UNIVERSITY OF BIRMINGHAM

Metallated Derivatives of Ammonia Borane with a view to their potential as Hydrogen Storage Materials

by

Ian C. Evans

Supervisor: Dr Paul A. Anderson

A thesis submitted to the University of Birmingham for the Degree of Doctor of Philosophy

The School of Chemistry

College of Engineering and Physical Sciences

The University of Birmingham

February 2011

Abstract

Ammonia borane, NH_3BH_3, has attracted growing interest in recent years in the field of hydrogen storage due to its high gravimetric hydrogen content. In this study the reaction of NH_3BH_3 with various metal hydrides was investigated. The reactions with hydrides of lithium and sodium required a molar ratio of 1:2 in favour of NH_3BH_3 and the reaction products were characterised as $[Li(NH_3)]^+[BH_3NH_2BH_3]^-$ and $[Na]^+[BH_3NH_2BH_3]^-$, respectively, through solid state ^{11}B and ^{23}Na MAS NMR and Raman spectroscopy. The reaction of CaH_2 with NH_3BH_3 required a reaction stoichiometry of 1:4 and this reaction proceeded through a different reaction mechanism, forming $Ca(BH_4)_2{\cdot}2NH_3$. The crystal structures of $Ca(BH_4)_2{\cdot}2NH_3$ and $Ca(BH_4)_2{\cdot}NH_3$ were determined by powder diffraction methods and the reaction pathway investigated through solid state ^{11}B MAS NMR spectroscopy.

The thermal desorption properties of these hydrogen rich materials were investigated and hydrogen was released from all the materials. However, under certain conditions ammonia was the major gaseous desorption product from $Ca(BH_4)_2{\cdot}2NH_3$ and was observed as a minor product from the decomposition of $[Li(NH_3)]^+[BH_3NH_2BH_3]^-$. Ammonia was also released during the synthesis of $[Na]^+[BH_3NH_2BH_3]^-$, but the decomposition of this material was free from ammonia release. Ramped thermal desorption studies of $[Na]^+[BH_3NH_2BH_3]^-$ and $[Li(NH_3)]^+[BH_3NH_2BH_3]^-$ to 350°C resulted in weight losses due to hydrogen desorption of 7.5 wt% and 12.5 wt%, respectively. Heating $Ca(BH_4)_2{\cdot}2NH_3$ to 350°C resulted in a total weight loss of 27.5 wt%, which was predominantly due to NH_3 desorption. Powder XRD and solid state ^{11}B MAS NMR spectroscopy were employed to identify the solid decomposition products and decomposition pathways were proposed. Metal borohydrides were identified in all cases as well as polymeric products possessing B–N chains.

Acknowledgements

Well the nightmare of writing a thesis has finally come to an end and for that I am exceptionally grateful. It has been a long and painful journey and I could not have got to the end without the support of so many people. Firstly, I would like to thank my supervisor, Paul, who has been eternally patient and helpful for the last few years as well as for our many football chats when we probably should have been discussing things a little more closely related to my PhD.

I'd like to thank the members of the Anderson group, past and present, for the last few years, with a special mention going to Dr Phil Chater for kindly synchronising his departure from the group with my submission day, as well as for all his help over the years with all things chemistry. Probably should mention the other group members to avoid an earful, so Alvaro, Matt, Alex, Dave, Tom C and Ivan, you have all been in the group. Thanks to the rest of Floor 5 for the fun and laughs while I've been there.

In Mat & Met Dan, Allan and Big Dave have been nice enough to let me use their equipment and help me out when things have not gone to plan. Tom Partridge at the University of Warwick is due a mention for the countless hours he spent collecting and interpreting NMR spectra, as well as John Hanna.

I am also thankful for having a fantastic set of mates, who I haven't really seen for the last 12 months, but that's about to change with some big nights out planned, starting today! So Bails, Evo, Jeff, Lairddog and Ugs, congratulations you have all made it in. And I have to mention the mighty Bournville Village and Village C football clubs for giving me a distraction from my thesis over the last year and keeping me sane. I'm sure some silverware is just around the corner!

Too many others to mention, but Nic, Ad and Deb are in for some brilliant times over the years.

Finally, and most importantly, thanks to my parents and grandparents, without their love and support I could never have achieved everything that I have in life.

Contents

Chapter 1

Introduction

1.1 The Current World Energy Situation

The world is currently heavily reliant on fossil fuels, with almost all mobile energy needs being met by petroleum, because they are a very convenient source of energy. However, with this source of energy rapidly running out, the need to find a replacement is becoming more critical. In pre-industrial times man used only biomass as an energy source, which had no effect on the atmosphere because carbon dioxide liberated from its combustion was offset by the absorption by plants during photosynthesis, producing a carbon neutral cycle. Since the industrial revolution world energy demand has drastically risen, with this increase mostly met by fossil fuels. The introduction of the steam engine provided the foundation for an industrialised society and a source of energy was needed in order to power it. This demand was met by coal. The use of fossil fuels led to an increase of the concentration of carbon dioxide in the atmosphere and because this is a greenhouse gas the burning of fossil fuels has been linked to global climate change. Alternatives to fossil fuels include biomass, nuclear, wind, solar, geothermal and hydrothermal energies. These energy sources may be especially useful in the production of electricity that is fed into the National Grid to be used in stationary applications. Their use in mobile applications is more challenging, which is where hydrogen may play an important role.

1.2 Hydrogen

Hydrogen offers potential to help provide a solution to the world's energy dilemma. Like electricity it is an energy carrier; however, electricity is at a disadvantage when

storage of energy is required. Hydrogen on the other hand could be suited to applications where storage of energy is required before use.

Figure 1.1 depicts how the nature of the world's main energy carrier has changed through history.

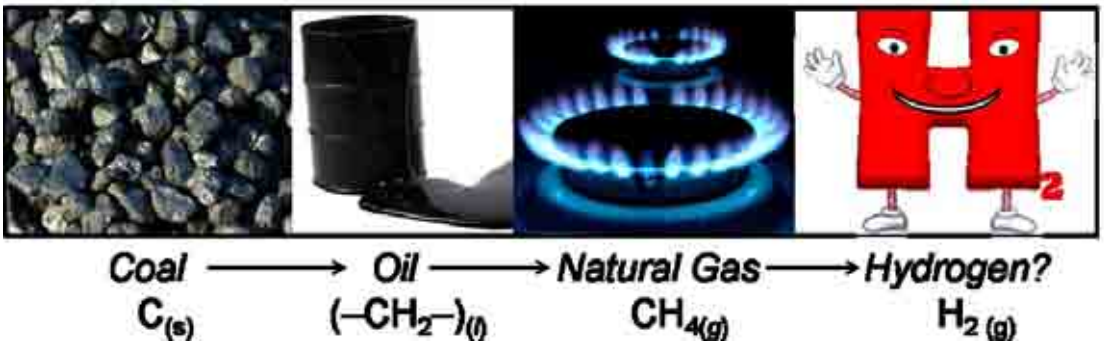

Figure 1.1 – Historical development of energy carriers

There are two trends that are observed in this progression. The first trend involves the physical state of the carrier, the transition from a solid to a liquid and then on to a gas state energy carrier is observed. Secondly, there is a trend towards using more hydrogen rich fuels. These two trends combined point in the direction of using pure hydrogen as an energy carrier in the future.

1.3 Hydrogen Production

Hydrogen is the most abundant element in the universe: it is estimated that 90% of all atoms are hydrogen which corresponds to 75% by mass of the universe. Further to this, it is thought that the heavier elements were and still are being made from hydrogen and helium. On Earth, hydrogen is also the most abundant element; however, only a small fraction, approximately one percent, exists as molecular hydrogen, the vast majority of it chemically bound in H_2O, with a further substantial amount bound in liquid or gaseous hydrocarbons. This means that the first step in using hydrogen as a fuel involves its production. In order to completely replace fossil fuels as the world's chief energy supplier, more than 3×10^{12} kg of hydrogen would need to be produced each year, which is approximately one hundred times greater than today's annual production.[1] The production of hydrogen adds extra cost to the use of hydrogen, which has not been experienced with fossil fuels. The only cost

involved with fossil fuels is that of the mining, which makes the cost of hydrogen fuel around three times greater than that of petroleum. This produces an economic challenge: to minimise the cost of hydrogen production as well as having to convince the world economy of the benefits of a synthetic fuel, as consumers must be willing to pay for the energy content of the fuel. An investment over five years, to the value of ten to one hundred trillion dollars, would be required to establish a new renewable energy production infrastructure, which is the same amount spent worldwide on energy over the same period.[1]

1.3.1 From Fossil Fuels

Currently hydrogen production in the world centres on fossil fuels and, specifically, the process of steam reforming as shown in reaction 1.1. In 2008, 96% of the world's hydrogen was produced using this process.[2] The hydrocarbon most frequently used for this reaction is methane. The process involves using high temperature steam, in the range 700 to 1000°C, in combination with a hydrocarbon to yield hydrogen and carbon monoxide. This is an endothermic reaction and hence consumes energy in the process.

$$-(CH_2)-_n + H_2O \rightarrow (n + 1)H_2 + CO \qquad \text{Reaction 1.1}$$

A second step, the water-gas shift reaction, reacts the synthesised carbon monoxide with steam to produce more hydrogen and carbon dioxide as shown in reaction 1.2.

$$CO + H_2O \rightarrow CO_2 + H_2 \qquad \text{Reaction 1.2}$$

Unfortunately, this method of production produces a significant amount of carbon dioxide emissions, in fact a similar amount to that of the direct combustion of fossil fuels. In the transition to a hydrogen economy, steam reforming would likely be the production method of choice during its infancy, with a predicted timescale of 20 years.[3] There are methods to reduce carbon dioxide emissions from steam reforming. The product gases are easily separated and carbon sequestration can be used to prevent carbon dioxide emissions to the atmosphere.

There is a second method of producing hydrogen from hydrocarbons that is free from carbon dioxide emissions. The thermal dissociation or cracking of hydrocarbons,

specifically methane, results in the production of hydrogen as well as carbon. The decomposition of methane is less endothermic than steam methane reforming: the energy required per mole of hydrogen produced is 37.8 kJ mol^{-1} H_2 for cracking compared with 63 kJ mol^{-1} H_2 for steam reforming. Carbon dioxide emissions can potentially be as low as 0.05 mol CO_2 / mol H_2 compared to 0.43 mol CO_2 / mol H_2 for the steam reforming process.[4] This process does, however, produce a vast amount of carbon and leaves the problem of how to dispose of it. Beneficially the product is solid, making it easily transported, handled and stored and one potential solution is to use it as a construction material.[5] The biggest drawback to this method though is it is again not sustainable as the resource employed is non-renewable.

1.3.2 Electrolysis

In order for hydrogen to be classified as a clean, sustainable and renewable fuel, its production must move away from fossil fuels, avoid the release of carbon dioxide into the atmosphere and utilise a renewable source of energy. One such possibility is that of water electrolysis. Electricity generated from renewable forms of energy including solar, wind and hydro can be used in this process. Electrolysis is simply the decomposition of water into oxygen and hydrogen, which makes it the cleanest way to produce hydrogen. An electric circuit is connected to two electrodes, made from inert metal, such as platinum, which are placed into the water. Two processes occur, reduction at the negatively charged cathode and oxidation at the positively charged anode, shown in reactions 1.3 and 1.4.

$$\text{Cathode}\quad 2H^+_{(aq)} + 2e^- \rightarrow H_{2(g)} \qquad \text{Reaction 1.3}$$

$$\text{Anode}\quad 2H_2O_{(l)} \rightarrow O_{2(g)} + 4H^+_{(aq)} + 4e^- \qquad \text{Reaction 1.4}$$

The process is thermodynamically unfavourable and so it is necessary to apply an electric potential. It is possible to increase the rate of electrolysis by adding an electrolyte to the water. The efficiency of electrolysis at ambient conditions is 65%, although improvements to the process including the use of activated electrodes and very thin membranes can help achieve increased efficiency to 85%.[6] Hydrogen produced in this way makes it sustainable in the long term as well as adding value to the renewable resources employed in the process.

1.3.3 Thermal Production

Hydrogen can also be produced directly from the thermal decomposition of water. This is, however, a very unfavourable process thermodynamically and requires temperatures in excess of 2000°C. This temperature can be lowered substantially to below 1000°C through the use of either a platinum or ruthenium catalyst. Following the thermal decomposition, the product gases must be separated to avoid recombination of the gases or the production of an explosive mixture. The advantage of this process is that it again uses a renewable source of energy in the form of sunlight. A solar furnace channels light energy from the sun onto a small area which achieves the very high temperatures required for the decomposition to proceed.[7]

1.3.4 Biomass

Biomass can be used to produce hydrogen in two ways. Firstly, through gasification; this is a process similar in nature to that of steam reforming. The biomass is thermally treated to yield a mixture of gases including hydrogen, carbon monoxide and methane. Further heat treatment through heated steam yields further hydrogen as well as carbon dioxide. However, as the carbon dioxide that is released as a result of this process was originally absorbed by the plant, this process can be regarded as carbon dioxide neutral. The process of fermentation can also be used to produce hydrogen through biomass. Hydrogen can be produced sustainably by anaerobic bacterial growth on carbohydrate rich substrates in the absence of light, to give organic fermentation end products, hydrogen and carbon dioxide. Sustainable hydrogen production in this way requires principally carbohydrate based organics, biomass produced from sustainable resources, biomass of sufficient concentration that fermentative conversion and energy recovery are energetically favourable, and biomass that requires minimal pre-treatment.[8] A significant advantage to this process is that biomass of low quality and low cost can be used. Again because the carbon dioxide released in the process was originally absorbed by the biomass it can be classed as a carbon dioxide neutral process.

1.4 Hydrogen as a Fuel

Chemical energy is related to valence electrons in atoms or molecules and their potential to form stable arrangements through reaction. The hydrogen atom is made up of only one proton and one electron making it an attractive chemical energy source as it has the highest number of valence electrons available for reaction per unit mass.

Following production, hydrogen is the cleanest burning fuel: the only exhaust gas when it is burnt with oxygen is water. Furthermore, hydrogen is a very energy rich fuel: its lower heating value, 120.1 MJ kg^{-1}, is three times greater than that of petroleum, 42.5 MJ kg^{-1}.[9] There are two methods of exploiting the chemical potential of hydrogen. First, as with petroleum, it can be combusted in an internal combustion engine producing mechanical power; or secondly, it can be used to produce electrical power by electrochemical means using a fuel cell.

Using hydrogen as a fuel also has the added benefits of dramatically cutting emissions of carbon dioxide, carbon monoxide and sulphur and nitrogen oxides. It has the potential to become a secure and abundant domestic supply of fuel, therefore significantly reducing the need to import other sources of energy such as oil or natural gas, in turn providing nations with energy independence and security. Finally, it would allow the transition from limited non-renewable supplies of fossil fuels to an unlimited, renewable fuel source.

1.4.1 Hydrogen Internal Combustion Engine

Internal combustion engines are a well established technology and the idea of using hydrogen as the fuel is not a modern one. The first internal combustion engine designed and built to run on a mixture of hydrogen and oxygen was built by François Isaac de Rivaz as early as 1807.[10] Hydrogen gas can be used directly in a petroleum internal combustion engine with only minor modifications required. The hydrogen is burnt in the same way as gasoline, the only difference being that hydrogen burns hotter than gasoline resulting in the need for minor modifications to the engine. The modifications include using fuel injectors designed for gas instead of liquid, harder valve and valve seats to compensate for the reduced lubricating properties of

hydrogen gas compared to liquid gasoline, and employing an exhaust system that is capable of sustaining water vapour produced from the combustion process.

Internal combustion engines running on hydrogen could pave the way for a transition to a Hydrogen Economy. The hydrogen internal combustion engine uses the current manufacturing infrastructure as well as allowing the opportunity to develop hydrogen infrastructure. A hydrogen internal combustion engine is currently much cheaper than a fuel cell running on hydrogen and therefore offers a cheaper temporary solution to using hydrogen as a fuel, until the cost of fuel cell technology starts to drop. A major advantage of using hydrogen instead of gasoline in an internal combustion engine is that the emissions of carbon dioxide are greatly reduced. A small amount of carbon dioxide is released when using hydrogen as the fuel, but this comes from engine oil in the cylinders of most engines and not from the fuel itself. It would require over 300 vehicles running on a hydrogen internal combustion engine to emit the same amount of carbon dioxide as one vehicle running on gasoline. However, there are relatively few car manufacturers that are actively researching a hydrogen internal combustion engine and of the major automotive manufacturers it is only BMW and Mazda that currently have an active research programme.

1.4.2 Fuel Cells

Fuel cells are emerging as a leading alternative technology to the more polluting internal combustion engine in both mobile and stationary applications. They are widely considered to be the green power source for the 21st century and could make the prospect of a Hydrogen Economy a reality.[11] However, they are not a recent invention, they were invented in 1839 by William Grove.[12] Fuel cells are electrochemical energy conversion devices which convert the chemical energy of the fuel, which is generally hydrogen, directly into electrical energy. There are numerous types of fuel cell, that are characterised by the type of electrolyte that is employed, the most common electrolytes being alkaline, solid oxide, molten carbonate, phosphoric acid and polymer membrane. Provided there is a constant source of fuel, fuel cells are capable of continuously producing energy.

Polymer electrolyte membrane fuel cells, PEMFC, also known as proton exchange membrane fuel cells have a number of advantages associated with their use. Primarily the only emission is water when using hydrogen as the fuel and oxygen as the oxidant. They are able to operate at temperatures below 100°C with high efficiency, which also results in them having rapid start-up times, making them attractive for use in mobile applications. Compared to other fuel cells, PEMFCs are capable of generating more power for a given weight or volume, making them compact and lightweight. A fuel cell stack, where many fuel cells are used in combination, is used in practice, allowing higher power densities to be achieved. The PEMFC uses a solid polymer membrane as the electrolyte which is permeable to protons when saturated with water but does not conduct electrons. Hydrogen gas is supplied to the anode, where a catalyst, usually platinum, splits it into protons and electrons. The protons permeate across the electrolyte to the cathode, while the electrons flow through an external circuit, producing electric power. Air, containing oxygen, flows past the cathode. At the cathode, oxygen combines with the electrons and the protons producing water. The reactions taking place are as follows and a schematic diagram of a PEMFC is shown in figure 1.2.

Anode	$2H_2 \rightarrow 4H^+ + 4e^-$	Reaction 1.5
Cathode	$O_2 + 4H^+ + 4e^- \rightarrow 2H_2O$	Reaction 1.6
Overall	$2H_2 + O_2 \rightarrow 2H_2O$	Reaction 1.7

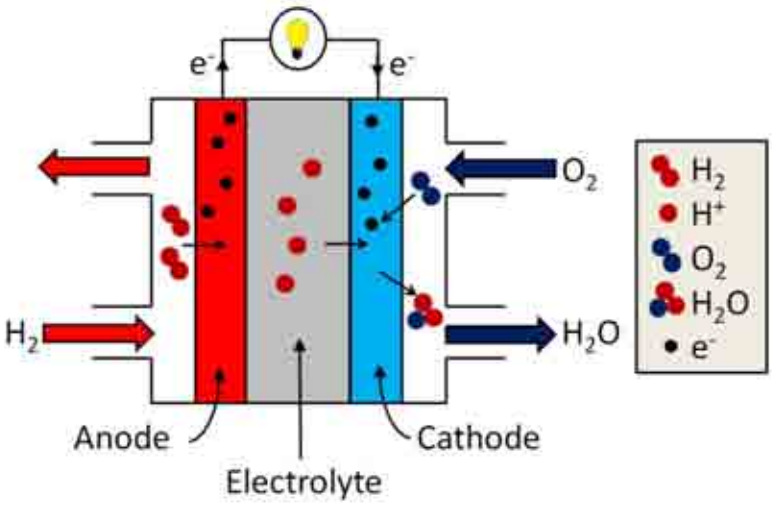

Figure 1.2 – A schematic diagram of a PEMFC[11]

PEMFCs suffer performance degradation as a result of impurities in the hydrogen supply such as carbon monoxide, hydrogen sulphide, ammonia and organic compounds, and also from NO_x and SO_x in air.[11] These contaminants can get into the membrane of the fuel cell, thereby competing with the protons for the SO_3^- sites and decreasing water content, resulting in a reduction in proton conductivity. Fuel cell performance has been shown to drop rapidly when exposed to a hydrogen supply containing 30 ppm ammonia, and could not be fully recovered after removal of the ammonia.[13]

1.5 Batteries

A different type of technology that has been proposed as a replacement for fossil fuels is that of batteries. Hydrogen has to be first produced, potentially through the process of electrolysis, before it is converted back into electrical energy in a fuel cell. As a result of these energy conversions, the efficiency of the fuel cell compared to directly using the electricity in batteries is lowered. In stationary applications, when using hydrogen and fuel cells, 51% of the electricity that could have been delivered directly remains following the conversions, whereas batteries are able to store and retrieve electricity with efficiencies greater than 75%.[14] In mobile applications it is estimated that by 2020 electric vehicles will have a range of 358 kilometres before a recharge is required. However, these recharges can take around four hours for a full recharge to be achieved. This is in contrast to fuel cells which are capable of running continuously provided there is sufficient fuel provided. Further to this the cost of lithium ion batteries is currently approximately three times too high for them to become a commercially viable alternative to internal combustion engine based vehicles. The development of alternative battery systems have shown particular improvements in recent years with respect to energy density, efficiency and cycling lifetimes, with an energy density of 125 W h / kg being achieved in lithium ion batteries offering a driving range of 250 kilometres.[15] A major advantage of using batteries is that the infrastructure for this technology is already in place, whereas there is the need for huge investment in order to use hydrogen as a fuel. In reality, it seems likely that fuel cell vehicles will use a combination of batteries and a fuel cell in order to meet the energy demands of automotive transport.[16]

1.6 Hydrogen Storage

At ambient temperature and pressure the hydrogen molecule exists as a gas, with a density of 0.0899 kg m^{-3}; below −262°C it exists as a solid with a much higher density of 76.3 kg m^{-3} and there is a small zone where the molecule is found in the liquid form with a density of 70.8 kg m^{-3} at −262°C.[1] The very low volumetric density of hydrogen gas shows the significant challenge of hydrogen storage. At ambient temperature and pressure 1 kg of hydrogen gas occupies a huge 11 m^3. On board energy storage in vehicles is required to be light, safe and affordable. A modern, commercially available car designed primarily for mobility has a range of 400 kilometres which burns 24 kilograms of petrol in a combustion engine.[17] In order to match this range, a combustion engine operating on hydrogen would require eight kilograms of fuel or an electric car running on fuel cells would require four kilograms of hydrogen. At room temperature and pressure, four kilograms of hydrogen occupies a volume of 45 m^3, which is not practical for a vehicle.

The term hydrogen storage essentially implies the reduction of this enormous volume of hydrogen gas. The goal is to pack hydrogen as closely as possible in order to achieve the highest possible volumetric density while minimising the amount of additional material. In order to achieve higher hydrogen densities either work must be applied to compress hydrogen or through liquefaction, both of which can be easily performed. However, both methods cause a reduction in gravimetric density due to the additional weight of the vessels required to maintain high pressures or low temperatures. A compromise must be made between increasing the volumetric capacity of the storage system while maintaining a usable gravimetric hydrogen capacity. An alternative approach is to minimise the repulsion between hydrogen molecules through the interaction with another material. Another important criterion for a hydrogen storage system is that it requires a reversible hydrogen uptake and release mechanism. This requirement means that all hydrocarbons are excluded as potential storage methods as the hydrogen can only be irreversibly released at temperatures above 800°C. There are a number of potential storage methods which can broadly be divided into two categories: either the storage of molecular hydrogen, which increases volumetric density through compression, liquefaction or adsorption

onto a surface, or the storage of atomic or ionic hydrogen through the reaction of hydrogen gas to form metal hydrides or complex hydrides.

1.6.1 Storing hydrogen as a gas

Conventionally hydrogen is stored at high pressures. High pressure tanks are traditionally made of relatively cheap steel and are routinely filled up to a pressure of 200 bar. However, this pressure would still require a total volume of 225 litres to store the 4 kilograms of hydrogen.[17] Furthermore, this equates to a gravimetric density of only about 1%, which is very low. New lightweight composite cylinders have been developed which are capable of withstanding pressures up to 800 bar, which results in a volumetric density of 36 kg m^{-3}.[18] However, as the storage pressure increases, the gravimetric hydrogen density decreases, because the walls of the pressure cylinder must increase in thickness to be able to cope with the increased pressure. The ideal material for a high pressure cylinder requires a high tensile strength, low density and to be inert towards hydrogen, with the majority of cylinders being made from stainless steel, copper or aluminium alloys. Recently light-weight high-density carbon fibre gas cylinders have been developed, which are capable of storing hydrogen up to pressures of 1000 bar, giving a gravimetric hydrogen density of 10 wt%.[19] These high pressure gas cylinders come with significant disadvantages. Additional pressure control would be required due to the large pressure drop when the fuel is made available, there is a high safety risk associated with having high pressure gas in automobiles and they are costly. A large amount of physical work is also required to be done on the gas with respect to compression in order to achieve the high pressures, which is energy that cannot be reclaimed when using the gas.[20] Industry has set itself a target of developing cylinders capable of storing hydrogen at a pressure of 700 bar, with a maximum weight of 110 kg, a gravimetric density of 6 wt% and a volumetric density of 30 kg m^{-3}.[21] However, this storage method looks unlikely to be adopted due to the low hydrogen density, safety concerns and high cost associated with it.

1.6.2 Liquid hydrogen storage

The storage of hydrogen as a cryogenic liquid has a high gravimetric density of 70.8 kg m^{-3} which is significantly higher than that of compressed gas.[18] Liquid hydrogen is stored in cryogenic tanks at temperatures below −252°C. These storage tanks have to be open systems due to problems with boil off, because the pressure in a closed system could rise to 10^4 bar. There are two main challenges associated with liquid hydrogen storage. Firstly, the energy-intensive liquefaction process, which has a significant energy penalty, because up to 30% of the energy content of hydrogen is required to liquefy it.[19] The second challenge is the thermal insulation of the cryogenic storage vessel in order to minimise the boil off of hydrogen. Even with the best available insulation vessels, boil off cannot be reduced below 1% per day for small tanks suitable for transportation usage. Further costs are also incurred because all of the components used for the delivery and storage of liquid hydrogen must be cooled. Due to these drawbacks, liquefaction is not a particularly efficient method of hydrogen storage. The high cost, large amount of energy required for liquefaction and the continuous boil off of hydrogen mean that this storage method is limited to applications where cost is not an important issue and the hydrogen is consumed in a relatively short time such as with air and space applications.

1.6.3 Solid state hydrogen storage

As the two conventional methods of hydrogen storage, compression and liquefaction, seem to be unlikely to be able to provide a solution to the problem, the most viable alternative, solid state hydrogen storage, could provide the answer. A suitable solid state hydrogen storage material should be able to store a high weight percent and high volume density of hydrogen, while being able to absorb and desorb hydrogen quickly close to room temperature and pressure. Furthermore, the material should be cheap, safe and reusable, and possess the capacity to be regenerated and readily recycled. Currently, there is no material that can meet all of these requirements.

Hydrogen can interact with the host material in a number of ways. Firstly, hydrogen molecules can be physically adsorbed onto the surface of the host material. The hydrogen can be chemically absorbed by the material through the formation of

chemical bonds. Finally, chemical hydrides can be formed which are characterised by distinct chemical covalent bonding.

1.6.4 Physisorption

Hydrogen is capable of being adsorbed onto a solid surface through van der Waals interactions. Physisorption is the weakest interaction between a solid and hydrogen, the energy of the interactions is generally very low, in the range 2 to 20 kJ mol^{-1} H_2.[1] As a consequence of this the majority of hydrogen can be desorbed from the surface by thermal energy at room temperature and as such significant physisorption is only observed at temperatures below 273 K. Liquid nitrogen, with a boiling point of 77 K, is often used as a coolant in order to maximise the physisorption interaction. The strongest binding of hydrogen occurs when the hydrogen is bound directly to the surface of the solid and although subsequent layers of hydrogen can be formed, the weakness of these interactions means that hydrogen molecules usually form a monolayer on the surface. Therefore, materials with very high surface areas are required for this type of hydrogen storage system in order to reach a desirable hydrogen storage capacity.

A number of types of high surface area solids have been studied including zeolites,[22] high surface area carbon,[23] metal organic frameworks (MOFs)[24] and polymers of intrinsic microporosity (PIMs).[25] Single walled carbon nanotubes have been shown to take up 2 wt% hydrogen at 77 K, with a high surface area of 1315 m^2 g^{-1}.[23] A zeolite-like carbon material was shown to exhibit improved and reversible hydrogen storage capacity showing an uptake of 6.9 wt% at 77 K and 20 bar.[26] At 1 bar the uptake was reduced to 2.6 wt%. The strength of hydrogen binding in zeolites has the potential to be improved by the inclusion of metal ions in the structure. Calcium exchanged zeolite X has been shown to take up 2.19 wt% hydrogen at 77 K and 15 bar.[22] This is an improvement compared to zeolites that do not contain metal cations, where about 1.5 wt% hydrogen can be absorbed under the same conditions.[27] Gravimetric capacities of 6.7 wt% have also been reported for MOFs where the binding to metal centres is suggested to improve the hydrogen storage capacity.[24] PIMs are polymers which behave like molecular sieves in the solid state, because they have rigid, contorted molecular structures that are unable to pack efficiently, which gives them

potential as hydrogen storage materials.[28] They have been shown to take up 2.7 wt% at 77 K and 10 bar.[25] Physisorption for hydrogen storage has the advantages of having relatively cheap materials and the storage systems are of a simple design. However, they suffer from relatively low gravimetric and volumetric densities and the low temperatures (and/or high pressures) required are significant drawbacks to their use.

1.6.5 Metallic Hydrides

A number of metals and alloys are capable of reversibly reacting with hydrogen to produce metal hydrides. The transition back to the metal can be achieved through either increasing the temperature or by reducing the pressure. Metals of group I and group II of the periodic table usually form stoichiometric ionic hydrides, such as LiH, whereas transition metals tend to form hydrides which have a variable non-stoichiometric composition, as is the case with $PdH_{0.6}$.[29] These non-stoichiometric hydrides form when hydrogen gas is dissociated at the metal surface and diffuses into the metal. During the desorption process, two hydrogen atoms recombine to form the hydrogen molecule. The lattice structure of non-stoichiometric hydrides is that of a typical metal with hydrogen atoms on the interstitial sites and hence they are also known as interstitial hydrides.

The formation of an interstitial hydride can be described in terms of a pressure-composition isotherm, as shown in figure 1.3.[1] Initially the host metal dissolves some hydrogen in low concentrations forming a solid solution, shown as the *α*-phase in figure 1.3. Increasing the pressure results in the concentration of hydrogen within the metal increasing and nucleation and growth of the ordered hydride *β*-phase begins. A plateau is observed where the two phases co-exist. During this plateau region, the composition of the metal hydride can be changed significantly with only small changes in temperature or pressure. This plateau region ends once a certain temperature, denoted Tc in figure 1.3, is reached. Above this temperature the transition from the *α* to the *β* phase is continuous.

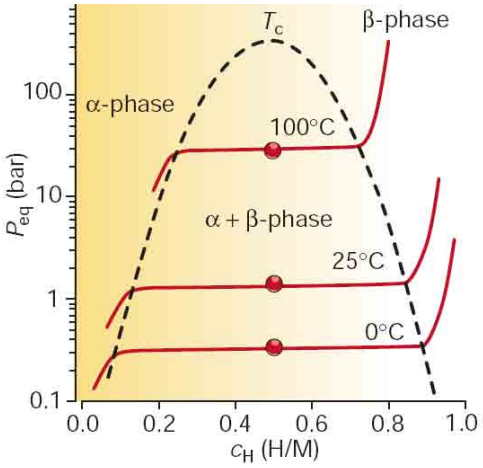

Figure 1.3 – A pressure–composition–temperature plot for a metal hydride[17]

Metal hydrides are very effective for storing hydrogen in a safe and compact way, capable of achieving very high volumetric hydrogen densities. $LaNi_5H_{6.5}$ for example has a high volumetric hydrogen density of 115 kg m^{-3}.[18] However, as the reversible hydrides usually consist of transition and/or rare earth metals, gravimetric densities are unable to reach more than about 3 wt%. There are several families of intermetallic compounds of interest to hydrogen storage which are summarised in table 1.1. These compounds consist of an A element, which is usually a rare earth or alkaline earth metal, with a high affinity to hydrogen, forming stable hydrides and a B element, generally a transition metal, which has a low affinity to hydrogen, forming unstable hydrides. The B element is often nickel as this is an excellent catalyst for hydrogen dissociation.

Table 1.1 – The families of hydride forming intermetallic compounds[17]

Type	Metal	Hydride	wt% H
Elemental	Pd	$PdH_{0.6}$	0.56
AB	FeTi	$FeTiH_2$	1.9
AB_2	ZrV_2	$ZrV_2H_{5.5}$	3
AB_3	$CeNi_3$	$CeNi_3H_4$	1.3
AB_5	$LaNi_5$	$LaNi_5H_{6.5}$	1.5
A_2B	Mg_2Ni	Mg_2NiH_4	3.6
A_2B_7	Y_2Ni_7	$Y_2Ni_7H_3$	0.5

The hydride of $LaNi_5$ shows some promising hydrogen storage properties, including fast and reversible hydrogen uptake, as well as being able to release all of its hydrogen at a pressure of less than 2 bar. However, lanthanum and nickel are both heavy elements, which means that only 1.5 wt% can be stored in the alloy. Higher hydrogen contents are obtainable through the use of light elements. Magnesium forms a hydride containing 7.7 wt% hydrogen; however, it suffers from very slow rates of de/rehydrogenation and releases hydrogen at temperatures in excess of 300°C.[30] The characteristics of hydrogen absorption and desorption can be modified by partial substitution of the constituent elements in the host lattice. For example, attempts to improve the hydrogen storage properties of MgH_2 have been made by alloying magnesium with nickel before hydriding, resulting in a hydride of 3.6 wt%, Mg_2NiH_4.[31] The rate of hydriding is improved, potentially due to nickel acting as a catalyst for the dissociation of hydrogen gas, but temperatures in excess of 280°C are still required for hydrogen release.[17] This temperature can be decreased further through mechanical alloying with transition metals.[32] Most metallic hydrides absorb hydrogen up to a metal to hydrogen ratio of two. Greater ratios are possible, as is the case with $BaReH_9$, containing a ratio of 4.5.[33]

1.6.6 Complex Hydrides

Light metals such as lithium, sodium and aluminium give rise to a large variety of metal-hydrogen complexes. They are amongst the most promising candidates for hydrogen storage due to their lightweight and the number of hydrogen atoms per metal atoms, which in many cases is two. The term complex hydride is generally given to materials where hydrogen is covalently bonded to a central atom in a complex anion.[34] These ionic hydrides include borohydrides, BH_4^-, alanates, AlH_4^- and amides, NH_2^-, where the negative charge of the anion is compensated by a cation of a light metal. They have some of the highest known gravimetric hydrogen densities, with lithium borohydride, $LiBH_4$, having a capacity of 18.5 wt%. However, the stability of the compounds can be problematic, as they decompose at elevated temperatures, often above the compound's melting point.

1.6.6.1 Alanates

The aluminium hydrides (alanates) of sodium and lithium can be synthesised either directly from reaction of the constituent elements or through the reaction of the metal hydride with aluminium halides in solution.[35] Both of these alanates have high gravimetric hydrogen contents, with lithium alanate containing 10.5 wt% and sodium alanate possessing 7.4 wt%. The compounds decompose through the release of hydrogen in a two step process, shown by reaction 1.8, lithium alanate decomposing at a slightly lower temperature of 201°C compared to 265°C for sodium alanate. The reverse reaction for the sodium system has been shown to proceed at 270°C under a hydrogen pressure of 175 bar.[34]

$$3MAlH_4 \rightarrow M_3AlH_6 + 2Al + 3H_2 \rightarrow 3MH + 3Al + 9/2H_2 \qquad \text{Reaction 1.8}$$

The practical use of alanates as materials for hydrogen storage was limited due to high kinetic barriers both towards hydrogenation and the reverse reaction. The kinetics of both uptake and release of hydrogen in sodium alanate have been shown to be dramatically improved through doping with titanium.[36] This allows hydrogen to be released from the material at 150°C, while the reversible reaction could proceed at a temperature as low as 170°C under 152 bar H_2. However, this was achieved at a cost of the hydrogen capacity of the material, this being reduced from an initial value of 5.6 wt% down to 3.1 wt% after thirty one cycles.

1.6.6.2 Borohydrides

Borohydrides were first synthesised as early as 1940 through the reaction of ethyllithium with diborane.[37] An alternative synthesis involves the reaction of metal hydride with diborane in ethereal solvents,[38] and direct synthesis from the metal, boron and hydrogen is also possible at elevated temperature and hydrogen pressure. Borohydrides have been widely used in organic synthesis as reducing agents, however, their potential as hydrogen storage materials has recently been investigated.[39, 40]

Lithium borohydride has a very high gravimetric hydrogen density of 18.5 wt% and therefore offers potential as a hydrogen storage material. The decomposition of

lithium borohydride begins at 280°C, which is accompanied by the melting of the material. Only a small amount of hydrogen is released at this temperature, with the main evolution of hydrogen occurring at a temperature in excess of 380°C.[39] During this process three of the four hydrogen atoms are released, leaving lithium hydride and boron, giving a theoretical hydrogen capacity of 13.9 wt%. The decomposition of lithium borohydride is shown in reaction 1.9.

$$2LiBH_4 \rightarrow 2LiH + 2B + 3H_2 \qquad \text{Reaction 1.9}$$

This desorption process can be catalysed by adding SiO_2, significantly lowering the onset temperature of hydrogen release.[39] The reverse rehydrogenation process has been shown to proceed at 600°C under a hydrogen pressure of 350 bar.[41] Following rehydrogenation the amount of hydrogen that can then be reversibly released has been shown to be 8.3 wt%.[42]

The decomposition of $LiBH_4$ can be modified by reaction with MgH_2, the alternative decomposition pathway shown in reaction 1.10.[43] The presence of MgH_2 improves the thermodynamics of both the hydrogenation and dehydrogenation pathways, while still maintaining a high gravimetric hydrogen density of 11.4 wt%.

$$LiBH_4 + ½MgH_2 \leftrightarrow LiH + MgB_2 + 2H_2 \qquad \text{Reaction 1.10}$$

The formation of MgB_2 stabilises the dehydrogenated state, consequently effectively destabilising the $LiBH_4$. Dehydrogenation begins from 270°C in a stepwise process, with a total of 8 wt% released by 450°C. Hydrogenation can be achieved to a value of 10 wt% at 400°C under a pressure of 24 bar.

The desorption of $NaBH_4$, which contains 10.7 wt% hydrogen, has also been investigated.[40] The compound undergoes dehydrogenation through a multi-step process, beginning at a temperature as low as 150°C, although there is only a relatively small release of hydrogen at this temperature, the main releases of hydrogen occur above the melting point of the material, 505°C, giving a total hydrogen release of 10.4 wt%, accounting for nearly all of the hydrogen in the initial material. Therefore, the decomposition of $NaBH_4$ differs slightly to that of $LiBH_4$, shown in reaction 1.11.

$$NaBH_4 \rightarrow Na + B + 2H_2 \qquad \text{Reaction 1.11}$$

This difference is most likely due to the lower decomposition temperature of NaH compared to LiH rather than any alternative decomposition pathway taking place. The equivalent reverse reaction of reaction 1.9 has been demonstrated for sodium hydride as well as calcium hydride.[44]

1.6.6.3 Amides

Alkali metal amides can be formed through the reaction of the molten metal with ammonia, through catalysing a metal–ammonia solution with Fe_2O_3 or by reaction of metal hydride with ammonia.[45] The thermal decomposition of lithium amide proceeds through the release of ammonia gas, forming lithium imide, shown in reaction 1.12, and hence, from this point of view, the potential of lithium amide as a hydrogen storage material is limited.[46]

$$2LiNH_2 \rightarrow Li_2NH + NH_3 \qquad \text{Reaction 1.12}$$

A breakthrough in amide hydrogen storage chemistry came in 2002, when Chen *et al.*[47] showed that lithium nitride, Li_3N, is capable of absorbing 9.3 wt% hydrogen at moderate temperature and pressure. This absorption was shown to be a two step process represented by reaction 1.13.

$$Li_3N + 2H_2 \leftrightarrow Li_2NH + LiH + H_2 \leftrightarrow LiNH_2 + 2LiH \qquad \text{Reaction 1.13}$$

Both steps of the reaction have been shown to be reversible, with a theoretical hydrogen capacity of 10.4 wt%. Furthermore, the reactions of $LiNH_2$ with LiH and Li_2NH with LiH were shown to release hydrogen, with only trace amounts of ammonia detected. However, the kinetics of the first step have been shown to be poor, with a very slow uptake of hydrogen and the Li_2NH and LiH reaction was shown to only release hydrogen above 320°C in a vacuum.[47] It is the amide–imide step that offers the most potential for hydrogen storage. This step has favourable thermodynamics and a reversible hydrogen capacity of 6.5 wt%, and as a result has been the subject of intensive research. The reaction mechanism has been investigated by isotopic exchange which led to the conclusion that the hydrogen release mechanism involved the combination of positively charged hydrogens present in $LiNH_2$ combining with the

negatively charged ones in LiH.[48] The effect of catalysis on the reaction has been investigated, with $TiCl_3$ shown to decrease the onset temperature of hydrogen release.[49] Ichikawa *et al.*[50] investigated the mechanism of hydrogen release and concluded that it occurs through two steps. Firstly, $LiNH_2$ decomposes to release ammonia, which in the second step rapidly reacts with the LiH present, producing Li_2NH and hydrogen. The lithium hydride acts as a 'scavenger' for ammonia and the reaction is so rapid that no ammonia release is detected. David *et al.*[51] used structural refinement of X-ray diffraction data to show that the mechanism of transformation between $LiNH_2$ and Li_2NH during hydrogen cycling involves a bulk reversible reaction that occurs in a non-stoichiometric manner within the cubic anti-fluorite-like Li–N–H structure. Variable stoichiometry was observed in this cubic structure, which suggested that the mechanism of absorption and desorption of hydrogen involves mobility of Li^+ and H^+. NH_3 in this mechanism is formed as a result of Li^+ migration to an adjacent, vacant, tetrahedral or octahedral site, resulting in unstable, charged species. Charge balance can be restored by the expulsion of a proton, leading to NH_3 formation, which when released reacts with LiH, releasing H_2. The hydrogenation mechanism involves surface migratory Li^+, which interacts with H_2, forming LiH and protonic hydrogen. The H^+ subsequently bonds with NH^{2-}, forming NH_2^- and ultimately $LiNH_2$.

The decomposition of $Mg(NH_2)_2$ has also been investigated and was shown to proceed by the release of ammonia.[52] Adding MgH_2 failed to inhibit the release of ammonia, whereas the presence of LiH resulted in only hydrogen being released. This is due to the reaction of MgH_2 with NH_3 being a slow reaction in the order of one day, whereas LiH and ammonia react in an ultrafast reaction in less than 25 ms.[53] Mixed metal amide–hydride systems have been the subject of research, with Li–Ca, and Li–Mg systems being proposed.[54] On substituting MgH_2 for LiH_2 in reaction 1.13, it was found that the onset temperature of hydrogen release was decreased and on dehydrogenation a mixed Li–Mg imide formed. The reaction was demonstrated to be reversible at 200°C and a hydrogen pressure of 32 bar. Further investigations showed that the hydrogenation reaction produced lithium hydride and magnesium amide in preference to the starting materials of lithium amide and magnesium hydride, shown by reaction 1.14.[54-56]

$$2LiNH_2 + MgH_2 \rightarrow Li_2Mg(NH)_2 + 2H_2 \leftrightarrow Mg(NH_2)_2 + 2LiH \qquad \text{Reaction 1.14}$$

Studies that started by looking at the magnesium amide and lithium hydride system settle on a 3:8 optimum molar ratio of the materials, with a reversible hydrogen content of 7 wt%. The hydrogenation reaction proceeds at 200°C under a pressure of 30 bar, with dehydrogenation proceeding at 170°C. Interestingly both dehydrogenation and hydrogenation mechanisms have been thought to rely on ammonia, although no ammonia release is actually detected, while there is no mention of a mixed Li–Mg imide due to the lower temperatures employed. The dehydrogenation reactions are shown by reactions 1.14a–c, rehydrogenation by reactions 1.15a–c, with the overall reaction shown in reaction 1.16.

$$3Mg(NH_2)_2 \rightarrow 3MgNH + 3NH_3 \rightarrow Mg_3N_2 + NH_3 \qquad \text{Reaction 1.14a}$$

$$4NH_3 + 4LiH \rightarrow 4LiNH_2 + 4H_2 \qquad \text{Reaction 1.14b}$$

$$4LiNH_2 \rightarrow 2Li_2NH + 2NH_3 \qquad \text{Reaction 1.14c}$$

$$4Li_2NH + 4H_2 \rightarrow 4LiH + 4LiNH_2 \qquad \text{Reaction 1.15a}$$

$$4LiNH_2 \rightarrow 2Li_2NH + 2NH_3 \qquad \text{Reaction 1.15b}$$

$$2NH_3 + \tfrac{1}{2}Mg_3N_2 \rightarrow \tfrac{3}{2}Mg(NH_2)_2 \qquad \text{Reaction 1.15c}$$

$$3Mg(NH_2)_2 + 8LiH \leftrightarrow Mg_3N_2 + 4Li_2NH + 8H_2 \qquad \text{Reaction 1.16}$$

The equivalent Li–Ca system forms a mixed Li–Ca imide at 300°C starting with either metal amide.[57] However, on rehydriding the mixed imide always results in $Ca(NH_2)_2$ and LiH. There is a significant hydrogen release, approaching the theoretical hydrogen capacity of 4.5 wt%, up to 200°C, although as with the Li–Mg example, this does not result in the mixed imide forming, rather the individual calcium and lithium imides.[58] The system is partly reversible at 180°C and 30 bar hydrogen pressure, shown in reaction 1.17.

$$2LiNH_2 + CaH_2 \rightarrow Li_2NH + CaNH + 2H_2 \rightarrow Li_2Ca(NH)_2 + 2H_2 \leftrightarrow Ca(NH_2)_2 + 2LiH \qquad \text{Reaction 1.17}$$

1.6.6.4 Mixed Amide Borohydrides

Reactions of metal amides and borohydrides have proven to produce new materials with potential for hydrogen storage. In the case of lithium, a 3:1 mixture of amide to borohydride forms a compound of ideal stoichiometry $Li_4BN_3H_{10}$.[59, 60] Structural investigations showed that both the NH_2 and BH_4 groups remained intact in the new mixed structure and so the compound should be regarded as $Li_4BH_4(NH_2)_3$. This material has a high hydrogen content of 11 wt% and decomposes through the release of hydrogen from 260°C.[59] This shows improvements over the hydrogen storage properties of both amides, as hydrogen release is preferential to ammonia, and borohydrides, as there is a lower onset temperature of hydrogen release. The preferential release of hydrogen has been suggested to be as a result of the presence of $H^{\delta+}$ in the amide group and $H^{\delta-}$ in the borohydride analogous to the LiH–$LiNH_2$ system. However, this system lacks reversibility, as the ultimate decomposition product is lithium boron nitride, Li_3BN_2, which is thermodynamically very stable. Other mixed amide borohydride compounds have been reported, with $Li_2BH_4NH_2$ containing a high hydrogen content of 13.5 wt% and $Na_2BH_4NH_2$, which releases hydrogen from 290°C although this is accompanied by a small amount of ammonia release.[61, 62] The quaternary hydride $Li_3BN_2H_8$, contains 11.9 wt% hydrogen, of which approximately 10 wt% can be released from 250°C, with a small amount of ammonia release also observed.[63]

1.6.7 Hydrogen Storage Targets

The greatest challenge facing hydrogen storage is where hydrogen is to be used in mobile applications. The United States Department of Energy have outlined a series of criteria that a hydrogen store should meet in order to find practical use in mobile applications.[64] The storage system should allow for a driving range of greater than 300 miles while also meeting packaging, cost, safety and performance requirements to be competitive with comparable vehicles already in the market place. The original targets set out by the US Department of Energy were intended to show how hydrogen could compete with petrol. However, these targets have since been shown to be very optimistic and have recently been adjusted to make them more realistic as

well as due to knowledge gained from hydrogen-fuelled vehicles produced since the release of the original targets. The current target for the gravimetric capacity of a hydrogen storage system is 5.5 wt%, to be achieved by the year 2015, with the ultimate goal of increasing this to 7.5 wt%. Some of the targets set out for a hydrogen storage system are shown in table 1.2.

Table 1.2 – Technical targets for an onboard hydrogen storage systems

Storage Parameter	2015 target	Ultimate target
System gravimetric capacity	5.5 wt%	7.5 wt%
System volumetric capacity	0.04 kg H_2 / L	0.07 kg H_2 / L
Min / Max delivery temperature	−40 / 85°C	−40 / 85°C
Operational cycle life	1500	1500
Delivery pressure	5 bar – Fuel Cell 35 bar – ICE	3 bar – Fuel Cell 35 bar – ICE
System fill time (5 kg H_2)	3.3 minutes	2.5 minutes

On top of the requirements detailed above, the system must also be completely and rapidly reversible as well as meet standards related to toxicity and safety. A further important requirement from a commercial point of view is that the hydrogen storage system is of low enough cost that it will be accepted into the marketplace.

It is important to note that the criteria are not specific to the hydrogen storage medium, but rather the hydrogen system as a whole. This includes the balance-of-plant components, the general term for all other components that are required for a hydrogen storage system to be used in conjunction with either a fuel cell or an ICE. Components such as pressure regulators, the storage tank and heat exchangers are all included in the storage system. Therefore, any hydrogen storage material must exceed the gravimetric and volumetric capacity targets so that the system as a whole is able to meet them.

There is also an important point to note in the case of chemical hydrides as materials for hydrogen storage. The gravimetric storage capacity of this system should be quoted from the hydrogen releasing reaction and not from the total hydrogen content of the material. It is often difficult to release the total hydrogen content of a material at moderate temperatures. An example of this being lithium borohydride, a compound that contains a total hydrogen content of 18.5 wt%. However, most of this hydrogen is released at elevated temperatures and as lithium hydride is one of the decomposition products, the amount of hydrogen actually released is reduced from this value until even higher temperatures are reached.

1.6.8 Thermodynamics of Hydrogen Storage

The relationship between the thermodynamic properties of a hydride and its hydrogen storage properties has been discussed in detail.[65] The behaviour of a hydride can be predicted from the decomposition reaction of a metal hydride, equation 1.1 and the related thermodynamic parameters, equation 1.2.

$$MH_n \rightarrow M + \tfrac{n}{2} H_{2(g)} \qquad \text{Equation 1.1}$$

$$\Delta G^{\circ}_{dec} = \Delta H^{\circ}_{dec} - T\Delta S^{\circ}_{dec} \qquad \text{Equation 1.2}$$

ΔH°_{dec} is equal to the negative of the standard enthalpy of formation of the hydride, ΔH°_{f}. The entropy change is primarily due to the evolution of molecular hydrogen gas, which is the entropy change on changing from hydrogen in an ordered solid to a disordered gas, $\Delta S^{\circ}_{dec} \approx S(H_2)^{\circ} = 130.7$ J mol^{-1} K^{-1}. In order for thermal decomposition of the hydride to proceed, the entropy contribution must overcome the enthalpy contribution. At a certain temperature, the formal decomposition temperature of the hydride, T_{dec}, the standard Gibbs enthalpy of the decomposition reaction, ΔG°_{dec}, drops below zero. At $\Delta G = 0$, the following is true for the thermal decomposition to proceed:

$$0 = \Delta H^{\circ}_{dec} - (\tfrac{n}{2}) T_{dec} S(H_2)^{\circ} \qquad \text{Equation 1.3}$$

From this the formal decomposition temperature can be shown to be:

$$T_{dec} = \left(\frac{\Delta H^{\circ}_{dec}}{n}\right)\left(\frac{2}{S(H_2)^{o}}\right) \text{K}$$

Equation 1.4

$\left(\Delta H^{\circ}_{dec} / n\right)$ is the negative enthalpy of formation of the hydride per hydrogen atom stored. Therefore, it can be shown that in order to reach an equilibrium pressure of 1 bar at room temperature, 27°C, the ideal standard enthalpy of hydride formation for each hydrogen atom stored is calculated to be 19.6 $kJmol_H^{-1}$. This value is a useful estimate in determining the potential reversibility of a hydrogen storage system, with the hydrogen releasing reaction ideally to be endothermic, so as to allow rehydriding to be thermodynamically favourable. However, this does not entirely rule out systems that do not meet this criterion. There is the possibility for systems that are irreversible under moderate pressure to become reversible as the pressure increases. Aside from the thermodynamics of the reaction, kinetics also play an important role in determining whether a storage system has potential. The kinetics must be sufficiently rapid to allow hydrogen to be supplied at a suitable rate to the fuel cell or ICE as well as allowing the system to meet recharging time targets. However, the kinetics of a reaction are not easily predicted.

1.7 Ammonia borane

1.7.1 Synthesis

Ammonia borane has recently attracted a growing amount of interest in the field of hydrogen storage.[66, 67] This is largely due to its high gravimetric hydrogen content of 19.6 wt% and its high volumetric content of 0.145 kg L^{-1}. Furthermore, it exists as a stable white solid at room temperature and pressure and it is non-flammable, non-toxic and non-explosive. The compound was first discovered in 1955 by Shore,[68] albeit through a stroke of luck. Previous work attempting to synthesise ammonia borane had proved unsuccessful. The reactions of Lewis acids with diborane had been well investigated, the products being monomeric donor-acceptor adducts; some examples are shown in reactions 1.18 and 1.19.[69]

$$B_2H_6 + 2CO \rightarrow 2BH_3CO \qquad \text{Reaction 1.18}$$

$$B_2H_6 + 2(CH_3)_3N \rightarrow 2(CH_3)_3NBH_3 \qquad \text{Reaction 1.19}$$

However, when the Lewis base was NH_3, it was shown that NH_3BH_3 was not synthesised and the reaction proceeded through a different reaction pathway, synthesising a compound represented by the empirical formula $B_2H_6.2NH_3$, which became known as the diammoniate of diborane, DADB.[70] The structure of this new compound provided much speculation in the 1940s and early 1950s with three distinct possibilities suggested. Firstly a structure containing an ammonium cation, I, was proposed by Schlesinger.[71] This structure was widely accepted until the discovery of the borohydride ion[37, 72, 73] which led to a second borohydride anion containing structure, II, becoming conceivable.[74] The final possibility discussed in the literature was that of a structure containing both an ammonium cation and a borohydride anion separated by an aminoborane, III.[75]

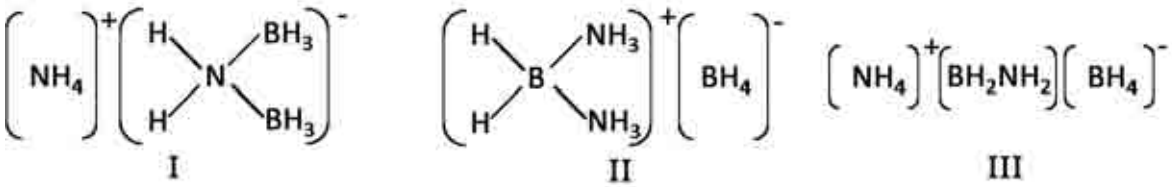

Finally, in the 1950s a series of papers were published by Parry and Shore[76-79] that proved that the structure of DADB involved an N–B–N chain and a borohydride anion, structure II shown above. One of the key steps in confirming this structure was looking at how DADB reacted with ammonium and borohydride salts. DADB was found to be unreactive towards borohydride salts, but did react with ammonium salts.[76] The steps in the reaction with ammonium bromide are shown in reaction 1.20 and the overall reaction in 1.21.

$$NH_4Br + DADB \rightarrow NH_4BH_4 + [NH_3BH_2NH_3]^+[Br]^- \qquad \text{Reaction 1.20a}$$

$$2NH_4BH_4 \rightarrow DADB + 2H_2 \qquad \text{Reaction 1.20b}$$

$$DADB + 2NH_4Br \rightarrow 2[NH_3BH_2NH_3]^+[Br]^- + 2H_2 \qquad \text{Reaction 1.21}$$

Shore[79] attempted to improve the synthesis of the halide salts and attempted a one step reaction using ether as a solvent and ammonium chloride, expecting to synthesise the chloride analogue of the product shown in reaction 1.21. In fact the reaction proceeded differently and resulted in the synthesis of the previously unobtained ammonia borane, NH_3BH_3, as shown in reaction 1.22.

$$DADB + NH_4Cl \xrightarrow[\text{Trace } NH_3]{\text{Ether}}{\text{Room Temperature}} H_3NBH_3 + [NH_3BH_2NH_3]^+[Cl]^- + H_2$$

Reaction 1.22

Subsequently it was proven that ammonia borane could be synthesised directly through the reaction of ammonium chloride and lithium borohydride as shown by reaction 1.23.[80]

$$LiBH_4 + NH_4Cl \xrightarrow[\text{Trace } NH_3]{\text{Ether}}{\text{Room Temperature}} H_3NBH_3 + LiCl + H_2$$

Reaction 1.23

As a result of this success the metathesis reaction in organic solvents has become one of the most widely used synthetic procedures to prepare ammonia borane. The reaction shown in reaction 1.23 produces ammonia borane in approximately a 30% yield. Attempts to modify this synthetic procedure have been undertaken in order to

improve the yield. Hu *et al.*[81] investigated the reactions of ammonium salts with sodium borohydride in THF. The best results were obtained through the reaction of ammonium carbonate with sodium borohydride in a solution of THF at a temperature of 45°C, ammonia borane being obtained in an 80% yield. This synthetic procedure is now widely used.[66, 67, 82-84] A second metathesis synthesis was investigated by Ramachandran *et al*.[85] Again ammonium salts were reacted with sodium borohydride initially in THF, however, the results showed that as the concentration of sodium borohydride in THF increased the purity and yield of ammonia borane decreased. The effects of solvent on the reaction were subsequently analysed. It was shown that ammonia borane could be obtained with 98% purity in 95% yield when ammonium formate and sodium borohydride were reacted using dioxane as a solvent at 40°C. This procedure has also been utilised by other research groups.[86, 87]

Progress has also been made in the direct reaction of diborane with ammonia. Research was carried out with respect to the role of the solvent in this reaction.[88] It was found that the reaction could be directed in the direction of either the asymmetric cleavage product of diborane, DADB, or the symmetric cleavage product, ammonia borane. DADB can be synthesised through passing diborane gas into liquid ammonia at −78°C. If diborane is first dispersed in THF, producing a BH_3.THF adduct, when ammonia is passed through the solution at −78°C, a 50/50 mixture of ammonia borane and DADB can be obtained. Ammonia borane can be removed from the mixture by extracting it with ether, giving a 50% yield. Mayer[89] showed that the basicity of the solvent had an influence on the competing asymmetric and symmetric pathways, with more basic solvents favouring ammonia borane formation. Ammonia borane could be prepared in 68 to 76 % yields in glyme after the addition of gaseous ammonia to diborane solutions of ether.

1.7.2 Structure

Following on from the discovery of ammonia borane, investigations into its structure began. As evidence for the discovery of the compound, the powder X-ray diffraction (XRD) pattern of ammonia borane was obtained.[80, 90] This data was used to determine a body centred tetragonal unit cell, with a = 5.255 Å and c = 5.048 Å at room temperature.[91] A proposed polar space group of *I*4*mm* (#107) was given, in

agreement with the expected dipole moment of the molecule. The NH_3BH_3 molecules were located at the vertices and body centre of the unit cell with all B–N bonds being oriented in the same direction, parallel to *c*, as shown in figure 1.4. However, the H atom positions could not be determined. A second study supported these conclusions.[92] However, it was also noted in this study that at low temperature, 230 ± 5 K, a phase transition occurred, causing the appearance of additional faint lines in the diffraction pattern.

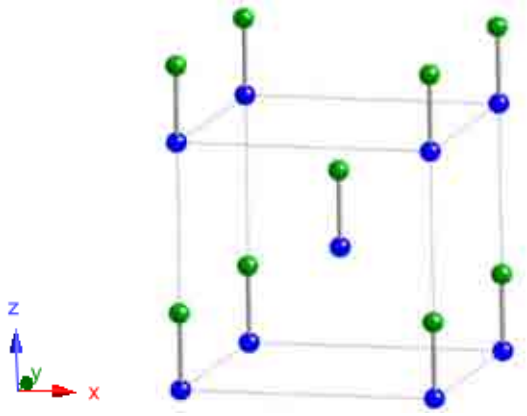

Figure 1.4 – The room temperature structure of NH_3BH_3, the B atoms are shown in green and N in blue (Hydrogen atoms not shown)[91]

This phase transition has been investigated, occurring at approximately 220 K. The low temperature phase has been shown to be orthorhombic with *a* = 5.395 Å, *b* = 4.887 Å and *c* = 4.986 Å and a space group of $Pmn2_1$ (#31).[93] The structure of the orthorhombic phase was first reported by Hoon[94] through X-ray powder diffraction techniques. A subsequent NMR study showed that in this low temperature phase both the BH_3 and NH_3 units are stationary, showing that the H atoms have well defined equilibrium positions.[95] However, this crystal structure showed discrepancies between experimental and calculated data.[96] A single crystal neutron diffraction study of the low temperature phase finally reported the definitive structure, figure 1.5.[93] This study located all of the hydrogen atoms and corrected the previously inaccurate assignment of the B and N locations of previous studies. This study showed that the B–N bond is not completely parallel to the *c*-axis. The phase transition is triggered by the reorientation of the BH_3 and NH_3 units, which leads to the tetragonal phase being more disordered than the orthorhombic phase, causing there to be a higher degree of entropy in the higher temperature tetragonal phase.

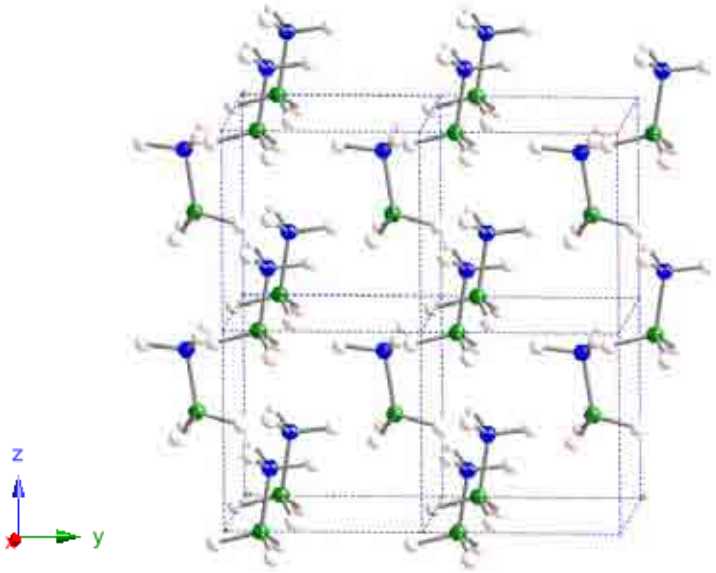

Figure 1.5 – The low temperature orthorhombic structure of NH_3BH_3, the B atoms are shown in green, N in blue and H in pale pink[93]

At room temperature ammonia borane exhibits some unusual physical properties. Despite being isoelectronic with ethane, which has a melting point of −181°C, the compound exists in the solid state and does not melt until 114°C. This comes from the fact that ammonia borane is a Lewis adduct. The B and N atoms are held together through a dative covalent bond, as the lone pair of the nitrogen interacts with an empty *p*-orbital of the boron. The intramolecular polarity of the molecule could contribute to the elevated melting point, however, a second compound isoelectronic to ethane, methyl fluoride, is also polar, but its melting point is only slightly elevated from that of ethane to −141 °C. The intramolecular polarity does in fact play a key role in the physical properties of ammonia borane; the hydrogen atoms bonded to nitrogen are protic in character whereas those bonded to boron are hydridic. This leads to a network of dihydrogen bonds, shown in figure 1.6, giving added stability to the structure.

$$H_3BH_2N{-}H^{\delta+} - - -{}^{\delta-}H{-}BH_2NH_3$$

Figure 1.6 – Dihydrogen bond found in ammonia borane

These interesting dihydrogen bonds found in ammonia borane differ to the conventional hydrogen bond. A typical hydrogen bond involves a protic hydrogen of an X–H bond, where X = N or O, the hydrogen bond donor, interacting with the basic

lone pair of an electronegative atom, the hydrogen bond acceptor. However, studies by Richardson *et al.*[97] showed that the bonding pair can lead to intramolecular hydrogen bonds of the type N–H---H–M and O–H---H–M. This study was further extended to boron and nitrogen containing compounds. Analysis of boron and nitrogen containing molecules showed that these interactions were found to have bond strengths between 12.6 and 29.3 kJ mol^{-1}, which is comparable to a classical hydrogen bond of average strength.[98] The H---H distances were found to be between 1.7 and 1.9 Å in length, which is much shorter than the sum of van der Waals radii for two hydrogen atoms of 2.4 Å. In ammonia borane these H---H interactions have a calculated bond strength of 25.5 kJ mol^{-1} and in the low temperature orthorhombic phase the H---H distance has been found to lie in the range 2.02 to 2.23 Å through neutron diffraction studies.[93, 98]

The room temperature tetragonal structure is highly disordered, due to the motion of the hydrogen atoms. The earliest studies on the room temperature structure failed to locate the hydrogen atoms,[91, 92] although in both cases it was stated that there must be disorder to agree with the four-fold symmetry. This four-fold rotation axis contradicts the three-fold symmetry expected from tetrahedral $–BH_3$ and $–NH_3$ units. There are two possibilities to account for this. Firstly, dynamic disorder, where the hydrogen atoms are free to rotate about the B and N atoms or secondly, static disorder, where individual $–BH_3$ and $–NH_3$ groups orient randomly with respect to the *a* and *b* directions. NMR spectroscopy has been utilised to study the motion of the hydrogen atoms in both phases. In the low temperature orthorhombic phase, hydrogen atoms exchange within each of the three sites available for both $–BH_3$ and $–NH_3$ groups.[95, 99] Motion occurs more rapidly in the $–NH_3$ group than the $–BH_3$ group meaning that they are independent of one another. The temperature dependence of the two rotations varies and as the phase transition temperature is approached, they rotate at similar rates. However, there are discrepancies in the literature about the nature of the rotations in the tetragonal phase. Either there is free rotation of the hydrogen atoms[95] or there is a whole molecule twelve fold rotation about the B–N bond.[99]

Studies have been undertaken into locating the hydrogen atoms in the room temperature phase. A powder XRD study by Hoon and Reynhardt[94] attempted to solve the crystal structure, however, the study was unsuccessful due to the disorder in the structure. It was proposed that due to the space group symmetry of the structure, *I*4*mm*, the vertices of the BH_3 and NH_3 groups can point in four mutually perpendicular directions, all perpendicular to the B–N axis, which means that each H atom can occupy any of twelve positions. A second study involving single crystal XRD was undertaken by Bowden *et al*.[100] The positions for boron and nitrogen refined simply to stable positions, but again the hydrogen positions proved problematic. A 3D Fourier difference map was calculated, which showed hydrogen atoms bonded to both boron and nitrogen are disordered in a halo-like arrangement perpendicular to the B–N bond. The symmetry of the halo, was weakly four-fold, as a consequence of the space group symmetry, meaning that the number of potential hydrogen positions has to be a multiple of four. A model accounting for the disorder was constructed, which proposed eight potential hydrogen positions around each boron and nitrogen atom, with an occupancy of 3/8 in order to maintain the stoichiometry. However, such a model was calculated to introduce new weak diffraction peaks into the XRD pattern, which an exhaustive search of the data failed to find. The results of the model therefore showed that hydrogen atoms do not occupy fixed positions in an ordered arrangement. The average hydrogen positions were therefore refined for the structure. A more recent powder neutron diffraction study attempted to solve the structure by analysing a fully deuterated sample of ammonia borane, ND_3BD_3.[101] Both the proposed models of Hoon and Reynhardt, twelve possible hydrogen positions, and Bowden *et al.*, eight possible hydrogen positions, were used to refine the structure. It was found that the best refinement was obtained with the eight possible positions model. Refined deuterium positions are published in this study. However, there are significant differences between this study and the single crystal XRD study with respect to atomic coordinates. To date, it has proved impossible to successfully refine the hydrogen positions in the room temperature tetragonal structure of ammonia borane due to the disorder observed in the structure.

1.7.3 Decomposition

The earliest studies of ammonia borane showed that it is subject to a slow loss of hydrogen even at room temperature.[90, 102] This loss of hydrogen was postulated to be accompanied by the formation of DADB. Pure ammonia borane was shown to dissolve completely in ethyl ether. However, a sample kept in a dry atmosphere for a short period was shown not to redissolve fully, suggesting a partial conversion to insoluble substances including DADB and polyaminoborane may have occurred. Further to this, ammonia borane dissolved in ether was observed to precipitate slowly an unidentified white solid. No observations about the behaviour of ammonia borane under thermal treatment were made during these studies.

The first study of the thermal decomposition of ammonia borane was carried out by Hu *et al*.[103] Thermogravimetric analysis, TGA, results showed that a rapid decrease in mass occurred between 120°C and 133°C, accompanied by a mass loss of 31.6%. As ammonia borane has a total hydrogen content of less than 20 wt%, hydrogen cannot be the sole decomposition product. A differential thermal analysis, DTA, study exhibited a sharp endothermic peak at 112°C. This corresponded well to the observed melting point of the compound, 112 – 114°C.[89] At 117°C a sharp exothermic peak is observed, reaching a maximum at 130°C. This peak was accompanied by a rapid voluminous expansion and the release of a large amount of gas. Finally a broad exothermic peak was observed from 150°C to 200°C. A combined pressure and temperature measurement showed that a sharp pressure increase was observed from 120°C, corresponding closely with the first exothermic peak. On reaching 145°C, the rate of pressure increase decreased, suggesting a second decomposition step. A final pyrolysis study involved heating ammonia borane to 200°C. 2.33 mmol of hydrogen were calculated to be released per mmol of ammonia borane and infra-red (IR) spectroscopy showed that both diborane and borazine were released as a result of decomposition. This two step decomposition mechanism was rationalised firstly by an exothermic release of hydrogen through either reaction 1.24 or reaction 1.25.

$$NH_3BH_3 \rightarrow (NH_2BH_2)_n + H_2 \qquad \text{Reaction 1.24}$$

$$2NH_3BH_3 \rightarrow NH_3BH_2NH_2BH_3 + H_2 \qquad \text{Reaction 1.25}$$

The exact nature of the step was not determined although both steps would lead to a material of BNH_4 composition. The exact composition of the product was not determined but from previous work was suggested to be made up of cyclodiborazane, $(BNH_4)_2$, cyclotriborazane, $(BNH_4)_3$, cyclopentaborazane, $(BNH_4)_5$, and polyaminoborane, $(BNH_4)_n$.[104] The vast number of potential products in this step shows the complex nature of the thermal decomposition of ammonia borane. The BNH_4 materials further undergo an exothermic hydrogen release step, producing a material of composition BNH_2, reaction 1.26.

$$(NH_2BH_2)_n \rightarrow (NHBH)_n + nH_2 \qquad \text{Reaction 1.26}$$

An IR spectrum taken of a sample of ammonia borane pyrolysed at 600°C showed features at 1390 and 810 cm^{-1}, which are also observed in boron nitride, showing this is the ultimate decomposition product.

Komm *et al.*[105] undertook a study related to the synthesis of poly(aminoborane), $(NH_2BH_2)_n$. Ammonia borane heated to 140°C frothed and released gas, which was presumed to be hydrogen. A white solid was collected after the experiment was completed in a yield of 30%. Elemental analysis of the product showed that it was of empirical formula BNH_4, however, molecular mass measurements proved unsuccessful due to the poor solubility of the material in solvents. This is consistent with either a cyclic or linear polymer of relatively high molecular weight, again showing the polymeric nature of the products from the thermal decomposition of ammonia borane.

A DTA study by Sit *et al.*[106] investigated how the heating rate affected the decomposition pathway. For all heating rates a sharp endothermic peak was followed by a sharp exothermic peak, however, the onset temperature of these processes was shown to be reliant on the heating rate, while features of the DTA curve became more distinct, with four separate processes being visible, with the lower heating rates. It was also observed that a slow heating rate resulted in the solid beginning to decompose at approximately 30°C below the melting point. The exothermic peaks

were again assigned to the formation of polyaminoboranes accompanied by hydrogen release and their subsequent decomposition, further releasing hydrogen.

Wolf *et al.*[66] further made progress in understanding the decomposition pathway through a study involving TGA, DSC, volumetric measurements and IR spectroscopy. DSC measurements showed that when a heating rate of 1°C min^{-1} was used, a previously unreported exothermic event was observed at 95°C, closely followed by an endothermic event and two further exothermic events at 113 and 125°C. There was considerable overlap between all of these events, each starting before the previous event had finished. A slower heating rate of 0.05°C min^{-1} significantly decreased the onset temperature of the first exothermic event to 82°C. Furthermore the endothermic event was no longer observed: the material completely decomposed below the melting point. Isothermal DSC measurements between 70 and 90°C show a single exothermic event, which was strongly dependent on temperature, occurring after forty minutes at 90°C and twenty four hours at 70°C. The mean enthalpy of reaction was calculated to be −21.7 kJ mol^{-1}. The solid residue produced after heating was determined to be mainly composed of polyaminoborane. Isothermal volumetric measurements carried out at 90°C showed the first decomposition step to be accompanied by the release of hydrogen, with one mole of hydrogen released per mole of ammonia borane. Although the rate of release was strongly dependent on temperature, the amount of hydrogen release was independent of temperature. TGA measurements coupled with DSC and IR spectroscopy showed a mass loss of 10 wt% for the first decomposition step. A one mole loss of hydrogen would correspond to a 6.5 wt% loss and hence volatile products such as borazine must account for the additional weight loss. IR spectroscopy identified monomeric aminoborane and borazine as products from this decomposition step. Monomeric aminoborane has been shown to be unstable at room temperature and rapidly polymerises.[107] These measurements also showed that borazine was detected after the release of monomeric aminoborane suggesting that borazine is released from decomposition products, potentially through the polymerisation of monomeric aminoborane and not directly from ammonia borane. This study showed that there are several reactions taking place simultaneously during the thermal decomposition of ammonia borane, the main decomposition product being polyaminoborane, along with other volatile

products including borazine. Furthermore, the decomposition process was shown to be strongly dependent on temperature.

A related study by Baitalow *et al.*[108] resulted in similar findings. A combined volumetric–TGA study showed two weight loss steps, which could be separated with a suitably slow ramp rate. 1.1 moles of hydrogen per mole of ammonia borane were calculated to be released during the first decomposition step, agreeing well with the formation of polyaminoborane. After heating to 200°C a total of 2.2 moles of hydrogen per mole of ammonia borane were released, which would correspond to a total mass loss of 14.3 wt%. However, the observed mass loss was in excess of this value and so additional volatile products must account for this difference. At a heating rate of 10°C min^{-1} the observed mass loss was as high as 33 wt%. Mass spectrometry revealed that hydrogen, borazine and monomeric aminoborane were released during the decomposition process. Hydrogen release was observed in both decomposition steps, independent of the heating rate. However, the heating rate did affect the release of volatiles. At a higher heating rate borazine and monomeric aminoborane were released in both steps, but when the heating rate was reduced, borazine release was suppressed in the first step. These two volatiles are released simultaneously and it is therefore reasonable to conclude that borazine is formed through the dehydrogenation of monomeric aminoborane, forming the highly reactive monomeric iminoborane, which then trimerises producing borazine. The total hydrogen release was again shown to be independent of both temperature and heating rate, although its slow release rate in isothermal experiments at temperatures below 90°C was discussed.

Up to this point only the thermodynamic properties of the thermal decomposition of ammonia borane had been reported, the mechanism of the release of gases was not fully understood. A study by Smith *et al.*[109] suggested that the decomposition pathway proceeded by a bimolecular mechanism. The gases released during thermolysis from a mixture of NH_3BH_3 and ND_3BD_3 were analysed and all three molecular species H_2, HD and D_2 were observed. This study also showed that hydrogen could be released at a temperature as low as 70°C in isothermal experiments, although there was a long delay before hydrogen release began. An *in*

situ solid state ^{11}B NMR study was undertaken by Stowe *et al.*[110] which analysed the decomposition of ammonia borane and the evolution of boron containing non-volatile intermediates and products at 88°C. The ammonia borane starting material was shown to have two observable peaks, due to quadrupolar coupling, centred about a chemical shift of −27.0 ppm. The first change in the spectrum saw the intensity of the starting material decrease and a new resonance grow at −23.0 ppm. Two new additional resonances then appeared corresponding to BH_2 and BH_4 at −13 and −38 ppm, the groups present in DADB. Pressure monitoring of ammonia borane decomposition at 88°C showed that there was very little pressure change during this time period, suggesting that little hydrogen is released at this time. The products formed during this period are precursors to hydrogen loss. This induction period was discussed as involving the disruption of the network of dihydrogen bonds, forming a new more mobile phase of ammonia borane. After DADB formation, hydrogen release began, evidenced by the broadening of the BH_2 feature and the appearance of a broad BH feature, consistent with polymerised species. The BH_4 signal remained constant after its appearance. DADB formation occurs during the nucleation step, this was identified as being the critical nucleation event that allows hydrogen release to commence. The final step in the decomposition was described as being a growth step. This step was described as initially involving the bimolecular reaction of DADB with unreacted ammonia borane resulting in the release of hydrogen and a DADB like species. This DADB like species then further reacts with ammonia borane to produce longer N–B chains, further releasing hydrogen and polyaminoborane precursors. The proposed mechanism of hydrogen release is shown in figure 1.7.

Bowden *et al.*[82] performed combined DSC–TG isothermal measurements. Two exothermic events were observed, which could be separated at lower temperatures. The first exotherm proceeded without any weight loss, whereas the second proceeded with a weight loss greater than 6.5 wt%, a larger weight loss than for the expected loss of one equivalent of hydrogen gas. This weight loss was larger at higher temperatures, due to the increased release of volatile species such as borazine. The first exothermic step was further analysed by optical microscopy and XRD. Microscopy observations showed significant changes in the molecular nature of ammonia borane without changes in the morphology of the crystals. It was concluded

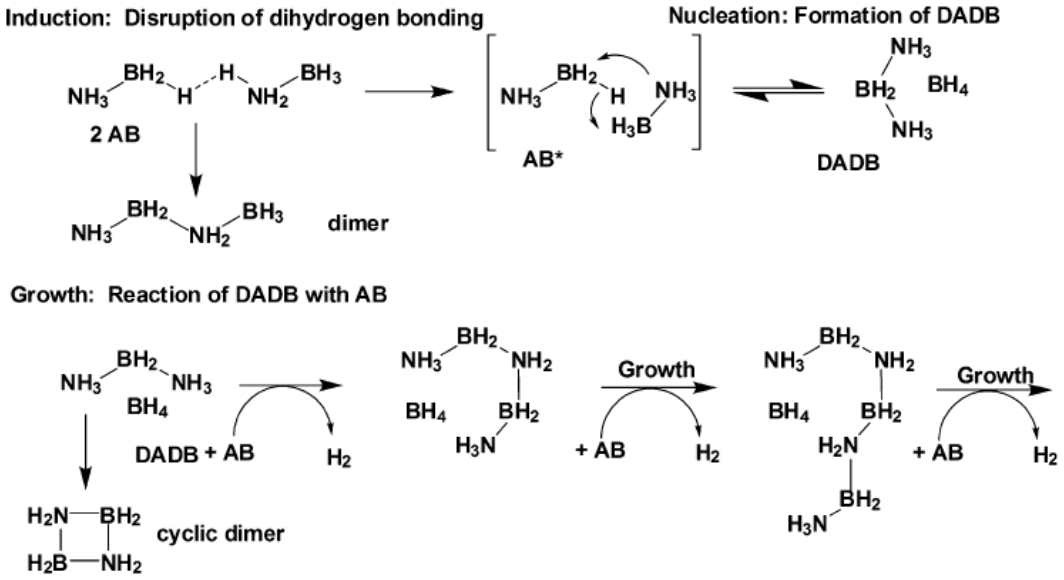

Figure 1.7 – The proposed thermal dehydrogenation mechanism of ammonia borane[110]

that the original alignment of polar B–N bonds along the *c* axis is disrupted during heating, removing the net polarity. This in turn means that the more mobile phase of ammonia borane involves more than just a disruption of the dihydrogen bonding network and there is a substantial disordering of the ammonia borane molecules. The XRD patterns showed that crystallinity was lost as temperature increased, at the same temperatures at which changes in the microscopy images were observed. The intensity of the peaks in the pattern decreased in a sigmoidal fashion, which is consistent with a nucleation and growth mechanism. Finally this study calculated an activation energy of 125 kJ mol^{-1} for the decomposition process. This value is close to the bond energy of the B–N dative bond,[111] which is consistent with the formation of DADB during the nucleation step as this requires the breaking of this bond.

The nature of the polymeric decomposition product, $(NH_2BH_2)_n$ has been investigated. A combined thermogravimetric–differential scanning calimetry (TG–DSC) study showed that three mass loss steps are observed, all exothermic in nature, rationalised by reactions 1.27 – 1.29.[112]

$$NBH_4 \rightarrow NBH_2 + H_2 \quad 6.9 \text{ wt\%} \qquad \text{Reaction 1.27}$$

$$NBH_2 \rightarrow NBH + \tfrac{1}{2}H_2 \quad 3.5 \text{ wt\%} \qquad \text{Reaction 1.28}$$

$$NBH \rightarrow NB + \tfrac{1}{2}H_2 \quad 3.5\ wt\% \qquad \text{Reaction 1.29}$$

However, observed total mass losses were greater than 14 wt% and so desorption of volatile substances, such as borazine, could account for the enhanced mass losses. Further to this it was noted that the sample history, with respect to its preparation had an effect on results; weight losses in the range 13.5 wt% to 32.0 wt% were observed. With such differences in results, it was suggested that there are competing decomposition pathways in addition to a stepwise hydrogen desorption mechanism.

Baumann *et al.*[113] further analysed the decomposition of polyaminoborane, synthesising the material through controlled decomposition of ammonia borane at 90°C. A DSC study showed an exothermic event at 115°C, consistent with the second exothermic event seen in the decomposition of ammonia borane.[66, 103] It was observed that, as with ammonia borane, increasing the heating rate caused an increase in the temperature at which polyaminoborane decomposes. The enthalpy of decomposition was shown to be dependent on heating rate; heating at 10 °C min^{-1} gave a value of −15.4 kJ mol^{-1}, whereas at 0.1°C min^{-1} a value of −23.9 kJ mol^{-1} was calculated. The effect of heating rate shows that different reaction pathways are possible, causing differences in decomposition products. Combined TG–FTIR and TG–MS results showed that monomeric NH_2BH_2, borazine, diborane and hydrogen were released. Although the amount of hydrogen released was independent of heating rate with 1.1 moles of hydrogen released per mole of polyaminoborane, the amount of monomeric NH_2BH_2 and borazine released increased with rising heating rate. The release of 1.1 moles of hydrogen is consistent with the formation of a second polymeric species, polyiminoborane, $(NHBH)_x$.

1.7.4 As a hydrogen storage material

The potential of ammonia borane as a hydrogen storage material was first discussed by Wolf *et al*.[66] The high hydrogen content, 19.6 wt%, moderate temperatures of the thermal decomposition process and the exothermic character of the decomposition process were cited as the reasons for the compound's potential. However, ammonia borane does not meet the previously discussed United States Department of Energy targets for onboard hydrogen storage systems.[67] Only 6.5 wt% of the compound's

hydrogen content can be released under isothermal conditions at temperatures below 100°C and this release suffers from a long induction period. Furthermore, the release of hydrogen occurs over a broad temperature range during temperature ramping experiments and occurs over a long time period under isothermal conditions below the operating system target temperature of 85°C. The two steps of hydrogen release have also proved difficult to separate at faster ramp rates and higher temperatures. The system also currently lacks reversibility, at least partly as a result of the exothermic release: attempts to directly rehydrogenate the system have proved unsuccessful.[114] Finally, the hydrogen release is readily polluted with other decomposition products, including monomeric ammonia borane, borazine and diborane.[67, 108] Borazine release during the decomposition of ammonia borane is so prominent that it has been used as a method of producing borazine on a laboratory preparation scale in high purity.[115] The release of borazine and subsequent entry of the gas into a fuel cell would poison the fuel cell and prevent it from working. For these reasons, interest in the solid state storage of hydrogen in ammonia borane has fallen off and interest has moved onto looking at how the system can be modified in order to improve its hydrogen storage properties.

1.8 Aims

Ammonia borane has been identified as having a great deal of potential as a material for hydrogen storage due to its high gravimetric hydrogen content. The interaction of hydridic boron-bound and protic nitrogen-bound hydrogen favours hydrogen release over other gases such as ammonia. The aim of the project was to investigate the potential for improving the hydrogen storage properties of the ammonia borane system through the introduction of metal cations. This was an area of hydrogen storage that had not been investigated at the start of this project.

The reactions of ammonia borane with metal hydrides, namely lithium, sodium and calcium hydrides were investigated. The interaction of lithium and sodium amides with ammonia borane was also explored. The chief method employed to characterise the reaction products was that of powder X-ray diffraction. In order to investigate the hydrogen storage properties of the synthesised materials, thermal desorption investigations were performed. Temperature programmed desorption experiments in conjunction with mass spectrometry were carried out to obtain information about the gases released during both synthesis and decomposition of the materials. Intelligent gravimetric analysis and thermogravimetric analysis were employed to further investigate the thermal decomposition properties of the synthesised materials by monitoring the weight losses experienced during heating as well as recording the gases released using a mass spectrometer. Reaction pathways were investigated with respect to the changes in boron environments within the samples using solid state ^{11}B magic angle spinning nuclear magnetic resonance spectroscopy. This method of analysis allowed information regarding amorphous reaction products to be obtained. In the case of the sodium hydride and ammonia borane reaction, the pathway was also investigated using solid state ^{23}Na magic angle spinning nuclear magnetic resonance spectroscopy. The final method of characterisation used to investigate the products of the various reactions was that of Raman spectroscopy in order to obtain information regarding the changes in bonds within the samples.

1.9 References

1. Züttel, A., Hydrogen storage methods. *Naturwissenschaften* **2004,** 91, (4), 157–172.

2. Balat, M., Potential importance of hydrogen as a future solution to environmental and transportation problems. *International Journal of Hydrogen Energy* **2008,** 33, 4013–4029.

3. Cherry, R. S., A hydrogen utopia? *International Journal of Hydrogen Energy* **2004,** 29, 125–129.

4. Muradov, N. Z.; Veziroğlu, T. N., From hydrocarbon to hydrogen – carbon to hydrogen economy. *International Journal of Hydrogen Energy* **2005,** 30, 225–237.

5. Steinberg, M., Fossil fuel decarbonization technology for mitigating global warming. *International Journal of Hydrogen Energy* **1999,** 24, 771–777.

6. Kreuter, W.; Hofmann, H., Electrolysis: The important energy transformer in a world of sustainable energy. *International Journal of Hydrogen Energy* **1998,** 23, (8), 661–666.

7. Baykara, S. Z., Hydrogen production by direct solar thermal decomposition of water, possibilities for improvement of process efficiency. *International Journal of Hydrogen Energy* **2004,** 29, 1451–1458.

8. Hawkes, F. R.; Dinsdale, R.; Hawkes, D. L.; Hussy, I., Sustainable fermentative hydrogen production: challenges for process optimisation. *International Journal of Hydrogen Energy* **2002,** 27, 1339–1347.

9. Bossel, U., Well-to-wheel studies, heating values, and the energy conservation principle. In *European Fuel Cell Forum Technical Report E10*, 2003.

10. Das, L. M., Hydrogen engines - A view of the past and a look into the future. *International Journal of Hydrogen Energy* **1990,** 15, 425–443.

11. Cheng, X.; Shi, Z.; Glass, N.; Zhang, L.; Zhang, J.; Song, D.; Liu, Z.-S.; Wang, H.; Shen, J., A review of PEM hydrogen fuel cell contamination: Impacts, mechanisms and mitigations. *Journal of Power Sources* **2007,** 165, 739–756.

12. Grove, W. R., On voltaic series and the combination of gases by platinum. *Philosophical Magazine, Series 3* **1839,** 14, 127–130.

13. Halseid, R.; Vie, P. J. S.; R., T., Effect of ammonia on the performance of polymer electrolyte membrane fuel cells. *Journal of Power Sources* **2006,** 154, 343–350.

14. Hammerschlag, R.; Mazza, P., Questioning hydrogen. *Energy Policy* **2005,** 33, 2039–2043.

15. van Mierlo, J.; Maggetto, G.; Lataire, P., Which energy source for road transport in the future? A comparison of battery, hybrid and fuel cell vehicles. *Energy Conversion and Management* **2006,** 47, 2748–2760.

16. Dunn, S., Hydrogen futures: Toward a sustainable energy system. *International Journal of Hydrogen Energy* **2002,** 27, 235–264.

17. Schlapbach, L.; Züttel, A., Hydrogen-storage materials for mobile applications. *Nature* **2001,** 414, 353–358.

18. Züttel, A., Materials for hydrogen storage. *Materials Today* **2003**, 24–33.

19. Edwards, P. P.; Kuznetsov, V. L.; David, W. I. F., Hydrogen energy. *Philosophical Transactions of the Royal Society A* **2007,** 365, 1043–1056.

20. Aceves, S. M.; Berry, G. D.; Martinez-Frias, J.; Espinosa-Loza, F., Vehicular storage of hydrogen in insulated pressure vessels. *International Journal of Hydrogen Energy* **2006,** 31, 2274–2283.

21. Zhou, L., Progress and problems in hydrogen storage methods. *Renewable and Sustainable Energy Reviews* **2005,** 9, 395–408.

22. Langmi, H. W.; Book, D.; Walton, A.; Johnson, S. R.; Al-Mamouria, M. M.; Speight, J. D.; Edwards, P. P.; Harris, I. R.; Anderson, P. A., Hydrogen storage in ion-exchanged zeolites. *Journal of Alloys and Compounds* **2005,** 404, 637–642.

23. Züttel, A.; Sudan, P.; Mauron, P.; Kiyobayashi, T.; Emmenegger, C.; Schlapbach, L., Hydrogen storage in carbon nanostructures. *International Journal of Hydrogen Energy* **2002,** 27, 203–212.

24. Lin, X.; Jia, J.; Zhao, X.; Thomas, K. M.; Blake, A. J.; Walker, G. S.; Champness, N. R.; Hubberstey, P.; Schroder, M., High H_2 adsorption by coordination-framework materials. *Angewandte Chemie International Edition* **2006,** 45, 7358–7364.

25. Budd, P. M.; Butler, A.; Selbie, J.; Mahmood, K.; McKeown, N. B.; Ghanem, B.; Msayib, K.; Book, D.; Walton, A., The potential of organic polymer-based hydrogen storage materials. *Physical Chemistry Chemical Physics* **2007,** 9, 1802–1808.

26. Yang, Z.; Xia, Y.; Mokaya, R., Enhanced hydrogen storage capacity of high surface area zeolite-like carbon materials. *Journal of the American Chemical Society* **2007,** 129, 1673–1679.

27. Langmi, H. W.; Walton, A.; Al-Mamouria, M. M.; Johnson, S. R.; Book, D.; Speight, J. D.; Edwards, P. P.; Gameson, I.; Anderson, P. A.; Harris, I. R., Hydrogen adsorption in zeolites A, X, Y and RHO. *Journal of Alloys and Compounds* **2003,** 356, 710–715.

28. McKeown, N. B.; Budd, P. M., Polymers of intrinsic microporosity (PIMs): Organic materials for membrane separations, heterogeneous catalysis and hydrogen storage *Chemical Society Reviews* **2006,** 35, 675–683.

29. van den Berg, A. W. C.; Arean, C. O., Materials for hydrogen storage: current research trends and perspectives. *Chemical Communications* **2008,** 6, 668–681.

30. Bogdanovic, B.; Bohmhammel, K.; Christ, B.; Reiser, A.; Schlichte, K.; Vehlen, R.; Wolf, U., Thermodynamic investigation of the magnesium–hydrogen system. *Journal of Alloys and Compounds* **1999,** 282, 84–92.

31. Reilly, J. J.; Wiswall, R. H., Reaction of hydrogen with alloys magnesium and nickel and formation of Mg_2NiH_4. *Inorganic Chemistry* **1968,** 7, 2254–2256.

32. Spassov, T.; Solsona, P.; Bliznakov, S.; Surinac, S.; Baro, M. D., Synthesis and hydrogen sorption properties of nanocrystalline $Mg_{1.9}M_{0.1}Ni$ (M = Ti, Zr, V) obtained by mechanical alloying. *Journal of Alloys and Compounds* **2003,** 356, 639–643.

33. Yvon, K., Complex transition metal hydrides. *Chimia* **1998,** 52, 613–619.

34. Orimo, S.; Nakamori, Y.; Eliseo, J. R.; Züttel, A.; Jensen, C. M., Complex hydrides for hydrogen storage. *Chemical Reviews* **2007,** 107, 4111–4132.

35. Bogdanovic, B.; Brand, R. A.; Marjanovic, A.; Schwickardi, M., Metal-doped sodium aluminium hydrides as potential new hydrogen storage materials. *Journal of Alloys and Compounds* **2000,** 302, 36–58.

36. Bogdanovic, B.; Schwickardi, M., Ti-doped alkali metal aluminium hydrides as potential novel reversible hydrogen storage materials *Journal of Alloys and Compounds* **1997,** 253, 1–9.

37. Schlesinger, H. I.; Brown, H. C., Metal borohydrides III. Lithium borohydride. *Journal of the American Chemical Society* **1940,** 62, 3429–3435.

38. Schlesinger, H. I.; Brown, H. C.; Hoekstra, H. R.; Rapp, L. R., Reactions of diborane with alkali metal hydrides and their addition compounds: New syntheses of borohydrides: Sodium and potassium borohydrides. *Journal of the American Chemical Society* **1953,** 75, 199–204.

39. Züttel, A.; Wenger, P.; Rentsch, S.; Sudan, P.; Mauron, P.; Emmenegger, C., $LiBH_4$ a new hydrogen storage material. *Journal of Power Sources* **2003,** 118, 1–7.

40. Urgnani, J.; Torres, F. J.; Palumbo, M.; Baricco, M., Hydrogen release from solid state $NaBH_4$. *International Journal of Hydrogen Energy* **2008,** 33, 3111–3115.

41. Orimo, S.; Nakamori, Y.; Kitahara, G.; Miwa, K.; Ohba, N.; Towata, S.; Züttel, A., Dehydriding and rehydriding reactions of $LiBH_4$. *Journal of Alloys and Compounds* **2005,** 404–406, 427–430.

42. Mauron, P.; Buchter, F.; Friedrics, O.; Remhof, A.; Bielmann, M.; Zwicky, C. N.; Züttel, A., Stability and reversibility of $LiBH_4$. *Journal of Physical Chemistry B* **2008,** 112, 906–910.

43. Vajo, J. J.; Skeith, S. L., Reversible storage of hydrogen in destabilized $LiBH_4$. *Journal of Physical Chemistry B* **2005,** 109, 3719–3722.

44. Barkhordarian, G.; Klassen, T.; Dornheima, M.; Bormann, R., Unexpected kinetic effect of MgB_2 in reactive hydride composites containing complex borohydrides *Journal of Alloys and Compounds* **2007,** 440, L18–L21.

45. Bergstrom, F. W.; Fernelius, W. C., The chemistry of the alkali amides. *Chemical Reviews* **1933,** 12, 43–179.

46. Juza, R.; Opp, K., Metallamide und metallnitride, 24. Mitteilung. Die kristallstruktur des lithiumamides. *Zeitschrift fur anorganische und allgemeine chemie* **1951,** 266, 313–324.

47. Chen, P.; Xiong, Z.; Luo, J.; Lin, J.; Tan, K. L., Interaction of hydrogen with metal nitrides and imides. *Nature* **2002,** 420, 302–304.

48. Chen, P.; Xiong, Z.; Luo, J.; Lin, J.; Tan, K. L., Interaction between lithium amide and lithium hydride. *Journal of Physical Chemistry B* **2003,** 107, 10967–10970.

49. Ichikawa, T.; Isobe, S.; Hanada, N.; Fujii, H., Lithium nitride for reversible hydrogen storage. *Journal of Alloys and Compounds* **2004,** 365, 271–276.

50. Ichikawa, T.; Hanada, N.; Isobe, S.; Leng, H.; Fujii, H., Mechanism of novel reaction from $LiNH_2$ and LiH to Li_2NH and H_2 as a promising hydrogen storage system. *Journal of Physical Chemistry B* **2004,** 108, 7887–7892.

51. David, W. I. F.; Jones, M. O.; Gregory, D. H.; Jewell, C. M.; Johnson, S. R.; Walton, A.; Edwards, P. P., A mechanism for non-stoichiometry in the lithium amide/lithium imide hydrogen storage reaction. *Journal of the American Chemical Society* **2007,** 129, 1594–1601.

52. Nakamori, Y.; Kitahara, G.; Orimo, S., Synthesis and dehydriding studies of Mg-N-H systems. *Journal of Power Sources* **2004,** 138, 309–312.

53. Hu, Y. H.; Ruckenstein, E., Ultrafast reaction between LiH and NH_3 during H_2 storage in Li_3N. *Journal of Physical Chemistry A* **2003,** 107, 9737–9739.

54. Xiong, Z.; Wu, G.; Hu, J.; Chen, P., Ternary imides for hydrogen storage. *Advanced Materials* **2004,** 16, 1522–1525.

55. Chen, Y.; Cheng-Zhang, W.; Wang, P.; Cheng, H., Structure and hydrogen storage property of ball milled $LiNH_2/MgH_2$ mixture. *International Journal of Hydrogen Energy* **2006,** 31, 1236–1240.

56. Rijssenbeek, J.; Gao, Y.; Hanson, J.; Huang, Q.; Jones, C.; Toby, B., Crystal structure determination and reaction pathway of amide-hydride mixtures. *Journal of Alloys and Compounds* **2008,** 454, 233–244.

57. Wu, G.; Xiong, Z.; Liu, T.; Liu, Y.; Hu, J.; Chen, P.; Feng, Y.; Wee, A. T. S., Synthesis and characterization of a new ternary imide $Li_2Ca(NH)_2$. *Inorganic Chemistry* **2007,** 46, 517–521.

58. Tokoyoda, K.; Hino, S.; Ichikawa, T.; Okamotoa, K.; Fujii, H., Hydrogen desorption/absorption properties of Li–Ca–N–H system. *Journal of Alloys and Compounds* **2007,** 439, 337–341.

59. Chater, P. A.; David, W. I. F.; Johnson, S. R.; Edwards, P. P.; Anderson, P. A., Synthesis and crystal structure of $Li_4BH_4(NH_2)_3$. *Chemical Communications* **2006**, 2439–2441.

60. Meisner, G. P.; Scullin, M. L.; Balogh, M. P.; Pinkerton, F. E.; Meyer, M. S., Hydrogen release from mixtures of lithium borohydride and lithium amide: A phase diagram study. *Journal of Physical Chemistry B* **2006,** 110, 4186–4192.

61. Chater, P. A.; David, W. I. F.; Anderson, P. A., Synthesis and structure of the new complex hydride $Li_2BH_4NH_2$. *Chemical Communications* **2007,** 45, 4770–4772.

62. Chater, P. A.; Anderson, P. A.; Prendergast, J. W.; Walton, A.; Mann, V. S. J.; Book, D.; David, W. I. F.; Johnson, S. R.; Edwards, P. P., Synthesis and characterisation of amide-borohydrides: New complex light hydrides for potential hydrogen storage. *Journal of Alloys and Compounds* **2007,** 446–447, 350–354.

63. Pinkerton, F. E.; Meisner, G. P.; Meyer, M. S.; Balogh, M. P.; Kundrat, M. D., Hydrogen desorption exceeding ten weight percent from the quaternary hydride $Li_3BN_2H_8$. *Journal of Physical Chemistry B* **2005,** 109, 6–8.

64. United States Department of Energy; Targets for onboard hydrogen storage systems for light-duty vehicles. *Office of Energy Efficiency and Renewable Energy and the FreedomCAR and Fuel Partnership technical report* **2009**.

65. Grochala, W.; Edwards, P. P., Thermal decomposition of the non-interstitial hydrides for the storage and production of hydrogen. *Chemical Reviews* **2004,** 104, 1283–1315.

66. Wolf, G.; Baumann, J.; Baitalow, F.; Hoffmann, F. P., Calorimetric process monitoring of thermal decomposition of B–N–H compounds. *Thermochimica Acta* **2000,** 343, 19–25.

67. Baumann, J.; Baitalow, F.; Wolf, G., Thermal decomposition of polymeric aminoborane $(H_2BNH_2)_x$ under hydrogen release. *Thermochimica Acta* **2005,** 430, 9–14.

68. Shore, S. G.; Parry, R. W., The crystalline compound ammonia borane, H_3NBH_3. *Journal of the American Chemical Society* **1955,** 77, 6084-6085.

69. Burg, A. B.; Schlesinger, H. I., Hydrides of boron. VII. Evidence of the transitory existence of borine (BH_3): Borine carbonyl and borine trimethylammine. *Journal of the American Chemical Society* **1937,** 59, 780–787.

70. Stock, A.; Pohland, E., *Ber. Dtsch. Chem. Ges.* **1925,** 58, 657.

71. Schlesinger, H. I.; Burg, A. B., Hydrides of boron. VIII. The structure of the diammoniate of diborane and its relation to the structure of diborane. *Journal of the American Chemical Society* **1938,** 60, 290–299.

72. Schlesinger, H. I.; Sanderson, R. J.; Burg, A. B., Metal borohydrides I. Aluminum borohydride. *Journal of the American Chemical Society* **1940,** 62, 3421–3425.

73. Burg, A. B.; Schlesinger, H. I., Metal borohydrides II. Beryllium borohydride. *Journal of the American Chemical Society* **1940,** 62, 3425–3429.

74. Burg, A. B., Proton-deuteron exchange between ammonia and ammoniated diborane. *Journal of the American Chemical Society* **1947,** 69, 747–750.

75. Schaeffer, G. W.; Adams, M. D.; Koenig, F. J., On the alkali metal salts derived from the diammoniate of diborane. *Journal of the American Chemical Society* **1956,** 78, 725–728.

76. Schultz, R. D.; Parry, R. W., Chemical evidence for the structure of the "Diammoniate of Diborane." I. Evidence for the borohydride ion and for the dihydro-diammine(III) cation. *Journal of the American Chemical Society* **1958,** 80, 4–8.

77. Shore, S. G.; Girardot, P. R.; Parry, R. W., Chemical evidence for the structure of the "Diammoniate of Diborane." V. A tracer study of the reaction between sodium and the "Diammoniate of Diborane". *Journal of the American Chemical Society* **1958,** 80, 20–24.

78. Parry, R. W.; Shore, S. G., Chemical evidence for the structure of the "Diammoniate of Diborane." IV. The reaction of sodium with Lewis acids in liquid ammonia. *Journal of the American Chemical Society* **1958,** 80, 15–20.

79. Shore, S. G.; Parry, R. W., Chemical evidence for the structure of the "Diammoniate of Diborane." III. The reactions of borohydride salts with lithium halides and aluminum chloride. *Journal of the American Chemical Society* **1958,** 80, 12–15.

80. Shore, S. G.; Parry, R. W., The crystalline compound ammonia-borane, H_3NBH_3. *Journal of the American Chemical Society* **1955,** 77, 6084–6085.

81. Hu, M. G.; van Paasschen, J. M.; Geanangel, R. A., New synthetic approaches to ammonia-borane and its deuterated derivatives. *Journal of Inorganic and Nuclear Chemistry* **1977,** 39, 2147-2150.

82. Bowden, M. E.; Autrey, T.; Brown, I.; Ryan, M., The thermal decomposition of ammonia borane: A potential hydrogen storage material. *Current Applied Physics* **2008,** 8, 498–500.

83. Graham, K. R.; Kemmitt, T.; Bowden, M. E., High capacity hydrogen storage in a hybrid ammonia borane-lithium amide material. *Energy and Environmental Science* **2009,** 2, 706–710.

84. Kang, X.; Fang, Z.; Kong, L.; Cheng, H.; Yao, X.; Lu, G.; Wang, P., Ammonia borane destabilized by lithium hydride: An advanced on-board hydrogen storage material. *Advanced Materials* **2008,** 20, 2756–2759.

85. Ramachandran, P.; Gagare, P. V., Preparation of ammonia borane in high yield and purity, methanolysis and regeneration. *Inorganic Chemistry* **2007,** 46, 7810–7817.

86. Xiong, Z.; Wu, G.; Chua, Y. S.; Hu, J.; He, T.; Xu, W.; Chen, P., Synthesis of sodium amidoborane ($NaNH_2BH_3$) for hydrogen production. *Energy and Environmental Science* **2008,** 1, 360–363.

87. Spielmann, J.; Jansen, G.; Bandmann, H.; Harder, S., Calcium amidoborane hydrogen storage materials: Crystal structures of decomposition products. *Angewandte Chemie-International Edition* **2008,** 47, 6290–6295.

88. Shore, S. G.; Boddeker, K. W., Large scale synthesis of $H_2B(NH_3)_2^+BH_4^-$ and H_3NBH_3. *Inorganic Chemistry* **1964,** 3, 914–915.

89. Mayer, E., Symmetrical cleavage of diborane by ammonia in solution. *Inorganic Chemistry* **1972,** 11, 866–869.

90. Shore, S. G.; Parry, R. W., The crystalline compound ammonia borane, H_3NBH_3. *Journal of the American Chemical Society* **1955,** 77, 6084–6085.

91. Hughes, E. W., The crystal structure of ammonia-borane, H_3NBH_3. *Journal of the American Chemical Society* **1956,** 76, 502–503.

92. Lippert, E. L.; Lipscomb, W. N., The structure of H_3NBH_3. *Journal of the American Chemical Society* **1956,** 78, 503–504.

93. Klooster, W. T.; Koetzle, T. F.; Siegbahn, P. E. M.; Richardson, T. B.; Crabtree, R. H., Study of the N–H---H–B dihydrogen bond including the crystal structure of BH_3NH_3 by neutron diffraction. *Journal of the American Chemical Society* **1999,** 121, 6337–6343.

94. Hoon, C. F.; Reynhardt, E. C., Molecular dynamics and structures of amine boranes of the type R_3NBH_3: I. X-ray investigation of H_3NBH_3 at 295 K and 110K. *Journal of Physics C: Solid State Physics* **1983,** 16, 6129–6136.

95. Reynhardt, E. C.; Hoon, C. F., Molecular dynamics and structures of amine boranes of the type R_3NBH_3: II NMR investigation of H_3NBH_3. *Journal of Physics C: Solid State Physics* **1983,** 16, 6137–6152.

96. Bühl, M.; Steinke, T.; von Ragué Schleyer, P.; Boese, R., Solvation effects on geometry and chemical shifts. An ab initio/IGLO reconciliation of apparent experimental inconsistencies on H_3BNH_3. *Angewandte Chemie-International Edition* **1991,** 30, 1160–1161.

97. Richardson, T. B.; de Gala, S.; Crabtree, R. H., Unconventional hydrogen bonds: Intermolecular B-H---H-N interactions. *Journal of the American Chemical Society* **1995,** 117, 12875-12876.

98. Crabtree, R. H.; Siegbahn, P. E. M.; Eisenstein, O.; Rheingold, A. L.; Koetzle, T. F., A new intermolecular interaction: Unconventional hydrogen bonds with element-hydride bonds as proton acceptor. *Accounts of Chemical Research* **1996,** 29, 348–354.

99. Penner, G. H.; Chang, Y. C. P.; Hutzal, J., A deuterium NMR spectroscopy study of solid BH_3NH_3. *Inorganic Chemistry* **1999,** 38, 2868–2873.

100. Bowden, M. E.; Gainsford, G. J.; Robinson, W. T., The room temperature structure of ammonia borane. *Australian Journal of Chemistry* **2007,** 60, 149–153.

101. Yang, J. B.; Lamsal, J.; Cai, Q.; James, W. J.; Yelon, W. B., Structural evolution of ammonia borane for hydrogen storage. *Applied Physics Letters* **2008,** 92, 091916–1–091916–3.

102. Shore, S. G.; Parry, R. W., Chemical evidence for the structure of the "Diammoniate of Diborane." II. The preparation of ammonia borane. *Journal of the American Chemical Society* **1958,** 80, 8–12.

103. Hu, M. G.; Geanangel, R. A.; Wendlandt, W. W., The thermal decomposition of ammonia borane. *Thermochimica Acta* **1978,** 23, 249–255.

104. Böddeker, K. W.; Shore, S. G.; Bunting, R. K., Boron-nitrogen chemistry. I. Synthesis and properties of new cycloborazanes, $(BH_2NH_2)_n$. *Journal of the American Chemical Society* **1966,** 88, 4396–4401.

105. Komm, R.; Geanangel, R. A.; Liepins, R., Synthesis and studies of poly(aminoborane), $(H_2NBH_2)_x$. *Inorganic Chemistry* **1983,** 22, 1684-1686.

106. Sit, V.; Geanangel, R. A.; Wendlandt, W. W., The thermal dissociation of NH_3BH_3. *Thermochimica Acta* **1986,** 113, 379-382.

107. Gerry, M. C. L.; Lewis-Bevan, W.; Merer, A. J.; Westwood, N. P. C., The infrared spectrum of gaseous aminoborane, $H_2N{=}BH_2$: Location of the fundamentals and rotational structure in the 4_{10} Band (BN Stretching vibration at 1337 cm^{-1}). *Journal of Molecular Spectroscopy* **1985,** 110, 153–163.

108. Baitalow, F.; Baumann, J.; Wolf, G.; Jaenicke-Rossler, K.; Leitner, G., Thermal decomposition of B–N–H compounds investigated by using combined thermoanalytical methods. *Thermochimica Acta* **2002,** 391, 159-168.

109. Smith, R. S.; Kay, B. D.; Schmid, B.; Li, L.; Hess, N.; Gutowski, M.; Autrey, T., Mechanistic studies of hydrogen formation from amineborane complexes. *Prep Paper American Chemical Society Division of Fuel Chemistry* **2005,** 50, 112-113.

110. Stowe, A. C.; Shaw, W. J.; Linehan, J. C.; Schmid, B.; Autrey, T., *In situ* solid state ^{11}B MAS-NMR studies of the thermal decomposition of ammonia borane: mechanistic studies of the hydrogen release pathways from a solid state hydrogen storage material. *Physical Chemistry Chemical Physics* **2007,** 9, 1831–1836.

111. Sana, M.; Leroy, G.; Wilante, C., Enthalpies of formation and bond energies in lithium, beryllium and boron derivatives. 2. Dative, single and triple bonds. *Organometallics* **1992,** 11, 781–787.

112. Geanangel, R. A.; Wendlandt, W. W., A TG–DSC study of the thermal dissociation of $(NH_2BH_2)_x$. *Thermochimica Acta* **1985,** 86, 375–378.

113. Baumann, J.; Baitalow, F.; Wolf, G., Thermal decomposition of polymeric aminoborane $(H_2BNH_2)_x$ under hydrogen release. *Thermochimica Acta* **2005,** 430, 9-14.

114. Wang, S.; Mao, W. L.; Autrey, T., Bonding in boranes and their interaction with molecular hydrogen at extreme conditions. *Journal of Chemical Physics* **2009,** 131, 144508–1 – 144508–6.

115. Wideman, T.; Sneddon, L. G., Convenient procedures for the laboratory preparation of borazine. *Inorganic Chemistry* **1995,** 34, 1002–1003.

Chapter 2

Experimental

2.1 Crystallography[1-3]

2.1.1 Crystal Systems and Unit Cells

In the solid state, all crystalline materials adopt a regular distribution of atoms or ions in three dimensions. This arrangement can be denoted by a repeatable unit, a unit cell. By definition the unit cell is the simplest portion of the structure that when repeated by translation shows the full symmetry of the crystal structure. A three dimensional unit cell is shown in figure 2.1.

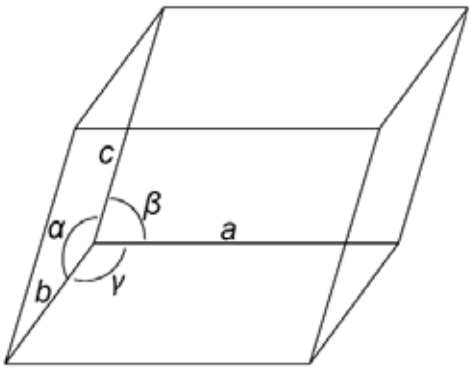

Figure 2.1 **–** General three-dimensional unit cell definition

The angles and lengths that define the unit cell size are the lattice parameters. In the unit cell in figure 2.1 the lattice parameters may take any values and as a result the cell shown has no symmetry. An increasing amount of symmetry in the unit cell produces relationships between the various cell parameters, which leads to the seven crystal systems, table 2.1. These are the only independent unit cell shapes possible in three-dimensional crystal structures.

Table 2.1 – The dimensions and essential symmetry features of the seven crystal systems

Crystal System	Unit Cell Dimensions	Essential Symmetry	Allowed Lattices
Cubic	$a = b = c$ $\alpha = \beta = \gamma = 90°$	Four threefold axes	P, I, F
Tetragonal	$a = b \neq c$ $\alpha = \beta = \gamma = 90°$	One fourfold axis	P, I
Orthorhombic	$a \neq b \neq c$ $\alpha = \beta = \gamma = 90°$	Three twofold axes	P, I, F, C
Hexagonal	$a = b \neq c$ $\alpha = \beta = 90°$ $\gamma = 120°$	One sixfold axis	P
Trigonal / Rhombohedral	$a = b = c$ $\alpha = \beta = \gamma \neq 90°$	One threefold axis	R
Monoclinic	$a \neq b \neq c$ $\alpha = \gamma = 90°$ $\beta \neq 90°$	One twofold axis	P, C
Triclinic	$a \neq b \neq c$ $\alpha \neq \beta \neq \gamma \neq 90°$	None	P

2.1.2 Lattices

For crystalline materials, the array of how atoms, ions or molecules are repeated is described as a lattice. Lattices provide no information about actual position of atoms or molecules, but show the translational symmetry of the material by locating equivalent positions, which are known as lattice points. The environment of an atom placed on one of these lattice points is identical to that placed on any other lattice point.

There are four potential lattice types for three-dimensional crystals. The simplest of which is a primitive cell, P, containing only a single lattice point, at the cell corners, the only purely translational symmetry is that of the unit cell. The body centred lattice, I, has an additional lattice point located at the cell centre, while the face centred lattice, F, has additional lattice points at the centre of all the unit cell faces. Lattices with lattice points in just one face are also known as face centred. Conventionally, these lattices are known as C-type lattices, where the additional lattice point is located at the centre of the face of the *ab* plane. It is also possible to have A and B centring, but redefining *a*, *b* and *c* directions results in a C type lattice.

The combination of the seven crystal classes with the four lattice types gives rise to 14 possible combinations, which are known as Bravais lattices, table 2.1.

2.1.3 Lattice Planes and Miller Indices

Lattice points which form a repeatable array in 3D can be connected by lattice planes. Each plane is part of a parallel set of equally spaced planes and each lattice point must lie on one of the lattice planes. These imaginary planes extend throughout the complete crystal structure, intersecting the unit cell at specific points, which are described by Miller indices. In a 3D structure three indices are required and are labelled h, k and l, which take values that are either positive or negative integers or zero. For a given set of planes the values of h, k and l are given by the reciprocal of the fractional intercepts along each of the cell directions. Where planes are parallel to one of the unit cell directions, the intercept is at infinity and therefore the Miller index for the axis is $^1/_\infty = 0$. Some examples of lattice planes and their Miller indices are shown in figure 2.2. The separation between equivalent planes is known as the d-spacing, d_{hkl}, which is also the perpendicular distance from the origin to the nearest plane. The relationship between the d-spacing and the lattice parameters can be determined geometrically, but is dependent on the crystal system. For a cubic system it can be calculated using the following equation:

$$d = \frac{a}{\sqrt{h^2 + k^2 + l^2}}$$

Equation 2.1

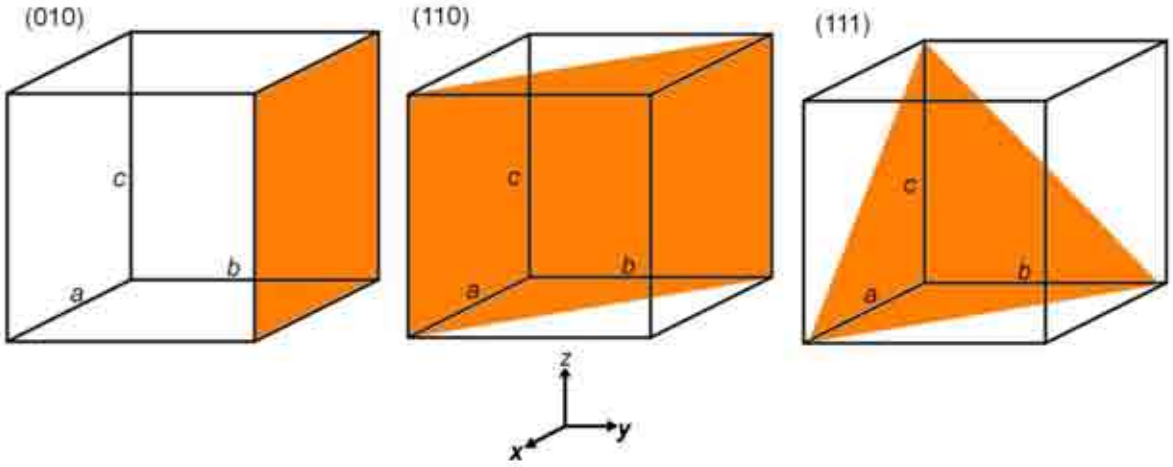

Figure 2.2 – Examples of lattice planes and their Miller indices

2.1.4 Crystal Structures

A crystal structure is described by lattice parameters, atomic positions within the unit cell and the symmetry of the unit cell. The inclusion of atoms within a unit cell can result in additional translational symmetry aspects to those that describe the Bravais lattices that must be considered. Atomic arrangements also result in screw axes and glide planes. The inclusion of all symmetry possibilities in 3D results in 230 space groups, which completely describe the symmetry of the unit cell.

2.2 X-Ray Diffraction[1, 2, 4]

2.2.1 Generation of X-rays

X-rays are a form of electromagnetic radiation that are able to interact with electrons in matter. They are produced when high energy particles such as electrons collide with matter, resulting in the particles slowing down or stopping. In the case of a standard laboratory X-ray diffractometer this matter is most commonly copper metal, as was the case in this study. The resultant X-ray spectrum is composed of two elements, a broad background formed from the bremsstrahlung radiation and a number of sharp maxima. These sharp maxima are produced by well defined electronic transitions, which occur when the collision is of sufficient energy to eject an electron from the metal atoms' core orbitals. The filling of this hole by electron decay from a higher energy orbital occurs with the emission of radiation. Figure 2.3a shows an outer electron from the 2p or 3p orbitals dropping down to fill the vacant 1s orbital; the energy released in this process appears as X-ray radiation. The transitions are accompanied by fixed values of wavelength; in the case of copper, the 2p → 1s transition is called K_α and has a wavelength of 1.5418 Å, while the 3p → 1s transition is referred to as K_β, with a wavelength of 1.3922 Å. The K_α transition occurs more frequently and with more intensity than K_β and is more commonly used in diffraction, as was the case in this study. Both K_α and K_β appear as close doublets due to the two possible spin states of the 2p electron. A typical X-ray spectrum for a copper X-ray source is shown in figure 2.3b.

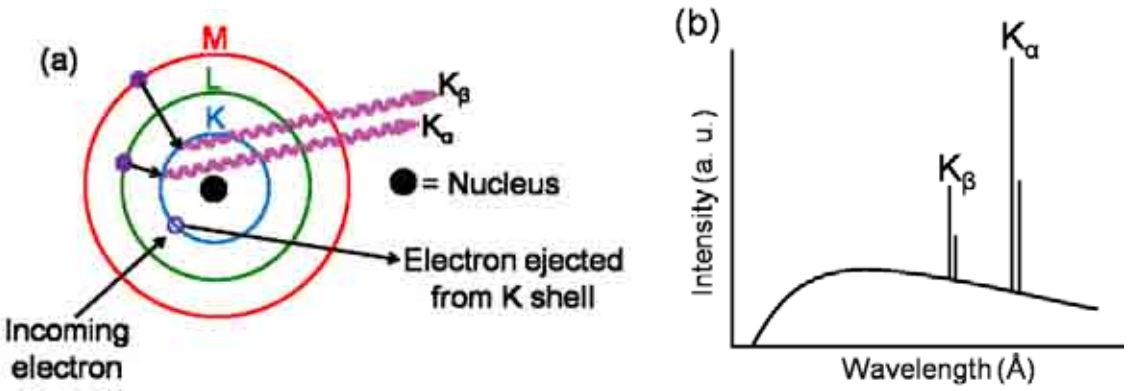

Figure 2.3 – (a) Generation of X-rays, (b) X-ray spectrum of copper

X-ray diffraction requires a single intense single X-ray wavelength. This is achieved through monochromation. In this study a single germanium crystal was employed. The crystal is oriented so that one set of planes which diffracts strongly is at the Bragg angle to the incident beam. The Bragg angle is calculated for the wavelength of $K_{\alpha 1}$ so that only the $K_{\alpha 1}$ rays are diffracted, resulting in monochromatic radiation.

2.2.2 Bragg's Law

The Bragg approach to diffraction is to regard crystals as built up in layers or planes so that each acts as a semi-transparent mirror. A proportion of the X-rays are reflected off a plane with the angle of reflection equal to the angle of incidence, while the remainder are transmitted and subsequently reflected by other later planes. The derivation of Bragg's law is shown in figure 2.4. Two X-ray beams, 1 and 2, are reflected from adjacent planes, A and B. Compared to beam 11' beam 22' has to travel the extra distance xyz and for the reflected beams 1' and 2' to be in phase, this distance must be equal to an integer number of wavelengths.

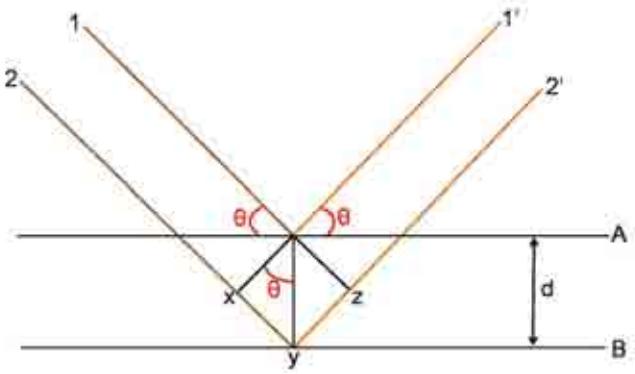

Figure 2.4 – Derivation of Bragg's law

The relationship between the d-spacing and the angle of incidence, θ, to the distance xy is given by:

$$xy = yz = d \sin\theta$$

$$\text{Hence, } xyz = 2d \sin\theta$$

$$\text{Enforcing the condition that, } xyz = n\lambda$$

$$\text{Gives Bragg's Law: } n\lambda = 2d \sin\theta \qquad \text{Equation 2.2}$$

When Bragg's law is satisfied, the reflected beams are in phase and there is constructive interference. At angles other than the Bragg angle the reflected beams are out of phase and destructive interference occurs. In real crystals thousands of planes are present, which means that if the incident angle is incorrect by more than a few tenths of a degree, complete cancellation of the reflected beam usually occurs.

2.2.3 Powder Diffraction

Powder samples contain a massive number of very small crystallites which randomly adopt every possible orientation, consequently the lattice planes are also present in every possible orientation. An X-ray beam incident on a powder sample will be diffracted in all possible directions as governed by the Bragg equation. The effect of this is that each lattice spacing in the crystal gives rise to a cone of diffraction, figure 2.5. These cones consist of a set of closely spaced dots, where each dot represents diffraction from a single crystallite within the sample. The positions of the various diffraction cones can be determined by a diffractometer, which uses an X-ray detector to measure the positions of diffracted beams. The detector scans a range of 2θ values at a constant angular velocity and produces a pattern, with the signal intensity being directly proportional to the amount of X-rays hitting the detector.

Powder diffraction allows the qualitative identification of crystalline phases present in a sample, but gives no direct information regarding their chemical composition. Every crystalline material has a characteristic powder pattern which can be used as a basis to identify the phases present in a pattern with the two variables in a pattern being peak position and intensity.

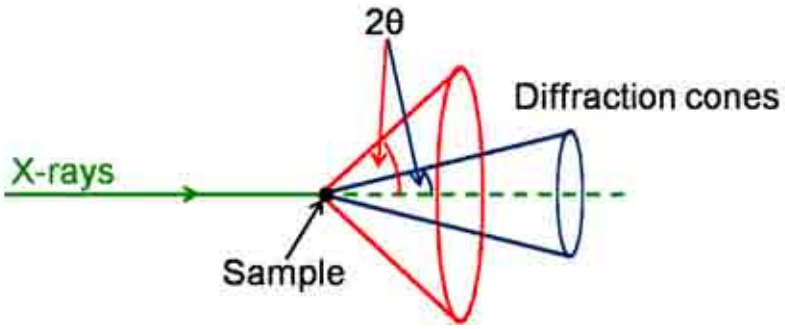

Figure 2.5 – Formation of cones of diffracted radiation

Peak positions are determined by the wavelength of radiation used for powder diffraction and the unit cell size, shape and symmetry. The peak positions correspond to the separation distances of lattice planes within the unit cell.

Peak intensities are important as they are necessary in order to solve crystal structures and they are required to identify phases present in a sample. Different parameters are capable of affecting either the absolute or relative intensities of the peaks. Absolute intensities are dependent on experimental factors such as data collection time and the scattering power of the sample as well as instrumental factors such as the intensity of the radiation source and the efficiency of the detector. The relative overall intensity of peaks for one phase compared to another is due to the relative abundance of that phase. The relative intensities of peaks for a specific phase are dependent on the types of atom present as well as their position in the unit cell. Preferred orientation can also affect the observed intensities. The sample is assumed to be a collection of crystallites of completely random orientation. However, if the crystallites are of a certain size or shape, such as plate-like or needle-like crystallites, they may align themselves into a non-random ordering. This ordering of crystallites can lead to errors in the observed intensities, with disproportionally high intensities from lattice planes in the aligned crystallographic plane.

The intensity of a Bragg peak can be calculated from the following equation:

$$I_{(hkl)} = K_{(hkl)} F^2_{(hkl)} m_{(hkl)} A_{(hkl)} Lp_{(hkl)}$$

Equation 2.3

The terms of equation 2.3 are described below.

$K_{(hkl)}$ = Proportionality constant

$m_{(hkl)}$ = The multiplicity of the Bragg reflection, taking into account the number of planes which contribute to a reflection

$A_{(hkl)}$ = An absorption correction factor, which takes into account the proportion of the incident and diffracted X-rays absorbed by the sample. The extent of absorption depends upon the sample composition and the sample thickness in the direction of diffraction

$Lp_{(hkl)}$ = This contains the Lorentz factor, which is the correction for the variation in the probability of observing a Bragg reflection at the diffraction angle and the Polarisation factor, which accounts for the polarisation of the X-ray beam

$F^2_{(hkl)}$ = The structure factor, which has the greatest influence upon the intensity of the Bragg peaks. It describes the interaction of the diffracted radiation with the atoms in the unit cell. It is calculated by:

$$F_{(hkl)} = \sum_n f_n N_n \exp[2\pi i(hx_n + ky_n + lz_N)] \exp\left[-\frac{B_n \sin^2\theta}{\lambda^2}\right] \quad \text{Equation 2.4}$$

The terms of equation 2.4 are described below.

f_n = The atomic scattering factor of the nth atom in the unit cell with the coordinates (x_n, y_n, z_n)

N_n = The site occupancy of the nth atomic site

x_n, y_n, z_n = Coordinates of the nth atom in the unit cell

$\left[-\frac{B_n \sin^2\theta}{\lambda^2}\right]$ = The thermal factor, which takes into account the reduction of intensity due to thermal vibrations of the atoms. B is proportional to the mean square oscillations of the atoms and is temperature dependent

2.2.4 Laboratory X-ray Diffraction

X-ray data were collected using a Bruker D8 diffractometer operating in transmission mode. Cu $K_{\alpha 1}$ radiation, λ = 1.5406 Å, was used, with a germanium crystal as a monochromator employed to focus the X-rays into a convergent beam. A movable position sensitive detector with a step size of approximately 0.02° was used. The samples were rotated in the plane perpendicular to the X-ray beam. Samples were prepared by grinding in an argon filled glove box and sealed from the atmosphere between two layers of Scotch® Magic™ tape.

2.3 Rietveld Analysis[5]

The principal aim of Rietveld analysis is to refine structural parameters in order to obtain a satisfactory fit for the diffraction data. The refinement is built upon a structural model using a collection of structural and experimental parameters that describe the crystal structure, which allows an accurate diffraction pattern to be calculated for a given crystal structure. In the 1960's it became apparent that a wealth of information could be obtained from a powder XRD pattern. Rietveld[6] developed a method for analysing powder diffraction patterns that focused on minimising the difference between observed and calculated patterns instead of minimising the difference between individual reflections. The Rietveld method uses a least-squares method where the structural and experimental parameters are varied until the best fit is obtained between the observed and calculated diffraction patterns. The function minimised during the least squares refinement is the residual, S_y, equation 2.5.

$$S_y = \sum_i w_i (y_i(obs) - y_i(calc))^2 \qquad \text{Equation 2.5}$$

where: $w_i = 1/y_i$

y_i(obs) = observed intensity at the i^{th} step

y_i(calc) = calculated intensity at the i^{th} step

The Rietveld method is concerned with refinement of a structural model rather than structure solution and so as good a starting model as possible is required. Despite this the method can play a very important role in structure solution, as well as playing a key role in the final step of structure determination, when the final refinement of the determined structure is performed. The determination of a crystal structure can be described in a series of steps. The diffraction pattern is first indexed and the crystal system and lattice parameters are determined. This is then followed by the identification of the space group and subsequent determination of an approximate structure. The final step is the refinement of the structure through the Rietveld method.

A visual inspection of a Rietveld plot with respect to the observed, calculated and difference plots is a good way of following the progress of a Rietveld refinement. For a perfect fit, the difference plot will be a straight line. However, a key feature of the method is that during refinement a number of statistics are produced to show how the fit is affected by variations in the parameters. These numerical values are a good indication of the "goodness of fit" of the refinement. A statistical value based on the fitting of the complete calculated to the observed pattern is that of the '*R*-weighted pattern,' R_{wp}, equation 2.6. This statistic is the best indication of how well the refinement is progressing as it contains the residual, S_y, (equation 2.5) being minimised. However, it is susceptible to producing artificially high values if not all the peaks in the pattern are accounted for, but in this case this should be identifiable from inspection of the difference plot. The value may also be artificially low if the refined background is high, because it is easier to obtain a good fit to a slowly varying background than to sets of Bragg reflection profiles. For this reason background corrected versions of this and other *R*-values, which can all be expressed as percentages, can be calculated. The example of the background corrected R_{wp} value is shown by equation 2.7.

$$R_{wp} = 100\left[\frac{\sum w_i\left[y_i(obs) - y_i(calc)\right]^2}{\sum w_i\left[y_i(obs)\right]^2}\right]^{1/2}$$

Equation 2.6

$$R_{wp}' = 100\left[\frac{\sum w_i[y_i(obs) - y_i(calc)]^2}{\sum w_i[y_i(obs) - Bkg_i]^2}\right]^{1/2}$$

Equation 2.7

The final R_{wp} value should approach the statistically expected R-value, R_{exp}, equation 2.8. which indicates the best possible R-value for a data set based on the quality of the data.

$$R_{exp} = 100\left[\frac{N - P - C}{\sum w_i[y_i(obs)]^2}\right]^{1/2}$$

Equation 2.8

N = Number of observables P = Number of refined parameters

C = Number of constraints used

A third useful numerical statistic is that of χ^2, equation 2.9, the square of the ratio between R_{wp} and R_{exp}; the lower the value of χ^2, the better the fit. This is a particularly useful statistic as it includes the number of refined parameters. The fit to the observed data can generally be improved by increasing the number of refined parameters. Very small values of χ^2 can show that errors due to poor quality of data outweigh the errors with structural model and a data set with a high background, which is easily modelled, can also significantly reduce this value.

$$\chi^2 = \left[\frac{R_{wp}}{R_{exp}}\right]^2$$

Equation 2.9

A final indication of the quality of a Rietveld refinement is the chemical sense of the structural model obtained. Atomic distances between bonding and non-bonding atoms as well as bond angles should be sensible and fractional occupancies should be consistent with the chemical composition of the sample.

2.4 Mass Spectrometry[7, 8]

Mass spectrometry is defined as the study of systems that causes the formation of gaseous ions which are subsequently characterised by their mass to charge ratios (m/z) and relative abundances. Selected m/z ratios can be analysed in order to determine their amount in a given sample. Mass spectrometry involves three main processes: ionisation, separation and detection.

Ionisation

Ionisation is the process that creates charged species by the removal or addition of an electron or proton. There are a number of ionisation techniques that can be used in mass spectrometry including chemical ionisation, electrospray ionisation and fast atom bombardment. However, the most common form of ionisation for gaseous analytes is that of electron impact. This was the only form of ionisation used in this study.

Electron impact uses a tungsten filament to generate a beam of electrons which is then accelerated in order to knock out an electron from neutral molecules to produce singly charged cations. Single ionisation can be promoted and multiple ionisation avoided by tuning the energy of the electron beam. This is favourable as multiple ionisation will affect the m/z values of the ions under analysis.

Ionisation can also result in fragmentation of ionic species. Excess energy from the ionisation process may be sufficient to result in the fragmentation of the ionic species into smaller fragments. The charged fragment can also be detected with a lower m/z ratio.

Ion Separation

Following ionisation a positively charged ion repeller forces the cations out of the ionisation chamber and they are then accelerated through a voltage, giving them all the same kinetic energy into a finely focused beam and into the analyser where separation occurs. Ion separation is based on the fact that the charged species have different m/z ratios. Quadrupole mass analysers are the most common method of ion

separation, and use an electric field provided by parallel electrodes to selectively stabilise or destabilise the paths of ions passing through it. The frequency of the electric field is varied to select which m/z value is stabilised and hence which ions are able to reach the detector. All other ions with different m/z values become neutralised through collisions and are therefore not detected. It is also important that the system operates under a vacuum so that the ions of interest do not collide with other species in the system during the ion separation process. Furthermore, the vacuum system is heated to minimise the amount of water present in the system.

Detection

The ions that reach the detector produce an ion current on collision with it, which the detector measures, outputting the data as a mass spectrum. For small samples, where high sensitivity is required, a secondary electron multiplier detector is used. Secondary electrons are produced by the initial collision of the ions with the detector, which is then amplified by a series of electrodes, each one at an increased potential. This results in increased sensitivity of the order of $\times 10^6$.

2.5 Temperature Programmed Desorption

Temperature programmed desorption (TPD) is a generic term for the controlled heating of a sample while the desorption products are monitored. A sample is heated under a flowing atmosphere at a controlled heating rate while the gaseous desorption products are analysed by mass spectrometry. A home built TPD apparatus was used in this study.

Temperature programmed desorption under a flowing argon atmosphere was monitored using a mass spectrometer, TPD–MS. The flow of argon within the apparatus was regulated using a mass flow controller (Hastings 200 Series, Teledyne) at a constant rate of 100 ml min^{-1}. The argon carrier gas flowed over the top of the reaction chamber. The sample (~0.1 g) was weighed into a quartz reaction tube (7 mm O/D, 4 mm I/D) inside an argon filled glove box and sealed vertically in the reaction chamber. The sealed reaction chamber was transferred to the TPD

apparatus while avoiding exposure of the sample to the atmosphere. An internal thermocouple, in contact with the sample, was used to control the sample temperature during experiments, with a barrel furnace surrounding the reaction chamber for heating. Endothermic and exothermic events were sometimes visible in the temperature trace of the TPD due to the thermocouple position within the sample. A quadrupole mass spectrometer (HPR–20, Hiden Analytical) was used to monitor the gaseous desorption products, with a secondary electron multiplier (SEM) detector. A schematic diagram of the TPD–MS setup is shown in figure 2.6.

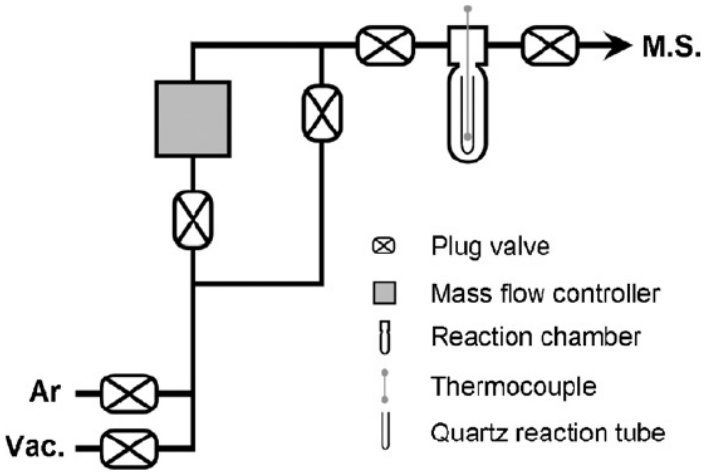

Figure 2.6 – Schematic diagram of the TPD–MS apparatus[9]

Calibration

A calibration gas (BOC Speciality Gases, 4736 ppm H_2, 4898 ppm NH_3, balance Ar) was used in order to determine the true sensitivity of the mass spectrometer with respect to H_2 and NH_3. There is a problem with detection of NH_3 in a mass spectrometer because the main fragment, NH_3^+, has the same m/z value as the OH^+ fragment of H_2O, which is often naturally present in vacuum systems. Therefore, the NH_2^+ fragment, approximately 80% the intensity of the NH_3^+ fragment, was used to determine the true amount of NH_3.

The calibration gas was flowed into the system and the observed partial pressures (P_n) for mass channels (m/z) 2 (H_2^+), 16 (NH_2^+), 17 (NH_3^+ / OH^+), 18 (H_2O^+), 28 (N_2^+), 32 (O_2^+) and 40 (Ar^+) were recorded until a consistent signal was achieved. The

background signals for mass channels (m/z) 2 (H_2^+) and 16 (NH_2^+) were also determined for the pure argon carrier gas.

The observed partial pressure signals for H_2 and NH_2 (P_2 and P_{16}) were converted to fractions (x_2 and x_{16}) of the observed argon signal (P_{40}):

$$x_2 = \frac{P_2}{P_{40}} \qquad x_{16} = \frac{P_{16}}{P_{40}}$$

Equation 2.10

The observed fractional signals determined for H_2 and NH_2 for the pure argon carrier gas (x_2^0 and x_{16}^0) were deducted from the respective fractional signals from the calibration gas, giving background subtracted fractional signals. Dividing these values by the true molar fraction provided with the calibration gas certificate, gives the relative sensitivity, R, values for H_2 and NH_3:

$$R_{H_2} = \frac{x_2 - x_2^0}{4.736 \times 10^{-3}} \qquad R_{NH_3} = \frac{x_{16} - x_{16}^0}{4.898 \times 10^{-3}}$$

Equation 2.11

The observed signals for H_2^+ and NH_2^+ from TPD–MS experiments could then be corrected by these determined relative sensitivity values, giving true values for H_2 and NH_3.

For the TPD–MS experiments the MS data was collected for an appropriate time before the TPD heating profile commenced to allow determination of the background signals for mass channels 2 (H_2^+) and 16 (NH_2^+) (x_2^0 and x_{16}^0). The MS data was again converted to a fraction of the argon signal and the background signals determined before starting the heating profile were subtracted. Corrected molar fractions of H_2 and NH_3 in the gas stream were obtained by dividing the corrected fractional signals by the determined R values, equation 2.12. These corrected values were able to give accurate relative amounts of H_2 and NH_3 released.

$$x_{H_2}^* = \frac{x_2 - x_2^0}{R_{H_2}} \qquad x_{NH_3}^* = \frac{x_{16} - x_{16}^0}{R_{NH_3}}$$

Equation 2.12

Simulated gravimetric data could be produced from further processing of the molar fractions of H_2 and NH_3 in the gas stream as a consequence of a mass flow controller being incorporated in the TPD setup. The corrected MS data detailed the molar fractions of H_2 and NH_3 present at time, t, ($x^*_{H_2}$(t) and $x^*_{NH_3}$(t)) at regular time intervals (δt, minutes) determined by the rate of MS data collection, which was approximately three complete mass spectra per minute. With the argon carrier gas flowing at a known rate of 100 ml min^{-1} it was possible to determine the volume of each gas (V_{H_2} and V_{NH_3}) released during the timescale for collection of one MS spectrum along with the total volume (ml) of each gas desorbed during a certain time interval, *V*(t):

$$V_{H_2}(t) = \sum_{t=0}^{t} 100 \times \delta t \times x^*_{H_2}(t) \quad V_{NH_3}(t) = \sum_{t=0}^{t} 100 \times \delta t \times x^*_{NH_3}(t)$$

Equation 2.13

H_2 and NH_3 have molar volumes of 24.804 l mol^{-1} and 24.532 l mol^{-1}, respectively, at room temperature and pressure. The calculated volume of gas released was used to provide an estimate of the number of moles of H_2 and NH_3 by multiplying the calculated volumes by 4.032 × 10^{-5} and 4.076 × 10^{-5}, respectively. Provided the initial sample mass and molecular mass were known it was possible to express the number of moles of each gas released in terms of the number of moles of the starting sample.

Multiplying the molecular mass of the gas by the calculated number of moles of the gas released gave a simulated mass of each gas released, equations 2.14 and 2.15. This calculated mass of gas released could then be subtracted from the initial sample mass (m_s, grams) and expressed as a percentage of the starting mass and hence a simulated gravimetric plot could be plotted.

$$wt\%(t) = 100 \times \frac{m_s - \sum_{t=0}^{t} VH_2(t) \times 4.032 \times 10^{-5} \times 2.02}{m_s}$$

Equation 2.14

$$wt\%(t) = 100 \times \frac{m_s - \sum_{t=0}^{t} VNH_3(t) \times 4.076 \times 10^{-5} \times 16.02}{m_s}$$

Equation 2.15

This form of data analysis is complicated, however, it does allow for a more complete analysis of the desorbed gases from the starting sample. It was particularly beneficial for analysis of samples of reaction mixtures where NH_3BH_3 was present. Upon heating NH_3BH_3 undergoes a voluminous swelling, which means it is unsuitable for analysis by more delicate methods of thermogravimetric analysis, whereas TPD–MS is much more resistant to poorly behaved samples.

2.6 Intelligent Gravimetric Analysis

An Intelligent Gravimetric Analyser (IGA, Hiden Analytical) is a pressure controlled thermo-gravimetric balance which allows complete control of the environment. The sample is inertly loaded into a quartz sample holder and placed onto a hang-down which is attached to a microbalance head. The sample mass is measured under different conditions so that the changes in weight can be monitored under temperature and pressure changes. The sample, microbalance head and counterbalance are all subject to the same environment which helps reduce buoyancy effects on the observed sample mass. An external furnace, surrounding the reaction tube, is used to heat the sample, with the sample temperature monitored by a positive temperature coefficient sensor located next to the sample.

In this study the IGA was used to obtain thermogravimetric data of the samples under investigation. A constant flow rate and pressure of the argon carrier gas was therefore established within the IGA reactor through external mass flow controllers. The argon carrier gas flowed directly over the sample at a rate of 100 ml min^{-1} and a pressure of 1 bar, which collected gaseous desorption products and transported them to a mass spectrometer (HPR20-QIC, Hiden Analytical) for analysis.

2.7 Thermogravimetric Analysis

Thermogravimetric analysis (TGA) involves the measurement of the mass of a sample with varying temperature. The sample is mounted onto a thermocouple within the furnace. Argon carrier gas flows over the sample and collects desorbed gases

before carrying them to a mass spectrometer for analysis. The thermocouple is connected to a microbalance which records the mass of the sample during the experiment.

2.8 Solid State Nuclear Magnetic Resonance Spectroscopy[10, 11]

Nuclear magnetic resonance (NMR) spectroscopy is an experimental method capable of providing structural information regarding the local environmental configuration of nuclei. It is especially useful when information obtainable by other methods, such as XRD is limited by the absence of long-range order in the sample being studied. The technique exploits the magnetic properties of atomic nuclei within a sample, which have an intrinsic nuclear spin angular momentum. All elements and all of their isotopes have a nuclear spin quantum number, I, which takes a value of $^{n}/_{2}$, where n is an integer. However, not all nuclei are NMR active: the spin quantum number must be non-zero and in these cases the nucleus will have a magnetic moment, μ, equation 2.16. The nuclei under investigation in this study, ^{11}B and ^{23}Na, both have a spin quantum number of $^{3}/_{2}$.

$$\mu = \frac{h\gamma}{2\pi}\left[I(I+1)\right]^{1/2}$$

Equation 2.16

γ = the gyromagnetic ratio (the ratio of magnetic dipole moment to angular momentum); this is characteristic of a particular isotope of a particular element.

When a magnetic field, B, is applied, the nuclear moments orient themselves, with a nucleus of spin I having 2I + 1 possible orientations, identified by the value of the magnetic quantum number, m_I, which takes the values I, I−1, I−2, ..., −I. For ^{11}B and ^{23}Na, m_I has the values $-^{3}/_{2}$, $-^{1}/_{2}$, $^{1}/_{2}$, $^{3}/_{2}$. The splitting of a nucleus of I = $^{3}/_{2}$ in an applied magnetic field is shown in figure 2.7. This is known as Zeeman splitting. The selection rule for NMR transitions dictates that $\Delta m_I = \pm 1$. The transition energy is given by equation 2.17. As $\Delta E = h\nu$, the difference in energy between the energy levels has a corresponding frequency given by equation 2.18. It is this energy transition that is measured by the NMR technique.

$$\Delta E = \frac{\gamma h B}{2\pi}$$ Equation 2.17

$$\nu = \frac{\gamma B_0}{2\pi}$$ Equation 2.18

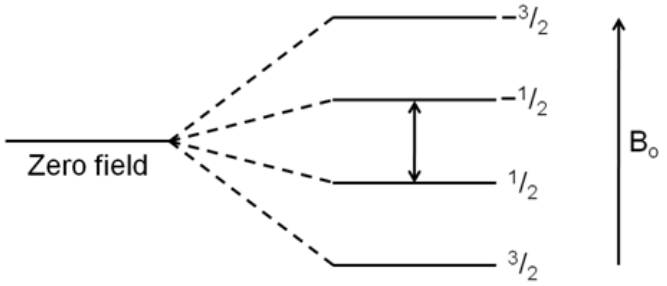

Figure 2.7 – Energy levels for a nucleus (I = $^3/_2$) in a magnetic field

When radiofrequency radiation of the same energy as the splitting between the spin states is applied, a transition between the levels is able to take place.

For a nucleus of spin I = $^1/_2$ there are two possible orientations of nuclear spin, m_I = $\pm^1/_2$. $m_I = +^1/_2$ is the lowest energy more stable state, α, and the upper state has m_I = $-^1/_2$, β. There are two allowed transitions ($\Delta m_I = \pm 1$), α→β, which corresponds to an absorption of energy and β→α corresponds to energy emission. The population difference between the spin states is governed by the Boltzmann distribution, equation 2.19. Increasing the field strength will increase the population difference and there will be a net absorption of energy and hence an increase in the strength of the signal.

$$\frac{N_\beta}{N_\alpha} = \exp\left(h\nu / kT\right)$$ Equation 2.19

The excess population in the lower state is often very low, ~1 in 10^5, which is the basic reason behind the low sensitivity of the NMR technique. The compensation for this is that the absorption coefficient for all nuclei is constant and therefore the NMR signal is directly proportional to the number of nuclei producing it. This is important for the interpretation of spectra because it means the area under a spectral peak is directly related to the number of nuclei giving rise to it and this can be determined by

integration. This allows determination of the relative abundance of the different sites for a specific nucleus within each sample.

The Chemical Shift

When a molecule containing the nuclei under consideration is subjected to the magnetic field, the electrons within the molecule shield the nuclei from the external applied field. The field experienced by the nucleus is therefore not equal to the applied field. The difference, referred to as the nuclear shielding, is proportional to the applied field.

The chemical shift is defined as the difference between the resonance frequency of a particular nucleus and that of a reference standard, equation 2.20. It is generally reported on the δ scale (ppm).

$$\delta = \left(\frac{\nu - \nu_{ref}}{\nu_{ref}} \right) \times 10^6$$

Equation 2.20

The factors that determine chemical shifts are due to atoms residing in different chemical environments which include coordination number, nearest neighbour type, type of next nearest neighbour and crystallographic inequivalence. A change in any of these environmental and chemical factors would result in a change in the electron density, hence modifying the shielding effect of the electrons and resulting in a change in the chemical shift.

Quadrupolar Interaction

The symmetry of the charge distribution of the nucleus plays a significant factor in the appearance of spectral lineshapes. Nuclei with I = ½ have spherical electric charge distributions, similar to a 1s orbital in hydrogen, which results in gaussian lineshapes. Those nuclei with I ≥ 1 have a non-uniform distribution of electric charge, resulting in distorted spheres and a charge gradient across the nucleus. These nuclei are quadrupolar, and both ^{11}B and ^{23}Na fall into this category. A non-spherical charge distribution can interact with an electric field gradient caused by asymmetry, resulting in a change in the energy level in addition to the Zeeman effect. The strength of the interaction is measured as the quadrupole moment. Linewidths are broadened as a

result of quadrupolar broadening, which can make it difficult to identify reliable chemical shifts.

For nuclei with a nuclear spin I > $^1/_2$, the non-spherically symmetrical nuclear electric charge distribution interacts with any electric field gradients present, disturbing the previously equally split Zeeman levels. In the case of ^{11}B and ^{23}Na where I = $^3/_2$, the application of a magnetic field results in the four previously degenerate states becoming distinct energy levels, described by the magnetic quantum number m_I, figure 2.7. The effect of the first-order quadrupolar interaction with the electric field gradient is to disrupt each of the nuclear energy levels by a small frequency. This disruption causes the non-central transitions ($m \neq ½$) to be sufficiently shifted so that they appear as satellite peaks either side of a more intense central peak due to the m = ±½ transition within the NMR spectrum. The central transition, $m_{½} \rightarrow m_{-½}$ is unaffected. The first-order disruption of the energy levels is shown in figure 2.8.

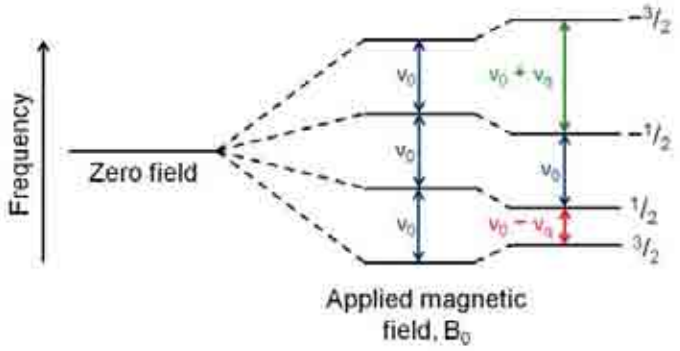

Figure 2.8 – Quadrupolar splitting of the nuclear energy levels within an applied magnetic field

In cases where the quadrupolar coupling is sufficiently strong a second-order disruption in addition to the first-order effect is observable, so that the energy bands are again shifted. This shift results in the central line undergoing a significant anisotropic broadening.

Recording spectra at high field helps to minimise the second order quadrupolar broadening, because the intensity of the quadrupolar interaction is inversely proportional to field strength; hence, at higher fields, sharper peaks can be obtained.[12] The effect of increased field strength on the quadrupolar lineshape is shown in figure 2.9.[13]

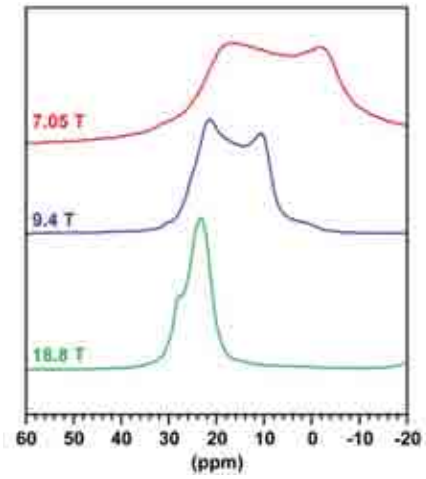

Figure 2.9 – ^{11}B MAS NMR spectra of polyborazylene recorded at various fields[13]

Magic Angle Spinning

In solution NMR the rapid molecular tumbling averages many line broadening interactions to zero. However, in the solid state these interactions are not reduced to zero and result in broad lines. Line broadening interactions that affect the NMR spectrum in the solid state are chemical shift anisotropy, dipolar and quadrupolar interactions. It is, however, possible to reduce this line broadening by the experimental technique of magic angle spinning, MAS. This technique involves rapidly rotating the sample about an axis inclined at θ to the magnetic field. The line broadening term contains the expression $3\cos^2\theta-1$, which becomes zero when θ = 54.7°. In some cases the maximum spinning rate is insufficient to remove all the interactions and the resulting spectrum consists of a central line flanked by spinning side bands. In the case of the quadrupolar interactions, they can only be suppressed to the first order as second order quadrupolar interactions have a different line broadening term, which has zero points when θ = 30.6° and 70.1°. This can be overcome by multiple quantum magic angle spinning NMR.

Boron Nitride

Boron nitride can serve as a good example of the aspects of solid state MAS NMR discussed above. As discussed the ^{11}B nucleus, I = $^3/_2$, possesses a quadrupolar moment, which gives rise to a quadrupolar interaction, the extent of which is strongly dependent on the distortion of the site from cubic symmetry. BN exists in two

polymorphs. The cubic form is composed of local BN_4 tetrahedra, with sp^3 hybridised boron environments, while the hexagonal structure possesses nearly planar B_3N_3 hexagons, with sp^2 B environments. The solid state ^{11}B MAS NMR spectra of the two polymorphs obtained by Marchetti *et al.*[14] are shown in figure 2.10.

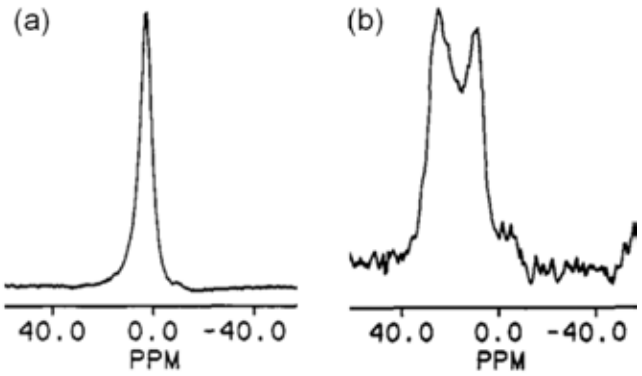

Figure 2.10 – Solid state ^{11}B MAS NMR spectra of (a) cubic BN and (b) hexagonal BN[14]

The lineshapes of the two polymorphs are clearly different, with a mainly symmetrical sharp resonance obtained for the cubic structure, while the hexagonal form produces a peak typical of a second order quadrupole lineshape for a nucleus of less than cubic symmetry.[11] The high symmetry of the boron environment within cubic BN means there is zero electric field gradient and hence zero quadrupole interaction. The asymmetrical boron present in hexagonal boron nitride implies the nucleus will possess an electric field gradient and so there is a significant quadrupolar interaction that broadens the peak over a large chemical shift range.

The chemical shifts of the resonances are also affected by the different boron environments. In cubic BN, the resonance has a chemical shift of 1.6 ppm, while hexagonal BN produces a resonance at 30 ppm. This is due to the difference in chemical shielding between the tetrahedral (sp^3 B) and trigonal (sp^2 B) environments. The increase in electron density around the boron nucleus in the tetrahedral geometry shields the nucleus from the external applied field and so the resonance is shifted upfield.

Finally, figure 2.10a shows that the line broadening interactions are averaged to zero through the use of the MAS technique for the cubic polymorph, whereas for the

hexagonal polymorph, figure 2.10b, the strong second-order quadrupolar interaction is only partially averaged and the characteristic lineshape of sp^2 boron environments is observed.

Solid state ^{11}B MAS NMR spectra in this study were collected using a 500 MHz Bruker Avance III spectrometer equipped with an 11.74 T magnet. The solid state ^{23}Na MAS NMR spectra were collected using a 400 MHz Bruker Avance spectrometer equipped with a 9.4 T magnet. All samples were loaded in a glove box under an argon atmosphere into a rotor. The rotor was sealed and then transferred onto the spectrometer and data collected without sample exposure to the atmosphere.

2.9 Raman Spectroscopy[15]

Raman spectroscopy is concerned with the study of molecular vibrations. Vibrational modes can be excited to higher energy through the absorption of radiation of appropriate frequency. A Raman spectrum is a plot of intensity of scattering as a function of frequency or wavenumber. In Raman spectroscopy, the sample is illuminated by monochromatic light, which is usually generated by a laser. A vibrational mode is Raman active if the polarisability of the molecule changes during the vibration. Changes in polarisability are not always easy to visualise and it is usually necessary to employ group theory in order to determine whether or not a mode will be Raman active.

During scattering, a short-lived excited state, known as a virtual state is created as a result of the incident radiation polarising the electron cloud surrounding the nuclei of the molecule under investigation. The excited state is unstable and rapidly relaxes through the release of a photon. Two types of scattered radiation are possible. Rayleigh scattering is essentially elastic, where only distortion of the electron cloud occurs and the energy difference between the incident and the scattered photons is minimal. Raman scattering events are inelastic, which occur when nuclear motions are induced in the molecule. The photon excites the molecule from the ground state to a virtual energy state and upon relaxation the molecule returns to a different

vibrational state. Figure 2.11 shows a diagram of the Rayleigh and Raman scattering processes. There are two types of Raman scattering, Stokes and anti-Stokes. Stokes scattering occurs when the Raman scattering event occurs from the ground vibrational state, $v = 0$, and results in the molecule absorbing energy and adopting an excited vibrational state, $v = 1$. The scattered photon is reduced in energy by the energy of this excited state compared to the incident photon. If the final vibrational state, $v = 0$, is lower in energy than the initial vibrational state, $v = 1$, then the excess energy is gained by the scattered photon, increasing its energy compared to the incident photon, this is known as anti-Stokes scattering.

Raman spectra in this study were collected using a Renishaw InVia Raman microscope using an Ar ion laser at a wavelength of 488 nm. All samples were loaded in a glove box under an argon atmosphere into a sample cell. The sample cell was sealed and then transferred onto the Raman microscope and data collected without sample exposure to the atmosphere.

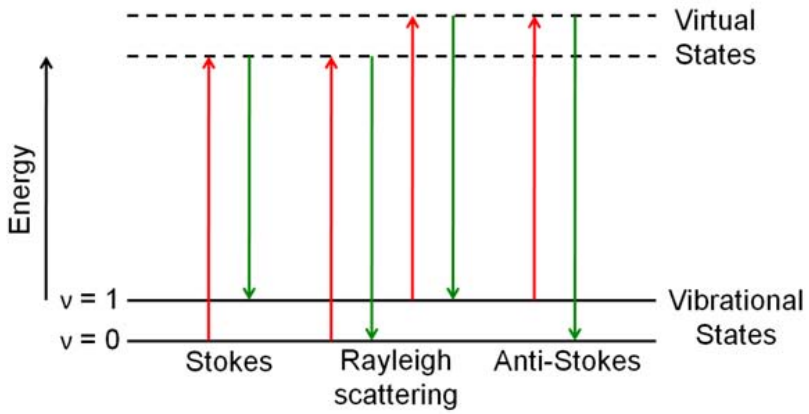

Figure 2.11 – The Rayleigh and Raman scattering processes. The incident energy is shown in red and the scattered energy in green

2.10 References

1. Giacovazzo, G.; Monaco, H. L.; Viterbo, D.; Scodary, F.; Gilli, G.; Zanotty, G.; Catti, M., Fundamentals of Crystallography. *Oxford Science Publications* **1998**.

2. West, A. R., Basic Solid State Chemistry. *John Wiley & Sons, LTD* **1999**.

3. Burns, G.; Grazer, A. M., Space Groups for Solid State Scientists. *Academic Press, INC* **1990**.

4. Hammond, C., The Basics of Crystallography and Diffraction. *Oxford University Press* **2001**.

5. Young, R. A., The Rietveld Method. *Oxford University Press* **1993**.

6. Rietveld, H. M., A profile refinement for nuclear and magnetic structures. *Journal of Applied Crystallography* **1969,** 2, 65–71.

7. Linscheid, M., Mass Spectrometry. *Ullmann's Encyclopedia of Industrial Chemistry* **2001**.

8. Mellon, F. A.; Self, R.; Startin, J. R.; Belton, P. S., Introduction to Principles and Practice of Mass Spectrometry. *RSC Publishing* **2000**.

9. Chater, P. A.; Anderson, P. A.; Prendergast, J. W.; Walton, A.; Mann, V. S. J.; Book, D.; David, W. I. F.; Johnson, S. R.; Edwards, P. P., Synthesis and characterisation of amide-borohydrides: New complex light hydrides for potential hydrogen storage. *Journal of Alloys and Compounds* **2007,** 446–447, 350–354.

10. Abraham, R. J.; Fisher, J.; Loftus, P., introduction to NMR Spectroscopy. *John Wiley & Sons, LTD* **1991**.

11. Smith, M. E.; van Eck, E. R. H., Recent advances in experimental solid state NMR methodology for half-integer spin quadrupolar nuclei. *Progress in Nuclear Magnetic Resonance Spectroscopy* **1999,** 34, 159–201.

12. Massiot, D.; Montouillout, V.; Magnenet, C.; Bessada, C.; Coutures, J.; Forster, H.; Steuernagel, S.; Mueller, D., Towards higher resolution for quadrupolar nuclei in solid state NMR at very high field. *Comptes Rendus de l'Academie des Sciences Serie II* **1998,** 1, 157–162.

13. Gervais, C.; Babonneau, F., High resolution solid state NMR investigation of various boron nitride preceramic polymers. *Journal of Organometallic Chemistry* **2002,** 657, 75–82.

14. Marchetti, P. S.; Kwon, D.; Schmidt, W. R.; Interrante, L. V.; Maciel, G. E., High-field ^{11}B Magic-Angle Spinning NMR characterization of boron nitrides. *Chemistry of Materials* **1991,** 3, 482–486.

15. Szymanski, H. A., Raman Spectroscopy : Theory and Practice. *Plenum Publishing Corporation* **1970**.

Chapter 3

The Thermal Decomposition of Ammonia Borane

3.1 Introduction

Prior to the commencement of this research there had been few published studies into the solid state thermal decomposition of ammonia borane. The majority of research related to ammonia borane had focused on determinations of the structure of the compound and any investigations into its decomposition generally involved organic solvents or hydrolysis. This research investigated the hydrogen desorption properties of the solid state material as well as spectroscopic investigations of the decomposition properties.

3.2 Experimental

The NH_3BH_3 starting material was placed into a quartz tube within an argon filled glove box (>10 ppm O_2, >1 ppm H_2O) and heated under a flowing argon atmosphere. The samples were reground and annealed at the target temperatures to allow for the samples to be collected as solids. Heating could not be carried out *in-situ* with respect to powder X-ray diffraction and solid state NMR spectroscopy due to the problem of ammonia borane undergoing a volume expansion while being heated.

3.3 Powder X-Ray Diffraction

The as-received ammonia borane was a white material with a high degree of plasticity. The powder X-ray diffraction, XRD, pattern of the ammonia borane starting material is shown in figure 3.1.

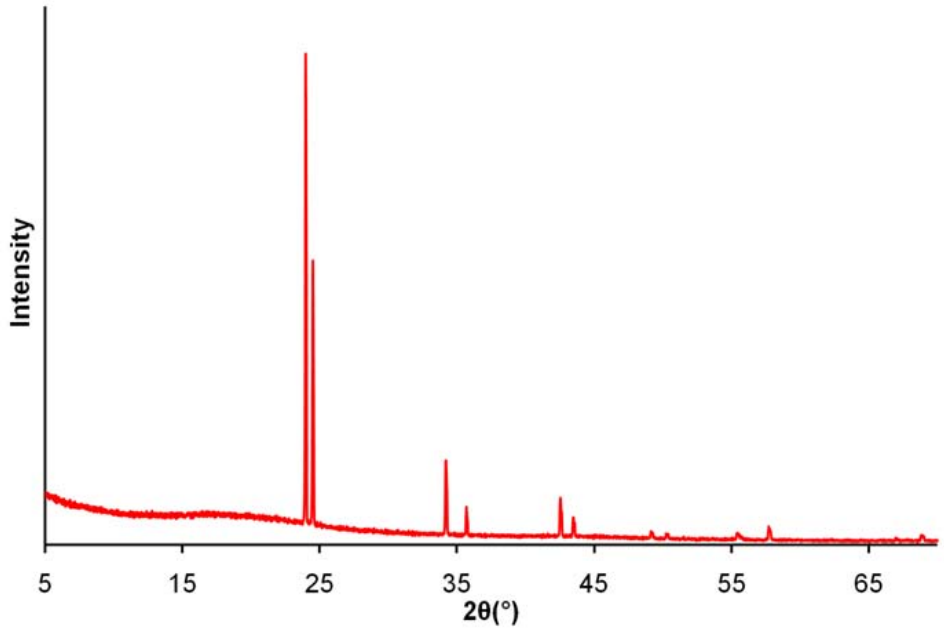

Figure 3.1 – The powder XRD pattern of ammonia borane at room temperature

On heating the material to 80°C a significant volume expansion occurred after a long induction period of 180 minutes, consistent with observations in other studies.[1, 2] After this volume expansion had occurred the ammonia borane became wet and required further heating, again to 80°C, for the sample to solidify. After the sample had been heated for a second time a white powder was obtained. This heating resulted in a loss of crystallinity in the sample: the original peaks observed in the powder XRD pattern were lost and only some low intensity peaks at approximately 24° 2θ are now observed. These peaks were assumed to be related to an intermediate solid labile form of ammonia borane that formed prior to the formation of the mobile form of ammonia borane in a liquid state, that formed during heating as a consequence of the disruption of the dihydrogen bonding network. This dramatically reduces the long range order within the structure, hence decreasing the crystallinity of the sample.[3] The major product after heating to 80°C has been shown to be the amorphous polyaminoborane, which is therefore not observed in the pattern.[2]

Additional heating of the ammonia borane starting material was carried out and the results analysed by powder XRD. The collected patterns are shown in figure 3.2.

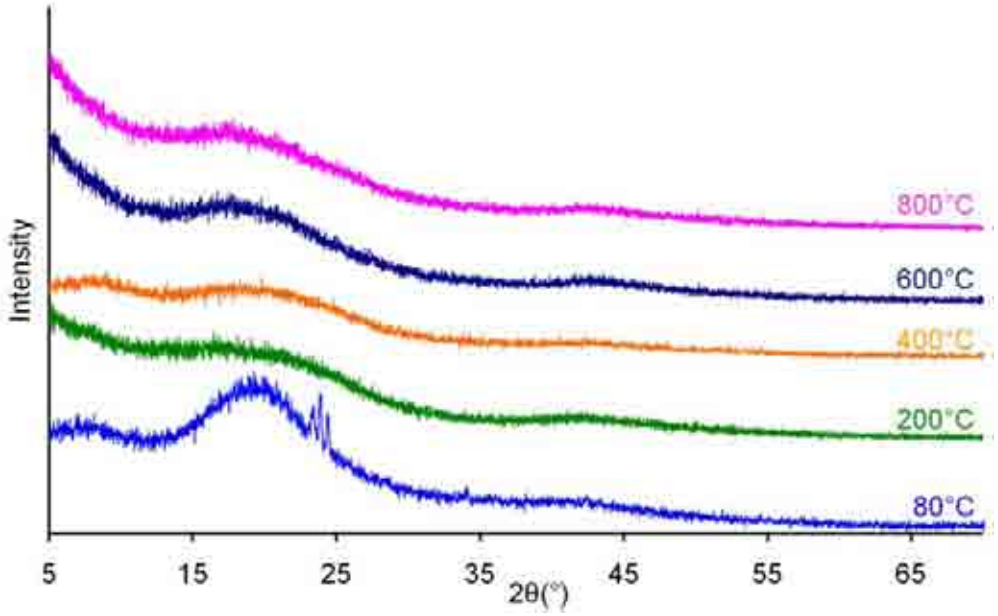

Figure 3.2 – Powder XRD patterns obtained after heating as-received ammonia borane to different temperatures

Further heating to 200°C produced a second amorphous product, polyiminoborane, again not detectable by X-rays.[4] This material was again obtained as a white powder. Literature data shows that further heating to 600°C begins to result in the formation of boron nitride.[4] Boron nitride is also a white powder and, consistent with this, the ammonia borane heated to 600°C resulted in a white powder. However, the powder XRD pattern obtained after heating at this temperature showed no peaks were present; the compound was again completely amorphous. It was possible that an amorphous form of boron nitride had formed. To confirm this, the product was further heated to 800°C to determine whether a crystalline phase could be obtained. The product obtained after heating to 800°C was again a white powder. However, the XRD pattern again showed that an amorphous phase had been produced. A large percentage of the hydrogen in the sample is released by this temperature and so it was concluded that an amorphous form of boron nitride was formed as the ultimate decomposition product. A study related to the decomposition of polyaminoborane has shown that a temperature of 1400°C is required before the decomposition product shows peaks due to the presence of crystalline boron nitride.[5]

3.4 Thermal Desorption Studies

The desorption profile of ammonia borane obtained on the home-built temperature programmed desorption, TPD, apparatus is shown in figure 3.3. The experiment was performed at a heating rate of 2°C min^{-1} to a temperature of 350°C. The TPD was connected to a mass spectrometer for analysis of the gases released during decomposition.

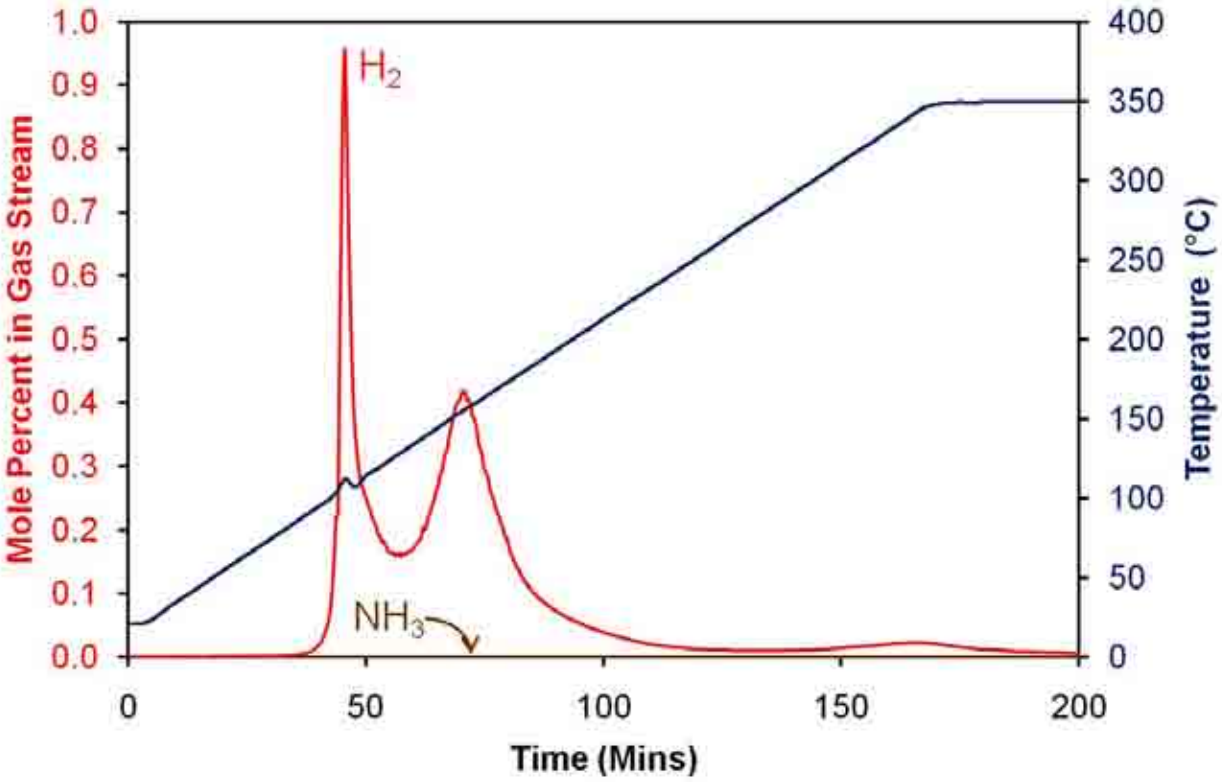

Figure 3.3 – TPD–MS analysis of a sample of NH_3BH_3. The temperature trace is shown in blue and the mole percentages of H_2 and NH_3 released are shown in red and brown, respectively

The plot shows that three releases of hydrogen were observed during the decomposition of ammonia borane, with a substantial overlap of the first two desorptions. The first hydrogen desorption was sharp and began at 85°C, peaking at 110°C. This release was accompanied by a bump in the temperature trace: the temperature increased at a rate faster than the ramp rate should have allowed. This showed that the release of hydrogen during this decomposition step was sufficiently exothermic to cause an increase in temperature in the sample holder. The exothermic nature of hydrogen release from ammonia borane has been

demonstrated in other studies.[2] Shortly after this exothermic event an endothermic event occurred, at 112°C, which was consistent with the melting point of ammonia borane.[6] Previous studies have shown that the melting of ammonia borane can be the thermal event that leads to the start of hydrogen release.[4, 7] However, at sufficiently slow ramp rates, the release of hydrogen can begin prior to the compound melting, which was similar to what was observed during this decomposition.[2] The second decomposition event began at 125°C and peaked at 150°C. This was a much broader hydrogen release than the first decomposition step. There was a long tail to this hydrogen release and the event did not completely end until a temperature of 260°C was reached. A final small release began at 290°C, which decreased once the target temperature of 350°C was reached, suggesting that this release was incomplete during the timescale of the experiment. There was no observed release of NH_3 during the desorption experiment, which is in accordance with other studies of the decomposition of ammonia borane.[3, 4, 7] The release of the volatile gas borazine has been detected in other studies at temperatures in excess of 200°C through the use of infra-red spectroscopy.[8] However, in this experiment no borazine release was detected by mass spectrometry. The appearance of borazine in the decomposition of ammonia borane has been shown to be related to the heating rate.[8] Therefore, it was possible that the heating rate in this experiment was sufficiently slow to suppress borazine release. Alternatively, borazine has been shown to dehydropolymerise readily at temperatures above 100°C, yielding another white solid, polyborazylene.[9] This reaction could therefore have taken place in the sample holder before borazine could be detected by the mass spectrometer. Powder XRD showed that the products obtained after the heating run were completely amorphous.

It is important to note that it has previously been discussed that the first step in hydrogen release from ammonia borane is the intermolecular rearrangement reaction resulting in DADB.[1, 3, 10] However, as this rearrangement does not release hydrogen it was not observed in this experiment although it can be concluded that this step takes place at temperatures below 85°C. The first step of hydrogen release results in the formation of aminoboranes,[2] as shown in reaction 3.1, which have been shown to rapidly associate,[11] resulting in a number of products of formula $(NBH_4)_x$[12], in the form of either cycloborazanes up to a maximum ring size of five BH_2NH_2 units; or

aminoborane oligomers, which following continued association result in long chain polymers, as shown in figure 3.4.[13] However, the cycloaminoboranes are crystalline materials.[12] Therefore, aminoboranes of this type can only have formed in very small amounts as the XRD patterns were completely amorphous with the exception of three peaks visible in the pattern obtained at 80°C. The mechanism of formation of these oligomers and cyclic products has been proposed as involving the reaction of DADB, or DADB-like species with ammonia borane, shown in reaction 3.2.[1] This mechanism shows that the first step of hydrogen release from ammonia borane results in a complex mixture of products.

$$NH_3BH_3 \rightarrow \frac{1}{x}(NH_2BH_2)_x + H_2 \qquad \text{Reaction 3.1}$$

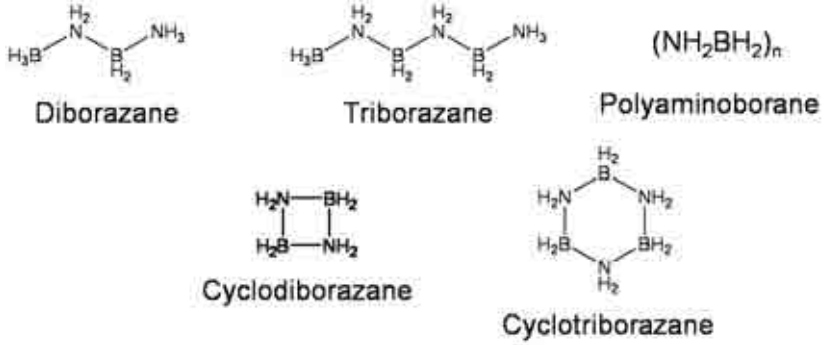

Figure 3.4 – Some potential association products of aminoborane

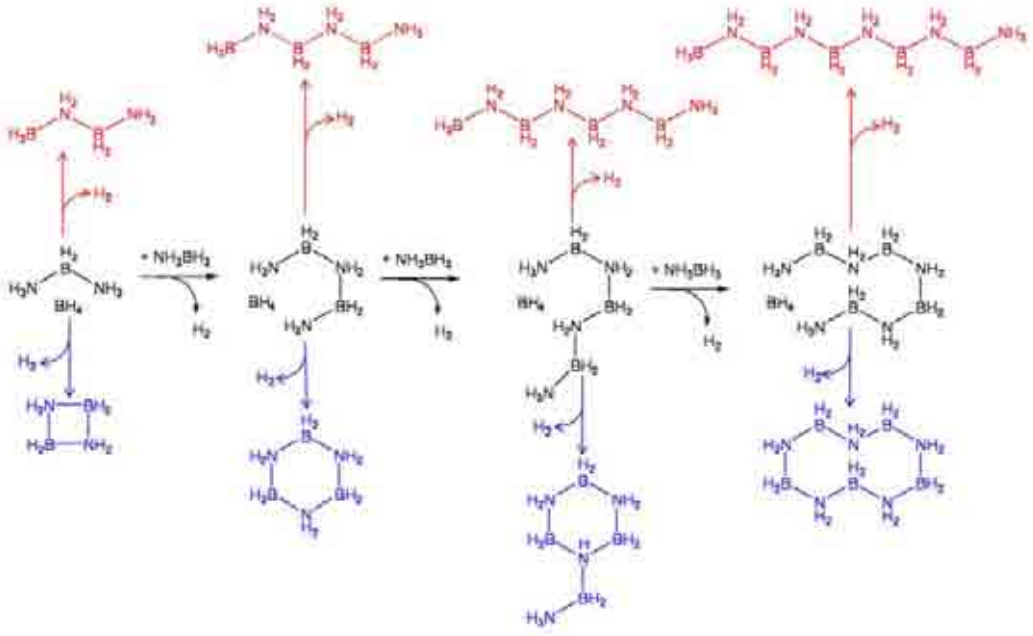

Reaction 3.2

Upon further heating the resulting cyclic products shown above undergo ring opening and the chain products decompose, both of which result in further loss of hydrogen during the second hydrogen release step. This hydrogen loss eventually results in the formation of compounds of general composition $(NBH_2)_x$, such as the polymeric chain species polyiminoborane, $(NHBH)_n$, shown in reaction 3.3.[7] These events occur during the second hydrogen desorption step. The decomposition of cycloborazanes and in particular cyclotriborazane has been shown to yield a solid residue similar in polymeric structure to the decomposition products of ammonia borane, as well as releasing borazine beginning at a temperature of around 150°C.[14] Ammonia borane is also prone to releasing borazine at a similar temperature,[15] which as mentioned earlier can polymerise to yield polyborazylene in this temperature range as shown in reaction 3.4. This reaction further contributes to the release of hydrogen during the second hydrogen release step observed in figure 3.3.

$$(NH_2BH_2)_x \rightarrow (NHBH)_x + H_2$$ Reaction 3.3

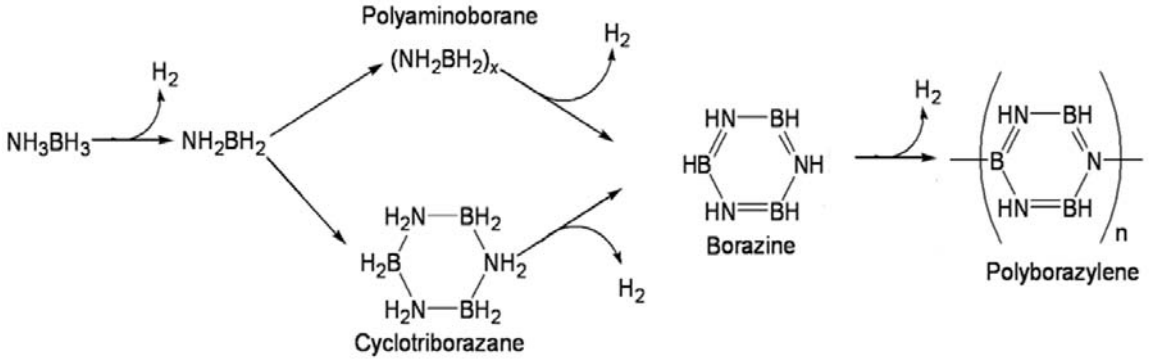

Reaction 3.4

The wide range of potential products formed during the first decomposition step resulted in the broad second step of hydrogen release as the decomposition of these products do not all commence at a single set temperature. The further higher temperature hydrogen release is suggested to be as a result of further decomposition of the products of formula $(NBH_2)_x$. This is at too low a temperature to be related to the formation of boron nitride, BN,[3] and has therefore been suggested to form products of formula $(NBH)_x$.[4] However, the difficulties in proposing structures for this compound mean that this is unlikely and hence this release could also be due to the

decomposition of products formed during the first hydrogen release step, of formula $(NBH_4)_x$, resulting in further products of lower hydrogen content.

3.5 Raman Spectroscopy

A comprehensive Raman spectroscopy study of the phase transition in ammonia borane has been carried out by Hess *et al*[16] and this will be used as the basis for the assignment of the vibrational modes observed in the obtained spectrum. Point group analysis of the symmetry of molecules enables the prediction of the number, symmetry and activity of vibrational modes. The free ammonia borane molecule possesses C_{3v} symmetry. The symmetry elements present in free ammonia borane are shown in figure 3.5.

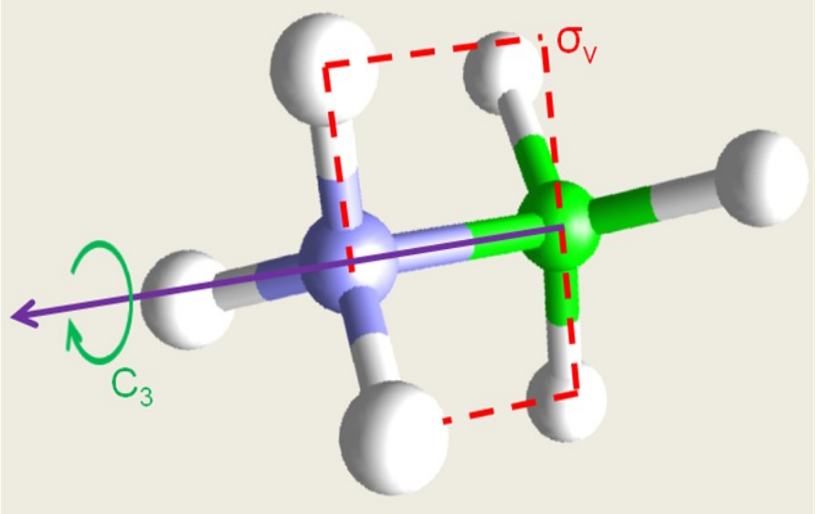

Figure 3.5 – The symmetry elements present in the free ammonia borane molecule

Using Cartesian displacement vectors for each of the atoms as the basis set it is possible to derive the normal vibrational modes. The reducible representation for this basis set (Γ_{red}) is shown in table 3.1 and the irreducible representation (Γ_{irr}) is given in table 3.2, where translational (Γ_{trans}) and rotational modes (Γ_{rot}) are removed to give the normal vibrational modes (Γ_{3n-6}). The irreducible representation of molecular ammonia borane is $5A_1 + A_2 + 6E$ which is consistent with $3n - 6 = 18$ degrees of freedom. The modes that are Raman active (Γ_{Raman}) are shown and assigned vibrational modes. The eleven Raman active modes were reported by Smith *et al*.[17]

Table 3.1 – Point group table for C_{3v}

	E	$2C_3$	$3\sigma_v$	Linear, Rotations	Quadratic
$\mathbf{A_1}$	1	1	1	z	$x^2 + y^2, z^2$
$\mathbf{A_2}$	1	1	−1	R_z	
E	2	−1	0	(x,y) (R_x, R_y)	(x^2-y^2, xy) (xz, yz)
Γ_{red}	24	0	4		

Table 3.2 – Deconvolution of Γ_{irr} for the free C_{3v} symmetry ammonia borane molecule

	Γ_{irr}	Γ_{trans}	Γ_{rot}	Γ_{vib}	Γ_{Raman}	Assignment
A_1	6	1	0	5	5	$\nu_1, \nu_2, \nu_3, \nu_4, \nu_5$
A_2	2	0	1	1	0	–
E	8	1	1	6	6	$\nu_7, \nu_8, \nu_9, \nu_{10}, \nu_{11}, \nu_{12}$

The vibrational A_1 modes ν_1, ν_2, ν_3, ν_4, ν_5 correspond to the N–H symmetric stretch, the B–H symmetric stretch, the N–H symmetric bend, the B–H symmetric bend and the B–N symmetric stretch, respectively. All of these modes are singly degenerate and are shown in figure 3.6. The vibrational E modes ν_7, ν_8, ν_9, ν_{10}, ν_{11}, ν_{12} correspond to the N–H asymmetric stretch, the B–H asymmetric stretch, the N–H asymmetric bend, the B–H asymmetric bend and two asymmetric rocking motions involving planes of hydrogen atoms of both the BH_3 and NH_3 groups, respectively. These modes are doubly degenerate and are shown in figure 3.7. The ν_6 mode corresponds to a BN torsion motion, however this is Raman inactive.

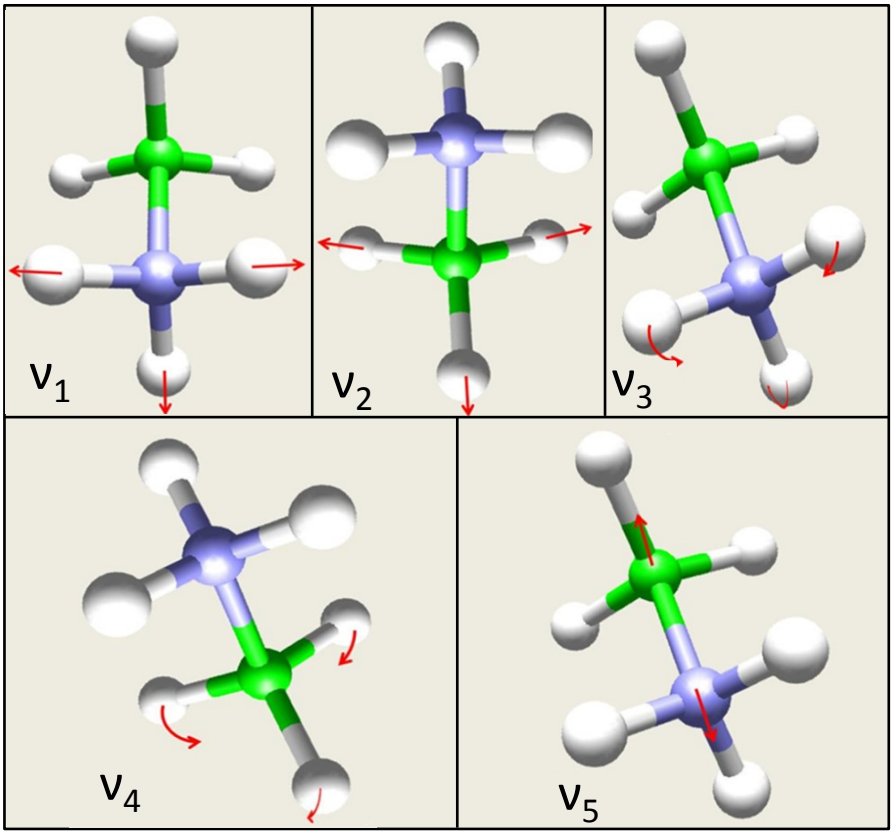

Figure 3.6 – The symmetric vibrational modes of the ammonia borane molecule

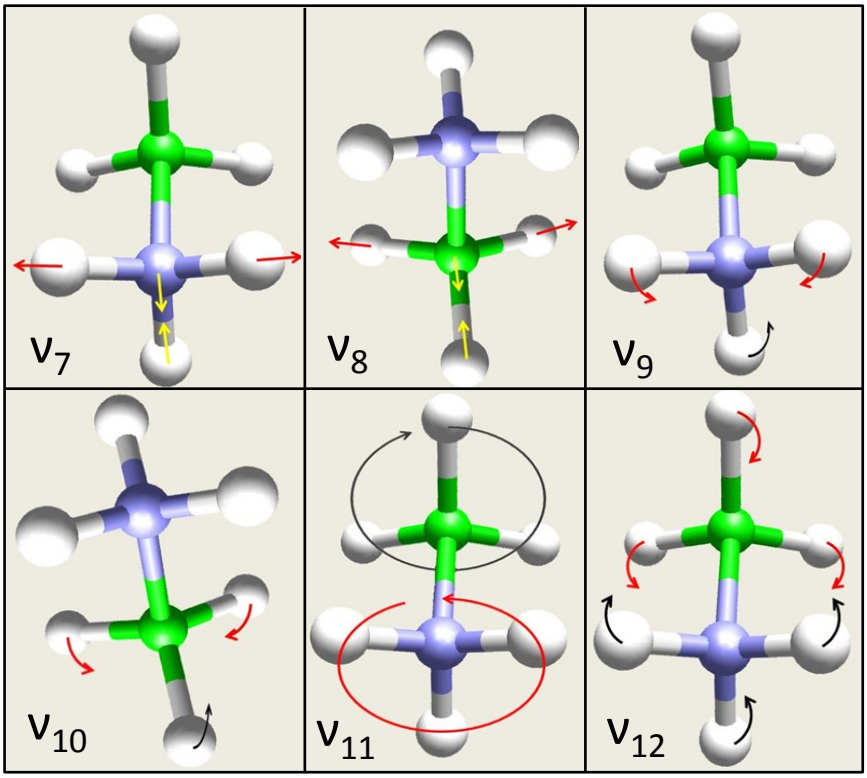

Figure 3.7 – The asymmetric vibrational modes of the ammonia borane molecule

For discussion purposes the Raman spectrum can be divided into five sections: the N–H stretching region, the B–H stretching region, N–H rocks and bends, B–H rocks and bends and the B–N stretching region. The room temperature Raman spectrum of ammonia borane is shown in figure 3.8.

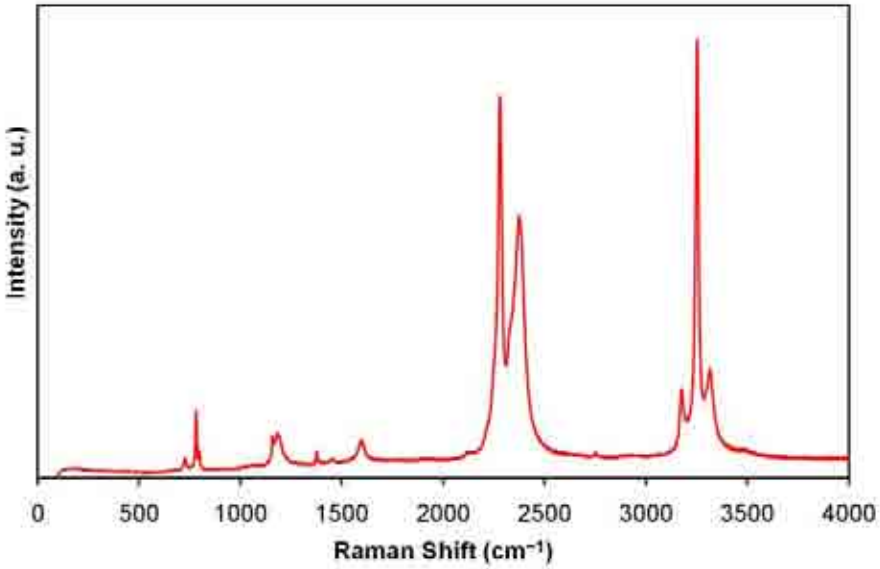

Figure 3.8 – The room temperature Raman spectrum of ammonia borane

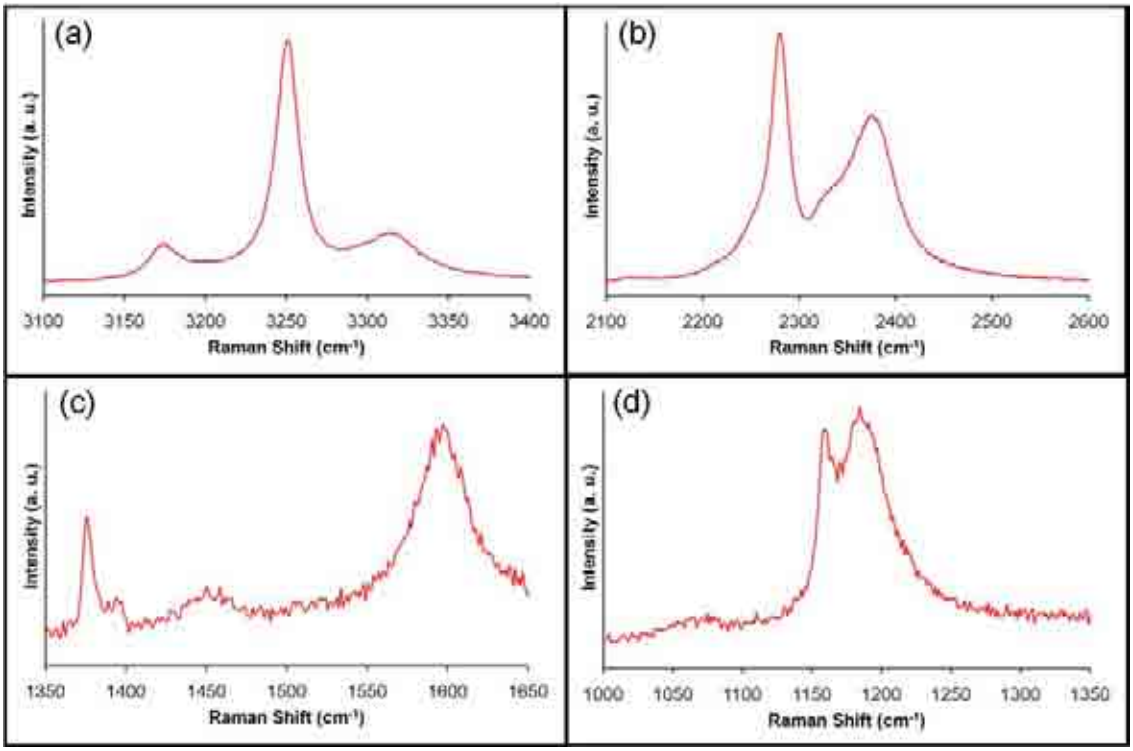

Figure 3.9 – Raman spectrum of the (a) N–H stretching region (b) B–H stretching region (c) NH_3 deformation region (d) BH_3 deformation region

The N–H stretching region is shown in figure 3.9a. The asymmetric *E* N–H stretch is found at 3317 cm^{-1} and the symmetric A_1 stretch located at 3252 cm^{-1}. There is a third peak at 3177 cm^{-1} which has been unassigned in some studies.[17-19] However, in the study by Hess *et al*.,[16] it was assigned as being due to the result of Fermi resonance of the overtone of a peak at 1600 cm^{-1}, an NH_3 deformation mode, and the N–H symmetric stretch at 3252 cm^{-1}.

The B–H stretching region, shown in figure 3.9b, is dominated by two peaks at 2377 and 2280 cm^{-1}. There is also a slight shoulder on the less intense peak at 2330 cm^{-1}. The assignment of these peaks has caused some dispute in the literature. Powder studies assigned the 2330 cm^{-1} peak to the asymmetric *E* B–H stretch and the symmetric A_1 B–H stretch to the more intense, sharper peak at 2280 cm^{-1}. Alternatively, the 2377 cm^{-1} peak has been assigned to the asymmetric B–H stretch by single crystal studies, although the symmetric stretch was assigned to either the 2330 cm^{-1} peak[18] or the 2280 cm^{-1} peak.[19] This discrepancy likely comes about as the single crystal results were both part of high pressure studies which observed the splitting of the peak at 2377 cm^{-1} but no splitting of the other two peaks. Polarised Raman studies by Hess *et al.*[16] show that the peaks at 2280 and 2377 cm^{-1} are both highly polarised whereas the 2330 cm^{-1} peak is depolarised, which agrees with the assignments from the powder studies.

The N–H bending region is shown in figure 3.9c. There are three peaks in this region: the most intense is located at 1600 cm^{-1}, a very low intensity peak is found at 1450 cm^{-1}, and the final peak is observed at 1375 cm^{-1}. There is good agreement regarding the assignment of the peaks at 1600 cm^{-1} and 1375 cm^{-1} in the literature. The remaining weak peak at 1450 cm^{-1} has not been reported in a number of studies. It has, however, been assigned as an overtone of low frequency rocking motions.[20]

The B–H bending region is shown in figure 3.9d. There is less agreement regarding the assignment of peaks in this region in other studies. Two features are observed at 1190 cm^{-1} and 1160 cm^{-1}. Asymmetric modes are generally observed at higher energy than symmetric modes, and so the peak at 1190 cm^{-1} has been assigned to the asymmetric *E* B–H bend.[17, 19] This assignment has been supported by polarised

studies which show that this mode is depolarised as well as high pressure studies which show that this peak splits under high pressure.[16, 18] The symmetric B–H bend has been assigned to a number of different peaks namely 1155 cm^{-1},[10] 1158 cm^{-1},[19] 1052 cm^{-1} [17] and 1026 cm^{-1}.[18] Polarised studies support the assignment of this mode as the peak observed at 1160 cm^{-1}.[16]

The B–N stretching region is shown in figure 3.10. The ^{11}B and ^{10}B contributions to the B–N symmetric stretch are observed at 783 and 800 cm^{-1} respectively.[21] The frequency difference of 17 cm^{-1} between these two peaks is in good agreement with *ab initio* calculations based on the mass difference of the two isotopes and a symmetric stretch.[19]

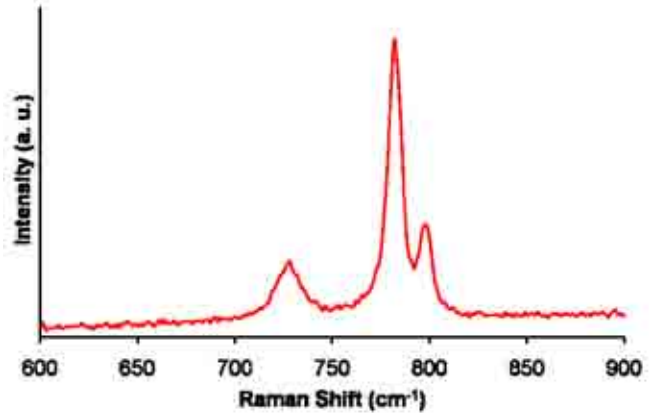

Figure 3.10 – Raman spectrum of the B–N stretching region

There are two remaining features that have yet to be assigned, firstly a weak feature at 1070 cm^{-1}, observable in figure 3.9d, and a second at 728 cm^{-1} seen in figure 3.10. These modes have been assigned as asymmetric rocking motions involving planes of hydrogen atoms in both BH_3 and NH_3 groups. The rocking motion which produces the peak at 1070 cm^{-1} involves the two planes of hydrogen atoms in a single NH_3BH_3 molecule remaining parallel to one another as the planes pivot about the B and N atoms. The lower frequency rocking motion also involves a pivoting motion of the planes of hydrogen atoms around the B and N atoms, however, in this motion the planes of hydrogen atoms in an individual molecule beat against each other.[16]

Table 3.3 shows a summary of the vibrational modes that are observed in the room temperature Raman spectrum of ammonia borane with the assignment of each mode.

Table 3.3 – Summary of peaks observed in the Raman spectrum of ammonia borane. st = stretch, d = deformation, ds = scissors, du = umbrella, r = rock, ov = overtone, dp = depolarised, p = polarised

Reference 5 (cm^{-1})	Assignment			This Study (cm^{-1})
3316	NH^{st}	*E*	ν_7	3317
3250	NH^{st}	A_1	ν_1	3252
3176	ov	p		3177
2375	Unknown	dp		2377
2328	BH^{st}	*E*	ν_8	2330
2279	BH^{st}	A_1	ν_2	2280
1600	NH_3^{ds}	*E*	ν_9	1600
1450	ov	dp		1450
1375	NH_3^{du}	A_1	ν_3	1375
1189	BH_3^{ds}	*E*	ν_{10}	1190
1155	BH_3^{du}	A_1	ν_4	1160
1065	NBH^{r}	*E*	ν_{11}	1070
800	$^{10}BN^{st}$	A_1	$\nu_{5'}$	800
784	$^{11}BN^{st}$	A_1	ν_5	783
727	NBH^{r}	*E*	ν_{12}	728
Not observed	BN torsion	A_2	ν_6	Not observed

The Raman spectrum of ammonia borane taken after heating to 80°C for 12 hours is shown in figure 3.11. This spectrum is compared to that of ammonia borane in figure 3.12, divided into the regions of N–H stretching, B–H stretching and the lower frequency region, containing the BH_3 and NH_3 deformations and the B–N stretch.

Figure 3.12a shows that the ν_7 and ν_1 N–H stretches as well as the overtone observed at room temperature in this region are still observed. Figure 3.12b shows that the B–H stretches, ν_8 and ν_2, are also still present. Analysis of the 600 – 1800 cm^{-1} region, figure 3.12c, shows that there is some evidence for the BH_3 deformation modes, ν_{10} and ν_4 still being present and ν_5, the B–N stretch, is observed. It is more difficult to state conclusively that the NH_3 deformation modes ν_9 and ν_3, the NBH

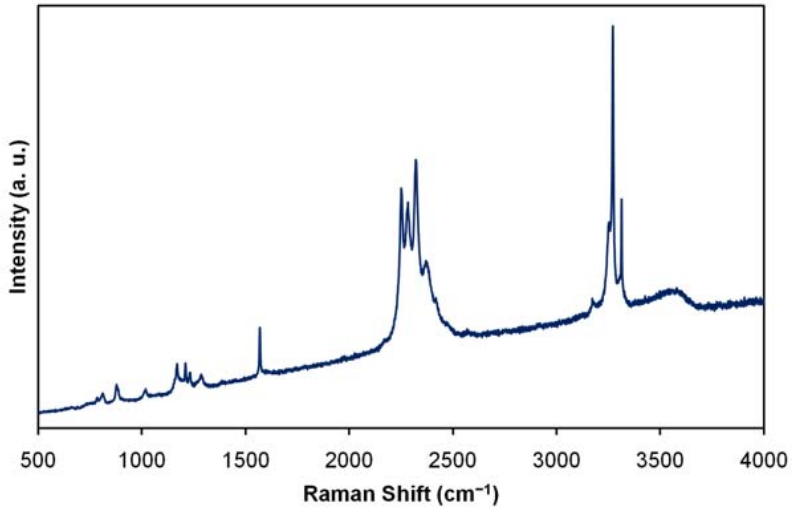

Figure 3.11 – The Raman spectrum of ammonia borane taken after heating to 80°C for 12 hours

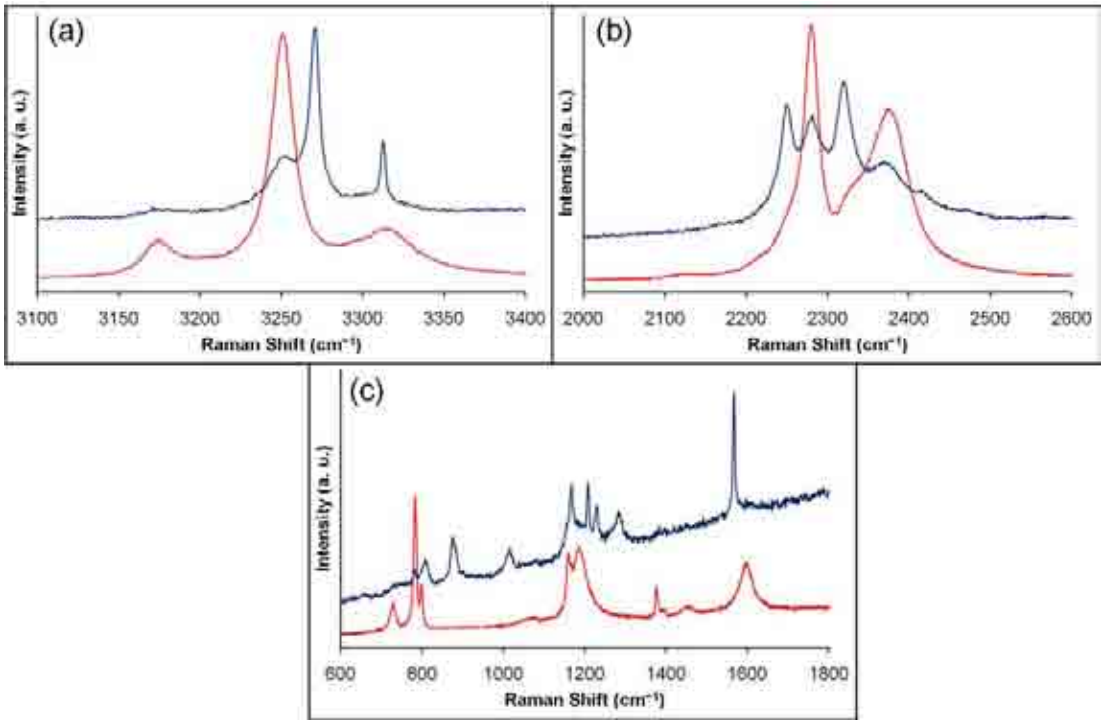

Figure 3.12 – Comparison of the Raman spectra of ammonia borane at room temperature (red) and after heating to 80°C (blue) showing (a) N–H stretching region (b) B–H stretching region (c) NH_3 deformation, BH_3 deformation and B–N stretching regions

rocking modes ν_{11} and ν_{12} and the overtone observed in this region at room temperature are still present due to the decreased intensity of these features. These peaks appear to be present albeit with low intensity, hidden partly in the background

of the spectrum. The observation of these features shows that the first step of decomposition is not yet complete, as these peaks are due to the presence of undecomposed ammonia borane. However, in each of the regions of the spectrum, there are now new features present.

The N–H stretching region now shows two additional peaks, the most intense found at 3270 cm^{-1} and a second at 3312 cm^{-1}. The Raman spectrum of sodium amide, $NaNH_2$, shows features at 3267 cm^{-1} due to the asymmetric, ν_3, N–H stretch and at 3218 cm^{-1} due to the symmetric, ν_1, N–H stretch.[22] This similarity suggests the presence of an NH_2. The N–H stretches in the decomposition product are blue shifted compared to those in $NaNH_2$ due to the presence of the metal cation. The B–H stretching region also displays additional peaks, two of approximately equal intensity at 2252 and 2322 cm^{-1} and a lower intensity, broad peak at 2422 cm^{-1}. The two intense modes in this region are probably due to B–H stretches of a BH_2 unit, with the asymmetric stretch at the higher frequency than the symmetric stretch. This is similar to the Raman spectrum of diborane, which contains terminal BH_2 units.[23] It is an interesting point to note here that the new peaks in the N–H stretching region are blue shifted compared to the original peaks, whereas in the B–H stretching region the new peaks have been red shifted. This can be explained through dihydrogen bonding. It has been well established that hydrogen stretching frequencies of X–H bonds, where X = O, N, show significant shifts to lower wavenumbers on formation of a hydrogen bond, with the most prominent spectral changes being observed in the region around 3500 cm^{-1}.[24, 25] Therefore, by analogy with the normal hydrogen bond, it would be expected that a similar effect would occur upon the formation of a dihydrogen bond. On decomposition, these dihydrogen bonds are broken and hence the N–H bonds present in the new compound will shift to a higher frequency.

The new peaks being produced are accompanied by hydrogen release and therefore it is reasonable to assume that they are due to NH_2 and BH_2 groups. There are also a number of new peaks in the region 600 – 1800 cm^{-1}, figure 3.12c. The peak found at 1566 cm^{-1} is also observed in the Raman spectrum of $NaNH_2$ and is assigned as being the symmetric, ν_2, N–H bend.[21] The other peaks observed in this region will be related to B–H bends and the B–N stretches. The B–H symmetric bend of the

terminal BH_2 group in the Raman spectrum of diborane is located at 1180 cm^{-1}.[26] Therefore, the modes observed at around this frequency are presumed to be as a result of the B–H bending vibrations, the asymmetric bend at 1208 cm^{-1} and the symmetric bend at 1167 cm^{-1}. The mode at 811 cm^{-1} is in the right region to be related to a B–N symmetric stretch, although the broad nature of the peak makes it difficult to identify the presence or absence of a ^{10}B–N stretch which would conclusively assign this mode. There are remaining unassigned features at 811, 876, 1230 and 1286 cm^{-1}. These features are also likely to be related to B–N stretches and B–H and N–H deformations due to the frequency range that they are found in. The potential variety of products produced at 80°C could result in a number of B–H and N–H environments being observed in the Raman spectrum.

The Raman spectrum of ammonia borane taken after heating to 200°C for 12 hours is shown in figure 3.13.

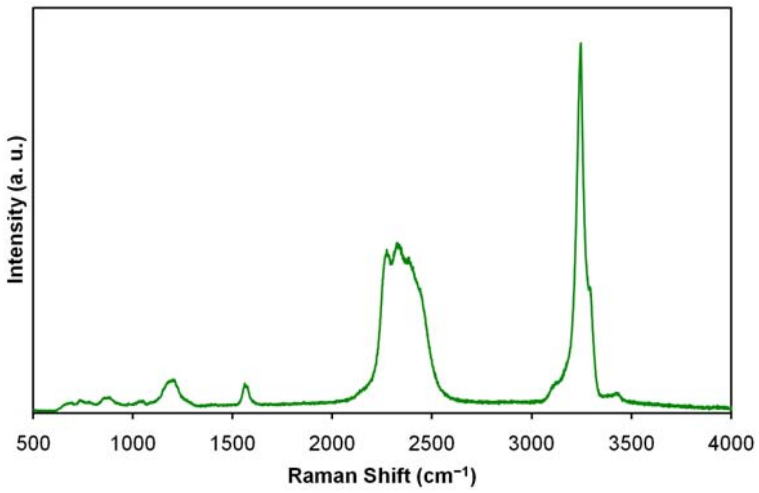

Figure 3.13 – The Raman spectrum of ammonia borane after heating to 200°C

It is immediately apparent that the sharp peak shapes characteristic of the features observed in the Raman spectrum collected at room temperature and 80°C have been lost and the features observed at 200°C are much broader in nature. This broadening occurs where there is increased disorder due to a loss of crystallinity; polymeric, amorphous materials give broader features than crystalline materials.[27] Non-crystalline polymers lack molecular symmetry and so the chemical repeat units cannot be viewed as also being physical repeat units, due to the geometrical

irregularity. It is often a good approximation to consider each chemical repeat unit as a separate molecule in its own local environment. Broad peaks are therefore expected due to group vibrations. The groups of atoms of the same kind in different regions of the polymer have slightly different vibrational frequencies as a consequence of the different physical environments of the units to which they belong, resulting in the observed broadening of the features. The change in nature of the two spectra highlights the transition from the crystalline ammonia borane to the products of decomposition, amorphous polymers. A comparison of the spectra obtained at room temperature, and after heating to 200°C, can be seen in figure 3.14.

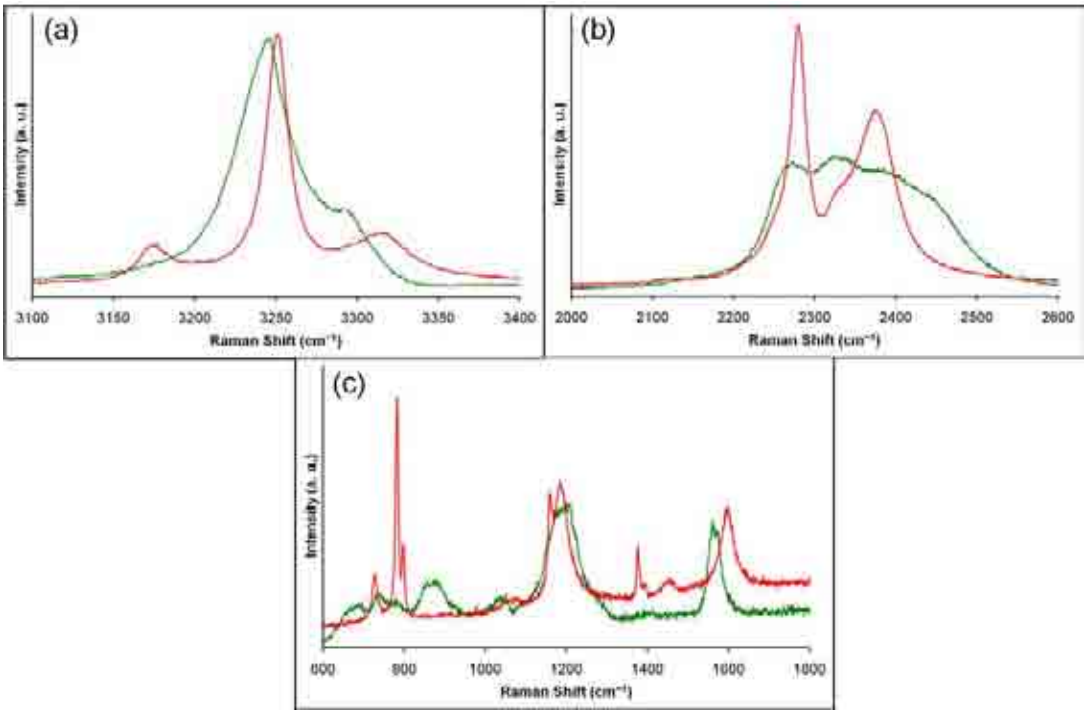

Figure 3.14 – Comparison of the Raman spectra of ammonia borane at room temperature (red) and after heating to 200°C (green) showing (a) N–H stretching region. (b) B–H stretching region. (c) NH_3 deformation, BH_3 deformation and B–N stretching regions

Analysis of figures 3.14a and 3.14b shows that there are no longer any N–H or B–H stretches present that can be attributed to ammonia borane as by this temperature all of the ammonia borane will have decomposed. Figure 3.14c shows that there is some alignment between the peaks observed in the room temperature and 200°C spectrum for B–H and N–H bends at 1190 and 1600 cm^{-1} respectively. However, as they originate from BH_3 and NH_3 units they are unlikely to be the same features in the

spectrum obtained from the sample heated to 200°C. A comparison between the spectra obtained from samples heated to 80°C and 200°C is shown in figure 3.15.

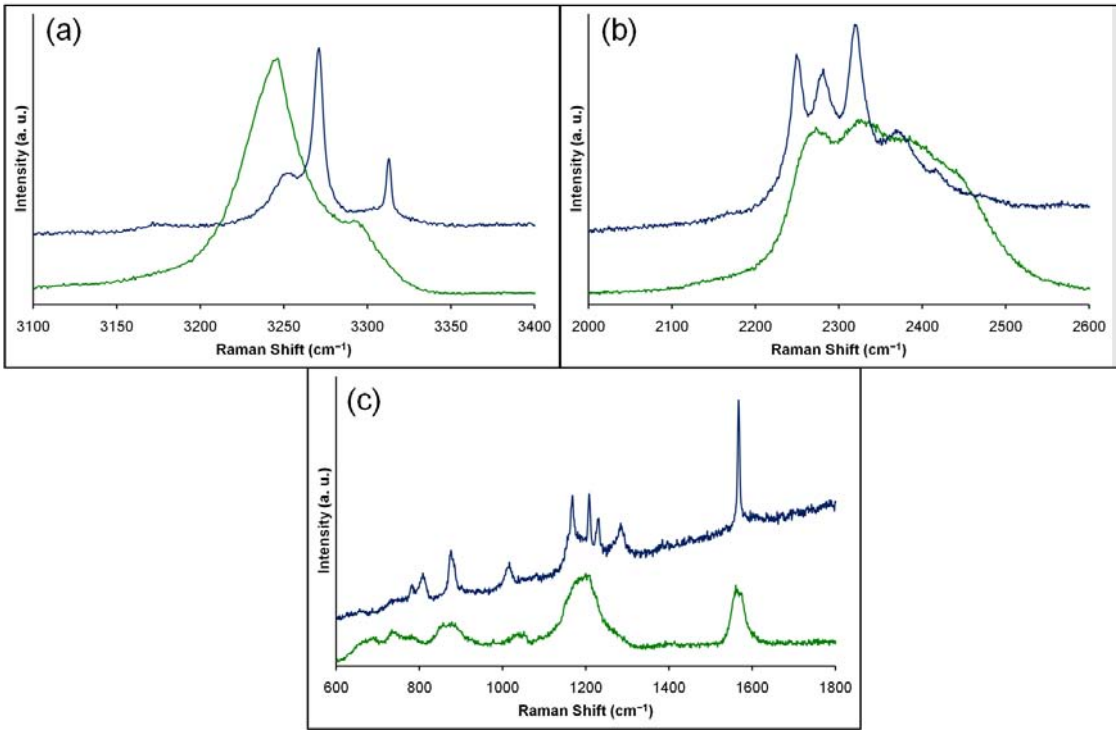

Figure 3.15 – Comparison of the Raman spectra of ammonia borane at 80°C (blue) and after heating to 200°C (green) showing (a) N–H stretching region. (b) B–H stretching region. (c) NH_3 deformation, BH_3 deformation and B–N stretching regions

The N–H stretching region shown in figure 3.15a shows that there are two broad peaks present, found at 3273 and 3339 cm^{-1}. They have a similar ratio of intensities to the peaks observed at 80°C, suggesting that they could be related to N–H stretches found in an NH_2 group. However, it is more likely that they are related to an NH group. The vibrational spectra of lithium amide, $LiNH_2$, and lithium imide, Li_2NH, have been reported.[28] It was observed that the N–H stretches in the amide shifted to lower frequencies on decomposition to the imide. Furthermore, a broadening of the peaks was observed due to increased disorder in the crystallite. Therefore, it is reasonable to suggest that the features in this region belong to an NH group, with the N–H asymmetric stretch found at 3339 cm^{-1} and the symmetric N–H stretch at 3273 cm^{-1}. The peaks found at 200°C are much broader than those at 80°C showing that this NH unit is found within a polymeric material. The B–H stretching region of the spectrum, figure 3.15b, is dominated by broad peaks which substantially overlap one

another and so it is difficult to obtain any meaningful information from this region of the spectrum with respect to the composition of the sample. Based on the number of hydrogen desorptions by 200°C and the fact that an NH group is present, it is likely that B–H stretches are present due to a BH unit, however, the spectrum provides inconclusive evidence for this. The features observed between 600 and 1800 cm^{-1}, figure 3.15c, are also broad in nature. There is some correlation with the peaks observed at 80°C and 200°C, specifically with respect to N–H and B–H bending vibrations. Unfortunately, the broad nature of the peaks again makes it difficult to assign them to particular stretching or bending modes. It is again predicted that a B–N stretch should be present in the spectrum as this bond should remain intact throughout the dehydrogenation process. The broad feature at 880 cm^{-1} could be due to this mode. Furthermore, a higher frequency B–N stretch may be expected in the spectrum due to the formation of a B=N double bond on dehydrogenation. However, the broad features again make it difficult to identify such a mode.

A table showing the changes in the Raman spectrum of ammonia borane as it was heated can be seen in Appendix 1.

3.6 Solid State ^{11}B MAS NMR Spectroscopy

The decomposition pathway of ammonia borane was investigated through solid state ^{11}B MAS NMR. The spectrum of the as-received ammonia borane is shown in figure 3.16. It can be seen that there is a single feature in this region, centred at −26.0 ppm. On closer inspection this feature is shown to have a shoulder at −24.5 ppm. The ammonia borane starting material possesses only one boron environment, namely an sp^3 hybridised boron atom present as H_3BN. The reason for the observation of two features is because of quadrupolar coupling.[1] The quadrupolar interaction is inversely proportional to the magnetic field and hence at higher magnetic fields only a single feature will be observed in the spectrum.[29]

The solid state ^{11}B NMR spectrum of ammonia borane after heating to 80°C for 12 hours is shown in figure 3.17. It is obvious that there has been a significant change in

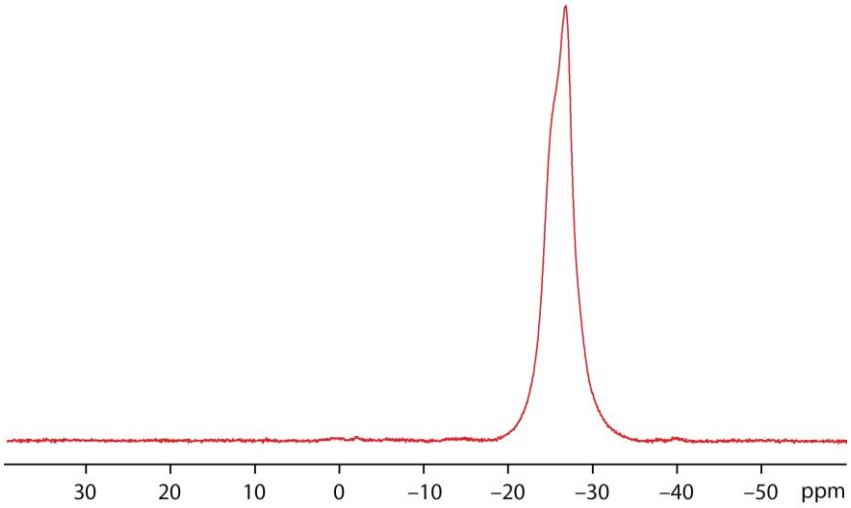

Figure 3.16 – The room temperature solid state ^{11}B MAS NMR spectrum of ammonia borane

the appearance of the spectrum compared to that at room temperature, with the emergence of several new boron environments observed in the spectrum. These features of polyaminoborane are formed by the loss of one equivalent of hydrogen from ammonia borane. As a general rule, the further downfield the feature, the less hydrogen there is attached to an sp^3 type boron.[10] Table 3.4 summarises the features that are observed in the spectrum.

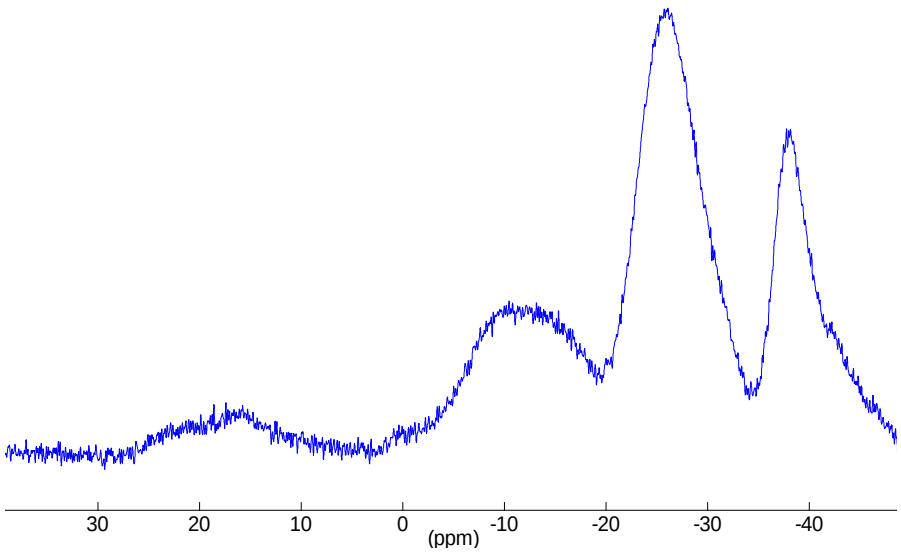

Figure 3.17 – The solid state ^{11}B MAS NMR spectrum of ammonia borane after heating to 80°C for 12 hours

Table 3.4 – Assignment of features observed in the solid state ^{11}B MAS NMR spectrum of ammonia borane after heating to 80°C for 12 hours[10]

Environment	Chemical Shift (ppm)
sp^3 B – BH_4	−38.0
sp^3 B – H_3BN	−26.0
sp^3 B – H_2BN_2	−13.0
sp^3 B – HBN_3	−0.5
sp^2 B	+27

The appearance of both H_2BN_2 and BH_4 features in the spectrum is due to the formation of DADB during the nucleation process, through the isomerisation of two ammonia borane molecules.[3] The appearance of this feature also confirms that the induction period, the disruption of the dihydrogen bonding network, has completed. Following DADB formation, the growth process occurs, whereby DADB reacts with ammonia borane, resulting in hydrogen loss.[1] This hydrogen loss leads to the appearance of hydrogen deficient features in the spectrum, namely polyaminoborane-like products. The observation of a number of boron environments in the spectrum suggests that the hydrogen releasing pathway is complex and cannot be summarised as simply as the reaction shown in reaction 3.5. This is in agreement with the solid state ^{11}B NMR spectrum of polymeric aminoborane.[30] The spectrum showed both sp^2 and sp^3 boron environments present in the sample, showing that the structure was not a simple long chain polymer.

$$NH_3BH_3 \rightarrow (NH_2BH_2)_n + H_2 \qquad \text{Reaction 3.5}$$

While this reaction can account for the appearance of the feature at −13 ppm due to sp^3 boron present as H_2BN_2, it cannot account for the other boron environments that are observed. Some of the boron environments could be explained by the following reactions:

BH_4, H_2BN_2	$2NH_3BH_3 \rightarrow [NH_3BH_2NH_3]^+[BH_4]^-$ (DADB)	Reaction 3.6
H_3BN	Unreacted NH_3BH_3	
H_2BN_2	$NH_3BH_3 \rightarrow (NH_2BH_2)_n + H_2$	Reaction 3.7
H_2BN_2, BH_4	DADB + $NH_3BH_3 \rightarrow [NH_3BH_2NH_2BH_2NH_3]^+[BH_4]^- + H_2$	Reaction 3.8

The reactions above along with ^{11}B NMR observations add weight to the published ammonia borane decomposition pathway, whereby the appearance and reactions of DADB play a key role in hydrogen release.[1, 3] The fact that there is still a substantial H_3BN feature along with the BH_4 presence suggests that the first step of hydrogen release was not completed under the conditions of this experiment, heating at 80°C for 12 hours, in agreement with the Raman spectra.

The final sp^3 B environment observed, due to HBN_3, was not accounted for in a previous study.[10] There is potential for competing cyclisation reactions to occur instead of the reaction of DADB or DADB like molecules with ammonia borane, as demonstrated below.[1]

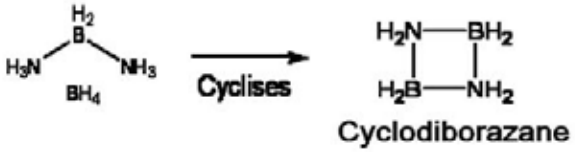

Reaction 3.9

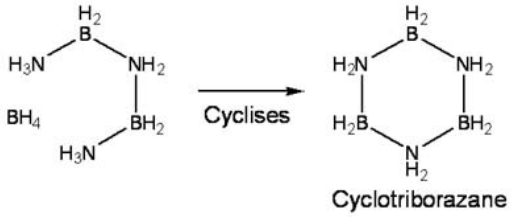

Reaction 3.10

Following cyclisation, further molecules containing sp^3 hybridised B in the form of H_2BN_2 are produced, again highlighting the complex nature of the decomposition pathway. These cyclic products could potentially react with ammonia borane giving rise to products containing HBN_3 units as shown in reaction 3.11, which plays an important role in the decomposition of ammonia borane in solution.[31] However, no

results have been published that provide evidence that this process occurs in the solid state.

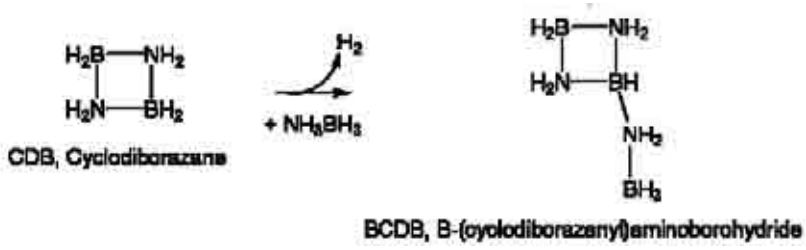

Reaction 3.11

There is also a small amount of sp^2 boron evident in the form of a broad feature observed at 27 ppm. The appearance of sp^2 boron in the spectrum would presumably be related to the loss of the second equivalent of hydrogen. This loss is generally associated with temperatures in excess of 100°C,[32] although the results here suggest that this loss can begin at temperatures as low as 80°C, possibly due to the long heating time of 12 hours. The low intensity of this feature shows that this hydrogen loss does not contribute significantly to the hydrogen release at temperatures up to 80°C. There are a number of pathways that could account for the appearance of sp^2 boron in the spectrum, two examples are shown below.

$$(NH_2BH_2)_n \rightarrow (NHBH)_n + H_2$$ Reaction 3.12

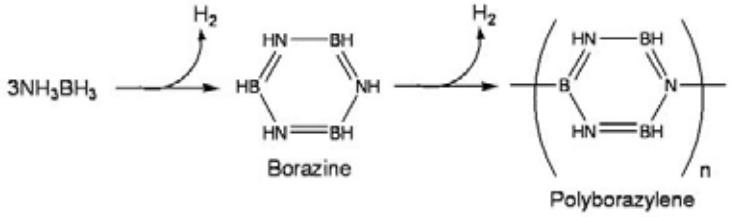

Reaction 3.13

The solid state ^{11}B NMR spectrum obtained after heating ammonia borane to 200°C is shown in figure 3.18. Again a number of features are observed, with similar chemical shifts, as observed with the spectrum obtained after heating to 80°C. However, there are significant differences between the two spectra with regards to the intensity of the features observed.

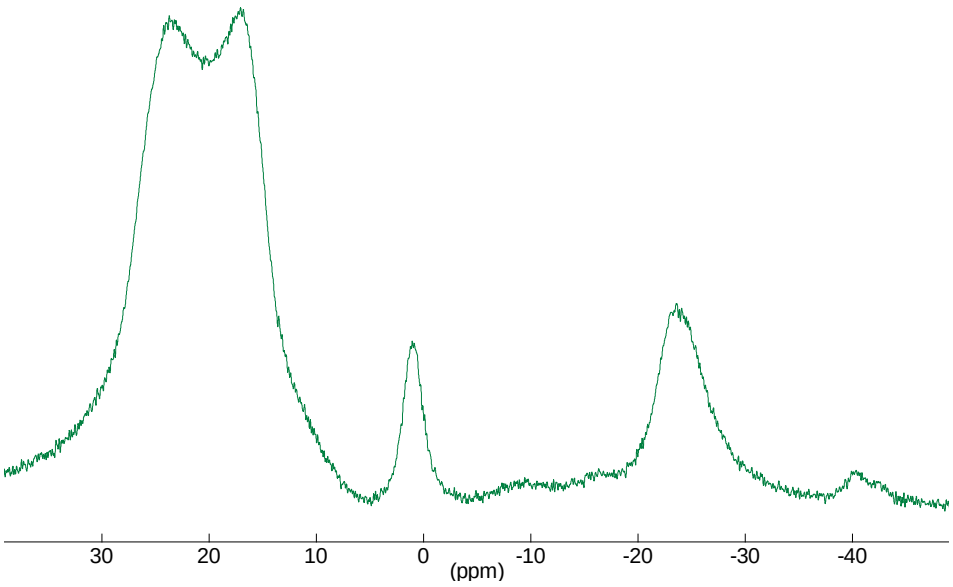

Figure 3.18 – The solid state ^{11}B MAS NMR spectrum of ammonia borane after heating to 200°C for 12 hours

The dominant feature in the spectrum is now that of sp^2 boron. There is still an sp^3 boron signal observed, namely due to HBN_3 observed at −23.7 ppm. The features due to BH_4 and H_2BN_2 have dramatically reduced in intensity and there is now only a small signal in the regions where these groups would be observed. This shows that the nucleation events have completed and there is only a minimal amount of DADB present in the sample and as such the release of the first equivalent of hydrogen has concluded.

The spectrum also showed the appearance of a feature at 1.0 ppm. This environment could have been related to BN. The solid state ^{11}B NMR spectrum of cubic BN shows a sharp resonance at 1.6 ppm and that of hexagonal BN shows a quadrupolar feature at similar chemical shift to the one observed in figure 3.18.[33, 34] Therefore there is a possibility that cross linking reactions had proceeded, producing BN_3 environments, reaction 3.14. The resulting trigonal planar B environments are consistent with those present in hexagonal BN and therefore the feature would be expected to be quadrupolar at approximately 30 ppm. Furthermore, the ultimate decomposition product of NH_3BH_3 has been observed to be hexagonal and not cubic BN.[5] The feature at 1.0 ppm may have been due to oxidation of the sample.

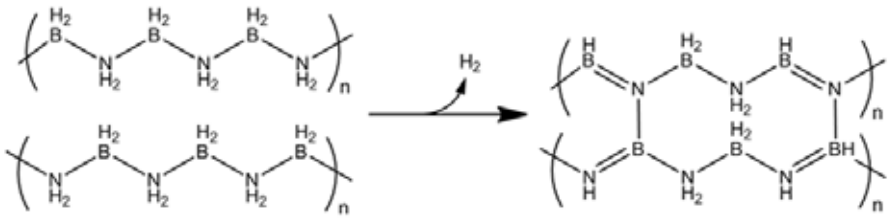

Reaction 3.14

The dominant quadrupolar sp^2 boron signal, +30 ppm, is due to the release of the second equivalent of hydrogen. The dominant reaction that produces this product is the loss of hydrogen from polyaminoborane, giving polyiminoborane, shown by reaction 3.15.

$$(NH_2BH_2)_n \rightarrow (NH{=}BH)_n + H_2 \qquad \text{Reaction 3.15}$$

As discussed previously there are a number of side reactions that can again contribute to this sp^2 boron feature, making it the most prominent feature in the spectrum.

The continued presence of a H_3BN sp^3 environment is a curious observation. Similar studies of ammonia borane decomposition show that by a temperature of 200°C this feature is lost.[30] The slight downfield shift of this feature to −23.7 ppm suggested that this feature was not due to NH_3BH_3 presence. A potential explanation is that a cyclic species such as cyclotriborazane has reacted with ammonia borane at lower temperatures, leading to B-(cyclotriborazanyl)aminoborohydride, BCTB. At temperatures approaching 200°C these species may lose hydrogen specifically from the ring, resulting in a product containing sp^2 boron in the ring and an sp^3 H_3BN boron environment in the side chain, shown by reaction 3.16, consistent with observations in the NMR spectrum. This product could also polymerise, further releasing hydrogen and leading to a structure similar in nature to polyborazylene, containing sp^2 boron with an NH_2BH_3 unit attached.

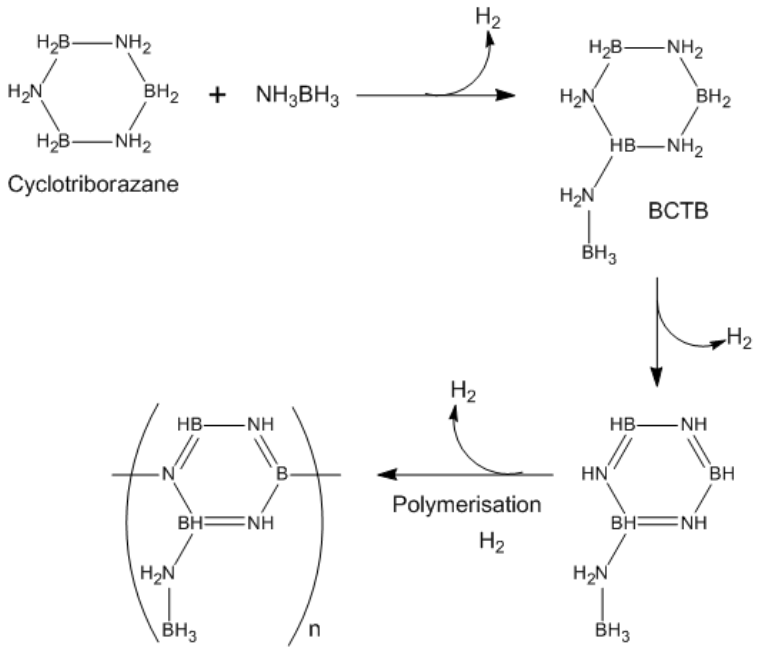

Reaction 3.16

A table showing the changes in the solid state ^{11}B MAS NMR spectrum of ammonia borane as it was heated can be seen in Appendix 1.

3.7 Conclusion

NH_3BH_3 shows potential as a hydrogen storage material due to its high gravimetric hydrogen content, 19.6 wt%. However, as shown by thermal desorption results, section 3.4, the desorption profile shows broad features. The complexity of these desorptions was highlighted by solid state ^{11}B MAS NMR results, section 3.6, where a number of B environments were present in the samples after heating NH_3BH_3 to 80°C and 200°C. Raman spectroscopic studies, section 3.5, showed that these products were polymeric, which implies that rehydrogenation of these decomposition products is not possible, a significant drawback for its potential use as a hydrogen storage material.

3.8 References

1. Stowe, A. C.; Shaw, W. J.; Linehan, J. C.; Schmid, B.; Autrey, T., *In situ* solid state ^{11}B MAS-NMR studies of the thermal decomposition of ammonia borane: mechanistic studies of the hydrogen release pathways from a solid state hydrogen storage material. *Physical Chemistry Chemical Physics* **2007,** 9, 1831–1836.

2. Wolf, G.; Baumann, J.; Baitalow, F.; Hoffmann, F. P., Calorimetric process monitoring of thermal decomposition of B–N–H compounds. *Thermochimica Acta* **2000,** 343, 19–25.

3. Bowden, M. E.; Autrey, T.; Brown, I.; Ryan, M., The thermal decomposition of ammonia borane: A potential hydrogen storage material. *Current Applied Physics* **2008,** 8, 498–500.

4. Hu, M. G.; Geanangel, R. A.; Wendlandt, W. W., The thermal decomposition of ammonia borane. *Thermochimica Acta* **1978,** 23, 249–255.

5. Kim, D.; Moon, K.; Kho, J.; Economy, J.; Gervais, C.; Babonneau, F., Synthesis and characterization of poly(aminoborane) as a new boron nitride precursor. *Polymers for Advanced Technologies* **1999,** 10, 702–712.

6. Mayer, E., Symmetrical cleavage of diborane by ammonia in solution. *Inorganic Chemistry* **1972,** 11, 866–869.

7. Sit, V.; Geanangel, R. A.; Wendlandt, W. W., The thermal dissociation of NH_3BH_3. *Thermochimica Acta* **1986,** 113, 379–382.

8. Baitalow, F.; Baumann, J.; Wolf, G.; Jaenicke-Rössler, K.; Leitner, G., Thermal decomposition of B–N–H compounds investigated by using combined thermoanalytical methods. *Thermochimica Acta* **2002,** 391, 159–168.

9. Fazen, P. J.; Remsen, E. E.; Beck, J. S.; Carrol, P. J.; McGhie, A. R.; Sneddon, L. G., Synthesis, properties and ceramic conversion reactions of polyborazylene. A high-yield polymeric precursor to boron nitride. *Chemistry of Materials* **1995,** 7, 1942–1956.

10. Heldebrant, D. J.; Karkamkar, A.; Hess, N.; Bowden, M. E.; Rassar, S.; Zheng, F.; Rappe, K.; Autrey, T., The effects of chemical additives on the induction phase in solid-state thermal decomposition of ammonia borane. *Chemistry of Materials* **2008,** 20, 5332–5336.

11. Wiberg, E.; Bolz, A.; Buchheit, P., Zur Borin-Hupothese der Borwasserstoff-Struktur. 1. Mitteilung uber Aminoderivate des Monoborlns BH_3 I: Der Verbindungstyp $BH_2(NR_2)$. *Zeitschrift für Anorganische Chemie* **1948,** 256, 285–306.

12. Böddeker, K. W.; Shore, S. G.; Bunting, R. K., Boron-nitrogen chemistry. I. Synthesis and properties of new cycloborazanes, $(BH_2NH_2)_n$. *Journal of the American Chemical Society* **1966,** 88, 4396–4401.

13. Denton, D. L.; Johnson, A. D.; Hickam, C. W.; Bunting, R. K.; Shore, S. G., Boron-nitrogen chemistry. II. Poly(aminoborane). *Journal of Inorganic and Nuclear Chemistry* **1975,** 37, 1037–1038.

14. Schellenberg, R.; Kriehme, J.; Wolf, G., Thermal decomposition of cyclotriborazane. *Thermochimica Acta* **2007,** 457, 103–108.

15. Gutowska, A.; Li, L.; Shin, Y.; Wang, C. M.; Li, X. S.; Linehan, J. C.; Smith, R. S.; Kay, B. D.; Schmid, B.; Shaw, W. J.; Gutowski, M.; Autrey, T., Nanoscaffold mediates hydrogen release and the reactivity of ammonia borane. *Angewandte Chemie-International Edition* **2005,** 44, 3578–3582.

16. Hess, N. J.; Bowden, M. E.; Parvanov, V. M.; Mundy, C.; Kathmann, S. M.; Schenter, G. K.; Autrey, T., Spectroscopic studies of the phase transition in ammonia borane: Raman spectroscopy of single crystal NH_3BH_3 as a function of temperature from 88 K to 330K. *The Journal of Chemical Physics* **2008,** 128, 034508–1 – 034508–11.

17. Smith, J.; Seshadri, K. S.; White, D., Infrared spectra of matrix isolated BH_3–NH_3, BD_3–ND_3 and BH_3–ND_3. *Journal of Molecular Spectroscopy* **1973,** 45, 327–337.

18. Trudel, S.; Gilson, D. F. R., High-pressure Raman spectroscopic study of the ammonia-borane complex. Evidence for the dihydrogen bond. *Inorganic Chemistry* **2003,** 42, 2814–2816.

19. Custalcean, R.; Dreger, Z. A., Dihydrogen bonding under high pressure: A Raman study of BH_3NH_3 molecular crystal. *Journal Of Physical Chemistry B* **2003,** 107, 9231–9235.

20. Allis, D. G.; Kosmowski, M. E.; Hudson, B. S., The inelastic neutron scattering spectrum of H_3B:NH_3 and the reproduction of its solid-state features by periodic DFT. *Journal of the American Chemical Society* **2004,** 126, 7756–7757.

21. Taylor, R. C.; Cluff, C. L., Vibrational frequency associated with the boron-nitrogen dative bond in amine boranes. *Nature* **1958,** 182, 390–391.

22. Cunningham, P. T.; Maroni, V. T., Laser Raman spectra of solid and molten $NaNH_2$: Evidence for hindered rotation of the NH_2^- ion. *The Journal of Chemical Physics* **1972,** 57, 1415–1418.

23. Anderson, T. F.; Burg, A. B., The Raman spectrum of liquid diborane. *Journal of Chemical Physics* **1938,** 6, 586–591.

24. Pimentel, G. C.; Sederholm, C. H., Correlation of Infrared stretching frequencies and hydrogen bond distances in crystals. *The Journal of Chemical Physics* **1956,** 24, 639–641.

25. Pimentel, G. C.; McClellan, A. L., The Hydrogen Bond. *W. H. Freeman And Company* **1960**.

26. Murli, C.; Song, Y., Pressure-induced transformations in diborane: A Raman spectroscopic study. *Journal Of Physical Chemistry B* **2009,** 113, 13509–13515.

27. Bower, D. I.; Maddams, W. F., The vibrational spectroscopy of polymers. **1989**.

28. Kojima, Y.; Kawai, Y., IR characterizations of lithium imide and amide. *Journal of Alloys and Compounds* **2005,** 395, 236–239.

29. Gervais, C.; Framery, E.; Duriez, C.; Maquet, J.; Vaultier, M.; Babonneau, F., ^{11}B and ^{15}N solid state NMR investigation of a boron nitride preceramic polymer prepared by ammonolysis of borazine. *Journal of the European Ceramic Society* **2005,** 25, 129–135.

30. Gervais, C.; Babonneau, F., High resolution solid state NMR investigation of various boron nitride preceramic polymers. *Journal of Organometallic Chemistry* **2002,** 657, 75–82.

31. Shaw, W. J.; Linehan, J. C.; Szymczak, N. S.; Heldebrant, D. J.; Yonker, C.; Camaioni, D. M.; Baker, R. T.; Autrey, T., In situ multinuclear NMR spectroscopic studies of the thermal decomposition of ammonia borane in solution. *Angewandte Chemie-International Edition* **2008,** 47, 7493–7496.

32. Xiong, Z.; Yong, C. K.; Wu, G.; Chen, P.; Shaw, W. J.; Karkamkar, A.; Autrey, T.; Jones, M. O.; Johnson, S. R.; Edwards, P. P.; David, W. I. F., High-capacity hydrogen storage in lithium and sodium amidoboranes. *Nature Materials* **2008,** 7, 138–141.

33. Jeschke, G.; Hoffbauer, W.; Jansen, M., A comprehensive NMR study of cubic and hexagonal boron nitride. *Solid State Nuclear Magnetic Resonance* **1998,** 12, 1–7.

34. Marchetti, P. S.; Kwon, D.; Schmidt, W. R.; Interrante, L. V.; Maciel, G. E., High-field ^{11}B Magic-Angle Spinning NMR characterization of boron nitrides. *Chemistry of Materials* **1991,** 3, 482–486.

Chapter 4

The Reaction of Sodium Hydride with Ammonia Borane

4.1 Introduction

At the beginning of this research there had been no reported investigations into the reactions of metal hydrides and ammonia borane. Initial investigations were targeted at synthesising the mixed amide borohydride of sodium, $Na_2BH_4NH_2$, which has been previously reported.[1] Initial investigations into the reaction of NaH and NH_3BH_3 in a molar ratio of 2:1 resulted in excess NaH in the product mixture. The 1:1 reaction mixture also resulted in excess NaH remaining at the end of the experiments. It was found that a stoichiometry of 1:2 in favour of NH_3BH_3 was required to yield a product free from starting materials. This new trigonal crystalline phase was found to be different from $Na_2BH_4NH_2$. The hydrogen desorption properties of this material were investigated and spectroscopic characterisations carried out.

4.2 Experimental

Sodium hydride (Sigma-Aldrich, 95% purity) and ammonia borane (Sigma-Aldrich, 97% purity) were ground together in a 1:2 molar ratio in an argon filled glove box (>10 ppm O_2, >1 ppm H_2O), and heated under a flowing argon atmosphere at 60°C. The sample was reground and annealed at 60°C to improve the crystallinity of the sample.

$NaNH_2BH_3$ synthesis was attempted through the reaction of $NaNH_2$ (Sigma-Aldrich, 95% purity) and NH_3BH_3 (Sigma-Aldrich, 97% purity) in a 1:1 molar ratio. The reagents were mixed together in an argon filled glove box (>10 ppm O_2, >1 ppm H_2O).

4.3 Powder X-Ray Diffraction

Following heating of the reaction mixture, powder X-Ray diffraction (XRD) patterns were collected for the products. Initial investigations showed that a new crystalline phase formed at a temperature of 60°C that had previously not been reported in the literature. This phase was collected as a white powder and the powder XRD pattern is shown in figure 4.1.

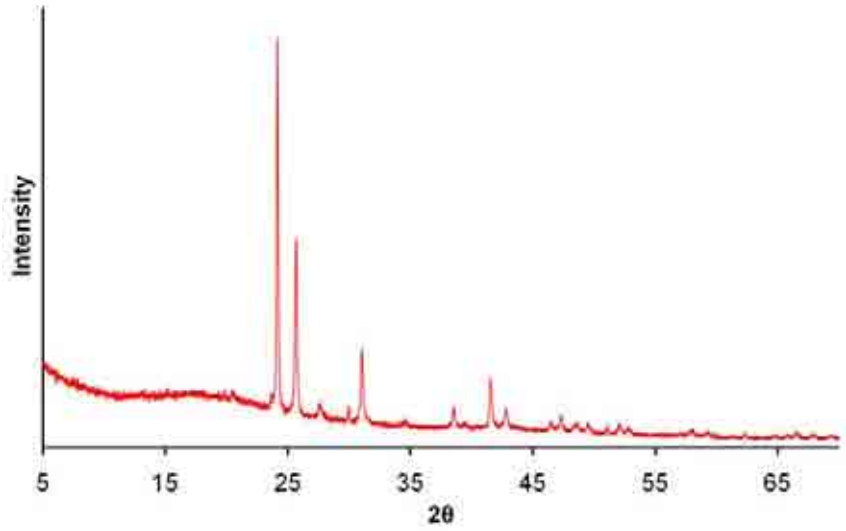

Figure 4.1 – The powder XRD pattern of the product of the reaction of NaH + $2NH_3BH_3$ at 60°C

Further experiments showed that this phase continued to exist up to a temperature of 110°C. At temperatures between 120°C and 400°C the only crystalline phase observed in the powder XRD patterns was that of sodium borohydride, $NaBH_4$. At 500°C and 800°C the powder XRD patterns showed no evidence of crystalline material.

Studies in the literature regarding the reaction of ammonia borane with sodium hydride have focused on a 1:1 reaction mixture, which have proved to produce the

crystalline phase sodium amidoborane, $NaNH_2BH_3$. Synthesis of this material can be carried out in solution, using tetrahydrofuran (THF) as solvent,[2, 3] or through ball milling the reagents.[4, 5] The synthesis of this material has not previously been reported through direct thermal solid state reaction of the starting materials. Investigations into the 1:1 reaction found that at a temperature as low as 40°C the desired 1:1 product could be obtained. The powder XRD pattern of this product is shown in figure 4.2.

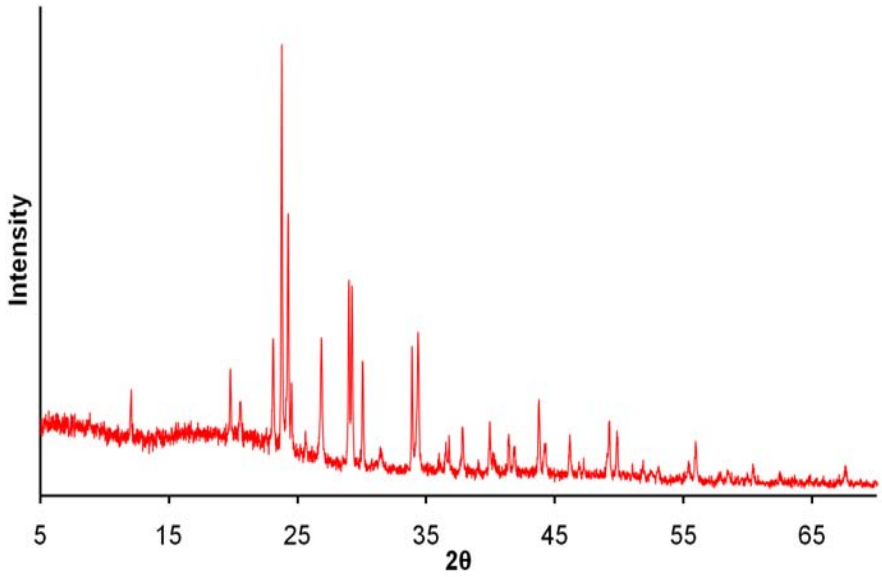

Figure 4.2 – The powder XRD pattern of the product of the reaction of NaH + NH_3BH_3 at 40°C

A stack plot of the powder XRD patterns obtained from the products of the 1:1 reaction at various temperatures is shown in figure 4.3. It can be seen that $NaNH_2BH_3$ was also formed in the 1:1 reaction at 50°C and was the dominant phase in the powder XRD pattern. There were also some lower intensity peaks present in this pattern which are not observed in figure 4.2. These peaks have similar 2θ values to the peaks observed in the unidentified crystalline phase from the 1:2 reaction, suggesting that this phase could also have formed during the reaction. At 60°C the powder XRD pattern contained no evidence of crystalline material and the pattern obtained after reaction at 200°C showed only the presence of NaH.

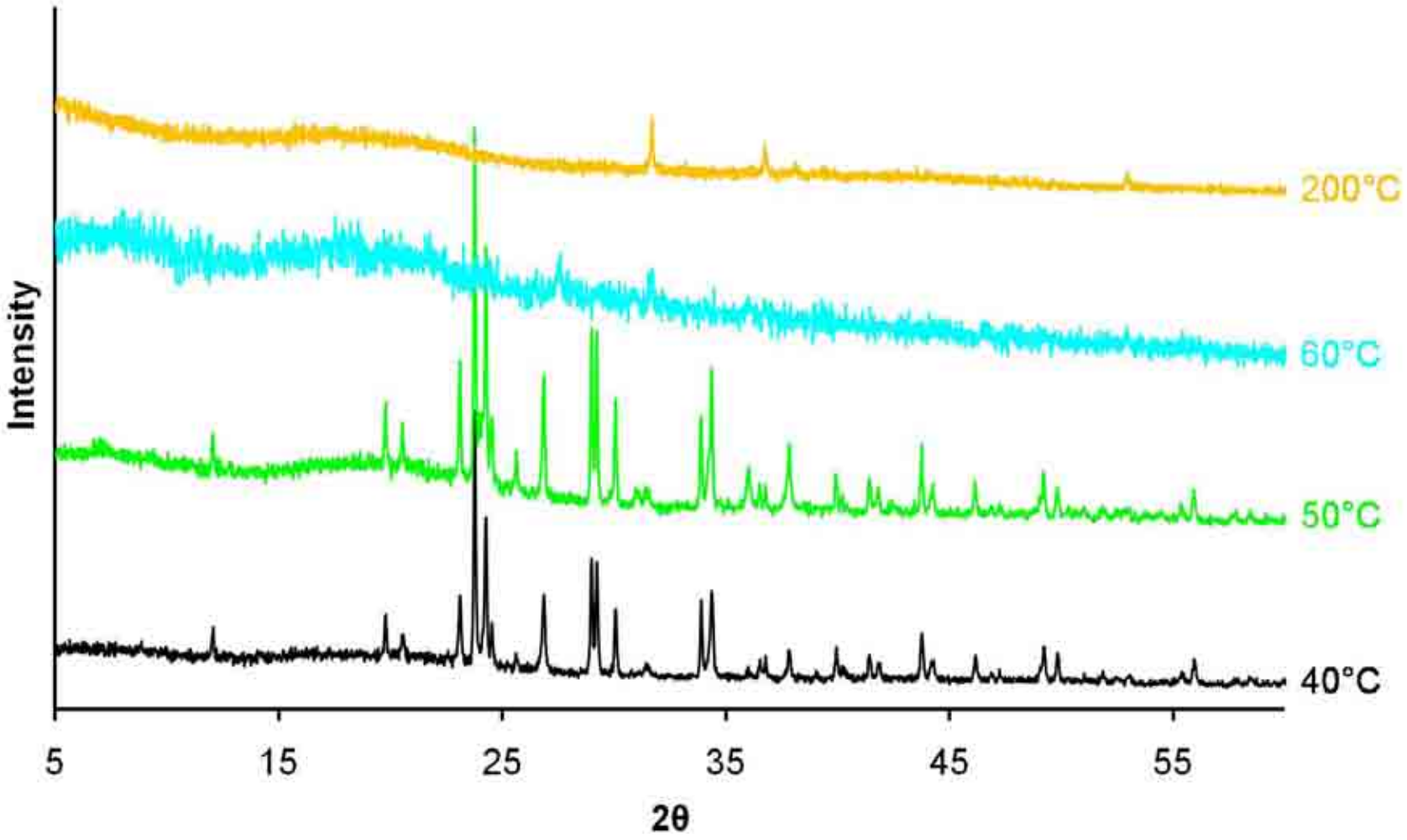

Figure 4.3 – Powder XRD patterns obtained from the products of the NaH + NH_3BH_3 reaction at various temperatures

The 1:2 reaction was subsequently investigated at lower temperatures following the successful synthesis of $NaNH_2BH_3$. A stack plot showing the crystalline phases formed through the NaH + $2NH_3BH_3$ reaction is shown in figure 4.4. After reaction at 40°C the powder XRD pattern showed the presence of $NaNH_2BH_3$ as well as unreacted NH_3BH_3. There were no peaks due to the presence of NaH. Reaction at 50°C again showed the presence of $NaNH_2BH_3$ in the product mixture as well as NH_3BH_3 and no NaH. This pattern also revealed that the unknown crystalline phase from reaction at 60°C had also begun to form. The plot clearly shows the initial formation of $NaNH_2BH_3$, followed by the emergence of the unidentified new crystalline phase and finally the appearance of $NaBH_4$ at higher temperatures. To aid the visibility of the peaks found around 24°, figure 4.5 shows a stack plot of the products of reaction at temperatures up to 110°C, between 22° and 30° 2θ.

Room temperature reactions of both 1:1 and 1:2 reaction mixtures were also carried out. Results showed that the 1:1 reaction would proceed to completion, the synthesis of $NaNH_2BH_3$, over a ten day period. The 1:2 reaction was also found to proceed at room temperature. The powder XRD pattern taken ten days after the reagents had been ground together showed the presence of $NaNH_2BH_3$ and NH_3BH_3, but that the NaH had been consumed by the reaction. Two months after the start of the reaction, the powder XRD pattern showed only the presence of the unidentified phase previously synthesised in 1:2 reactions.

The formation of $NaNH_2BH_3$ has also been reported through the reaction of sodium amide, $NaNH_2$, with ammonia borane in a 1:1 ratio using THF as solvent.[3] This was, however, shown to be a much slower reaction than the reaction of NaH with NH_3BH_3. The solid state reaction, in contrast, showed the opposite. While the 1:1 reaction involving NaH was shown to require ten days to reach completion at room temperature, the reaction of $NaNH_2$ and NH_3BH_3 was instantaneous. On mixing the reagents, white smoke was observed to be given off from the reaction and the reaction mixture became wet before rapidly drying. The powder XRD pattern of the product showed that $NaNH_2BH_3$ had formed, figure 4.6, although there was still substantial presence of $NaNH_2$, despite there no longer being any NH_3BH_3 present.

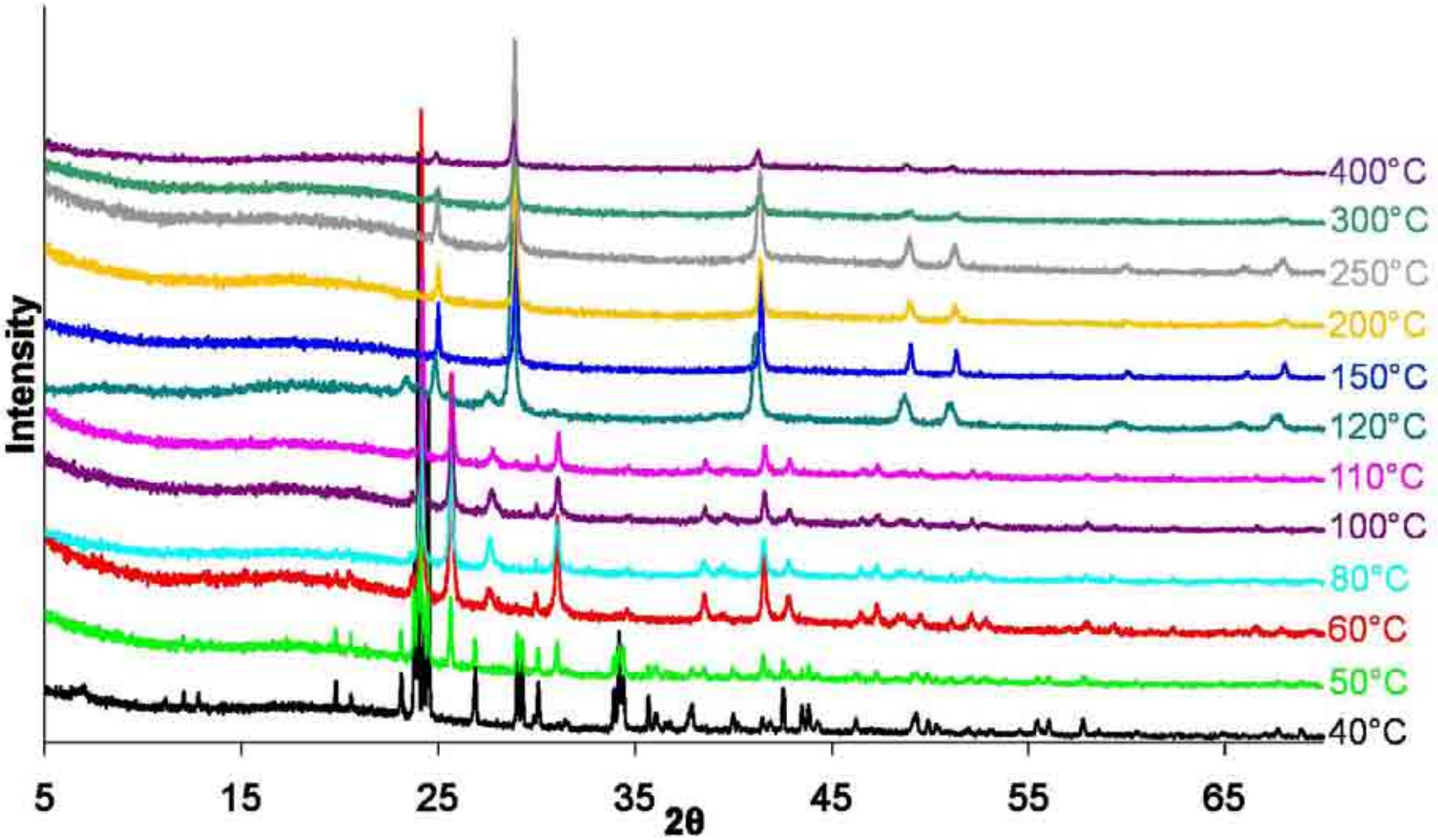

Figure 4.4 – Powder XRD patterns obtained from the products of the NaH + $2NH_3BH_3$ reaction at various temperatures

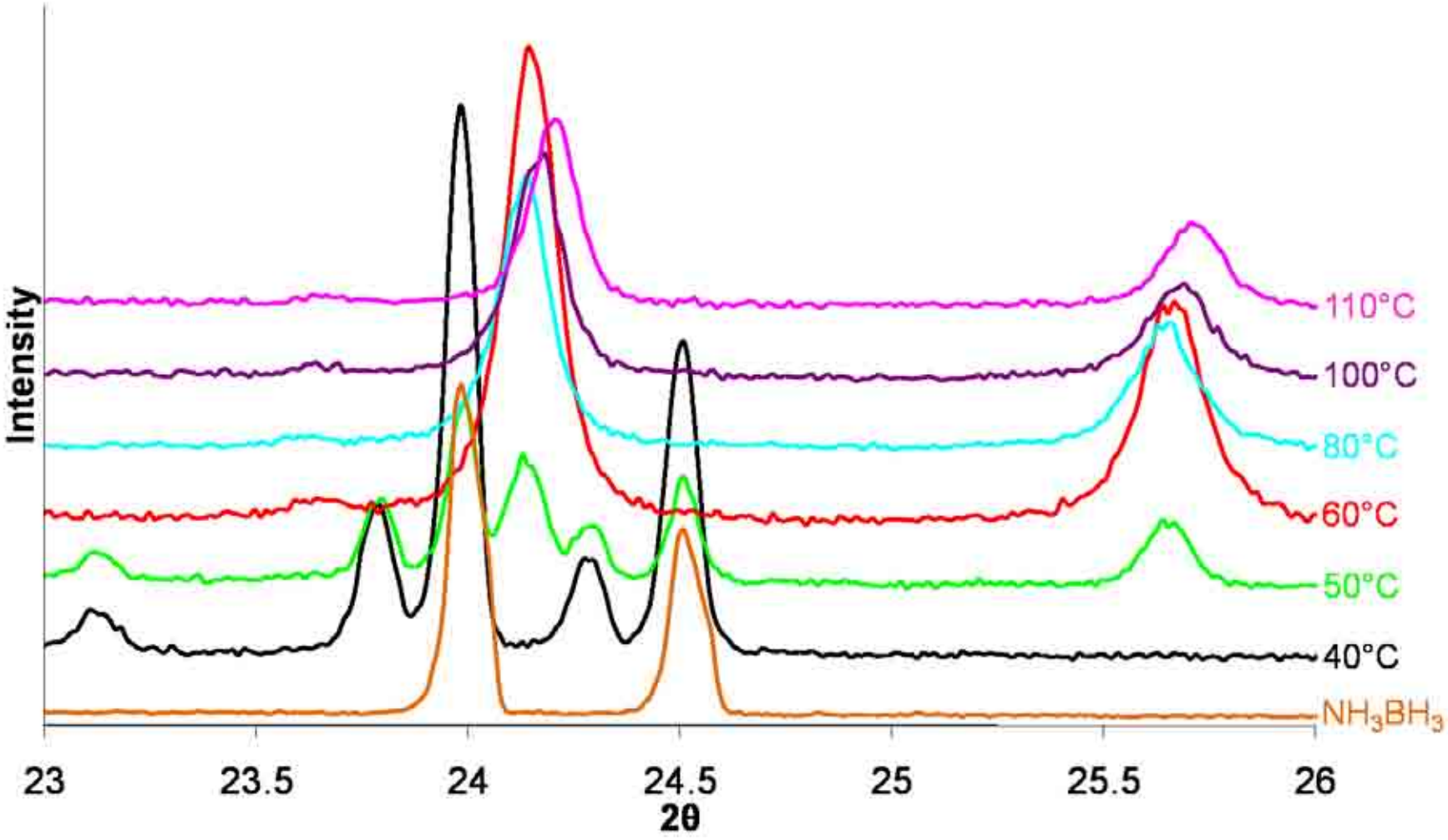

Figure 4.5 – Powder XRD patterns between 23° and 26° 2θ obtained from the products of the NaH + $2NH_3BH_3$ reaction at temperatures before the appearance of $NaBH_4$

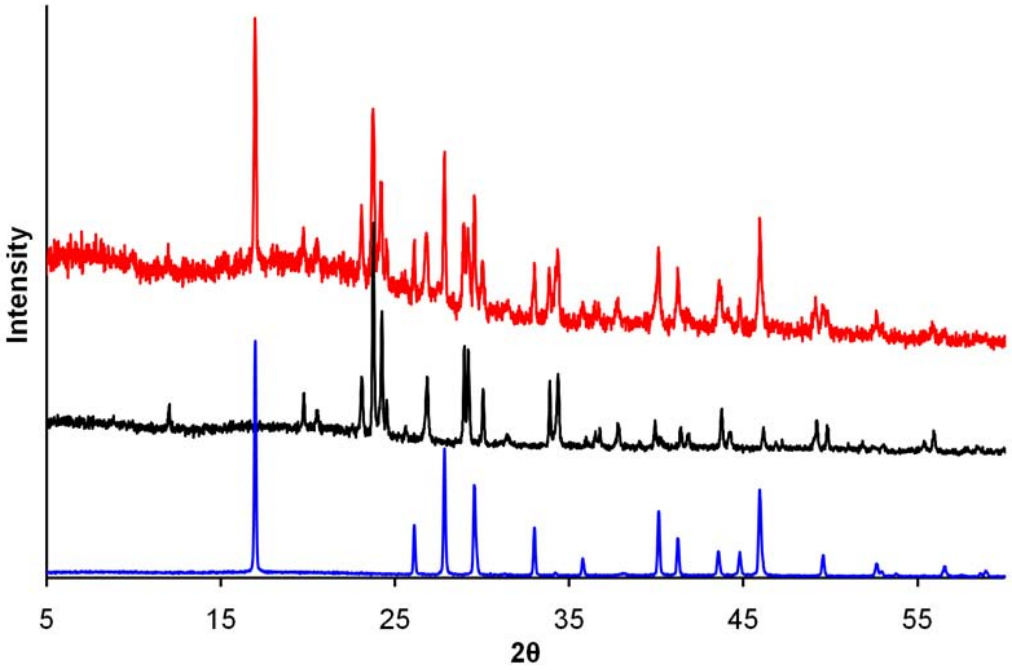

Figure 4.6 – The powder XRD pattern of the product of the reaction of $NaNH_2$ + NH_3BH_3 at room temperature (red), the XRD patterns of $NaNH_2BH_3$ (black) and $NaNH_2$ (blue) are shown for comparison

4.3.1 Discussion

From the powder XRD patterns it can be concluded that the previously unreported crystalline phase formed at a temperature of 60°C and underwent decomposition above 110°C. $NaBH_4$ was the only crystalline decomposition product, implying that amorphous N containing material also formed. This was similar to the decomposition of ammonia borane, where amorphous decomposition products were also observed, see chapter 3.4.

$NaBH_4$ is known to begin thermal decomposition at 400°C,[6] although the major decomposition steps do not commence until a temperature of 565°C is reached as shown in reaction 4.1.[7]

$$NaBH_4 \rightarrow Na + B + 2H_2 \qquad \text{Reaction 4.1}$$

This is in disagreement to results observed here, where the XRD pattern of the product from reaction at 500°C was amorphous, implying that $NaBH_4$ had already undergone decomposition. $NaBH_4$ treated under the same conditions showed only partial decomposition with some Na being evident in the powder XRD pattern. This

suggested that the amorphous decomposition product effectively decreased the decomposition temperature of $NaBH_4$. Further to this the lack of Na in the powder XRD pattern of the product from the NaH + $2NH_3BH_3$ reaction at 500°C suggested an alternative decomposition pathway to that shown in reaction 4.1. The onset temperature of $NaBH_4$ decomposition has been shown to be lowered through the interaction of the material with $LiAlH_4$[8] and MgH_2[9] resulting in a modified decomposition pathway. However, because the composition of the amorphous material remains unknown it is not possible to determine how the decomposition pathway was modified.

A difference between ammonia borane decomposition and this reaction was the lack of volume expansion on heating. Ammonia borane undergoes a significant volume expansion at 80°C, but this was not observed either during synthesis or decomposition of the unidentified crystalline phase. Therefore, it can be deduced that the induction phase, the disruption of the dihydrogen bonds, observed during the decomposition of ammonia borane, which is responsible for the volume expansion, did not have to occur during the reaction of NaH with NH_3BH_3.

The 1:1 reaction pathway closely resembled that published in the literature. Following synthesis of $NaNH_2BH_3$, powder XRD analysis of the decomposition products after heating to 90°C revealed the sample to be amorphous and further heating to 200°C showed NaH to be the only crystalline phase observed.[3] An interesting observation in the powder pattern of the reaction at 50°C was the emergence of peaks at similar 2θ to those observed in the unidentified crystalline phase. This suggested there may have been competing reactions taking place: firstly the synthesis of $NaNH_2BH_3$ and secondly the synthesis of the unidentified crystalline phase. However, the lower temperature 1:2 reactions showed the reactions were not in fact competing but the synthesis of $NaNH_2BH_3$ was the first step in the synthesis of the unidentified crystalline phase. This was further substantiated through the reaction of $NaNH_2BH_3$, previously synthesised through a 1:1 reaction at 40°C, with NH_3BH_3 at 60°C. The powder XRD pattern, figure 4.7, of the product showed that the unidentified crystalline phase from the 1:2 reaction was synthesised.

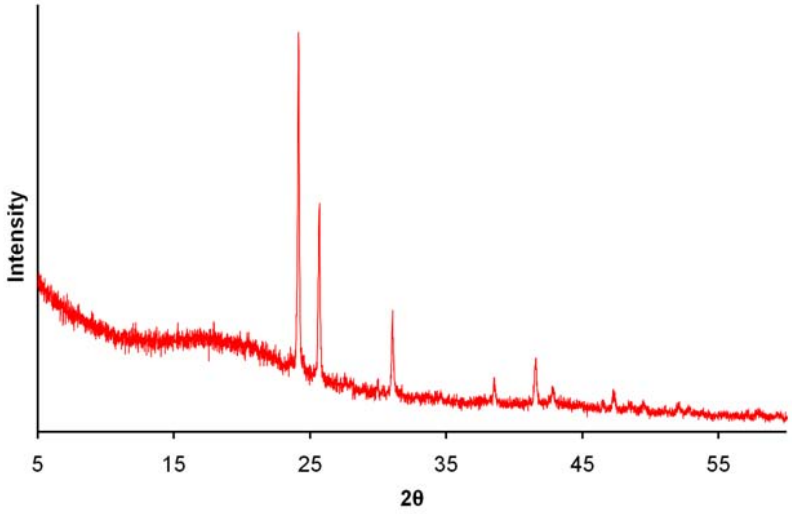

Figure 4.7 – The powder XRD pattern of the product of the reaction of $NaNH_2BH_3$ + NH_3BH_3 at 60°C

The fact that both the 1:1 and 1:2 reactions proceeded at room temperature highlights the fact that these reactions must have been thermodynamically favoured, with a significant driving force and no significant kinetic barriers to the reactions. NaH has a negatively charged hydride ion and as previously discussed NH_3BH_3 has protic hydrogens associated with the nitrogen atoms. Therefore, there is potentially an attractive force between hydrogens of this nature which can combine to form a hydrogen molecule, leaving a sodium cation and an NH_2BH_3 anion which crystallise as $NaNH_2BH_3$. This reaction mechanism will be substantiated further in subsequent sections of this chapter that investigate the gases released during the reaction pathway. In terms of the reaction of $NaNH_2BH_3$ with NH_3BH_3, little can be determined about the driving force for the reaction from powder XRD patterns alone and this will be discussed further in the following sections of this chapter.

The solid state reaction between $NaNH_2$ and NH_3BH_3 was shown to synthesise $NaNH_2BH_3$, which implied that the white gas given off was NH_3, reaction 4.2. This assumption also agreed with the observation that NH_3 was released during the THF mediated reaction.[3]

$$NaNH_2 + NH_3BH_3 \rightarrow NaNH_2BH_3 + NH_3 \qquad \text{Reaction 4.2}$$

There are two possible mechanisms that could have proceeded, both resulting in the same product. The NH_2^- anion could have acted as a nucleophile, attacking the B in

NH_3BH_3 through an S_N2 type reaction, shown in reaction 4.3 or acted as a base and removed a proton from the NH_3 group in NH_3BH_3 as shown by reaction 4.4.

Reaction 4.3

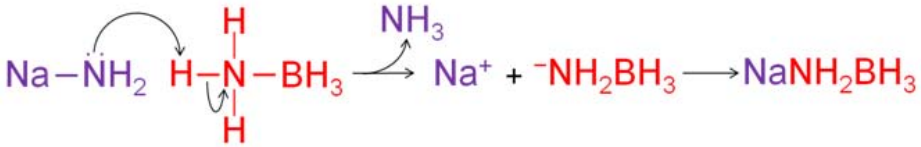

Reaction 4.4

It has been established in other studies that in the solid state the NH_2^- anion appears to act as a nucleophile, whereas in solution the anion acts as a base.[10] Therefore, it can be assumed that reaction 4.3 was responsible for the synthesis of $NaNH_2BH_3$, although no evidence for this can be offered by this study. In order to determine the correct mechanism a deuterated sample of $NaND_2$ would be required as a starting material. The product of reaction would then either be $NaND_2BH_3$ if an S_N2 reaction proceeded or $NaNH_2BH_3$ if the base mediated mechanism took place.

This solid state reaction of NH_3BH_3 with $NaNH_2$ was shown to be a poor method of synthesis of $NaNH_2BH_3$ as there was a significant presence of $NaNH_2$ remaining in the powder XRD pattern, whereas all of the NH_3BH_3 was consumed in the reaction. Had the reaction been stoichiometric then all of the $NaNH_2$ and NH_3BH_3 would have been consumed. The fact that $NaNH_2$ remained after reaction showed that the competing pathway most likely involved NH_3BH_3. The spontaneous nature of the reaction suggests that the reaction could have been sufficiently exothermic to trigger the decomposition of NH_3BH_3. Assuming an S_N2 reaction took place, there are a number of other similar type reactions that could have proceeded as detailed below.

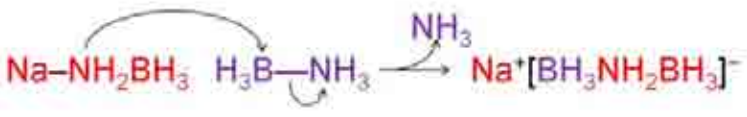

Reaction 4.5

Reaction 4.6

Reaction 4.5 would have competed with the main S_N2, reaction 4.3, consuming NH_3BH_3 and leaving unreacted $NaNH_2$. The second possible S_N2 reaction, reaction 4.6, would have formed $NaNH_2$ as a product of the reaction. Both reactions would form $Na^+[BH_3NH_2BH_3]^-$. As this material is crystalline, see section 4.4, the fact that it was not observed in the powder XRD pattern of the product of this reaction shows that these reactions were not responsible for the observation of excess $NaNH_2$. The continued presence of $NaNH_2$ at the end of the reaction must therefore have been a consequence of partial NH_3BH_3 decomposition in the reaction mixture.

The information gained from powder XRD patterns about the 2:1 reaction pathway is summarised in reaction 4.7, and the 1:1 reaction and $NaNH_2$ reaction pathways are shown in reactions 4.8 and 4.9.

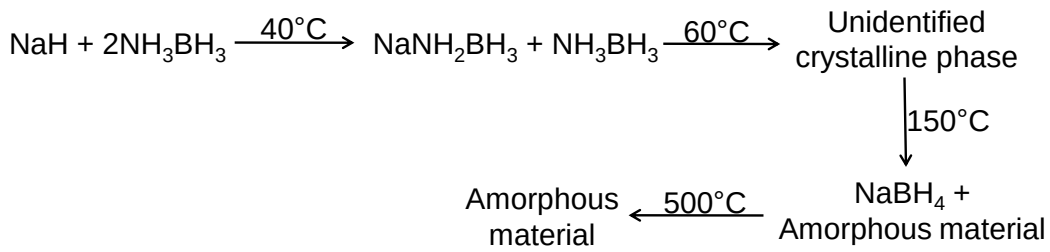

Reaction 4.7

$$NaH + NH_3BH_3 \rightarrow NaNH_2BH_3 \rightarrow \text{Amorphous material} \rightarrow NaH + \text{Amorphous material}$$

Reaction 4.8

$$NaNH_2 + NH_3BH_3 \rightarrow (1-x)NaNH_2 + xNaNH_2BH_3 + xNH_3 + \text{Amorphous material}$$

Reaction 4.9

4.3.2 Indexing

The peak positions observed in the product of the $NaH + 2NH_3BH_3$ reaction at 60°C were run through the indexing routine of Topas.[11] The most probable assignment was for a trigonal unit cell with a = 4.34 Å and c = 17.86 Å, with a suggested space group of $P31c$. The a and c lattice constants were refined through a Pawley fit using Topas[11] to values of 4.3389(4) Å and 17.859(1) Å, respectively, giving a unit cell volume of 291.16(5) Å^3. The refinement is shown in figure 4.8. It can be seen from

this refinement that the product was impure as there were a few broad peaks present, at 20.5°, 27.6° and 39.4° 2θ, that were not accounted for by the indexed trigonal phase. The fact that they were broad indicated that they were most likely an impurity. The very large *c*:*a* ratio of approximately 4:1 led to the question as to whether this was a realistic unit cell. It was found that refinement of anisotropic peak broadening in trigonal symmetry using the method described by Stephens[12] gave rise to a significantly improved fit to the observed data with significantly sharper peaks in the (001) direction. This observation was taken as evidence for the validity of the determined trigonal unit cell.

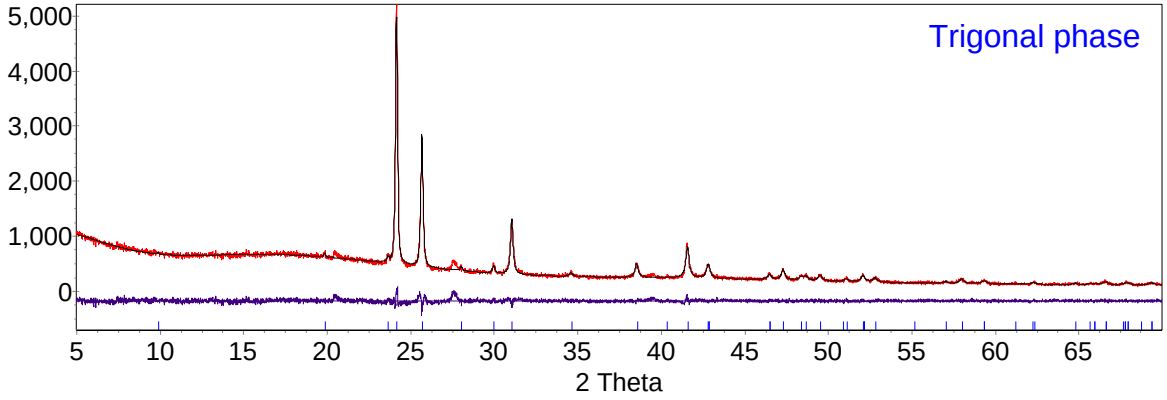

Figure 4.8 – Pawley refinement for the product synthesised through the NaH + $2NH_3BH_3$ reaction at 60°C. The observed pattern is shown in red, the calculated pattern in black and the difference in blue. Blue tick marks indicate the peak positions of the trigonal phase. R_{wp} = 6.186%, χ^2 = 1.540

The procedure was repeated for the peak positions observed for this new phase synthesised in reactions up to a temperature of 110°C. The results are shown in table 4.1 and the refinements can be seen in Appendix 2. The impurity peaks observed in the powder pattern of the products from reaction at 60°C were present in all patterns throughout this temperature range, with the intensity of these peaks being greatest at 80°C.

The refinement of the trigonal phase synthesised through the reaction of $NaNH_2BH_3$ with NH_3BH_3 at 60°C is shown in figure 4.9. Unlike the 1:2 reaction, all of the peaks in this pattern are indexed meaning there were no crystalline impurities in the product. The refined lattice constants and cell volume are shown in table 4.1.

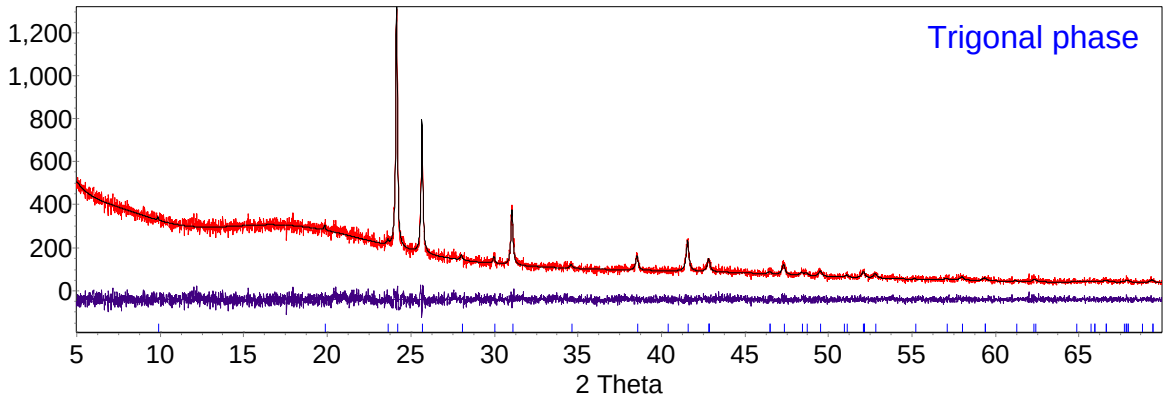

Figure 4.9 – Pawley refinement for the product synthesised through the $NaNH_2BH_3$ + NH_3BH_3 reaction at 60°C. The observed pattern is shown in red, the calculated pattern in black and the difference in blue. Blue tick marks indicate the peak positions of the trigonal phase. R_{wp} = 5.982%, χ^2 = 1.148

Table 4.1 – Refined values of the *a* and *c* lattice constants and cell volume for the trigonal phase observed in the NaH + $2NH_3BH_3$ reaction

Reaction Temperature (°C)	*a* (Å)	*c* (Å)	Cell volume (Å^3)
60	4.3389(4)	17.859(1)	291.16(5)
80	4.3392(5)	17.854(2)	291.12(8)
100	4.3363(6)	17.844(2)	290.59(8)
110	4.3393(5)	17.857(2)	291.19(7)
$NaNH_2BH_3$ + NH_3BH_3 60°C	4.3379(6)	17.848(2)	290.85(8)

As discussed earlier, inspection of the powder XRD pattern of the product from reaction at 120°C, showed that $NaBH_4$ was the dominant crystalline phase present.

$NaBH_4$ has a face centred cubic unit cell with space group $Fm\bar{3}m$. The lattice constants were obtained through a Rietveld refinement using the crystal structure published by Filinchuk and Hagemann.[13] Subsequently, the value of the lattice parameter *a* was refined to 6.1883(7) Å. The refinement for this product can be seen in figure 4.10. Inspection of the fit shows that there were again some unindexed peaks, which are found at 23.4°, 24.0° and 27.6° 2θ. The two peaks observed at 23.4° and 24.0° are unrelated to the trigonal phase observed at 110°C. However, the peak at 27.6° is consistent with an impurity peak from lower temperature reactions.

$NaBH_4$ is the only crystalline phase observed above this temperature, up to a reaction temperature of 400°C. The Rietveld refinements of the powder XRD patterns are shown in Appendix 2. Throughout the reaction temperature range of 120°C to 400°C all of the peaks in the powder XRD patterns can be indexed to $NaBH_4$ with no evidence of any crystalline impurities. Above 500°C the powder XRD patterns were completely amorphous and so no refinements could be performed.

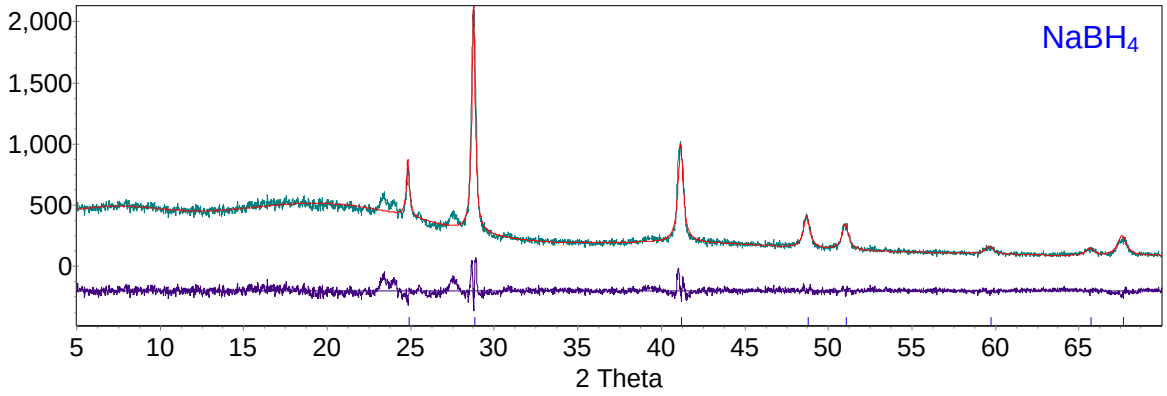

Figure 4.10 – Pawley refinement for the product synthesised through the NaH + $2NH_3BH_3$ reaction at 120°C. The observed pattern is shown in aqua, the calculated pattern in red and the difference in blue. Blue tick marks indicate the peak positions of $NaBH_4$. R_{wp} = 8.141%, χ^2 = 1.785

A Rietveld refinement was performed on the $NaNH_2BH_3$ phase synthesised through the 1:1 reaction at 40°C using the crystal structure published by Wu *et al.*[14] for the isostructural $LiNH_2BH_3$ and the lattice constants published by Xiong *et al.*[5] for $NaNH_2BH_3$. Initially, only the *a*, *b* and *c* lattice constants were refined, however, the resultant refinement was unsatisfactory due to significant differences between the calculated and observed diffraction patterns. Therefore, the refinement moved on to include the atomic coordinates of the heaviest elements in the unit cell, namely sodium, nitrogen and boron. Hydrogen atoms were removed from the refinement as they are poor scatterers of X-rays. The calculated pattern had a much more acceptable fit following this refinement. A selection of refined parameters is shown in table 4.2 along with the original published structure values, and the refined powder XRD pattern shown in figure 4.11. Table 4.2 shows there is good agreement between the two unit cells with respect to lattice constants although there are slight discrepancies with respect to bond lengths. However, this is likely due to the poorer quality of data collected in this study; the acquisition of synchrotron X-ray diffraction

data would likely see these discrepancies reduced. The collection of neutron diffraction data of deuterated samples would also aid refinement of the hydrogen positions. As a consequence of the differences in the quality of data between the two studies, these discrepancies can be deemed acceptable. Not all of the peaks in the powder XRD pattern are accounted for by the $NaNH_2BH_3$ phase. There are two impurity peaks located at 25.6° and 36.0° 2θ, which are not related to either starting material.

Table 4.2 – Refined lattice constants and selected bond lengths of $NaNH_2BH_3$ synthesised in the reaction of NaH + NH_3BH_3 at 40°C

Parameter	Ref 5	NaH + NH_3BH_3 40°C
***a* (Å)**	7.46931(7)	7.4711(5)
***b* (Å)**	14.65483(16)	14.6421(10)
***c* (Å)**	5.65280(8)	5.6600(3)
Na–N bond length (Å)	2.35	2.413(4)
B–N bond length (Å)	1.56	1.460(2)

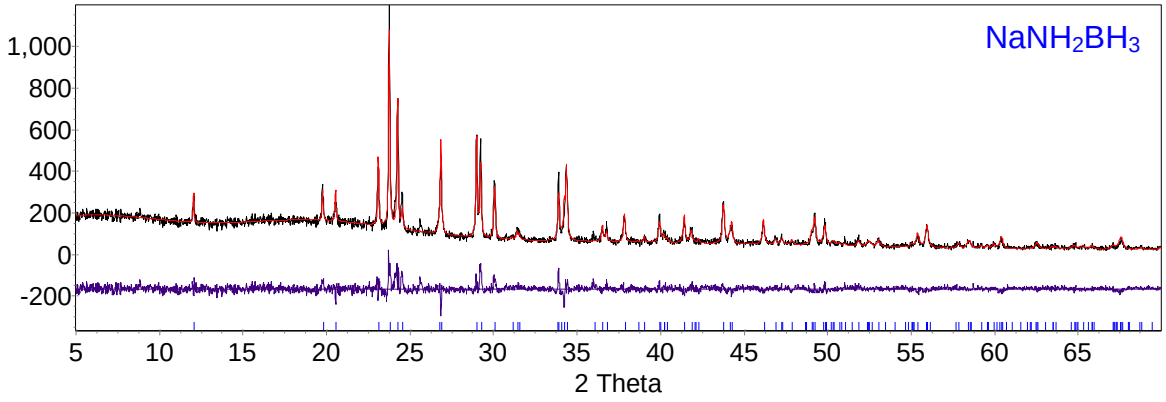

Figure 4.11 – Rietveld refinement of $NaNH_2BH_3$ synthesised from reaction of NaH + NH_3BH_3 at 40°C. The observed pattern is shown in black, the calculated pattern in red and the difference in blue. Blue tick marks indicate the peak positions of $NaNH_2BH_3$. R_{wp} = 13.053%, χ^2 = 1.621

The powder XRD pattern of the product from the NaH + $2NH_3BH_3$ reaction at 40°C was shown to contain both $NaNH_2BH_3$ and NH_3BH_3, and these phases were refined using structures published by Wu *et al*.[14] and Bowden *at al*.,[15] respectively. For the $NaNH_2BH_3$ phase, the *a*, *b* and *c* lattice constants were refined along with the atomic positions of the sodium, nitrogen and boron atoms. The refinement for NH_3BH_3 was carried out with respect to the *a* and *c* lattice constants only. The result is shown in figure 4.12 and the refined values shown in table 4.3. There is good agreement between the published and refined parameters for both $NaNH_2BH_3$ and NH_3BH_3 as shown by table 4.3. The refinement also indicates that there is more NH_3BH_3 in the product of reaction than $NaNH_2BH_3$, and the refinement of NaH showed that this material was consumed by the reaction. The refinement also highlighted some impurities, with unrefined peaks located at 11.1°, 12.8°, 29.9°, 36.0°, 37.7°, 39.6° and 54.5° 2θ.

Table 4.3 - Refined lattice constants and selected bond lengths of $NaNH_2BH_3$ and NH_3BH_3 resulting from the reaction of NaH + $2NH_3BH_3$ at 40°C

Parameter	Ref 5 – $NaNH_2BH_3$	Ref 14 – NH_3BH_3	$NaNH_2BH_3$	NH_3BH_3
***a* (Å)**	7.46931(7)	5.2630(4)	7.4671(4)	5.2373(2)
***b* (Å)**	14.65483(16)	5.2630(4)	14.6316(8)	5.2373(2)
***c* (Å)**	5.65280(8)	5.0504(8)	5.6549(3)	5.0237(3)
Na–N bond length (Å)	2.35	Not applicable	2.43(1)	Not applicable
B–N bond length (Å)	1.56	1.597(3)	1.46(2)	1.589

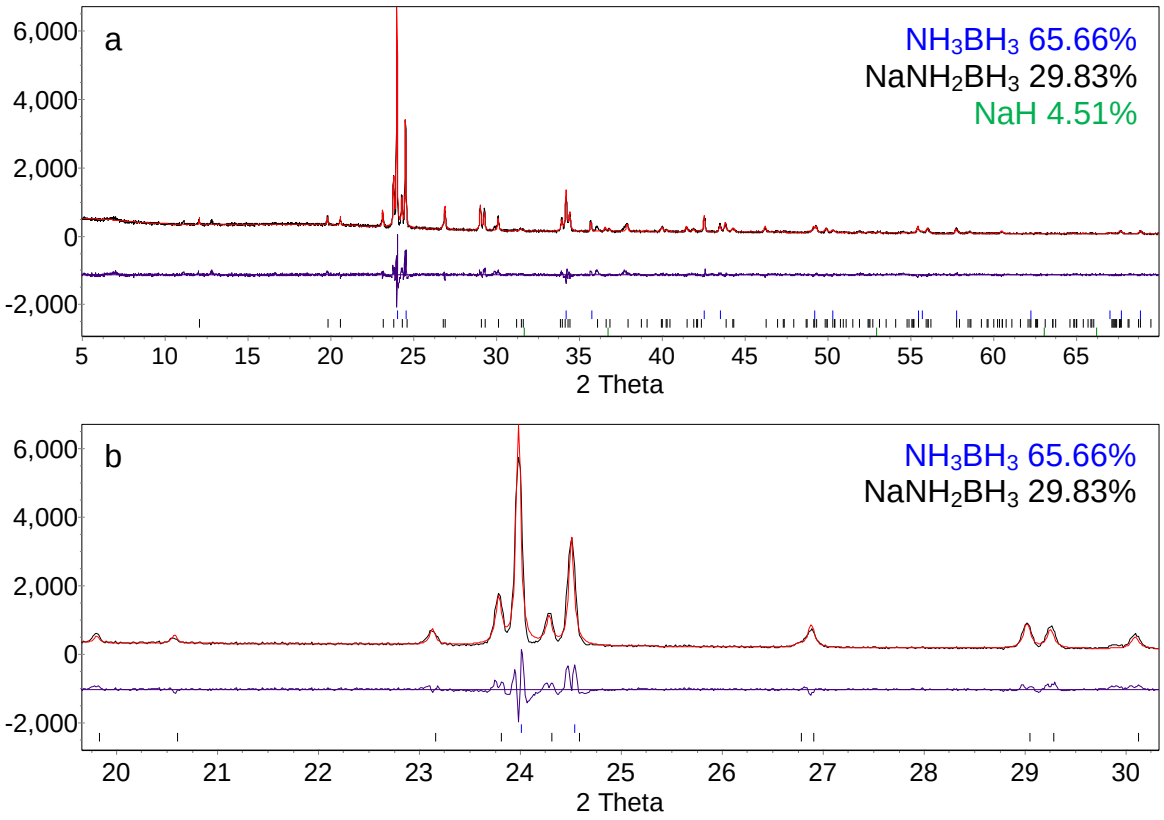

Figure 4.12 – Rietveld refinement for the product synthesised through the NaH + $2NH_3BH_3$ reaction at 40°C (a) the full 2θ range (b) 20 - 30° 2θ. The observed pattern is shown in black, the calculated pattern in red and the difference in blue. Bragg peak positions due to NH_3BH_3 (blue), $NaNH_2BH_3$ (black) and NaH (green) are indicated. R_{wp} = 11.711%, χ^2 = 3.247

The reaction at 50°C produced a powder XRD pattern containing multiple phases. The phases present were refined and the results are shown in table 4.4 and figure 4.13. Rietveld refinements were performed for the known crystalline phases, $NaNH_2BH_3$ and NH_3BH_3 and a Pawley refinement for the unidentified trigonal phase. There is only one unassigned peak in the pattern, observed at 36.1° 2θ. There is good agreement between literature values and the refined parameters, and the NaH refinement again shows that this material has been consumed by the reaction. The refinement also suggests that there is a similar amount of $NaNH_2BH_3$ and NH_3BH_3 in the product.

Table 4.4 - Refined lattice constants and selected bond lengths of $NaNH_2BH_3$, NH_3BH_3 and the trigonal phase synthesised in the reaction of NaH + $2NH_3BH_3$ at 50°C

Parameter	Ref 5 – $NaNH_2BH_3$	Ref 14 – NH_3BH_3	$NaNH_2BH_3$	NH_3BH_3	Trigonal Phase
***a* (Å)**	7.46931(7)	5.2630(4)	7.4570(4)	5.2298(3)	4.3370(3)
***b* (Å)**	14.65483(16)	5.2630(4)	14.6120(9)	5.2298(3)	4.3370(3)
***c* (Å)**	5.65280(8)	5.0504(8)	5.6494(4)	5.0178(4)	17.852(2)
Na–N bond length (Å)	2.35	Not applicable	2.45(2)	Not applicable	Not applicable
B–N bond length (Å)	1.56	1.597(3)	1.49(2)	1.587	Not applicable

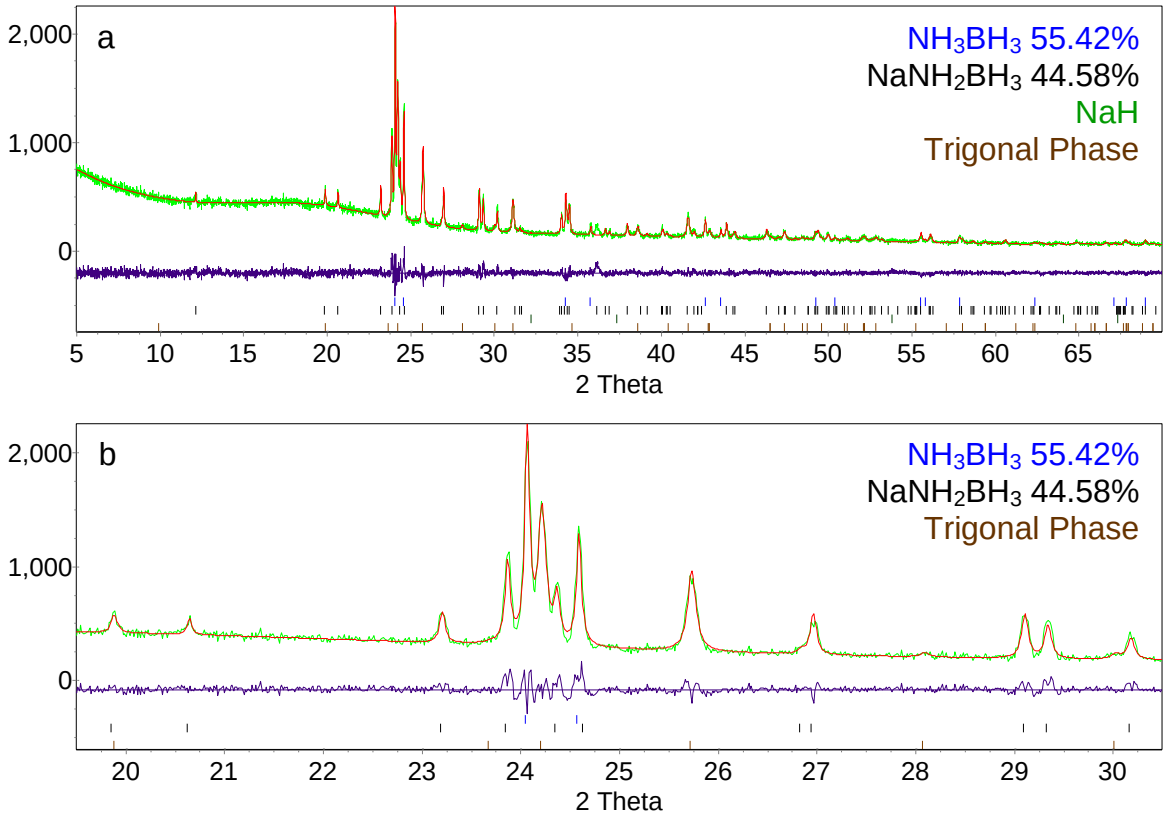

Figure 4.13 - Rietveld refinement of the product synthesised through the NaH + $2NH_3BH_3$ reaction at 50°C (a) the full 2θ range (b) 20 - 30° 2θ. The observed pattern is shown in green, the calculated pattern in red and the difference in blue Bragg peak positions due to NH_3BH_3 (blue), $NaNH_2BH_3$ (black), NaH (green) and the trigonal phase (brown) are indicated. R_{wp} = 7.781%, χ^2 = 1.540

After ten days reaction at room temperature the phases present in the powder XRD pattern could be refined as $NaNH_2BH_3$ and NH_3BH_3. After two months of reaction at room temperature, the phase present in the powder XRD pattern was indexed to a trigonal unit cell and then refined through a Pawley fit. After ten days of reaction the refinements showed that $NaNH_2BH_3$ made up 41.47 mol% of the product compared to 58.05 mol% NH_3BH_3 with a small amount of unreacted NaH. The refined lattice constants of all phases and the refined powder XRD patterns are shown in Appendix 2.

The refined values of phases observed in the products of the series of 1:1 reactions carried out between temperatures of 50°C and 200°C are summarised in table 4.5. The refined powder XRD patterns can be viewed in Appendix 2. The structure published by Shull *et al.*[16] was used for the Rietveld refinement of NaH. At 50°C the only phase that could be refined was that of $NaNH_2BH_3$. Other peaks were present in the pattern, at similar 2θ values to peaks observed both for NH_3BH_3 and the trigonal phase; however, the poor resolution of these peaks made these phases impossible to refine.

Table 4.5 – Refined *a*, *b* and *c* lattice constants observed in the NaH + NH_3BH_3 reaction between temperatures of 50°C and 200°C

Reaction Temperature (°C)	Phase	*a* (Å)	*b* (Å)	*c* (Å)
50	$NaNH_2BH_3$	7.47534(6)	14.648(1)	5.6639(4)
60	Amorphous	Not applicable	Not applicable	Not applicable
200	NaH	4.8833(10)	*a*	*a*
Ref 5	$NaNH_2BH_3$	7.46931(7)	14.65483(16)	5.65280(8)
Ref 15	NaH	4.89	*a*	*a*

Following the room temperature reaction of $NaNH_2$ with NH_3BH_3 the powder XRD pattern could be refined to show the continued presence of $NaNH_2$ and the formation of $NaNH_2BH_3$. The structure published by Nagib *et al.*[17] was used as the starting model for the Rietveld refinement of $NaNH_2$. The refinement showed a significant amount of $NaNH_2$ remained after reaction, as well as some impurity peaks appearing

at 24.0°, 25.6°, 27.5° and 39.3° 2θ. The refined parameters are shown in table 4.6 and the refined diffraction patterns can be found in Appendix 2.

Table 4.6 - Refined lattice constants and selected bond lengths for $NaNH_2BH_3$ and $NaNH_2$ from the reaction of $NaNH_2$ + NH_3BH_3

Parameter	Ref 5 – $NaNH_2BH_3$	Ref 16 – $NaNH_2$	$NaNH_2BH_3$ RT	$NaNH_2$ RT
***a* (Å)**	7.46931(7)	8.964(3)	7.4770(9)	8.973(10)
***b* (Å)**	14.65483(16)	10.456(3)	14.671(2)	10.464(1)
***c* (Å)**	5.65280(8)	8.073(3)	5.6641(8)	8.0809(9)
Na–N bond length (Å)	2.35	2.437	2.44(2)	2.442
B–N bond length (Å)	1.56	Not applicable	1.52(3)	Not applicable

4.3.2.1 Impurities

Following refinement of the powder XRD patterns, impurity peaks were highlighted in most of the patterns. These peaks are listed in table 4.7. With respect to the NaH + $2NH_3BH_3$ reactions, where the trigonal phase was formed, there were consistently impurity peaks at approximately 27.6° and 39.4°. These peaks remain unidentified, but do show that there are competing reactions taking place in addition to the formation of the trigonal phase. These impurities were also observed in the $NaNH_2$ + NH_3BH_3 reactions, as well as in the NaH + NH_3BH_3 reaction at 80°C. Grochala *et al*.[4] reported three low intensity peaks in the powder XRD pattern of $NaNH_2BH_3$ at 10.83°, 12.85° and 25.67°, which were unidentified. In this study these impurity peaks were also observed in the reactions where $NaNH_2BH_3$ was synthesised along with a further impurity peak at 36.0°. The positions of impurity peaks in the NaH + NH_3BH_3 reactions at approximately 24.1°, 25.6° and 31.0° are consistent with the most intense peaks of the trigonal phase, suggesting that the trigonal phase formed to a minor extent during this reaction. The emergence of $NaNH_2BH_3$ as the main product of this reaction raised the possibility of this phase reacting with NH_3BH_3 to form the

trigonal phase. There were also a number of other peaks which appear in different patterns, although there was no apparent pattern with the appearance of these impurities, again highlighting that these reactions are not clean due to competing pathways. Interestingly there were no impurities in the product of the reaction between $NaNH_2BH_3$ and NH_3BH_3. This implies that separating the two steps involved in the synthesis of the trigonal phase leads to a purer product by restricting the extent to which side reactions can occur. There were a number of impurity peaks in the 1:2 reaction product at 40°C. The impurity peaks in the 1:1 reaction at 40°C were mostly related to the trigonal phase formation. Therefore, the excess NH_3BH_3 present in this first step must have been responsible for increasing the potential for side reactions to occur. In the second step there may also have been more potential for other side reactions to occur, with a 1:2 reaction mixture compared to the $NaNH_2BH_3$ + NH_3BH_3 reaction mixture, due to the presence of impurities, resulting in a significantly less pure product. The impurity at 28.9° in the 1:2 reaction at 110°C is consistent with the most intense (002) Bragg peak of $NaBH_4$, showing that the trigonal phase begins to decompose to $NaBH_4$ at this temperature. The two impurity peaks in the pattern of the product from the 1:2 reaction at 120°C are assumed to be related to the decomposition of the trigonal phase. The large number of impurity peaks shows the complex nature of both the synthesis reactions and the decomposition pathway. Further to this it was only possible to identify crystalline impurities from powder XRD patterns, the question of amorphous impurities or indeed major phases cannot be answered by this method of analysis.

Table 4.7 – The peak positions of impurities observed in powder XRD patterns
$^{¥}$ = $NaBH_4$, † = Trigonal phase, ^{ξ} = Unknown impurity

Reaction	Temp (°C)	Peak positions, 2θ						
NaH + $2NH_3BH_3$	RT, 10 days	36.0^{ξ}						
	RT, 2 months	27.5^{ξ}	39.3^{ξ}					
	40	7.0^{ξ}	11.1^{ξ}	12.8^{ξ}	29.9^{ξ}	36.0^{ξ}		
	50	36.1^{ξ}						
	60	20.5^{ξ}	27.6^{ξ}	39.4^{ξ}				
	80	20.5^{ξ}	27.6^{ξ}	39.4^{ξ}				
	100	27.7^{ξ}	39.5^{ξ}					
	110	27.7^{ξ}	28.9$^{¥}$	39.5^{ξ}				
	120	23.4^{ξ}	24.0^{ξ}	27.5^{ξ}				
NaH + NH_3BH_3	40	24.1†	25.6†	36.0^{ξ}				
	50	12.8^{ξ}	24.0^{ξ}	24.1†	25.6†	31.0†	36.0^{ξ}	42.4^{ξ}
	80	27.5^{ξ}	31.6^{ξ}	36.0^{ξ}	46.7^{ξ}			
$NaNH_2BH_3$ + NH_3BH_3	60	None						
$NaNH_2$ + NH_3BH_3	RT	27.5^{ξ}						

4.3.2.2 Refined Lattice Constants

The changes in the values of the *a* and *c* lattice constants with reaction temperature for the trigonal phase are shown in figure 4.14. It can be seen that there were no particular trends in either of these parameters and the changes in the values were negligible.

The variations of the *a*, *b* and *c* lattice constants of the $NaNH_2BH_3$ phase are shown in figure 4.15. For both the 1:1 and 1:2 reactions, the changes in the values of the

constants upon heating were all within 0.4% rendering them negligible, although the variation was greater for the product from the 1:1 reaction.

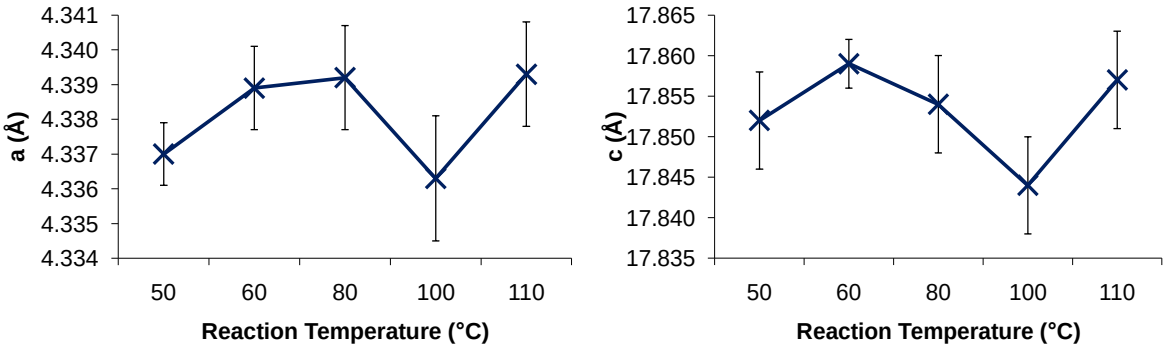

Figure 4.14 – Lattice constants for the trigonal phase

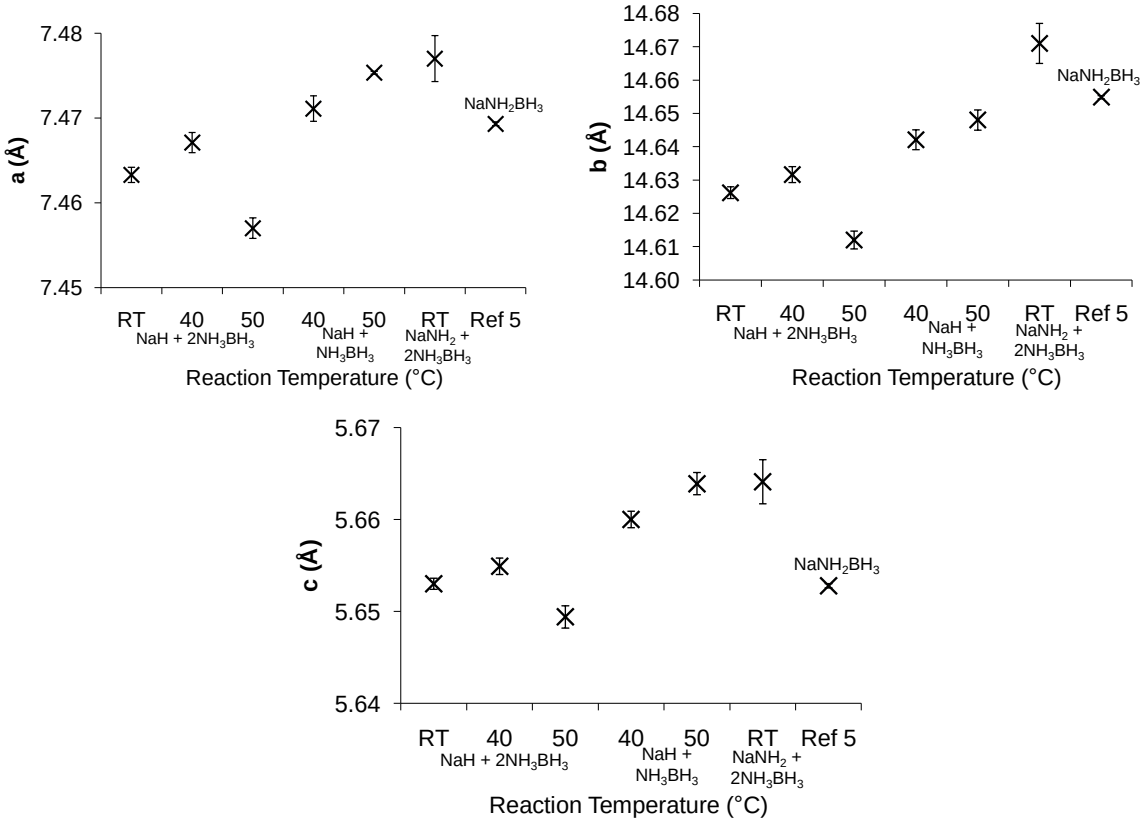

Figure 4.15 – Lattice constants for $NaNH_2BH_3$

Figure 4.16 shows the changes in B–N and Na–N bond lengths in the $NaNH_2BH_3$ phase. There are noticeable differences between the bond lengths calculated for both the Na–N bond and B–N bond compared to the structure published by Xiong *et al*.[5] As discussed previously, this is most probably due to the difference in quality of data collected. The B–N bond is shorter in $NaNH_2BH_3$ than in NH_3BH_3, which can be

attributed to stronger bonding between the B and N atoms in $NaNH_2BH_3$, a consequence of substituting a hydrogen atom in NH_3BH_3 for a more electron donating alkali metal. The longer the Na–N bond, the more electron rich the N atom should be and a shorter B–N bond would be expected. Therefore, it seems that the quality of data collected was insufficient to draw comparisons between these bond lengths.

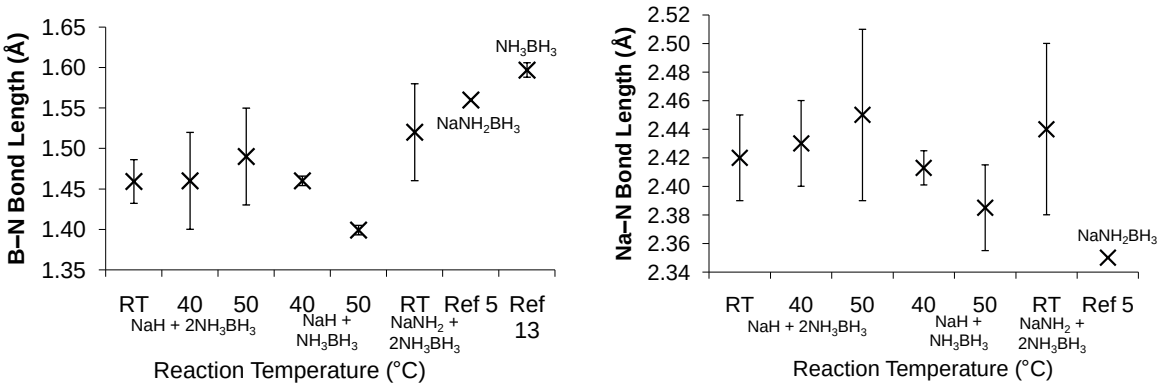

Figure 4.16 – Bond lengths for $NaNH_2BH_3$

The first step in the 1:2 reaction produces $NaNH_2BH_3$ and leaves excess NH_3BH_3. If this were to proceed stoichiometrically, the mole percentage of $NaNH_2BH_3$ and NH_3BH_3 in the product would be 50%. The values calculated from Rietveld refinements are shown in table 4.8 and are similar to the theoretical values for the 50°C reaction, although it is slightly lower for $NaNH_2BH_3$ but much lower after reaction at 40°C. These discrepancies again highlight the fact that there are competing pathways taking place producing amorphous materials. The unexpectedly low value of $NaNH_2BH_3$ in the 40°C reaction could be due to intermolecular reactions involving $NaNH_2BH_3$ molecules, whereas at 50°C $NaNH_2BH_3$ preferentially reacts with NH_3BH_3 resulting in the trigonal phase.

Table 4.8 – Mole percentage of phases in products from Rietveld refinements

Reaction	$NaNH_2BH_3$	NH_3BH_3
NaH + $2NH_3BH_3$ 40°C	31.24%	68.76%
NaH + $2NH_3BH_3$ 50°C	44.58%	55.42%
NaH + $2NH_3BH_3$ RT	41.67%	58.33%

4.4 Thermal Desorption Studies

4.4.1 $NaNH_2BH_3$

The thermal desorption properties of $NaNH_2BH_3$ were investigated using TGA–MS. A sample of the pre-synthesised $NaNH_2BH_3$ was inertly loaded into a TGA connected to a mass spectrometer. Figure 4.17 shows a combination of the thermogravimetric data and the mass spectrometric data. The heated sample showed a two step weight loss pathway. The first desorption step began at 70°C, peaking at 140°C. This desorption step was completely finished before the onset temperature, 230°C, of the second desorption step was achieved, which reached a maximum at 315°C. A total mass loss of 5.25 wt% was observed. The first step showed a loss of 3.5 wt% with a further loss of 1.75 wt% during the second step. The only gaseous desorption product detected by mass spectrometry was hydrogen.

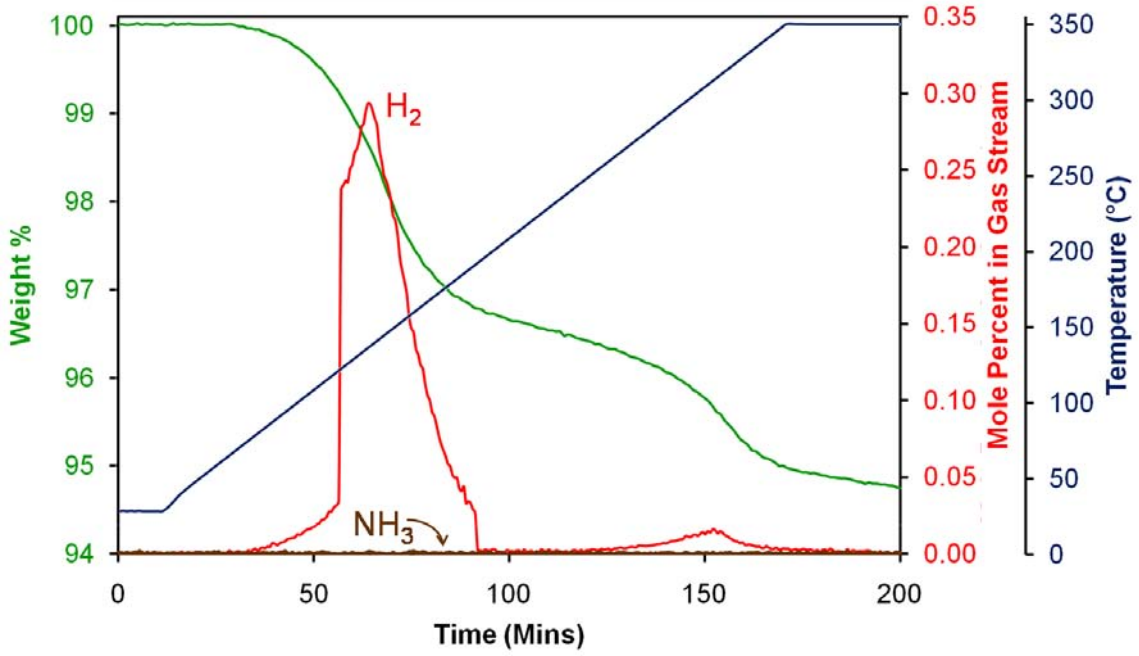

Figure 4.17 – TGA of $NaNH_2BH_3$. The gravimetric trace is shown in green, the temperature trace in blue and the mole percentages of H_2 and NH_3 detected by mass spectrometry shown in red and brown, respectively.

Discussion

There have been conflicting reports with respect to $NaNH_2BH_3$ decomposition in the literature. Two independent studies have shown the material to release exclusively hydrogen, with a total weight loss of 7.5 wt%. The first of these studies was carried out isothermally at 91°C, and a heat treatment duration of 19 hours was required to effect the total mass loss.[5] The second study used temperature ramping and showed weight loss over a two step release process with a first release step at 87°C releasing 4.4 wt% (1.15 equiv H_2) and a second step at 174°C releasing a further 3.1 wt% (0.85 equiv H_2).[3] A third study analysed nine independent samples and found weight loss varied from 5.5 to 9.5 wt% in the temperature range 75 to 105 °C, with an average weight loss of 6.6 wt%.[4] A further loss of 1.9 wt% was observed above 140°C. However, the hydrogen release was significantly contaminated with ammonia.

Compared to the earlier studies, the results here showed an unexpectedly low weight loss. However, the first weight loss step is consistent with the loss of roughly one equivalent of hydrogen as shown by reaction 4.10. This reaction would account for a weight loss of 3.8 wt%, similar to the observed value of 3.5 wt%, leaving a material of composition $NaNHBH_2$. Powder XRD analysis in section 4.3.1 showed that the only crystalline product observed after decomposition of $NaNH_2BH_3$ was NaH, therefore this material must be amorphous and, by analogy with the decomposition products of NH_3BH_3, is probably a polymeric material.

$$nNaNH_2BH_3 \rightarrow (NaNHBH_2)_n + nH_2 \qquad \text{Reaction 4.10}$$

The next desorption step must result in NaH, in order to be consistent with powder XRD patterns. There was a slight discrepancy in temperatures: NaH was observed in powder XRD patterns after heating to 200°C, whereas the second weight loss did not commence until a temperature of 230°C was achieved. This could be due to the different experimental conditions: the reaction mixture was held at the reaction temperature for twelve hours during gas line experiments, but was heated at a rate of 2°C min^{-1} during the TGA experiment. Therefore it would be reasonable to expect this event to occur at a higher temperature in the ramped TGA experiment. It is also plausible that NaH formed without gas evolution before the higher temperature

weight loss event. The sodium atom present could combine with an adjacent hydridic hydrogen bonded to boron, resulting in NaH and $(NHBH)_n$, polyimidoborane, as shown in reaction 4.11. The higher temperature weight loss would consequently be associated with the thermal decomposition of polyimidoborane; this event was observed at a similar temperature in the desorption profile of NH_3BH_3 (Chapter 3.4).

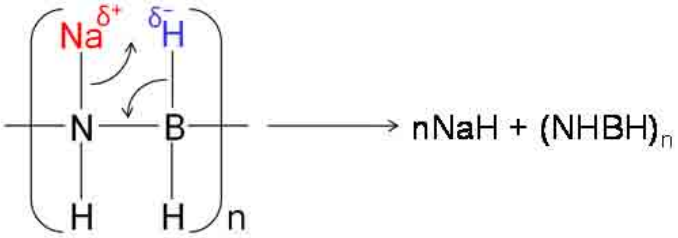

Reaction 4.11

Xiong *et al.*[3] proposed that $NaNH_2BH_3$ decomposition results in the formation of NaH and BN, with calculated and observed weight losses of 7.5 wt%. However, this was challenged in a later study by Fijalkowski and Grochala[4] on the grounds that the temperature was insufficient to lead to BN formation and that the hydrogen release was contaminated by NH_3. The authors instead speculated that an intermolecular reaction, secondary to the main decomposition pathway, between $NaNH_2BH_3$ molecules led to intermediates which decomposed to NaH and $BH_2NHNaBH_2$. However, this pathway involved the release of NH_3 and so cannot have taken place during our TGA study. The weight loss observed in the second decomposition step was also insufficient to account for a release of a second equivalent of hydrogen. Assuming reaction 4.11 does account for NaH formation, the release of the second equivalent of hydrogen would not have been expected to be complete at the maximum temperature, 350°C, of this experiment because $(NHBH)_n$ requires temperatures in excess of 400°C to decompose fully to BN, which supports the relatively small weight loss.[18] The combination of TGA and powder XRD results leads to the proposed decomposition of $NaNH_2BH_3$ shown in reaction 4.12.

$$nNaNH_2BH_3 \rightarrow (NaNHBH_2)_n + nH_2 \rightarrow nNaH + (NHBH)_n \rightarrow nNaH + nBN + nH_2$$

Reaction 4.12

4.4.2 NaH + NH_3BH_3

The thermal desorption properties of a ground sample of NaH and NH_3BH_3 were investigated using TPD–MS, heated at a ramp rate of 2°C min^{-1} to 350°C. The data is shown in figure 4.18.

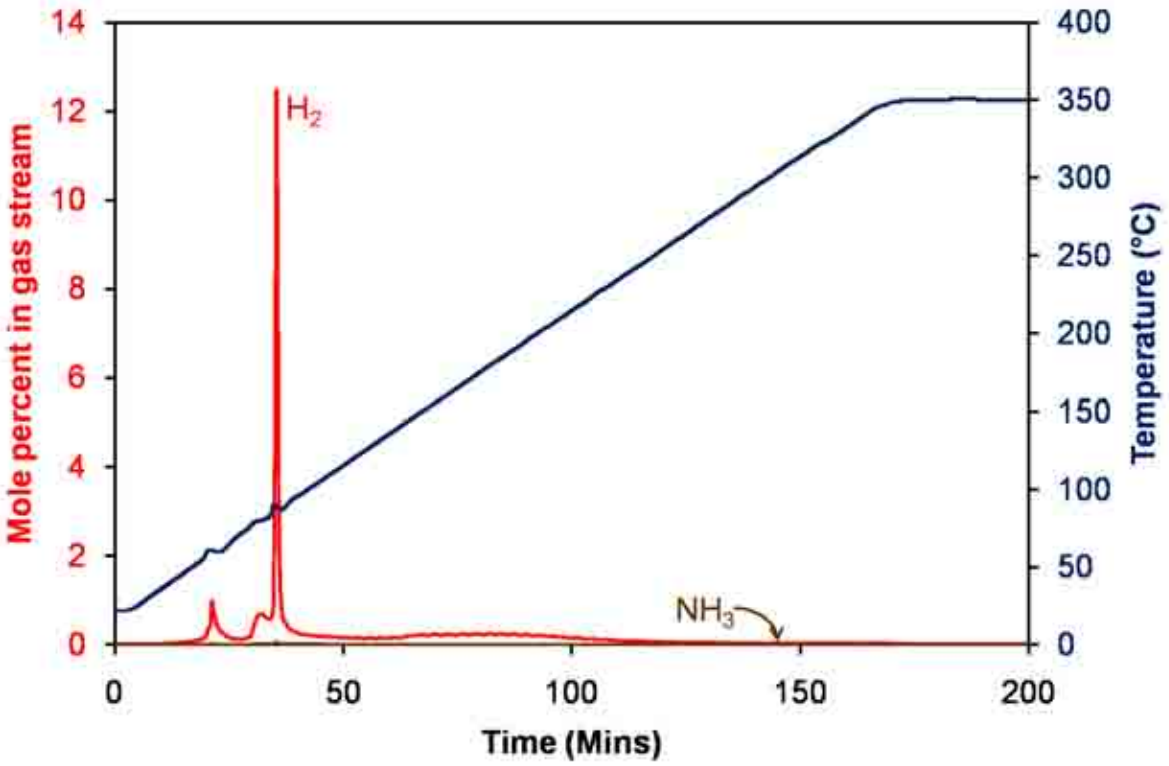

Figure 4.18 – TPD–MS analysis of a ground reaction mixture of NaH + NH_3BH_3. The temperature trace is shown in blue and the mole percentages of H_2 and NH_3 released are shown in red and brown, respectively

There were three exothermic events observed in the temperature trace, at 50°C, 75°C and 85°C, with each event accompanied by hydrogen release. The first release at 50°C can be associated with the reaction of NaH and NH_3BH_3, forming $NaNH_2BH_3$, accompanied by the release of one equivalent of hydrogen. The temperature of the event was in good agreement with gas line reactions, where it was shown that this reaction occurred at 40°C, however, the release appeared to be much smaller than expected. This is substantiated by processing the TPD–MS data to show gravimetric data as discussed in chapter 2.5. The processed data is shown in figure 4.19. It can be seen that the first hydrogen release step evolved less than 0.2 equivalents of H_2. The reaction potentially commenced on grinding the reagents and proceeded during

the delay between loading the sample onto the TPD apparatus and beginning the experiment. The hydrogen evolved during this time period would hence have not been detected during the desorption experiment.

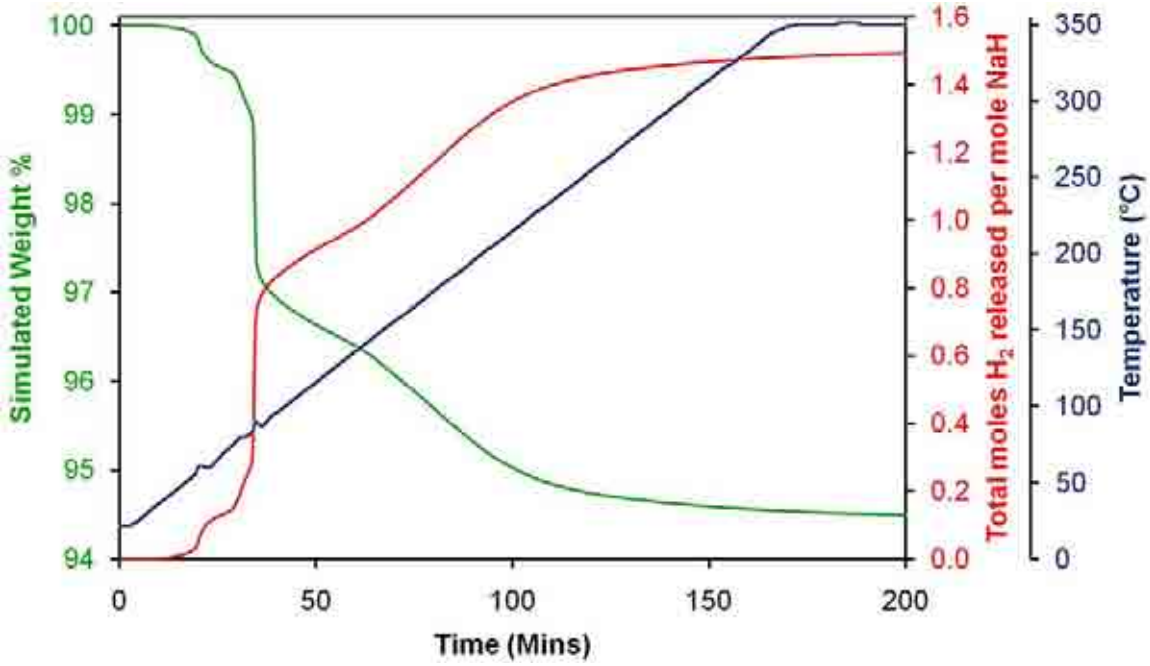

Figure 4.19 – Thermal decomposition analysis of NaH + NH_3BH_3 reaction mixture in a TPD with simulated gravimetric data. The temperature trace is shown in blue, the moles of H_2 released in red, and simulated gravimetric data in green

The main hydrogen release event occurred at 85°C and was observed to be a very sharp release of hydrogen, which, in agreement with TGA data in chapter 4.4.1 and results in the literature,[3-5] can be assigned to the decomposition of the $NaNH_2BH_3$ phase resulting in formation of $(NaNHBH_2)_n$. The increase in the temperature trace that occurred simultaneously with this hydrogen release highlights the exothermic nature of this decomposition. The theoretical weight loss for this step is calculated to be 3.7 wt% and the simulated value, 3.4 wt%, from figure 4.19 is similar to this. The discrepancy can be assumed to come from the fact that the sample was weighed before grinding the reagents and the mass at the start of the experiment was assumed to be equal to this. However, as discussed above there was potential for gas to have been released prior to the start of the experiment, the true sample mass at the start of the experiment would therefore have decreased and hence the actual weight loss would have been greater.

The third exothermic event observed in figure 4.18 occurred at 75°C between the two steps discussed above. There is no apparent third event in this temperature range that would account for this step. This event could potentially have been related to either the reaction of NaH with NH_3BH_3 or the decomposition of $NaNH_2BH_3$, although it could also have been due to side reactions. This hydrogen release was also evident in the TPD plot published by Xiong *et al.*,[3] however, the release was not discussed.

There was a final broad hydrogen release, which commenced at 140°C and continued until 230°C, with weight loss above 140°C totalling 1.8 wt%. This agrees very well with the study by Fijalkowski and Grochala[4] but less so with our TGA experiment on $NaNH_2BH_3$, in terms of the onset temperature for this desorption event, although there was good agreement between the two weight loss values. The thermal desorption data of $NaNH_2BH_3$ obtained from the TGA experiment and the TPD-MS data for the NaH + $2NH_3BH_3$ sample are compared in figure 4.20.

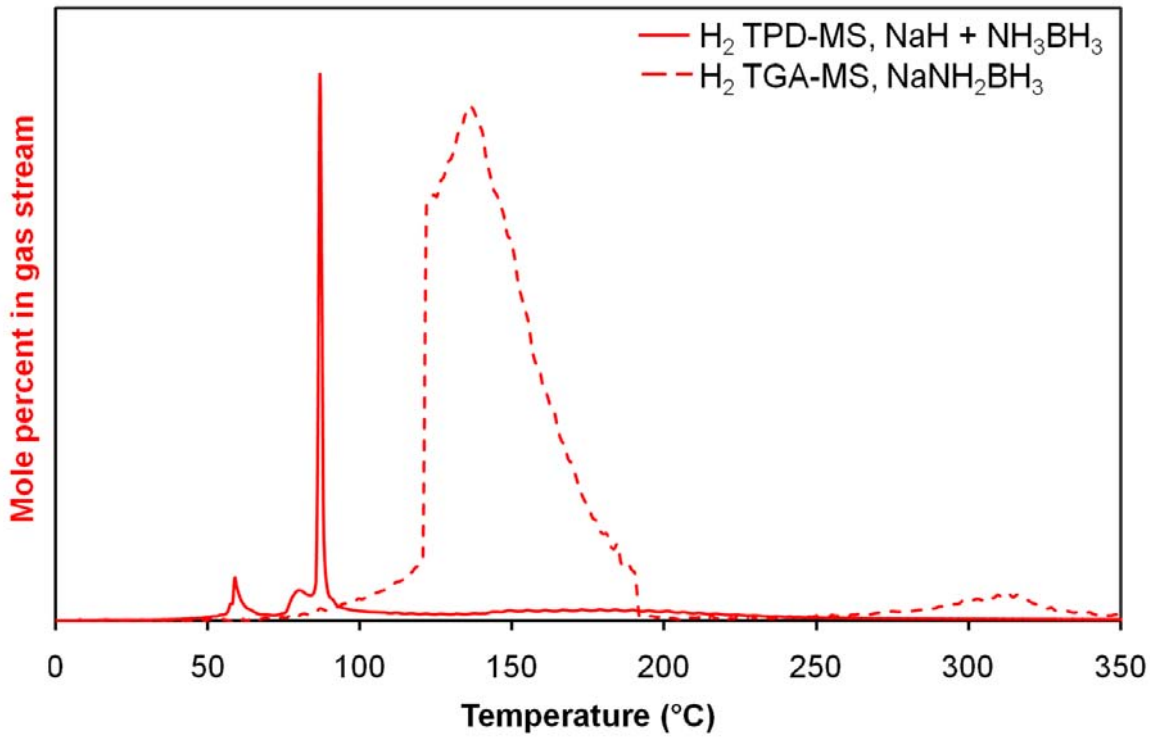

Figure 4.20 – Comparison of thermal desorption data for a sample of NaH + NH_3BH_3 in a TPD and $NaNH_2BH_3$ in a TGA

There is an apparent difference in the appearance of the two profiles: the main desorption event in the TGA experiment occurred at a higher temperature than in the TPD and the release was much broader. Interestingly though, the onset temperature of this major desorption event was consistent at approximately 75°C. The two events have both been assigned to the same desorption event, however, this comparison suggests that these two reactions did not necessarily follow the same pathway. There are a number of factors that could explain the discrepancies between the two traces. Primarily the sample in the TGA had been pre-synthesised in a gas line reaction at 40°C, whereas the sample in the TPD was a reaction mixture offering potential for side reactions to occur. Secondly, the experimental setups were not the same and so could have contributed to the differences in the desorption events. The powder XRD pattern of the product obtained from the TPD experiment is shown in figure 4.21. The diffraction pattern shows that the only crystalline decomposition product was NaH, which supports reaction 4.12. Unfortunately, due to the small quantity of sample required for a TGA experiment, insufficient sample was recovered for powder XRD analysis.

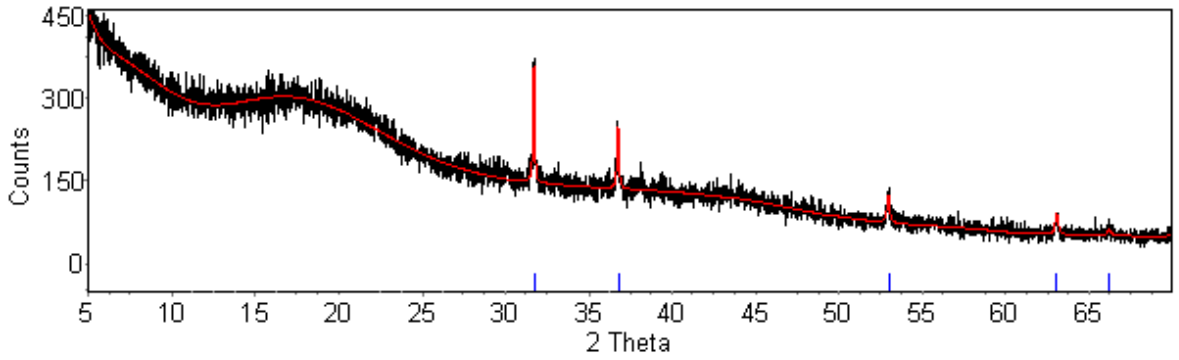

Figure 4.21 – Powder XRD pattern of the NaH + NH_3BH_3 sample collected after heating to 350°C at a rate of 2°C min^{-1} in a TPD. Bragg peak positions due to NaH are shown in blue

4.4.3 NaH + $2NH_3BH_3$

The desorption profile of the NaH + $2NH_3BH_3$ reaction mixture collected in a TPD–MS apparatus is shown in figure 4.22. The profile was acquired at a heating rate of 2°C min^{-1} to a temperature of 350°C.

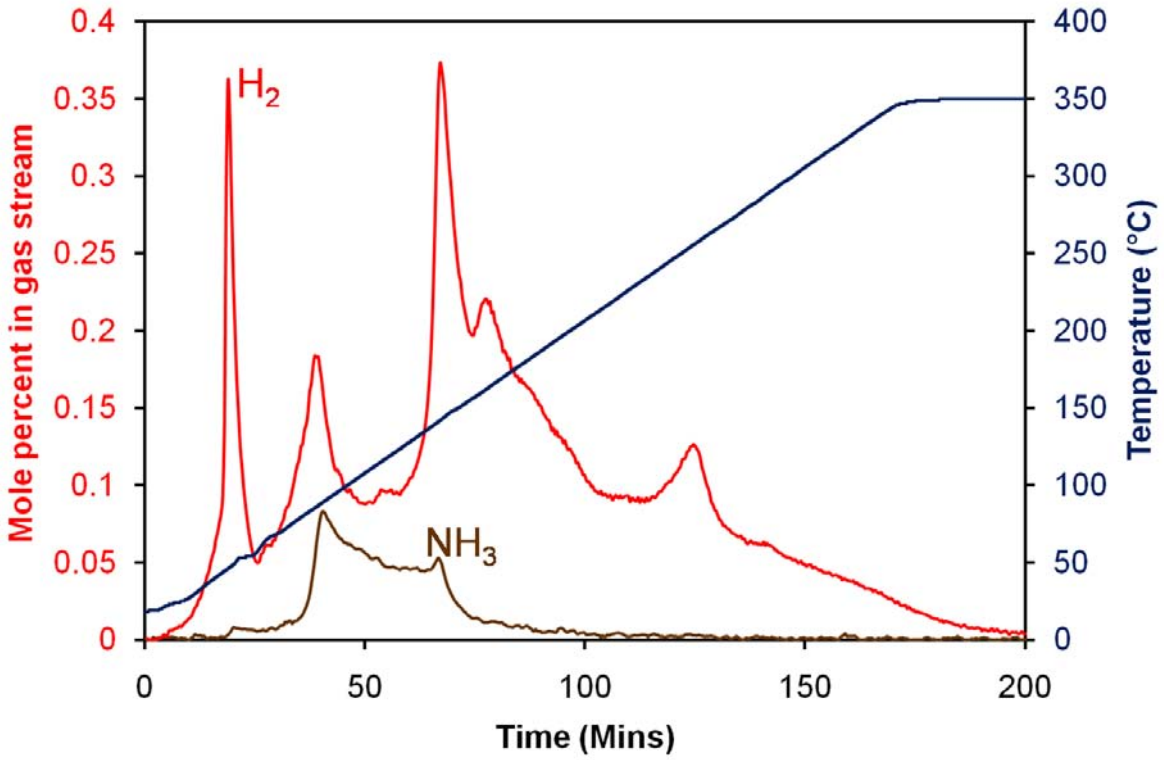

Figure 4.22 – The TPD profile of the NaH + $2NH_3BH_3$ reaction mixture. The temperature trace is shown in blue and the mole percentages of H_2 and NH_3 released shown in red and brown respectively

Hydrogen release can be seen to commence almost simultaneously with the beginning of heating. The first peak was observed at 40°C. This was followed by a slight endotherm in the temperature trace at 50°C. A second desorption of hydrogen began at 55°C and peaked at 80°C. The next desorption of hydrogen began at 115°C; this peaked at 140°C, followed by a fourth desorption, which peaked at 155°C. The onset of the final hydrogen release was observed at 230°C, peaking at 250°C. Hydrogen release continued until the target temperature of 350°C was reached. There was a substantial amount of overlap of these desorption events. There was also a significant amount of ammonia release observed during the desorption experiment. A small amount of release occurred at 40°C, shortly after the onset of hydrogen release, with the main broad release beginning at 65°C and peaking at 80°C. The broad release continued until a temperature of 140°C was achieved when the ammonia signal tailed off, although a small release continued until 245°C.

Figure 4.23 shows the TPD–MS data processed so as to give simulated gravimetric data, as discussed in chapter 2.5. The total hydrogen content in the reagents was 15.3 wt%, which was greater than the total weight loss calculated from the observed mass spectrometry data of 12.9 wt%; however, as observed in figure 4.22, NH_3 also contributed to this weight loss. The powder XRD pattern, shown in figure 4.24, taken after the desorption run showed only $NaBH_4$. If this were the only product, then a far higher weight loss of 55.9 wt% would have been observed. Therefore, although $NaBH_4$ is the only crystalline desorption product, there must also be amorphous products present.

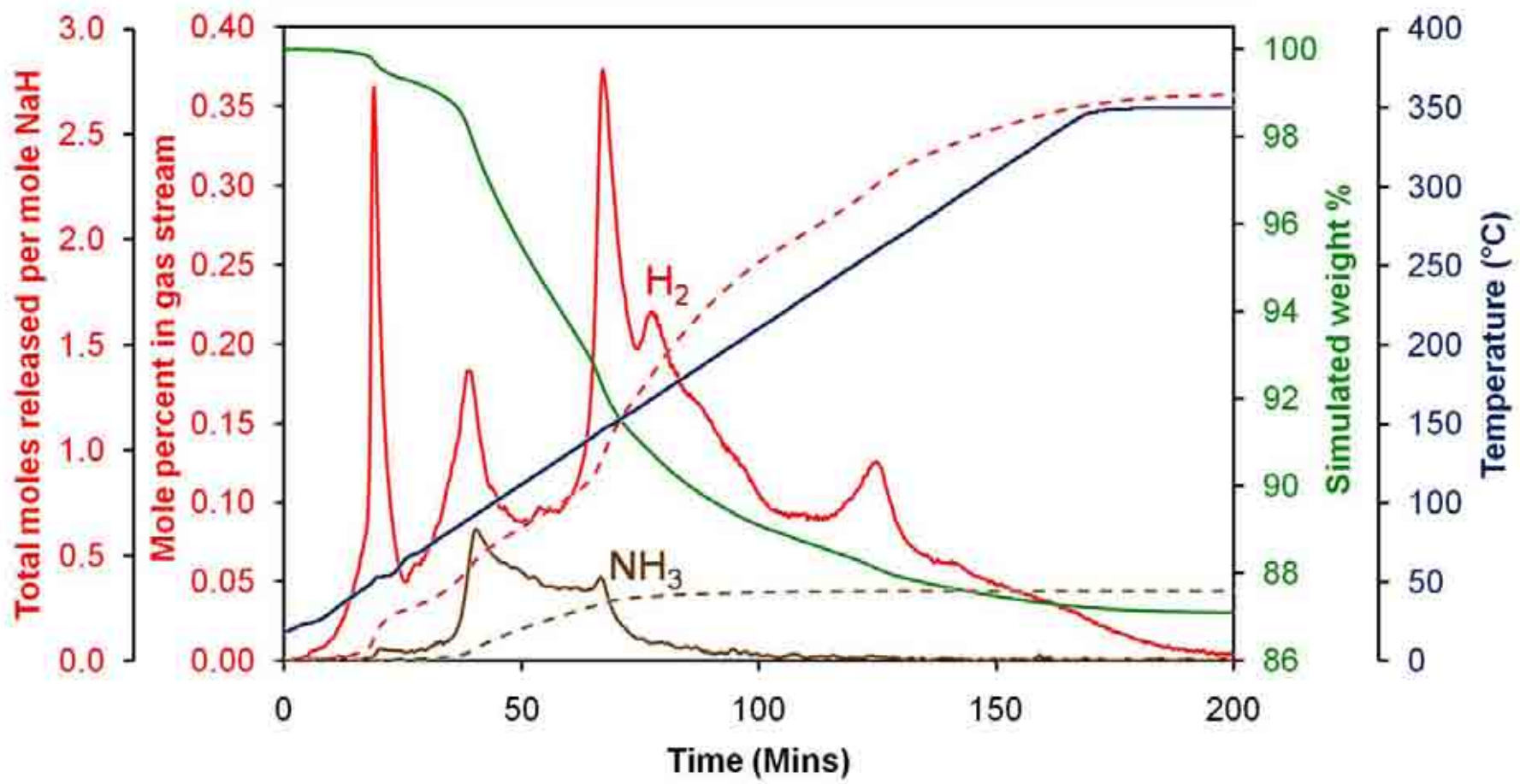

Figure 4.23 – Thermal desorption analysis of a NaH + $2NH_3BH_3$ reaction mixture in a TPD apparatus with simulated gravimetric data. The mole percentages are shown by continuous lines and the moles of the gases released by broken lines, with H_2 shown in red and NH_3 in brown. The simulated gravimetric data is shown in green and the temperature trace in blue

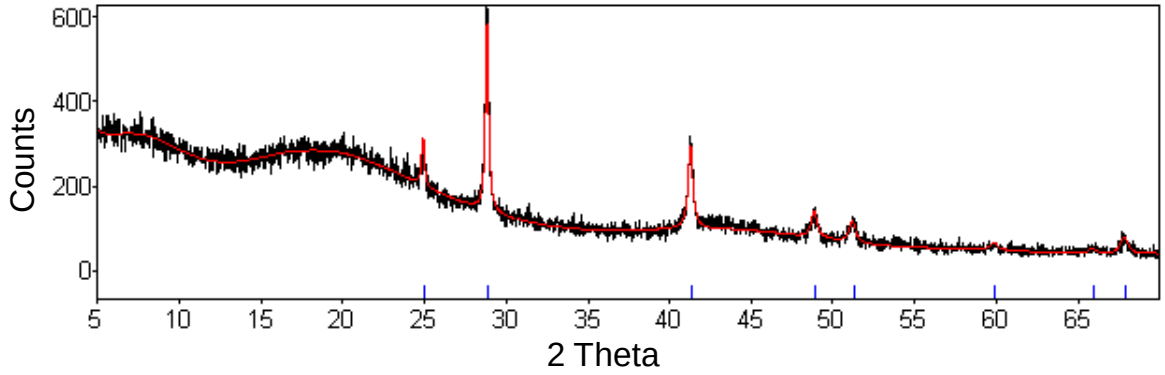

Figure 4.24 – Powder XRD pattern of the NaH + $2NH_3BH_3$ sample collected after heating to 350°C at a rate of 2°C min^{-1} in a TPD. Bragg Peak positions due to $NaBH_4$ are shown in blue. R_{wp} = 9.724%, χ^2 = 1.121

Figure 4.25 shows the amount of weight loss due to H_2 and NH_3 plotted as a function of temperature. From a combination of figures 4.23 and 4.25 it can be seen that a total of 2.7 moles of H_2 (6.3 wt%) and 0.33 moles of NH_3 (6.6 wt%) were released.

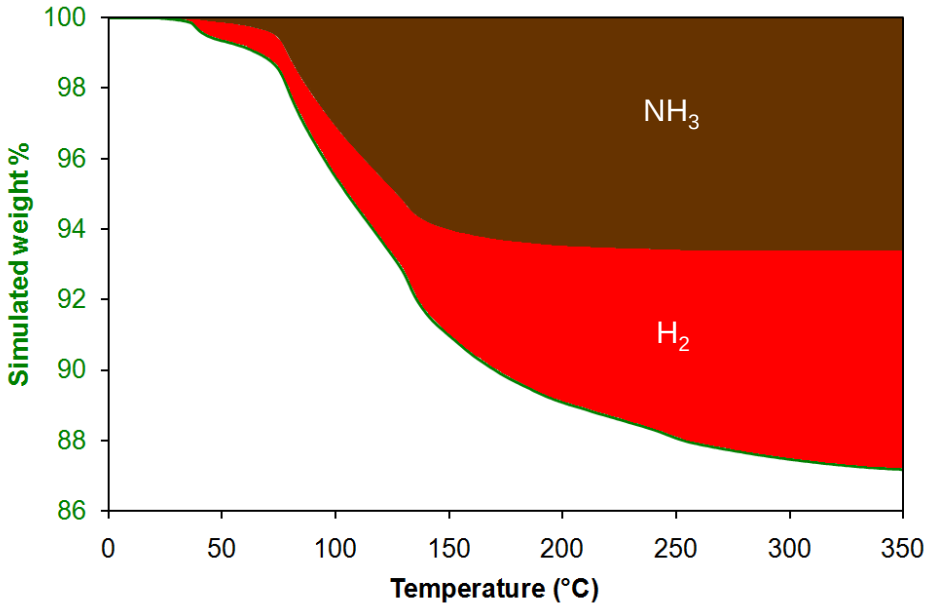

Figure 4.25 – Simulated thermogravimetric analysis of a NaH + $2NH_3BH_3$ reaction mixture in a TPD apparatus. The simulated gravimetric trace is shown in purple, with the proportion of the weight loss due to H_2 and NH_3 shown in red and brown, respectively

Figure 4.23 shows how much of each desorbed gas in terms of moles were released during each desorption step. The first desorption was shown to release 0.2 equivalents of hydrogen and a further 0.5 equivalents were released during the

second hydrogen release step. The major hydrogen desorption, which incorporated two peaks in the hydrogen trace released a total of 1.3 equivalents of hydrogen, with 0.5 equivalents released after the first peak and a further 0.8 equivalents associated with the second broader peak. The remaining 0.7 equivalents of hydrogen were released during the remainder of the experiment, with 0.35 equivalents released during the fifth peak of the hydrogen trace. As a consequence of the ammonia trace showing only one broad feature, the 0.33 equivalents released could not be broken down into different decomposition events.

Discussion

The NaH + $2NH_3BH_3$ reaction pathway has been shown to be complex, with a number of overlapping desorption events occurring, which offered potential for unidentified side reactions to proceed. The first desorption step occurred at a sufficiently low temperature to be related to the 1:1 reaction of NaH with NH_3BH_3, synthesising $NaNH_2BH_3$ which agrees with the reaction pathway proposed in reaction 4.7, inferred from the results of powder XRD. This 1:1 reaction should release 1 equivalent of hydrogen. However, as with the results of the simulated gravimetric data of the NaH + NH_3BH_3 reaction mixture from TPD data, figure 4.19, the calculated number of moles of hydrogen released was much lower than expected. This may again be attributed to the facile nature of the reaction, with it commencing and releasing hydrogen before the TPD experiment had begun, although competing side reactions may also have suppressed this release.

The second step in the reaction pathway involved the simultaneous release of NH_3 and H_2. This implied that at this point in the pathway, competing reactions were taking place. An insight into these pathways can be found by comparing the desorption profiles of the 1:1 and 1:2 reaction mixtures as shown in figure 4.26. The second hydrogen desorption correlates well with the small desorption event observed prior to the main sharp desorption in the TPD profile of a 1:1 reaction mixture, figure 4.18. In the 1:1 reaction this desorption released 0.15 equivalents of hydrogen, whereas in the 1:2 reaction mixture 0.5 equivalents were released. The increased amount of hydrogen released in the 1:2 reaction during this desorption step suggested this event involved NH_3BH_3 in a side reaction. The main difference

between the two desorption profiles was that ammonia was released from the 1:2 reaction mixture. This release may have therefore been associated with the formation of the crystalline trigonal phase. The most reasonable explanation for the release of ammonia would be through the reaction of $NaNH_2BH_3$ with NH_3BH_3 resulting in a phase of composition $Na^+(BH_3NH_2BH_3)^-$, reaction 4.13.

$$NaNH_2BH_3 + NH_3BH_3 \rightarrow Na^+(BH_3NH_2BH_3)^- + NH_3 \qquad \text{Reaction 4.13}$$

0.33 equivalents of NH_3 were calculated to have been released during the TPD experiment. If this had been a clean reaction then 1 equivalent of NH_3 would have been released, but because of the competing side reactions, this reaction could not proceed in a 1:1 fashion and so the amount of NH_3 released was less than what was expected. This lower than expected release of NH_3 also suggested $NaNH_2BH_3$ was not initially stoichiometrically formed. It can also be seen that shortly after hydrogen release had commenced, through the reaction of NaH with NH_3BH_3, NH_3 release began. This supports the notion that NH_3 release arose from the reaction of $NaNH_2BH_3$ with NH_3BH_3, because it would have been unable to occur without $NaNH_2BH_3$ presence. The sharp hydrogen desorption observed in the TPD profile of the 1:1 reaction at 90°C, assigned to $NaNH_2BH_3$ decomposition, was not present in the profile of the 1:2 reaction mixture, suggesting $NaNH_2BH_3$ did not undergo decomposition in the presence of NH_3BH_3. This is further evidence for the occurrence of reaction 4.13.

Figure 4.27 shows a comparison of the thermal desorption trace of NH_3BH_3 versus the NaH + $2NH_3BH_3$ reaction mixture. It can be seen that the first two desorption events in the 1:2 reaction mixture trace were complete before the first NH_3BH_3 desorption step began and so cannot be related to NH_3BH_3 decomposition. However, there was a small peak in the hydrogen trace of the 1:2 reaction mixture at 110°C which correlated well with the first decomposition step of NH_3BH_3 suggesting the two events could have been related.

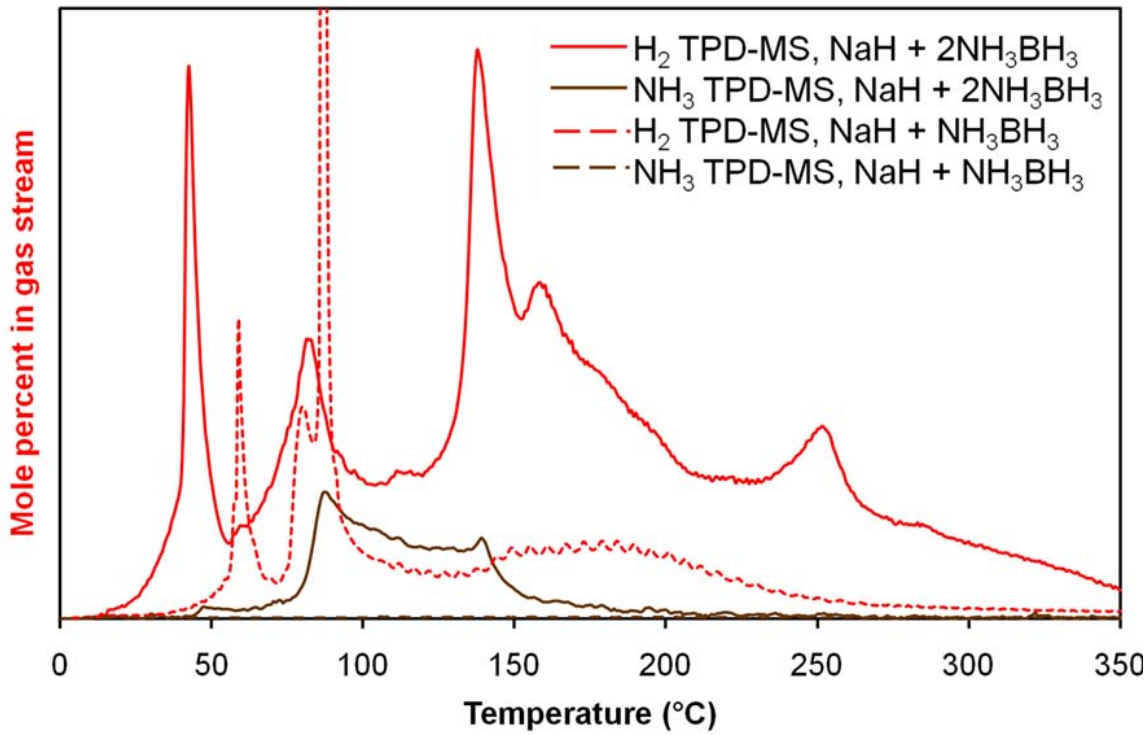

Figure 4.26 – A comparison of the TPD–MS data collected for NaH + NH_3BH_3 and NaH + $2NH_3BH_3$ reaction mixtures. The desorption profile of the 1:1 reaction mixture has the most intense sharp release cut off to allow better comparison of the less intense desorptions

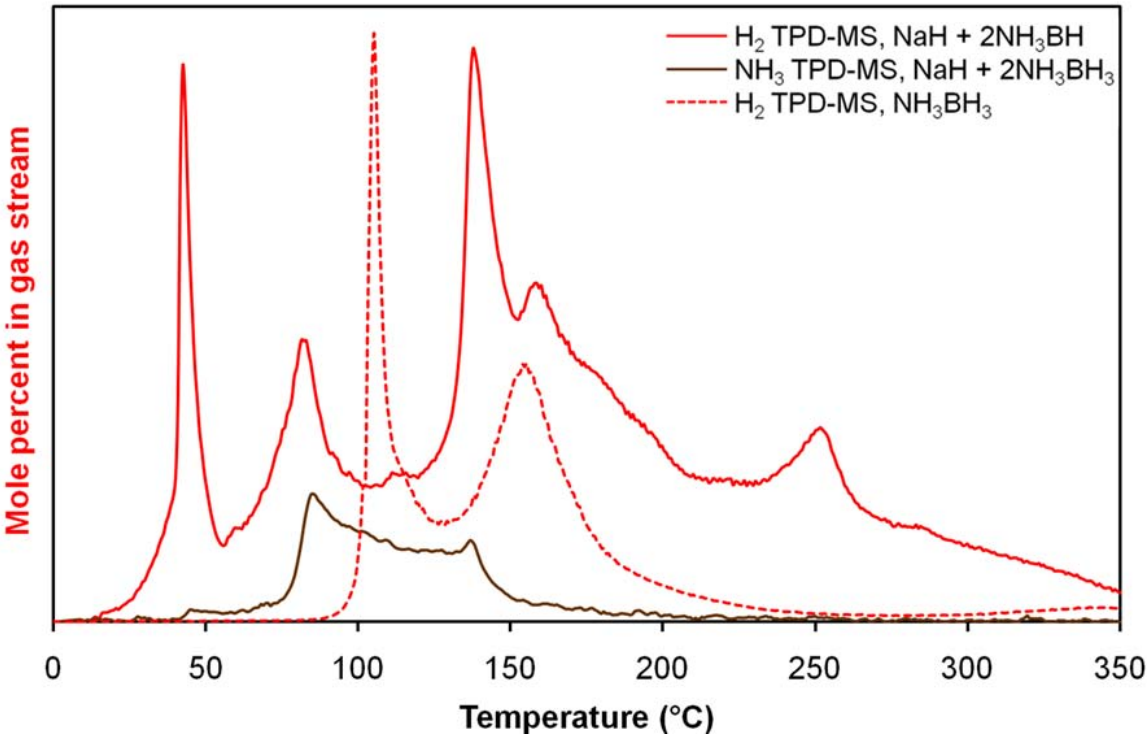

Figure 4.27 – A comparison of the TPD-MS data collected for the NaH + $2NH_3BH_3$ reaction mixture and NH_3BH_3

Information garnered from powder XRD patterns showed that the next step in the reaction pathway was the formation of $NaBH_4$. $NaBH_4$ does not appear in either the decomposition pathway of NH_3BH_3 or $NaNH_2BH_3$ and hence should be related to the decomposition of the $Na^+(BH_3NH_2BH_3)^-$ phase. From XRD data collected it was shown that $NaBH_4$ formation occurred at a temperature of 120°C. The third desorption step in the TPD trace of the 1:2 reaction mixture that began at 115°C could therefore be related to this desorption step. The NH_3 signal showed a decline as this step began and therefore it can be assumed that the decomposition of $Na^+(BH_3NH_2BH_3)^-$ involved only the release of H_2. The ratio of Na to B atoms in this phase is 1:2, whereas the ratio in $NaBH_4$ is 1:1. The lack of any N containing gaseous decomposition products also means there is nitrogen that has been unaccounted for. This leaves a B:N ratio of 1:1. The temperature of this decomposition step was too low to have led to BN formation and only 0.5 equivalents of H_2 were released. Any other decomposition products must also have been amorphous and so it would seem likely that a polyimidoborane-like phase had formed. This decomposition step can be represented in reaction 4.14.

$$nNa^+(BH_3NH_2BH_3)^- \rightarrow nNaBH_4 + (BHNH)_n + nH_2 \qquad \text{Reaction 4.14}$$

This step was accompanied by the release of 0.5 equivalents of hydrogen, whereas, reaction 4.14 shows that a release of one equivalent of hydrogen would have been expected. This lower release can be explained by the fact that the reaction forming $Na^+(BH_3NH_2BH_3)^-$ was inhibited by other competing pathways and the amount of hydrogen released during this step was calculated from the original reaction mixture and not from the amount of $Na^+(BH_3NH_2BH_3)^-$ that formed.

The fourth hydrogen desorption peak, at 155°C, shows fairly good correlation with the second desorption event in the ammonia borane trace, as shown in figure 4.27. As discussed previously, some NH_3BH_3 decomposition was expected to have taken place during the desorption experiment and hence the products of this step would have subsequently undergone further decomposition, releasing hydrogen.

The final high temperature hydrogen release was also due to competing pathways to the main $Na^+(BH_3NH_2BH_3)^-$ synthesis–decomposition pathway. This can be verified

by the fact that the powder XRD results showed that the $Na^+(BH_3NH_2BH_3)^-$ phase had completely undergone decomposition at this higher temperature and $NaBH_4$ was the only crystalline product. Further to this, $NaBH_4$ has been shown to undergo decomposition only at temperatures in excess of 400°C.[7]

4.4.4 Alternative Thermal Desorption Studies

There are no direct reports of $Na^+(BH_3NH_2BH_3)^-$ or its decomposition in the literature, although its existence was postulated by Fijalkowski and Grochala.[4] This study also raised a number of points which are relevant to the discussion here. Alternative studies had shown exclusive hydrogen release from $NaNH_2BH_3$,[2, 3, 5] however, Fijalkowski observed emission of a substantial amount of NH_3 in the desorbed gases, both during synthesis of $NaNH_2BH_3$ and its subsequent decomposition. A DSC study of the decomposition of $NaNH_2BH_3$ revealed an endothermic event at 55°C. This endothermic event was also evident in the TPD trace of the $NaH + 2NH_3BH_3$ reaction mixture shown in figure 4.22. Fijalkowski hypothesised that this event was due to a thermally activated intermolecular head to tail dimerisation, reaction 4.14, which is also an important step in the decomposition of NH_3BH_3.[19] The resulting ionic salt is analogous to the topological isomer of DADB, $[BH_3(NH_2)BH_3]^-[NH_4]^+$. Reaction 4.15 shows the postulated decomposition steps of this compound.

$$2NaNH_2BH_3 \rightarrow [NH_3Na]^+[BH_3(NHNa)BH_3]^- \qquad \text{Reaction 4.14}$$

$$[NH_3Na]^+[BH_3(NHNa)BH_3]^- \rightarrow Na^+[BH_3(NHNa)BH_3]^- + NH_3\uparrow \rightarrow$$

$$NaH + BH_3(NHNa)BH_2 \rightarrow BH_2(NNa)BH_2 + H_2\uparrow \rightarrow (BH(NNa)BH)_n + H_2\uparrow$$

Reaction 4.15

The endothermic event observed in this study cannot be related to a melting of either a reagent or $NaNH_2BH_3$, as all of these compounds melt at higher temperatures.[4, 20] Therefore, an intermolecular rearrangement reaction would seem to have occurred. The rearrangement reaction shown in reaction 4.14 offers one such possibility. However, as the subsequent decomposition steps, shown in reaction 4.15, result in the formation of NaH, which was not observed in powder XRD patterns, this excludes this possibility. Reaction 4.14 shows the reverse rearrangement reaction to the one

taking place during DADB formation from NH_3BH_3. The rearrangement reaction more closely related to DADB formation is shown in reaction 4.16.

$$2NaNH_2BH_3 \rightarrow [NaNH_2BH_2NH_2Na]^+[BH_4]^- \qquad \text{Reaction 4.16}$$

Following the endothermic event, both H_2 and NH_3 were released in both this study and that by Fijalkowski. Therefore, the ionic salt that forms must provide a pathway for these gases to be released. There would appear to be no suitable pathway for the release of NH_3 from this compound and hence reaction 4.16 cannot be the main reaction related to the endothermic event.

The 1:2 reaction mixture of this study provided the opportunity for a number of other rearrangement reactions to proceed through the intermolecular reaction of $NaNH_2BH_3$ with NH_3BH_3, which following the first step in the reaction pathway would have been present in a 1:1 ratio. These reactions are shown below.

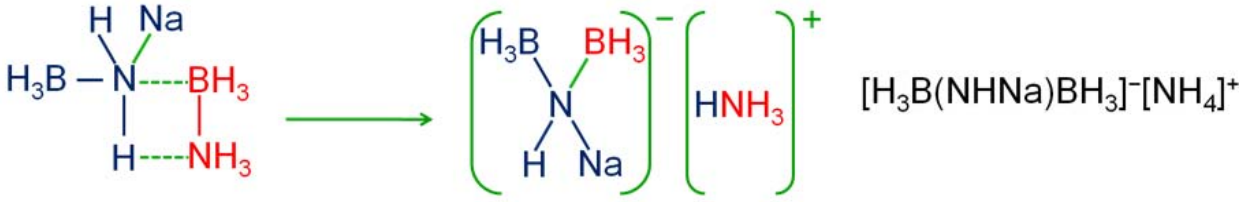

Reaction 4.17

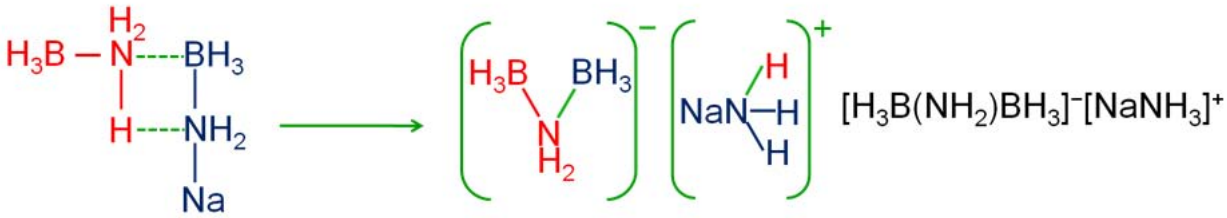

Reaction 4.18

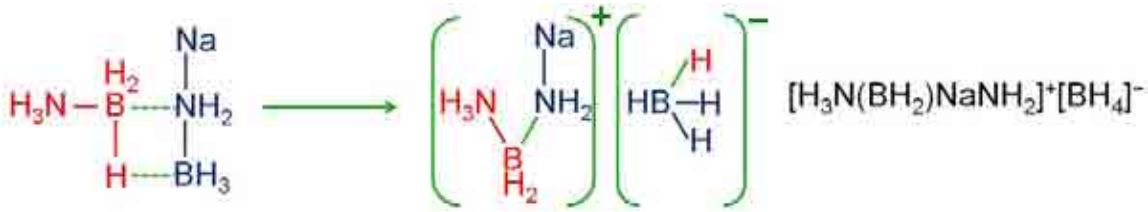

Reaction 4.19

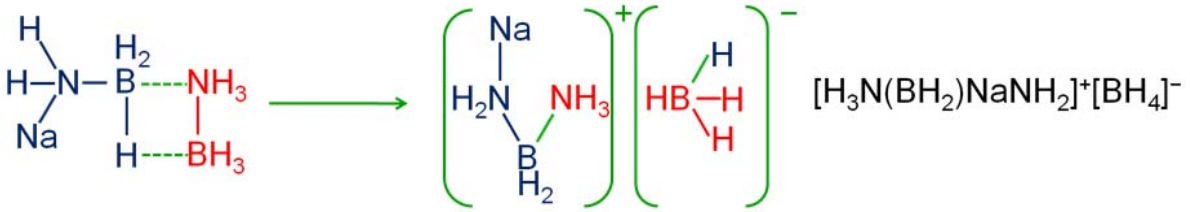

Reaction 4.20

The products from reactions 4.19 and 4.20 are seen to be identical, however, the four reactions offer three additional products to those already proposed. In order for the reaction product to be consistent with the desorption data, NH_3 must be released either simultaneously or soon after this formation step. Reaction 4.18 would appear to provide the product most susceptible to NH_3 release, as the cation involves an NH_3 molecule bound to sodium.

Therefore, the endothermic event at 50°C is assigned to be largely related to this reaction and hence the main reaction pathway. However, the possibility that these other rearrangements occurred during the reaction pathway cannot be ignored and again highlight the complex nature of the reaction mechanism, providing side reactions that could have led to the observed H_2 release concomitant with the NH_3 release. Further evidence for the product of reaction 4.18 being the main product of the $NaH + 2NH_3BH_3$ reaction will be offered in section 4.5.

An intermolecular reaction is not the only reaction mechanism that can yield the product $[Na]^+[BH_3NH_2BH_3]^-$. This product could also have been achieved through a simple nucleophilic attack by the NH_2BH_3 anion of $NaNH_2BH_3$ at the B of the NH_3BH_3, with NH_3 expelled as the B is approached by the N of the anion, reaction 4.21. This S_N2 reaction would yield a negatively charged species of composition $[BH_3NH_2BH_3]^-$, which would subsequently crystallise with the remaining cation, Na^+.

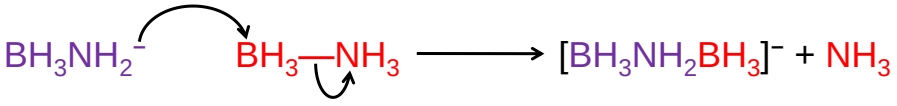

Reaction 4.21

Fijalkowski hypothesised that the bimolecular reaction between $NaNH_2BH_3$ molecules, reaction 4.14, was responsible for the release of NH_3 observed during the decomposition of $NaNH_2BH_3$. However, NH_3 release was also observed during the ball milling process that synthesised the $NaNH_2BH_3$ phase. Fijalkowski proposed the

intermolecular reaction between unreacted NH_3BH_3 and $NaNH_2BH_3$ was responsible for this release, shown in reaction 4.22.

$$NaNH_2BH_3 + NH_3BH_3 \rightarrow [NaNH_3]^+[BH_3(NH_2)BH_3]^- \rightarrow Na^+[BH_3(NH_2)BH_3]^- + NH_3\uparrow$$

Reaction 4.22

The results described here provide support for this assignment, although as discussed they are equally consistent with an S_N2 reaction. Fijalkowski proposed that the decomposition of this material would proceed as shown by reaction 4.23.

$$Na^+[BH_3(NH_2)BH_3]^- \rightarrow BH_3(NHNa)BH_2 + H_2\uparrow \qquad \text{Reaction 4.23}$$

Our results do not agree with this proposed reaction, because $NaBH_4$ was shown to be a decomposition product, also accompanied by H_2 release. However, the results of a ^{11}B NMR study by Fijalkowski revealed the presence of BH_4^- during the reaction. Fijalkowski commented that any number of pathways could be responsible for BH_4^- formation. The two reactions that were put forward are shown below.

$$2NaNH_2BH_3 \rightarrow [(NH_2Na)(BH_2)(NH_2Na)]^+[BH_4]^- \qquad \text{Reaction 4.24}$$

$$2NaNH_2BH_3 \rightarrow NaBH_4 + NaNH_2 + (NH_2BH_2)_n \qquad \text{Reaction 4.25}$$

Our results are able to provide an alternative answer for the appearance of this BH_4^- signal, through the decomposition of the $Na^+[BH_3(NH_2)BH_3]^-$ phase. Reaction 4.24 could still be in part responsible for BH_4^- formation. However, a contribution from reaction 4.25 is not supported by the results of this study because there were no Bragg peaks due to $NaNH_2$ observed in any of the powder XRD patterns, section 4.3.

4.4.5 $Na^{+}(BH_3NH_2BH_3)^{-}$ Phase

The gaseous thermal desorption properties of pre-synthesised $Na^{+}[BH_3(NH_2)BH_3]^{-}$ through a gas line reaction at 60°C were investigated using TPD–MS and IGA–MS. The decomposition pathway was found to be independent of the method of desorption employed with hydrogen the only gas evolved in both techniques.

4.4.5.1 TPD–MS

Thermal desorption data collected from a pre-synthesised sample of the trigonal phase heated at a ramp rate of 2°C min^{-1} to 350°C is shown in figure 4.28.

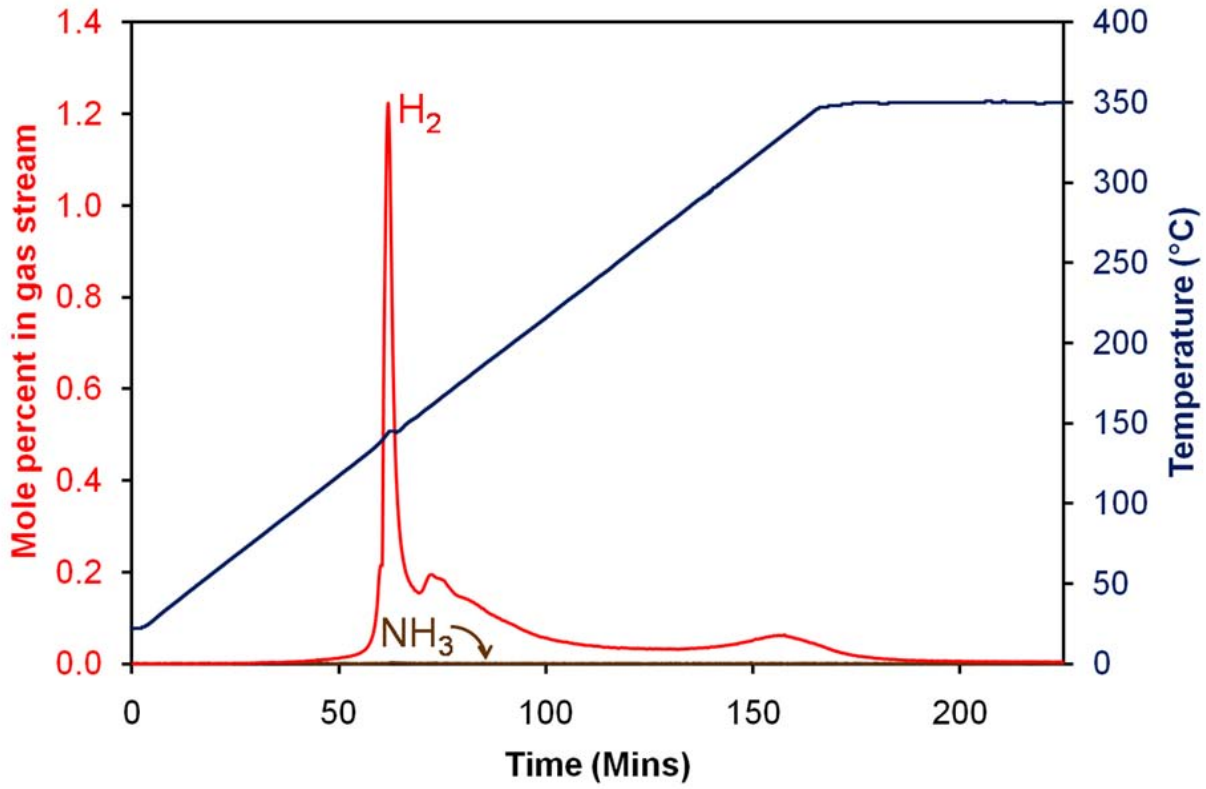

Figure 4.28 – TPD–MS analysis of pre-synthesised $Na^{+}[BH_3(NH_2)BH_3]^{-}$. The temperature trace is shown in blue and the mole percentages of H_2 and NH_3 released are shown in red and brown, respectively

The sample had previously been heated on an argon gas line at 60°C during synthesis and therefore no gas release would have been expected below this temperature. Hydrogen release began at 100°C and was followed by a sharp release peaking at 140°C, this was accompanied by a slight exotherm in the temperature trace. A second broader release of hydrogen began at 145°C and peaked at 155°C.

The release then tailed off, although it did continue slowly until the maximum temperature of the experiment, 350°C, was reached. During this temperature range another peak was observed at 325°C.

The powder XRD pattern of the sample collected after the desorption experiment, shown in figure 4.29, showed the crystalline decomposition product to be $NaBH_4$, in agreement with gas line reactions, as discussed in section 4.3.

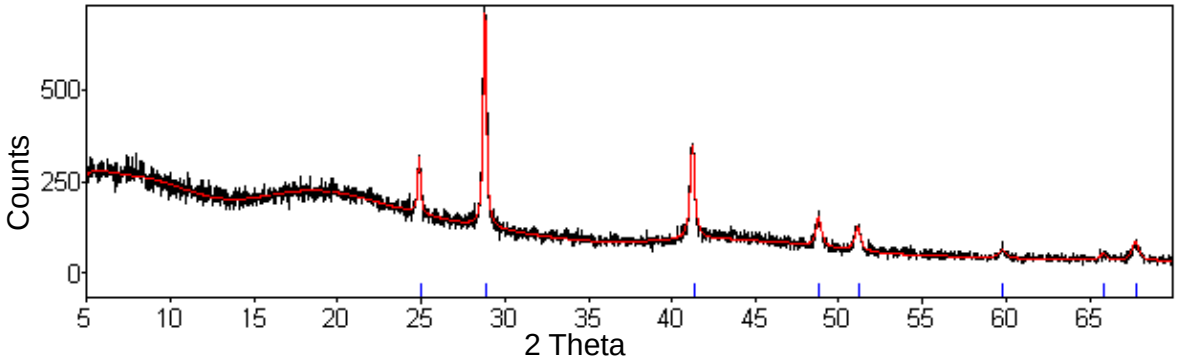

Figure 4.29 – Powder XRD pattern of the product of the TPD experiment after heating $Na^+[BH_3(NH_2)BH_3]^-$ to 350°C at 2°C min^{-1}. Bragg peak positions due to $NaBH_4$ are indicated in blue. R_{wp} = 8.775%, χ^2 = 1.309

4.4.5.2 IGA–MS

A sample of the pre-synthesised trigonal phase (73 mg) was inertly loaded into an IGA connected to a mass spectrometer. Figure 4.30 shows the thermogravimetric data overlaid with the mass spectrometric data for the observed desorption products. The same conditions as employed in the TPD experiment were used, with the sample heated at a rate of 2°C min^{-1} to a target temperature of 350°C.

The sample heated in the IGA showed a similar desorption trace to that of the TPD experiment, with only hydrogen desorbed. The onset of this release was observed at 135°C, with the first release involving a sharp release of hydrogen, peaking at 145°C. As with the TPD experiment this release was accompanied by a slight exotherm in the temperature trace. Following this desorption step the release of hydrogen levelled out at 155°C and there was a plateau in the release until 180°C. The release continued albeit slowly until the target temperature of 350°C was achieved. A small

broad release was observed towards the end of the experiment, with a slight peak at 305°C.

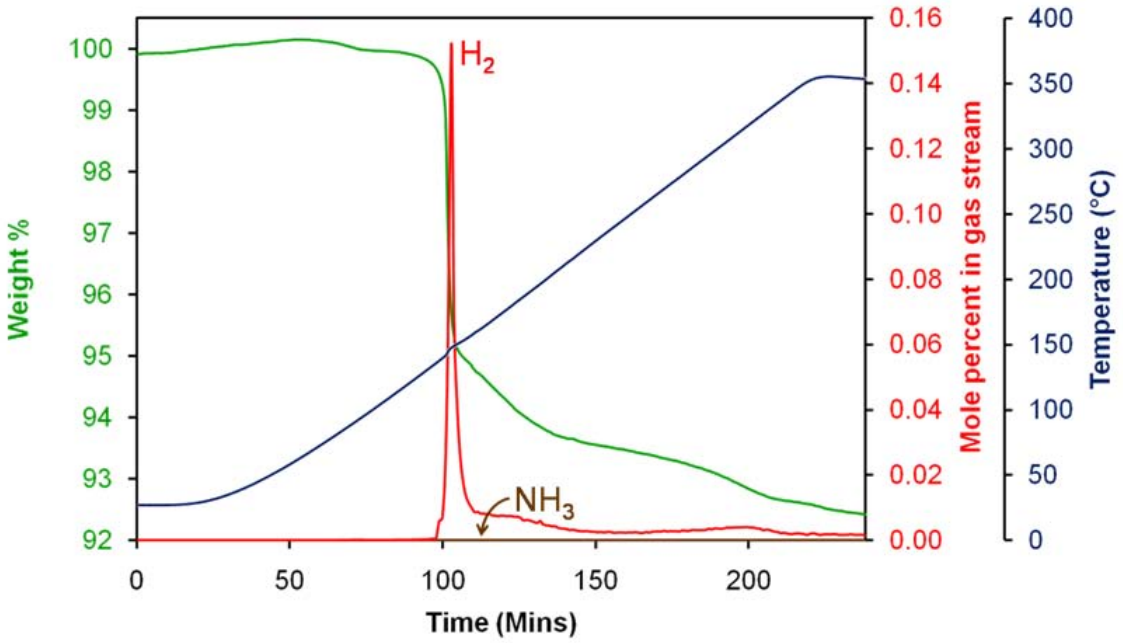

Figure 4.30 – Thermogravimetric analysis of $Na^{+}[BH_3(NH_2)BH_3]^{-}$ in an IGA. The gravimetric trace is shown in green, the temperature trace in blue and the mole percentages of H_2 and NH_3 released are shown in red and brown, respectively

A total mass loss of 7.5 wt% was observed, although as can be seen in figure 4.30 neither the weight loss nor the hydrogen release were complete at the end of the experiment. The main hydrogen desorption step was accompanied by a weight loss of 5 wt%; the observed plateau of hydrogen release was accompanied by a further 1.2 wt% loss and the final 1.3 wt% was lost slowly up until the end of the experiment.

4.4.5.3 Discussion

A comparison of the thermal desorption profile of the trigonal phase from TPD–MS and IGA–MS experiments is made in figure 4.31. The IGA and TPD profiles of the trigonal phase show very similar desorption profiles, with both the main desorption of hydrogen and the higher temperature desorption occurring at similar temperatures. The two desorption profiles correlated reasonably well with the third hydrogen desorption peak in the TPD profile of the NaH + $2NH_3BH_3$ reaction mixture, figure 4.31, suggesting that they are all related to the same desorption event. Although, it can be seen that the desorption profile is much less well defined in the reaction

mixture. The main hydrogen desorption peak in the profiles of the trigonal phase would be due to the decomposition of this phase, as this event occurred at a similar temperature to which the phase change from $Na^+[BH_3(NH_2)BH_3]^-$ to $NaBH_4$ was observed through powder XRD analysis. The desorption events above 150°C were likely due to side reactions or the decomposition of amorphous materials formed as part of the main reaction pathway. There was a good agreement between the desorption event at 160°C for the reaction mixture and pre-synthesised trigonal phase. However, the higher temperature desorption event occurred at a lower temperature in the reaction mixture profile. This discrepancy was likely to have been due to side reactions.

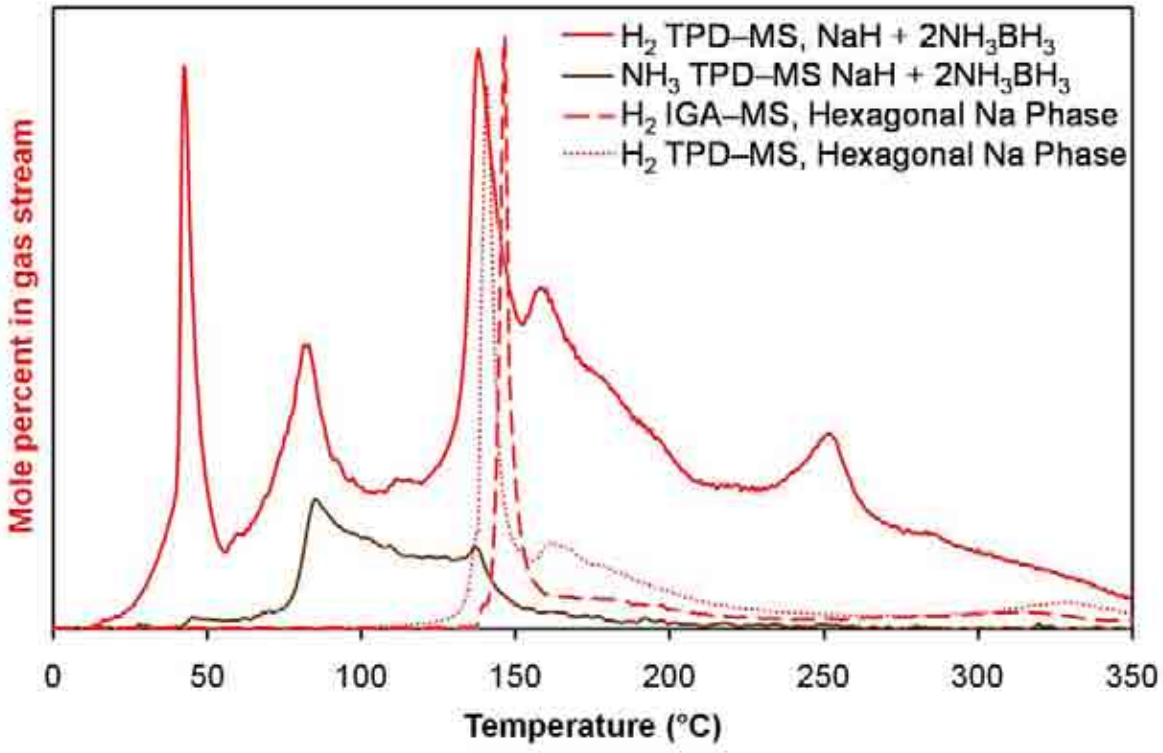

Figure 4.31 – Comparison of TPD–MS and IGA–MS thermal desorption data for the trigonal phase as well as TPD–MS thermal desorption data for a NaH + $2NH_3BH_3$ reaction mixture

Further to this, there was no NH_3 loss observed from the pre-synthesised $Na^+[BH_3(NH_2)BH_3]^-$ phase, which confirmed that NH_3 release was specific to the formation of this phase.

The hydrogen content of $Na^+[BH_3(NH_2)BH_3]^-$ is 12.1 wt% and therefore this material can theoretically account for the total observed hydrogen weight loss of 7.5 wt% during the IGA–MS experiment. However, as discussed previously a number of side reactions potentially occurred during synthesis and therefore the sample used in this experiment would probably not have been pure $Na^+[BH_3(NH_2)BH_3]^-$. The main sharp hydrogen desorption has been assigned to the decomposition of this phase, forming $NaBH_4$, reaction 4.26.

$$nNa^+[BH_3(NH_2)BH_3]^- \rightarrow nNaBH_4 + (NH_2BH_2)_n + nH_2 \qquad \text{Reaction 4.26}$$

This reaction yields the polymeric material polyaminoborane, which itself undergoes decomposition upon heating above 150°C and hence would also have decomposed, releasing hydrogen, reaction 4.27.[18]

$$(NH_2BH_2)_n \rightarrow (NHBH)_n + nH_2 \qquad \text{Reaction 4.27}$$

The decomposition of $Na^+[BH_3(NH_2)BH_3]^-$ would therefore be expected to release two equivalents of hydrogen, equal to a weight loss of 6.0 wt%. The observed weight loss associated with this step was less than this, 5.0 wt%. This shows that the initial sample loaded into the IGA was not purely $Na^+[BH_3(NH_2)BH_3]^-$ or that side reactions were proceeding during the experiment. The higher temperature weight losses were likely due to side reactions as both $(NHBH)_n$ and $NaBH_4$ do not undergo decomposition until temperatures in excess of the maximum temperature reached during the experiment.[7, 18]

4.5 Solid State ^{11}B MAS NMR Spectroscopy

The $NaH + NH_3BH_3$ and $NaH + 2NH_3BH_3$ reaction pathways were studied using solid state ^{11}B MAS NMR spectroscopy to determine how the B environments changed as the reactions progressed, in particular to provide information on the amorphous components of the reaction mixtures. The reactions were carried out on an argon gas line as described in section 4.2 and the ^{11}B NMR spectra collected at room temperature. The data was collected in collaboration with the University of Warwick.

All deconvolution of the spectra was carried out by Tom Partridge at the University of Warwick.

4.5.1 NaH + NH_3BH_3 Reaction

The solid state ^{11}B MAS NMR spectrum of $NaNH_2BH_3$ synthesised through the solid state reaction of a 1:1 mixture of NaH and NH_3BH_3 at 40°C is shown in figure 4.32. There is a single feature observed in the spectrum, at −22.9 ppm, which is identical to that reported by Xiong *et al.*[5] for the spectrum of $NaNH_2BH_3$. This feature can be assigned to the sp^3 boron found in an NBH_3 environment.

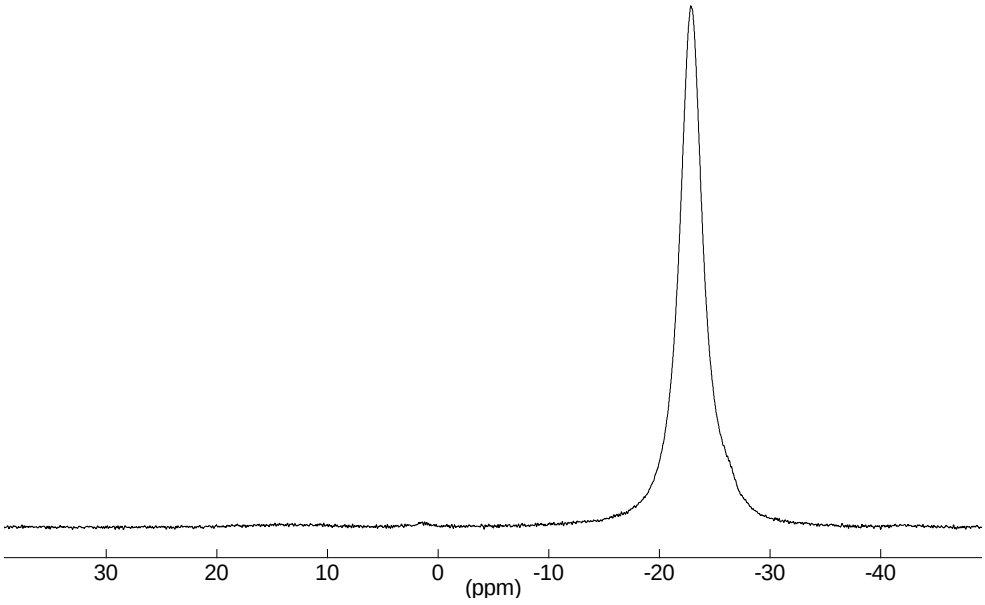

Figure 4.32 – The solid state ^{11}B MAS NMR spectrum of $NaNH_2BH_3$, synthesised through the NaH + NH_3BH_3 reaction at 40°C

The spectrum obtained after heating the 1:1 reaction mixture to 60°C is shown in figure 4.33. The feature previously observed at −22.9 ppm, showed a slight shift upfield to −23.3 ppm as well as a significant broadening. Two small features were observed, at −42.7 ppm and 1.0 ppm. A broad complex feature at 30.4 ppm was also present. The shape of the feature is due to the quadrupolar interaction of this B environment.

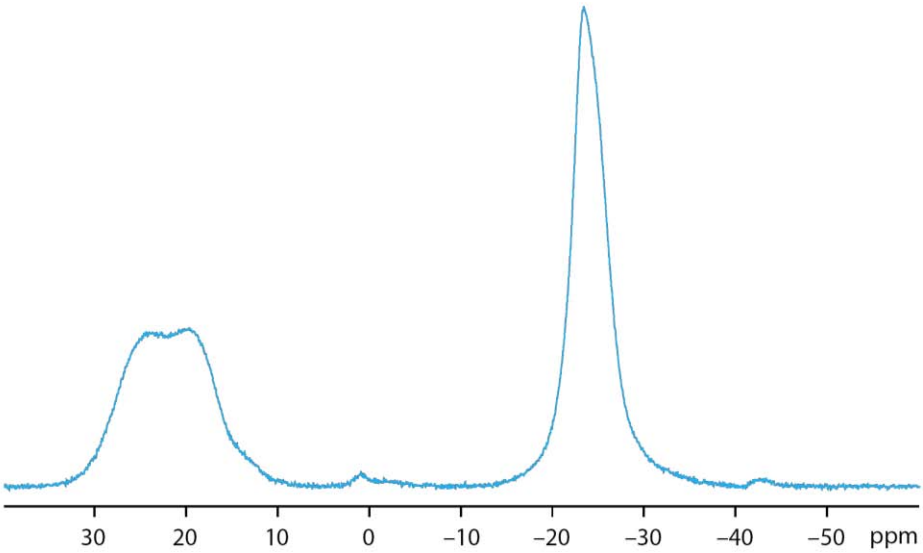

Figure 4.33 – The solid state ^{11}B MAS NMR spectrum of the product of the NaH + NH_3BH_3 reaction at 60°C

The ^{11}B NMR spectrum of the sample obtained after heating to 200°C is shown in figure 4.34. A broad feature, 30.4 ppm, was again observed in the spectrum, but had now become the dominant resonance in the spectrum. The NBH_3 signal, observed at −23.3 ppm was again broad, however, the intensity was much reduced compared to its appearance in the spectrum after heating to 60°C. There were again low intensity features observed at 1.0 ppm and −42.7 ppm.

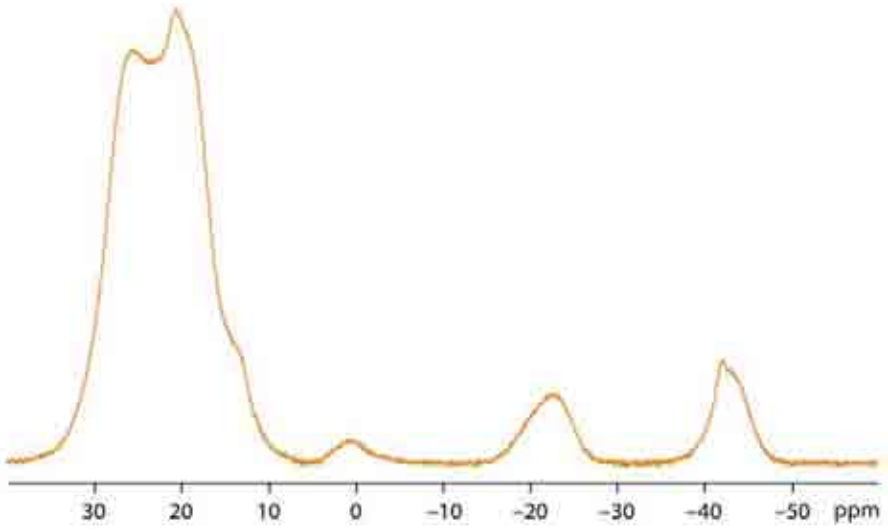

Figure 4.34 – The solid state ^{11}B MAS NMR spectrum of the product of the NaH + NH_3BH_3 reaction at 200°C

Discussion

The single feature observed in the spectrum of $NaNH_2BH_3$ implied that the product was relatively pure, although there was some evidence for residual NH_3BH_3. The spectra of $NaNH_2HB_3$ and NH_3BH_3 are compared in figure 4.35. The spectra were similar in that both showed only a single resonance. This downshift of the BH_3 signal on substitution of a hydrogen by sodium has been observed in previous solid state and solution ^{11}B NMR studies.[2, 4] The substitution of hydrogen by the more electron donating sodium increases the strength of the B–N bond. It was noted in section 4.3 that the B–N bond length in $NaNH_2BH_3$ is slightly shorter (1.46 Å) than in NH_3BH_3 (1.597 Å[15]) highlighting this change. The observed downfield shift of the NBH_3 resonance supports the increased strength of this bond.

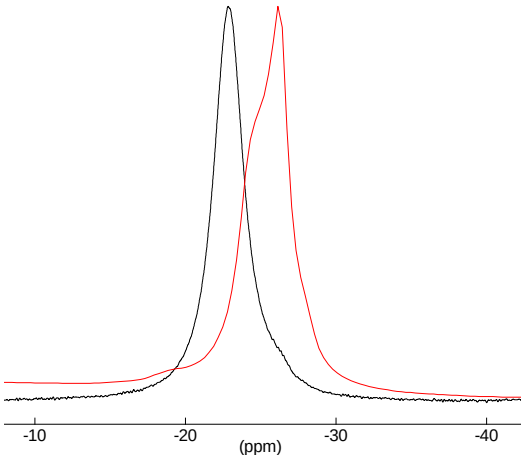

Figure 4.35 – The solid state ^{11}B MAS NMR spectra of $NaNH_2BH_3$ (black) and NH_3BH_3 (red)

The XRD pattern of the sample collected after heating the NaH + NH_3BH_3 reaction to 60°C showed that no crystalline phases were observed, suggesting that $NaNH_2BH_3$ had completely decomposed. However, the observation of a feature at −23.3 ppm in the ^{11}B NMR spectrum of this sample suggested that decomposition was incomplete at 60°C. The fact that the resonance had broadened suggested that there was an increased amount of disorder in this environment, making $NaNH_2BH_3$ undetectable by XRD. The broad feature at 30.4 ppm can be assumed to be related to the most prominent decomposition pathway. As discussed in section 4.4, the first step in the decomposition of $NaNH_2BH_3$ involved the release of H_2 which was expected to yield

a BH_2 containing species, similar to the decomposition of NH_3BH_3. However, a boron found in a tetrahedral BH_2 environment will give rise to a feature between +5 and −15 ppm.[21, 22] If the main decomposition product had possessed a tetrahedral BH_2 environment, the intensity of a feature in this range would have been much greater than the very low intensity of the peak observed at 1.0 ppm. This feature was more likely due to a small amount of oxidation of the sample, resulting in a B–O environment. The absence of a tetrahedral BH_2 feature means that either a BH_2 unit was not involved in $NaNH_2BH_3$ decomposition or any species that formed containing a BH_2 unit was rapidly consumed. The complex broad feature observed at 30.4 ppm is characteristic of sp^2 B in either an N_3B or N=BH–N environment.[23, 24] The slight shift observed in the position of the NBH_3 resonance could have meant that this was not in fact related to the $NaNH_2BH_3$ material and the decomposition product could have possessed terminal NBH_3 and internal N=BH–N environments. The final feature at −42.7 ppm was related to a BH_4 unit.[19] The absence of any N_2BH_2 feature in the spectrum showed that this could not have been related to DADB or a DADB analogue. The chemical shift of this peak was inconsistent with that of $NaBH_4$.

Further heating to 200°C showed that the ultimate decomposition product primarily involved boron in an sp^2 environment. Xiong *et al.*[5] proposed the decomposition product of $NaNH_2BH_3$ to be $(NaNBH)_n$. The spectrum observed by Xiong *et al.* after heating $NaNH_2BH_3$ to 200°C is reproduced in figure 4.36. This spectrum shows resonances with very similar intensities and chemical shifts to those in figure 4.34. However, Xiong *et al.* did not identify NaH as a decomposition product. Deconvolution of this broad quadrupolar feature, figure 4.37, showed there were in fact two sp^2 boron environments present in the product. The dominant sp^2 signal was observed at a chemical shift of 30.4 ppm and the secondary site at 23.5 ppm. The ^{11}B NMR spectrum of $(NHBH)_n$ possesses only a broad sp^2 feature with a chemical shift of 31.0 ppm, similar to the dominant sp^2 feature observed here.[23, 24] As will become clear in subsequent chapters, the secondary quadrupolar site at 23.5 ppm was exclusive to the NaH + NH_3BH_3 reaction pathway, which suggests that $(NaNBH)_n$ may also have been a decomposition product. Further evidence for this will be presented in section 4.6. The main decomposition pathway of $NaNH_2BH_3$ can therefore be represented by reaction 4.28. The fact that other boron environments

were observed in the spectrum of the decomposition product, namely BH_4 and NBH_3, shows that there must have been competing side reactions to this main pathway.

$$nNaNH_2BH_3 \rightarrow nNaH + (NHBH)_n + nH_2 \qquad \text{Reaction 4.28}$$

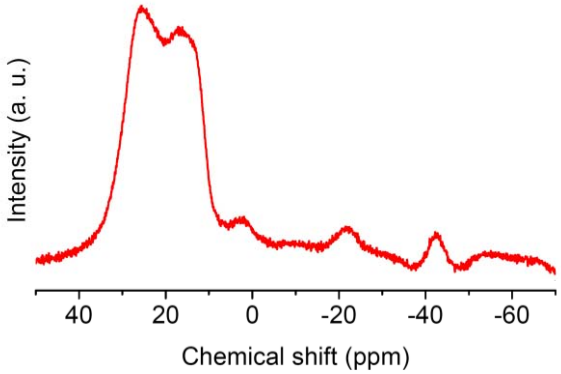

Figure 4.36 – The solid state ^{11}B NMR spectrum of the decomposition product of $NaNH_2BH_3$ heated at 200°C[5]

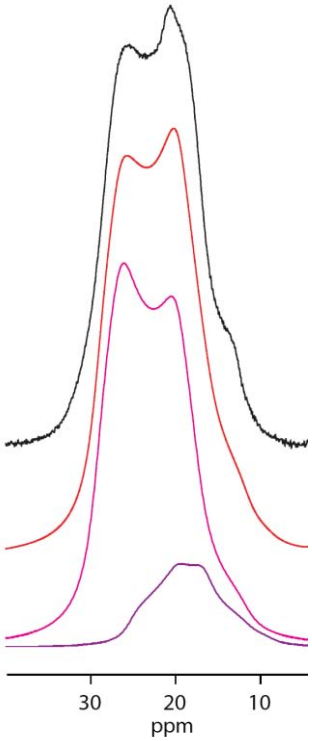

Figure 4.37 – Deconvolution of the broad quadrupolar feature observed in the solid state ^{11}B MAS NMR spectrum collected for the product of the NaH + NH_3BH_3 reaction at 200°C. The observed spectrum is shown in black, deconvolution of the site in pink and purple and the cumulative simulated spectrum in red

4.5.2 NaH + $2NH_3BH_3$ Reaction

The solid state ^{11}B MAS NMR spectrum of the sample obtained after reaction at 40°C along with the deconvolution of the spectrum is shown in figure 4.38. The spectrum contained features in the region of the spectrum where NBH_3 environments are expected. Deconvolution showed that there were two separate boron environments of this nature: which had chemical shifts of −23.0 ppm and −26.1 ppm. These peaks had the same chemical shifts as the features previously observed in the ^{11}B NMR spectra of $NaNH_2BH_3$ and NH_3BH_3, respectively. The spectra obtained after heating the 1:2 reaction mixture to 40°C is compared to those of NH_3BH_3 and $NaNH_2BH_3$ in figure 4.39.

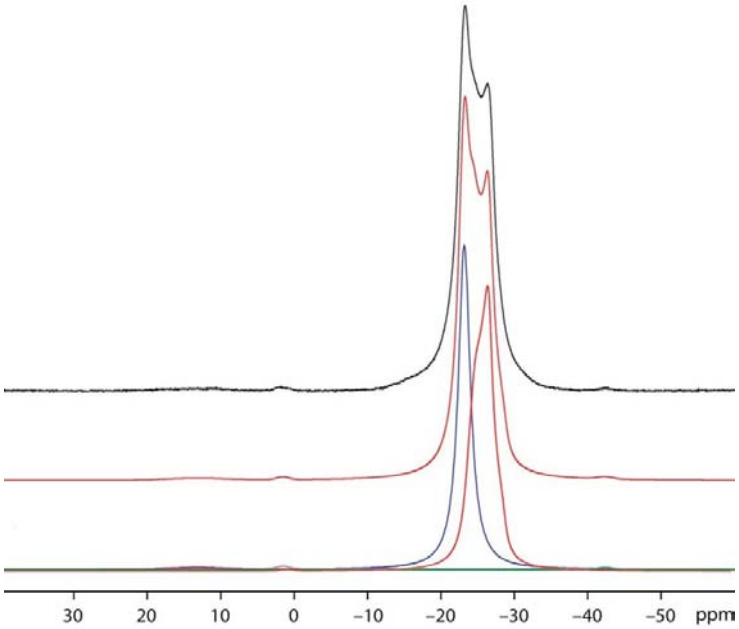

Figure 4.38 – The observed solid state ^{11}B MAS NMR spectrum of the product of the NaH + $2NH_3BH_3$ reaction at 40°C (black). Deconvolution of the spectrum is shown, with the cumulative simulated spectrum shown in red

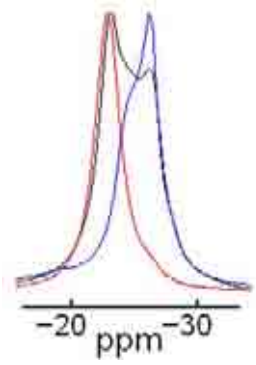

Figure 4.39 – Comparison of the solid state ^{11}B MAS NMR spectra of the product of the NaH + $2NH_3BH_3$ reaction at 40°C (black), $NaNH_2BH_3$ (red) and NH_3BH_3 (blue) in the region −20 to −30 ppm

The NMR spectrum of the sample obtained after reaction at 60°C along with the deconvolution of the spectrum is shown in figure 4.40. Deconvolution showed there had been a change in the appearance of the resonances found in the NBH_3 region of the spectrum. The resonances assigned to NH_3BH_3 and $NaNH_2BH_3$ were no longer present and had been replaced by a single resonance at −24.2 ppm. A number of low intensity resonances were also observed, with features at −42.9 ppm, −7.3, −15.7 ppm and 1.0 ppm along with a quadrupolar site at 29.3 ppm.

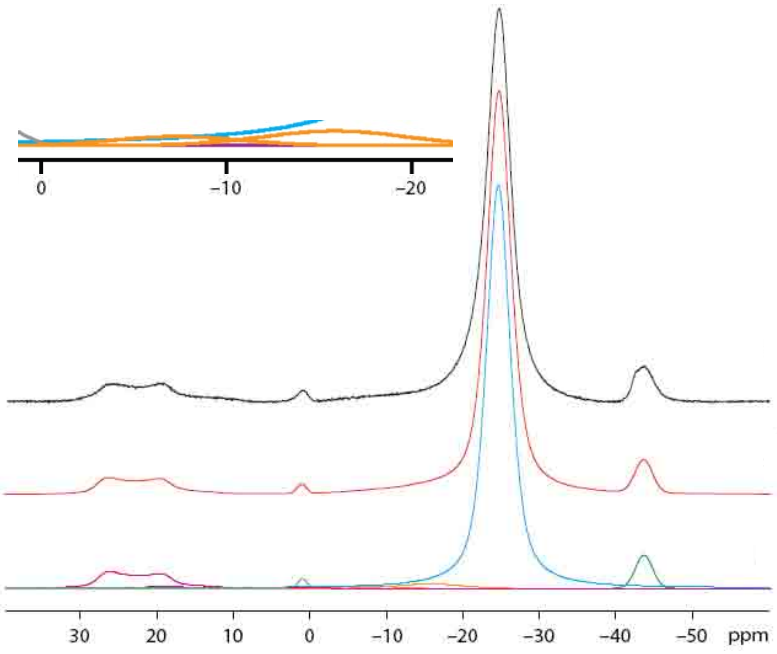

Figure 4.40 – The observed solid state ^{11}B MAS NMR spectrum of the product of the NaH + $2NH_3BH_3$ reaction at 60°C (black). Deconvolution of the spectrum is shown, with the cumulative simulated spectrum shown in red

The pathway of the NaH + $2NH_3BH_3$ reaction as viewed by solid state ^{11}B NMR spectroscopy results with respect to the changes in B environments during the pathway is shown in figure 4.41. It can be seen that there were few changes in the spectra collected from the products of the 80°C and 100°C reactions compared to the product of the 60°C reaction. The spectra were dominated by the intense resonance at −24.2 ppm, as well as both spectra showing the previously observed low intensity features at −42.8 ppm, −15.7 ppm, −7.3 ppm and 1.0 ppm. The quadrupolar feature was again observed at 29.3 ppm in both spectra. However, deconvolution of this site showed that at 100°C there appeared to be a second B environment present, with a chemical shift of 25.7 ppm, figure 4.42.

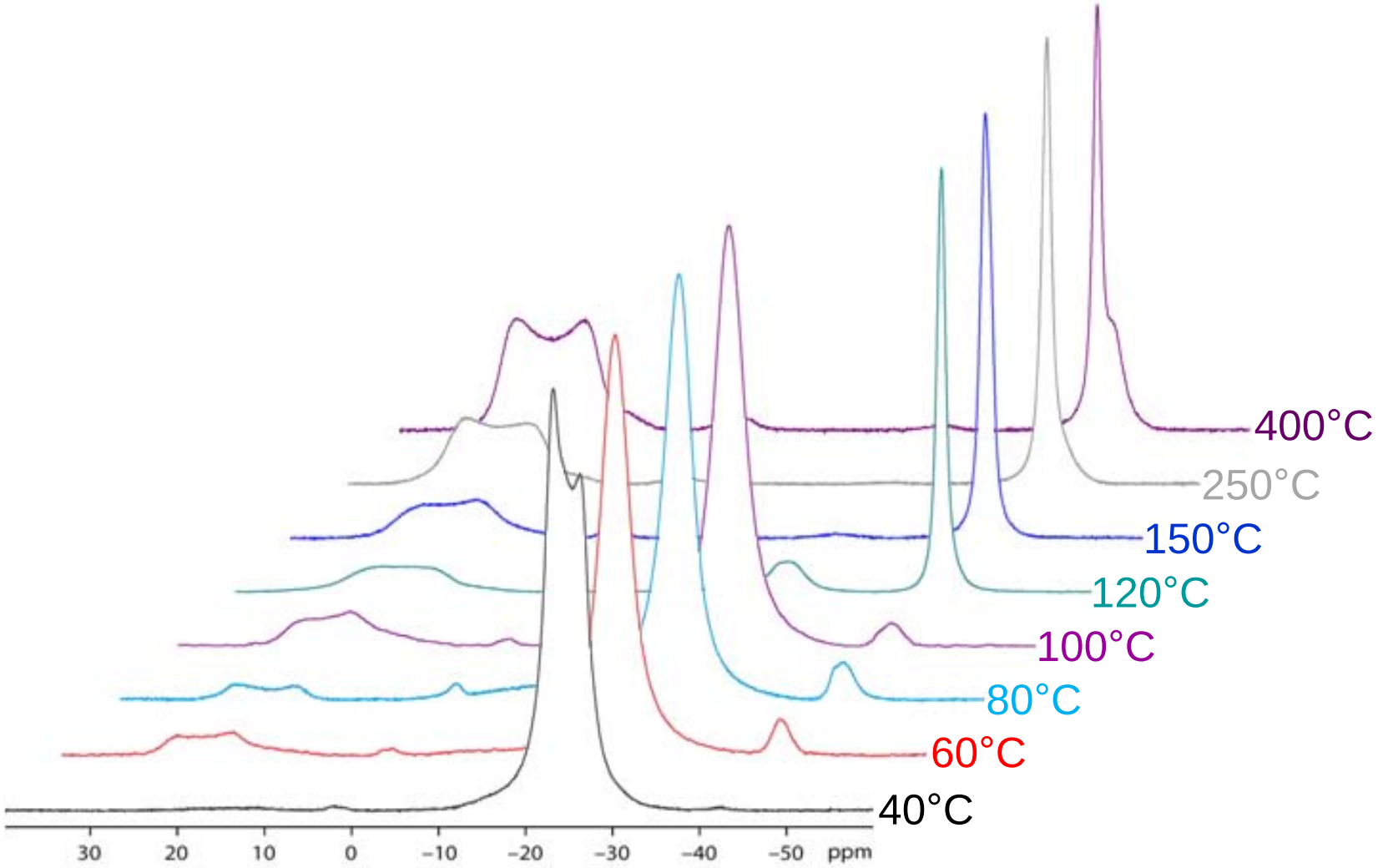

Figure 4.41 – Solid state ^{11}B MAS NMR spectra obtained from the products of the NaH + $2NH_3BH_3$ reaction at various temperatures

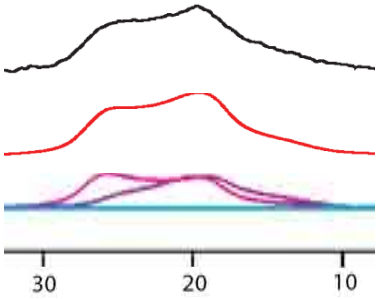

Figure 4.42 – Deconvolution of the quadrupolar site observed in the ^{11}B MAS NMR spectrum of the product of the NaH + $2NH_3BH_3$ reaction at 100°C

Figure 4.41 shows that a significant change in the ^{11}B NMR spectra was observed on increasing the reaction temperature from 100°C to 120°C. The spectrum collected after reaction at 120°C is presented in figure 4.43 along with the deconvolution of the sites. The dominant resonance at −24.2 ppm at lower temperature was still present although its intensity had substantially reduced and the spectrum was now dominated by a sharp resonance at −42.0 ppm. The quadrupolar boron environment at 29.3 ppm was still present and deconvolution of this site again showed evidence that there was a secondary site at 25.7 ppm. At a reaction temperature of 120°C and above, the previously observed low intensity features at −42.8 ppm, −15.7 ppm and −7.3 ppm were not evident in any spectra, while the resonance at 1.0 ppm was present in most spectra.

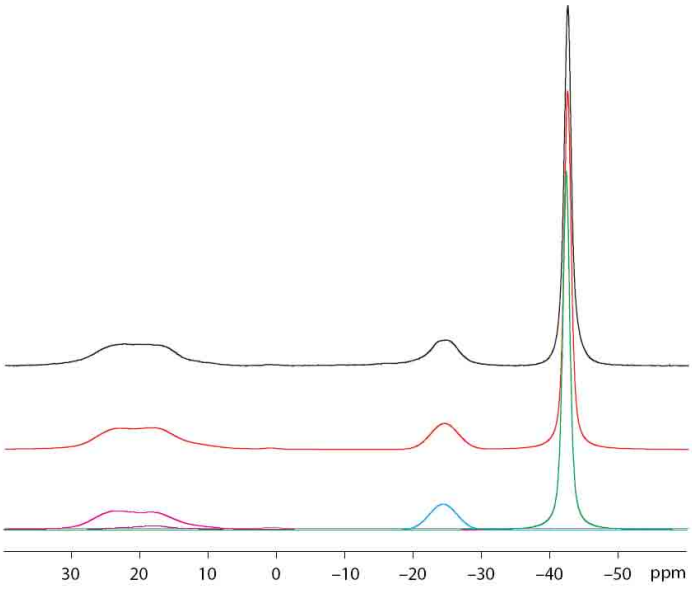

Figure 4.43 – The observed solid state ^{11}B MAS NMR spectrum of the product of the NaH + $2NH_3BH_3$ reaction at 120°C (black). Deconvolution of the spectrum is shown, with the cumulative simulated spectrum shown in red

Above 120°C the resonance at −24.2 ppm disappeared while the resonance with a chemical shift of −42.0 ppm remained the most intense feature in the spectra. Between 150°C and 400°C there was an increase in the cumulative intensity of the quadrupolar environments at 29.3 ppm. Deconvolution of the sites showed that the secondary site at 25.7 ppm was present throughout this temperature range, with it being most prominent after reaction at 150°C, figure 4.44. After reaction at 250°C and 400°C deconvolution revealed that a new resonance appeared in the spectra at −44.3 ppm, the intensity of which grew with temperature increase, figure 4.45.

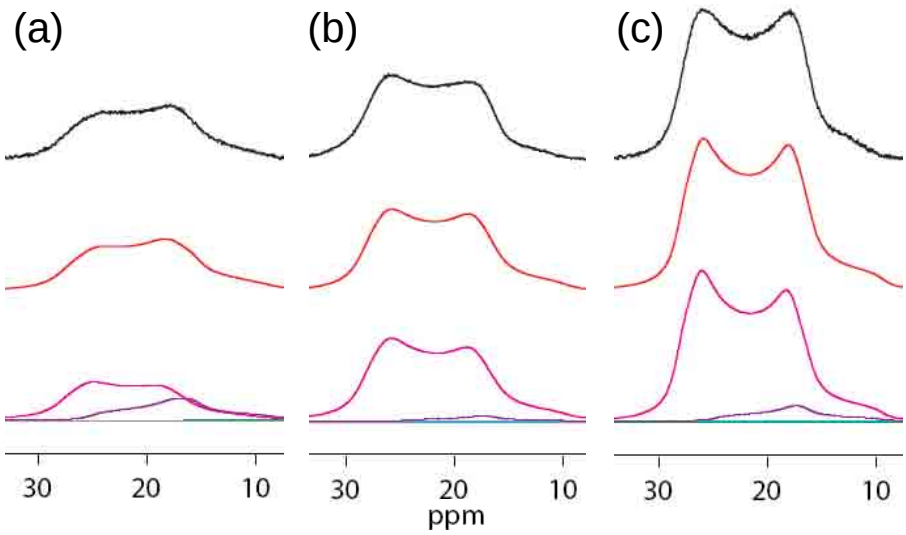

Figure 4.44 – Deconvolution of the quadrupolar B site observed in the solid state ^{11}B MAS NMR spectra collected from the products of the NaH + $2NH_3BH_3$ reaction at (a) 150°C (b) 250°C and (c) 400°C

Discussion

The first step in the NaH + $2NH_3BH_3$ reaction has been shown by powder XRD to involve the synthesis of $NaNH_2BH_3$ at 40°C with the excess NH_3BH_3 remaining in the reaction mixture. This was also shown to be the case by ^{11}B NMR. The fact that no other resonances were observed in the spectrum implied that this step was free from side reactions.

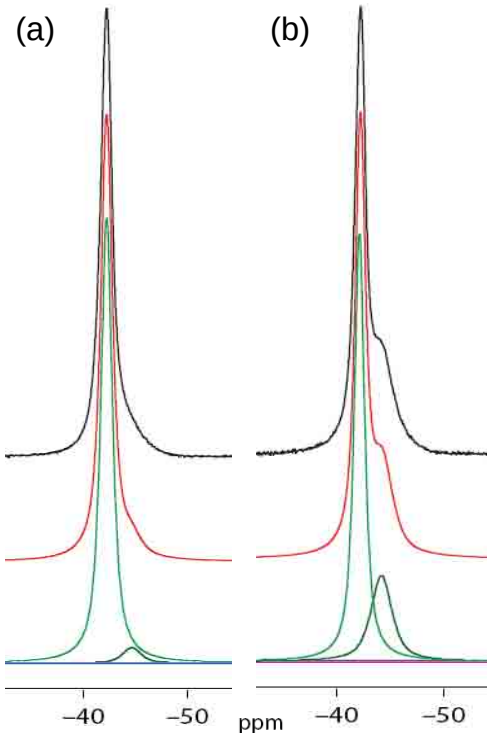

Figure 4.45 – Deconvolution of the resonance observed at −42.0 ppm in the solid state ^{11}B MAS NMR spectra collected from the products of the NaH + $2NH_3BH_3$ reaction at (a) 250°C and (b) 400°C

Powder XRD results showed that the product of the 1:2 reaction at 60°C was a previously unreported trigonal crystalline phase, section 4.3. Following analysis of gas desorption data, section 4.4, this phase was assigned the chemical formula $Na^+[BH_3NH_2BH_3]^-$. After reaction at 60°C the resonances of $NaNH_2BH_3$ and NH_3BH_3 were no longer observed and had been replaced by a dominant feature at −24.2 ppm. This resonance supported the $Na^+[BH_3NH_2BH_3]^-$ assignment. The chemical shift of this resonance is consistent with an sp^3 boron in an NBH_3 environment.[5, 19] Due to the reaction stoichiometry two boron atoms were required to be in the reaction product. Figure 4.46 shows the percentage change of boron in the observed environments as a function of reaction temperature. It can be seen that after reaction at 60°C over 80% of the boron in the sample was present in the environment at −24.2 ppm. This shows that the two boron atoms within the product must have both been present in this environment and because the proposed product $Na^+[BH_3NH_2BH_3]^-$ has only one boron environment, this result supports this assignment. The observed chemical shift of this resonance offers further support for this composition. The resonance appears downfield of the resonance observed in the spectrum of NH_3BH_3

but upfield of that in $NaNH_2BH_3$. Electron donation from the Na causes the resonance to shift downfield compared to NH_3BH_3. However, the fact that this downfield shift was reduced compared to that observed with $NaNH_2BH_3$ shows that there was a reduced amount of electron donation, as would be expected with $Na^+[BH_3NH_2BH_3]^-$.

The decreased intensity of the $Na^+[BH_3NH_2BH_3]^-$ resonance after reaction at 120°C showed decomposition of this phase had occurred. This was accompanied by the appearance of the resonance at −42.0 ppm. Powder XRD results showed that $NaBH_4$ formed at 120°C and consistent with this, the observed resonance has a chemical shift associated with an alkali metal borohydride and can therefore be assigned to $NaBH_4$.[25] Whereas powder XRD could not identify other products of this decomposition, ^{11}B NMR revealed that a second product formed, which produced the quadrupolar boron resonance at 29.3 ppm. As $NaBH_4$ showed an increased amount of hydrogen bound to boron, this site should show reduced hydrogen compared to a BH_3. Quadrupolar boron sites have been identified for sp^2 boron at similar chemical shifts to those identified in the spectra presented here.[26] Two environments that satisfy this requirement are BHN_2 and BN_3, which have both been identified by Gervais *et al.*[27] in the structure of polyborazylene. The chemical shifts of these were identified as 31 ppm and 27 ppm for the BHN_2 and BN_3 environments, respectively. The observed chemical shift of the quadrupolar boron resonance in our study is similar to that of the BHN_2 environment, suggesting that the amorphous decomposition product of $Na^+[BH_3NH_2BH_3]^-$ likely possesses this environment. Hexagonal BN also possesses sp^2 boron and both Marchetti *et al.*[26] and Jeschke *et al.*[28] have observed this quadrupolar resonance at 30 ppm and 30.4 ppm, respectively. However, it is unlikely that this compound was responsible for the resonance observed in our study as temperatures in excess of 800°C are required for its synthesis.[23] The second quadrupolar site identified at 25.7 ppm shows a similar upfield shift to the BN_3 environment observed by Gervais *et al.* as did the BHN_2 environment. Figure 4.44 showed that this secondary site did not show a correlation with reaction temperature increase. It is therefore probable that this environment formed as a consequence of side reactions, possibly related to cross linking reactions between polymers possessing BHN_2 environments, which would release H_2 and form polymers containing BN_3 environments, as observed in the decomposition

of polyaminoborane.[29] Figure 4.46 showed that the sp^2 and $NaBH_4$ environments were present in approximately equal amounts following decomposition of $Na^+[BH_3NH_2BH_3]^-$. This implied that all of the sodium in the decomposed products was present as $NaBH_4$. This will be considered further in section 4.6.

Above 250°C a second BH_4 resonance was observed in the spectra of the products at −44.3 ppm, whose appearance and subsequent growth was accompanied by a decrease in the amount of $NaBH_4$ and increase in sp^2 boron in the sample. This would therefore be expected to be related to $NaBH_4$ decomposition. However, the decomposition of $NaBH_4$ has only been reported in the temperature range 400°C to 565°C.[7, 30, 31] Therefore, the changes in B environment observed at 250°C would not have been related to this decomposition. The fact that a second BH_4 environment appeared in the spectrum may be an indication that a phase transition occurs during the decomposition of $NaBH_4$. Phase transitions in the decomposition of both $LiBH_4$ and $Ca(BH_4)_2$ have previously been reported.[32, 33] However, there no literature reports have identified such a transition for $NaBH_4$. The reason behind the appearance of this resonance therefore remains unknown. The decomposition of $NaBH_4$ has been shown to proceed through either reaction 4.29 or reaction 4.30.[34]

$$NaBH_4 \rightarrow Na + B + 2H_2 \qquad \text{Reaction 4.29}$$

$$NaBH_4 \rightarrow NaH + B + 3/2H_2 \qquad \text{Reaction 4.30}$$

The absence of Na and NaH in the powder XRD patterns of the reaction products suggested that $NaBH_4$ decomposition did not proceed. Therefore the changes in the spectra were likely due to unidentified side reactions involving $NaBH_4$.

Below 120°C a third BH_4 resonance was observed at −42.8 ppm, along with two resonances at −7.3 ppm and −15.7 ppm. Stowe *et al.*[19] identified resonances at similar chemical shifts during the thermal decomposition of NH_3BH_3, which were assigned to the formation of DADB. The amount of boron in BH_2 and BH_4 environments was similar at temperatures below 120°C and both sites disappeared above this temperature. This collective behaviour was a good indication that the two sites were related. NH_3BH_3 decomposes to $(NH_2BH_2)_n$ through DADB formation and this polymer further decomposes to $(NHBH)_n$ above 130°C.[18] Therefore above 120°C

it can be concluded that the BH_2 environments released H_2 to form sp^2 boron and the BH_4 crystallised with Na to form $NaBH_4$.

Finally the low intensity resonance at approximately 1 ppm, observed in most spectra, was thought to be due to a small amount of sample oxidation.

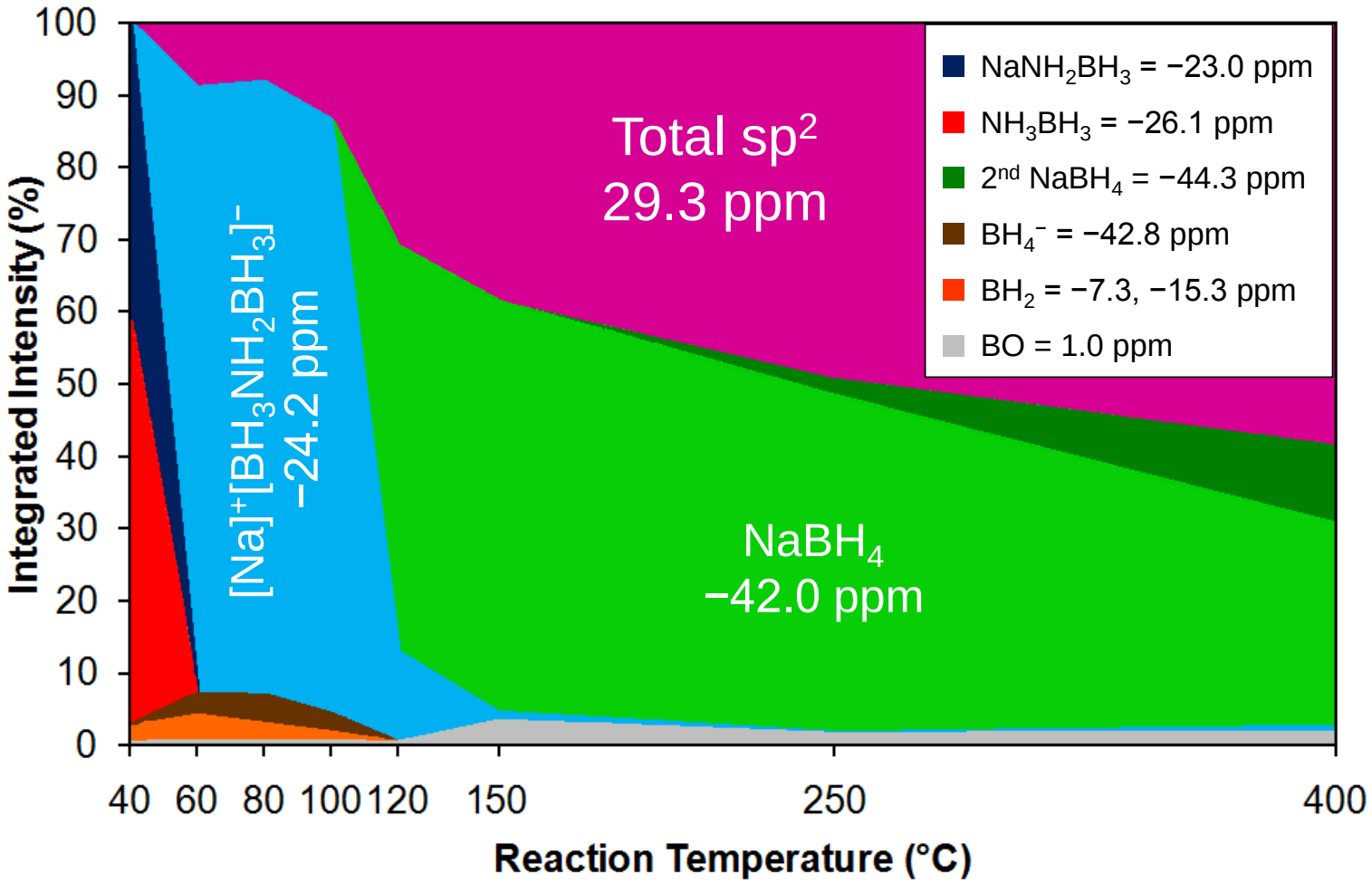

Figure 4.46 – A plot of the integrated intensities of the phases present in the NaH + $2NH_3BH_3$ reaction pathway as deduced from solid state ^{11}B MAS NMR

4.6 Solid State ^{23}Na MAS NMR Spectroscopy

The 1:2 sodium reaction pathway was also investigated through solid state ^{23}Na MAS NMR spectroscopy. The data was collected in collaboration with the University of Warwick. All deconvolution of the spectra was carried out by Tom Partridge at the University of Warwick. The collected spectra are displayed in figure 4.47.

Figure 4.47 shows that throughout the reaction pathway there were only three sodium environments. Initially two environments were present, a quadrupolar environment at 7.5 ppm and a resonance at −4.6 ppm. After reaction at 60°C only the resonance at −4.6 ppm was observed. Only this single site remained in the spectra up to 110°C, before the final site appeared, with a chemical shift of −8.3 ppm. The resonance at −4.6 ppm was present in both the spectra collected from the products of reactions at 120°C and 150°C, although the intensity of the resonance was low. Above 200°C only the resonance at −8.3 ppm was observed.

Discussion

The quadrupolar site observed at 7.5 ppm was identified as $NaNH_2BH_3$ through comparison with the solid state ^{23}Na MAS NMR spectrum, figure 4.48, collected from the product of the NaH + NH_3BH_3 reaction at 40°C, previously established to be $NaNH_2BH_3$. This spectrum possessed a dominant quadrupolar sodium environment with a chemical shift of 7.5 ppm, identical to the resonance observed in the 1:2 reactions at low temperature. As this resonance disappeared from the spectrum it was replaced by the increased intensity of the feature at −4.6 ppm, figure 4.49. From comparisons with powder XRD and solid state ^{11}B MAS NMR results, this resonance can be assigned to the $Na^+[BH_3NH_2BH_3]^-$ phase. This resonance was also unexpectedly observed in the spectrum of the 40°C reaction product and may have been due to the time delay between performing the 40°C reaction and collecting the ^{23}Na NMR spectrum, giving enough time for $NaNH_2BH_3$ to react slowly with NH_3BH_3 in the sample, yielding this product. Above 120°C the resonance observed at −8.3 ppm can be assigned to $NaBH_4$.

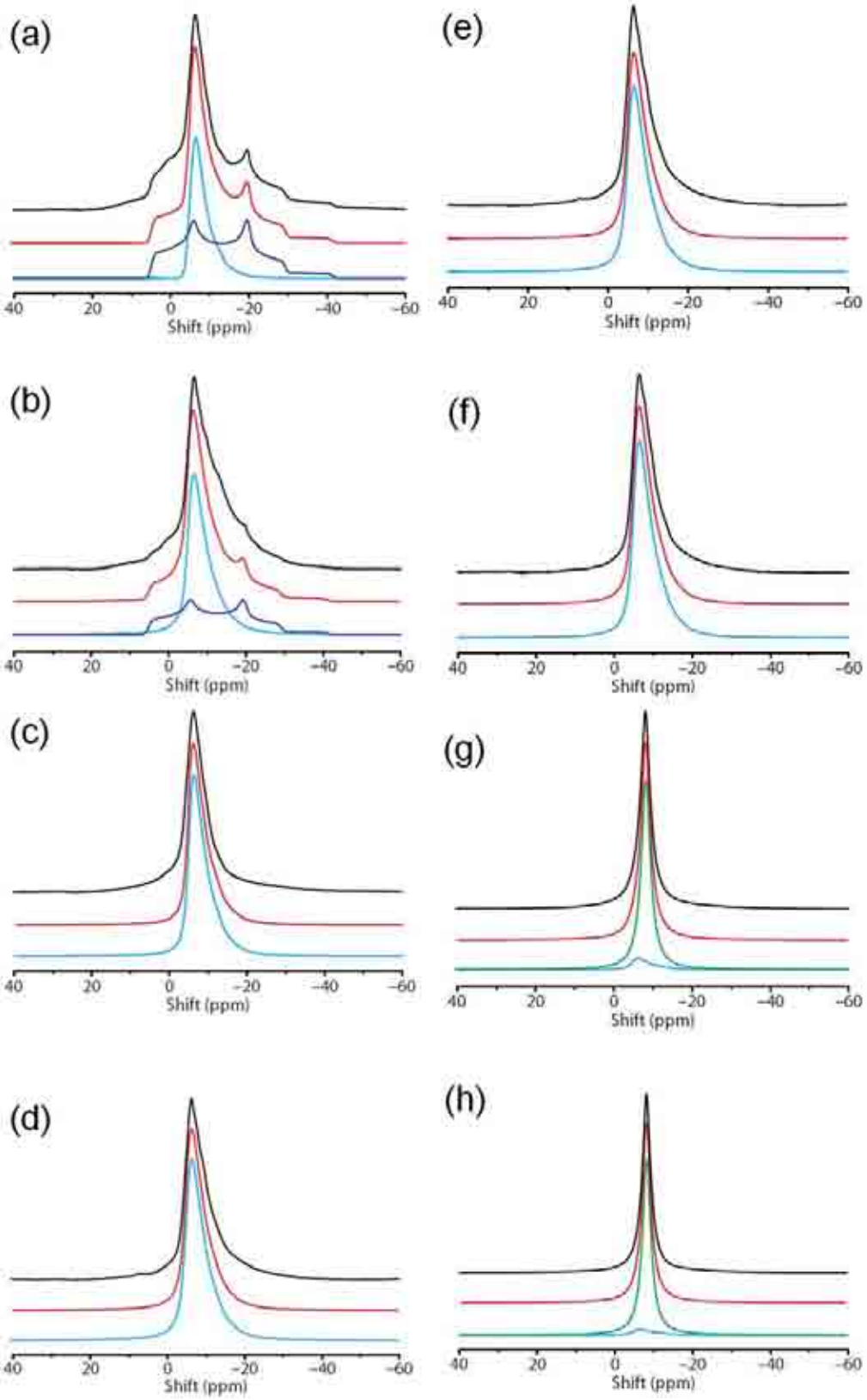

Figure 4.47 – Solid state ^{23}Na MAS NMR spectra collected from the products of the $NaH + 2NH_3BH_3$ reaction at (a) 40°C (b) 50°C (c) 60°C (d) 80°C (e) 100°C (f) 110°C (g) 120°C (h) 150°C

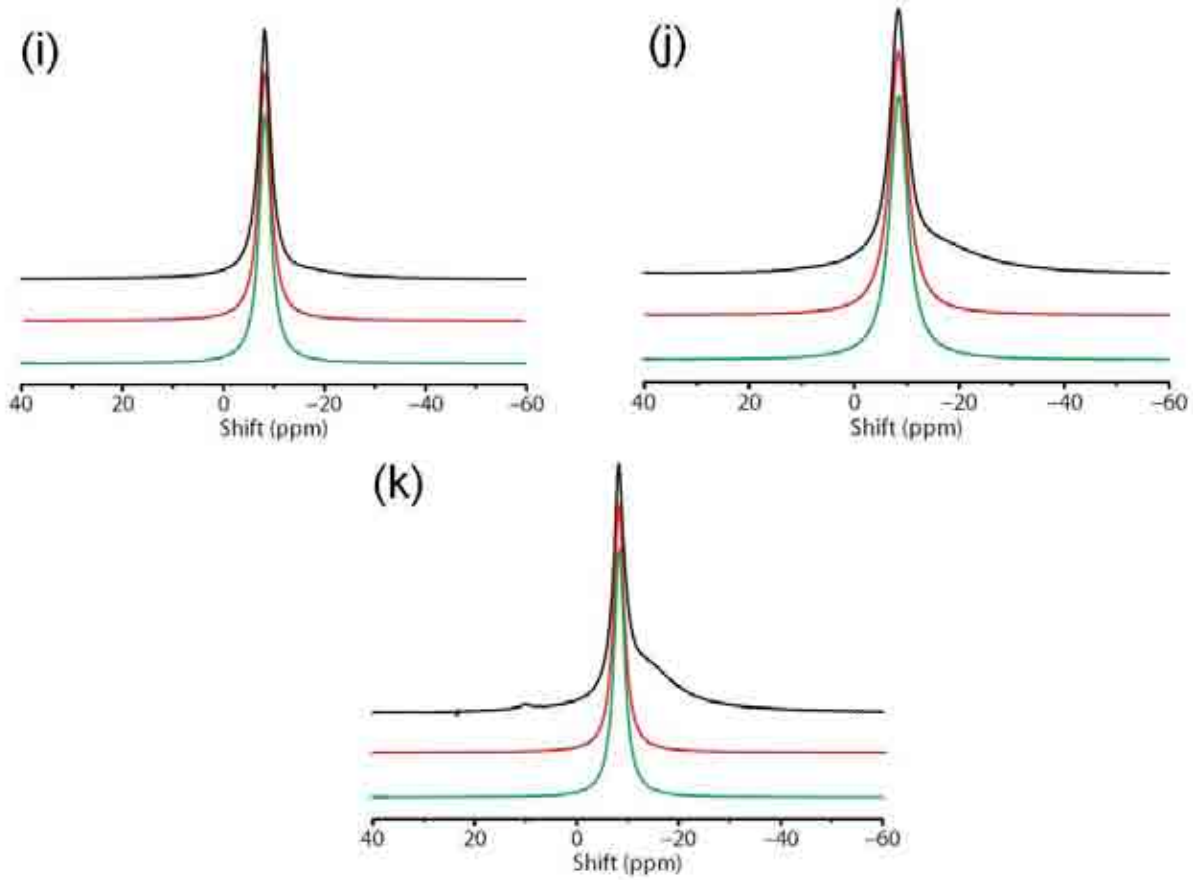

Figure 4.47 (cont.) – Solid state ^{23}Na MAS NMR spectra collected from the products of the NaH + $2NH_3BH_3$ reaction at (i) 200°C (j) 300°C (k) 400°C

Figure 4.49 shows that following decomposition of $Na^+[BH_3NH_2BH_3]^-$ all of the sodium was present as $NaBH_4$ and therefore the decomposition product possessing sp^2 boron was free of sodium. Combining the solid state ^{11}B and ^{23}Na MAS NMR results suggests that the main amorphous product from the decomposition of $Na^+[BH_3NH_2BH_3]^-$ was similar to that of NH_3BH_3, $(NHBH)_n$. The main decomposition pathway of $Na^+[BH_3NH_2BH_3]^-$ can hence be represented by reaction 4.31, although side reactions likely play a part.

$$nNa^+[BH_3NH_2BH_3]^- \rightarrow nNaBH_4 + (NHBH)_n + nH_2 \qquad \text{Reaction 4.31}$$

The results of the solid state ^{23}Na NMR experiments also gave further insight into the 1:1 reaction pathway. Solid state ^{11}B NMR results showed that the decomposition products of $NaNH_2BH_3$ and $Na^+[BH_3NH_2BH_3]^-$ both possessed two sp^2 boron environments. The dominant sp^2 environment in both decomposition products produced similar chemical shifts of 30.4 ppm and 29.3 ppm, which in both reactions

was determined to be due to $(NHBH)_n$ formation. The secondary quadrupolar site showed a larger discrepancy between the chemical shifts of this environment, being observed in the decomposition products of $NaNH_2BH_3$ and $Na^+[BH_3NH_2BH_3]^-$ at 23.5 ppm and 25.7 ppm, respectively. This discrepancy may be due to the presence of sodium. The ^{23}Na NMR results showed that sodium was not present in the amorphous decomposition products of $Na^+[BH_3NH_2BH_3]^-$, which may imply that the product responsible for the environment observed at 23.5 ppm did possess sodium.

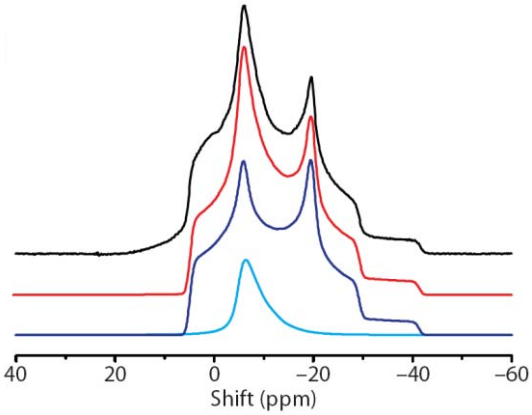

Figure 4.48 – The solid state ^{23}Na MAS NMR spectrum collected from the product of the NaH + NH_3BH_3 reaction at 40°C

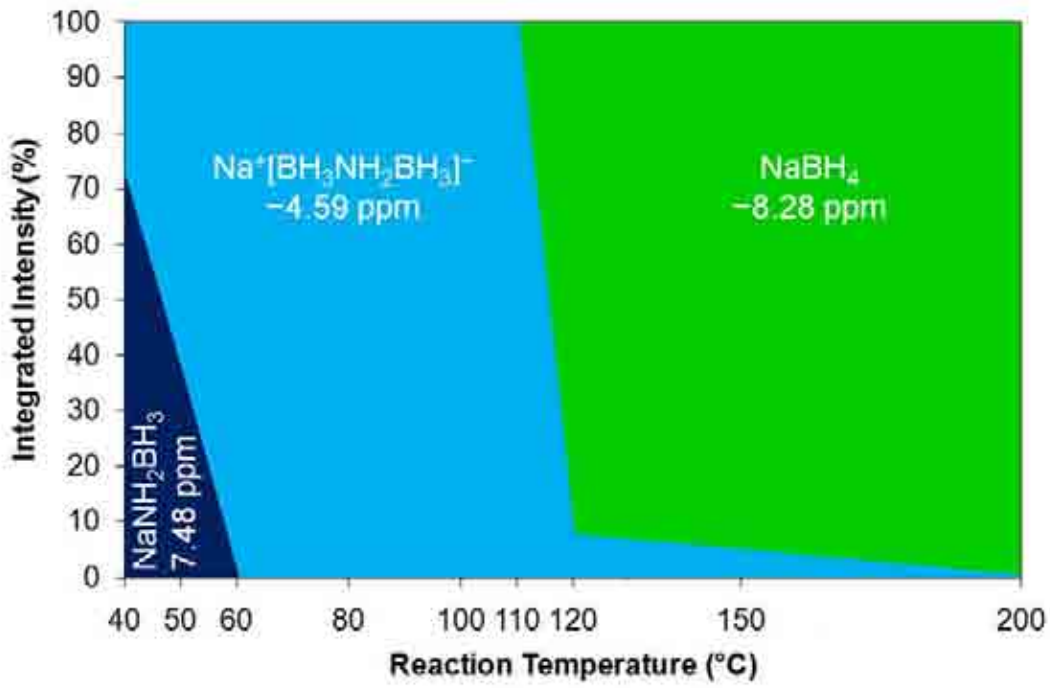

Figure 4.49 – A plot of the integrated intensities of the phases present in the NaH + $2NH_3BH_3$ reaction pathway as deduced from solid state ^{23}Na MAS NMR

4.7 Raman Spectroscopy

4.7.1 $NaNH_2BH_3$

The product of the NaH + NH_3BH_3 reaction, $NaNH_2BH_3$, has C_s symmetry and as such the only symmetry element the molecule possesses is a mirror plane as shown in figure 4.50.

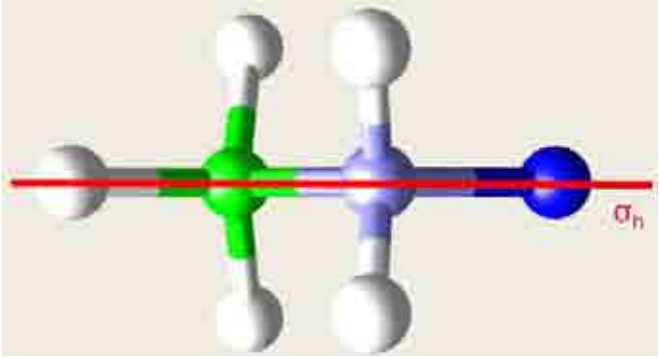

Figure 4.50 – The horizontal mirror plane present in the $NaNH_2BH_3$ molecule, sodium is shown in dark blue, nitrogen in blue, boron in green and hydrogen in white

Using Cartesian displacement vectors for each of the atoms as the basis set it is possible to derive the normal vibrational modes. The reducible representation for this basis set (Γ_{red}) is shown in table 4.9 and the irreducible representation (Γ_{irr}) is given in table 4.10, where translational (Γ_{trans}) and rotational modes (Γ_{rot}) are removed to give the normal vibrational modes (Γ_{3n-6}). The irreducible representation of molecular $NaNH_2BH_3$ is 11A' + 7A'' which is consistent with 3n − 6 = 18 degrees of freedom. The modes that are Raman (Γ_{Raman}) active are shown and assigned vibrational modes.

Table 4.9 – Point group table for C_s

	E	σ_h	Linear, Rotations	Quadratic
A'	1	1	x, y, R_z	x^2, y^2, z^2, xy
A''	1	-1	z, R_x, R_y	yz, xz
Γ_{red}	24	4		

Table 4.10 – Deconvolution of Γ_{irr} for the $NaNH_2BH_3$ molecule of C_s symmetry

	Γ_{irr}	Γ_{trans}	Γ_{rot}	Γ_{vib}	Γ_{Raman}	Assignment
A'	14	2	1	11	11	$\nu_1, \nu_2, \nu_3, \nu_4, \nu_5, \nu_6, \nu_7, \nu_8, \nu_9, \nu_{10}, \nu_{11}$
A''	10	1	2	7	7	$\nu_{12}, \nu_{13}, \nu_{14}, \nu_{15}, \nu_{16}, \nu_{17}, \nu_{18}$

The Raman spectrum of $NaNH_2BH_3$ is shown in figure 4.51. For discussion purposes the Raman spectrum is divided into different regions and compared to that of ammonia borane as shown in figure 4.52. The decreased symmetry of $NaNH_2BH_3$ (C_s) compared to NH_3BH_3 (C_{3v}) is reflected in the increased number of vibrational bands in the spectrum of $NaNH_2BH_3$.

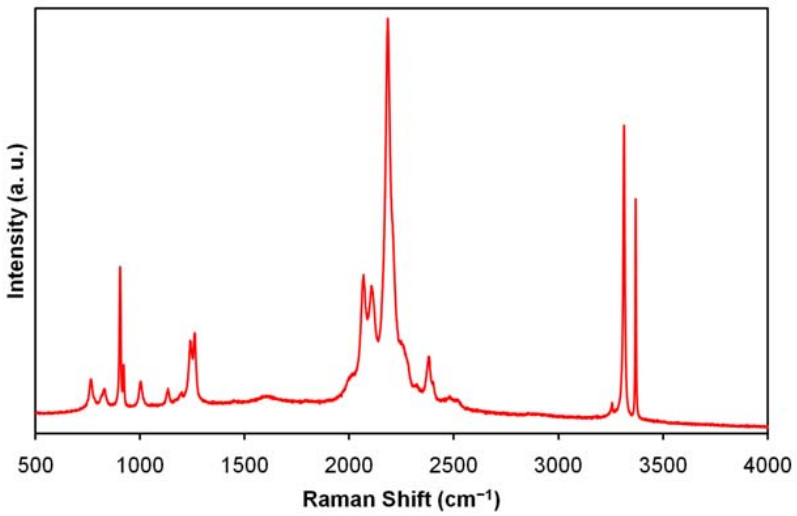

Figure 4.51 – The Raman spectrum of $NaNH_2BH_3$

The reaction of NaH with NH_3BH_3 results in a substitution of a hydrogen associated with the nitrogen by the sodium. Therefore, the most significant changes in the Raman spectrum could reasonably be expected in the N–H stretching and bending regions. Figure 4.52a shows the N–H stretching region and it can be seen that there is a significant difference between the spectra of NH_3BH_3 and $NaNH_2BH_3$. There is a very weak feature observed at 3275 cm^{-1} along with two prominent strong bands at 3369 cm^{-1} and 3313 cm^{-1}, which are assigned to the N–H asymmetric and symmetric stretches, respectively. These vibrational modes are shown in figure 4.53. The final band in the N–H stretching region at 3259 cm^{-1} is assigned to an overtone.

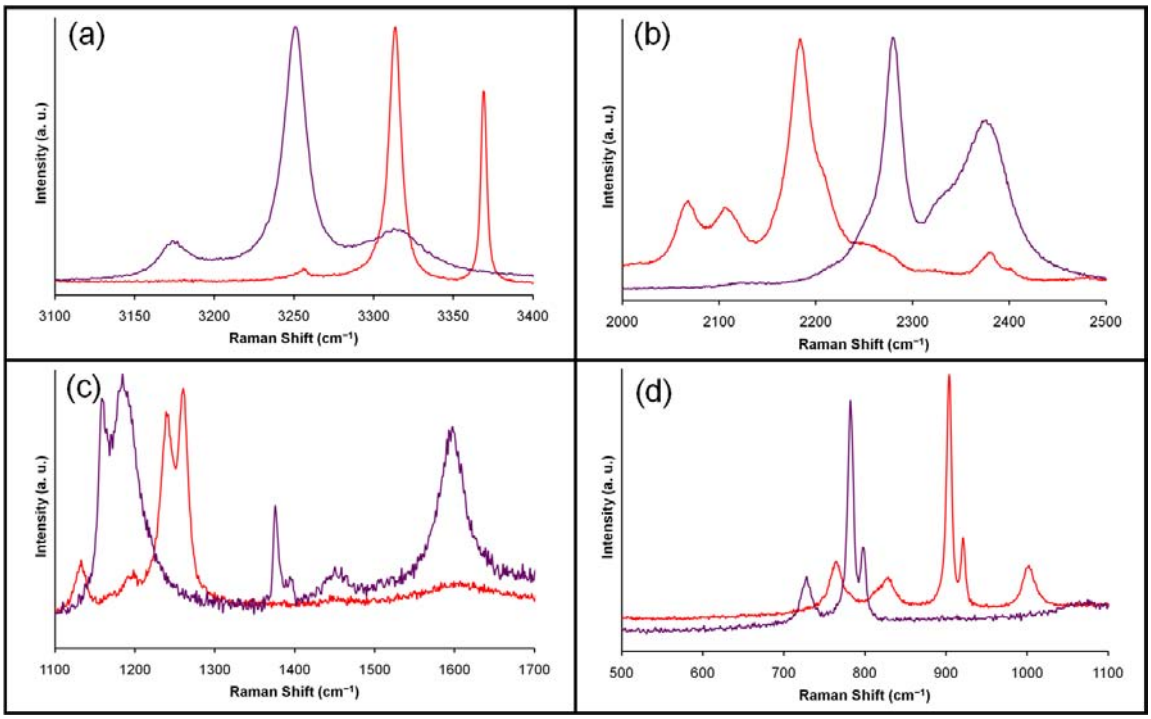

Figure 4.52 – The Raman spectrum of $NaNH_2BH_3$ (red) compared to that of NH_3BH_3 (purple) showing (a) the N–H stretching region, (b) the B–H stretching region, (c) the deformation region and (d) the B–N stretching region

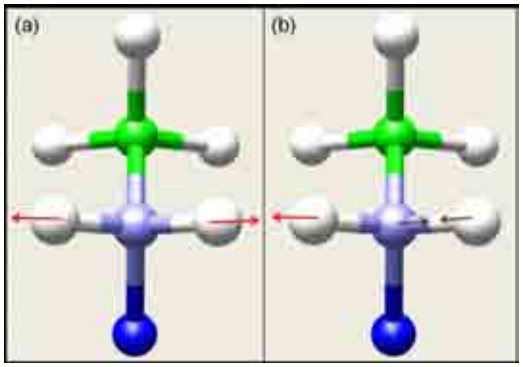

Figure 4.53 – The N–H stretches in the $NaNH_2BH_3$ molecule (a) symmetric stretch (b) asymmetric stretch

The deformation modes of the NH_2 group are limited to the symmetric bend, as an asymmetric bend is not possible. This mode was assigned to the weak band at 1607 cm^{-1} observed in figure 4.52c. A total of three N–H vibrations were observed in the spectrum, which is in agreement with the Raman spectrum of $NaNH_2$.[35]

The ^{11}B-N stretch can be observed at 904 cm^{-1} in figure 4.52d and as with NH_3BH_3 the ^{10}B-N isotopic contribution is also observed at 921 cm^{-1}, the frequency difference of 17 cm^{-1} between the two bands is identical for both molecules. The bands were

significantly blue shifted in $NaNH_2BH_3$ due to the increased electron donating strength of sodium compared to hydrogen, which resulted in a strengthening of the B–N bond, as evidenced in section 4.3.

The B–H stretching region also shows significant differences between NH_3BH_3 and $NaNH_2BH_3$, figure 4.52b, and in fact resembles the B–H stretching region of $NaBH_4$ more closely, figure 4.54. In the crystal structure of $NaBH_4$ the BH_4^- anion occupies a site of ideal symmetry, having point group T_d, figure 4.55. The similarity between the spectra may be explained by considering that the BH_4^- ions rotate around 3-fold axes, effectively becoming BH_3-like, having C_{3v} symmetry. A similar rotation of the BH_3 within $NaNH_2BH_3$ can also lead to this group possessing pseudo C_{3v} symmetry. The dihydrogen bonding present in NH_3BH_3 prevents this rotation and this is reflected in the Raman spectrum.

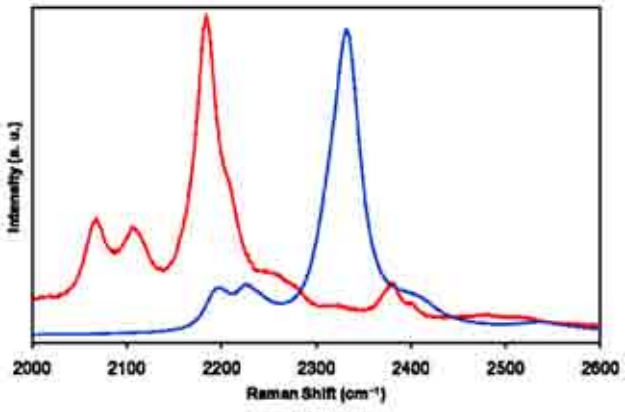

Figure 4.54 – The B–H stretching region of $NaBH_4$ (blue) and $NaNH_2BH_3$ (red)

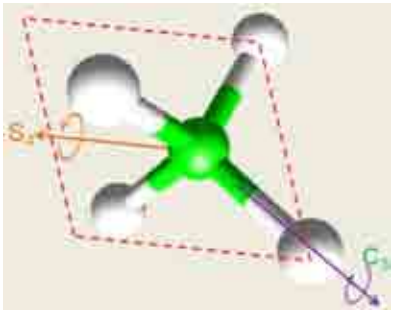

Figure 4.55 – The symmetry of the BH_4^- anion in $NaBH_4$ with the symmetry elements labelled

For the tetrahedral BH_4^- anion it is possible to derive the normal vibrational modes using Cartesian displacement vectors for each of the atoms as the basis set. Table

4.11 shows the reducible representation for this basis set (Γ_{red}) and the irreducible representation (Γ_{irr}) is given in table 4.12, where translational (Γ_{trans}) and rotational modes (Γ_{rot}) are removed to give the normal vibrational modes (Γ_{3n-6}). The irreducible representation of BH_4^- is $A_1 + E + 2T_2$ which is consistent with $3n - 6 = 9$ degrees of freedom. The modes that are Raman (Γ_{Raman}) active are shown and assigned vibrational modes.

Table 4.11 – Point group table for T_d

	E	$8C_3$	$3C_2$	$6S_4$	$6\sigma_d$	Linear, Rotations	Quadratic
A_1	1	1	1	1	1		$x^2 + y^2 + z^2$
A_2	1	1	1	-1	-1		
E	2	-1	2	0	0		$(2z^2 - x^2 - y^2, x^2 - y^2)$
T_1	3	0	-1	1	-1	(R_x, R_y, R_z)	
T_2	3	0	-1	-1	1	(x, y, z)	(xy, xz, yz)
Γ_{red}	15	0	-1	-1	3		

Table 4.12 – Deconvolution of Γ_{irr} for BH_4^- ion of T_d symmetry

	Γ_{irr}	Γ_{trans}	Γ_{rot}	Γ_{vib}	Γ_{Raman}	Assignment
A_1	1	0	0	1	1	ν_1
A_2	0	0	0	0	0	
E	1	0	0	1	1	ν_2
T_1	1	0	1	0	0	
T_2	3	1	0	2	2	ν_3, ν_4

The vibrational modes ν_1 (A_1), ν_2 (E), ν_3 (T_2) and ν_4 (T_2) correspond to the singly degenerate symmetric stretch, the doubly degenerate symmetric bend, the triply

degenerate asymmetric stretch and the triply degenerate asymmetric bend, respectively, as shown in figure 4.56.

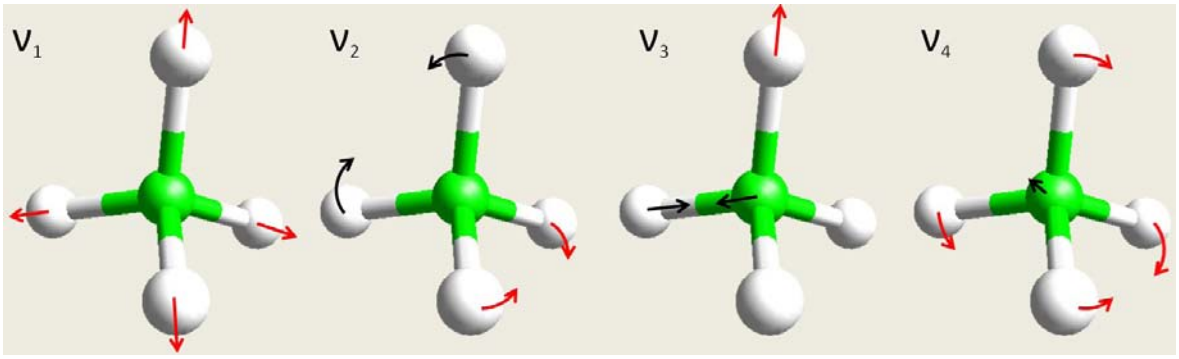

Figure 4.56 – Vibrational modes of the BH_4^- anion in $NaBH_4$

In terms of $NaNH_2BH_3$, the B–H symmetric and asymmetric stretches shown in figure 4.56 are still possible vibrational modes. However, the ν_2 symmetric bend which involves two pairs of H atoms moving towards each other and the ν_4 asymmetric bend where one pair of H atoms move towards each other and the other pair of H atoms away from each other will not be possible when a hydrogen atom is replaced by the [$NaNH_2$] group in $NaNH_2BH_3$. This change in environment results in a reversal of the assignment of these vibrational modes. The BH_4 to BH_3 change means that the ν_2 symmetric bend now resembles the ν_{10} asymmetric bend of the BH_3 group of ammonia borane and the ν_4 asymmetric bend becomes similar to the ν_3 symmetric bend of the same group, see figures 3.6 and 3.7 in chapter 3.5. Therefore, it may be expected that the B–H stretching region of $NaNH_2BH_3$ will resemble that of $NaBH_4$, whereas the B–H deformation bands may resemble those of NH_3BH_3.

The B–H deformation modes of NH_3BH_3 are shown in figure 4.52c. Two bands of similar appearance are observed at slightly higher energy in the $NaNH_2BH_3$ spectrum and it is therefore reasonable to assign these two bands as the B–H symmetric (scissors) and asymmetric (umbrella) deformations at 1241 cm^{-1} and 1262 cm^{-1}, respectively. There are two bands at approximately twice the wavenumber of these two bands, 2486 and 2523 cm^{-1}, and so they are assigned as overtones of these deformation modes.

The Raman spectrum of $NaBH_4$ has been fully assigned by Renaudin *et al*.[36] Using these literature assignments the bands in the B–H stretching region can be assigned. In $NaBH_4$ the asymmetric bend is observed as a shoulder of the symmetric stretch band at lower wavenumber, however, for $NaNH_2BH_3$ this shoulder occurs at a higher wavenumber. Asymmetric stretches are observed at higher wavenumbers, so this shoulder is assigned to the asymmetric B–H stretch and the most intense band at 2185 cm^{-1} is assigned to the symmetric B–H stretch. There are number of other bands in the B–H stretching region which have not been assigned to any vibration. These bands may arise because the BH_3 group in $NaNH_2BH_3$ does not adopt an ideal tetrahedral arrangement and could theoretically adopt the symmetry of the $NaNH_2BH_3$ molecule as a whole, C_s. The effect of reducing the ideal tetrahedral symmetry can be seen by constructing a symmetry correlation table, table 4.13, and the corresponding correlation diagram, figure 4.57.

Table 4.13. – Correlation table for T_d and C_s point groups

C_s	E				σ	
A'	1				1	
A''	1				-1	
T_d	**E**	**$8C_3$**	**$3C_2$**	**$6S_4$**	**$6\sigma_d$**	**Species of C_s**
A_1	1	1	1	1	1	**A'**
A_2	1	1	1	-1	-1	**A''**
E	2	-1	2	0	0	**A' + A''**
T_1	3	0	-1	1	-1	**A' + 2A''**
T_2	3	0	-1	-1	1	**2A' + A''**

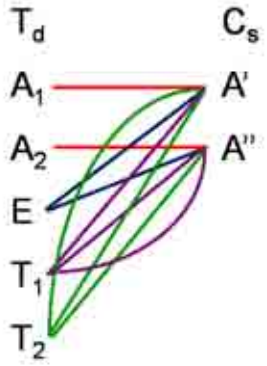

Figure 4.57 – Correlation diagram for T_d and C_s symmetries

Figure 4.57 shows that the ν_1 (A_1) symmetric stretch remains (A'), the doubly degenerate ν_2 (E) symmetric bend splits to A' and A'' and the two triply degenerate ν_3 and ν_4 (T_2) vibrations split to 2A' + A'' modes. Therefore, it could be expected that some of the vibrational modes split so that more vibrations are observed in the Raman spectrum. The bands observed at 2071 cm^{-1} and 2112 cm^{-1} and 2384 cm^{-1} with a shoulder at 2403 cm^{-1} could be related to these band splittings. The complete assignment of the bands observed in the Raman spectrum of $NaNH_2BH_3$ is shown in figure 4.58.

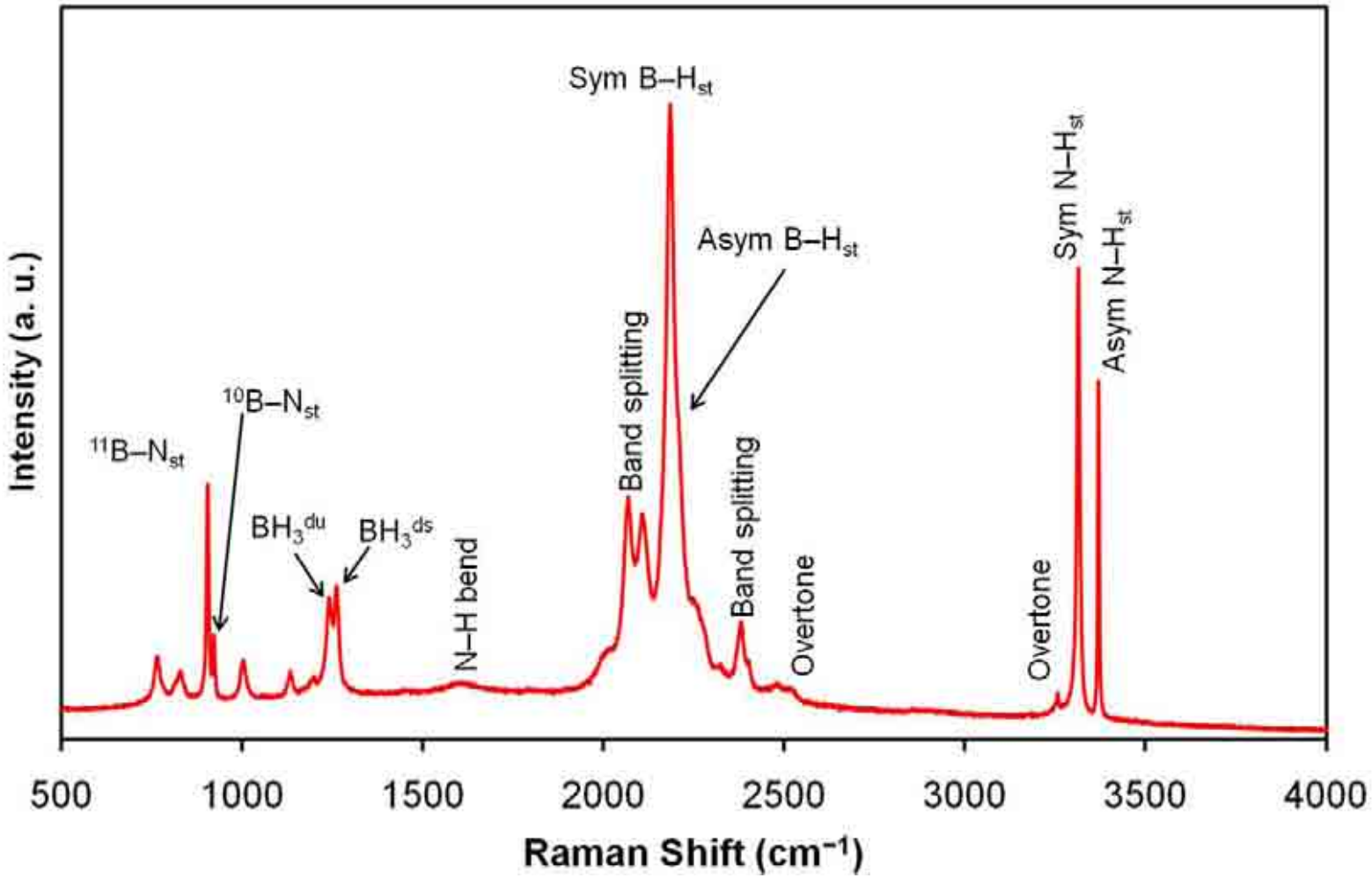

Figure 4.58 – The Raman spectrum of $NaNH_2BH_3$ with the proposed assignment of the observed bands, du = umbrella deformation, ds = scissors deformation

4.7.2 $Na^+[BH_3NH_2BH_3]^-$

The Raman spectrum collected from the product of the NaH + $2NH_3BH_3$ reaction at 60°C is shown in figure 4.59.

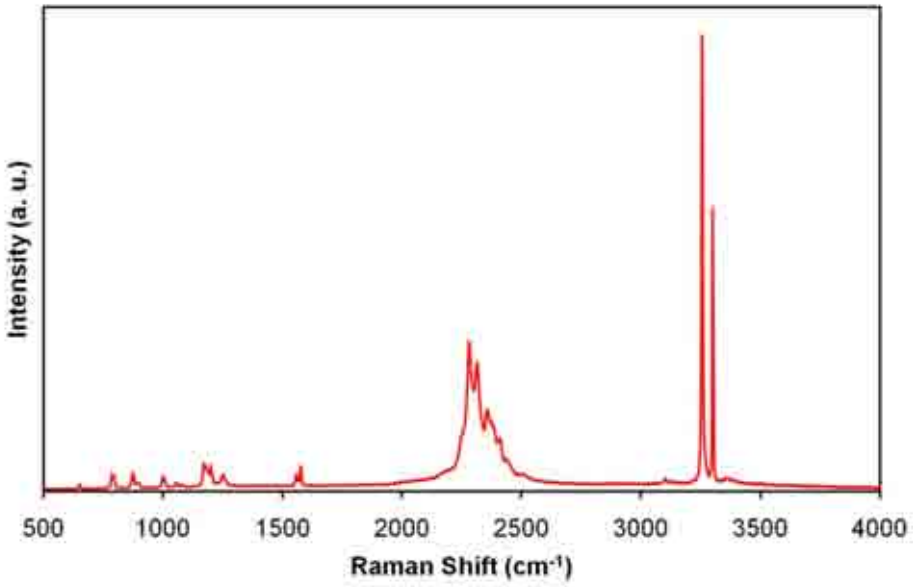

Figure 4.59 – The Raman spectrum collected from the product of the NaH + $2NH_3BH_3$ reaction at 60°C, $Na^+[BH_3NH_2BH_3]^-$

The N–H stretching region of the spectrum is shown in figure 4.60. Only two peaks were observed, at 3255 cm^{-1} and 3300 cm^{-1}, and therefore they can be simply assigned as the N−H symmetric and asymmetric stretches, respectively. This offers confirmation that the product contains an NH_2 group.

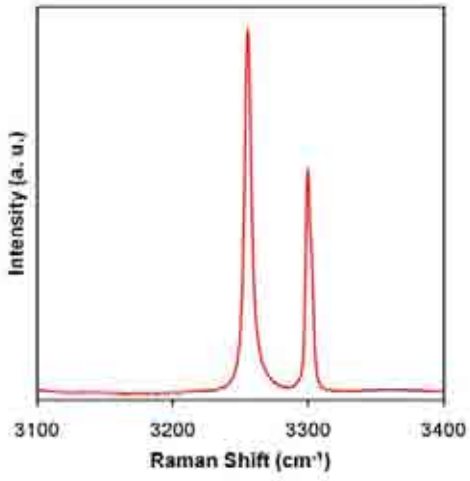

Figure 4.60 – The N–H stretching region of the Raman spectrum collected from the product of the NaH + $2NH_3BH_3$ reaction at 60°C

The B–H stretching region, figure 4.61 of the product was more complicated than the N–H stretching region with a number of features observed. Bands were observed at 2249, 2282, 2314, 2358, 2382, 2411, 2440 and 2508 cm^{-1}.

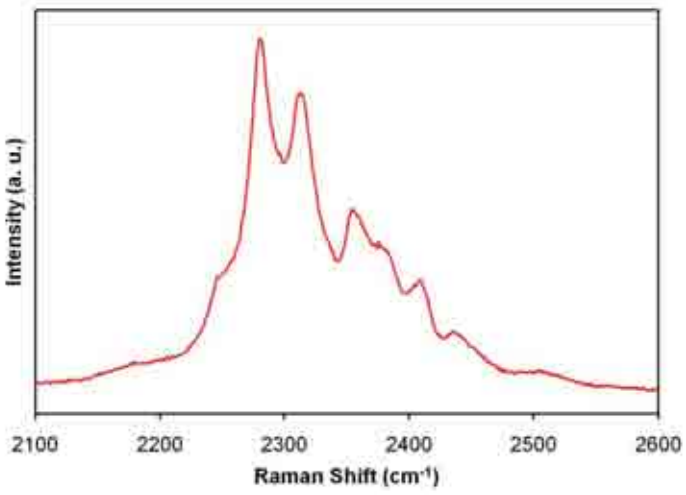

Figure 4.61 – The B–H stretching region of the Raman spectrum collected from the product of the NaH + $2NH_3BH_3$ reaction at 60°C

As the $Na^+[BH_3NH_2BH_3]^-$ molecule possesses BH_3 a comparison with the Raman spectrum of NH_3BH_3 can again help to identify some of the modes, figure 4.62. It can be seen that there was a good correlation between the B–H symmetric stretch of NH_3BH_3 at 2280 cm^{-1} and the most intense peak of the spectrum of $Na^+[BH_3NH_2BH_3]^-$ at 2282 cm^{-1} in terms of the Raman shift, shape and relative intensity of these peaks. Therefore the band at 2282 cm^{-1} was assigned to a B–H symmetric stretch. The asymmetric B–H stretch of NH_3BH_3 was observed at 2330 cm^{-1}, on the shoulder of another feature at 2377 cm^{-1} in the spectrum of NH_3BH_3. The increased number of bands observed in the spectrum of $Na^+[BH_3NH_2BH_3]^-$ compared to NH_3BH_3 meant that it was not possible to observe the asymmetric stretch, but the observation of a band at 2382 cm^{-1} implied that this stretch was still present. The separation between these B–H symmetric and asymmetric stretches was 100 cm^{-1}. It can be seen from figure 4.61 that there were two other bands in the spectrum with a separation of ~100 cm^{-1}, which also had similar shapes and relative intensities to those observed at 2282 and 2382 cm^{-1}. By manually shifting the NH_3BH_3 B–H symmetric stretch to a Raman shift of 2314 cm^{-1} this correlation can be better observed, figure 4.62. The two bands at 2314 and 2411 cm^{-1} correlate well

with these shifted stretches, implying that they were also related to B–H symmetric and asymmetric stretches, respectively. The B–H stretching region of the spectrum therefore supported the presence of two BH_3 groups within the product of the NaH + $2NH_3BH_3$ reaction. There were a number of other bands present in this region of the spectrum, the most intense of which was observed at 2358 cm^{-1}. This band and the low intensity bands may be related to side reactions.

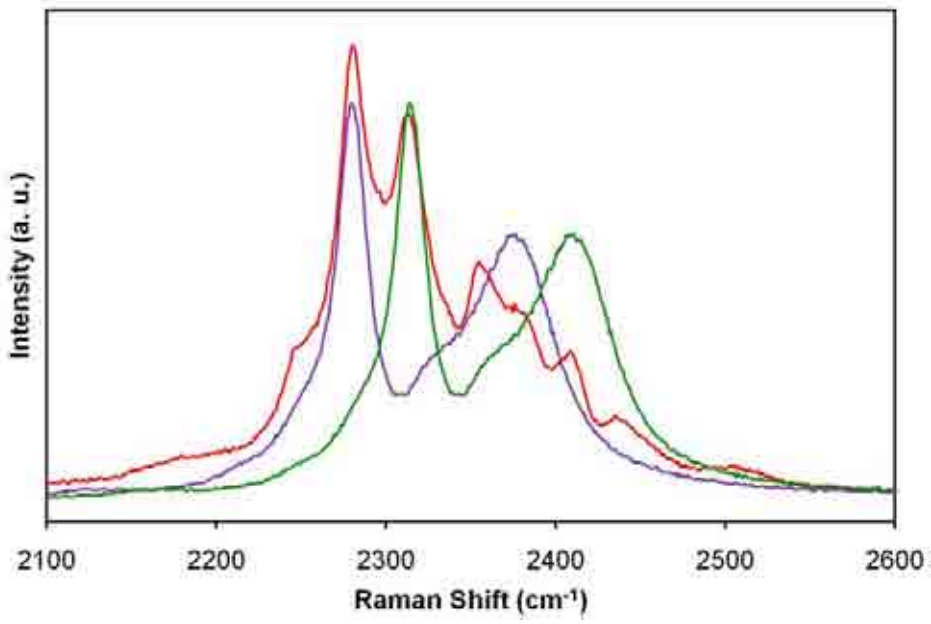

Figure 4.62 – The B–H stretching regions of the Raman spectrum collected of the product of the NaH + $2NH_3BH_3$ reaction at 60°C (red) and NH_3BH_3 (purple) and the spectrum of NH_3BH_3 blue shifted by 34 cm^{-1} (green)

The region of the Raman spectrum where BH_3 and NH_3 deformation modes as well as B–N stretches are expected to be observed is shown in figure 4.63. The Raman spectrum of NH_3BH_3, also shown in figure 4.63, was used as a basis for the assignment of modes in this region. The B–N stretch was observed at 870 cm^{-1} and again the ^{10}B contribution to this stretch was present at 894 cm^{-1}, confirming the continued presence of a B–N bond in the reaction product. The B–N stretch was blue shifted compared to its position in NH_3BH_3, but red shifted compared to $NaNH_2BH_3$. This showed that the $Na^+[BH_3NH_2BH_3]^-$ B–N bond was stronger than in NH_3BH_3 but weaker than in $NaNH_2BH_3$, which showed that electron donation from the Na was sufficient to increase the bond strength but to a lesser extent than in $NaNH_2BH_3$, where an Na–N bond was present. The BH_3 deformation modes were observed at

1169 and 1198 cm^{-1}, while the NH_3 deformation mode was assigned to the band at 1575 cm^{-1}. Rocking motions of the H atoms associated with the BH_3 groups would also be expected to produce two bands in the spectrum, with these vibrations assigned to the bands observed at 652 and 1001 cm^{-1}. The number of bands observed in this region of the spectrum was greater than that of the spectrum of NH_3BH_3, with the increased number of bands due to two different BH_3 groups present.

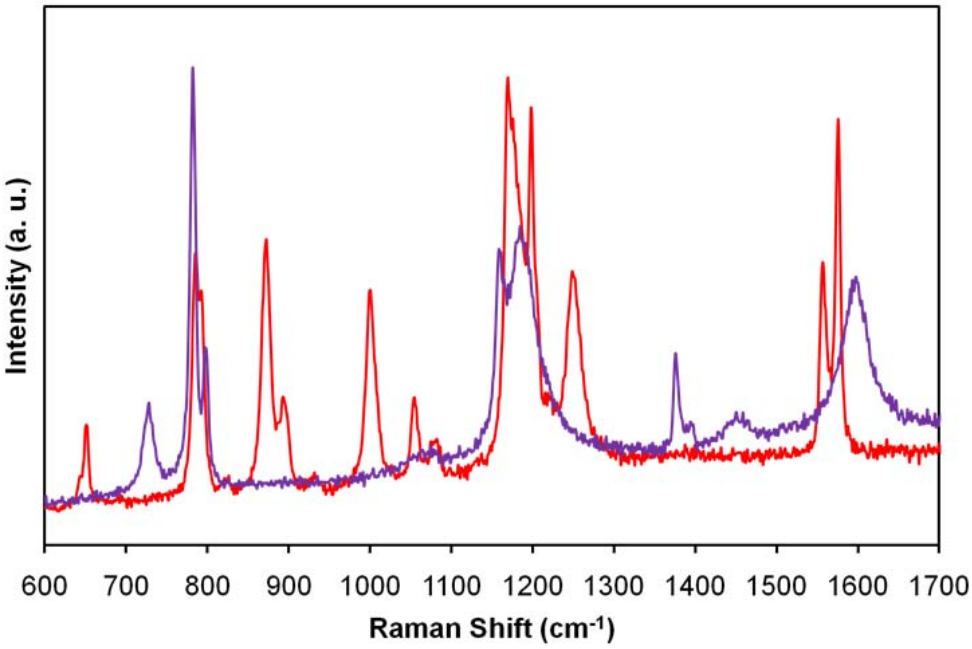

Figure 4.63 – The NH_3 deformation, BH_3 deformation and B–N stretching region of the Raman spectrum collected from the product of the NaH + $2NH_3BH_3$ reaction at 60°C (red) and NH_3BH_3 (purple)

4.8 Overall Discussion and Conclusion

4.8.1 The NaH + NH_3BH_3 Reaction Pathway

The first step in the reaction pathway was the solid state reaction of 1 mole of NaH with 1 mole of NH_3BH_3 to yield the previously reported $NaNH_2BH_3$, reaction 4.32.[5]

$$NaH + NH_3BH_3 \rightarrow NaNH_2BH_3 + H_2 \qquad \text{Reaction 4.32}$$

This reaction could be effected at a temperature as low as 40°C, although gaseous thermal desorption data showed that the reaction began at temperatures lower than this. The reaction product was confirmed through powder XRD and solid state ^{11}B MAS NMR spectroscopy. TPD-MS data showed that the only gas released during the synthesis of this phase was H_2. A key feature of this reaction was likely to have been the high affinity for a protic hydrogen atom in the NH_3 group of NH_3BH_3 to combine with the negatively charged hydrogen present in NaH forming H_2. The resultant $NH_2BH_3^-$ anion and Na^+ cation would have subsequently combined to form the $NaNH_2BH_3$ product.

As shown by powder XRD, $NaNH_2BH_3$ initially decomposed to an amorphous material. Thermal desorption studies revealed the exclusive release of H_2 and solid state ^{11}B NMR showed two dominant boron environments, with both sp^2 and sp^3 (NBH_3) hybridised boron present, as well as a small amount of BH_4^-. Thermogravimetric data showed that this decomposition step was accompanied by the release of one equivalent of H_2. A key property of $NaNH_2BH_3$ in terms of hydrogen storage is the presence of both hydridic and protic hydrogens due to the different electronegativities of boron and nitrogen. This is similar to amide borohydride materials, where H_2 release is enhanced through the combination of $H^{\delta+}$ and $H^{\delta-}$.[1] For NH_3BH_3, the overall loss of H_2 can be written:

$$nNH_3BH_3 \rightarrow (NH_2BH_2)_n + nH_2 \qquad \text{Reaction 4.33}$$

However, it is well established that the mechanism of H_2 loss involves DADB. The appearance of a resonance due to BH_4^- in the solid state ^{11}B MAS NMR spectrum of decomposed $NaNH_2BH_3$, figures 4.33 and 4.34, suggests that a similar mechanism

may have taken place during $NaNH_2BH_3$ decomposition with two $NaNH_2BH_3$ molecules reacting to form a DADB like molecule, reaction 4.34. If this species had then reacted further with other $NaNH_2BH_3$ molecules, similar to the growth step in NH_3BH_3 decomposition, H_2 would have been released and a polymeric species formed, reaction 4.35.

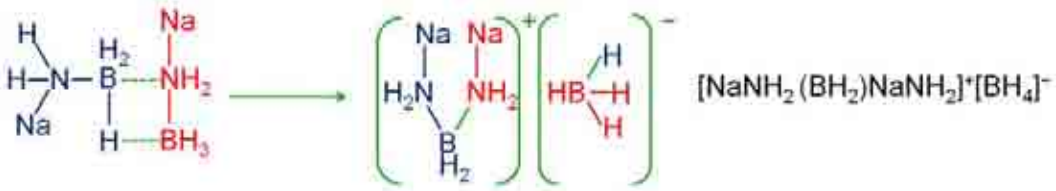

Reaction 4.34

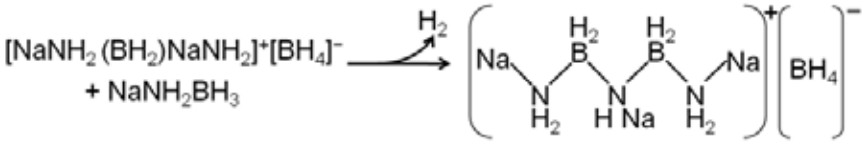

Reaction 4.35

Reaction 4.34 yields a polymeric species, implying the product would likely have been amorphous, in agreement with the XRD result. However, neither of the proposed reactions form products that possess sp^2 boron and both possess N_2BH_2 environments, which disagrees with ^{11}B NMR results. Therefore, if either reaction is involved in the decomposition pathway the N_2BH_2 environments must be short lived. However, further H_2 loss from these species below 60°C would not agree with the thermal desorption studies. This suggests that the initial decomposition product was not in fact polymeric. H_2 loss from $[NaNH_2(BH_2)NaNH_2]^+[BH_4]^-$ may have occurred intramolecularly through the combination of oppositely charged H atoms, reaction 4.36. A competing reaction to this may also have been possible, with H_2 lost intramolecularly from a single $NaNH_2BH_3$ molecule, reaction 4.37. These competing reactions yield products consistent with the ^{11}B NMR study. The low intensity of the BH_4^- feature after reaction at 60°C, figure 4.33, suggests reaction 4.37 may have been initially responsible for H_2 loss.

$$[NaNH_2(BH_2)NaNH_2]^+[BH_4]^- \rightarrow [NaNH{=}BHNH_2Na]^+[BH_4]^- + H_2 \qquad \text{Reaction 4.36}$$

$$NaNH_2BH_3 \rightarrow Na^+NH{=}BH_2^- + H_2 \qquad \text{Reaction 4.37}$$

At 200°C, the decomposition products included NaH and amorphous material containing two sp^2 boron environments and BH_4^-. TGA study of $NaNH_2BH_3$ showed this step released less than one equivalent of H_2. Again competing reactions may have taken place. The products of reactions 4.36 and 4.37 had the potential to further release H_2. $[NaNH{=}BHNH_2Na]^+[BH_4]^-$ could have reacted with $NaNH_2BH_3$ molecules, reaction 4.38, or $Na^+NH{=}BH_2^-$ may have polymerised, reaction 4.39.

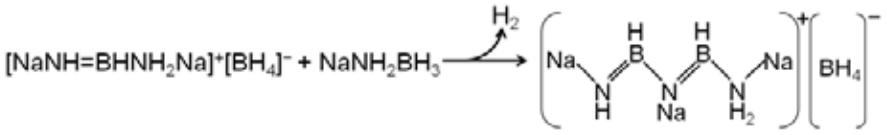

Reaction 4.38

$$nNa^+NH{=}BH_2^- \rightarrow (NaNBH)_n + nH_2 \qquad \text{Reaction 4.39}$$

Both of these products agree at least in part with the ^{11}B NMR data, however, neither account for the appearance of NaH in the XRD pattern. The reactions were assumed to proceed through the combination of oppositely charged hydrogens. However, a second possibility would have been for the Na, also possessing a positive charge, to have combined with a negatively charged H atom, forming NaH as follows. This competition between H_2 release and NaH formation could explain why H_2 release was observed above 200°C in thermal desorption studies, but the amount released was less than one equivalent.

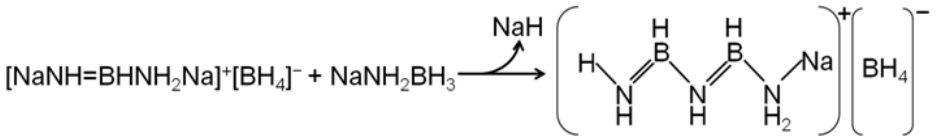

Reaction 4.40

$$nNa^+NH{=}BH_2^- \rightarrow (NHBH)_n + nNaH \qquad \text{Reaction 4.41}$$

The results of solid state ^{11}B and ^{23}Na MAS NMR suggested that the dominant decomposition product was free from sodium, while a side reaction yielded a product containing sodium, therefore suggesting that reactions 4.40 and 4.41 were the dominant decomposition pathways. The fact that there are competing reaction pathways in the first step of $NaNH_2BH_3$ decomposition as well as further competition between H_2 and NaH expulsion within each pathway highlights the complex nature of

this decomposition. The dominant NaH + NH_3BH_3 reaction pathway is concluded to have proceeded according to the overall reaction 4.42.

$$nNaH + nNH_3BH_3 \rightarrow nNaNH_2BH_3 + nH_2\uparrow \rightarrow (NHBH)_n + nNaH + nH_2\uparrow \quad \text{Reaction 4.42}$$

4.8.2 The NaH + $2NH_3BH_3$ Reaction Pathway

The first step in the 1:2 pathway was identical to that observed in the 1:1 pathway, the reaction of NaH with NH_3BH_3 forming $NaNH_2BH_3$ and releasing H_2. Thermal desorption data showed that the subsequent reaction pathway step involved the desorption of NH_3, yielding a previously unreported crystalline phase. This crystalline phase was indexed to a trigonal unit cell with *a* = 4.3389(4) Å and *c* = 17.859(1) Å and a unit cell volume of 291.16(5) $Å^3$. The composition of this trigonal phase was proposed to be $Na^+[BH_3NH_2BH_3]^-$ and support for this assignment was provided by solid state ^{11}B MAS NMR and Raman spectroscopy. Two pathways may have led to the formation of this product: either an intermolecular rearrangement reaction, reaction 4.43, or an S_N2 reaction, reaction 4.44.

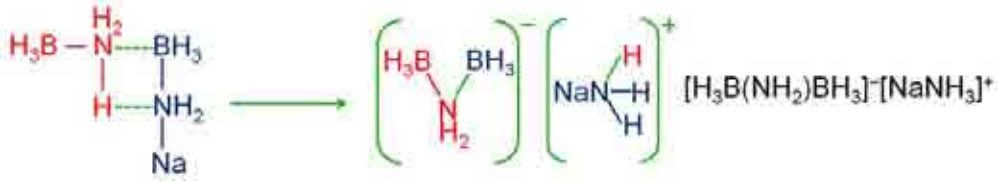

Reaction 4.43

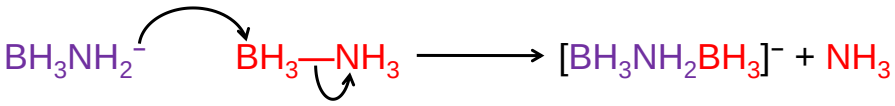

Reaction 4.44

There are only two reports of $Na^+[BH_3NH_2BH_3]^-$ in the literature. It was first hypothesised as early as 1938 by Schaeffer *et al.*[37] as a product of the reaction of DADB with Na in NH_3, reaction 4.45. However, this was based on the incorrect structure of DADB ($[NH_4]^+[BH_3NH_2BH_3]^-$) previously proposed by Schlesinger and Burg.[38] Shore *et al.*[39] later showed that the products of the reaction of Na with DADB were in fact $NaBH_4$ and $(NH_2BH_2)_n$, reaction 4.46.

$$Na + [NH_4]^+[BH_3NH_2BH_3]^- \rightarrow [Na]^+[BH_3NH_2BH_3]^- + NH_3 + \tfrac{1}{2}H_2 \quad \text{Reaction 4.45}$$

$$nNa + n[NH_3BH_2NH_3]^+[BH_4]^- \rightarrow nNaBH_4 + (NH_2BH_2)_n + nNH_3 + \tfrac{1}{2}nH_2 \quad \text{Reaction 4.46}$$

A recent study by Daly *et al.*[40] reported the compound $Na^+[BH_3NH_2BH_3]^-$. The reaction of NH_3BH_3 with excess Na in THF at room temperature synthesised $NaNH_2BH_3$, but when heated at reflux $Na^+[BH_3NH_2BH_3]^-$ formed along with a white by-product that precipitated from the solution. The reaction of $NaNH_2$ with NH_3BH_3 in a 1:2 molar ratio in refluxing THF was also shown to form this compound; however, in both cases THF could not be completely removed and so the authors were unable to obtain crystals of sufficient quality to study by XRD.

Decomposition of $Na^+[BH_3NH_2BH_3]^-$ led to the formation of $NaBH_4$, as well as an amorphous material, and was accompanied by H_2 release. Solid state ^{11}B MAS NMR results showed that the amorphous phase was primarily constituted of sp^2 boron in an NBH_2 environment. Further to this, solid state ^{23}Na MAS NMR investigations showed that no sodium was present in the amorphous materials. $NaBH_4$ formation may have taken place through an intermolecular rearrangement reaction, reaction 4.47, expelling Na^+, which along with the BH_4^- also produced would have crystallised as $NaBH_4$. As with the growth step of NH_3BH_3 decomposition, this rearrangement would be a chain growth mechanism, leading to a polymeric decomposition product. $Na^+[BH_3NH_2BH_3]^-$ decomposition occurred above 120°C, at which temperature $(NH_2BH_2)_n$ decomposes through H_2 release and therefore the polymer formed in this reaction would have been susceptible to H_2 release, ultimately yielding $(NHBH)_n$.

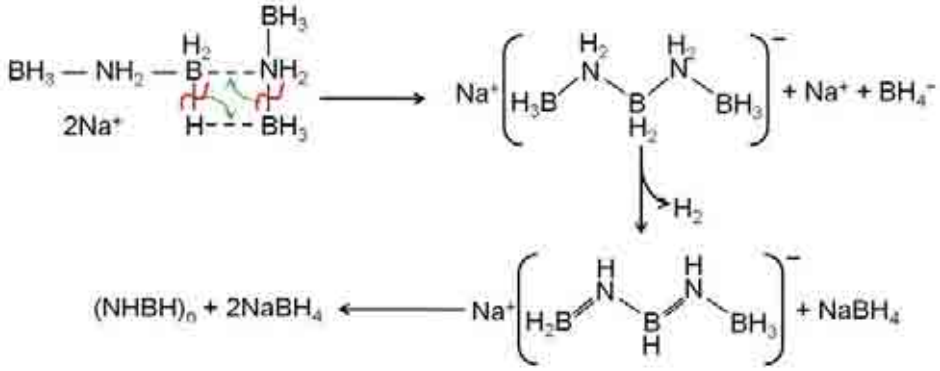

Reaction 4.47

The NaH + $2NH_3BH_3$ reaction pathway is concluded to have proceeded by the overall reaction 4.48.

$$NaH + 2NH_3BH_3 \rightarrow NaNH_2BH_3 + NH_3BH_3 + H_2\uparrow \rightarrow Na^+[BH_3NH_2BH_3]^- + NH_3\uparrow \rightarrow NaBH_4 + (NHBH)_n + H_2\uparrow$$

Reaction 4.48

4.8.3 Potential as Hydrogen Storage Materials

The lower onset temperature of H_2 release from $NaNH_2BH_3$ (70°C) compared to $Na^+[BH_3NH_2BH_3]^-$ (100°C) suggests $NaNH_2BH_3$ has more potential as a hydrogen storage material. However, $NaNH_2BH_3$ has a lower hydrogen content (9.5 wt%) than $Na^+[BH_3NH_2BH_3]^-$ (12.5 wt%). Thermogravimetric studies also showed that upon heating to 350°C $Na^+[BH_3NH_2BH_3]^-$ showed the higher weight loss of 7.5 wt% compared to 5.25 wt% from $NaNH_2BH_3$, with both weight losses due to H_2 only. The use of $Na^+[BH_3NH_2BH_3]^-$ is, however, complicated by the desorption of NH_3 during its synthesis from $NaNH_2BH_3$ and NH_3BH_3.

A key advantage of $NaNH_2BH_3$ is the presence of oppositely charged hydrogens which aids the desorption of H_2 from the material. These oppositely charged hydrogens are also present in $Na^+[BH_3NH_2BH_3]^-$. As shown in reaction 4.47 these opposite charges were not involved in the initial decomposition step of $Na^+[BH_3NH_2BH_3]^-$ but following the formation of polymeric material, H_2 release would have been promoted due to their presence.

As with the parent material NH_3BH_3, both materials show initial sharp desorptions of H_2. Following this initial release, the broad desorption of H_2 observed for NH_3BH_3 is avoided. Despite this, the ultimate decomposition products of both $NaNH_2BH_3$ and $Na^+[BH_3NH_2BH_3]^-$ involve the formation of $(NHBH)_n$, an amorphous polymer, also a decomposition product of NH_3BH_3. Therefore, for all three materials the reversibility of the system is significantly hampered by the rehydriding of $(NHBH)_n$. Furthermore, the crystalline decomposition products of $NaNH_2BH_3$ and $Na^+[BH_3NH_2BH_3]^-$ are NaH and $NaBH_4$, respectively. Clearly, these materials cannot be rehydrogenated individually. In fact the only material that offers the potential for recycling individually is $(NHBH)_n$. Therefore following the initial dehydrogenation and rehydrogenation cycle, $NaNH_2BH_3$, $Na^+[BH_3NH_2BH_3]^-$ and NH_3BH_3 would all lead to NH_3BH_3 being regenerated, eliminating the initial advantages that the $NaNH_2BH_3$ and $Na^+[BH_3NH_2BH_3]^-$ storage systems held over their parent material. In the case of $NaNH_2BH_3$ this may be avoided if the decomposition pathway leading to $(NaNBH)_n$ formation can be promoted, giving the potential for $NaNH_2BH_3$ to be regenerated. This is not a possibility with $Na^+[BH_3NH_2BH_3]^-$ as all of the Na in the decomposition

products is found in the form of $NaBH_4$. However, this does not rule out the possibility of these materials being able to react with other dehydrogenation products in the presence of H_2. As has been shown NaH reacts with NH_3BH_3 and so there may be potential for NaH or $NaBH_4$ to react with the amorphous decomposition products, yielding sodium containing products, which could offer the storage system a recyclable pathway.

4.9 References

1. Chater, P. A.; Anderson, P. A.; Prendergast, J. W.; Walton, A.; Mann, V. S. J.; Book, D.; David, W. I. F.; Johnson, S. R.; Edwards, P. P., Synthesis and characterisation of amide-borohydrides: New complex light hydrides for potential hydrogen storage. *Journal of Alloys and Compounds* **2007,** 446–447, 350–354.

2. Autrey, T.; Luedtke, A., Hydrogen release studies of alkali metal amidoboranes. *Inorganic Chemistry* **2010,** 49, 3905–3910.

3. Xiong, Z.; Wu, G.; Chua, Y. S.; Hu, J.; He, T.; Xu, W.; Chen, P., Synthesis of sodium amidoborane ($NaNH_2BH_3$) for hydrogen production. *Energy and Environmental Science* **2008,** 1, 360–363.

4. Fijalkowski, K. J.; Grochala, W., Substantial emission of NH_3 during thermal decomposition of sodium amidoborane, $NaNH_2BH_3$. *Journal of Materials Chemistry* **2009,** 19, 2043-2050.

5. Xiong, Z.; Yong, C. K.; Wu, G.; Chen, P.; Shaw, W. J.; Karkamkar, A.; Autrey, T.; Jones, M. O.; Johnson, S. R.; Edwards, P. P.; David, W. I. F., High-capacity hydrogen storage in lithium and sodium amidoboranes. *Nature Materials* **2008,** 7, 138–141.

6. Zuttel, A.; Wenger, P.; Rentsch, S.; Sudan, P.; Mauron, P.; Emmenegger, C., $LiBH_4$ a new hydrogen storage material. *Journal of Power Sources* **2003,** 118, 1-7.

7. Orimo, S.; Nakamori, Y.; Züttel, A., Material properties of MBH_4 (M = Li, Na and K). *Materials Science and Engineering* **2004,** B108, 51–53.

8. Mao, J. F.; Yu, X. B.; Guo, Z. P.; Poh, C. K.; Liu, H. K.; Wu, Z.; Ni, J., Improvement of the $LiAlH_4$-$NaBH_4$ system for reversible hydrogen storage. *Journal Of Physical Chemistry C* **2009,** 113, 10813–10818.

9. Mao, J. F.; Yu, X. B.; Guo, Z. P.; Liu, H. K.; Wu, Z.; Ni, J., Enhanced hydrogen storage performances of $NaBH_4$–MgH_2 system. *Journal of Alloys and Compounds* **2009,** 479, 619–623.

10. Burrell, A. K., Los Alamos National Laboratory. *Personal Communication*.

11. Coelho, A. A. *Topas, General Profile and Structure Analysis Software for Powder Diffraction Data*, Bruker AXS, Karlsruhe, Germany, 3rd edition: 2004.

12. Stephens, P. W., Phenomenological model of anisotropic peak broadening in powder diffraction. *Journal of Applied Crystallography* **1999,** 32, 281–289.

13. Filinchuk, Y.; Hagemann, H., Structure and properties of $NaBH_4.2H_2O$ and $NaBH_4$. *European Journal of Inorganic Chemistry* **2008,** 20, 3127-3133.

14. Wu, H.; Zhou, W.; Yildirim, T., Alkali and alkaline-earth metal amidoboranes: Structure, crystal chemistry, and hydrogen storage properties. *Journal of the American Chemical Society* **2008,** 130, 14834–14839.

15. Bowden, M. E.; Gainsford, G. J.; Robinson, W. T., The room temperature structure of ammonia borane. *Australian Journal of Chemistry* **2007,** 60, 149–153.

16. Shull, C. G.; Wollan, E. O.; Morton, G. A.; Davidson, W. L., Neutron diffraction studies of NaH and NaD. *Physical Review* **1948,** 73, 842–847.

17. Nagib, M.; Kistrup, H.; Jacobs, H., Neutron diffraction by sodium-deuteroamide, $NaND_2$. *Atomkernenergie* **1975,** 26, 87–90.

18. Bowden, M. E.; Autrey, T.; Brown, I.; Ryan, M., The thermal decomposition of ammonia borane: A potential hydrogen storage material. *Current Applied Physics* **2008,** 8, 498–500.

19. Stowe, A. C.; Shaw, W. J.; Linehan, J. C.; Schmid, B.; Autrey, T., *In situ* solid state ^{11}B MAS-NMR studies of the thermal decomposition of ammonia borane: mechanistic studies of the hydrogen release pathways from a solid state hydrogen storage material. *Physical Chemistry Chemical Physics* **2007,** 9, 1831–1836.

20. Mayer, E., Symmetrical cleavage of diborane by ammonia in solution. *Inorganic Chemistry* **1972,** 11, 866–869.

21. Bluhm, M. E.; Bradley, M. G.; Butterick III, R.; Kusari, U.; Sneddon, L. G., Amineborane-based chemical hydrogen storage: Enhanced ammonia borane dehydrogenation in ionic liquids. *Journal of the American Chemical Society* **2006,** 128, 7748–7749.

22. Miller, A. J. M.; Bercaw, J. E., Dehydrogenation of amine–boranes with a frustrated Lewis pair. *Chemical Communications* **2010,** 46, 1709–1711.

23. Gervais, C.; Babonneau, F., High resolution solid state NMR investigation of various boron nitride preceramic polymers. *Journal of Organometallic Chemistry* **2002,** 657, 75–82.

24. Gervais, C.; Framery, E.; Duriez, C.; Maquet, J.; Vaultier, M.; Babonneau, F., ^{11}B and ^{15}N solid state NMR investigation of a boron nitride preceramic polymer prepared by ammonolysis of borazine. *Journal of the European Ceramic Society* **2005,** 25, 129–135.

25. Hwang, S.-J.; Bowman Jr, R. C.; Reiter, J. W.; Rijssenbeek, J.; Soloveichik, G. L.; Zhao, J.-C.; Kabbour, H.; Ahn, C. C., NMR confirmation for formation of $[B_{12}H_{12}]^{2-}$ complexes during hydrogen desorption from metal borohydrides. *The Journal of Physical Chemistry C* **2008,** 112, 3164–3169.

26. Marchetti, P. S.; Kwon, D.; Schmidt, W. R.; Interrante, L. V.; Maciel, G. E., High-field ^{11}B Magic-Angle Spinning NMR characterization of boron nitrides. *Chemistry of Materials* **1991,** 3, 482–486.

27. Gervais, C.; Maquet, J.; Babonneau, F.; Duriez, C.; Framery, E.; Vaultier, M.; Florian, P.; Massiot, D., Chemically derived BN ceramics: Extensive ^{11}B and ^{15}N solid-state NMR study of a preceramic polyborazilene. *Chemistry of Materials* **2001,** 13, 1700–1707.

28. Jeschke, G.; Hoffbauer, W.; Jansen, M., A comprehensive NMR study of cubic and hexagonal boron nitride. *Solid State Nuclear Magnetic Resonance* **1998,** 12, 1–7.

29. Kim, D.; Moon, K.; Kho, J.; Economy, J.; Gervais, C.; Babonneau, F., Synthesis and characterization of poly(aminoborane) as a new boron nitride precursor. *Polymers for Advanced Technologies* **1999,** 10, 702–712.

30. Schlesinger, H. I.; Brown, H. C.; Hoekstra, H. R.; Rapp, L. R., Reactions of diborane with alkali metal hydrides and their addition compounds. New synthesis of borohydrides. Sodium and potassium borohydrides. *Journal of the American Chemical Society* **1953,** 75, 199–204.

31. Martelli, P.; Caputo, R.; Remhof, A.; Mauron, P.; Borgschulte, A.; Züttel, A., Stability and decomposition of $NaBH_4$. *Journal of Physical Chemistry C* **2010,** 114, 7173–7177.

32. Züttel, A.; Rentsch, S.; Fischer, P.; Wenger, P.; Sudan, P.; Mauron, P.; Emmenegger, C., Hydrogen storage properties of $LiBH_4$. *Journal of Alloys and Compounds* **2003,** 356-357, 515–520.

33. Filinchuk, Y. E.; Rönnebro, E.; Chandra, D., Crystal structures and phase transformations in $Ca(BH_4)_2$. *Acta Materialia* **2009,** 57, 732–738.

34. Urgnani, J.; Torres, F. J.; Palumbo, M.; Baricco, M., Hydrogen release from solid state $NaBH_4$. *International Journal of Hydrogen Energy* **2008,** 33, 3111–3115.

35. Cunningham, P. T.; Maroni, V. T., Laser Raman spectra of solid and molten $NaNH_2$: Evidence for hindered rotation of the NH_2^- ion. *The Journal of Chemical Physics* **1972,** 57, 1415–1418.

36. Renaudin, G.; Gomes, S.; Hagemann, H.; Keller, L.; Yvon, K., Structural and spectroscopic studies on the alkali borohydrides MBH_4 (M = Na, K, Rb, Cs). *Journal of Alloys and Compounds* **2004,** 375, 98–106.

37. Schaeffer, G. W.; Adams, M. D.; Koenig, F. J., On the alkali metal salts derived from the diammoniate of diborane. *Journal of the American Chemical Society* **1956,** 78, 725–728.

38. Schlesinger, H. I.; Burg, A. B., Hydrides of boron. VIII. The structure of the diammoniate of diborane and its relation to the structure of diborane. *Journal of the American Chemical Society* **1938,** 60, 290–299.

39. Shore, S. G.; Girardot, P. R.; Parry, R. W., Chemical evidence for the structure of the "Diammoniate of Diborane." V. A tracer study of the reaction between sodium and the "Diammoniate of Diborane". *Journal of the American Chemical Society* **1958,** 80, 20–24.

40. Daly, S. R.; Bellott, B. J.; Kim, D. Y.; Girolami, G. S., Synthesis of the long sought unsubstituted aminodiboranate Na($H_3BNH_2BH_3$) and its *N*-Alkyl analogs. *Journal of the American Chemical Society* **2010,** 132, 7254–7255.

Chapter 5

The Reaction of Lithium Hydride with Ammonia Borane

5.1 Introduction

At the commencement of this research there had been no reported investigations into the interaction of lithium hydride with ammonia borane. This investigation was initially focused on the attempted synthesis of $Li_2BH_4NH_2$, a previously reported material.[1] The reaction mixture of LiH and NH_3BH_3 in a molar ratio of 2:1 left excess LiH at the end of the experiment. The 1:1 reaction mixture also resulted in the formation of a product which was contaminated with the LiH starting material. A stoichiometry of 1:2 in favour of NH_3BH_3 was subsequently found to be required to yield a crystalline product free from starting materials. This new tetragonal crystalline phase differed from $Li_2BH_4NH_2$. The hydrogen desorption properties of this material were investigated and spectroscopic characterisation carried out.

5.2 Experimental

Lithium hydride (Sigma-Aldrich, 95% purity) and ammonia borane (Sigma-Aldrich, 97% purity) were ground together in a 1:2 molar ratio in an argon filled glove box (>10 ppm O_2, >1 ppm H_2O), and heated under a flowing argon atmosphere at 50°C. The sample was reground and annealed at 50°C to improve the crystallinity of the product.

The synthesis of $LiNH_2BH_3$ was attempted through the reaction of $LiNH_2$ (Sigma-Aldrich, 95% purity) and NH_3BH_3 (Sigma-Aldrich, 97% purity) in a 1:1 molar ratio. The reagents were mixed together in an argon filled glove box (>10 ppm O_2, >1 ppm H_2O). The nature of the reaction dictated that the reagents could not be ground together, because the reaction mixture became wet upon mixing and took several hours to dry under ambient conditions in the glove box.

5.3. Powder X-Ray Diffraction

Powder XRD patterns were collected for the products following the heating of the reaction mixture. It was found that a new crystalline phase formed at a temperature of 50°C, which was collected as a white powder at the end of the experiment. No reports of this phase had previously appeared in the literature. The powder XRD pattern of this phase is shown in figure 5.1.

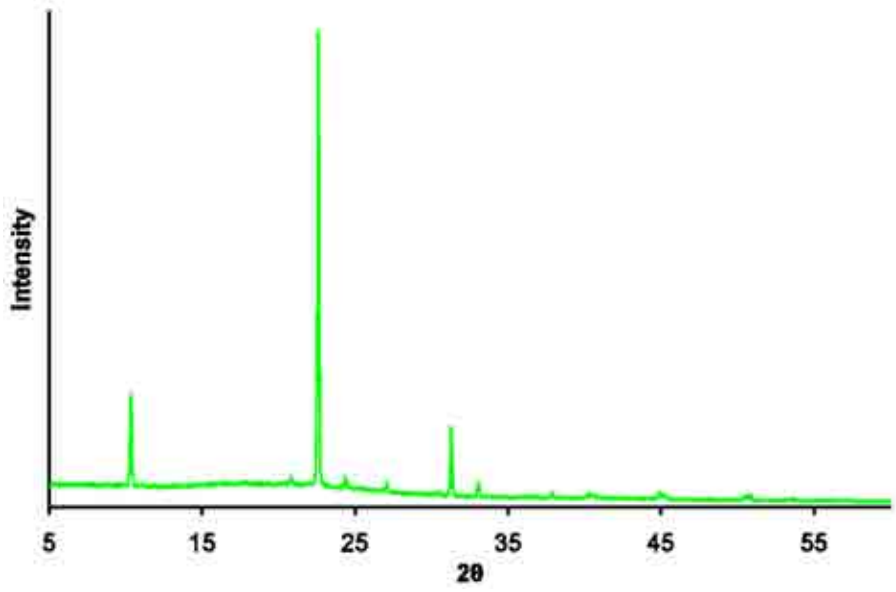

Figure 5.1 – The powder XRD pattern collected from the product of the reaction of $LiH + 2NH_3BH_3$ at 50°C

Higher temperature reactions showed that this phase persisted up to a temperature of 120°C. At reaction temperatures above 120°C no crystalline phases were observed in the powder XRD pattern, showing that only amorphous phases remained. The ultimate decomposition product of the reaction was investigated using

an elevated reaction temperature of 800°C and, as can be seen in figure 5.2, this product was also amorphous.

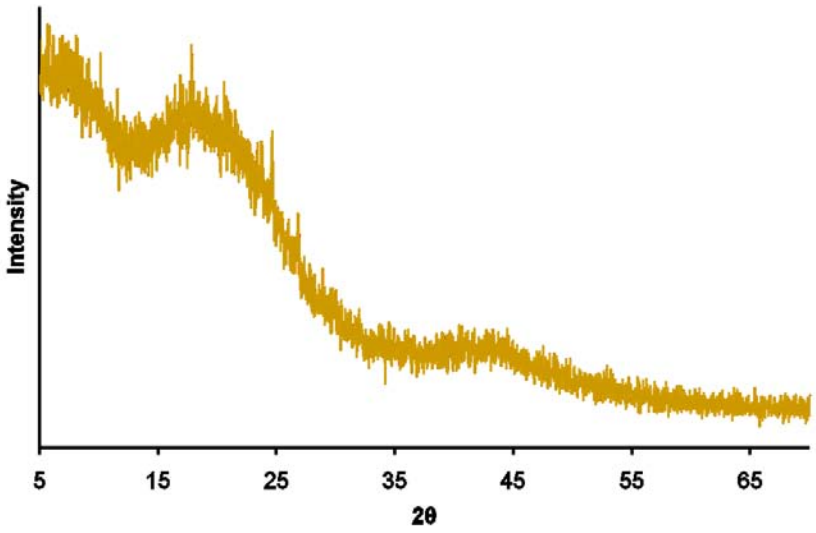

Figure 5.2 – The powder XRD pattern of the product of the reaction of LiH + $2NH_3BH_3$ at 800°C

Reported studies into the reaction of LiH with NH_3BH_3 have focused on the 1:1 reaction, which have been shown to synthesise the crystalline phase lithium amidoborane, $LiNH_2BH_3$. Similar to $NaNH_2BH_3$ there are two recent synthetic procedures that have been outlined to form this material. The reaction can proceed in solution using THF as a solvent[2, 3] or through ball milling of the reagents.[4, 5] A third preparative procedure has previously been reported for this material, through the reaction of NH_3BH_3 with *n*-butyllithium in THF at 0°C.[6] As with $NaNH_2BH_3$, the synthesis of $LiNH_2BH_3$ has not previously been reported through direct thermal solid state reaction of LiH and NH_3BH_3. Investigations into the 1:1 reaction in this study revealed that this material could not be synthesised through a thermal reaction, even at low temperatures. Analysis by powder XRD (figure 5.3) revealed two phases present in the product: peaks related to the product of the 1:2 reaction along with peaks due to the continued presence of LiH were observed.

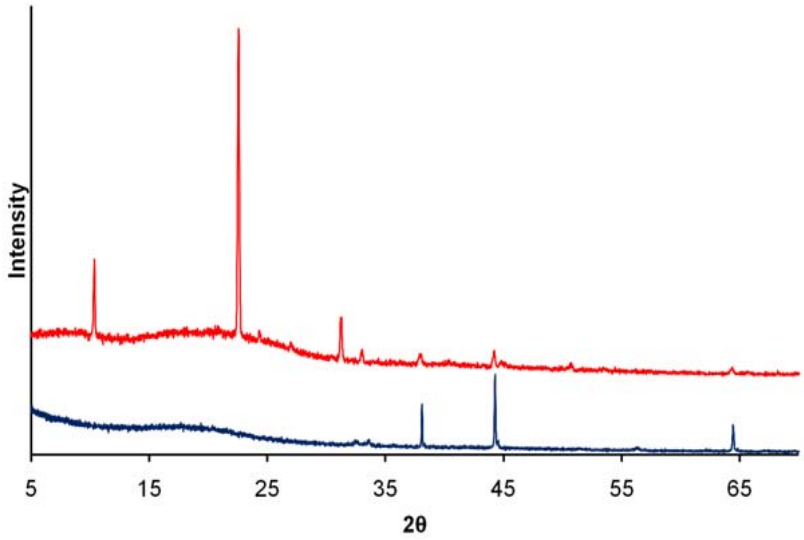

Figure 5.3 – The powder XRD pattern of the product of the reaction of LiH + NH_3BH_3 at 60°C (red). The powder XRD pattern of LiH is shown for comparison (blue)

The progression of the reaction with temperature increase as observed by powder XRD is shown in figure 5.4. It can be seen that powder XRD shows only two steps in the pathway. The first step involved the formation of the unknown crystalline phase at a reaction temperature of 50°C. This crystalline phase existed until a temperature of 140°C. Above this temperature it mostly underwent decomposition to an amorphous material as shown by the absence of any significant amount of crystalline phases in any of the diffraction patterns. A small amount of $LiBH_4$ was observed just above the background of the diffraction patterns collected from the products after reaction at 140°C and 150°C, which was absent after reaction at 250°C.

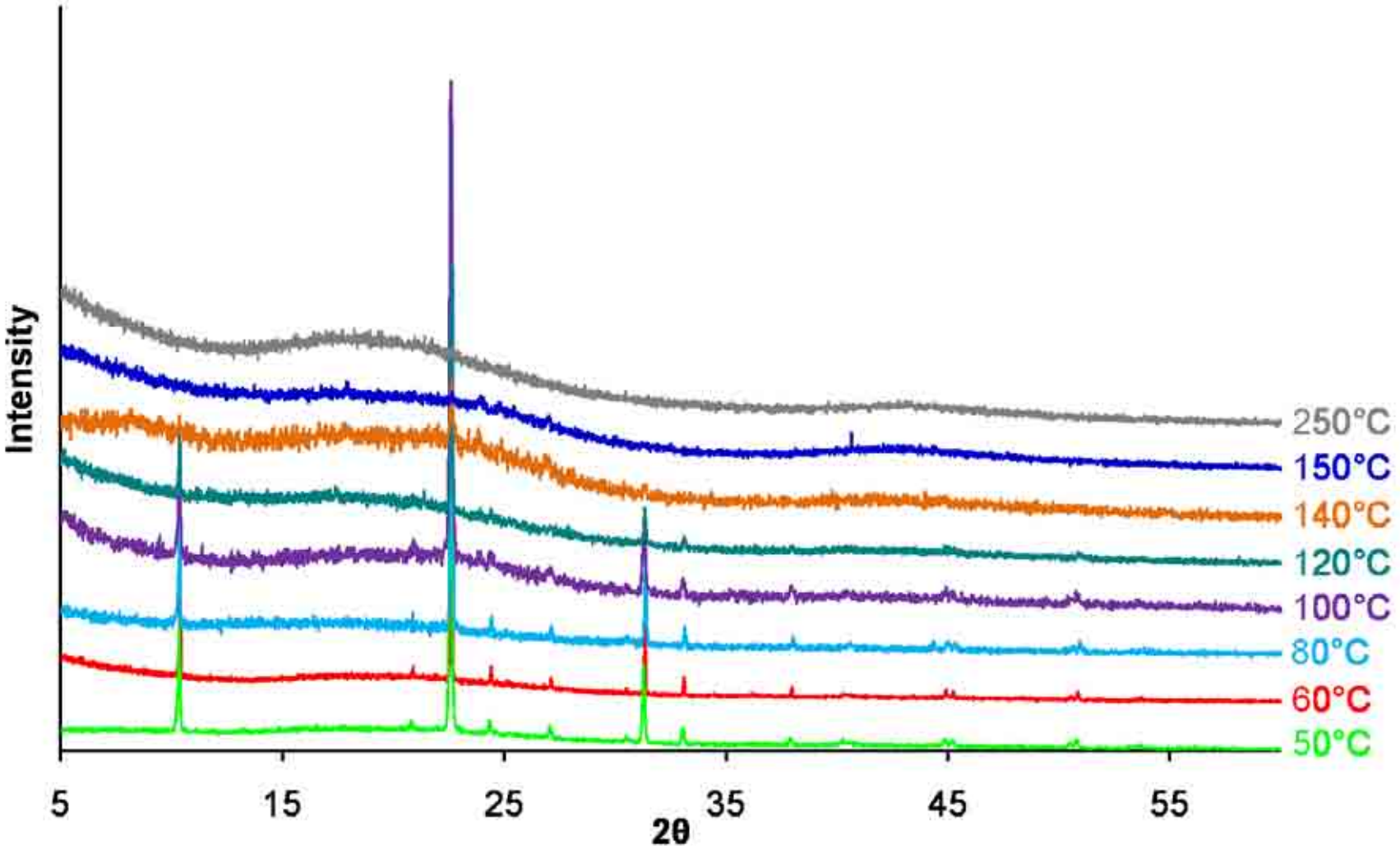

Figure 5.4 – Powder XRD patterns obtained from the products of the LiH + $2NH_3BH_3$ reaction at various temperatures

The LiH + $2NH_3BH_3$ reaction was also investigated at room temperature and it was found that the reaction proceeded, albeit slowly, over a period of two months, to yield the same unidentified crystalline phase discussed previously, shown in figure 5.5. At no point during the reaction was there any evidence of the formation of a 1:1 phase, either in the form of $LiNH_2BH_3$ or otherwise. It was also found that this reaction would proceed at 40°C with an extended reaction time of 80 hours. The product of the reaction was the unidentified crystalline phase, again no evidence of the formation of $LiNH_2BH_3$ was observed.

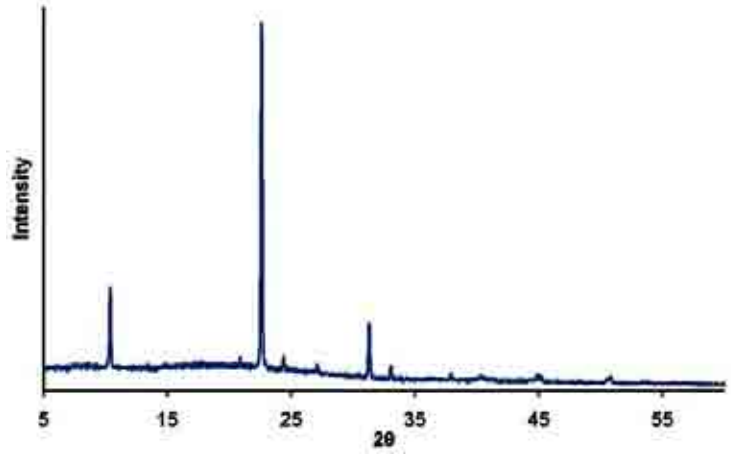

Figure 5.5 – The powder XRD pattern of the LiH + $2NH_3BH_3$ reaction two months after the reagents had been ground together at room temperature

The unknown crystalline phase was also found to be the product of the reaction of $LiNH_2BH_3$, previously synthesised through the reaction of $LiNH_2$ and NH_3BH_3, with NH_3BH_3 at 50°C, figure 5.6.

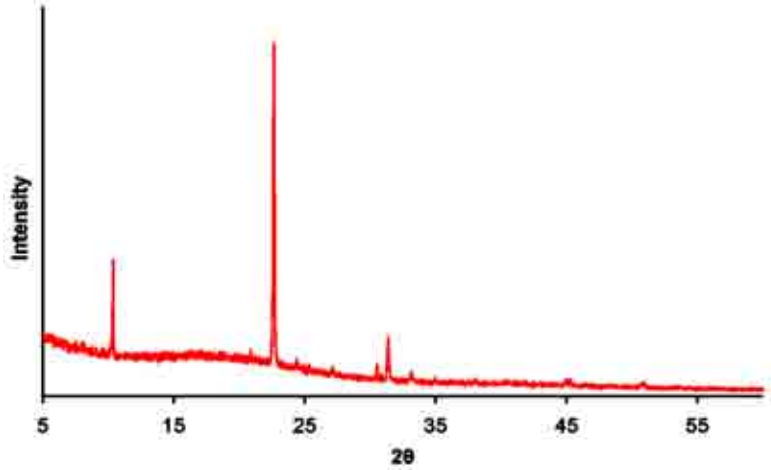

Figure 5.6 – The powder XRD pattern of the product of the reaction of $LiNH_2BH_3$ + NH_3BH_3 at 50°C

Unlike the $NaNH_2$ + NH_3BH_3 reaction, there have been no reports in the literature that have detailed the successful synthesis of $LiNH_2BH_3$ through a $LiNH_2$ + NH_3BH_3 reaction using either solid state or solution synthesis. On mixing the reagents an exothermic reaction appeared to proceed instantaneously, evidenced by the reaction mixture becoming wet only a few seconds after combining the reagents. There was no visible evidence of any gases being given off and the reaction mixture dried when it was left to stand for several hours, leaving a white powder. The powder XRD pattern of this sample, figure 5.7, showed that $LiNH_2BH_3$ was the main product of the reaction with a small amount of unreacted $LiNH_2$ remaining, although NH_3BH_3 was completely consumed in the reaction. The excess $LiNH_2$ that remained after reaction was possibly due to the reaction being sufficiently exothermic to initiate the decomposition of NH_3BH_3, hence altering the stoichiometry of the reaction from the desired 1:1 molar ratio. $LiNH_2$ is stable to a much higher temperature than NH_3BH_3 and so would not have undergone decomposition.[7] The solitary report in the literature regarding the $LiNH_2$ + NH_3BH_3 reaction stated that the solid state reaction yielded an amorphous hybrid material of approximate composition $LiNH_2BH_3NH_3$, although similar observations regarding the state of the reaction mixture were made.[8] This hybrid material is of the same chemical composition as $Li(NH_3)NH_2BH_3$, an amorphous material synthesised by Xia *et al.*[9] through the treatment of $LiNH_2BH_3$ with NH_3 at room temperature. There is a possibility that these materials were the same, however, as both were amorphous, XRD cannot determine this.

The effect of heating the $LiNH_2BH_3$ material to 50°C is shown in figure 5.8. This did not result in any changes to the XRD pattern, $LiNH_2BH_3$ remained the dominant phase in the pattern, with $LiNH_2$ still observed. Further heating to 100°C proved to result in the decomposition of the $LiNH_2BH_3$ phase as the only crystalline phase present in the XRD pattern was $LiNH_2$. This showed that the decomposition product of $LiNH_2BH_3$ was an amorphous material. The $LiNH_2$ present throughout was likely to have been unreacted starting material rather than a product of decomposition.

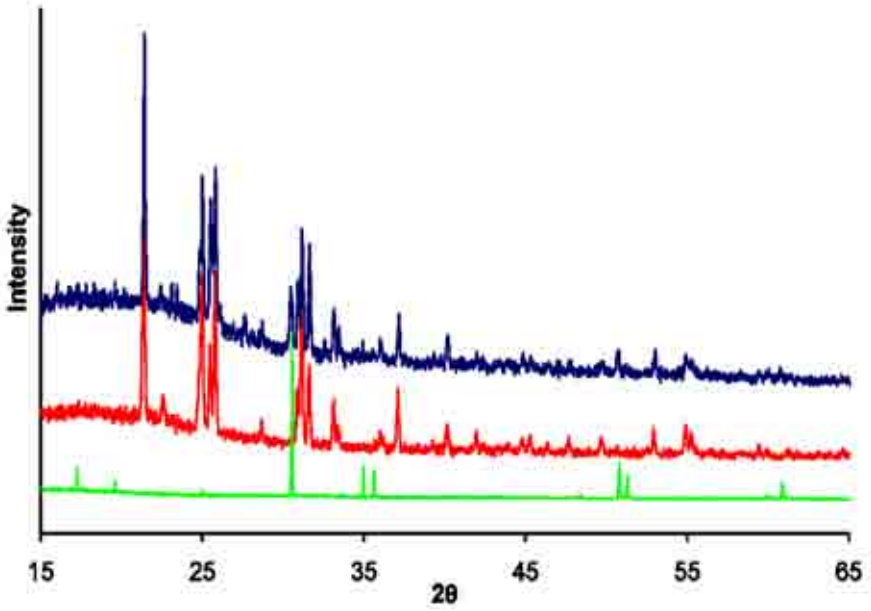

Figure 5.7 – The powder XRD pattern of the product of the reaction of $LiNH_2$ and NH_3BH_3 at room temperature (blue). The powder XRD patterns of $LiNH_2BH_3$[10] (red), and $LiNH_2$ (green) are shown for comparison

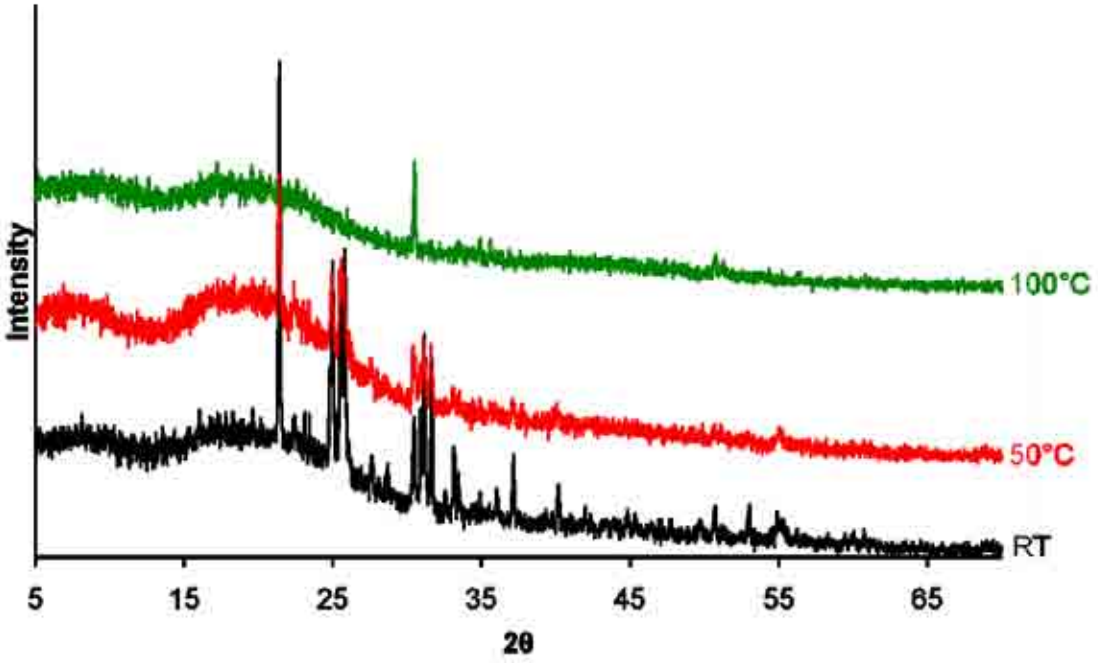

Figure 5.8 – Powder XRD patterns obtained from the products of the $LiNH_2$ + NH_3BH_3 reaction at specified temperatures

5.3.1 Indexing

The peak positions observed in the product of the LiH + $2NH_3BH_3$ reaction at 50°C were run through the indexing routine of Topas.[11] The most probable assignment was for a tetragonal unit cell with *a* = 4.03 Å and *c* = 17.01 Å, with a suggested space group of $P4_2mc$. The *a* and *c* lattice parameters were refined through Topas[11], using a Pawley fit, to values of 4.0288(2) Å and 16.958(2) Å, respectively, giving a unit cell volume of 275.26(5) $Å^3$. The fit is shown in figure 5.9. There was only one broad peak present in the pattern that was not indexed as part of this tetragonal crystalline phase, observed at 40.5°, shown in figure 5.10.

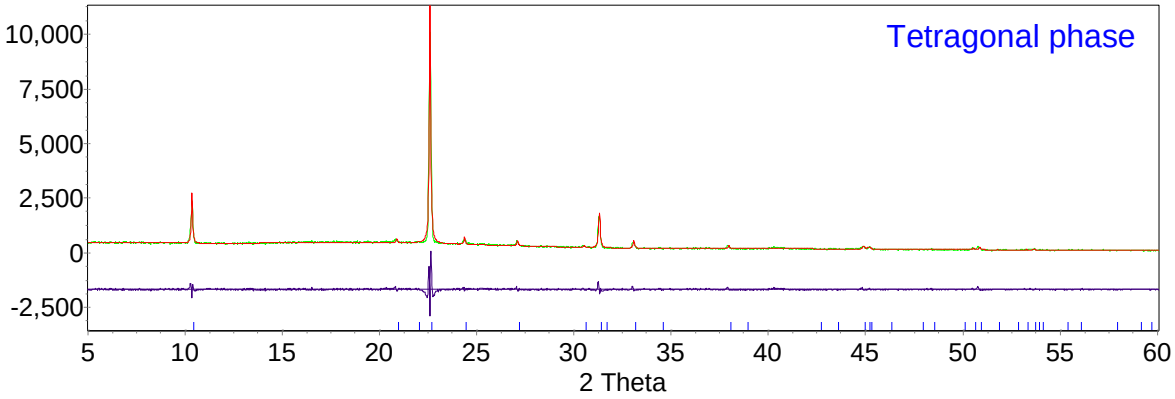

Figure 5.9 – Pawley refinement for the product synthesised through the LiH + $2NH_3BH_3$ reaction at 50°C. The observed pattern is shown in green, the calculated pattern in red and the difference in purple. Bragg peak positions of the tetragonal phase are indicated in blue. R_{wp} = 9.304%, χ^2 = 2.931

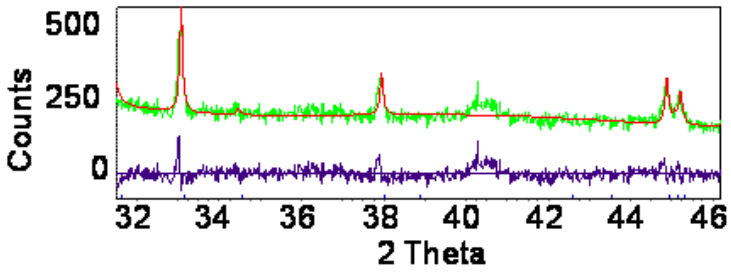

Figure 5.10 – The impurity peak in the Pawley refinement of the tetragonal phase synthesised through the LiH + $2NH_3BH_3$ reaction at 50°C

The procedure was repeated for the peak positions observed for this new phase synthesised in reactions up to a temperature of 140°C. The results are shown in table 5.1 and the Pawley fits can be seen in Appendix 3. No regular trend between lattice

constants and reaction temperature was observed. There was variation in the lattice constants, but these differences were relatively small. The impurity peak observed in the powder pattern of the product from reaction at 50°C was observed in all patterns up to a reaction temperature of 120°C. The intensity of this peak was greatest at temperatures up to 80°C; at 100°C and 120°C its intensity was decreased and after heating to 140°C the peak was no longer visible. The structure published by Soulié *et al.*[12] was used as a starting model for Rietveld refinements of the powder XRD patterns collected from the products of the LiH + $2NH_3BH_3$ reaction at 140°C and 150°C to show the presence of $LiBH_4$. The refined patterns can be seen in figures 5.11 and 5.12. The product of the $LiNH_2BH_3$ + NH_3BH_3 reaction was also indexed to the same tetragonal cell, although there was no sign of the impurity peak at 40.5°; the Pawley fit for this refinement can be seen in Appendix 3. There has been one study reported in the literature on the subject of the LiH + $2NH_3BH_3$ reaction, with a ball milled reaction mixture shown to produce $LiNH_2BH_3{\cdot}NH_3BH_3$ in the $P2_1/c$ space group with a monoclinic unit cell.[13] No peaks in any of the powder XRD patterns could be indexed to this monoclinic phase.

Table 5.1 – Refined values of the *a* and *c* lattice constants and cell volume for the tetragonal phase observed in the LiH + $2NH_3BH_3$ reaction

Reaction Temperature (°C)	*a* (Å)	*c* (Å)	Cell volume (Å^3)
Literature[14]	4.0320(4)	17.023(4)	276.73(8)
RT	4.0293(3)	16.944(3)	275.09(6)
40	4.0403(1)	17.1213(8)	279.48(2)
50	4.0288(2)	16.958(2)	275.26(5)
60	4.0331(1)	16.989(1)	276.34(3)
80	4.0184(3)	16.913(2)	273.11(5)
100	4.0313(5)	16.990(4)	276.12(10)
120	4.0251(4)	16.963(3)	274.83(7)
140	4.032(1)	16.955(6)	275.6(2)
$LiNH_2BH_3$ + NH_3BH_3 50°C	4.0223(4)	16.963(4)	274.44(8)

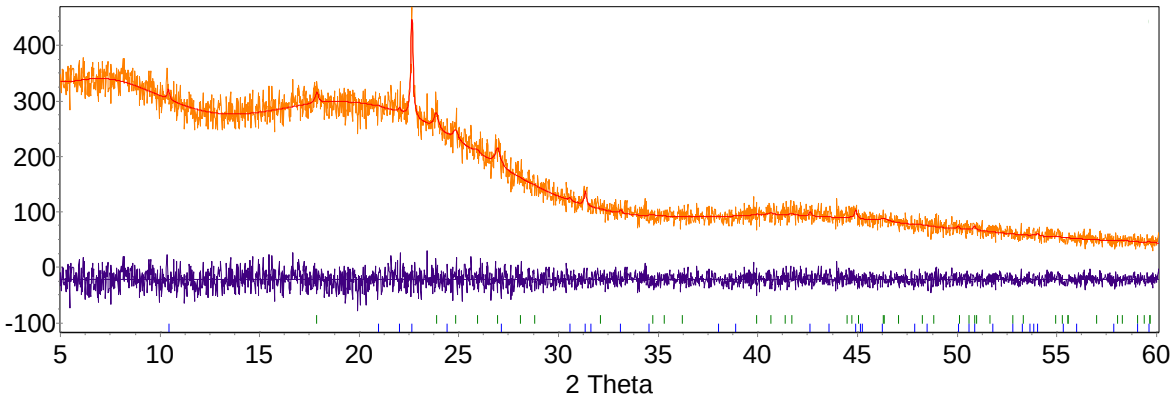

Figure 5.11 – The refined powder XRD pattern of the LiH + $2NH_3BH_3$ reaction at 140°C. The observed pattern is shown in orange, the calculated pattern in red and the difference in purple. Bragg peak positions of the tetragonal phase are indicated in blue and $LiBH_4$ in green. R_{wp} = 8.578%, χ^2 = 1.026

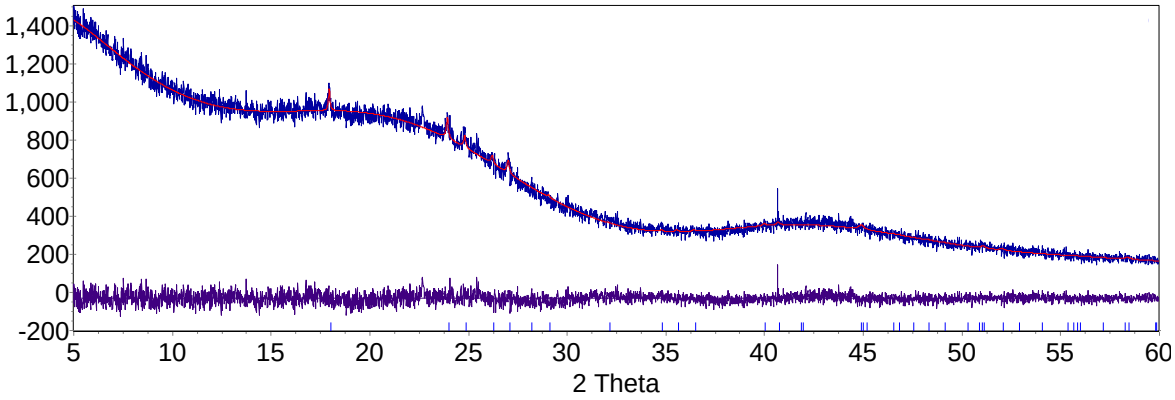

Figure 5.12 – Pawley refinement for the product synthesised through the LiH + $2NH_3BH_3$ reaction at 150°C. The observed pattern is shown in blue, the calculated pattern in red and the difference in purple. Bragg peak positions of $LiBH_4$ are indicated in blue. R_{wp} = 4.678%, χ^2 = 1.136

Following the room temperature reaction of $LiNH_2$ with NH_3BH_3, the powder XRD pattern was refined to show the continued presence of $LiNH_2$ as well as the formation of $LiNH_2BH_3$. The starting model used for the Rietveld refinement of the $LiNH_2BH_3$ phase was obtained from previous reports in the literature.[4, 15] The *a*, *b* and *c* lattice constants were refined along with the atomic coordinates of lithium, nitrogen and boron. Hydrogen atoms were not included in the refinement as they are poor scatterers of X-rays. The structure published by Jacobs *et al.*[16] was used as the starting model for the Rietveld refinement of $LiNH_2$. The refined powder XRD pattern can be seen in figure 5.13. There was a good fit between the observed and

calculated patterns following this refinement. Table 5.2 shows a selection of refined parameters along with the original published structure values.

Table 5.2 – Refined lattice constants and selected bond lengths of $LiNH_2BH_3$ and $LiNH_2$ synthesised in the reaction of $LiNH_2$ + NH_3BH_3 at room temperature

Parameter	NH_3BH_3[17]	$LiNH_2BH_3$[4, 15]	$LiNH_2$[16]	$LiNH_2BH_3$	$LiNH_2$
a	5.2630(4)	7.1051(8)	5.037	7.1147(7)	5.0433(9)
b	5.2630(4)	13.930(1)	5.037	13.945(1)	5.0433(9)
c	5.0504(8)	5.1477(7)	10.278	5.1524(6)	10.264(4)
Li–N bond length (Å)	0.85(7) (H–N)	1.98	2.06 – 2.21	2.028(2)	2.06812
B–N bond length (Å)	1.597(3)	1.56	Not applicable	1.571(2)	Not applicable

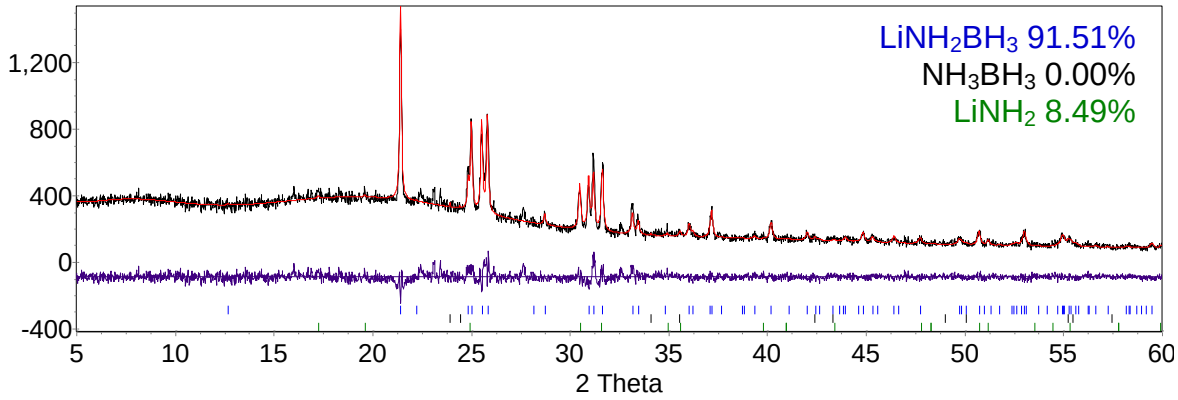

Figure 5.13 – Rietveld refinements for the phases observed in the product of the $LiNH_2$ + NH_3BH_3 reaction at room temperature. The observed pattern is shown in black, the calculated pattern in red and the difference in purple. Bragg peak positions of $LiNH_2BH_3$ (blue), NH_3BH_3 (black) and $LiNH_2$ (green) are indicated. R_{wp} = 8.343%, χ^2 = 1.498

The refinement showed that the major product of the reaction was $LiNH_2BH_3$ with a small amount of unreacted $LiNH_2$ remaining in the sample. The reason behind the continued presence of $LiNH_2$ will be discussed in section 5.3.2. The refined lattice constant values of both $LiNH_2BH_3$ and $LiNH_2$ agreed well with literature values. The substitution of a protic H in NH_3BH_3 for Li resulted in a decrease of the B–N bond length in $LiNH_2BH_3$ compared to NH_3BH_3. The decreased B–N bond length shows that this bond increased in strength following the Li for H substitution, which agreed with predictions previously reported by Armstrong *et al*.[18] The increased B–N bond

strength is due to the presence of the more electron donating Li, compared to H in NH_3BH_3.

5.3.2 Discussion

A tetragonal crystalline phase was synthesised through the reaction of LiH + $2NH_3BH_3$ at 50°C, which underwent decomposition above 140°C. This phase was also shown to form at 40°C and even at room temperature, although the reaction time required was substantially increased. The major decomposition products of the tetragonal phase were found to be amorphous, similar to the decomposition of NH_3BH_3. Only a very small amount of $LiBH_4$ was formed around 150°C which was different from the decomposition of $Na^+[BH_3NH_2BH_3]^-$, where $NaBH_4$ was a significant decomposition product. The low intensity of $LiBH_4$ peaks in the powder XRD patterns may have been due to the material not being able to crystallise under the reaction conditions. It has been commented on in other studies that $LiBH_4$ is unable to crystallise under dehydrogenation conditions and so is often not observed in powder XRD patterns despite it being an expected decomposition product.[13]

A striking observation of all these reactions was the fact that a significant volume expansion was observed during heating, at which point the sample became wet, although the final product collected following annealing was a powder. This volume expansion is a key step in the decomposition of ammonia borane, whereas it was not observed in any reaction involving NaH and NH_3BH_3. This provided an insight into the mechanism of the crystalline phase formation. The hydride ion of MH is a strong base and is potentially capable of removing a protic H from the NH_3 group in NH_3BH_3. In the case of the more basic NaH, deprotonation of NH_3BH_3 was facile and so $NaNH_2BH_3$ could form. Lithium is less electron donating than sodium, meaning the H^- is a weaker base and so it was not capable of acquiring a protic H from NH_3BH_3. This meant that the NaH reaction could proceed when NH_3BH_3 was in its most stable state, before disruption of the dihydrogen bonding network. The LiH reaction, however, required the more labile form of NH_3BH_3, present after volume expansion and the disruption of the dihydrogen bonding network, in order for the reaction to proceed. This may have resulted in the lithium reaction proceeding through a different reaction mechanism to the sodium pathway.

The tetragonal phase has been identified in a number of literature studies as being a side product to the main reaction under investigation. A study by H. Wu *et al.*,[15] primarily focused on investigating the 1:1 reaction, was the first to discuss the product of the LiH + $2NH_3BH_3$ reaction. Following ball milling of a 1:1 reaction mixture a number of low intensity unindexed peaks in the powder XRD pattern were observed along with peaks due to $LiNH_2BH_3$. The intensity of the unindexed peaks increased on decreasing the ratio of LiH to NH_3BH_3 to 1:2 in the reaction mixture. The majority of these peaks did not appear in our powder XRD pattern of the product of the LiH + $2NH_3BH_3$ reaction, although the three dominant peaks observed at 2θ = 10.4°, 22.6° and 31.3° were present. However, both the observed and unobserved peaks were indexed to the same crystalline material and the product was concluded to have the chemical formula $LiNH_2BH_3{\cdot}NH_3BH_3$. A structure was subsequently solved in the $Cmc2_1$ space group, with lattice constants a = 13.992 Å, b = 10.742 Å and c = 10.110 Å. The fact that a number of the peaks in this XRD pattern occurred in the powder XRD pattern of our product from the LiH + $2NH_3BH_3$ reaction suggested that the product observed by H. Wu *et al.* was in fact multiphase.

A second study by C. Wu *et al.*[13] focused on the synthesis of the $LiNH_2BH_3{\cdot}NH_3BH_3$ phase through ball milling of LiH + $2NH_3BH_3$ and $LiNH_2BH_3$ + NH_3BH_3 reaction mixtures. The XRD pattern of the product was similar to the one observed by H. Wu *et al.*[15] However, the three peaks observed at 2θ = 10.3°, 22.7° and 31.4° were assigned as impurities in the $LiNH_2BH_3{\cdot}NH_3BH_3$ XRD pattern. The intensities of these peaks were also greatly reduced compared to those observed in the study by H. Wu *et al*.[15] Consequently, the two determined structures of $LiNH_2BH_3{\cdot}NH_3BH_3$ were significantly different. It was noted that the $LiNH_2BH_3{\cdot}NH_3BH_3$ material underwent decomposition slowly at room temperature and subsequently the three impurity peaks at 2θ = 10.3°, 22.7° and 31.4° increased in intensity while the peaks indexed to the $LiNH_2BH_3{\cdot}NH_3BH_3$ phase disappeared from the pattern. It can therefore be concluded that the data used by H. Wu *et al.* to solve the structure of $LiNH_2BH_3{\cdot}NH_3BH_3$ did in fact contain two phases. Heating $LiNH_2BH_3{\cdot}NH_3BH_3$ to 100°C resulted in the decomposition of this material. The XRD pattern obtained after heating $LiNH_2BH_3{\cdot}NH_3BH_3$ to 100°C resembled that of the tetragonal phase, with the three dominant peaks observed at 2θ = 10.4°, 22.6° and 31.3° present in both

patterns. These observations therefore suggested that the tetragonal phase was a product of the decomposition of $LiNH_2BH_3{\cdot}NH_3BH_3$.

A further study by C. Wu *et al.*[14] investigated the phase transitions during the ball milled LiH + NH_3BH_3 reaction forming $LiNH_2BH_3$. The reaction pathway, reaction 5.1, was proposed to involve formation of $LiNH_2BH_3{\cdot}NH_3BH_3$ as an intermediate.

$$2LiH + 2NH_3BH_3 \rightarrow LiH + LiNH_2BH_3{\cdot}NH_3BH_3 + H_2 \rightarrow 2LiNH_2BH_3 + 2H_2$$

Reaction 5.1

An impurity phase was identified in most samples, the most intense peak of which was observed in the XRD pattern at 22.7°, consistent with our observations. Furthermore, this crystalline phase was indexed to a tetragonal unit cell with lattice constants a = 4.0320(4) Å and c = 17.023(4) Å and a unit cell volume of 276.73(8) $Å^3$. These parameters showed good agreement with those calculated for the tetragonal phase formed in our study, confirming that the same crystalline phase had formed. This impurity phase was thought to have originated from the decomposition of the $LiNH_2BH_3{\cdot}NH_3BH_3$ phase during the reaction.

From comparisons of the literature reports to the results outlined here, it can be concluded that the thermal LiH + $2NH_3BH_3$ reaction did not result in the crystalline phase $LiNH_2BH_3{\cdot}NH_3BH_3$. Literature studies showed the $LiNH_2BH_3{\cdot}NH_3BH_3$ material was synthesised through room temperature ball milling of the reagents whereas this study used thermal treatment of the reagents in order to effect a reaction. C. Wu *et al.* [13, 14] showed that $LiNH_2BH_3{\cdot}NH_3BH_3$ decomposed slowly at room temperature, with the resulting XRD pattern showing the presence of the tetragonal phase.[13, 14] Due to the LiH + $2NH_3BH_3$ reaction being carried out at temperatures in excess of 50°C, any formation of $LiNH_2BH_3{\cdot}NH_3BH_3$ would have been rapidly followed by the transition to the tetragonal phase and so this material was not detected in the powder XRD patterns of the products. These results do, however, suggest that $LiNH_2BH_3{\cdot}NH_3BH_3$ may have been involved in the LiH + $2NH_3BH_3$ reaction mechanism.

The product of the $LiNH_2BH_3$ + NH_3BH_3 reaction at 50°C was also the tetragonal phase, suggesting that $LiNH_2BH_3$ was also involved in the reaction mechanism,

despite not being observed in any of the powder XRD patterns of the products of the LiH + $2NH_3BH_3$ reactions. Therefore, if $LiNH_2BH_3$ was involved in the reaction mechanism it must have undergone a rapid reaction with the second molar equivalent of NH_3BH_3 forming the tetragonal phase and, as discussed above, possibly through $LiNH_2BH_3{\cdot}NH_3BH_3$ as an intermediate. The relative rates of the LiH + NH_3BH_3 and $LiNH_2BH_3$ + NH_3BH_3 reactions can be determined through the LiH + NH_3BH_3 reaction. The powder XRD pattern, figure 5.3, showed the presence of the tetragonal phase and unreacted LiH, showing that $LiNH_2BH_3$ + NH_3BH_3 was the faster reaction. The LiH + $2NH_3BH_3$ reaction pathway can hence be broken down into a two step process as shown in reaction 5.2.

$$LiH + 2NH_3BH_3 \xrightarrow[\text{limiting}]{\text{Rate}} LiNH_2BH_3 + NH_3BH_3 \xrightarrow{\text{Fast}} \text{Tetragonal Phase}$$

Reaction 5.2

The rationale for the first step being rate limiting has been previously discussed and is related to the fact that in order for the reaction to proceed the NH_3BH_3 starting material had to undergo a structural change with respect to the disruption of the dihydrogen bonding network. Following this step a much more reactive, mobile form of NH_3BH_3 was present in the reaction mixture and hence the second step in the pathway, NH_3BH_3 reaction with $LiNH_2BH_3$ was able to proceed more rapidly.

The rationale that neither $LiNH_2BH_3$ nor $LiNH_2BH_3{\cdot}NH_3BH_3$ were observed in the powder XRD patterns was that the reaction temperatures were sufficient to effect subsequent reaction of $LiNH_2BH_3$ with NH_3BH_3 or $LiNH_2BH_3{\cdot}NH_3BH_3$ decomposition. Therefore, at room temperature these thermal events may have been avoided. However, at no point during the room temperature reaction were either of these phases observed in the powder XRD pattern. $LiNH_2BH_3$ absence could be justified if the room temperature reaction of $LiNH_2BH_3$ + NH_3BH_3 was fast. However, this reaction was not shown to proceed instantly at room temperature; the powder XRD pattern obtained one week after grinding the reaction mixture, figure 5.14, showed that both starting materials as well as the tetragonal phase were present. This result can, however, be used to justify the absence of $LiNH_2BH_3{\cdot}NH_3BH_3$ in any of the powder XRD patterns of the reaction products, because even at room temperature it was shown that this material was unable to form. It can hence be concluded that

$LiNH_2BH_3$ was not involved in the $LiH + 2NH_3BH_3$ reaction pathway. This conclusion is further validated by the results published by C. Wu *et al.*[14] which investigated the 1:1 reaction pathway. Reaction 5.1 shows that $LiNH_2BH_3{\cdot}NH_3BH_3$ was in fact an intermediate in the formation of $LiNH_2BH_3$, therefore disproving reaction 5.2. This fact shows why it was not possible to form $LiNH_2BH_3$ from a reaction mixture of LiH and NH_3BH_3 at any reaction stoichiometry. $LiNH_2BH_3{\cdot}NH_3BH_3$ has been shown to be unable to form in thermal reactions and instead the product was observed to be the tetragonal phase. This means that the second step in reaction 5.1, would have been unable to proceed, signifying that $LiNH_2BH_3$ formation was prevented. This also means that the first step in reaction 5.2 resulted in the tetragonal phase and excess LiH and not a mixture of $LiNH_2BH_3$ and unreacted NH_3BH_3 as speculated.

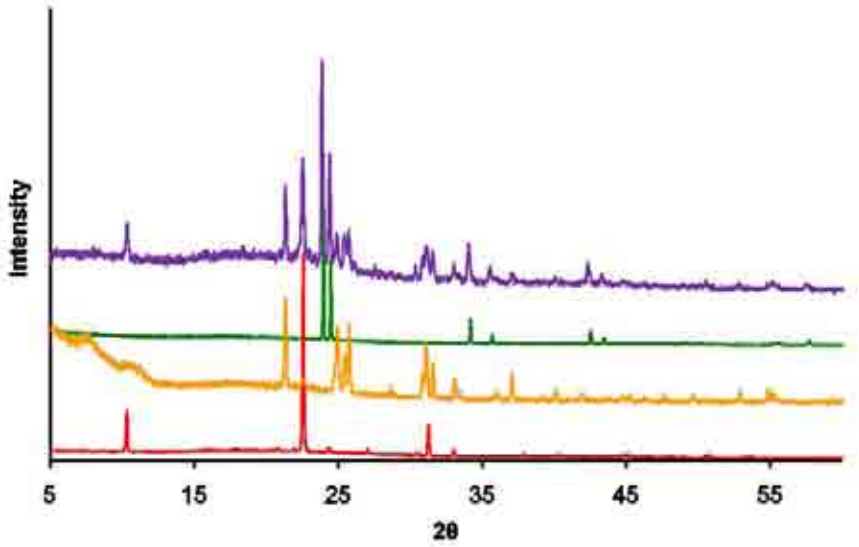

Figure 5.14 – The powder XRD pattern of the products of reaction of $LiNH_2BH_3$ + NH_3BH_3 at room temperature, one week after grinding the reagents (purple). The powder XRD patterns of NH_3BH_3 (green), $LiNH_2BH_3$ (orange) and the tetragonal phase (red) are shown for comparison

The conclusion that $LiNH_2BH_3$ does not have a role in the $LiH + 2NH_3BH_3$ reaction mechanism poses the question of what the reaction mechanism could involve. As discussed previously the reaction mixture was observed to undergo a voluminous swelling on heating, showing that the metal hydride reacted with the more mobile phase of ammonia borane. During this volume expansion, the dihydrogen bonding network is disrupted and the NH_3BH_3 molecules have increased freedom. In the

decomposition of NH_3BH_3 a nucleation step then occurs, which involves the rearrangement of two NH_3BH_3 molecules, forming DADB, reaction 5.3.

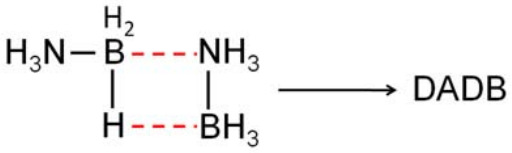

Reaction 5.3

If LiH was to react with this mobile form of NH_3BH_3, before DADB formation, it would effectively be reacting with two NH_3BH_3 molecules and hence explain why a 1:2 molar ratio of reagents was required. The crystal structure of $LiNH_2BH_3{\cdot}NH_3BH_3$ showed that the structure consists of alternate layers of $LiNH_2BH_3$ and NH_3BH_3.[13] This structure was shown to contain both ionic bonds, between Li^+ and $NH_2BH_3^-$ ions, and dihydrogen bonds between adjacent NH_3BH_3 and $LiNH_2BH_3$ molecules. It is presumably these dihydrogen bonds that give the structure the ability to exist, similar to the role they play in the structure of NH_3BH_3.[19] In thermal reactions it is possible that the reaction temperatures are sufficiently high to inhibit formation of these dihydrogen bonds and hence $LiNH_2BH_3{\cdot}NH_3BH_3$ formation, and consequently, the tetragonal phase would have formed instead. This proposal is supported by the lengths of the dihydrogen bonds found in $LiNH_2BH_3{\cdot}NH_3BH_3$ and NH_3BH_3. The shortest dihydrogen bonds present in pure NH_3BH_3 have been experimentally determined to be 1.91(5) Å in length,[17] although DFT calculations determined them to be shorter, 1.897 Å.[20] The dihydrogen bond lengths in the NH_3BH_3 layers in the $LiNH_2BH_3{\cdot}NH_3BH_3$ structure were also calculated and determined to be 1.902 Å in length.[13] The dihydrogen bond lengths are similar in both structures and therefore it can be assumed that the dihydrogen bonding networks break at approximately the same temperature. In fact these bonds have been shown to break at lower temperature in $LiNH_2BH_3{\cdot}NH_3BH_3$, evidenced by its lower melting point, 58°C, than NH_3BH_3, 95°C.[13] The thermal LiH + $2NH_3BH_3$ reaction was shown to not proceed until the NH_3BH_3 became labile and so $LiNH_2BH_3{\cdot}NH_3BH_3$ would not be expected to form, with the tetragonal phase forming instead.

The solid state reaction of $LiNH_2$ and NH_3BH_3 produced the crystalline phase $LiNH_2BH_3$, although the product was contaminated with unreacted $LiNH_2$, despite all of the NH_3BH_3 starting material being consumed during the reaction. The observation

of the reaction mixture foaming and becoming wet almost simultaneously with the mixing of the reagents showed that there was no significant kinetic barrier to the reaction. The product of the reaction being $LiNH_2BH_3$ implied that NH_3 release accompanied the formation of this phase as shown in reaction 5.4.

$$LiNH_2 + NH_3BH_3 \rightarrow LiNH_2BH_3 + NH_3 \qquad \text{Reaction 5.4}$$

The release of NH_3 from this reaction was consistent with the $NaNH_2$ + NH_3BH_3 reaction. The reaction mechanism can therefore be assumed to have been the same as for the $NaNH_2$ + NH_3BH_3 reaction, chapter 4.3, with the NH_2^- anion acting as a nucleophile and attacking the B through an S_N2 reaction, although there was still the possibility that the NH_2^- anion acted as a base, forming the same product. $LiND_2$ would be required as a starting material to substantiate the reaction mechanism.

The release of NH_3 from these reactions also gave the potential for a second reaction to proceed. Exposing $LiNH_2BH_3$ to ammonia has been shown to yield a coordination compound, $Li(NH_3)NH_2BH_3$.[9] This material is amorphous in nature at room temperature and exists as a sticky liquid, although it does crystallise at lower temperature. The observation that the $LiNH_2$ + NH_3BH_3 reaction mixture became wet on mixing the reagents suggested that this NH_3 adduct could have formed, although as it would have formed as an amorphous material it would not have been detected by powder XRD. This possible reaction will be discussed further in section 5.4.

The continued presence of $LiNH_2$ in the powder XRD pattern after reaction again showed that competing reactions must have been taking place. Two such competing reactions were proposed for the $NaNH_2$ + NH_3BH_3 reaction in chapter 4.3, reactions 4.5 and 4.6. The product of both reactions was $Na^+[BH_3NH_2BH_3]^-$. The powder XRD pattern of this material is now known, but it was not observed in the product of the $NaNH_2$ + NH_3BH_3 reaction, showing that these reactions probably did not proceed. Neither is there any evidence that the lithium analogue, $Li^+[BH_3NH_2BH_3]^-$, formed during the $LiNH_2$ + NH_3BH_3 reaction. The continued presence of $LiNH_2$ at the end of the reaction is therefore attributed to the partial decomposition of NH_3BH_3 during the exothermic reaction upon mixing the reagents.

The information gained from powder XRD patterns about the 2:1 reaction pathway is summarised in reaction 5.5, the 1:1 pathway in reaction 5.6 and the $LiNH_2$ reaction is shown in reaction 5.7.

$$LiH + 2NH_3BH_3 \rightarrow \text{Tetragonal phase} \rightarrow \text{Amorphous product} + LiBH_4$$ Reaction 5.5

$$LiH + NH_3BH_3 \rightarrow \tfrac{1}{2}LiH + \text{Tetragonal phase}$$ Reaction 5.6

$$LiNH_2 + NH_3BH_3 \rightarrow xLiNH_2BH_3 + (1-x)LiNH_2 \rightarrow \text{Amorphous product}$$ Reaction 5.7

5.4 Thermal Desorption Studies

5.4.1 TPD Study of $LiNH_2BH_3$

The gaseous thermal desorption properties of pre-prepared $LiNH_2BH_3$, through the $LiNH_2 + NH_3BH_3$, reaction were investigated using TPD–MS. The sample was heated at a ramp rate of 2°C min^{-1} to 350°C. The collected data are shown in figure 5.15.

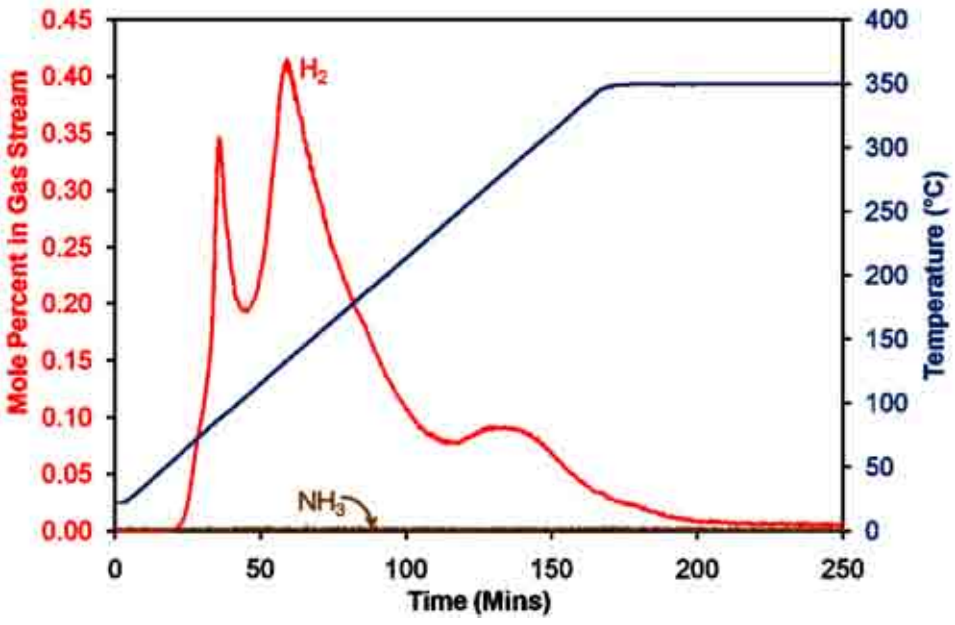

Figure 5.15 – Thermal desorption analysis of a sample of $LiNH_2BH_3$ using a TPD apparatus. The temperature trace is shown in blue and the mole percentages of H_2 and NH_3 released are shown in red and brown, respectively

It can be seen that there were three hydrogen release steps during the desorption experiment, which were free from ammonia pollution. The first release commenced at 55°C and peaked at 87°C, with the second release beginning at 100°C and peaking at 130°C and also seeing a greater amount of hydrogen released. The final broad release started at 245°C and reached a maximum at 275°C.

Discussion

Literature reports regarding the thermal desorption of $LiNH_2BH_3$ have shown that exclusively hydrogen is released. Temperature ramping experiments have shown that the material vigorously releases H_2 below 100°C, with this sharp release observed at either 92°C[4, 15] or 86°C.[5] These studies also identified a second small broad H_2 desorption at 120°C. These earlier reports did not agree with the thermal desorption profile presented here. This may have been due to the presence of other amorphous materials in the sample. As discussed in section 5.3.2, the release of NH_3 during the $LiNH_2$ + NH_3BH_3 reaction led to the possibility of the amorphous material $Li(NH_3)NH_2BH_3$ also forming. Xia *et al.*[9] reported that this material releases H_2 at a lower temperature than $LiNH_2BH_3$, with desorption commencing at 40°C and peaking at 71°C. NH_3 release was also observed in the desorption profile between 25 and 150°C. The amorphous material $LiNH_2BH_3NH_3$ identified by Graham *et al.*[8] was also shown to release H_2 at a lower temperature than $LiNH_2BH_3$, with the release commencing at approximately 40°C and peaking at 60°C. Therefore figure 5.15 suggests that the sample contained both amorphous $Li(NH_3)NH_2BH_3$, which was responsible for the first H_2 desorption and crystalline $LiNH_2BH_3$, which was responsible for the second H_2 desorption.

None of the literature studies were heated to a sufficiently high temperature to observe the third higher temperature hydrogen release. This higher temperature desorption was due to further H_2 loss from the polymeric decomposition products of both $Li(NH_3)NH_2BH_3$ and $LiNH_2BH_3$.

5.4.2 TPD Study of LiH + $2NH_3BH_3$ Reaction Mixture, Heated to 350°C at a rate of 2°C min^{-1}

The gaseous thermal desorption properties the LiH + $2NH_3BH_3$ reaction mixture were investigated using TPD–MS. The sample was heated at a ramp rate of 2°C min^{-1} to 350°C. The collected data are shown in figure 5.16.

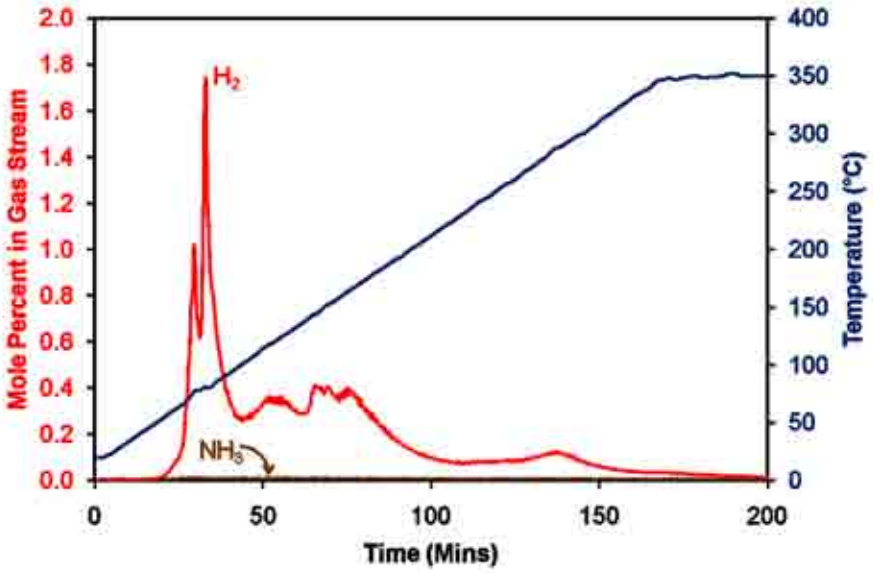

Figure 5.16 – Thermal desorption analysis of the LiH + $2NH_3BH_3$ reaction mixture using a TPD apparatus. The temperature trace is shown in blue and the mole percentages of H_2 and NH_3 released are shown in red and brown, respectively

The onset temperature of H_2 release was observed at 50°C and was followed by two sharp releases, the first of which peaked at 75°C and the second at 80°C. Analysis of the temperature trace showed that both of these events were exothermic, as can be seen by the augmented rate of temperature increase, shown more clearly in figure 5.17. Following these two sharp desorptions the release became much broader in nature. On reaching a temperature of 100°C a third release of H_2 began, which peaked at 120°C. The H_2 trace began to decrease briefly before increasing again at 135°C and this fourth release peaked at 150°C before tailing off. A final small release of H_2 was observed at higher temperatures, which had a peak at 285°C. No NH_3 desorption was observed at any point in the TPD profile.

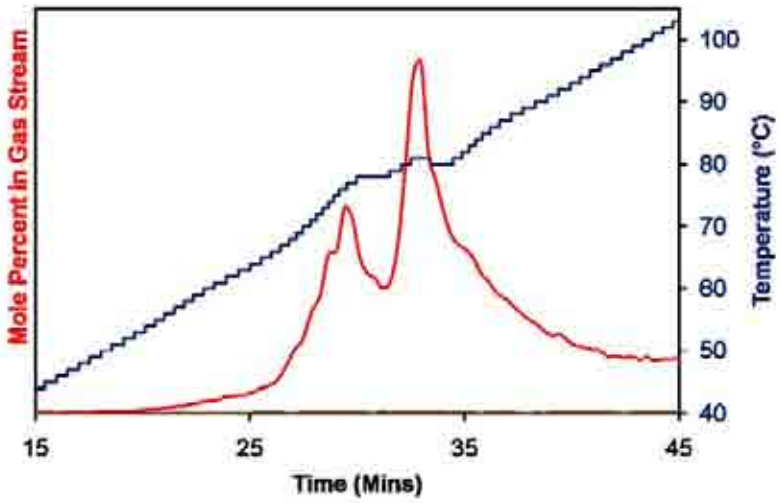

Figure 5.17 – The exothermic events in the TPD profile of the LiH + $2NH_3BH_3$ reaction mixture

Discussion

The powder XRD patterns showed two events in the LiH + $2NH_3BH_3$ reaction pathway. A reaction temperature of 50°C resulted in the formation of the tetragonal crystalline phase and this was followed by the decomposition of this material to an amorphous product, which was completed at a reaction temperature of 150°C. Of the first two desorption events in the TPD profile, observed below a temperature of 80°C, at least one must have been related to the formation of the tetragonal phase. Two possible pathways may have proceeded in the room temperature to 80°C range of the desorption profile. Firstly, only one of these H_2 desorptions was related to the formation of the tetragonal phase, with the second release being related to an alternative reaction pathway, resulting in amorphous products. However, in light of the results of other studies, it would appear to be more rational to assign both of these desorption events to the formation of the tetragonal phase.[13, 14] As previously discussed reports in the literature detailed that the tetragonal phase formation arose from $LiNH_2BH_3{\cdot}NH_3BH_3$ decomposition. However, due to the thermal nature of the reactions in our study, this material was unstable and subsequently led to the rapid formation of the tetragonal phase. Both of these steps have been shown to release exclusively H_2. The initial release may therefore have been related to the mechanism that forms $LiNH_2BH_3{\cdot}NH_3BH_3$. Furthermore the formation of this material has been shown to be an exothermic event, which explains why an exotherm was observed in

the temperature trace of the TPD study.[13] However, because $LiNH_2BH_3{\cdot}NH_3BH_3$ melts at 58°C, it would not have been able to crystallise, with the sample instead being constituted of a mixture of $LiNH_2BH_3$ and NH_3BH_3, in amorphous or liquid forms, and unreacted LiH. This first release began to decrease before the second H_2 release commenced, which suggested that the melt briefly existed in the reaction mixture. The second release of H_2 would consequently have been due to the formation of the tetragonal phase, which agreed with the reported decomposition temperature of $LiNH_2BH_3{\cdot}NH_3BH_3$ of 80°C in temperature ramping experiments.[13]

The reported desorption profile of $LiNH_2BH_3{\cdot}NH_3BH_3$, which proceeds through the tetragonal phase, showed a second strong desorption of H_2 at 140°C and a third weak desorption at 160°C. The two H_2 release events observed between 100°C and 160°C in figure 5.16, can therefore be assigned to the decomposition of the tetragonal phase. The fact that there were differences in the amount of H_2 released in these two steps between this study and the desorption profile found in the literature was possibly down to different experimental setups. Powder XRD results showed that the product of the $LiH + 2NH_3BH_3$ reaction at temperatures above 150°C was amorphous, therefore these two desorption events resulted in the formation of an amorphous material. The literature study of the desorption profile of $LiNH_2BH_3{\cdot}NH_3BH_3$ was not heated to a sufficient temperature to observe the higher temperature release observed at 285°C in this study. This desorption can be assigned to further decomposition of the amorphous material.

5.4.3 TPD Study of LiH + $2NH_3BH_3$ Reaction Mixture, Heated to 60°C at a rate of 0.1°C min^{-1}

In order to further investigate the initial steps in the LiH + $2NH_3BH_3$ reaction pathway, namely the formation of the tetragonal phase, the TPD experiment was repeated with experimental parameters that imitated the conditions employed during the synthesis of the tetragonal phase. Thermal desorption data was collected using a ramp rate of 0.1°C min^{-1} to a target temperature of 60°C. The collected data are shown in figure 5.18.

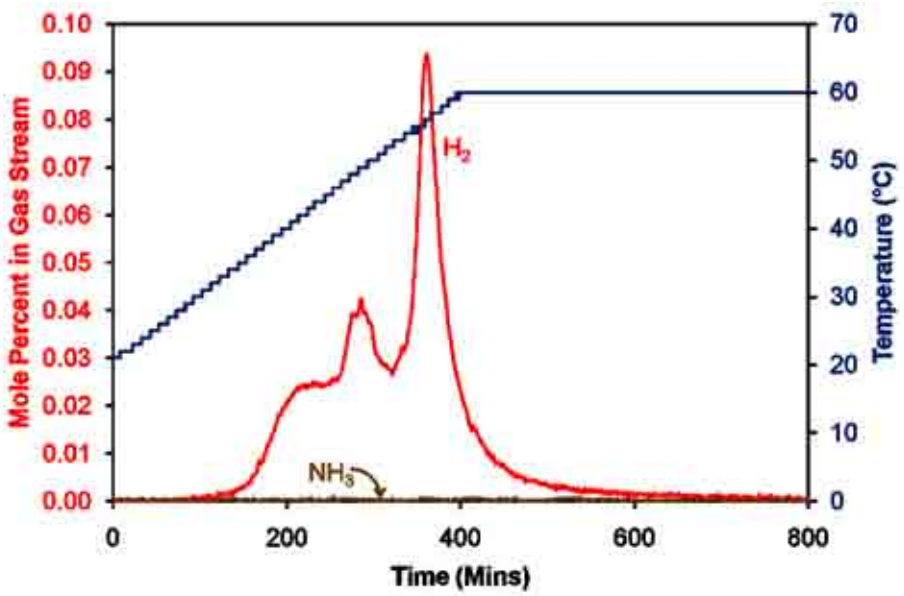

Figure 5.18 – Thermal desorption analysis of the LiH + $2NH_3BH_3$ reaction mixture using a TPD apparatus, under conditions employed during the synthesis of the tetragonal phase. The temperature trace is shown in blue and the mole percentages of H_2 and NH_3 released are shown in red and brown, respectively

It can be seen that there were three events observed in the desorption profile. H_2 was exclusively released from the reaction mixture, with the release effected at a temperature as low as 30°C. The release increased before reaching a plateau at 40°C. A second release occurred between 45 and 50°C, with a peak at 47°C. The final release commenced at 50°C and peaked at 55°C, before decreasing prior to the achievement of the target temperature of 60°C.

Figure 5.19 shows this TPD–MS data processed so as to give simulated gravimetric data, as discussed in chapter 2.5. There was a total weight loss of 3.1 wt%, which equated to the loss of approximately one equivalent of H_2.

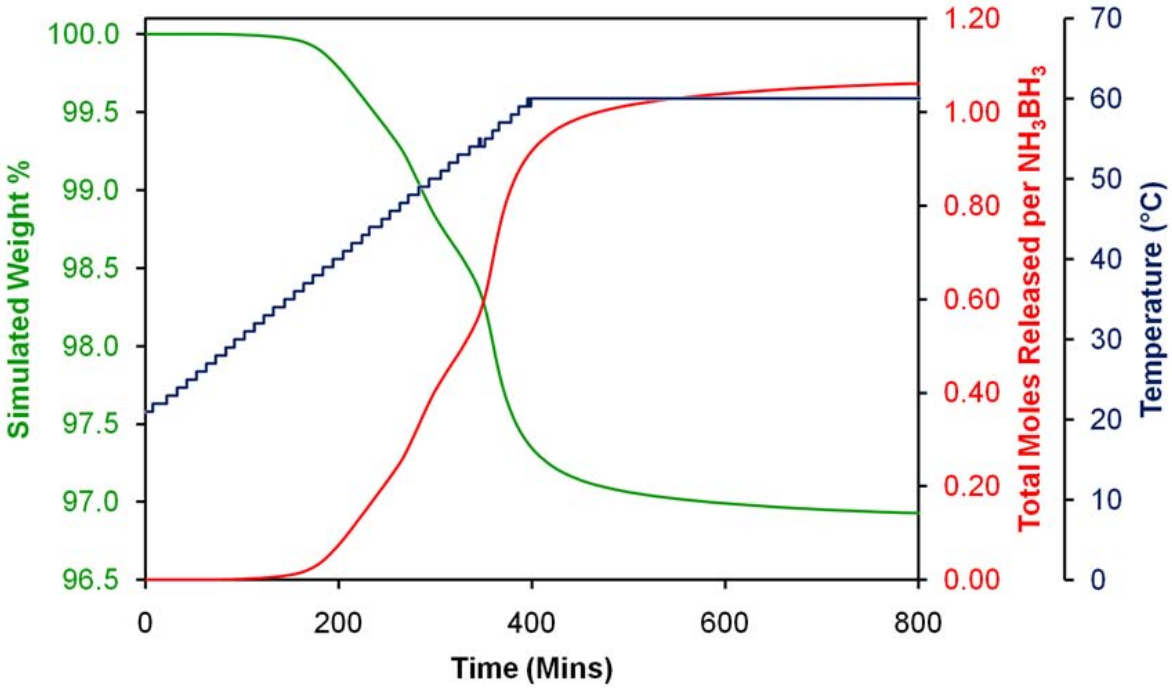

Figure 5.19 – Thermal desorption analysis of a LiH + $2NH_3BH_3$ reaction mixture in a TPD apparatus processed to give simulated gravimetric data. The temperature trace is shown in blue, the moles of H_2 released are shown in red and the simulated gravimetric data in green

Discussion

The release of only one equivalent of H_2 was an interesting result because the study by Wu *et al.*[13] concluded that thermal decomposition of $LiNH_2BH_3{\cdot}NH_3BH_3$ resulted in the tetragonal phase formation through the desorption of two equivalents of H_2, meaning a total of three equivalents of H_2 were desorbed from a LiH + $2NH_3BH_3$ reaction mixture before the tetragonal phase formed. The release of one equivalent of H_2, with a weight loss of 3.1 wt% from the starting mixtures suggested that reaction 5.8 had taken place.

$$LiH + 2NH_3BH_3 \rightarrow LiNH_2BH_3{\cdot}NH_3BH_3 + H_2 \qquad 2.9\ wt\%\ H_2 \qquad \text{Reaction 5.8}$$

Following the TPD experiment the sample could not be recovered for analysis by powder XRD analysis. However, as the conditions employed were identical to those

used in the thermal reactions carried out on an argon gas line, it was reasonable to assume that the products were the same and hence that the sample left at the end of the TPD experiment was that of the unidentified tetragonal phase. This suggested that the $LiNH_2BH_3{\cdot}NH_3BH_3$ to tetragonal phase change was not in fact due to decomposition through H_2 desorption, but in fact a rearrangement reaction that proceeded without desorption of H_2 or any other gas. The discrepancy with the study by Wu *et al.* may have been due to the fact that Wu *et al.* pre-synthesised $LiNH_2BH_3{\cdot}NH_3BH_3$ through ball milling and so it was present in the sample at the start of the experiment. Two reaction pathways may have therefore competed, the decomposition of $LiNH_2BH_3{\cdot}NH_3BH_3$ to amorphous material but also the rearrangement reaction leading to the tetragonal phase, subsequently Wu *et al.* would only have observed the crystalline product through XRD analysis. In our study it has been proposed that the thermal reactions prevented the formation of $LiNH_2BH_3{\cdot}NH_3BH_3$. The fact that the tetragonal phase was able to form during thermal reactions showed that it was more stable than $LiNH_2BH_3{\cdot}NH_3BH_3$ and so formation of the tetragonal phase was favoured.

5.4.4 TPD–MS Study of the Tetragonal Phase

The gaseous thermal desorption properties from the pre-synthesised tetragonal phase through a gas line reaction at 50°C were investigated using TPD–MS. The desorption profile collected at a ramp rate of 2°C min^{-1} to a target temperature of 350°C is shown in figure 5.20.

The desorption profile showed that H_2 was exclusively desorbed from the tetragonal phase. H_2 release began at 65°C when a small broad release began, the peak of which occurred at 120°C. This was followed by the largest H_2 desorption event, which commenced at 130°C and peaked at 150°C. A final small release began at 240°C and peaked at 275°C.

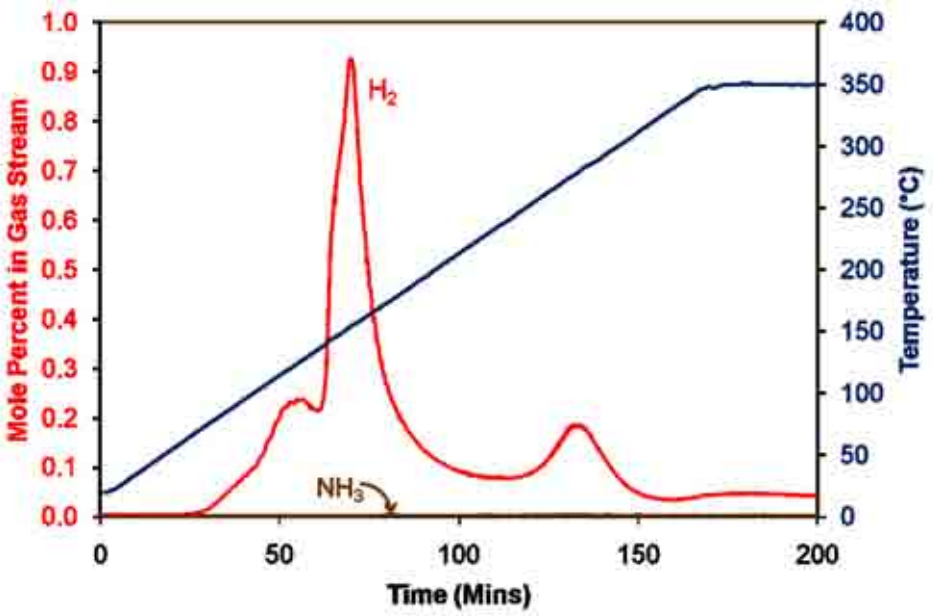

Figure 5.20 – Thermal desorption analysis of a sample of the tetragonal phase using a TPD apparatus. The temperature trace is shown in blue and the mole percentages of H_2 and NH_3 released are shown in red and brown, respectively

Discussion

Powder XRD results showed that the tetragonal phase decomposed at a reaction temperature of 140°C. Therefore the large H_2 desorption event peaking at 150°C can be assigned to the decomposition of the tetragonal phase. This release of H_2 from the tetragonal phase resulted in the formation of amorphous material. The higher temperature release of H_2 was due to the decomposition of this amorphous material. The lower temperature desorption event was at too low a temperature for it to be expected to be related to the decomposition of the tetragonal phase. Therefore the tetragonal phase may not have been the only phase present in the sample showing that the LiH + $2NH_3BH_3$ reaction was subject to side reactions. $LiNH_2BH_3{\cdot}NH_3BH_3$ has been shown to decompose in this temperature range.[13] $LiNH_2BH_3{\cdot}NH_3BH_3$ was not observed in the powder XRD patterns in this study, because the dihydrogen bonding network that gives the structure added stability was unable to form. If there was an amorphous form of this material present in the sample it may have undergone decomposition at similar temperatures, offering an explanation for the low temperature H_2 desorption.

5.4.5 IGA–MS Study of the Tetragonal Phase

A sample of the pre-synthesised tetragonal phase (81 mg) was inertly loaded into an IGA connected to a mass spectrometer. Figure 5.21 shows the thermogravimetric data overlaid with the mass spectrometric data for the observed desorption products. The same conditions as employed in the TPD experiment were used, with the sample heated at a rate of 2°C min^{-1} to a target temperature of 350°C.

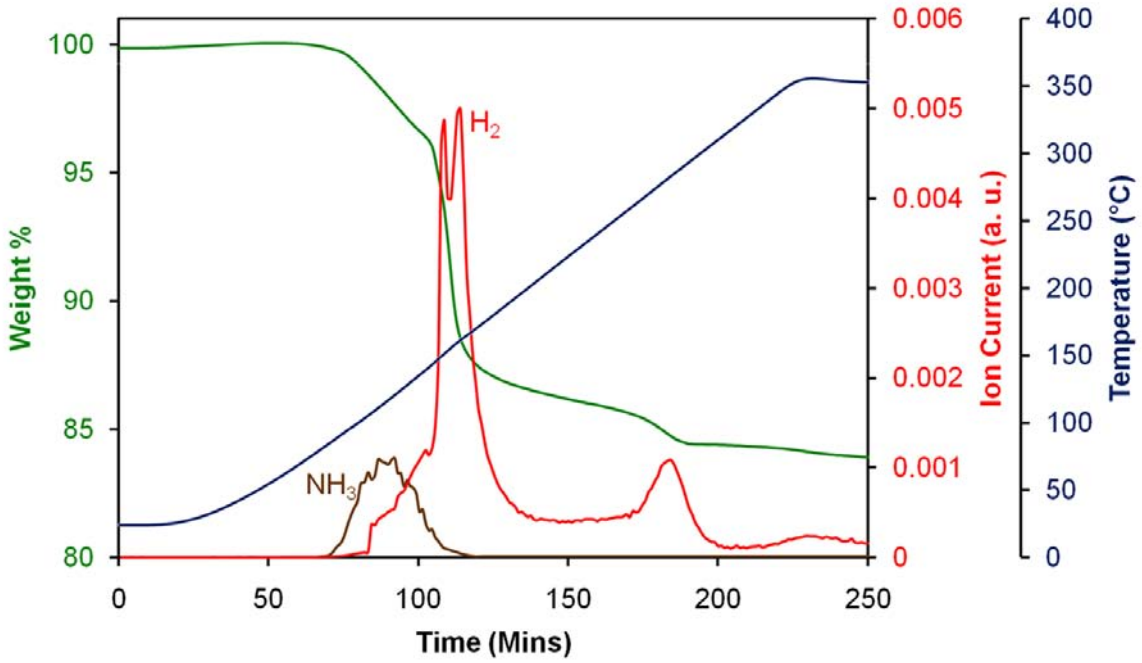

Figure 5.21 – Thermogravimetric analysis of the tetragonal lithium phase in an IGA. The gravimetric trace is shown in green, the temperature trace in blue and the signals detected by mass spectrometry of H_2 in red and NH_3 (×100) in brown

The IGA–MS trace showed that H_2 release began at 100°C, the release of H_2 initially increased steadily, until a temperature of 135°C was achieved, at which point a significant increase in the amount of H_2 release occurred. This desorption event showed two peaks at 145°C and 160°C. A small desorption of H_2 was observed to commence at 255°C, peaking at 275°C and a final small release was observed above 330°C. This desorption profile was very similar to that observed in the TPD–MS experiment, however, the IGA–MS experiment also showed NH_3 desorption from the tetragonal phase. This desorption began at 75°C and peaked at 110°C, with no NH_3 release observed above 150°C.

The rate of weight loss from the sample showed five separate events. The first of which showed a weight loss of 3.6 wt% up to a temperature of 145°C, which was primarily due to NH_3 release, although H_2 desorption would also have contributed to this weight loss. The largest H_2 desorption was accompanied by a weight loss of 9.4 wt%. Between 165°C and 255°C, where the H_2 desorption profile reached a plateau, a further weight loss of 1.4 wt% occurred. The H_2 desorption between 255°C and 275°C was accompanied by a weight loss of 1.1 wt% and above this temperature a further weight loss of 0.6 wt% was observed. This was a total weight loss of 16.1 wt% from the sample, with H_2 desorption being responsible for a loss of approximately 12.5 wt%.

Discussion

The low temperature NH_3 release offered an alternative explanation to the reason behind the observed H_2 desorption below the decomposition temperature of the tetragonal phase in both the TPD and IGA studies of the tetragonal phase. NH_3 desorption has been shown to be dependent on the setup of the desorption experiment. In a flowing system, NH_3 release is detectable, whereas in a closed system H_2 is often detected instead.[21, 22] In the flowing system the carrier gas removes the NH_3 from the surroundings of the sample, whereas in a closed system the NH_3 is able to interact with the sample and this can result in the release of H_2 instead. The TPD setup was such that the argon carrier gas did not flow directly over the sample and so any NH_3 released may have been able to interact with the sample, therefore resulting in H_2 being detected by the mass spectrometer. In the IGA experiment, the argon carrier gas passed directly over the sample and hence the NH_3 was removed quickly meaning it was detectable. The H_2 desorption below 130°C in the IGA experiment could have been related to the decomposition of the tetragonal phase.

The higher temperature H_2 desorptions occurred at similar temperature to those in the TPD experiment. Therefore the previous assignments that the main H_2 release at 135°C was due to decomposition of the tetragonal phase and H_2 release above 255°C was due to further release from the decomposition products of this material are valid.

The weight loss of 12.5 wt% due to H_2 release gave an insight into the composition of the tetragonal phase. Wu *et al.*[13] have previously proposed that the tetragonal phase has the composition $LiN_2B_2H_7$. However, a material of this composition contains only 11.1 wt % H_2 and therefore it cannot account for all the observed weight loss. Furthermore, the structure of the material was proposed to be either $LiNHBH_2{\cdot}NH_2BH_2$ or $LiNH_2BH{=}NHBH_3$ and neither of these compositions would appear to be capable of desorbing NH_3. The reported weight loss from $LiNH_2BH_3{\cdot}NH_3BH_3$ due to H_2 desorption is 14.3 wt%.[13, 14] This material contains a total hydrogen content of 16.4 wt% and therefore this material or an isomer of it could have accounted for the observed weight loss in the IGA experiment. This hence adds weight to the proposal that the tetragonal phase formed through a rearrangement reaction from $LiNH_2BH_3{\cdot}NH_3BH_3$ rather than it being a decomposition product of this material.

The release of NH_3 from the tetragonal phase provided an interesting insight into the composition of this material as it showed that the material must have had the potential to desorb NH_3. An isomer of $LiNH_2BH_3{\cdot}NH_3BH_3$ is $[Li(NH_3)]^+[BH_3NH_2BH_3]^-$ which is similar in nature to the material synthesised through the $NaH + 2NH_3BH_3$ reaction, $[Na]^+[BH_3NH_2BH_3]^-$. This material has the potential to release NH_3 as well as having a total H_2 content of 16.4 wt%.

As has been previously discussed the $LiH + 2NH_3BH_3$ reaction was only able to proceed once labile NH_3BH_3 was present in the reaction mixture. LiH would have been able to react with one mole of NH_3BH_3 to form $LiNH_2BH_3$, reaction 5.9, but as the second mole of NH_3BH_3 was also labile, a subsequent reaction of $LiNH_2BH_3$ with NH_3BH_3 would also have been able to proceed. Due to the thermal nature of the reactions, dihydrogen bonds and subsequently $LiNH_2BH_3{\cdot}NH_3BH_3$ would have been unable to form. The $LiNH_2BH_3 + NH_3BH_3$ reaction could have proceeded by either an S_N2 reaction, reaction 5.10, or through a rearrangement mechanism similar to the one that takes place during DADB formation from two NH_3BH_3 molecules, reaction 5.11.

$$LiH + NH_3BH_3 \rightarrow LiNH_2BH_3 + H_2 \qquad \text{Reaction 5.9}$$

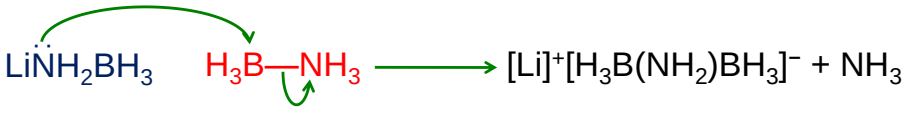

Reaction 5.10

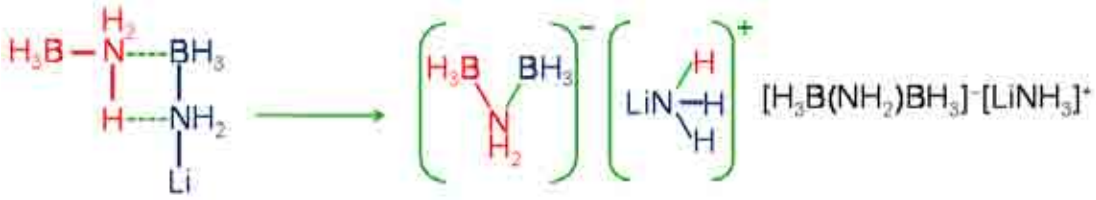

Reaction 5.11

Reactions 5.10 and 5.11 are the same reactions that were proposed for the reaction of $NaNH_2BH_3$ and NH_3BH_3. Thermal desorption investigations of this reaction mechanism showed a significant amount of NH_3 was released during the reaction, chapter 4.4, whereas the formation of the tetragonal phase did not involve NH_3 desorption. The lithium cation is a stronger Lewis acid than the sodium cation and so it is more facile for the released NH_3 to form an adduct with the lithium cation compared to sodium.[23] The calculated binding energy of NH_3 to the sodium cation has been shown to be significantly weaker than to the lithium cation.[24] Therefore the reaction temperatures employed would have been sufficient to prevent bond formation between the sodium cation and NH_3, hence resulting in NH_3 release. Whereas in the lithium reaction mechanism the binding energy was sufficient to allow an adduct to form, hence preventing immediate NH_3 release.

The tetragonal phase formed from a combination of reaction 5.9 and reaction 5.10 or 5.11. Together these reactions show only the release of one equivalent of H_2, which agreed with the simulated gravimetric data from the TPD study of a $LiH + 2NH_3BH_3$ reaction mixture.

With respect to the observation of the tetragonal phase forming from the decomposition of $LiNH_2BH_3{\cdot}NH_3BH_3$ in the literature, this can be explained by the disruption of the dihydrogen bonding network present in this material.[13, 14] The crystal structure, figure 5.22, of this material shows that the $LiNH_2BH_3$ and NH_3BH_3 molecules form layers, held together by dihydrogen bonds.[13] As this material is heated, these bonds break, leaving labile $LiNH_2BH_3$ and NH_3BH_3, which can then react either through reaction 5.10 or reaction 5.11, forming the tetragonal phase.

These reactions occur on heating and because $LiNH_2BH_3{\cdot}NH_3BH_3$ has a low decomposition temperature, 57°C, decomposition of this material can also take place, explaining why these studies observed H_2 desorption during formation of the tetragonal phase.

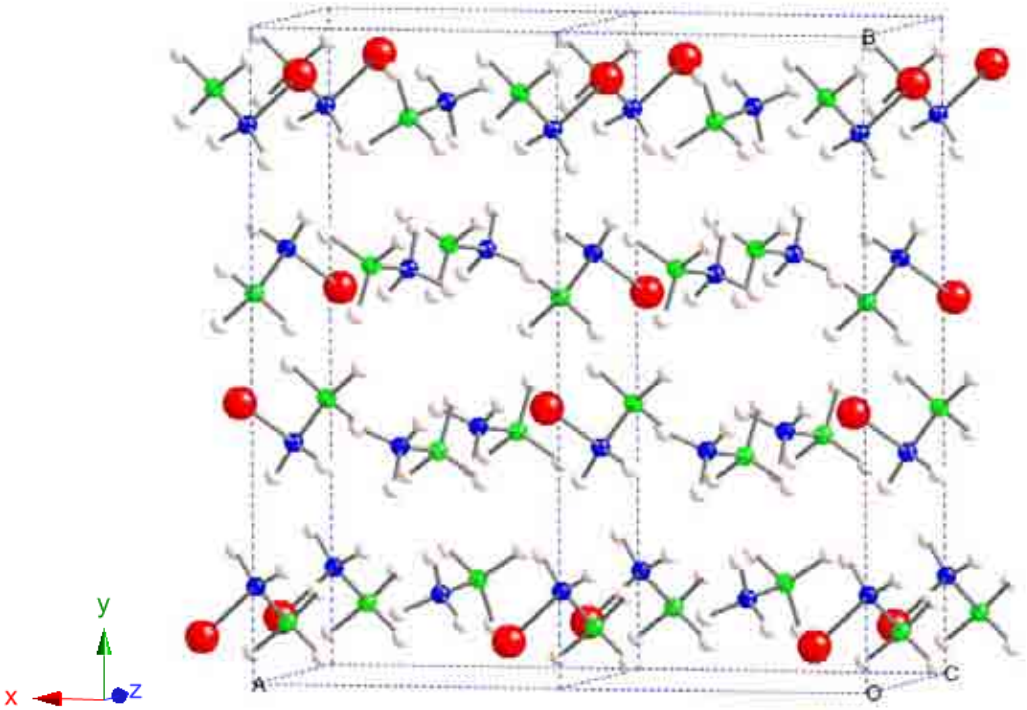

Figure 5.22 – The crystal structure of $LiNH_2BH_3{\cdot}NH_3BH_3$. The lithium atoms are shown in red, nitrogen in blue, boron in blue and hydrogen in pale pink

The weight loss of 16.1 wt% from the tetragonal phase upon heating to 350°C was due to a combination of NH_3 and H_2 desorption. It was estimated that the weight loss due to H_2 release was approximately 12.5 wt%. The release of four equivalents of H_2 from $[Li(NH_3)]^+[BH_3NH_2BH_3]^-$ gives a theoretical weight loss of 11.9 wt%, which would leave a sample of composition $LiN_2B_2H_3$ and the desorption of five equivalents of H_2 would result in a theoretical weight loss of 14.9 wt%, leaving a sample of composition LiN_2B_2H. The composition of the decomposition products will be discussed further in section 5.5.

5.4.6 Comparison of H_2 desorption from the LiH + $2NH_3BH_3$ reaction mixture and $[Li(NH_3)]^+[BH_3NH_2BH_3]^-$ to NH_3BH_3

Figure 5.23 shows a comparison of the TPD profiles of H_2 desorption from as-received NH_3BH_3, the LiH + $2NH_3BH_3$ reaction mixture and $[Li(NH_3)]^+[BH_3NH_2BH_3]^-$. It can be seen that the reaction mixture has a lower onset of H_2 release compared to NH_3BH_3, with the onset temperature decreased from 85°C to 50°C when LiH is present. However, the main H_2 desorption from $[Li(NH_3)]^+[BH_3NH_2BH_3]^-$ occurred at a higher temperature than the first H_2 desorption of NH_3BH_3 and at a similar temperature to that of the second H_2 desorption from NH_3BH_3.

In terms of improving the H_2 release properties of NH_3BH_3, it can be seen that the presence of LiH has a positive effect, by decreasing the onset temperature of H_2 release, while also maintaining the sharp nature of this low temperature release. However, the pre-synthesised $[Li(NH_3)]^+[BH_3NH_2BH_3]^-$ material showed higher temperature release as well as the release being over a broad temperature range. A positive feature in terms of hydrogen storage is the high H_2 content of this material, 16.4 wt%, with approximately 12.5 wt% H_2 being released below 350°C. However, due to this material containing an NH_3 adduct, there is the problem of NH_3 desorption polluting the released H_2, as shown by the IGA–MS results in figure 5.21.

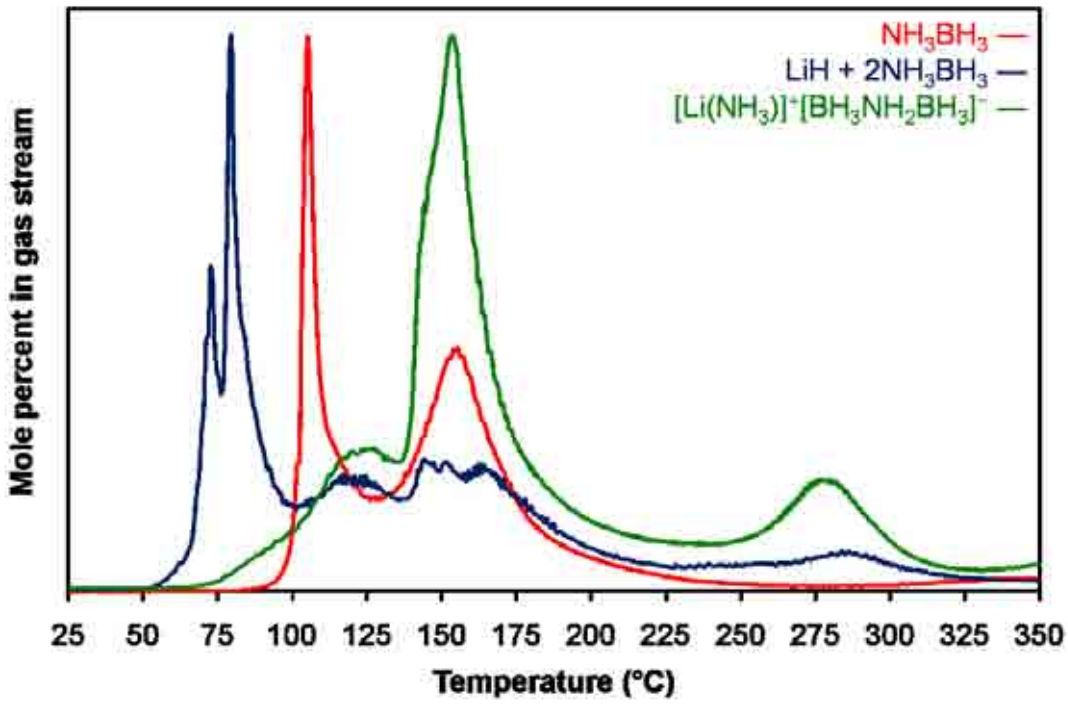

Figure 5.23 – A comparison of the H_2 desorption profiles from samples of NH_3BH_3 (red), a LiH + $2NH_3BH_3$ reaction mixture (blue) and $[Li(NH_3)]^+[BH_3NH_2BH_3]^-$ (green) from TPD experiments

5.5 Solid State ^{11}B MAS NMR Spectroscopy

The LiH + $2NH_3BH_3$ reaction pathway was studied using solid state ^{11}B MAS NMR spectroscopy to determine how the boron environments changed as the reaction progressed and in particular to provide information regarding the amorphous components of the reaction products. The thermal reactions were carried out on an argon gas line as described in section 5.2. The NMR spectra of the samples were collected at room temperature. The data was collected in collaboration with the University of Warwick. All peak fitting was carried out by Tom Partridge at the University of Warwick.

The solid state ^{11}B MAS NMR spectrum of the product of the $LiNH_2$ + NH_3BH_3 reaction is shown in figure 5.24. A dominant feature was observed at −23.7 ppm, which is characteristic of sp^3 boron in an NBH_3 environment.[25] The second most intense feature was a broad resonance, at 29.9 ppm, which was a quadrupolar feature due to the presence of boron in an sp^2 environment.[26] There was also a very

low intensity resonance present at −40.5 ppm, which can be assigned to a BH_4^- environment.[27]

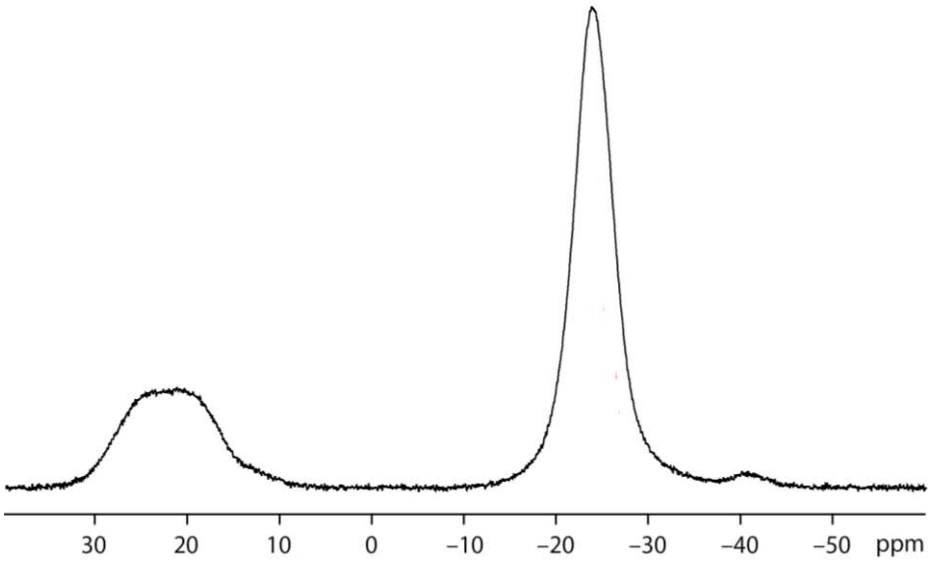

Figure 5.24 – The solid state ^{11}B MAS NMR spectrum of the product of the $LiNH_2$ + NH_3BH_3 reaction at room temperature

The NMR spectrum of the sample obtained after reaction at 50°C is shown in figure 5.25. There are a number of distinct boron environments in the spectrum. The most intense of which was observed at −24.0 ppm, which is characteristic of a NBH_3 environment. The broad quadrupolar feature at 29.9 ppm showed the presence of boron in an sp^2 environment and the low intensity feature found at −41.0 ppm is characteristic of BH_4 type boron.

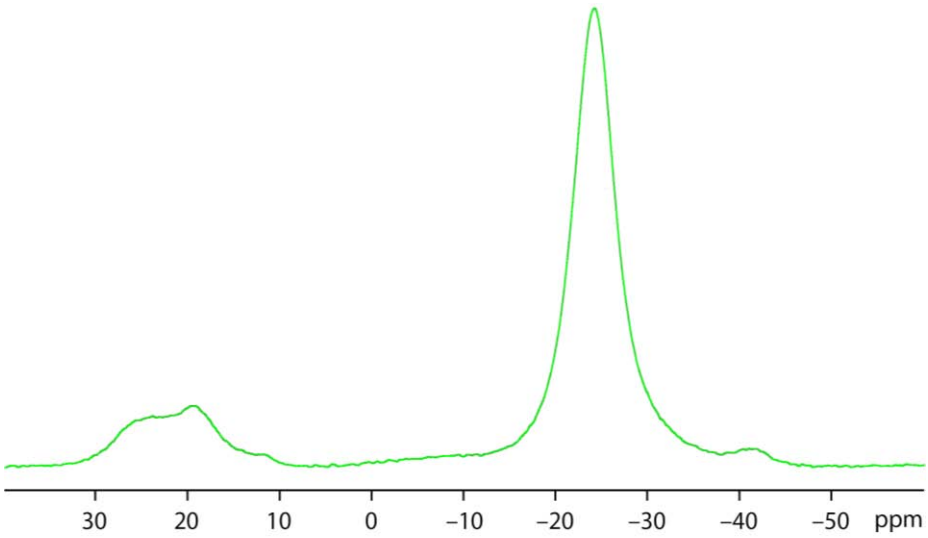

Figure 5.25 – The solid state ^{11}B MAS NMR spectrum of the product of the LiH + $2NH_3BH_3$ reaction at 50°C

The complete LiH + $2NH_3BH_3$ reaction pathway as viewed from solid state ^{11}B MAS NMR spectra is shown in figure 5.26. The spectra show that there were only small changes in the boron environments within the samples upon increasing the reaction temperature from 50°C to 100°C. Throughout this temperature range the most intense feature in the spectra was the one due to boron within an sp^3 environment. This feature was again observed at −24.0 ppm at 60°C but shifted slightly after reaction at 80°C and 100°C to −23.8 ppm. The BH_4 feature remained low intensity up to a temperature of 80°C, consistently with a chemical shift of −41.0 ppm, before its intensity increased slightly at 100°C and a slight downfield shift to −40.5 ppm occurred. The broad quadrupolar feature due to an sp^2 boron environment retained the same chemical shift at these reaction temperatures, 29.9 ppm. A steady increase in the intensity during this temperature range was observed for this feature.

After reaction at 120°C, a significant change was observed in the NMR spectrum. The sp^3 boron feature showed a considerable decrease in intensity and also shifted downfield slightly to −23.5 ppm. This was accompanied by substantial increases in the intensities of both of the features due to boron in sp^2 and BH_4 environments. No change in the chemical shift of the quadrupolar sp^2 feature was observed, although the BH_4 resonance shifted upfield to a chemical shift of −41.4 ppm. There was minimal change in the spectrum upon heating to 150°C, the relative intensities of the features remained the same, while there were only slight changes in the chemical shifts of the sp^3 feature, to −24.1 ppm, and the BH_4 feature to −41.2 ppm.

Further changes to the spectrum were observed after reaction at 250°C. The feature due to boron in an sp^3 environment was of very low intensity and had also shifted downfield slightly to −23.3 ppm. The BH_4 feature also showed decreased intensity and had a chemical shift of −41.3 ppm. The most intense feature in the spectrum was that of the broad sp^2 resonance. Reaction at 400°C produced a spectrum that was dominated by the broad sp^2 resonance. There was no evidence of a feature due to boron in an sp^3 environment and only a very weak feature at −41.0 ppm showing the sample contained a small amount of boron in a BH_4 environment.

A number of the spectra possessed a low intensity feature at 0.7 ppm, this resonance was due to oxidation of the samples and will not be discussed further.

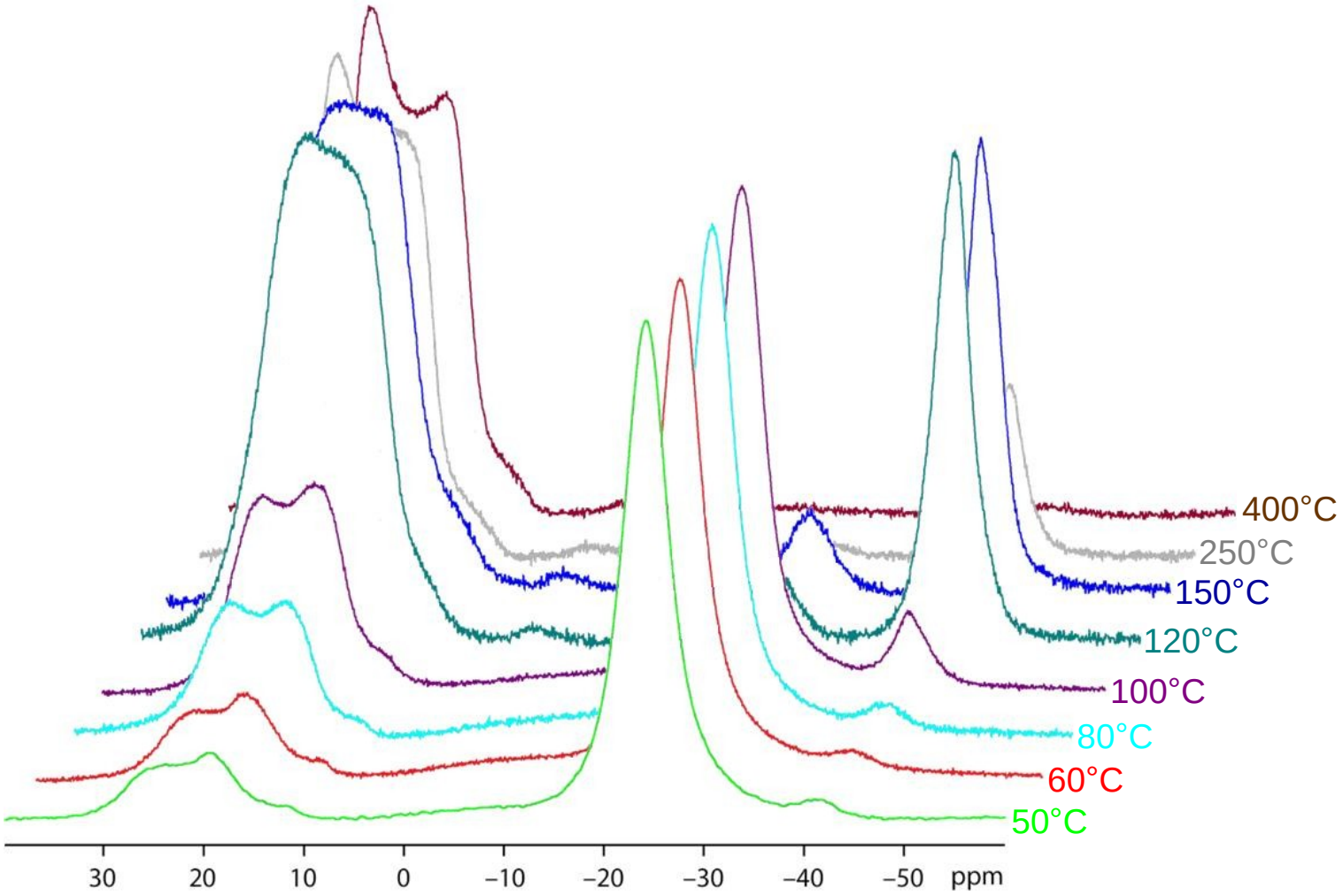

Figure 5.26 – Solid state ^{11}B MAS NMR spectra obtained from the products of the LiH + $2NH_3BH_3$ reaction at specified temperatures

5.5.1 Discussion

Powder XRD results showed that the crystalline product of the $LiNH_2$ + NH_3BH_3 reaction was $LiNH_2BH_3$, although thermal desorption investigations suggested that the amorphous phase $Li(NH_3)NH_2BH_3$ had also formed. Literature studies have shown that these two materials produce different ^{11}B NMR spectra. The solid state ^{11}B NMR spectrum of $LiNH_2BH_3$ shows a single resonance at −22.9 ppm,[4] while that of the ammoniated material has a single resonance at −23.2 ppm.[9] Therefore it may have been expected that the NMR spectrum of the product of the $LiNH_2$ + NH_3BH_3 reaction displayed two resonances at similar chemical shifts to these materials. The single resonance observed in the spectrum, however, disagreed with this hypothesis. The chemical shift, −23.7 ppm, of this resonance was also shifted upfield compared to the literature values of $LiNH_2BH_3$ and $Li(NH_3)NH_2BH_3$. The NMR spectrum therefore showed that the sample contained only one BH_3 environment. The fact that the chemical shift of this environment was shifted upfield compared to $LiNH_2BH_3$ was a good indication that the product of the $LiNH_2$ + NH_3BH_3 reaction was an ammoniated material. Similar observations have been made when ammoniating $Ca(BH_4)_2$, with the chemical shift of $Ca(BH_4)_2$ observed at −32.7 ppm, while that of the ammoniated compound was observed at −34.7 ppm.[22] Ammoniated $Ca(NH_2BH_3)_2$ also shows an upfield shift from −17 ppm in $Ca(NH_2BH_3)_2$ to −21 ppm.[21] The presence of coordinated NH_3 results in electron donation to the lithium and consequently an upfield shift in the position of the BH_3 resonance due to increased shielding. Therefore the material responsible for the resonance at −23.7 ppm was most likely $Li(NH_3)NH_2BH_3$. However, it is unclear as to why $LiNH_2BH_3$ would have been absent from the sample. This may in part have been due to the delay between sample synthesis and spectrum collection, with residual NH_3 in the glove box binding to $LiNH_2BH_3$, forming the ammoniated material. It seems unlikely, however, that this would have resulted in the complete absence of $LiNH_2BH_3$ from the sample.

In section 5.3.2 it was hypothesised that remaining $LiNH_2$ in the product of the $LiNH_2$ + NH_3BH_3 reaction was due to the decomposition of NH_3BH_3. This hypothesis was supported by the ^{11}B NMR spectrum of this product. The broad quadrupolar resonance due to the presence of boron in an sp^2 environment at 29.9 ppm is also

observed in the decomposition product of NH_3BH_3, see chapter 3.6. Therefore, this resonance could at least in part have been due to decomposed NH_3BH_3. The appearance of a resonance at −41.0 ppm has been observed in the ^{11}B NMR spectra of both decomposed $LiNH_2BH_3$ and $Li(NH_3)NH_2BH_3$.[4, 9] These spectra also showed that the decomposition products of these materials primarily possessed boron in an sp^2 environment. The broad quadrupolar feature at 29.9 ppm and the low intensity feature at −40.5 ppm can therefore be assigned to decomposition of these materials.

Peak fitting of the ^{11}B NMR spectra obtained from the products of the $LiH + 2NH_3BH_3$ reactions allowed the percentages of the different boron environments within the samples to be determined. The results are shown in figure 5.27.

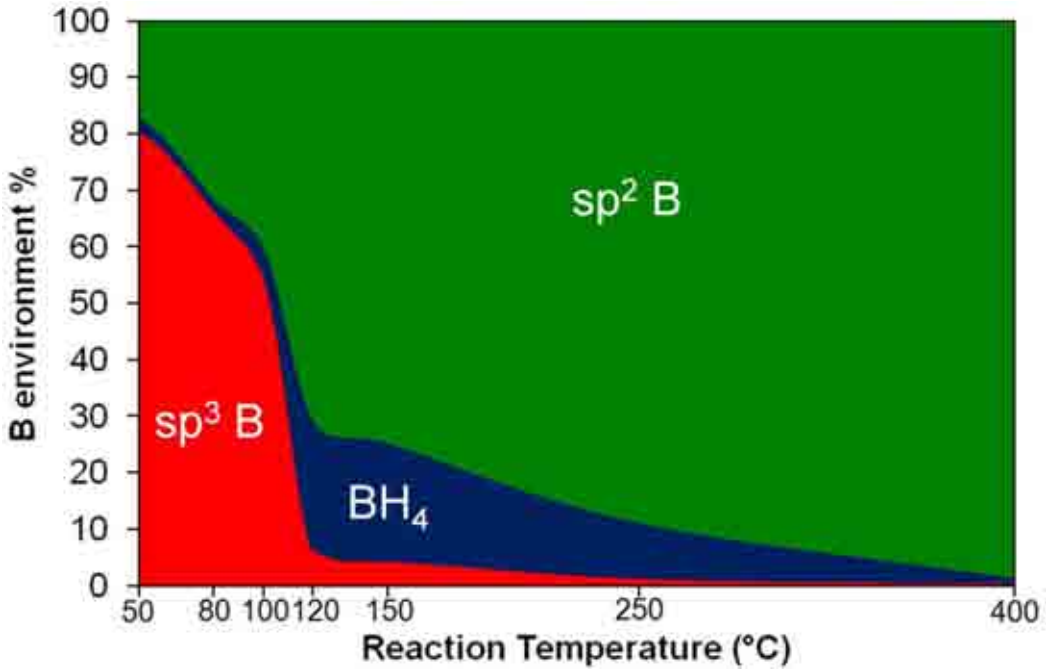

Figure 5.27 – The percentage of boron in different environments in the samples collected from the $LiH + 2NH_3BH_3$ reactions at various temperatures, determined from peak fitting of the solid state ^{11}B MAS NMR spectra

Thermal desorption investigations of the tetragonal phase, resulted in the conclusion that this phase was of composition $[Li(NH_3)]^+[BH_3NH_2BH_3]^-$. Due to the symmetrical nature of the $BH_3NH_2BH_3$ chain only one resonance would be expected in the solid state ^{11}B NMR spectrum related to boron in an sp^3 environment, at approximately −23 ppm as observed in $LiNH_2BH_3$.[4] Peak fitting of the ^{11}B NMR spectrum of the product of the $LiH + 2NH_3BH_3$ reaction at 50°C showed that around 80% of the boron

in the product was in an sp^3 environment, with 2.5% present as BH_4 and 17.5% in an sp^2 environment. This spectrum showed that the main product of the LiH + $2NH_3BH_3$ reaction at 50°C was primarily that of $[Li(NH_3)]^+[BH_3NH_2BH_3]^-$, however, the presence of both BH_4 and sp^2 boron environments showed that other reactions were also taking place. The chemical shift of the main resonance in the spectrum, −24.0 ppm, was supportive of the proposal that the tetragonal phase contained an NH_3 molecule bound to the Li cation. The chemical shifts of BH_3 groups in the metal amidoboranes are observed at lower chemical shifts than this and several NMR studies on ammoniating materials have shown that the resonance experiences a shift upfield due to electron donation from the NH_3 to the metal cation.[4, 9, 21, 22] The chemical shift of this boron resonance therefore supports the presence of an NH_3 adduct within the tetragonal phase.

On increasing the reaction temperature to 100°C there was a decrease in the percentage of boron within an sp^3 environment, which was accompanied by an increase in the amount of sp^2 boron. This showed that the decomposition of $[Li(NH_3)]^+[BH_3NH_2BH_3]^-$ led to the formation of a material possessing boron only in an sp^2 environment. During this temperature range there was no increase in the amount of boron present as BH_4. This partial decomposition of $[Li(NH_3)]^+[BH_3NH_2BH_3]^-$ below 100°C also showed that the observed H_2 release from this material below this temperature in thermal desorption studies, section 5.4, was related to this decomposition as well as the other possibilities previously discussed. Figure 5.27 shows that reaction at 120°C resulted in a significant amount of decomposition of $[Li(NH_3)]^+[BH_3NH_2BH_3]^-$ with the change in boron environment mostly from sp^3 to sp^2, although there was also an increase in the amount of boron present as BH_4. The appearance of BH_4 in the reaction pathway was only detected by powder XRD patterns in minimal amounts. The chemical shift of the BH_4 resonance was consistent with that observed in crystalline $LiBH_4$.[28] Furthermore, because $NaBH_4$ was observed in the decomposition pathway of $[Na]^+[BH_3NH_2BH_3]^-$ it would be reasonable to expect $LiBH_4$ to form during the decomposition of $[Li(NH_3)]^+[BH_3NH_2BH_3]^-$. The reaction temperatures employed may have been insufficient to promote the crystallisation of $LiBH_4$ and hence it was not observed in powder XRD patterns. The percentage of BH_4 in the sample decreased upon heating to 250°C, showing that the $LiBH_4$ had

partly decomposed and after reaction at 400°C there was very little $LiBH_4$ remaining in the sample. The decomposition of $LiBH_4$ after heating to 250°C has been reported, although the main decomposition event occurs at 453°C.[29] The decreased BH_4 resonance was accompanied by an increase in the sp^2 resonance. This is a discrepancy with the known decomposition pathway of $LiBH_4$. The ultimate decomposition product has been shown to be elemental boron, which produces a broad resonance in ^{11}B NMR spectra over 2 ppm.[30] Further to this a number of studies have identified an intermediate product in the decomposition pathway as $Li_2B_{12}H_{12}$, which produces a resonance at −12 ppm.[30] Neither of these two resonances were observed in any of the spectra of this study, suggesting that the non-crystalline state of $LiBH_4$ must have affected its decomposition pathway.

The weight loss observed in the IGA–MS study of $[Li(NH_3)]^+[BH_3NH_2BH_3]^-$, section 5.4, implied that the decomposition product of this material was of composition $LiN_2B_2H_3$. This composition was probably a combination of a number of materials. It has been established that one of the decomposition products involved the BH_4^- ion. The remaining decomposition products must have contained boron in an sp^2 environment. Therefore potential products included Li_3BN_2, $(LiNBH)_n$, $(NHBH)_n$ and BN. All of these materials produce broad quadrupolar resonances in solid state ^{11}B NMR spectra at similar chemical shifts and therefore it was not possible to determine which of these sp^2 boron containing materials formed.[4, 31-33]

Wu *et al.*[13] concluded that the tetragonal phase was of composition $LiN_2B_2H_7$ and could be either $LiNHBH_2{\cdot}NH_2BH_2$ or $LiNH_2BH{=}NHBH_3$. These compositions were based on solid state ^{11}B NMR measurements, which showed the tetragonal phase produced resonances at −24.1 ppm and 29.9 ppm, in agreement with the results presented here. The $LiNH_2BH{=}NHBH_3$ possibility does not appear to fit with the NMR results, as this material possesses boron in two environments, both of which would account for 50% of the boron in the compound, which disagrees with the results from peak fitting. The authors noted that the NMR spectrum resembled that of polyaminoborane, which suggested that the $LiNHBH_2{\cdot}NH_2BH_2$ was a polymeric product.[25, 31] However, as discussed above, the weight loss observed in IGA

experiments along with the observed NH_3 desorption showed that the tetragonal phase could not have been of this composition.

5.6 Raman Spectroscopy

The Raman spectrum collected from the product of the LiH + $2NH_3BH_3$ reaction heated to 50°C is shown in figure 5.28, showing the different regions of the spectrum.

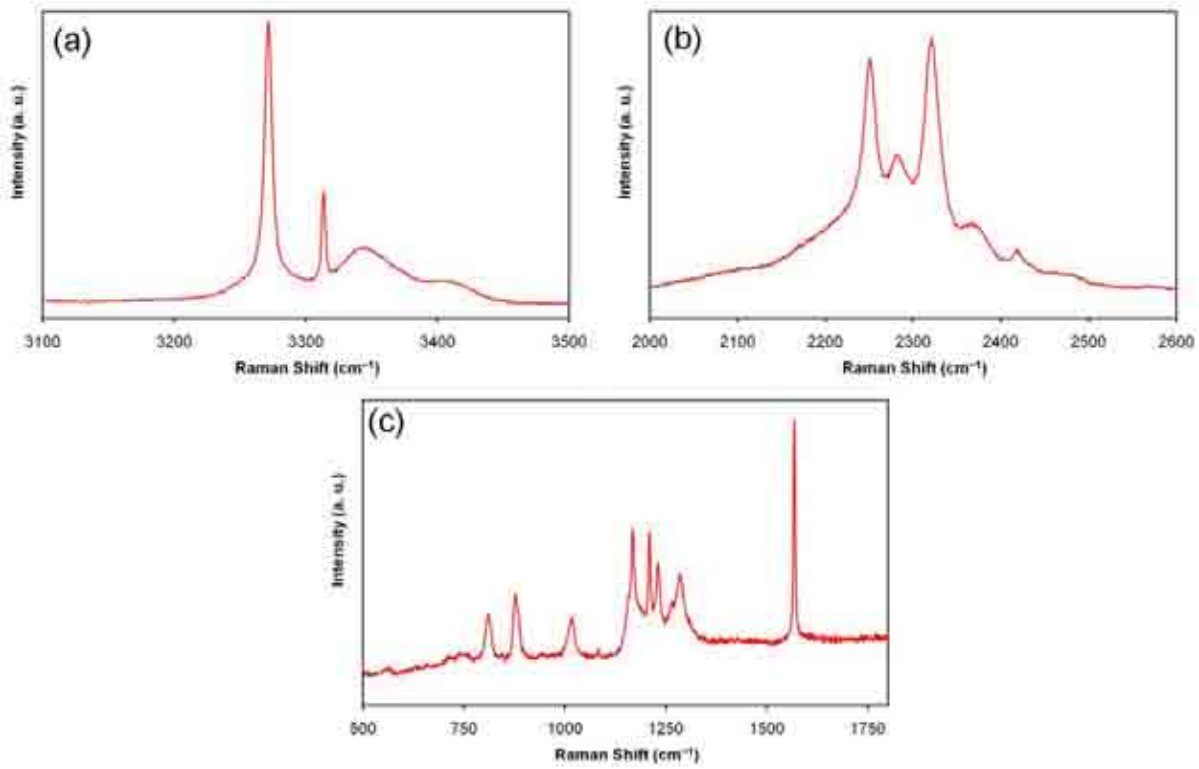

Figure 5.28 – The Raman spectrum collected from the product of the LiH + $2NH_3BH_3$ reaction at 50°C, $[Li(NH_3)]^+[BH_3NH_2BH_3]^-$, showing (a) the N–H stretching region, (b) the B–H stretching region, (c) the deformation region

The N–H stretching region, figure 5.28a, shows two distinct shapes of peaks, with two sharp bands observed at 3271 cm^{-1} and 3314 cm^{-1} and two broader less intense bands at 3347 cm^{-1} and 3410 cm^{-1}. The two sharp bands are characteristic of N–H symmetric and asymmetric stretches respectively, similar to those observed in $LiNH_2$, confirming the existence of an NH_2 unit in the product. Broad N–H stretches, similar in nature to those present in figure 5.28a, have been observed in ammonia adducts of inorganic materials.[34, 35] The Raman spectrum of NH_3 has been reported by Ninet

et al.[36] and using these assignments the bands observed at 3347 cm^{-1} and 3410 cm^{-1} can be assigned to the N–H symmetric and asymmetric stretches, respectively. The asymmetric stretching mode of NH_3 is observed at 3444 cm^{-1} and upon coordination with a Lewis acid it red-shifts, consistent with the observation here. This provides evidence for coordinated NH_3 within the product of the LiH + $2NH_3BH_3$ reaction at 50°C and as such is consistent with the proposed $[Li(NH_3)]^+[BH_3NH_2BH_3]^-$ composition.

The B–H stretching region of the spectrum, figure 5.28b is more complex than the N–H stretching region, with a number of features observed. Comparing this region with that of $Na^+(BH_3NH_2BH_3)^-$, figure 5.29, shows that there are a similar number of bands in each, the main difference being that the bands in the spectrum of the lithium product are slightly red shifted. The good resemblance between the two spectra suggests that the same B–H stretches are present in both compounds, indicating the presence of two BH_3 groups in the product of the lithium reaction. Again this is consistent with the proposed $[Li(NH_3)]^+[BH_3NH_2BH_3]^-$ composition.

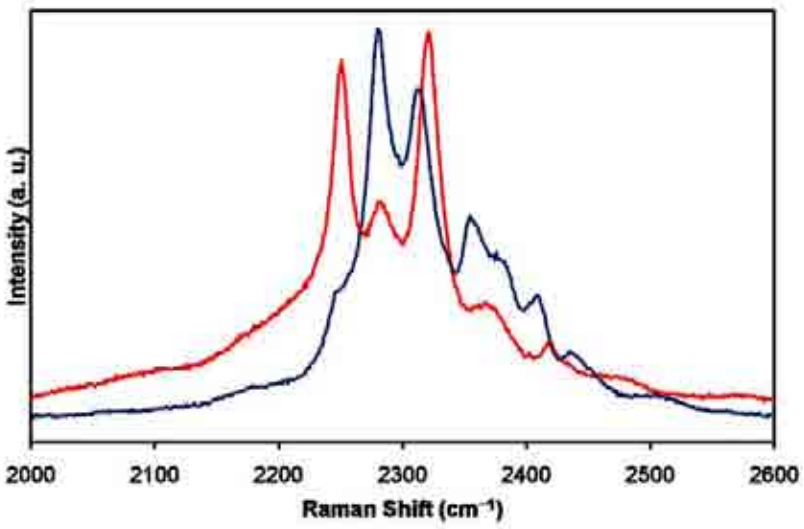

Figure 5.29 – The B–H stretching regions of the Raman spectra of $[Li(NH_3)]^+[BH_3NH_2BH_3]^-$ (red) and $Na^+(BH_3NH_2BH_3)^-$ (blue)

The deformation region of the spectrum is also complex. BH_3 deformations are evident at 1207 cm^{-1} and 1231 cm^{-1} while the intense, sharp band at 1569 cm^{-1} is likely related to an NH_3 deformation as this mode is observed at 1627 cm^{-1} in the Raman spectrum of NH_3.[36] The B–N stretch is difficult to identify as the ^{10}B–N stretch

appears to be obscured by other more intense bands. The band observed at 1167 cm^{-1} is tentatively assigned to this vibrational mode. The other bands in this region of the spectrum remain unassigned.

The Raman spectrum collected from the product of the LiH + $2NH_3BH_3$ reaction at 150°C is shown in figure 5.30a. This spectrum shows similarities to that of $LiBH_4$, the B–H stretching regions of the two spectra are compared in figure 5.30b. The Raman spectrum of $LiBH_4$ has been fully assigned by Gomes *et al.*,[37] and using these assignments some of the bands observed in figure 5.30a can be allocated modes. The vibrational modes of $LiBH_4$ can be seen in chapter 4.7 and the assigned bands in table 5.3.

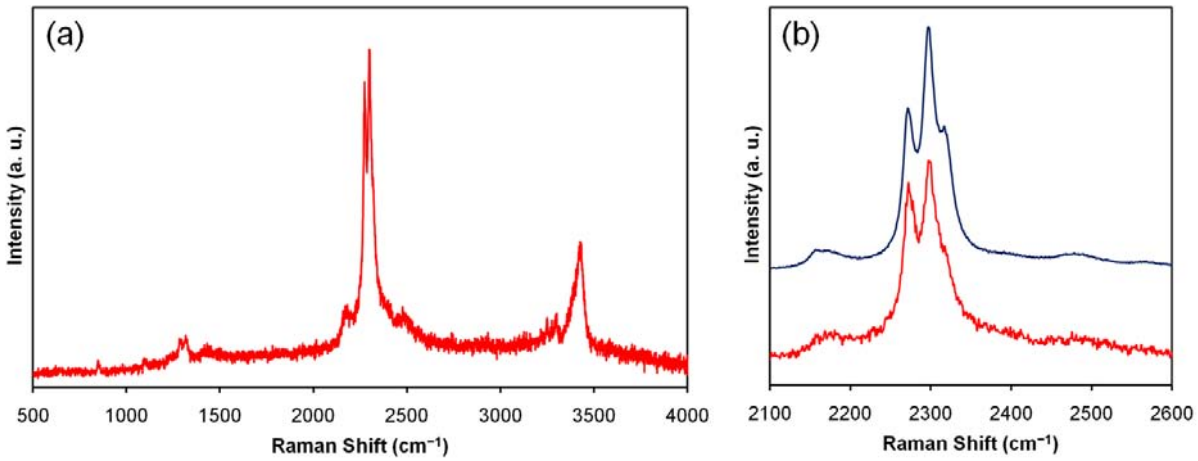

Figure 5.30 – (a) The Raman spectrum collected from the product of the LiH + $2NH_3BH_3$ reaction at 150°C. (b) The B–H stretching region of the product (red) is compared to $LiBH_4$ (blue)

The good agreement between the literature and observed spectra of $LiBH_4$ with some of the bands observed in the spectrum of the product from the LiH + $2NH_3BH_3$ reaction offers strong evidence that despite the lack of crystalline evidence for $LiBH_4$, it was, in an amorphous form, a decomposition product of $[Li(NH_3)]^+[(BH_3NH_2BH_3)]^-$. The spectrum also showed evidence of other decomposition products being present, with features observed in the N–H stretching region (>3000 cm^{-1}) and a number of low intensity features in the deformations region (<1500 cm^{-1}). However, the broad nature of these features meant it was not possible to identify any of the modes.

Table 5.3 – Literature and observed Raman shifts and assignments for $LiBH_4$ with observed data for the product of the LiH + $2NH_3BH_3$ reaction at 150°C

$LiBH_4$			**Product of LiH + $2NH_3BH_3$ at 150°C**
Literature[37]		Observed	Observed
Assignment	Raman shift (cm^{-1})	Raman shift (cm^{-1})	Raman shift (cm^{-1})
v_4	1090	1095	1099
v_4'	1099		
$3v_L$	1235	1237	1236
v_2	1286	1288	1289
v_2'	1316	1320	1322
$2v_4$	2157	2161	2163
$2v_4$'	2177	2178	2179
v_3	2275	2274	2274
v_1	2301	2299	2300
v_3'	2321 (sh)	2319	2318
com	2391	2395	
com	2491	2487	2485
com	2572	2571	2560

sh = shoulder, com = combination bands

5.7 Overall Discussion and Conclusion

5.7.1 The LiH + $2NH_3BH_3$ Reaction Pathway

The LiH + $2NH_3BH_3$ reaction proved to synthesise a compound, $[Li(NH_3)]^+[BH_3NH_2BH_3]^-$, similar to the product of the NaH + $2NH_3BH_3$ reaction, $Na^+(BH_3NH_2BH_3)^-$. The difference between the two compounds being that the lithium product possessed an NH_3 adduct, due to the high affinity of lithium containing compounds to bind with NH_3. However, the mechanism of formation of these materials appeared to differ. The sodium reaction proceeded through the formation of $NaNH_2BH_3$, whereas $LiNH_2BH_3$ was not detected in any sample by powder XRD. Furthermore, the LiH + $2NH_3BH_3$ reaction mixture was observed to undergo a volume expansion during heating, implying that the disruption of the dihydrogen bonding network present within NH_3BH_3 was required before the reaction could proceed. The labile NH_3BH_3 could then react with LiH to form $LiNH_2BH_3$, however, the labile nature of the reaction mixture also meant that this underwent a rapid reaction with NH_3BH_3, forming $[Li(NH_3)]^+[BH_3NH_2BH_3]^-$, shown below.

Reaction 5.12

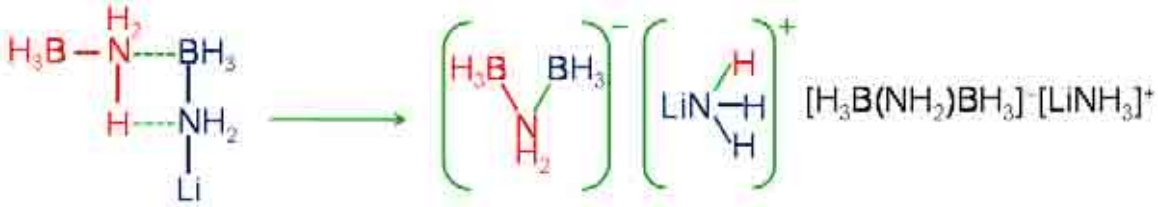

Reaction 5.13

The powder XRD pattern of $[Li(NH_3)]^+[BH_3NH_2BH_3]^-$ was indexed to a tetragonal unit cell with a = 4.0288(2) Å and c = 16.958(2) Å. Literature reports have shown that a ball milled reaction mixture of LiH + $2NH_3BH_3$ yields $LiNH_2BH_3{\cdot}NH_3BH_3$, which has been reported to undergo decomposition to form the same tetragonal phase.[13, 14] It was concluded that this material was of composition $LiN_2B_2H_7$. However, the results of our study do not support this assignment. Thermal desorption studies showed that the tetragonal phase experiences a weight loss of 12.5 wt% due to H_2 release, which

cannot be accounted for by a material of composition $LiN_2B_2H_7$. Furthermore, our solid state ^{11}B MAS NMR results were inconsistent with the proposed $LiNHBH_2{\cdot}NH_2BH_2$ and $LiNH_2BH{=}NHBH_3$ compositions. We therefore conclude that the tetragonal phase is $[Li(NH_3)]^+[BH_3NH_2BH_3]^-$ and is formed from a rearrangement reaction during melting of $LiNH_2BH_3{\cdot}NH_3BH_3$, at which point a labile mixture of $LiNH_2BH_3$ and NH_3BH_3 is effectively present in the reaction mixture, hence allowing either reaction 5.12 or 5.13 to proceed.

The decomposition of $[Li(NH_3)]^+[BH_3NH_2BH_3]^-$ led to predominantly amorphous products, possessing sp^2 boron environments. However, there was evidence that $LiBH_4$ had formed in trace amounts. The formation of this material may have proceeded in a similar fashion to $NaBH_4$ formation during $Na^+(BH_3NH_2BH_3)^-$ decomposition, reaction 5.14. This decomposition pathway may also have been responsible for the observed NH_3 release.

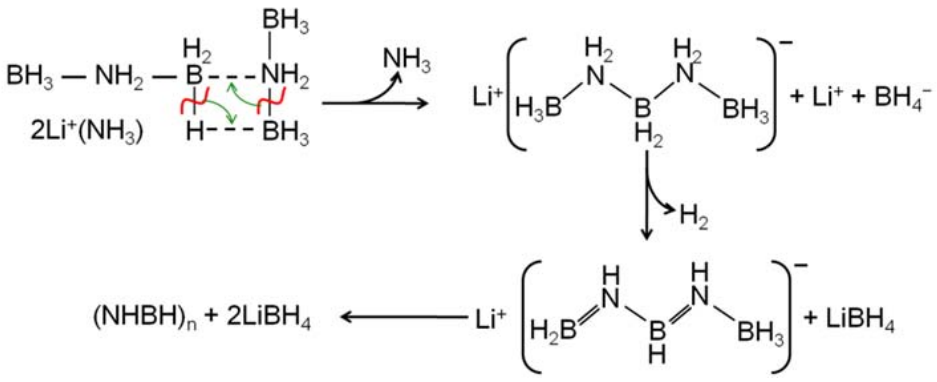

Reaction 5.14

The decomposition of $[Li(NH_3)]^+[BH_3NH_2BH_3]^-$ was however more complicated than that of $Na^+(BH_3NH_2BH_3)^-$, as shown by the fact that $LiBH_4$ was a minor decomposition product and this may have been due to the presence of the NH_3 adduct. NH_3 release was shown to be dependent on experimental conditions and it was not released in a stoichiometric quantity in experiments when it was detected. The main decomposition pathway may have therefore involved the formation of polymeric material such as $(LiNBHNHBH)_n$ accompanied by H_2 release, reaction 5.15. The theoretical weight loss from this reaction, 11.9 wt%, is in good agreement with the observed weight loss in thermogravimetric studies, 12.5 wt%.

$$n[Li(NH_3)]^+[BH_3NH_2BH_3]^- \rightarrow (LiNBHNHBH)_n + 4H_2 \qquad \text{Reaction 5.15}$$

5.7.2 Potential as a Hydrogen Storage Material

The high hydrogen content, 16.4 wt%, of $[Li(NH_3)]^+[BH_3NH_2BH_3]^-$ suggests that this material may have potential as a material for hydrogen storage. It also shows moderate temperature H_2 desorption, with a sharp release at 150°C. This is at a slightly higher temperature than the initial release of H_2 from the parent compound NH_3BH_3, but the subsequent broad desorptions are avoided. The final mixture of decomposition products may offer potential for reactions to occur in the presence of H_2, offering a rehydrogenation pathway.

A drawback to the use of this material as a hydrogen store is that under certain conditions NH_3 can be released. This release must be suppressed in order for the material to reach its full potential in the field of hydrogen storage.

5.8 References

1. Chater, P. A.; David, W. I. F.; Anderson, P. A., Synthesis and structure of the new complex hydride $Li_2BH_4NH_2$. *Chemical Communications* **2007**, 4770–4772.

2. Xiong, Z.; Chua, Y. S.; Wu, G.; Xu, W.; Chen, P.; Shaw, W. J.; Karkamkar, A.; Linehan, J. C.; Smurthwaite, T.; Autrey, T., Interaction of lithium hydride and ammonia borane in THF. *Chemical Communications* **2008**, 5595–5597.

3. Autrey, T.; Luedtke, A., Hydrogen release studies of alkali metal amidoboranes. *Inorganic Chemistry* **2010,** 49, 3905–3910.

4. Xiong, Z.; Yong, C. K.; Wu, G.; Chen, P.; Shaw, W. J.; Karkamkar, A.; Autrey, T.; Jones, M. O.; Johnson, S. R.; Edwards, P. P.; David, W. I. F., High-capacity hydrogen storage in lithium and sodium amidoboranes. *Nature Materials* **2008,** 7, 138–141.

5. Kang, X.; Fang, Z.; Kong, L.; Cheng, H.; Yao, X.; Lu, G.; Wang, P., Ammonia borane destabilized by lithium hydride: An advanced on-board hydrogen storage material. *Advanced Materials* **2008,** 20, 2756–2759.

6. Myers, A. G.; Yang, B. H.; Kopecky, D. J., Lithium amidotrihydroborate, a powerful new reductant. Transformation of tertiary amides to primary alcohols. *Tetrahedron Letters* **1996,** 37, 3623–3626.

7. Juza, R.; Opp, K., Metallamide und metallnitride, 24. Mitteilung. Die kristallstruktur des lithiumamides. *Zeitschrift fur anorganische und allgemeine chemie* **1951,** 266, 313–324.

8. Graham, K. R.; Kemmitt, T.; Bowden, M. E., High capacity hydrogen storage in a hybrid ammonia borane-lithium amide material. *Energy and Environmental Science* **2009,** 2, 706–710.

9. Xia, G.; Yu, X.; Guo, Y.; Wu, Z.; Yang, C.; Liu, H.; Dou, S., Amminelithium amidoborane $Li(NH_3)NH_2BH_3$: A new coordination compound with favourable dehydrogenation characteristics. *Chemistry – A European Journal* **2010,** 16, 3763–3769.

10. The powder XRD pattern of $LiNH_2BH_3$ was collected from a sample received from the University of Oxford, synthesised through ball milling a mixture of LiH and NH_3BH_3 in a 1:1 molar ratio.

11. Coelho, A. A. *Topas, General Profile and Structure Analysis Software for Powder Diffraction Data*, Bruker AXS, Karlsruhe, Germany, 3rd edition: 2004.

12. Soulié, J. P.; Renaudin, G.; Cerny, R.; Yvon, K., Lithium boro-hydride $LiBH_4$ I. Crystal structure. *Journal of Alloys and Compounds* **2002,** 346, 200–205.

13. Wu, C.; Wu, G.; Xiong, Z.; Han, X.; Chu, H.; He, T.; Chen, P., $LiNH_2BH_3$•NH_3BH_3: Structure and hydrogen storage properties. *Chemistry of Materials* **2010,** 22, 3−5.

14. Wu, C.; Wu, G.; Xiong, Z.; David, W. I. F.; Ryan, K. R.; Jones, M. O.; Edwards, P. P.; Chu, H.; Chen, P., Stepwise phase transition in the formation of lithium amidoborane. *Inorganic Chemistry* **2010,** 49, 4319−4323.

15. Wu, H.; Zhou, W.; Yildirim, T., Alkali and alkaline-earth metal amidoboranes: Structure, crystal chemistry, and hydrogen storage properties. *Journal of the American Chemical Society* **2008,** 130, 14834–14839.

16. Jacobs, H.; Juza, R., Neubestimmung der Kristallstruktur des Lithiumamids. *Zeitschrift für anorganische und allgemeine Chemie* **1972,** 391, 3247–3259.

17. Bowden, M. E.; Gainsford, G. J.; Robinson, W. T., The room temperature structure of ammonia borane. *Australian Journal of Chemistry* **2007,** 60, 149–153.

18. Armstrong, D. R.; Perkins, P. G.; Walker, G. T., The electronic structure of the monomers, dimers, a trimer, the oxides and the borane complexes of the lithiated ammonias. *Journal of Molecular Structure (Theochem)* **1985,** 122, 189–203.

19. Klooster, W. T.; Koetzle, T. F.; Siegbahn, P. E. M.; Richardson, T. B.; Crabtree, R. H., Study of the N–H---H–B dihydrogen bond including the crystal structure of BH_3NH_3 by neutron diffraction. *Journal of the American Chemical Society* **1999,** 121, 6337–6343.

20. Lee, S. M.; Kang, X.; Wang, P.; Cheng, H.; Lee, Y. H., A comparative study of the structural, electronic and vibrational properties of NH_3BH_3 and $LiNH_2BH_3$: Theory and experiment. *Chemical Physics and Physical Chemistry* **2009,** 10, 1825–1833.

21. Chua, Y. S.; Wu, G.; Xiong, Z.; He, T.; Chen, P., Calcium Amidoborane Ammoniate – Synthesis, Structure, and Hydrogen Storage Properties. *Chemistry of Materials* **2009,** 21, 4899–4904.

22. Chu, H.; Wu, G.; Xiong, Z.; Guo, J.; He, T.; Chen, P., Structure and hydrogen storage properties of calcium borohydride diammoniate. *Chemistry of Materials* **2010,** 22, 6021–6028.

23. Brown, I. D.; Skowron, A., Electronegativity and Lewis acid strength. *Journal of the American Chemical Society* **1990,** 112, 3401–3403.

24. Magnusson, E., Binding of polar molecules to Li^+, Na^+, KS, Mg^{2+}, and Ca^{2+} in single-ligand adducts M^+L and $M^{2+}L$ (L = H_2O, NH_3, H_2S, PH_3). *Journal of Physical Chemistry* **1994,** 98, 12558–12569.

25. Gervais, C.; Babonneau, F., High resolution solid state NMR investigation of various boron nitride preceramic polymers. *Journal of Organometallic Chemistry* **2002,** 657, 75–82.

26. Gervais, C.; Framery, E.; Duriez, C.; Maquet, J.; Vaultier, M.; Babonneau, F., ^{11}B and ^{15}N solid state NMR investigation of a boron nitride preceramic polymer prepared by ammonolysis of borazine. *Journal of the European Ceramic Society* **2005,** 25, 129–135.

27. Mosegaard, L.; Møller, B.; Jørgensen, J. E.; Bosenberg, U.; Dornheim, M.; Hanson, J. C.; Cerenius, Y.; Walker, G.; Jakobsen, H. J.; Besenbacher, F.; Jensen, T. R., Intermediate phases observed during decomposition of $LiBH_4$. *Journal of Alloys and Compounds* **2007,** 446–447, 301–305.

28. Johnson, S. R.; Anderson, P. A.; Edwards, P. P.; Gameson, I.; Prendergast, J. W.; Al-Mamouri, M.; Book, D.; Harris, I. R.; Speight, J. D.; Walton, A., Chemical activation of MgH_2; a new route to superior hydrogen storage materials. *Chemical Communications* **2005**, 2823–2825.

29. Züttel, A.; Wenger, P.; Rentsch, S.; Sudan, P.; Mauron, P.; Emmenegger, C., LiBH4 a new hydrogen storage material. *Journal of Power Sources* **2003,** 118, 1–7.

30. Hwang, S.-J.; Bowman Jr, R. C.; Reiter, J. W.; Rijssenbeek, J.; Soloveichik, G. L.; Zhao, J.-C.; Kabbour, H.; Ahn, C. C., NMR confirmation for formation of $[B_{12}H_{12}]^{2-}$ complexes during hydrogen desorption from metal borohydrides. *The Journal of Physical Chemistry C* **2008,** 112, 3164–3169.

31. Kim, D.; Moon, K.; Kho, J.; Economy, J.; Gervais, C.; Babonneau, F., Synthesis and characterization of poly(aminoborane) as a new boron nitride precursor. *Polymers for Advanced Technologies* **1999,** 10, 702–712.

32. Worle, M.; Meyer zu Altenschildescheb, H.; Nesper, R., Synthesis, properties and crystal structures of α-$Ca_3(BN_2)_2$ and $Ca_{9+x}(BN_2, CBN)_6$ – two compounds with BN_2^{3-} and CBN^{4-} anions. *Journal of Alloys and Compounds* **1998,** 264, 107–114.

33. Marchetti, P. S.; Kwon, D.; Schmidt, W. R.; Interrante, L. V.; Maciel, G. E., High-field ^{11}B Magic-Angle Spinning NMR characterization of boron nitrides. *Chemistry of Materials* **1991,** 3, 482–486.

34. Fahys, B.; Herlem, M.; Daher, J.; Robert, G., Lithium perchlorate ammoniate ionic liquid, $LiClO_4 \cdot 4NH_3$. *Journal of the Electrochemical Society* **1988,** 135, 2679–2682.

35. Mikuli, E.; Hetmańczyk, Ł.; Medycki, W.; Kowalska, A., Phase transitions and molecular motions in $[Zn(NH_3)_4](BF_4)_2$ studied by nuclear magnetic resonance, infrared and Raman spectroscopy. *Journal of Physics and Chemistry of Solids* **2007,** 68, 96–103.

36. Ninet, S.; Datchi, F.; Saitta, A. M.; Lazzeri, M.; Canny, B., Raman spectrum of ammonia IV. *Physical Review B* **2006,** 74, 104101.

37. Gomes, S.; Hagemann, H.; Yvon, K., Lithium boro-hydride $LiBH_4$ II. Raman spectroscopy. *Journal of Alloys and Compounds* **2002,** 346, 206–210.

Chapter 6

The Reaction of Calcium Hydride with Ammonia Borane

6.1 Introduction

Prior to the start of this research there had been no reported studies into the reaction of calcium hydride with ammonia borane. Mixed amide borohydride materials have previously been reported for the alkali metals lithium and sodium, but the synthesis of the alkaline earth metal analogues has yet to be reported.[1-8] The study was initially focused on the potential synthesis of calcium mixed amide borohydrides. The CaH_2 + NH_3BH_3 reaction was investigated with different molar ratios and it was found that a molar ratio of 1:4 seemed to be stoichiometric. This stoichiometry yielded a crystalline phase free from starting materials at a reaction temperature of 80°C, which was identified to be $Ca(BH_4)_2{\cdot}2NH_3$. Further heating of the reaction mixture to 120°C formed a second crystalline phase, $Ca(BH_4)_2{\cdot}NH_3$, and when the reaction temperature was increased to 225°C, $Ca(BH_4)_2$ was observed. The hydrogen desorption properties of the reaction pathway were investigated and spectroscopic characterisation of the crystalline phases by solid state ^{11}B MAS NMR was carried out. The crystal structures of both $Ca(BH_4)_2{\cdot}2NH_3$ and $Ca(BH_4)_2{\cdot}NH_3$ were solved, with the crystal structure of $Ca(BH_4)_2{\cdot}NH_3$ being previously unreported.

6.2 Experimental

Calcium hydride (Sigma-Aldrich, 99.99%) and ammonia borane (Sigma-Aldrich, 97%) were ground together in a 1:4 molar ratio in an argon filled glove box (>10 ppm O_2,

>1 ppm H_2O) and heated under a flowing argon atmosphere at 80°C. The sample was reground and annealed again at 80°C to improve the crystallinity of the sample.

6.3 Powder X-Ray Diffraction

Powder XRD patterns were taken of the products following the heating of the reaction mixture. It was found that a crystalline phase (Phase A) formed at a temperature of 80°C, which was collected as a white powder at the end of the experiment. The powder XRD pattern of this phase is shown in figure 6.1.

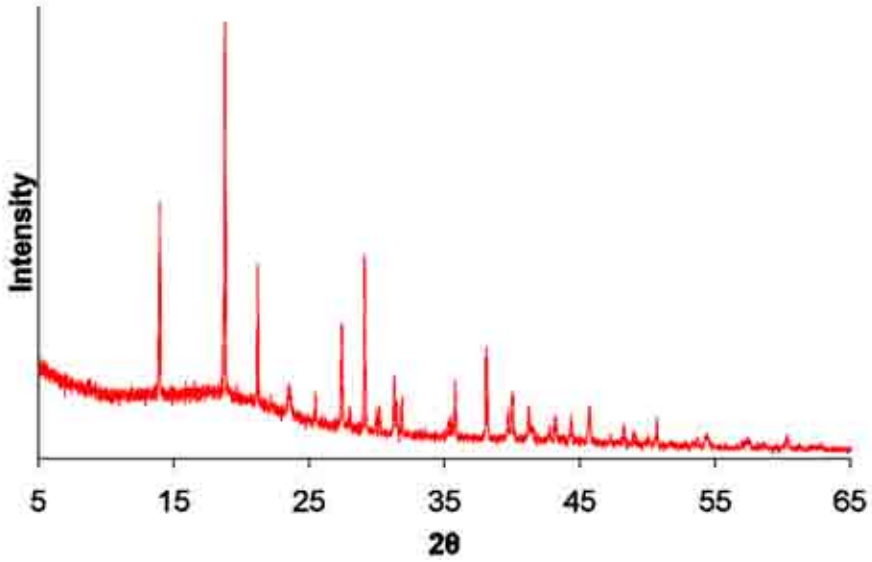

Figure 6.1 – The powder XRD pattern of the product of the reaction of CaH_2 + $4NH_3BH_3$ at 80°C

Further experiments and powder XRD patterns of the reaction products showed that Phase A was the sole crystalline product of the CaH_2 + $4NH_3BH_3$ reaction up to a reaction temperature of 90°C. The highest reaction temperature employed where this phase was observed in the powder XRD pattern of the collected sample was 110°C. After reaction at 100°C, the powder XRD pattern showed that a second crystalline phase had formed during the reaction. This crystalline phase (Phase B) was the solitary crystalline product of reaction after heating the starting materials to 120°C. This sample was also collected as a white powder. The powder XRD pattern of this phase is shown in figure 6.2. Powder XRD patterns showed that Phase B existed up to a reaction temperature of 200°C; above this temperature, no evidence of its presence was observed in powder XRD patterns.

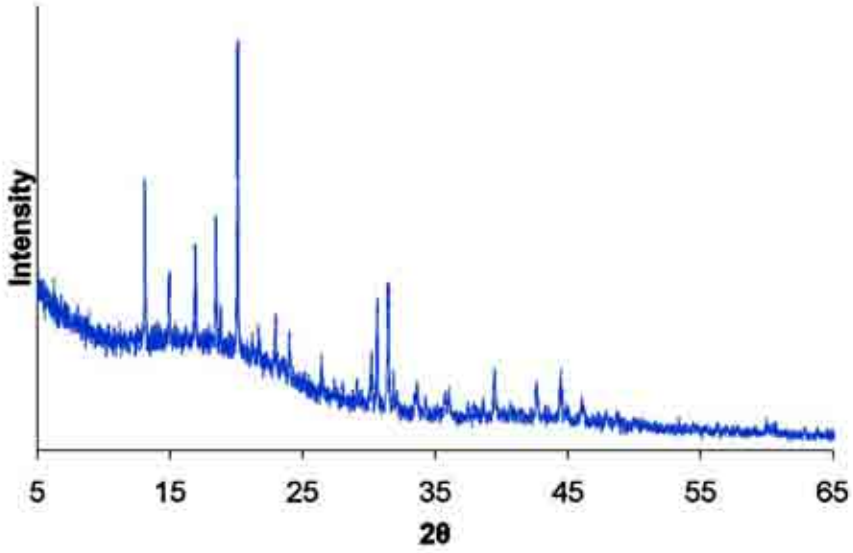

Figure 6.2 – The powder XRD pattern of the product of the reaction of CaH_2 + $4NH_3BH_3$ at 120°C

After reaction at 200°C the powder XRD pattern showed that the sample contained a second crystalline phase. Inspection of this pattern showed that this second phase was α-$Ca(BH_4)_2$. At 225°C α-$Ca(BH_4)_2$ was the only crystalline phase present in the powder XRD pattern, but partly underwent a phase transition at 250°C, giving a mixture of α and β $Ca(BH_4)_2$ in the powder XRD pattern. At 275°C, the powder XRD pattern showed no evidence of crystalline products, although after heating to 300°C and 400°C, there was evidence of a small amount of a crystalline phase, which was identified through inspection as CaH_2. Elevated heating to 800°C produced a poorly crystalline material. It was also established that the CaH_2 + $4NH_3BH_3$ reaction was unable to proceed at temperatures below 80°C, even with extended reaction times. The reaction pathway of the CaH_2 + $4NH_3BH_3$ reaction as viewed by powder XRD results is shown in figure 6.3.

It was observed during the experiments that the samples underwent a significant volume expansion at approximately 80°C, similar in nature to the observed expansion when heating the NH_3BH_3 starting material as discussed in chapter 3.3. This volume expansion was observed to take place after heating the reaction mixture for a period of 70 minutes.

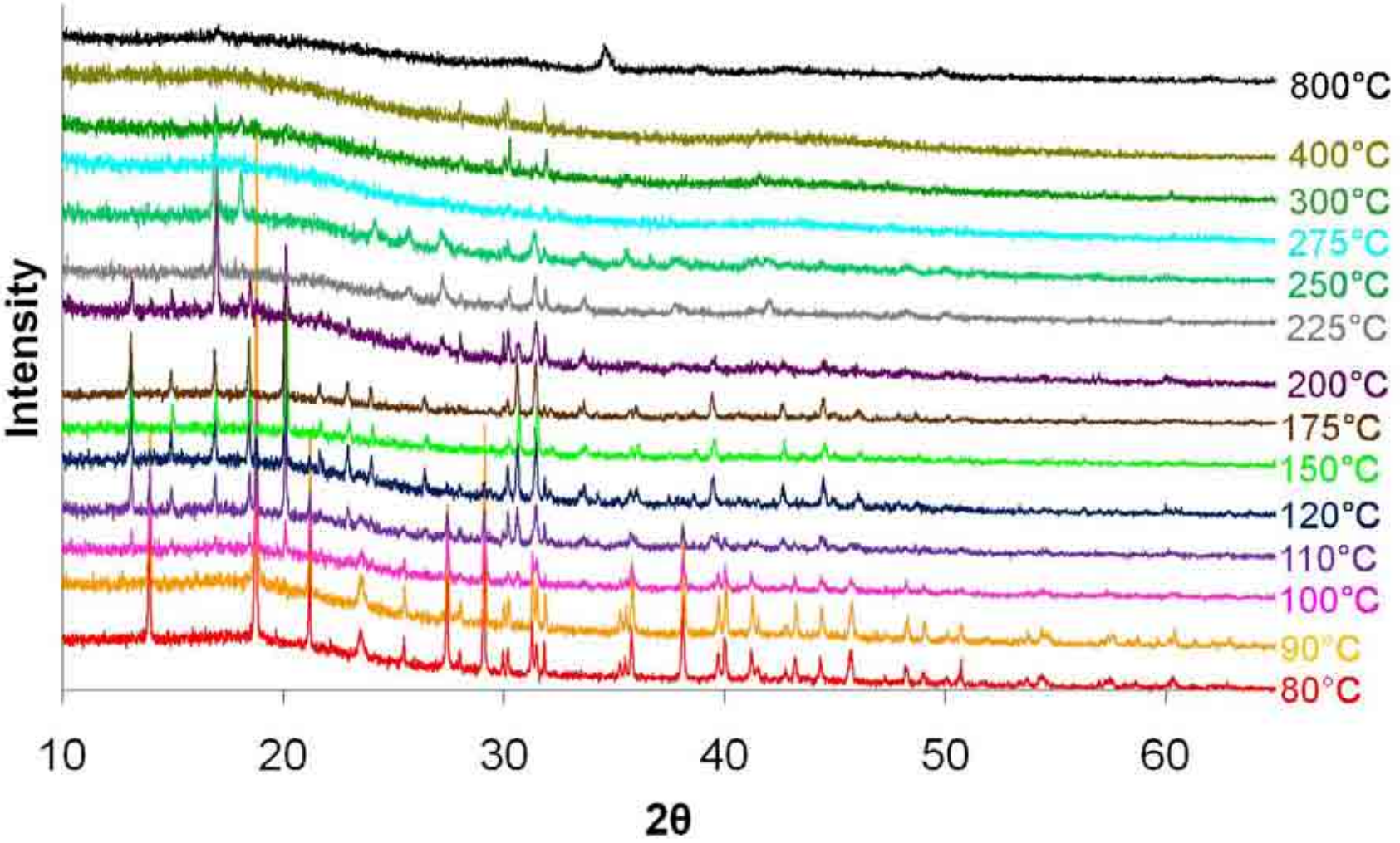

Figure 6.3 – Powder XRD patterns obtained from the products of the $CaH_2 + 4NH_3BH_3$ reaction at various temperatures

Analysis by powder XRD of the product obtained from a CaH_2 + $2NH_3BH_3$ reaction heated to 80°C for 72 hours revealed that there were two crystalline phases present in the sample. Peaks were observed in the pattern, figure 6.4, which were due to the formation of Phase A as well as unreacted CaH_2.

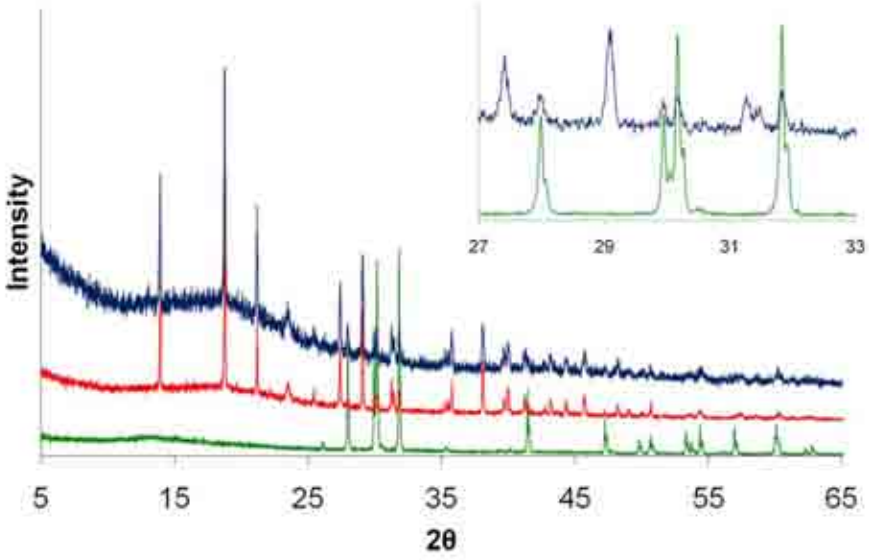

Figure 6.4 – The powder XRD pattern of the product of the reaction of CaH_2 + $2NH_3BH_3$ heated at 80°C for 72 hours (blue). The powder XRD pattern of CaH_2 (green) and Phase A (red) are shown for comparison. The inset shows a closer comparison of the 1:2 reaction product with CaH_2 between 27° and 33° 2θ

6.3.1 Discussion

Even now, there are few reported investigations into the reaction of CaH_2 and NH_3BH_3. The reports that have appeared in the literature have studied the reaction with a stoichiometry of 1:2 in favour of NH_3BH_3. The reaction has been carried out in solution, using THF as a solvent, which proved to form $Ca(thf)_2(NH_2BH_3)_2$. Vacuum drying this product overnight led to the THF being removed from the compound yielding $Ca(NH_2BH_3)_2$. However, small amounts of THF were still detected in the product, albeit in amounts well below stoichiometric ratios.[9] The THF free product has been prepared through ball milling a CaH_2 + $2NH_3BH_3$ reaction mixture.[10, 11] An ammoniated derivative of $Ca(NH_2BH_3)_2$, $Ca(NH_2BH_3)_2{\cdot}2NH_3$, has also been reported through ball milling a reaction mixture of $Ca(NH_2)_2$ and NH_3BH_3 in a 1:2 mole ratio.[12] The ammonia can be removed from this material through heating at 100°C, which results in $Ca(NH_2BH_3)_2$. The synthesis of $Ca(NH_2BH_3)_2$ or a derivative of this

compound has not been reported through direct solid state thermal reaction of CaH_2 and NH_3BH_3. Investigations into the 1:2 reaction in this study revealed that $Ca(NH_2BH_3)_2$ could not be synthesised through thermal methods even at low reaction temperatures or with extended reaction times.

The chemical compositions of both Phase A and Phase B were identified through comparisons with the results of a recent study published by Chu *et al*.[13] This study investigated the reaction of $Ca(BH_4)_2$ with NH_3 and a number of ammoniated forms of $Ca(BH_4)_2$; the NH_3 content varied between a maximum of $Ca(BH_4)_2{\cdot}6NH_3$ and $Ca(BH_4)_2{\cdot}NH_3$. The published powder XRD pattern of $Ca(BH_4)_2{\cdot}2NH_3$ was identical to that of Phase A synthesised in the 1:4 CaH_2 and NH_3BH_3 reactions in this study. Furthermore the published $Ca(BH_4)_2{\cdot}NH_3$ powder XRD pattern matched that of Phase B. It can therefore be concluded that the first step in the $CaH_2 + 4NH_3BH_3$ reaction resulted in the formation of $Ca(BH_4)_2{\cdot}2NH_3$. As a consequence of these observations the initial steps in the $CaH_2 + 4NH_3BH_3$ reaction can be summarised through reaction 6.1.

$$CaH_2 + 4NH_3BH_3 \longrightarrow \underset{\text{Phase A}}{Ca(BH_4)_2{\cdot}2NH_3} \longrightarrow \underset{\text{Phase B}}{Ca(BH_4)_2{\cdot}NH_3} \longrightarrow \alpha\text{-}Ca(BH_4)_2$$

Reaction 6.1

The question of what gases are released during the reaction pathway will be addressed in section 6.6, although from analysis of reaction 6.1 it would be reasonable to assume that the pathway involves the release of NH_3. It is also evident that the stoichiometry shown in reaction 6.1 is incorrect. The reaction suggests that the actual stoichiometry was $CaH_2 + 2NH_3BH_3$, as Phase A is B, N and H deficient with respect to the 1:4 starting mixture. However, as discussed previously a reaction stoichiometry of 1:2 was shown to leave unreacted CaH_2 in the product. Therefore, it would be reasonable to conclude that the reaction pathway may have involved the formation of amorphous products containing the remaining B, N and H, which would have been undetectable by powder XRD.

There have been a number of studies regarding the structure and decomposition products of the polymorphs of $Ca(BH_4)_2$. A number of polymorphs have been

identified with reports relating to the existence of α,[14-21] α',[17] β,[14, 16-23] γ[16, 20, 22-24] and δ[22, 23] phases presented in the literature. The first polymorph observed in this study was that of the α phase, after carrying out the CaH_2 + $4NH_3BH_3$ reaction at 200°C, which on further heating to 250°C showed evidence of a phase transition to the β polymorph. Literature studies regarding the decomposition pathway of $Ca(BH_4)_2$ have also detailed this phase transformation, with it being shown to be completed by a temperature of 300°C.[17, 18] However, none of the collected samples in this study produced powder XRD patterns that showed only the presence of β-$Ca(BH_4)_2$. The transformation of the α polymorph to the β phase must therefore have completed during the reaction carried out at 275°C. This powder XRD pattern was observed to be amorphous and therefore the decomposition of the β polymorph must have also taken place during the timescale of this reaction. The α' polymorph has been observed as the first step in the α to β phase transition by Filinchuk *et al*.[17] There was no evidence of the α' polymorph forming in this study during the α to β phase transition, however, the study by Filinchuk *et al.* is the sole report that has identified the existence of this polymorph. The δ polymorph has also not been widely reported in the literature and furthermore it is only observed in trace amounts, forming in the temperature range 290 – 330°C from either the γ or β polymorphs.[22, 23] Formation of both the α' and δ polymorphs are therefore very specific to the reaction conditions and it is hence unsurprising that they were not observed in this study. The remaining polymorph that was not observed in this study, the γ phase, is not involved in the α to β phase transition. This polymorph has been observed following heating $Ca(BH_4)_2$·2THF at 100°C under vacuum. The main product collected after THF removal was the α polymorph, but this was contaminated by a small amount of the γ polymorph.[20] The γ polymorph can be synthesised in greater amounts by wet chemical synthesis, through the reaction of CaH_2 with triethylamine borane, $Et_3N{\cdot}BH_3$.[16, 22-24] There have been no reports regarding a phase transformation of the α form of $Ca(BH_4)_2$ to the γ phase and therefore because the CaH_2 + $4NH_3BH_3$ reaction pathway initially led to the formation of the α polymorph, the γ phase is not expected to form.

The decomposition of the β phase has been reported to commence at temperatures above 330°C.[14, 20-23] This is not entirely consistent with our observations that there

was no evidence of any polymorph of $Ca(BH_4)_2$ in powder XRD patterns above a reaction temperature of 250°C. At 275°C the powder XRD pattern showed no evidence of crystalline phases and hence decomposition of the material had at least begun. The discrepancy between the literature reports and the results of this study was likely due to differences in reaction conditions. Whereas the studies in the literature reported temperature ramping experiments, with a heating rate of 2°C min^{-1}, the reactions of this study were heated slowly to the target temperature and then held for 12 hours. This difference could result in the observed difference in apparent decomposition temperature. It should also be considered that $Ca(BH_4)_2$ was unlikely to have been the only decomposition product, with amorphous products also present in the sample. Previous studies have shown that the decomposition temperature of $Ca(BH_4)_2$ can be reduced through the interaction with other materials.[25-27] Therefore the possibility that these amorphous materials could have interacted with the $Ca(BH_4)_2$ and lowered its decomposition temperature cannot be ignored. The decomposition of $Ca(BH_4)_2$ has been shown consistently to result in the crystalline material CaH_2.[14, 15, 18, 20-23, 28] This was reflected in the powder XRD patterns collected at 300°C and 400°C, where CaH_2 was observed to be the only crystalline product. The other products of the decomposition of $Ca(BH_4)_2$ have not been completely identified, although there have been a number of studies related to identifying these unknown products. The decomposition pathway of $Ca(BH_4)_2$ has been postulated to involve one or both of the following reactions.[15, 18, 20, 21]

$$Ca(BH_4)_2 \rightarrow {}^{2}/_{3}CaH_2 + {}^{1}/_{3}CaB_6 + {}^{10}/_{3}H_2 \qquad \text{Reaction 6.2}$$

$$Ca(BH_4)_2 \rightarrow CaH_2 + 2B + 3H_2 \qquad \text{Reaction 6.3}$$

The identification of B and CaB_6 through powder XRD has proved unsuccessful with the majority of studies not observing these phases in the powder XRD patterns of decomposed $Ca(BH_4)_2$ as they are present in amorphous forms. Only two studies have identified the possible presence of CaB_6 through XRD patterns.[20, 23] However, in both of these studies this identification was limited to an observation that there was a broad increase in the background of the powder XRD pattern at the 2θ position, 30.4°, where the most intense peak in the CaB_6 would be found and both studies used Raman spectroscopy to confirm the presence of this material. In both of these

literature studies the broad feature was only observed upon heating $Ca(BH_4)_2$ in excess of 480°C and therefore the only sample where any evidence of CaB_6 in this study may be expected would be in that of the sample heated to 800°C. A section of this pattern is shown in figure 6.5.

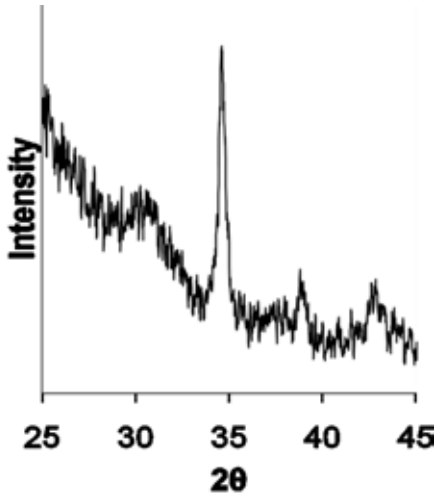

Figure 6.5 – The powder XRD pattern of the $CaH_2 + 4NH_3BH_3$ pattern showing two broad features at 30.5° and 37.5° 2θ, which give some indication that CaB_6 may be present in the sample

There are two broad features at 30.5° and 37.5° 2θ observed in this pattern which could be due to the presence of CaB_6. Investigations into the decomposition pathway of $Ca(BH_4)_2$ have also led to the identification of an unknown intermediate crystalline phase that has been shown to form between 320°C and 390°C.[18, 20, 21, 23] This intermediate has been indexed to an orthorhombic unit cell, with a suggested composition of either CaB_2H_2 or $Ca(B_{12}H_{12})$.[21, 23] The intermediate phase may have formed and subsequently decomposed during the reactions carried out at 400°C and 800°C, as it was not identified in any of the powder XRD patterns of the $CaH_2 + 4NH_3BH_3$ reactions in this study. Upon further heating this intermediate undergoes decomposition to CaH_2 and an amorphous boron containing material. CaH_2 was observed in the powder XRD pattern of the reaction performed at 400°C and hence some of this material may have been present as a consequence of the intermediate phase decomposing as well as being formed directly from $Ca(BH_4)_2$ decomposition. The crystalline phase observed at 800°C was identified by comparison with the published XRD pattern of $Ca_3(BN_2)_2$.[29] The poor crystallinity of this material was due to an insufficient temperature to allow the phase to crystallise, with a temperature of

1200°C shown to be required for the material to form with good crystallinity.[29] This was an interesting observation considering the Ca within the reaction, as far as XRD showed, was present in the form of $Ca(BH_4)_2$ and CaH_2 prior to the formation of $Ca_3(BN_2)_2$. The appearance of nitrogen in a calcium containing phase at 800°C therefore suggested that an amorphous Ca, B and N containing phase formed during the reaction pathway and began to crystallise as $Ca_3(BN_2)_2$ after heating to 800°C. Alternatively $Ca_3(BN_2)_2$ could have formed as a result of the decomposition of CaH_2, which has been shown to take place at a temperature of 700°C, leaving Ca metal and releasing H_2.[30] The Ca metal may have subsequently reacted with an amorphous B and N containing compound, such as BN. However, the stability of BN renders the synthesis of $Ca_3(BN_2)_2$ from such a reaction unlikely. The formation of $Ca_3(BN_2)_2$ will be discussed further in section 6.7. The formation of $Ca_3(BN_2)_2$ offered proof that there was an amorphous nitrogen containing compound present in the sample, although the composition of the material cannot be determined from powder XRD investigations.

6.4 Crystal Structure Determination of $Ca(BH_4)_2 \cdot 2NH_3$ (Phase A)

The crystal structure of $Ca(BH_4)_2 \cdot 2NH_3$ was determined from powder diffraction data using the computer program Topas.[31] The structure was found to consist of octahedral Ca^{2+} surrounded by four BH_4^- and two NH_3 units.

6.4.1 Indexing

The observed peak positions from the $Ca(BH_4)_2 \cdot 2NH_3$ phase were run through the indexing routine of the computer program Topas.[32] The most probable assignment was for an orthorhombic unit cell with *a* = 12.67 Å, *b* = 8.38 Å and *c* = 6.40 Å, which was similar to the assignment of Chu *et al.*[13] The suggested space group was $Pca2_1$ (#29), see table 6.1. The lattice constants and unit cell volume were refined in a Pawley fit using Topas as *a* = 12.6717(4) Å, *b* = 8.3665(3) Å, *c* = 6.3966(2) Å, giving a unit cell volume of 678.10(4) $Å^3$.

Table 6.1 – Special positions available in the space groups $Pca2_1$ and *Pbcn*

***Pca*2$_1$ (# 29)**			
Multiplicity	**Wyckoff letter**	**Site symmetry**	**Coordinates**
4	*a*	1	(*x*, *y*, *z*)
***Pbcn* (# 60)**			
Multiplicity	**Wyckoff letter**	**Site symmetry**	**Coordinates**
8	*d*	1	(*x*, *y*, *z*)
4	*c*	2	(0, *y*, ¼)
4	*b*	$\bar{1}$	(0, ½, 0)
4	*a*	$\bar{1}$	(0, 0, 0)

On closer inspection of the Pawley fit it was noticed that there were a number of predicted reflections with zero intensity, see figure 6.6, in the $Pca2_1$ (#29) space group and therefore other space groups were tested. Chu *et al.* indexed the XRD pattern of $Ca(BH_4)_2{\cdot}2NH_3$ to an orthorhombic unit cell with *a* = 6.4160 Å, *b* = 8.3900 Å and *c* = 12.7020 Å with a space group of *Pbcn* (#60), table 6.1. It was found that this space group better suited the set of observed reflections, figure 6.7, with the lattice constants refined in a Pawley fit as *a* = 6.3967(3) Å, *b* = 8.3668(3) Å and *c* = 12.6714(6) Å. The unit cell volume was calculated to be 678.17(5). It can be seen from figures 6.6 and 6.7 that the main difference between the two space groups was due to the peak at 23.6° 2θ. This peak was included in the fit in the $Pca2_1$ space group (the (310) peak, *d*-spacing of 3.77 Å), but excluded from that of *Pbcn*. Close inspection of the (310) peak revealed that the peak was significantly broader than the other peaks due to $Ca(BH_4)_2{\cdot}2NH_3$ and that the exact peak position did not completely match that of the predicted (310) reflection. It was concluded that this peak was most likely due to an impurity phase, rather than $Ca(BH_4)_2{\cdot}2NH_3$. Structure solution of the $Ca(BH_4)_2{\cdot}2NH_3$ material was therefore attempted using these lattice constants in the space group *Pbcn*, which had a minimal number of predicted reflections with zero intensity.

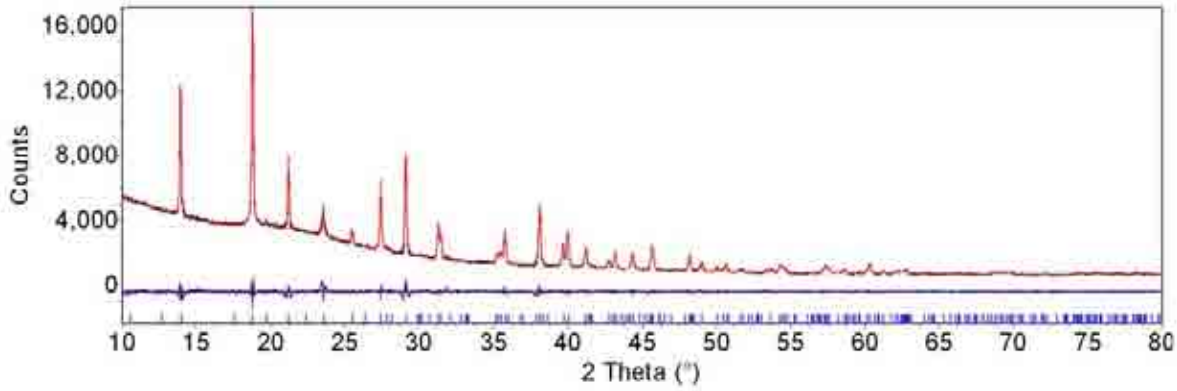

Figure 6.6 – Pawley refinement of the $Ca(BH_4)_2 \cdot 2NH_3$ powder XRD pattern in the *Pca*2_1 (#29) space group. The observed (black), calculated (red) and difference (blue) plots are shown. The predicted peak positions are shown in blue. R_{wp} = 3.632%, χ^2 = 2.615

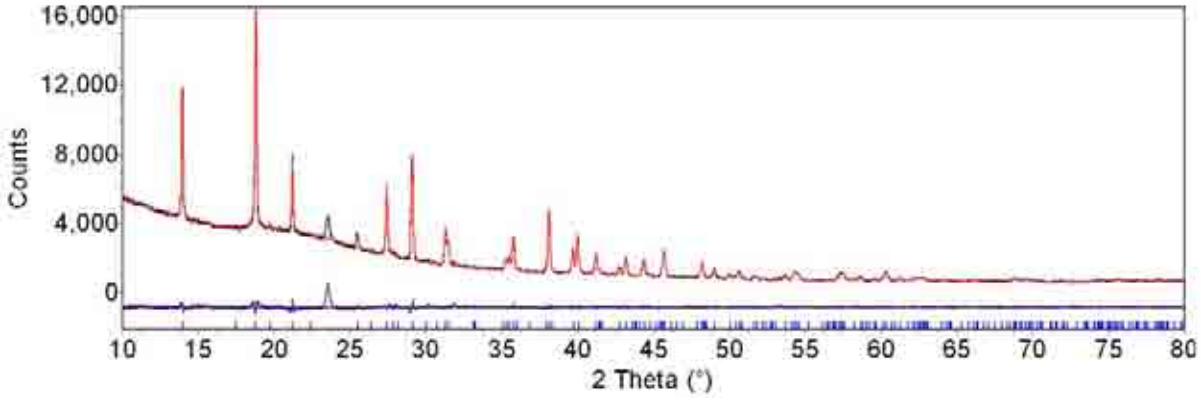

Figure 6.7 – Pawley refinement of the $Ca(BH_4)_2 \cdot 2NH_3$ powder XRD pattern in the *Pbcn* (#60) space group. The observed (black), calculated (red) and difference (blue) plots are shown. The predicted peak positions are shown in blue. R_{wp} = 3.881%, χ^2 = 2.958

6.4.2 Determining the Number of Formula Units in the Unit Cell and Producing a Model

The volume of the α-$Ca(BH_4)_2$ unit cell has been determined to be 863.07 Å^3, with eight $Ca(BH_4)_2$ molecules within the unit cell, which means that a single $Ca(BH_4)_2$ unit occupies a volume of approximately 107.9 Å^3.[33] The calculated unit cell volume of $Ca(BH_4)_2 \cdot 2NH_3$ was 678.17 Å^3, which would allow 6.35 $Ca(BH_4)_2$ units within the unit cell. The *Pbcn* space group allows sites of multiplicity of four or eight (table 6.1) and therefore because a $Ca(BH_4)_2 \cdot 2NH_3$ unit will occupy a larger volume than a $Ca(BH_4)_2$ unit, it was concluded that there would most likely be four formula units per unit cell.

Throughout the structure solution process the region of the XRD pattern between 22.9° and 24.0° 2θ was excluded from refinements as the peak observed in this range was due to a reflection that was unrelated to the *Pbcn* space group. The strongest scatterer of X-rays within the compound is calcium and therefore this was the first element to be introduced into the unit cell as part of the structure solution process. There are three available special positions in the *Pbcn* space group with a multiplicity of four (4*a*, 4*b* and 4*c*) and these were all considered as possible sites for Ca. Ca atoms were introduced on each of these sites and the occupancy as well as the atomic position of the 4*c* site were determined using the simulated annealing routine within Topas. It was found that the occupation of the 4*a* and 4*b* sites refined to zero, whereas the occupancy of the 4*c* site, (0, *y*, ¼) refined to one, giving the 4*c* site as the Ca position.

Boron and nitrogen have similar X-ray scattering strengths and they were hence both introduced to the structure as the next step. There were a number of ways in which it was possible to introduce the required 8B and 8N to the unit cell due to the *Pbcn* space group possessing multiple special positions. The candidate models that involved occupation of two of the sites of multiplicity four proved to produce models that were poor both visually and statistically. In contrast, occupation of the 8*d* site for both B and N provided a much better candidate model.

The final step in the structure solution was to introduce the H atoms into the unit cell. The H atoms could not be treated as separate entities due to their poor X-ray scattering capability and the quality of the laboratory based diffraction data. Therefore rigid bodies in the form of BH_4 and Ca–NH_3 units were introduced. These rigid bodies were introduced to the structure at the refined positions of B and N respectively. Ca–NH_3 was chosen as a rigid body instead of just NH_3 to enforce the geometry of the nitrogen lone pair bonding to Ca. The BH_4 unit was initially restrained to ideal tetrahedral geometry with a fixed B–H bond length of 1.2 Å, while the N–H bonds within the NH_3 unit were fixed to 1.1 Å and the bond angles fixed at 109.5°. The Ca–N bond length was allowed to vary from a starting value of 2.5 Å. The rotation of these rigid bodies was refined, followed by the refinement of all of the atomic positions. During these refinements the constraints applied to the rigid bodies

were maintained. This model gave a fit that was both visually, figure 6.8, and statistically, R_{wp} = 4.608%, satisfactory. At this point the number of terms in the background function was increased in order to improve the fit. A satisfactory model had now been produced to proceed with a full Rietveld refinement.

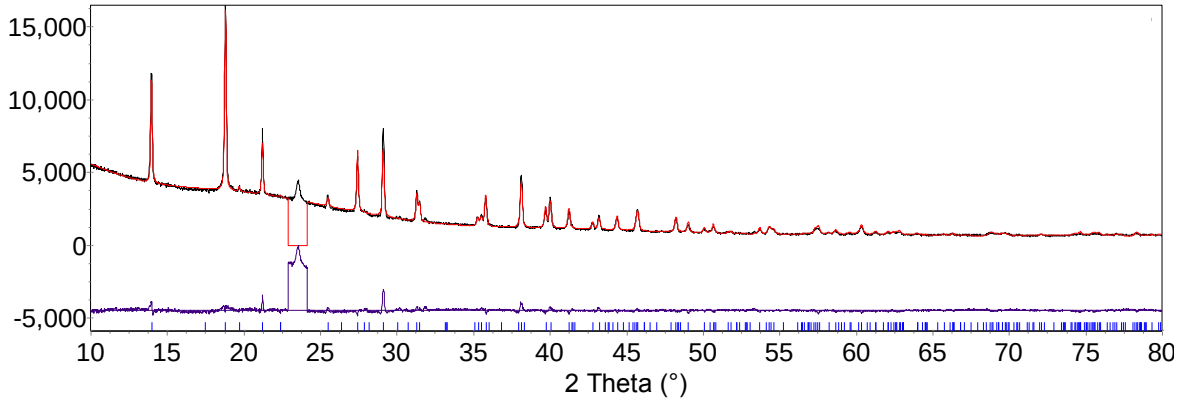

Figure 6.8 – The fit for $Ca(BH_4)_2{\cdot}2NH_3$ with refined Ca, B and N positions and refined BH_4 and Ca–NH_3 rigid bodies within the *Pbcn* space group. The observed (black), calculated (red) and difference (blue) plots are shown. The predicted peak positions are shown in blue. R_{wp} = 4.608%, χ^2 = 2.124

6.4.3 Full Rietveld Refinement

A complete Rietveld refinement was performed in Topas by refining a zero point error, a pseudo-Voigt peak shape (6 parameters) and a Chebyshev background function (17 parameters). Atomic positions were determined within the enforced geometry of the rigid bodies described in section 6.4.2 by refining the translation and rotation of the rigid bodies (6 parameters for each rigid body). The Ca–N bond length was refined, however, attempts to refine the N–H and B–H bond lengths resulted in the bond lengths reaching the minimum applied limit (0.8 Å) and so the N–H and B–H bond lengths were fixed at the values published by Chu *et al.*[13] (1.03 Å and 1.23 Å, respectively). It was not possible to obtain accurate H positions from room temperature laboratory diffraction data. Higher quality diffraction data, obtained at low temperature to minimise thermal motion, would be advantageous. Isotropic thermal parameters (B_{eq}) were also introduced to the refinement for Ca, B, N and H, and refined from starting values of 1 Å^2. Refinement of these parameters resulted in non-sensible values in every case except Ca, and so values for B, N and H were fixed at 1 Å^2. The final refinement contained 40 refined parameters. The resultant crystal

structure and Rietveld plot are shown in figures 6.9 and 6.10 respectively. The refined crystallographic data is shown in table 6.2. The atomic coordinates obtained from the cif file provided in the electronic supplementary information by Chu *et al.*[13] are shown for comparison. Mapping the structure determined by Chu *et al.* onto our structure required inversion of their *x* and *y* axes.

Table 6.2 – Refined crystallographic data for $Ca(BH_4)_2{\cdot}2NH_3$†

Atom	Site	This study			Chu *et al.*[13]		
		x	*y*	*z*	*x*	*y*	*z*
B1	8*d*	0.271(3)	0.513(3)	0.1612(5)	0.242	0.489	0.1473
H1	8*d*	0.142	0.567	0.1025	0.0850	0.5577	0.1157
H2	8*d*	0.388	0.429	0.1126	0.3813	0.5063	0.0827
H3	8*d*	0.367	0.620	0.2015	0.2986	0.5421	0.2330
H4	8*d*	0.185	0.436	0.2284	0.1980	0.3469	0.1554
N1	8*d*	0.753	0.745	0.0987	0.737	0.765	0.105
H5	8*d*	0.712	0.633	0.0826	0.7197	0.6563	0.0685
H6	8*d*	0.626	0.809	0.1170	0.5912	0.7930	0.1345
H7	8*d*	0.823	0.794	0.0355	0.7646	0.8454	0.0450
Ca1	4*c*	0	0.748(2)	0.25	0	0.754	0.25

†Space group *Pbcn* (#60), a = 6.3969(2) Å, b = 8.3670(3) Å, c = 12.6717(4) Å.

R_{wp} = 3.426%, R_{exp} = 2.377%, R_{wp}' = 16.054%, R_{exp}' = 11.140%, χ^2 = 2.078.

rCaN = 2.483(4), B_{eq}(Ca) = 2.6(1)

BH_4 rigid body. Rotational values: R_x = 196(4)°, R_y = 310(4) and R_z = 131(4); Translational values: x = 0.271(3), y = 0.513(3), z = 0.1612(5).

Ca–NH_3 rigid body. Rotational values: R_x = 140.7(1)°, R_y = 357(2) and R_z = 267(2); Translational values: x = 0, y = 0.748(2), z = 0.25.

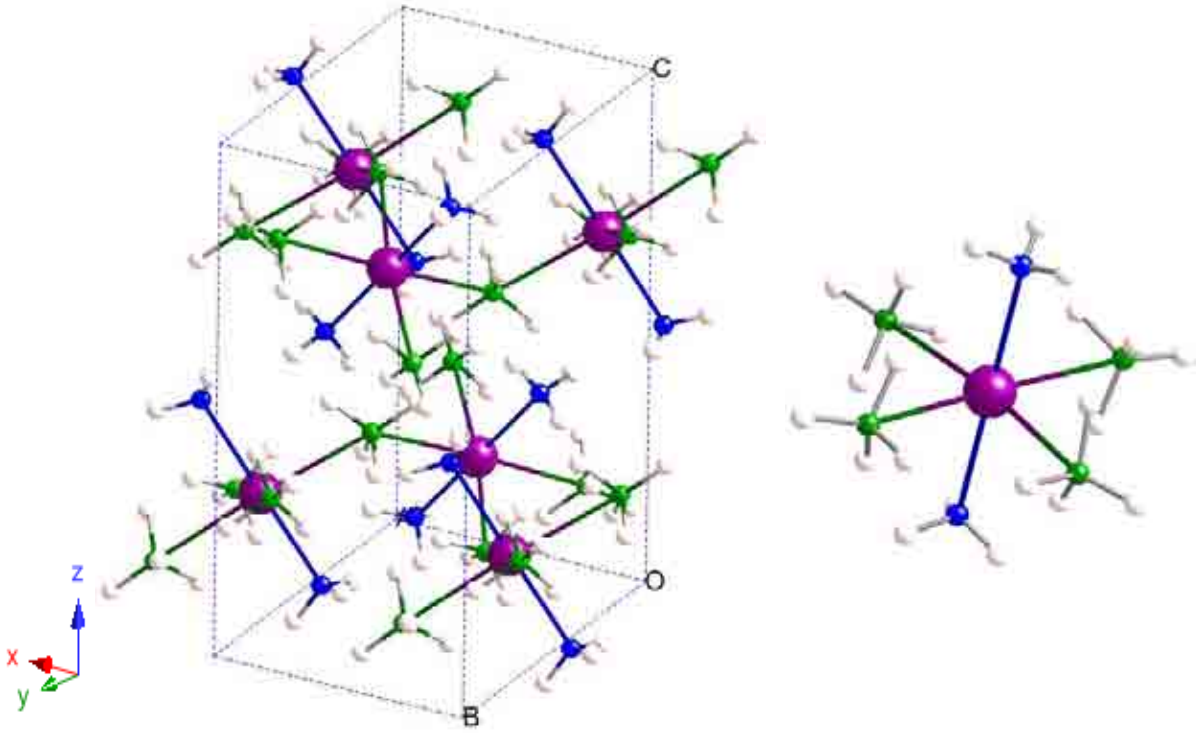

Figure 6.9 – Refined crystal structure of $Ca(BH_4)_2 \cdot 2NH_3$. The coordination environment of the Ca^{2+} cation is shown. Each Ca^{2+} coordinates with two NH_3 and four BH_4 groups. Ca is shown in purple, N in blue, B in green and H in pale pink

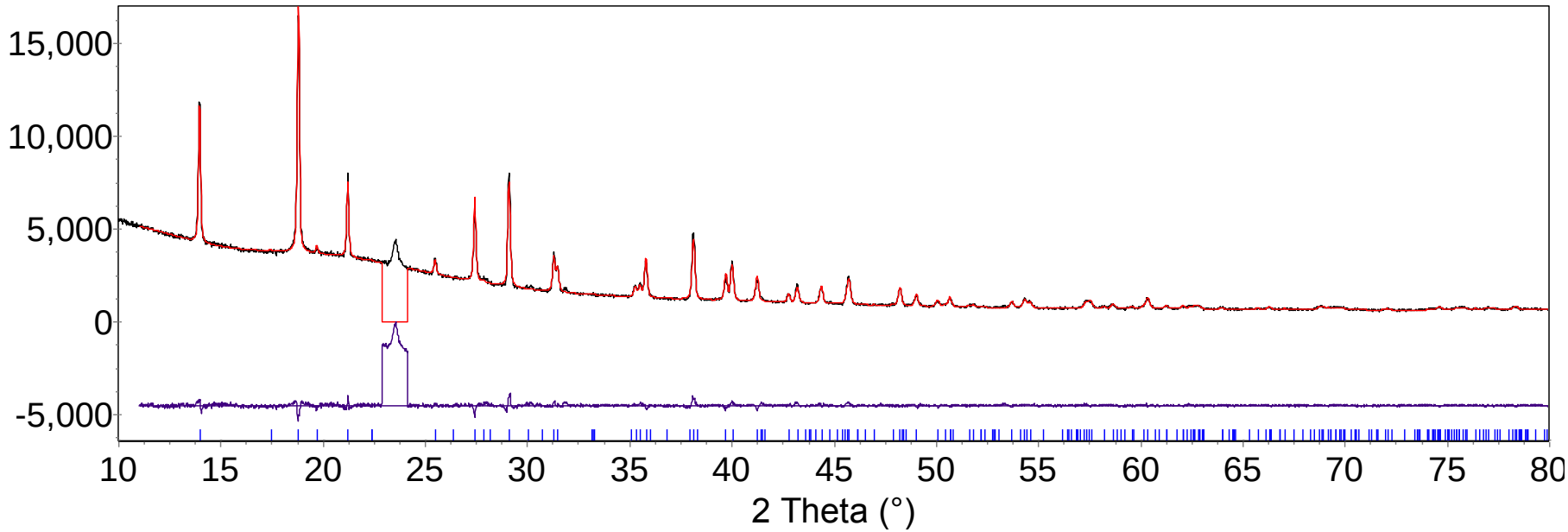

Figure 6.10 – Final Rietveld plot for $Ca(BH_4)_2 \cdot 2NH_3$. The observed pattern is shown in black, the calculated in red and the difference in blue. The calculated peak positions are indicated. R_{wp} = 3.426%, χ^2 = 2.078

6.5 Crystal Structure Determination of $Ca(BH_4)_2 \cdot NH_3$ (Phase B)

The crystal structure of $Ca(BH_4)_2 \cdot NH_3$ was determined from powder diffraction data using the computer program Topas.[32] The structure was found to consist of octahedral Ca surrounded by five BH_4^- and one NH_3 units.

6.5.1 Indexing

The observed peak positions from the $Ca(BH_4)_2 \cdot NH_3$ phase were run through the indexing routine of the computer program Topas.[31] The most probable assignment was for an orthorhombic unit cell with *a* = 8.18 Å, *b* = 11.81 Å and *c* = 5.82 Å, which agreed with the assignment of Chu *et al.*[13] The suggested space group was *Pna*2_1 (#33), which shares identical predicted hkl values with space group *Pnma* (#62), so both possible space groups were considered. Due to the ordering of the lattice constants, the non-standard space group setting *Pnam* was considered instead of *Pnma*. The special positions available in these two possible space groups are shown in table 6.3. The lattice constants and the unit cell volume refined in a Pawley refinement using Topas as *a* = 8.1986(3) Å, *b* = 11.8410(5) Å, *c* = 5.8368(2) Å and the unit cell volume as 566.63(4) $Å^3$.

Table 6.3 – Special positions available in the space groups *Pna*2_1 and *Pnam*

***Pna*2_1 (No. 33)**			
Multiplicity	**Wyckoff letter**	**Site symmetry**	**Coordinates**
4	*a*	1	(*x*, *y*, *z*)
***Pnam* (No. 62)**			
Multiplicity	**Wyckoff letter**	**Site symmetry**	**Coordinates**
8	*d*	1	(*x*, *y*, *z*)
4	*c*	m	(*x*, *y*, ¼)
4	*b*	$\bar{1}$	(0, ½, 0)
4	*a*	$\bar{1}$	(0, 0, 0)

6.5.2 Determining the Number of Formula Units in the Unit Cell and Producing a Model

The volume of the α-$Ca(BH_4)_2$ unit cell has been determined to be 863.07 $Å^3$, with eight $Ca(BH_4)_2$ molecules within the unit cell, which means that a single $Ca(BH_4)_2$ unit occupies a volume of approximately 107.9 $Å^3$.[33] As discussed in section 6.4, the unit cell volume of $Ca(BH_4)_2{\cdot}2NH_3$ was determined to be 678.3 $Å^3$, with four formula units per unit cell and so each formula unit occupied a volume of 169.6 $Å^3$. An estimated volume for one formula unit of $Ca(BH_4)_2{\cdot}NH_3$ can be made by taking an average of these two volumes, with the calculation giving a value of 138.75 $Å^3$. From this value, the number of formula units of $Ca(BH_4)_2{\cdot}NH_3$ within the unit cell can be estimated to be approximately four. This estimate provides a good argument that there are four $Ca(BH_4)_2{\cdot}NH_3$ units within the unit cell.

The first step in the structure solution process was to introduce the heaviest X-ray scatterer in the compound, Ca, to the unit cell, firstly within the *Pna*2_1 (#33) space group. There is only one general position within this space group and therefore the Ca atom was introduced on a general position (*x*, *y*, *z*). Using the simulated annealing function within Topas, the Ca position within the unit cell was determined.

This procedure was repeated for the *Pnam* (#62) space group. Three available special positions with a multiplicity of 4 (4*a*, 4*b* and 4*c*) were considered as possible Ca sites. Ca atoms were introduced on each of these sites and the occupancy as well as the atomic position of the 4c site were determined using the simulated annealing routine within Topas. It was found that the occupancy of the 4*a* and 4*b* sites refined to zero, whereas the occupancy of the 4*c* site (*x*, *y*, ¼) refined to one, giving the 4*c* site as the Ca position.

Refining the Ca atom positions in both the *Pna*2_1 and *Pnam* space groups gave similar visual fits to the observed diffraction data, see figures 6.11 and 6.12, and therefore both space groups were considered for the next stage of the structure solution process. The statistics for these refinements were also similar with an R_{wp} value of 9.506% for the *Pna*2_1 space group and 9.696% for *Pnam*.

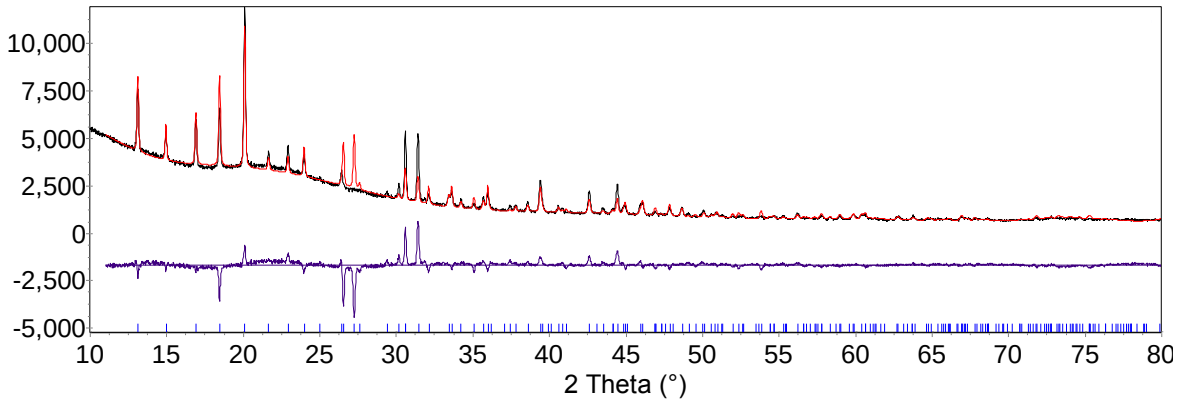

Figure 6.11 – Rietveld plot upon refinement of the Ca positions within the *Pna*2$_1$ (#33) space group. R_{wp} = 9.506%, χ^2 = 10.524

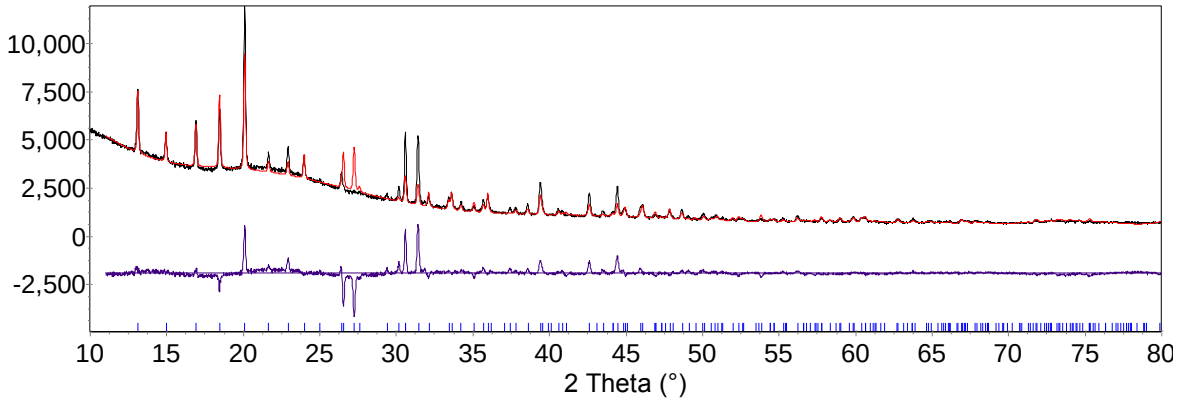

Figure 6.12 – Rietveld plot upon refinement of the Ca positions within the *Pnam* (#62) space group. R_{wp} = 9.696%, χ^2 = 10.731

B and N were then added to the structural models and their positions determined using simulated annealing, with Ca fixed at its previously determined position. In space group *Pna*2$_1$, two B positions and one N position were added on the 4*a* general position.

In space group *Pnam*, the presence of multiple special positions meant that there were a number of possible ways to introduce the 8B and 4N required in the unit cell, each of which was tested. The occupation of 4*a* and 4*b* sites was always unfavoured, with the site occupancy refining to zero. Occupation of the 8d site was tested as a possible B site, but the presence of a mirror plane perpendicular to the shortest lattice parameter (*c* = 5.84 Å) meant that the maximum possible B–B distance was 2.9 Å. This distance is significantly shorter than in the determined structures of both $Ca(BH_4)_2{\cdot}NH_3$, see section 6.4, and in α-$Ca(BH_4)_2$ (> 4 Å),[33] and so occupation of the

8*d* site was deemed to be unfavourable. This unfavourable arrangement of boron atoms is shown in figure 6.13. The best visual and statistical fit was obtained with boron occupying two 4*c* sites and N occupying one 4*c* site.

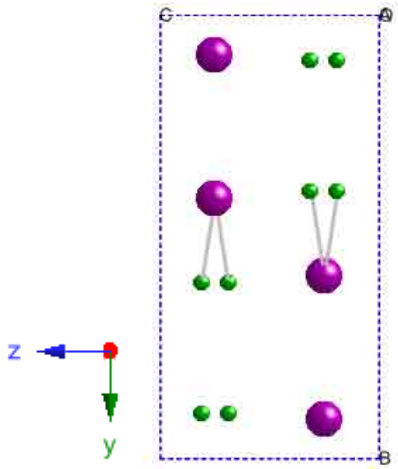

Figure 6.13 – The unit cell of $Ca(BH_4)_2{\cdot}NH_3$ with only Ca and B atoms present, with Ca occupying a 4*c* site and B occupying an 8*d* site in the *Pnam* space group. The Ca atoms are shown in purple and the B atoms shown in green

After refining the Ca, B and N atom positions in both the *Pna*2_1 and *Pnam* space groups, it was still difficult to determine which space group would provide the most suitable structure for the compound as the visual fit and statistical data were very similar. The fits are shown in figures 6.14 (*Pna*2_1) and 6.15 (*Pnam*), with R_{wp} values of 4.294% for the *Pna*2_1 space group and 4.331% for *Pnam*. Due to the very similar fits it was decided to proceed with the structure solution using only the higher symmetry space group, *Pnam*.

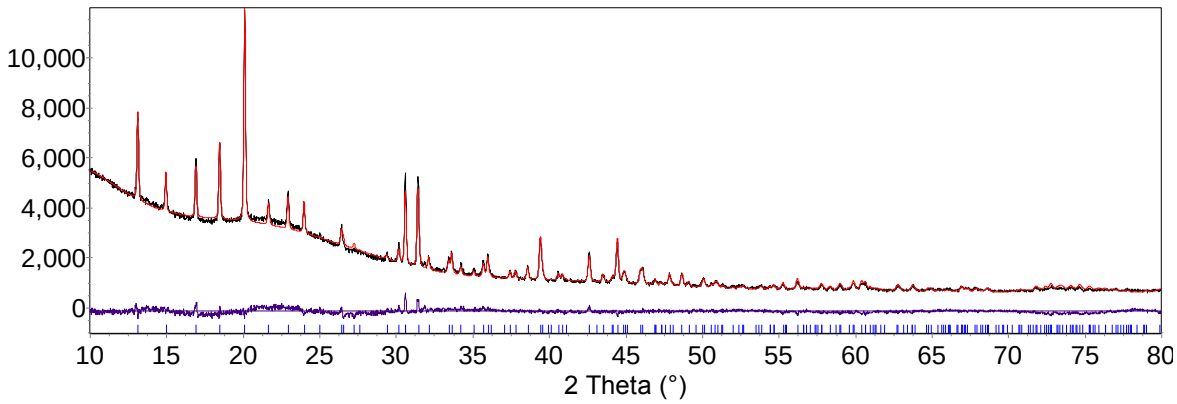

Figure 6.14 – Rietveld plot upon refinement of the Ca, B and N positions within the *Pna*2_1 (#33) space group. R_{wp} = 4.294%, χ^2 = 3.272

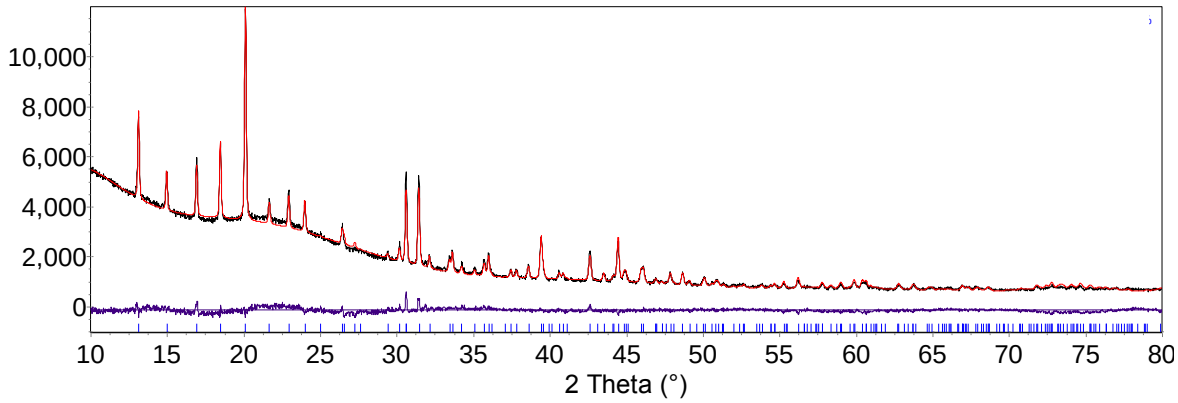

Figure 6.15 – Rietveld plot upon refinement of the Ca, B and N positions within the *Pnam* (#62) space group. R_{wp} = 4.331%, χ^2 = 3.327

Progress in solving the structure now required the incorporation of the H atoms into the unit cell. Due to the poor X-ray scattering of H and the quality of the laboratory based diffraction data, it was not possible to treat the H atoms as separate entities. In order to include the H atoms, rigid bodies were therefore used in the form of BH_4 and Ca–NH_3. Ca–NH_3 was chosen as a rigid body instead of just NH_3 to enforce the geometry of the nitrogen lone pair bonding to Ca. The BH_4 and Ca–NH_3 rigid bodies were introduced to the structure at the refined positions for B and Ca, respectively, in the *Pnam* space group. The BH_4 unit was initially restrained to its ideal tetrahedral geometry with a fixed B–H bond length of 1.2 Å. The Ca–NH_3 rigid body was initially restrained to an N–H bond length of 1.1 Å, a Ca–N bond length of 2.5 Å and the bond angles within the NH_3 group were fixed at 109.5°. The rotation of these rigid bodies was refined, followed by the refinement of all of the atomic positions. The constraints applied to the rigid bodies were maintained during these refinements. This model gave a good visual, figure 6.18, and statistical fit, R_{wp} = 4.089%, to the observed data. The number of terms in the background function was increased at this point to improve the fit. A satisfactory model had now been produced to proceed with a full Rietveld refinement.

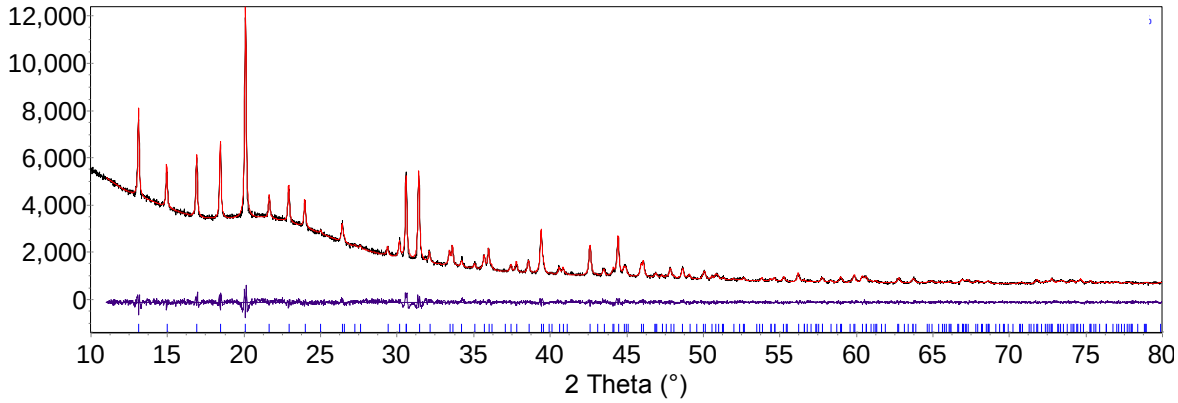

Figure 6.16 – The fit for $Ca(BH_4)_2{\cdot}NH_3$ with refined Ca, B and N positions and refined BH_4 and Ca–NH_3 rigid bodies within the *Pnam* (#33) space group. R_{wp} = 4.089%, χ^2 = 2.946

6.5.3 Full Rietveld Refinement

A complete Rietveld refinement was performed in Topas by refining a zero point error, a pseudo-Voigt peak shape (6 parameters) and a Chebyshev background function (17 parameters). Atomic positions were determined within the enforced geometry of the rigid bodies described in section 6.5.2 by refining the translation and rotation of the rigid bodies (6 parameters for each rigid body). The Ca–N bond length was refined, however, attempts to refine the N–H and B–H bond lengths resulted in the bond lengths reaching the minimum applied limit (0.8 Å) and so the N–H and B–H bond lengths were fixed at the values published by Chu *et al.*[13] for the structure of $Ca(BH_4)_2{\cdot}2NH_3$ (1.03 Å and 1.23 Å, respectively). It was not possible to obtain accurate H positions from room temperature laboratory diffraction data. Higher quality diffraction data, obtained at low temperature to minimise thermal motion, would be advantageous. Isotropic thermal parameters (B_{eq}) were also introduced to the refinement for Ca, B, N and H, and refined from starting values of 1 $Å^2$. Refinement of these parameters resulted in non-sensible values in every case except Ca, and so values for B, N and H were fixed at 1 $Å^2$. The final refinement contained 53 refined parameters. The resultant crystal structure and Rietveld plot are shown in figures 6.17 and 6.18 respectively. The refined crystallographic data is shown in table 6.4. The large errors associated with the rotational values of the Ca–NH_3 rigid body are indicative of a large degree of thermal motion in the bound NH_3. This could be overcome by the acquisition of higher quality data at lower temperature.

Table 6.4 – Refined crystallographic data for $Ca(BH_4)_2{\cdot}NH_3$[†]

Atom	Site	*x*	*y*	*z*
B1	4*c*	0.058(1)	0.2818(9)	0.25
H1	4*c*	0.164	0.2068	0.25
H2	4*c*	0.929	0.2348	0.25
H3	4*c*	0.074	0.3409	0.081
H4	4*c*	0.074	0.3409	0.419
B2	4*c*	0.350(1)	0.4317(8)	0.75
H5	4*c*	0.213	0.4725	0.75
H6	4*c*	0.342	0.3290	0.75
H7	4*c*	0.425	0.4636	0.582
H8	4*c*	0.425	0.4636	0.918
N	4*c*	0.6899	0.9098	0.25
H9	4*c*	0.6381	0.8849	0.415
H10	4*c*	0.6381	0.8849	0.085
H11	4*c*	0.7931	0.8621	0.25
Ca	4*c*	0.8375(3)	0.0906(2)	0.25

[†]Space group *Pnam* (#62), a = 8.1993(3) Å, b = 11.8410(4) Å, c = 5.8369(2) Å.

R_{wp} = 3.321%, R_{exp} = 2.392%, R_{wp}' = 19.668%, R_{exp}' = 14.164%, χ^2 = 1.929.

rCaN = 2.46(2), H–N–H = 115.2°(7), B_{eq}(Ca) = 1.0(1)

$B1H_4$ rigid body. Rotational values: R_x = 283(2)°, R_y = 202(1) and R_z = 214(2);
Translational values: x = 0.058(1), y = 0.2818(9), z = 0.25.

$B2H_4$ rigid body. Rotational values: R_x = 289(3)°, R_y = 20(3) and R_z = 40(3);
Translational values: x = 0.350(1), y = 0.4317(8), z = 0.75.

$Ca–NH_3$ rigid body. Rotational values: R_x = 143(33)°, R_y = 265(2) and R_z = 278(34);
Translational values: x = 0.8375(3), y = 0.0906(2), z = 0.25.

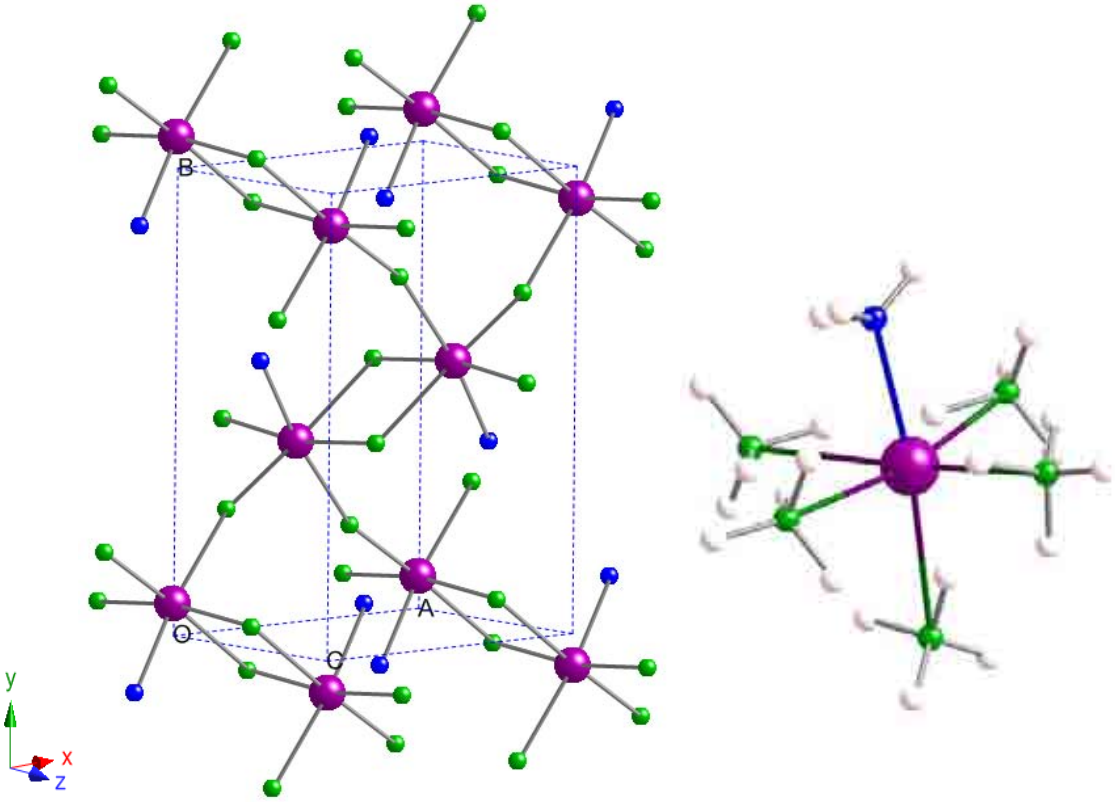

Figure 6.17 – Refined crystal structure of $Ca(BH_4)_2 \cdot NH_3$ (H atoms not shown). The coordination environment of the Ca^{2+} cation is shown. Each Ca^{2+} coordinates with one NH_3 and five BH_4 groups. Ca is shown in purple, N in blue, B in green and H in pale pink

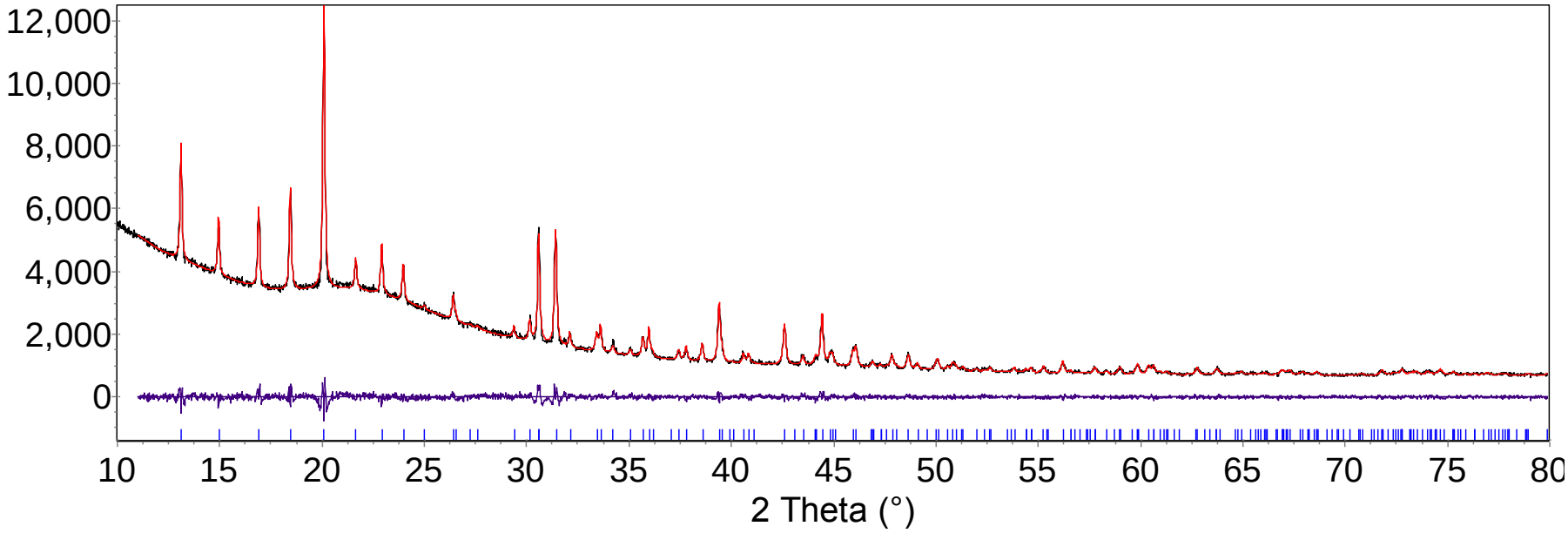

Figure 6.18 – Final Rietveld plot for $Ca(BH_4)_2{\cdot}NH_3$. The observed pattern is shown in black, the calculated in red and the difference in blue. The calculated peak positions are indicated. R_{wp} = 3.321%, χ^2 = 1.929

6.6 Thermal Desorption Studies

6.6.1 TPD Study of a $CaH_2 + 4NH_3BH_3$ Reaction Mixture

The thermal desorption properties of a ground sample of a $CaH_2 + 4NH_3BH_3$ reaction mixture were investigated using TPD–MS. The sample was heated to 350°C with a heating rate of 2°C min^{-1}. The data collected are shown in figure 6.19.

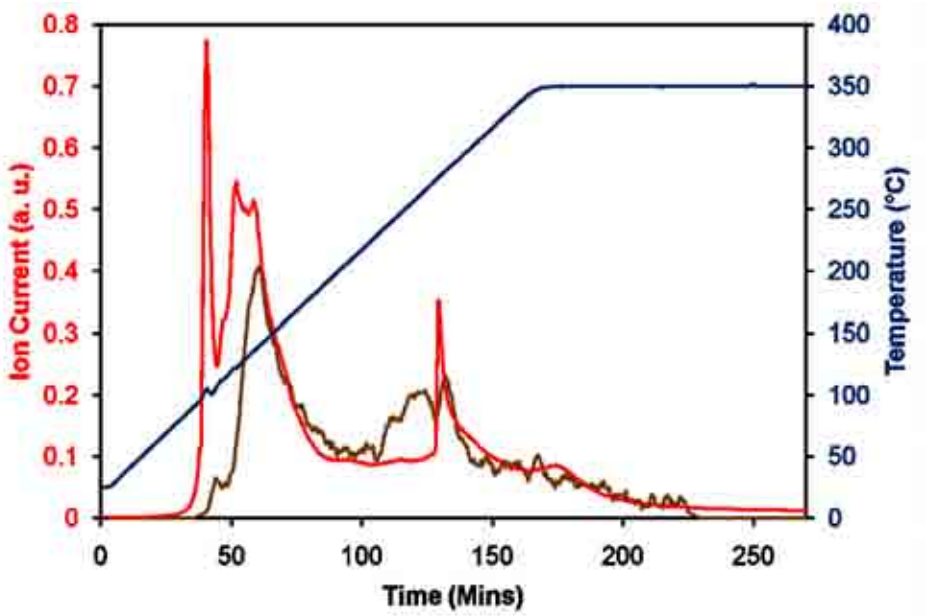

Figure 6.19 – TPD–MS analysis of a ground reaction mixture of $CaH_2 + 4NH_3BH_3$. The temperature trace is shown in blue and the mole percentages of H_2 and NH_3 (×200) released are shown in red and brown, respectively

It can be seen from the temperature trace that an exothermic event occurred at around 100°C, which was accompanied by a sharp H_2 release. A second broader H_2 desorption began at 105°C which peaked at 130°C. The amount of H_2 being released decreased, before reaching a constant rate at 190°C. This plateau of H_2 release continued up to 270°C when a sharp release occurred. A final small broad release began just before the target temperature of 350°C was achieved, this release may not have completed during the timescale of the experiment. NH_3 was also released from the reaction mixture. There were two broad NH_3 releases, the first began soon after the onset of H_2 release at approximately 100°C, reaching a maximum at 135°C. The second release of NH_3 began at 220°C and peaked at 255°C. Following this second broad release, the amount of NH_3 being released from the sample

decreased, although it did continue until the maximum temperature of 350°C was reached.

Discussion

From the knowledge of the $CaH_2 + 4NH_3BH_3$ reaction pathway garnered from powder XRD patterns, the desorptions observed in the TPD experiment would be expected to be related to events in the reaction pathway. The steps of the reaction pathway observed through powder XRD are shown below as well as the expected desorbed gases.

$$CaH_2 + 4NH_3BH_3 \rightarrow Ca(BH_4)_2{\cdot}2NH_3 + B_2N_2H_{(12-2n)} + nH_2 \qquad \text{Reaction 6.4}$$

$$Ca(BH_4)_2{\cdot}2NH_3 \rightarrow Ca(BH_4)_2{\cdot}NH_3 + NH_3 \qquad \text{Reaction 6.5}$$

$$Ca(BH_4)_2{\cdot}NH_3 \rightarrow \alpha\text{-}Ca(BH_4)_2 + NH_3 \qquad \text{Reaction 6.6}$$

$$\alpha\text{-}Ca(BH_4)_2 \rightarrow \beta\text{-}Ca(BH_4)_2 \qquad \text{Reaction 6.7}$$

$$\alpha + \beta\text{-}Ca(BH_4)_2 \rightarrow {}^{2}/_{3}CaH_2 + {}^{1}/_{3}CaB_6 + {}^{10}/_{3}H_2 \qquad \text{Reaction 6.8}$$

The two desorptions of NH_3 can hence be assigned to reactions 6.5 and 6.6. These reactions were shown to be completed at 150°C and 225°C, respectively, by powder XRD. The first NH_3 desorption correlated well with this temperature, with the majority of this first desorption being completed below 180°C. The majority of the second NH_3 desorption took place below a temperature of 300°C, with the peak rate of release at 255°C. This discrepancy in temperature could have been due to the different experimental setups: the TPD experiment was heated at 2°C min^{-1} whereas the gas line reactions were held for 12 hours at the reaction temperature. Therefore, events in the TPD trace were likely to occur at higher temperatures than in gas line reactions. As shown in the structural model of $Ca(BH_4)_2{\cdot}2NH_3$, section 6.4, each Ca centre was coordinated with two NH_3 molecules. The relatively low onset temperature of NH_3 release, 100°C, highlighted that the NH_3 molecules were coordinated to the Ca. This was a much lower temperature release of NH_3 compared to $Ca(NH_2)_2$ (347°C) and $LiNH_2$ (380°C), where the N is more strongly bound to the metal atom.[34,

[35] However, the low levels of NH_3 detected in this experiment suggested that an alternative pathway, favouring H_2 release, was at work.

The α to β phase transition in $Ca(BH_4)_2$, reaction 6.7, took place at 250°C according to powder XRD results. Investigations into this change outlined in the literature have shown that this was a structural phase transition that took place without the release of any gases.[17, 18, 21] Therefore, it can be concluded that none of the gas desorption events were related to this transition.

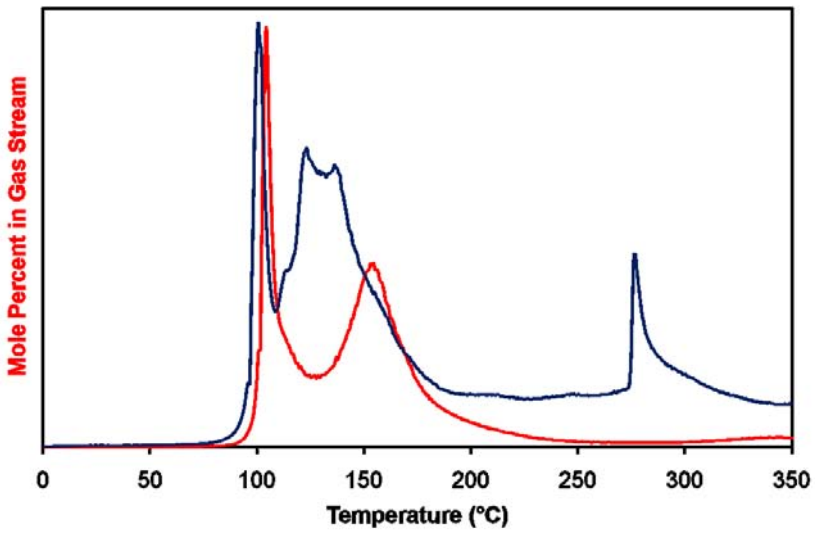

Figure 6.20 – A comparison of the H_2 TPD profiles of the $CaH_2 + 4NH_3BH_3$ reaction mixture (blue) and as-received NH_3BH_3 (red)

Figure 6.20 compares the H_2 desorption traces of the $CaH_2 + 4NH_3BH_3$ reaction mixture and NH_3BH_3. There was a strong correlation between the first H_2 desorptions from NH_3BH_3 and the $CaH_2 + 4NH_3BH_3$ reaction mixture, which suggested that NH_3BH_3 decomposition may have played some role in the reaction pathway. The first step in the reaction pathway inferred from powder XRD patterns showed the formation of $Ca(BH_4)_2{\cdot}2NH_3$, reaction 6.4. A $CaH_2 + xNH_3BH_3$ reaction mixture would be presumed to proceed in a 1:2 ratio in order to provide the correct stoichiometry to synthesise $Ca(BH_4)_2{\cdot}2NH_3$ without side products. However, as shown by powder XRD, figure 6.4, this stoichiometry resulted in excess CaH_2 being present in the product. Despite the fact that the presumed excess of NH_3BH_3 in a 1:4 reaction mixture appeared to follow its established decomposition pathway, we may conclude that this excess NH_3BH_3 could have played a role in the pathway of the CaH_2 +

$4NH_3BH_3$ reaction, because it was only at this stoichiometry that the starting materials were completely consumed during the reaction. The possible role of NH_3BH_3 in the reaction mechanism will be discussed in section 6.8. The first H_2 desorption step in the decomposition of NH_3BH_3 results in the formation of the amorphous material polyaminoborane, $(NH_2BH_2)_n$, see chapter 3.4. As the only crystalline phase observed in the powder XRD pattern of the product of the CaH_2 + $4NH_3BH_3$ reaction at 80°C was $Ca(BH_4)_2{\cdot}2NH_3$, the remaining B, N and H must have been present in an amorphous material. The first H_2 desorption may therefore involve the following reaction:

$$CaH_2 + 4NH_3BH_3 \rightarrow Ca(BH_4)_2{\cdot}2NH_3 + 2(NH_2BH_2)_n + 2H_2 \qquad \text{Reaction 6.9}$$

A key observation of the reaction was that during heating the sample underwent a significant volume expansion, a phenomenon also observed during the thermal decomposition of as-received NH_3BH_3, which supports the notion that NH_3BH_3 decomposition was involved in the reaction pathway. Furthermore, this decomposition is an exothermic process, explaining the observed exothermic event in figure 6.19. Following this first step, two separate desorption pathways could then proceed: firstly as discussed above the two step NH_3 release from $Ca(BH_4)_2{\cdot}2NH_3$ and secondly, as discussed in chapter 3.4, further H_2 release from $(NH_2BH_2)_n$. Figure 6.20 shows that the second desorption of NH_3BH_3 occurred as a shoulder on the broad desorption from the mixture. This provided evidence that the decomposition of $(NH_2BH_2)_n$, yielding $(NHBH)_n$ took place, reaction 6.10, but that other desorption events also proceeded, underlining the complicated nature of the desorption pathway.

$$2(NH_2BH_2)_n \rightarrow 2(NHBH)_n + 2nH_2 \qquad \text{Reaction 6.10}$$

The broad desorption of H_2 between the two NH_3BH_3 related desorptions occurred just after the onset of NH_3 release. A study by Chu *et al.*[13] with respect to the decomposition of $Ca(BH_4)_2{\cdot}2NH_3$ reported that under flowing conditions NH_3 was the only desorbed product, whereas H_2 was exclusively released in a closed system. This was rationalised by the fact that in a closed system the NH_3 would remain in close proximity to $Ca(BH_4)_2$, giving the potential to interact with nearby species and

leading to the dissociation of both N–H and B–H bonds, forming H_2; the proposed desorption reaction after heating the sample to 250°C is shown in reaction 6.11. The TPD–MS experimental setup was not a closed system, but because the NH_3 was not moved away quickly from the sample, it did offer potential for significant amounts of NH_3 to remain close to the sample. The low levels of NH_3 detected by mass spectrometry suggested that pathways similar to that proposed by Chu *et al.* proceeded, and hence H_2 desorption at a similar temperature to NH_3 in TPD–MS experiments was observed.

$$Ca(BH_4)_2{\cdot}2NH_3 \rightarrow \tfrac{1}{4}Ca(BH_4)_2 + \tfrac{1}{4}Ca_3(BN_2)_2 + BN + 6H_2 \qquad \text{Reaction 6.11}$$

The higher temperature H_2 desorption events, primarily the sharp release of H_2 at 270°C, were likely related to $Ca(BH_4)_2$, reaction 6.8. The shape of this desorption meant it could not have been associated with the decomposition pathway of NH_3BH_3, as the higher temperature H_2 desorption event in this decomposition is broad in nature. In contrast to this, the first H_2 desorption in $Ca(BH_4)_2$ decomposition has been observed as a sharp release.[18, 21-23] However, the onset temperature of this H_2 desorption in this study was significantly lower than what has been reported in literature studies regarding $Ca(BH_4)_2$, casting doubt on the validity of this assignment. The lowest reported onset temperature of H_2 release from $Ca(BH_4)_2$ is 320°C, which is 50°C higher than that observed in the TPD–MS experiment of this study.[20] The results of powder XRD, section 6.3, also supported this low decomposition temperature of $Ca(BH_4)_2$. The literature study also employed a heating rate of 2°C min^{-1} and therefore the heating rates were not responsible for the observed differences. The initial low temperature H_2 desorption, between 100°C and 150°C, due to unidentified side reactions possibly related to NH_3 release being suppressed, may have led to the formation of other materials, such as $Ca_3(BN_2)_2$ (reaction 6.11) hence complicating the reaction mixture and resulting in further side reactions at higher temperatures. The sharp H_2 desorption at 270°C may have been one such side reaction that involved $Ca(BH_4)_2$.

The highest temperature release of H_2 at 350°C could potentially be related to one of two events. Firstly, in the desorption profile of NH_3BH_3, see chapter 3.4, a desorption of H_2 was observed at a similar temperature and therefore it could be assigned to the

release of H_2 from $(NHBH)_n$. However, H_2 release from $Ca(BH_4)_2$ has been observed as a two step process, with the second desorption step being much broader in nature than the first.[20-23] This second step has been shown to take place at temperatures above 400°C and therefore would not have been expected to have been observed in the TPD–MS experiment of this study. However, as discussed above, the potential reaction of $Ca(BH_4)_2$ with other components of the reaction mixture may have led to H_2 release at a lower temperature than what is observed from isolated $Ca(BH_4)_2$ and so it follows that further reactions may have occurred instead of the second H_2 desorption from $Ca(BH_4)_2$.

Hydrogen loss from $(NHBH)_n$ has been shown to occur at temperatures as low as 350°C, but this release is not completed below a temperature of 600°C.[36] Therefore, it seems likely that the two H_2 desorptions observed above 270°C were due to a combination of decomposition of $Ca(BH_4)_2$ and $(NHBH)_n$, the sharp release at 270°C being related to the decomposition of $Ca(BH_4)_2$, resulting in CaH_2 and an unidentified intermediate, and the higher temperature release at 350°C originating from $(NHBH)_n$. Evidence for at least one of these desorption events being related to $Ca(BH_4)_2$ decomposition was observed in the powder XRD pattern taken of the sample after the TPD–MS experiment. The pattern, figure 6.21, showed only CaH_2 presence, a decomposition product of $Ca(BH_4)_2$.

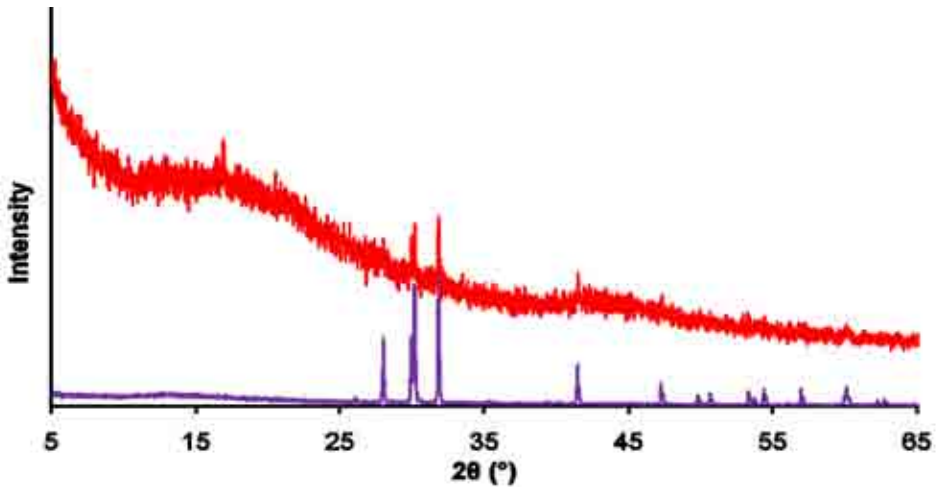

Figure 6.21 – The powder XRD pattern of the sample collected after heating a reaction mixture of $CaH_2 + 4NH_3BH_3$ to 350°C at a rate of 2°C min^{-1} in a TPD (red). The powder XRD pattern of CaH_2 is shown for comparison (purple)

6.6.2 IGA Study of a CaH_2 + $4NH_3BH_3$ Reaction Mixture

The synthesis of the crystalline material $Ca(BH_4)_2{\cdot}2NH_3$, was investigated using IGA–MS. A sample of the reaction mixture (24.6 mg) was inertly loaded into the IGA connected to a mass spectrometer. Figure 6.22 shows the thermogravimetric data overlaid with the mass spectrometric data for the observed desorption products. The sample was heated at a rate of 1°C min^{-1} to an initial target temperature of 70°C. This target temperature was subsequently raised to 90°C because neither any desorbed gases nor a weight loss were observed at 70°C.

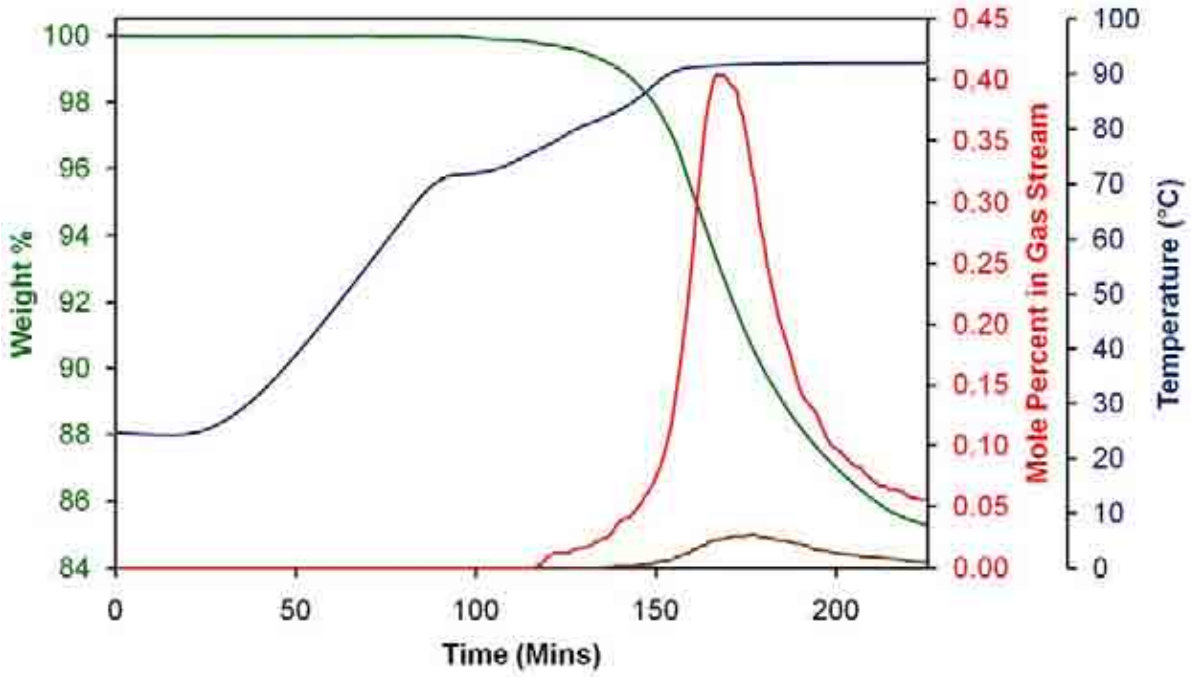

Figure 6.22 – Thermogravimetric analysis of the CaH_2 + $4NH_3BH_3$ reaction mixture in an IGA. The gravimetric trace is shown in green, the temperature trace in blue and the mole percentages of H_2 and NH_3 released are shown in red and brown, respectively

Weight loss from the sample began at around 74°C, with the majority of mass lost above 88°C, when the temperature was maintained at 90°C. This weight loss was accompanied by both H_2 and NH_3 release. H_2 release began first, with the onset of NH_3 release at 84°C. The initial slow weight loss from the sample between 74°C and 84°C was exclusively due to H_2, with the main weight loss above 88°C being due to desorption of both H_2 and NH_3. Both the onset temperatures of H_2 and NH_3 desorption were lower in the IGA–MS experiment compared to the TPD–MS

experiment. This was probably related to the lower heating rate employed in the IGA–MS experiment. The sample showed a weight loss of 14.7 wt% during the timescale of the experiment.

Discussion

The release of both H_2 and NH_3 during the IGA–MS experiment suggested that decomposition of NH_3BH_3 to $(NH_2BH_2)_n$ had occurred, resulting in H_2 release, along with formation of $Ca(BH_4)_2{\cdot}2NH_3$ and its subsequent decomposition, releasing NH_3 to yield $Ca(BH_4)_2{\cdot}NH_3$. The theoretical weight losses for these two events are shown below.

$$CaH_2 + 4NH_3BH_3 \rightarrow Ca(BH_4)_2{\cdot}2NH_3 + 2(NH_2BH_2)_n + 2H_2 \qquad 2.4\ wt\%$$

$$Ca(BH_4)_2{\cdot}2NH_3 \rightarrow Ca(BH_4)_2{\cdot}NH_3 + NH_3 \qquad 10.3\ wt\%$$

These two reactions account for a weight loss of 12.7 wt% from the initial sample, which was lower than the observed weight loss of 14.7 wt%. The additional weight loss must have therefore been due to either the next steps in the reaction pathways or side reactions.

6.6.3 Thermal Desorption Studies of Product A

6.6.3.1 TPD Study of Product A

The thermal desorption properties of the product of the $CaH_2 + 4NH_3BH_3$ reaction heated at 80°C were investigated using TPD–MS. Powder XRD of the sample prior to the TPD–MS experiment confirmed that the sample contained the crystalline phase $Ca(BH_4)_2{\cdot}2NH_3$. The sample was heated to 350°C with a heating rate of 2°C min^{-1}. The data collected are shown in figure 6.23.

The desorption profile (figure 6.23) showed that both H_2 and NH_3 were released from the sample, with the onset of H_2 release at a lower temperature, 95°C, than that of NH_3, 125°C. The first desorption of H_2 peaked at 135°C, which was shortly followed

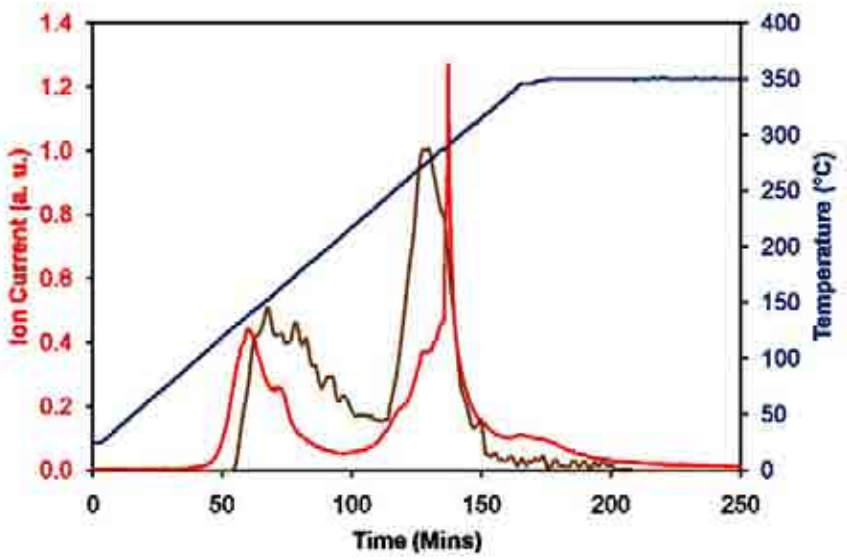

Figure 6.23 – TPD–MS analysis of a sample of Product A. The temperature trace is shown in blue and the mole percentages of H_2 and NH_3 (×50) released are shown in red and brown, respectively

by the maximum of the first NH_3 desorption at 155°C. A shoulder was observed on the first H_2 desorption peak at 155°C. A second broader H_2 desorption began at 215°C, continuing until a temperature of 275°C was reached, at which point a sharp desorption of H_2 occurred. This was possibly due to two overlapping H_2 desorption events. A second desorption of NH_3 commenced at 230°C and reached a maximum at 270°C. This desorption was completed at a temperature of 300°C and no further release of NH_3 were observed. A final small broad release of H_2 was observed at 320°C, which tailed off while the sample was held at 350°C.

6.6.3.2 IGA Study of Product A

A sample (61 mg) of the product of the $CaH_2 + 4NH_3BH_3$ reaction pre-heated at 80°C was inertly loaded into an IGA connected to a mass spectrometer. Figure 6.24 shows the thermogravimetric data overlaid with the mass spectrometric data for the observed desorption products. The same conditions as employed in the TPD experiment were used, with the sample heated at a rate of 2°C min^{-1} to a target temperature of 350°C.

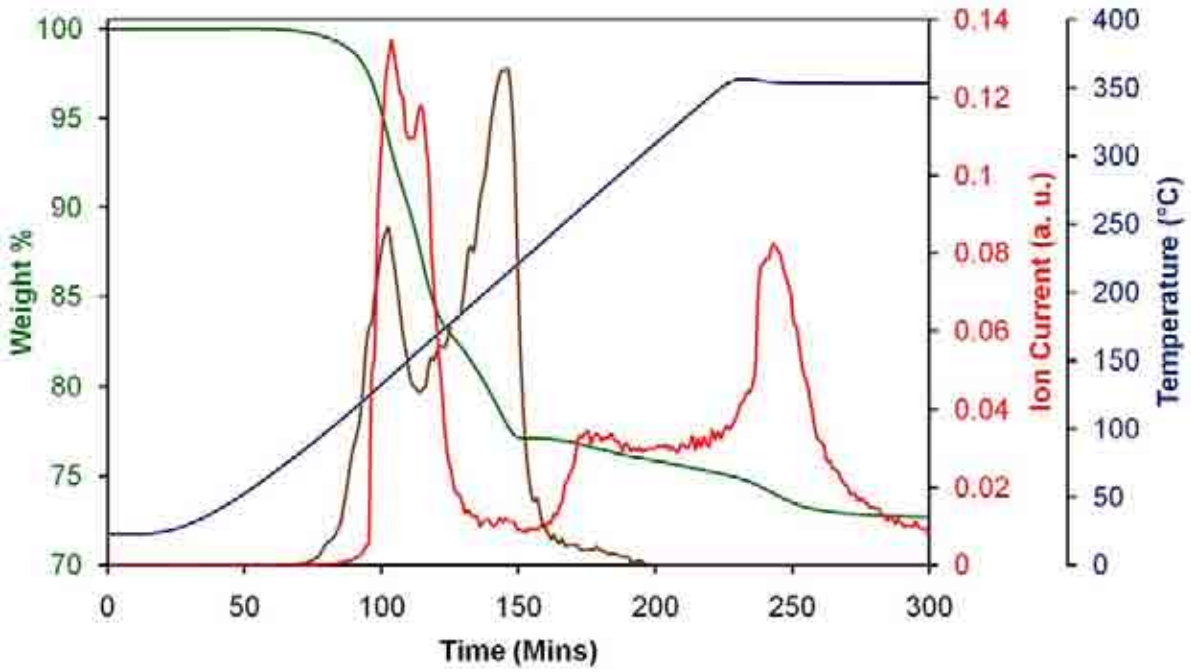

Figure 6.24 – Thermogravimetric analysis of a sample of Product A in an IGA. The gravimetric trace is shown in green, the temperature trace in blue and the mole percentages of H_2 and NH_3 (×100) released are shown in red and brown, respectively

A total weight loss of 27.5 wt% from the sample was observed on heating the sample to 350°C. The initial weight loss began at 80°C and continued until a temperature of 165°C was reached. This step involved the loss of 15.5 wt%. This weight loss was accompanied by both the desorption of NH_3 and H_2. Unlike the TPD experiment, the onset of NH_3 release (80°C) was observed at a lower temperature than H_2 (95°C). The weight loss continued above 165°C, although the rate of loss decreased, implying that a second event in the reaction pathway was responsible. This step showed a weight loss of 7.1 wt% and was complete at 215°C. A second release of NH_3 was observed between 150°C and 220°C, with only a small amount of H_2 desorption during this temperature range. The second weight loss was therefore related to the desorption of NH_3. A third weight loss began at 240°C and at 350°C the rate of weight loss increased, implying a fourth weight loss event. The third event was responsible for a weight loss of 2.5 wt% and the final weight loss contributed 2.4 wt%. NH_3 release above 235°C was minimal and no NH_3 release was observed at all above 295°C. Conversely, H_2 desorption increased at 235°C and a plateau of H_2 release was observed between 255°C and 340°C, at which temperature a final sharp

release occurred, which peaked at 350°C. As 350°C was the highest temperature that the sample was exposed to, the experiment seemed to have captured an isothermal desorption. The two higher temperature weight losses were clearly due to the desorption of H_2.

6.6.3.3 Discussion

The TPD–MS results (figure 6.23) showed the expected two step NH_3 desorption pathway, for the decomposition of $Ca(BH_4)_2{\cdot}2NH_3$ to $Ca(BH_4)_2{\cdot}NH_3$, followed by its subsequent decomposition to $Ca(BH_4)_2$. The low levels of NH_3 detected again suggested that this was in fact a minority pathway within this experimental setup. The initial H_2 desorption was similar to what was observed from the reaction mixture, figure 6.19, with the initial release being related to alternative desorption pathways previously discussed, section 6.6.1, and the shoulder of this release being due to $(NH_2BH_2)_n$ decomposition. The broad higher temperature H_2 release at 320°C may subsequently have been associated with the decomposition of $(NHBH)_n$. H_2 release between 215°C and 320°C was not observed during the TPD study of NH_3BH_3, chapter 3.4, and therefore it cannot have been associated with this decomposition pathway. Hence, this H_2 release was likely associated with $Ca(BH_4)_2$, with the possibility of side reactions or unexpected interactions between compounds present in the two main desorption pathways being responsible. As with the TPD–MS study of the $CaH_2 + 4NH_3BH_3$ reaction mixture, the temperature at which the sharp release of H_2 occurred at, 275°C, was lower than what would be expected for isolated $Ca(BH_4)_2$. Therefore, the rationale discussed previously for this lower than expected H_2 release in section 6.6.1 can also be applied here. The fact that this H_2 release occurred shortly after the peak of the second NH_3 desorption showed that the formation of $Ca(BH_4)_2$ was rapidly followed by either its decomposition or involvement in side reactions.

The IGA desorption study of $Ca(BH_4)_2{\cdot}2NH_3$ revealed a total weight loss of 27.5 wt%, with a 22.6 wt% loss below 215°C. The majority of the NH_3 desorption took place below this temperature. Theoretically the release of one equivalent of NH_3 from $Ca(BH_4)_2{\cdot}2NH_3$ would result in a weight loss of 16.4 wt% and as two equivalents would be lost on forming $Ca(BH_4)_2$ the expected weight loss for the IGA study was

32.8 wt%. The much lower observed weight loss offers support to the notion that there was amorphous material present in the sample, such as $(NH_2BH_2)_n$. The calculated weight losses from the initial sample assuming a composition of $Ca(BH_4)_2{\cdot}2NH_3 + 2(NH_2BH_2)_n$ are shown below for the desorption events observed below 215°C.

$$Ca(BH_4)_2{\cdot}2NH_3 + 2(NH_2BH_2)_n \rightarrow Ca(BH_4)_2{\cdot}NH_3 + 2(NH_2BH_2)_n + NH_3 \qquad 10.5\ wt\%$$

$$Ca(BH_4)_2{\cdot}NH_3 + 2(NH_2BH_2)_n \rightarrow Ca(BH_4)_2{\cdot}NH_3 + 2(NHBH)_n + 2H_2 \qquad 2.5\ wt\%$$

$$Ca(BH_4)_2{\cdot}NH_3 + 2(NHBH)_n \rightarrow Ca(BH_4)_2 + 2(NHBH)_n + NH_3 \qquad 10.5\ wt\%$$

This gives a total theoretical weight loss of 23.5 wt% which agrees well with the observed weight loss. The slight discrepancy was due to the fact that there was a small amount of NH_3 released above 215°C. The loss of 4.9 wt% above 215°C was primarily due to H_2 desorption although it was slightly contaminated with NH_3. Below 215°C the observed weight loss was 0.9 wt% less than the theoretical value due to NH_3 loss not being completed. Therefore it can be assumed that above 215°C, H_2 desorption caused a weight loss of 4.0 wt%, which was equal to a desorption of three equivalents of H_2. H_2 desorption from $Ca(BH_4)_2$ and $(NHBH)_n$ could both have contributed to this weight loss. Thermogravimetric studies of $Ca(BH_4)_2$ have shown that weight loss totalled 6 wt%, equal to two equivalents of H_2, up to a temperature of 350°C.[18, 20, 21] Therefore, two of the three equivalents of H_2 released above 215°C in the IGA–MS study can be assigned to $Ca(BH_4)_2$ decomposition with the remaining one equivalent desorbed from amorphous material in the sample. The good agreement between the theoretical and calculated weight losses suggests that in the IGA study the two pathways operated more or less separately and that side reactions were less of an issue. Significant support for this comes from the higher temperature H_2 release. The release at 350°C agrees much better with the reported decomposition temperature of $Ca(BH_4)_2$, implying that in the IGA experiment this phase was not involved in side reactions.

There were a number of differences between the TPD–MS and IGA–MS experiments. In the TPD–MS experiment, the onset of NH_3 release was at a higher temperature than that of H_2, whereas this was reversed for the IGA–MS experiment.

These observations supported the proposal that when the NH_3 was not quickly removed from the sample (TPD) it was able to effect side reactions, resulting in H_2 release. In the IGA experiment the NH_3 release was carried away as soon as it was desorbed, as the argon carrier gas flowed directly over the sample and so H_2 was not desorbed until the decomposition of $(NH_2BH_2)_n$ began. The lower than expected temperature of desorption events compared to values reported in the literature was a feature of the TPD data. This was most apparent in the higher temperature H_2 desorptions, where the peak in the H_2 desorption trace of the IGA–MS experiment at 350°C showed much better agreement with the known decomposition temperature of $Ca(BH_4)_2$ compared to the peak observed at 275°C in the TPD–MS trace.[20, 22, 23, 28] As discussed this may have in part been due to side reactions caused by NH_3 interacting with the sample following its desorption. A second difference between the two experiments was that a larger sample was used in the TPD experiment, which may have been more prone to inhomogeneities in temperature or local composition. A further factor to consider was that the side reactions occurring in the TPD experiment may have led to the formation of a material that melted during the timescale of the experiment, producing a labilizing effect and hence lower temperature H_2 release.

6.6.4 Thermal Desorption Studies of Product B

6.6.4.1 TPD Study of Product B

The thermal desorption properties of the product of the $CaH_2 + 4NH_3BH_3$ reaction heated at 150°C were investigated using TPD–MS. Powder XRD of the sample prior to the TPD–MS experiment confirmed that the sample contained the crystalline phase $Ca(BH_4)_2{\cdot}NH_3$. The sample was heated at a rate of 2°C min^{-1} to a maximum temperature of 350°C. The data collected is shown in figure 6.25.

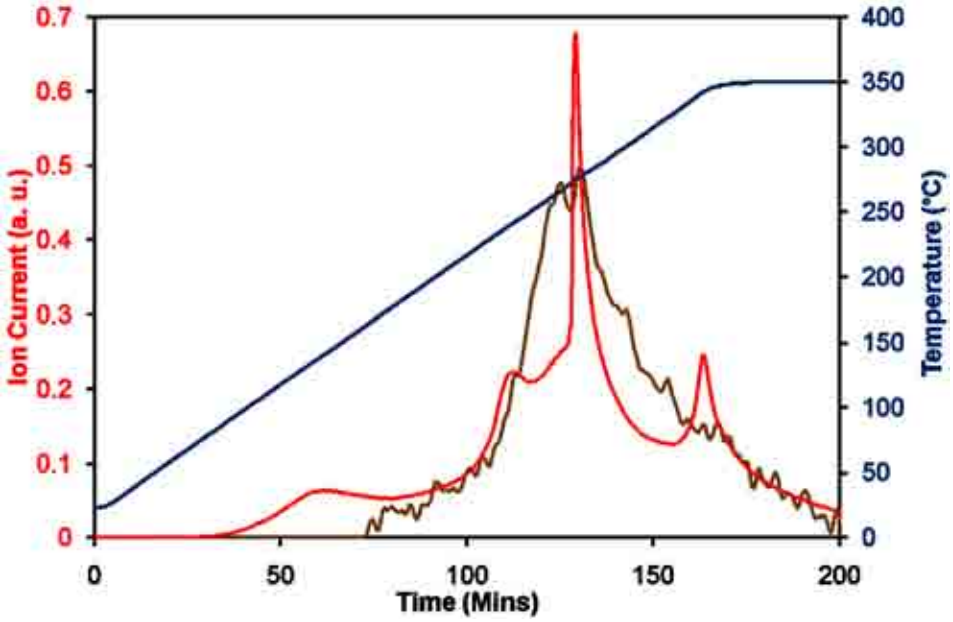

Figure 6.25 – TPD–MS analysis of a sample of Product B. The temperature trace is shown in blue and the mole percentages of H_2 and NH_3 (×75) released are shown in red and brown, respectively

Both H_2 and NH_3 desorptions were observed during the TPD experiment. The onset of H_2 release was at a lower temperature than that of NH_3, occurring at 80°C. There was an initial small broad release of H_2, between 80°C and 165°C, which reached a maximum at 130°C. The main H_2 desorption event began at 165°C and the shape of the H_2 trace suggested that at least two H_2 desorptions occurred between 165°C and 300°C. A broad release proceeded in this temperature range, as well as a sharp release of H_2, that reached a maximum at 275°C. A final higher temperature release of H_2 began at 315°C, reaching a maximum at 335°C. There was a single broad NH_3 desorption which began at 160°C, the peak of which occurred at 270°C.

6.6.4.2 TGA Study of Product B

The thermogravimetric and thermal desorption properties of a sample of Product B were investigated using a TGA connected to a mass spectrometer. Figure 6.26 shows the thermogravimetric data overlaid with the mass spectrometric data for the observed desorption products. The same conditions as employed in the TPD experiment were used, with the sample heated at a rate of 2°C min^{-1} to a target temperature of 350°C.

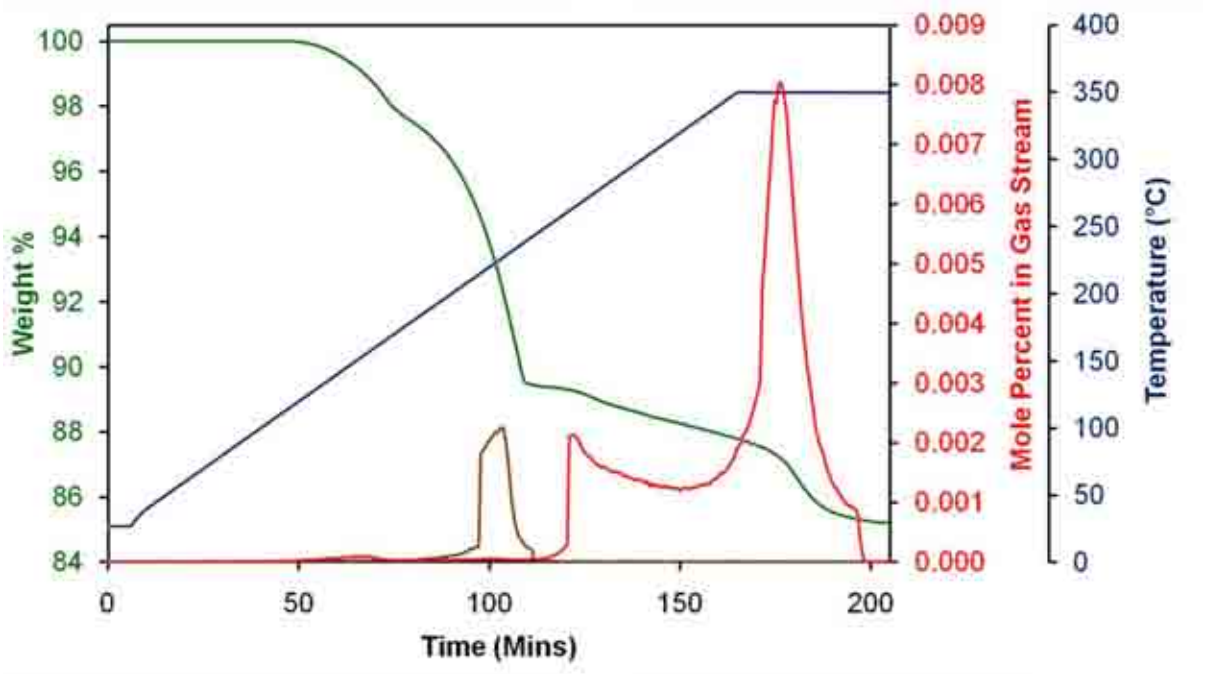

Figure 6.26 – Thermogravimetric analysis of a sample of Product B in a TGA. The gravimetric trace is shown in green, the temperature trace in blue and the mole percentages of H_2 and NH_3 released shown in red and brown, respectively

The thermogravimetric data showed that a total weight loss of 14.8 wt% took place during the experiment. There were a number of weight loss events that took place, with the initial weight loss beginning at a temperature of 120°C. A second weight loss event appeared to start before the completion of the first at 160°C, due to a change in the rate of weight loss. The sample lost 2.2 wt% up to a temperature of 160°C. The second weight loss was completed at 235°C and a further 8.4 wt% was lost from the sample during this temperature range. Further weight loss was observed above 260°C in a two step process. The sample lost weight slowly between 260°C and 350°C, with a loss of 1.8 wt%. A final weight loss of 2.4 wt% took place while the sample was maintained at a temperature of 350°C. Analysis of the gases desorbed showed that the first two weight loss events were almost exclusively accompanied by NH_3 release. NH_3 desorption began at 125°C, with an initially slow rate of desorption. The rate of desorption increased greatly at 210°C and the majority of NH_3 was released above this temperature in a single step desorption, peaking at 220°C. This desorption was complete at 240°C, with no further NH_3 desorbed above this temperature. Only a minimal amount of H_2 was released below 240°C, with two very small releases of H_2 at 140°C and 235°C. The main H_2 release occurred above

250°C, with two desorptions evident above this temperature. The absence of NH_3 release above this temperature showed that the two higher temperature weight losses were due entirely to H_2 loss. There was a sharp increase in the amount of H_2 released at 250°C, while the rate of H_2 release decreased slowly until a temperature of 345°C was reached, when a sharp release of H_2 began.

6.6.4.3 Discussion

Desorption of H_2 below 150°C was unexpected because the sample was synthesised at this temperature prior to the desorption experiments. This low temperature H_2 release in the TPD–MS experiment could have been due to the presence of $(NH_2BH_2)_n$ in the sample. The NH_3 desorbed in both the experiments was due to the decomposition of $Ca(BH_4)_2{\cdot}NH_3$, the discrepancy in the observed temperature of the desorption being due to the different experimental setups as discussed in section 6.6.3. Assuming the initial sample contained $Ca(BH_4)_2{\cdot}NH_3$ and $(NH_2BH_2)_n$, the theoretical weight loss for this decomposition step is 11.7 wt%. The observed weight loss due to NH_3 release was less than this, 10.6 wt%, this difference was possibly due to sample degradation, due to NH_3 release, during the delay between synthesising the sample and running the TGA experiment. The weight loss of 4.2 wt% above 260°C was exclusively due to H_2 desorption, which meant that three equivalents of H_2 were desorbed. This was the same result as for the IGA–MS study of $Ca(BH_4)_2{\cdot}2NH_3$, as would be expected and therefore the same conclusion can be drawn: two equivalents of H_2 were desorbed due to the decomposition of $Ca(BH_4)_2$ and the other equivalent desorbed from polymeric material in the sample.

The H_2 desorption trace from $Ca(BH_4)_2{\cdot}NH_3$ again showed the same discrepancy as with $Ca(BH_4)_2{\cdot}2NH_3$, where the H_2 desorption assumed to be related to the decomposition of $Ca(BH_4)_2$ occurred at a lower temperature than expected in the TPD–MS experiment, whereas the TGA experiment showed the release at the expected temperature. The H_2 desorption from the TGA experiment was very similar to that observed in the IGA trace of Product A at high temperature, which suggests this data may be more reliable than TPD. The TGA experiment was similar in nature to that of IGA–MS, in the sense that the argon carrier gas flowed directly over the sample. This supports the proposal that the interaction of NH_3 with sample

components resulted in different desorption pathways in the TPD experiment. A difference between the TPD–MS desorption data of $Ca(BH_4)_2{\cdot}2NH_3$ and $Ca(BH_4)_2{\cdot}NH_3$ was the observation of a sharp H_2 desorption at 350°C from the $Ca(BH_4)_2{\cdot}NH_3$ sample, compared to a broad release from $Ca(BH_4)_2{\cdot}2NH_3$. A sharp release would be unexpected from a polymeric product such as $(NHBH)_n$. This release may therefore have been related to the decomposition of $Ca(BH_4)_2$.

6.7 Solid State ^{11}B MAS NMR Spectroscopy

The $CaH_2 + 4NH_3BH_3$ reaction pathway was also investigated through solid state ^{11}B MAS NMR spectroscopy to determine how the boron environments changed as the reaction progressed, in particular to provide information about amorphous components of reaction mixtures. The samples were prepared through thermal reactions as described in section 6.2 and the ^{11}B NMR spectra collected at room temperature. The data was collected in collaboration with the University of Warwick. All deconvolution of the spectra was carried out by Tom Partridge at the University of Warwick. Figure 6.27 shows the ^{11}B NMR spectrum collected of the product of the $CaH_2 + 4NH_3BH_3$ reaction at 80°C along with the deconvolution of the spectrum.

The ^{11}B NMR spectrum of the sample collected after heating to 80°C was dominated by a strong resonance at −34.8 ppm; deconvolution showed there was also a weak resonance at −33.2 ppm. There were also a number of low intensity features present at −21.9, −17.3, −13.1 and −7.1 ppm: inset figure 6.27. Deconvolution of the quadrupolar resonance showed that there were two environments present; at 30.3 and 25.3 ppm.

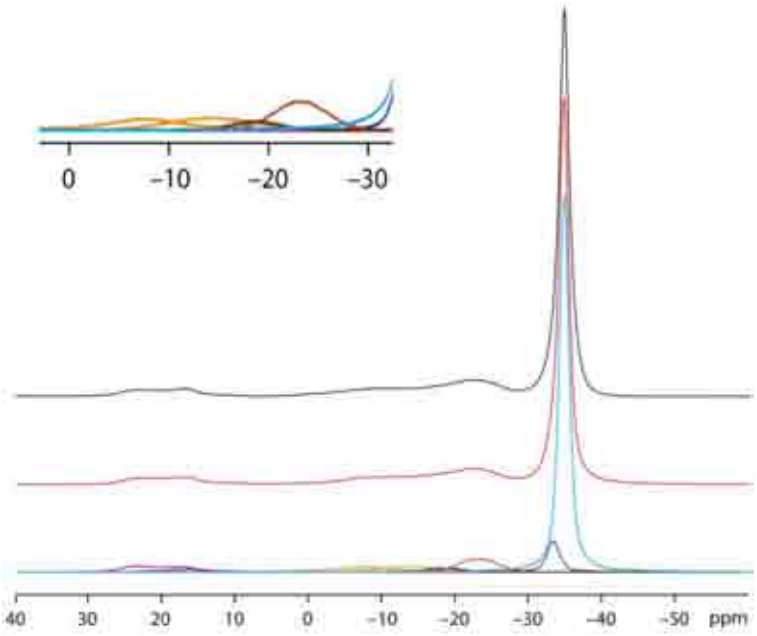

Figure 6.27 – The solid state ^{11}B MAS NMR spectrum collected from the product of the CaH_2 + $4NH_3BH_3$ reaction at 80°C (black). Deconvolution of the spectrum is shown, with the cumulative simulated spectrum shown in red

The pathway of the CaH_2 + $4NH_3BH_3$ reaction as viewed by solid state ^{11}B MAS NMR spectroscopy is shown in figure 6.28. The spectrum collected after reaction at 90°C was identical to the one collected after reaction at 80°C, but further heating to 100°C resulted in the appearance of a shoulder on the most intense feature at −34.7 ppm, figure 6.29. Deconvolution of this spectrum showed that the shoulder was composed of two separate resonances at −32.2 and −33.2 ppm. The quadrupolar boron environments showed slight increases in intensity, while the low intensity resonances between −7.0 ppm and −22.0 ppm were still present.

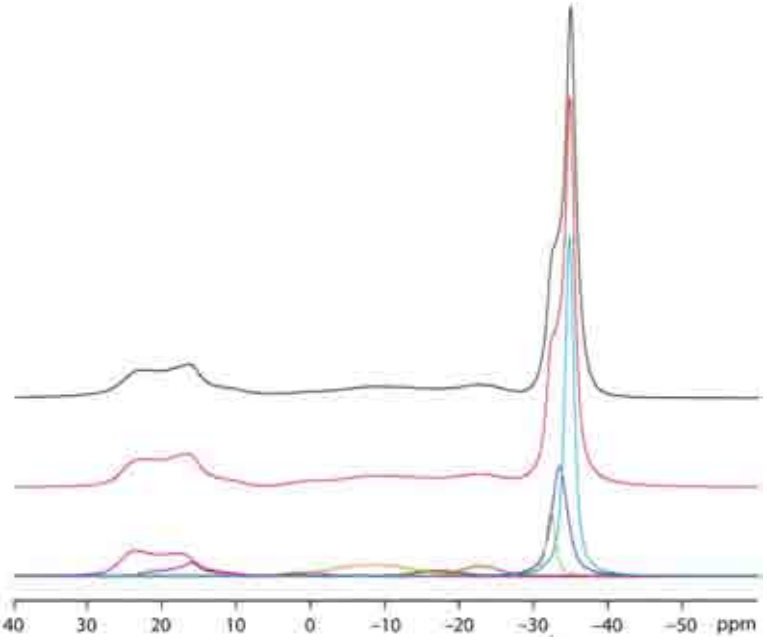

Figure 6.29 – The solid state ^{11}B MAS NMR spectrum collected from the product of the CaH_2 + $4NH_3BH_3$ reaction at 100°C (black). Deconvolution of the spectrum is shown, with the cumulative simulated spectrum shown in red

Further heating to 110°C showed that the shoulder feature, made up of the two resonances at −32.3 and −33.2 ppm had increased in intensity and had become the most intense feature in the spectrum, figure 6.30. The previously observed resonance at −34.7 ppm was also still present. The low intensity features previously observed between −7.0 ppm and −22.0 ppm were also present, although their intensity had decreased, while the quadrupolar environments showed a slight increase in intensity.

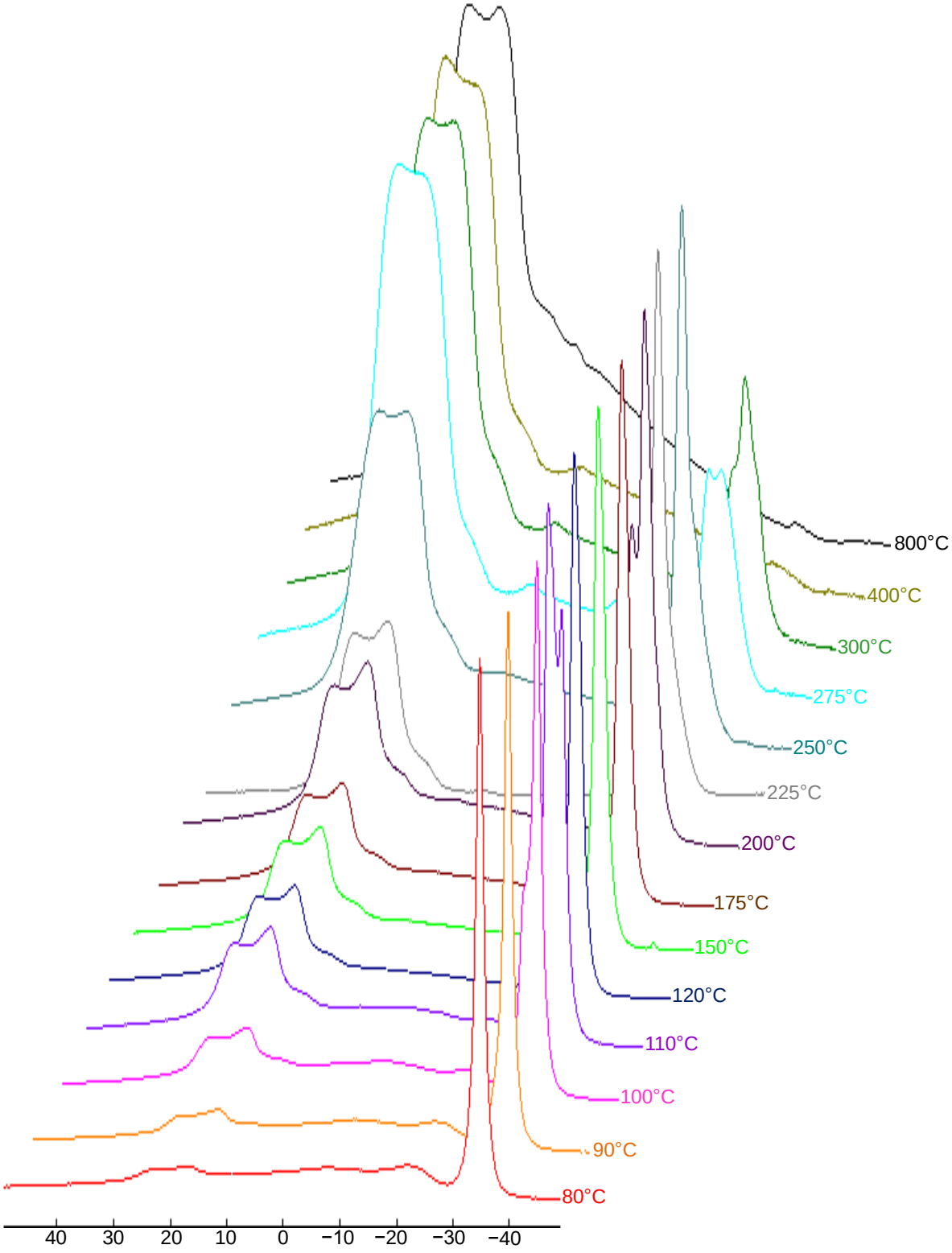

Figure 6.28 – Solid state ^{11}B MAS NMR spectra obtained from the products of the $CaH_2 + 4NH_3BH_3$ reaction at various temperatures

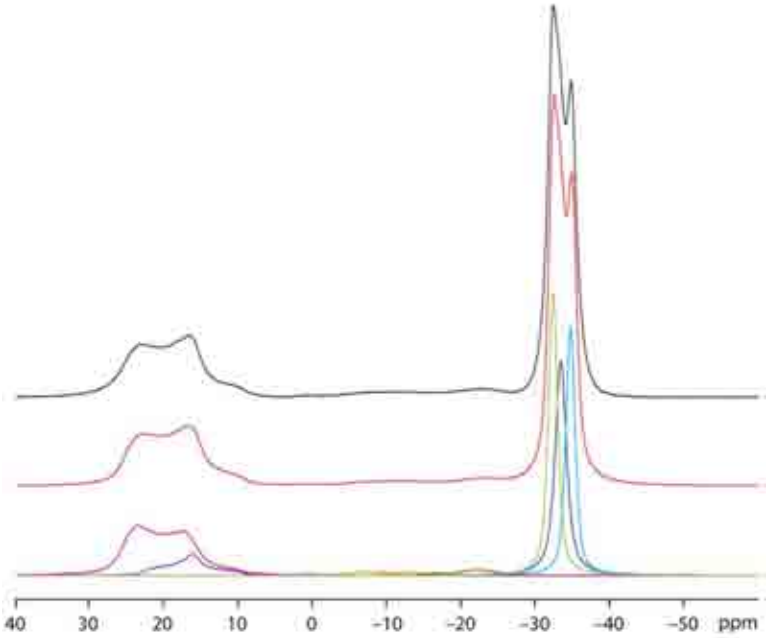

Figure 6.30 – The solid state ^{11}B MAS NMR spectrum collected from the product of the $CaH_2 + 4NH_3BH_3$ reaction at 110°C (black). Deconvolution of the spectrum is shown, with the cumulative simulated spectrum shown in red

The resonance at −34.7 ppm was no longer evident in the ^{11}B NMR spectrum after reaction at 120°C, figure 6.31. Further to this the low intensity resonances between −7.0 and −22.0 ppm were also no longer present. The spectrum comprised only the quadrupolar boron environments and the two overlapping resonances at −32.3 and −33.2 ppm.

Figure 6.28 shows that the spectra collected from the products of the reactions at 150°C and 175°C were almost identical to that of the one collected after reaction at 120°C, which showed that there had been no change in the boron environments during this temperature range.

After reaction at 200°C the ^{11}B NMR spectrum, figure 6.32, showed the appearance of a new boron environment at −30.1 ppm. The most intense feature in the spectrum was observed at −32.3 ppm which was again fitted to two boron environments with chemical shifts of −32.3 ppm and −33.2 ppm. The quadrupolar boron environments had increased in intensity.

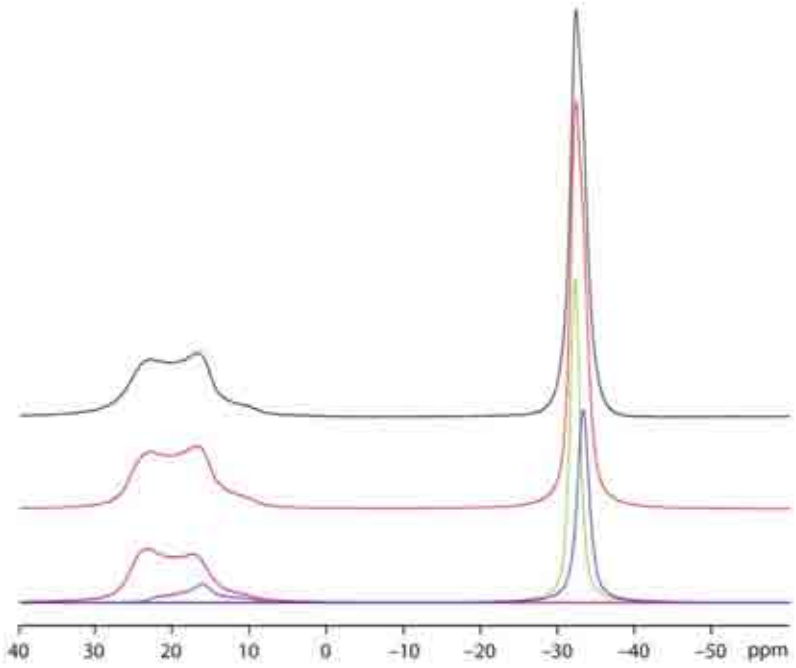

Figure 6.31 – The solid state ^{11}B MAS NMR spectrum collected from the product of the $CaH_2 + 4NH_3BH_3$ reaction at 120°C (black). Deconvolution of the spectrum is shown, with the cumulative simulated spectrum shown in red

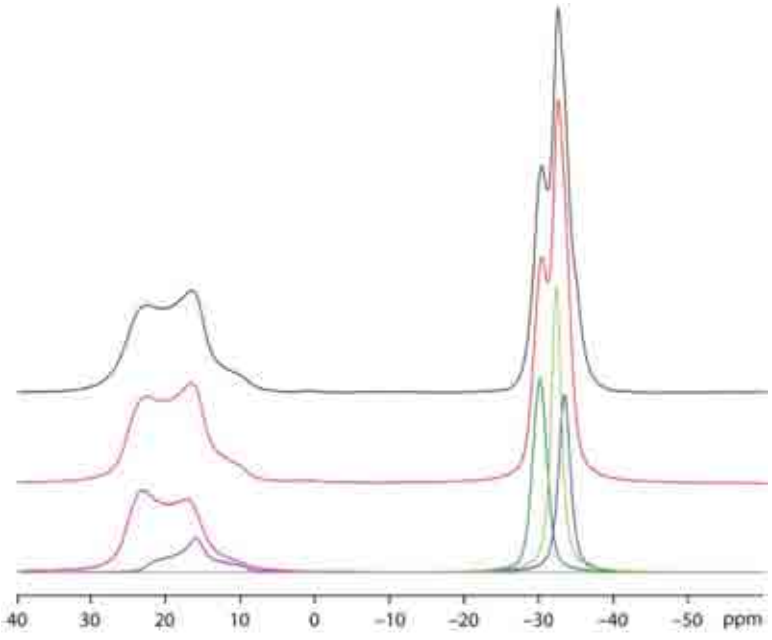

Figure 6.32 – The solid state ^{11}B MAS NMR spectrum collected from the product of the $CaH_2 + 4NH_3BH_3$ reaction at 200°C (black). Deconvolution of the spectrum is shown, with the cumulative simulated spectrum shown in red

The intensity of the quadrupolar boron environments increased after reaction at 225°C, and further still after the 250°C reaction, figure 6.33. There was also a

significant change in the intensities of the features around −32.0 ppm between reactions at 200°C and 225°C, figure 6.34a. The resonance at −30.1 ppm became the most intense feature in the spectrum, while the intensities of the features at −32.3 ppm and −33.2 ppm were greatly reduced. Similar observations were made in this chemical shift range in the spectrum obtained after heating to 250°C, figure 6.34b, with the most intense resonance observed at −30.0 ppm. One difference was that deconvolution of the spectrum suggested the initial dominant boron environment observed after reaction at 80°C (−34.8 ppm) was again present, although its intensity was low. A second difference was that the intensity of the resonance at −32.3 ppm had increased while the resonance at −33.2 ppm had decreased. This was the first time that the intensities of these two features had diverged.

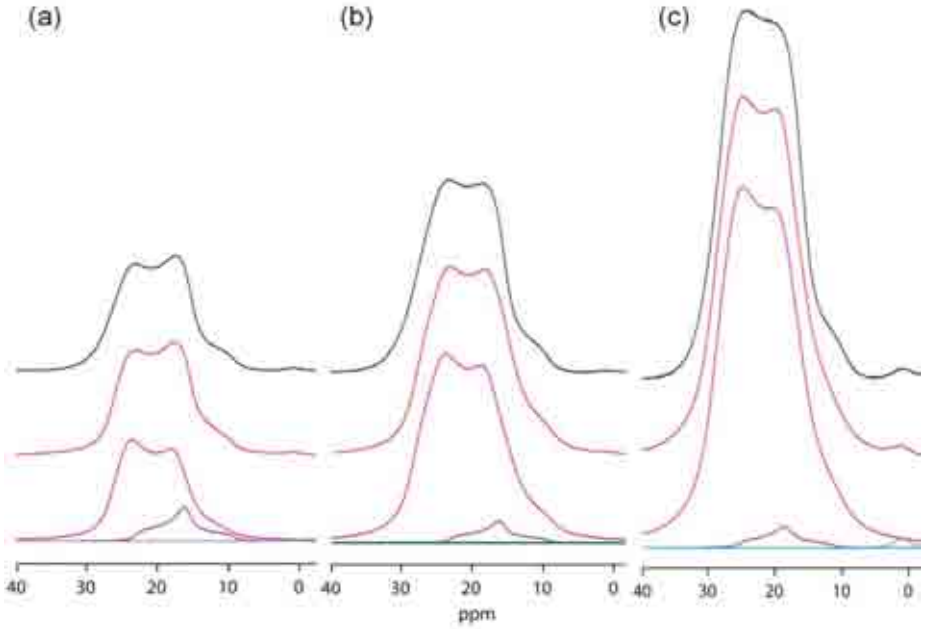

Figure 6.33 – Deconvolution of the quadrupolar boron site observed in the solid state ^{11}B MAS NMR spectra collected from the products of the $CaH_2 + 4NH_3BH_3$ reaction at (a) 225°C (b) 250°C and (c) 275°C

After reaction at 275°C the quadrupolar resonance had become the dominant resonance in the spectrum, figure 6.33c, and as can be seen in figure 6.28, this remained the most intense feature up to the maximum reaction temperature of 800°C. At 275°C, figure 6.34c, the boron environment at −30.2 ppm had dramatically decreased in intensity compared to this resonance in the spectrum obtained after reaction at 250°C. The resonance at −33.2 ppm again showed a slight reduction in

intensity, but conversely the intensity of the resonance at −32.3 ppm again showed a slight increase. The intensity of the feature at −34.8 ppm had also increased slightly. A broad resonance was also observed at −16.3 ppm.

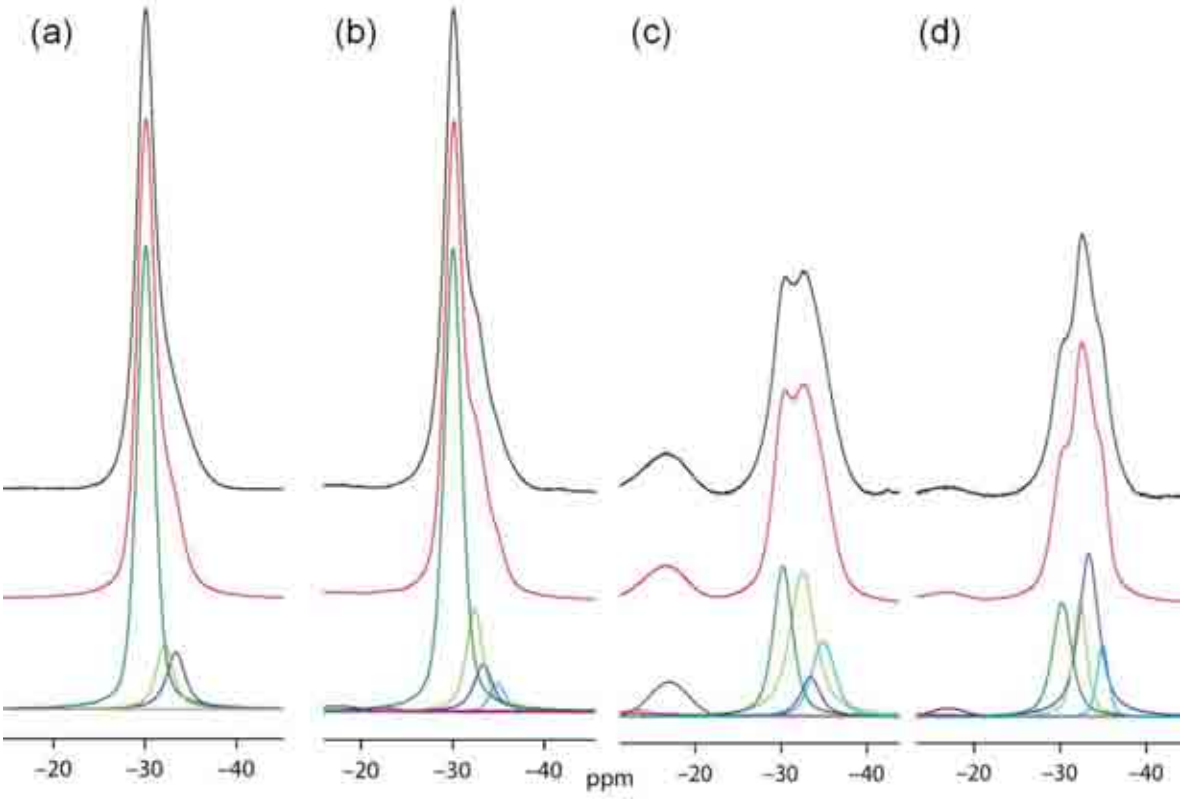

Figure 6.34 – Deconvolution of the resonances observed around −30 ppm in the solid state ^{11}B MAS NMR spectra collected from the products of the $CaH_2 + 4NH_3BH_3$ reaction at (a) 225°C (b) 250°C (c) 275°C and (d) 300°C

The spectrum collected after reaction at 300°C, figure 6.34d, showed decreased intensity of the resonances at −34.8 ppm and −32.3 ppm, with little change of the resonance at −30.2 ppm, while a noticeable increase in intensity of the resonance at −33.2 ppm occurred compared to those observed after reaction at 275°C. A broad low intensity resonance was again observed at −16.3 ppm. Higher temperature reactions at 400°C and 800°C resulted in spectra dominated by the quadrupolar resonance, neither spectrum showed any other well defined features.

In a number of spectra a resonance at 1.0 ppm was observed. This resonance was due to oxidation of the sample and is therefore not discussed further.

Discussion

Table 6.5 shows a summary of the resonances observed in the ^{11}B NMR spectra of the products from the CaH_2 + $4NH_3BH_3$ reaction at various temperatures. Peak deconvolution was used to calculate the percentage of each environment in the spectra.

Table 6.5 – Summary of the observed resonances in the ^{11}B NMR spectra of the products from the CaH_2 + $4NH_3BH_3$ reaction at various temperatures, showing the percentage of each environment present in the samples

Reaction Temperature (°C)	Chemical Shift (ppm)								
	−34.7	−33.2	−32.2	−30.1	−21.9	−17.3	−13.1	−7.1	30.3
80	66.68	6.89			2.08	7.52	4.13	5.04	7.13
90	60.26	12.84			2.30	5.19	4.20	2.49	12.38
100	36.87	20.68	6.89		1.66	3.77	7.11	0.47	21.50
110	20.34	22.59	23.44		0.41	1.50	1.10	0.72	29.62
120		25.17	34.55						40.28
150		23.16	35.63						40.95
175		24.39	32.47						42.88
200		15.87	22.49	19.35					42.10
225		5.53	5.52	35.81					52.94
250	1.23	2.90	5.40	23.57	0.63	0.15		0.09	65.97
275	3.13	1.63	7.56	5.60	2.22		0.02	0.49	78.80
300	1.59	7.24	3.26	4.58	0.48			0.10	82.34
400	0.58	0.32	0.23	0.17	0.55				97.58
800		0.17	0.13						99.45

From the results of powder XRD some of the products of each reaction are already known and consequently assignment of the observed boron environments can be attempted. At 80°C, the crystalline phase $Ca(BH_4)_2{\cdot}2NH_3$ was the only product observed by powder XRD. The published ^{11}B NMR spectrum of $Ca(BH_4)_2{\cdot}2NH_3$ shows that this material has a single resonance at −34.7 ppm, which is a similar chemical shift to the one observed in this study.[13] Therefore, the resonance can be assigned to the BH_4 groups in this material. The determined crystal structure of $Ca(BH_4)_2{\cdot}2NH_3$, section 6.4, showed there was only one boron environment and therefore only one boron environment would be expected in the spectrum. Due to the

effect of two NH_3 groups donating electrons to the calcium and consequently increased shielding at the boron sites, this resonance was the furthest upfield.

The next crystalline phase observed by powder XRD was $Ca(BH_4)_2{\cdot}NH_3$; this was the only phase observed after reaction at 120°C and so either of the resonances observed at −33.2 ppm or −32.2 ppm could have been related to this material. In order to make the correct assignment the other crystalline phases observed in powder XRD patterns should be considered. α-$Ca(BH_4)_2$ was first observed in powder XRD patterns after reaction at 200°C and after reaction at 225°C was the only crystalline phase observed. The resonance at −30.1 ppm was not observed in the NMR spectra until reaction at 200°C and furthermore this was the dominant resonance in the spectrum of the product of the reaction at 225°C. Assignment of this resonance to the boron environment in α-$Ca(BH_4)_2$ is therefore justified. This assignment also agreed with that of Reiter *et al*.[37]

The β polymorph of $Ca(BH_4)_2$ was first observed by powder XRD after reaction at 275°C. Interestingly no resonance in the ^{11}B NMR spectra first appeared at this temperature, but by a process of elimination the boron environment within this compound must have produced a resonance at either −33.2 ppm or −32.2 ppm. These two resonances were therefore due to $Ca(BH_4)_2{\cdot}NH_3$ and β-$Ca(BH_4)_2$. Again the presence of the electron donating group, NH_3, in the monoammoniate would have caused a downfield shift in the position of the BH_4 environment within this material and so the resonance at −33.2 ppm was assigned to $Ca(BH_4)_2{\cdot}NH_3$ and the resonance at −32.2 ppm was assigned to β-$Ca(BH_4)_2$. This assignment for β-$Ca(BH_4)_2$ also agreed with that of Reiter *et al*.[37]

Below 300°C $Ca(BH_4)_2{\cdot}2NH_3$, $Ca(BH_4)_2{\cdot}NH_3$, α-$Ca(BH_4)_2$ and β-$Ca(BH_4)_2$ were the only crystalline phases observed in powder XRD patterns. Therefore, the resonances observed at −21.9 ppm, −17.3 ppm, −13.1 ppm and −7.1 ppm could not have been present as crystalline material. As discussed in section 6.6, the decomposition pathway of NH_3BH_3 has been inferred to play a role in the $CaH_2 + 4NH_3BH_3$ reaction pathway. Stowe *et al.*[38] conducted a solid state ^{11}B NMR investigation into the thermal decomposition of NH_3BH_3 at 88°C. Resonances were observed at −38 ppm and −13 ppm which were assigned to the BH_4 and BH_2 environments present in

DADB respectively. No resonance at −38 ppm was observed in any spectra in this study. However, the initial formation of $Ca(BH_4)_2{\cdot}2NH_3$ would have required the presence of a BH_4^- ion in the reaction mixture. DADB formation could have provided this ion and hence the pathway to form $Ca(BH_4)_2$. This reaction would also explain why there was no BH_4 resonance due to DADB presence observed in the NMR spectra. The BH_2 resonances at −7.1 and −13 ppm observed by Stowe *et al.* were, however, observed in this study between 80°C and 110°C. Despite the consumption of the BH_4^- ion from DADB, the decomposition of NH_3BH_3 would have still been able to proceed to form polymeric NH_2BH_2, and therefore a BH_2 environment would be expected in the NMR spectrum. As NH_3BH_3 decomposition proceeded Stowe *et al.* noted that these resonances broadened and decreased in intensity due to continued polymerisation. Similar observations were noted in this study, with the intensities of both of these resonances decreasing as well as the peaks broadening with increasing reaction temperature. The ^{11}B NMR spectrum obtained after reaction at 120°C no longer showed these two resonances, indicating that the first two steps in NH_3BH_3 decomposition, reaction 6.12, were complete. The product of these steps $(NHBH)_n$ possessed boron only in an sp^2 environment. Boron in an sp^2 environment is observed in the range 0 ppm to 40 ppm.[39-42] This decomposition product was shown by thermal desorption studies to form at around 150°C and therefore the broad feature at 30.3 ppm can be assigned to this decomposition product up to this reaction temperature.

$$nNH_3BH_3 \rightarrow (NH_2BH_2)_n + nH_2 \rightarrow (NHBH)_n + nH_2 \qquad \text{Reaction 6.12}$$

The resonances at −21.9 ppm and −17.3 ppm were observed between 80°C and 110°C; however, only $Ca(BH_4)_2{\cdot}2NH_3$ and $Ca(BH_4)_2{\cdot}NH_3$ were detected by powder XRD in this temperature range. Therefore, a literature search was undertaken in an attempt to assign these features. Chua *et al.*[12] studied the reaction of $Ca(NH_2)_2$ with NH_3BH_3 in a 1:2 molar ratio and found that an ammoniated derivative of $Ca(NH_2BH_3)_2$ was synthesised, $Ca(NH_2BH_3)_2{\cdot}2NH_3$. The NH_3 was desorbed upon heating this material above 73°C. Solid state ^{11}B NMR investigations of these materials showed that the boron environments within $Ca(NH_2BH_3)_2{\cdot}2NH_3$ and $Ca(NH_2BH_3)_2$ were observed at −21 and −17 ppm, respectively. Re-examination of

our powder XRD patterns produced no evidence that either of these products were present. However, the CaH_2 + $4NH_3BH_3$ reaction does offer the potential to form $Ca(NH_2BH_3)_2$ through the same reaction mechanism that led to $NaNH_2BH_3$ formation from NaH and NH_3BH_3 starting materials. If this material had formed it could also have become ammoniated in the same way that ammoniated forms of $Ca(BH_4)_2$ were produced. The resonances observed at −21.9 and −17.3 ppm in this study were broad, low intensity peaks suggesting that the boron environments were disordered. This disorder may have explained why these phases were not detected by powder XRD. Although, there was no overwhelming evidence for the assignment of these resonances to $Ca(NH_2BH_3)_2$ and $Ca(NH_2BH_3)_2{\cdot}2NH_3$, this was the most satisfactory assignment that could be made based on the information available. The full assignment of the observed resonances in the solid state ^{11}B NMR spectra is shown in table 6.6.

Table 6.6 – The assignment of boron environments to the observed resonances in the solid state ^{11}B NMR spectra

Chemical Shift (ppm)	Assignment
−34.7	$Ca(BH_4)_2{\cdot}2NH_3$
−33.2	$Ca(BH_4)_2{\cdot}NH_3$
−32.2	β-$Ca(BH_4)_2$
−30.1	α-$Ca(BH_4)_2$
−21.9	$Ca(NH_2BH_3){\cdot}2NH_3$
−17.3	$Ca(NH_2BH_3)_2$
−13.1	BH_2 – DADB / NH_3BH_3 decomposition products
−7.1	BH_2 – DADB / NH_3BH_3 decomposition products
20.0	sp^2 B

Peak deconvolution of the various resonances allowed the percentages of each phase to be determined at the various reaction temperatures. The results are shown in figure 6.35. The percentage of crystalline phases present in the samples was also calculated from powder XRD patterns using Topas and the results are shown in figure 6.36.[32] A comparison of the two figures shows that the results broadly agreed, the major difference being that XRD does not account for the amorphous content of the samples, while ^{11}B NMR could not detect CaH_2. A slight discrepancy was that the

resonances due to ammoniated phases reappeared in the spectra above 250°C. This was probably because during cooling, any NH_3 that had remained in the vicinity of $Ca(BH_4)_2$ following its earlier release, was able to recombine with this material and reform the ammoniates. As powder XRD did not reveal this phase at these temperatures, the material may have been finely divided or highly disordered.

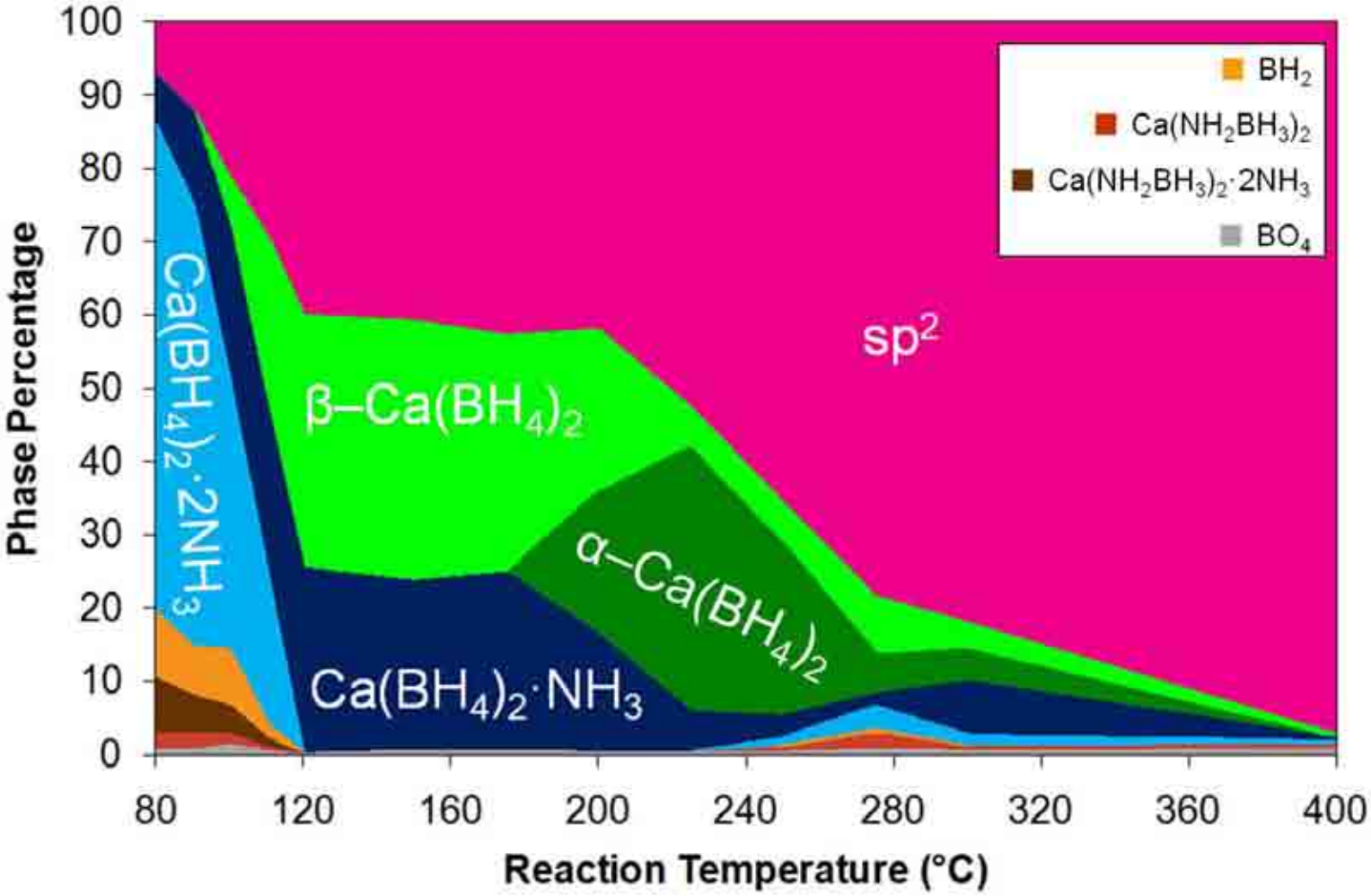

Figure 6.35 – The calculated percentages from peak fitting solid state ^{11}B NMR spectra of each boron environment in the samples collected after reaction at various temperatures

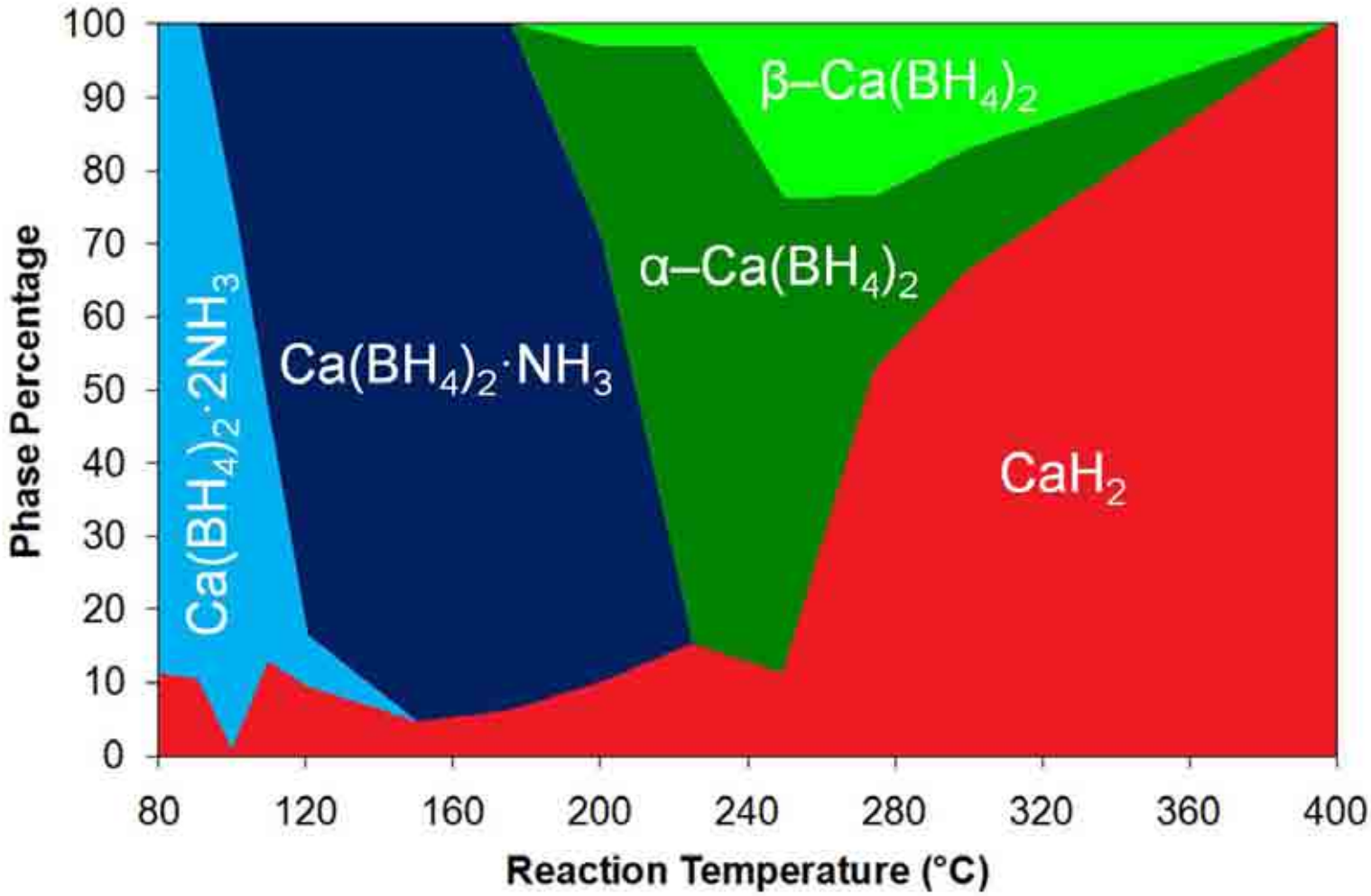

Figure 6.36 – The percentage of crystalline phases present in the products of the $CaH_2 + 4NH_3BH_3$ reaction at various temperatures calculated from powder XRD patterns

Figure 6.35 showed that the decrease in boron present as $Ca(BH_4)_2{\cdot}2NH_3$ was accompanied by an increase in the boron environment within $Ca(BH_4)_2{\cdot}NH_3$. However, this percentage decrease in the former was significantly greater than the observed increase in the latter. Further to this the resonance at −32.2 ppm was observed from 100°C onwards, previously assigned to β-$Ca(BH_4)_2$. This is a significant discrepancy with the results of thermal desorption studies, where the second release of NH_3 did not occur until temperatures in excess of 200°C and powder XRD results revealed that it was in fact the α polymorph that formed first. The crystal structure determination of $Ca(BH_4)_2{\cdot}NH_3$, section 6.5, revealed that this structure contains two distinct boron positions within the unit cell, with the B1–Ca and B2–Ca distances shorter and longer than 2.9 Å, respectively. The B–Ca distance in β-$Ca(BH_4)_2$ is longer than 2.9 Å suggesting the B2 site of $Ca(BH_4)_2{\cdot}NH_3$ may have been similar to the boron site in β-$Ca(BH_4)_2$, hence producing a resonance with a similar chemical shift.[17] Therefore, between reaction temperatures of 100°C and 225°C the resonance assigned to β-$Ca(BH_4)_2$ may actually have been due to a second boron environment within $Ca(BH_4)_2{\cdot}NH_3$. This is substantiated by the fact that the percentage traces of $Ca(BH_4)_2{\cdot}NH_3$ and 'β-$Ca(BH_4)_2$' follow each other relatively closely in this temperature range. Above 225°C the percentage of β-$Ca(BH_4)_2$ present showed an increase whereas that of $Ca(BH_4)_2{\cdot}NH_3$ decreased, which was also the temperature at which powder XRD showed the presence of crystalline β-$Ca(BH_4)_2$ within the product, and so above this temperature the resonance at −32.2 ppm was genuinely due to β-$Ca(BH_4)_2$.

As expected from powder XRD patterns the percentage decrease of boron in the environments of $Ca(BH_4)_2{\cdot}NH_3$ was accompanied by the increase of α-$Ca(BH_4)_2$ within the sample. Once the reaction temperature had surpassed the onset temperature for the α to β phase transition, the percentage of the α polymorph began to decrease and the percentage of the β polymorph increased, although the decrease in α was greater than the increase in β. There was, however, also an increase in the percentage of boron in an sp^2 environment within the sample and this must therefore also have been related to the decrease of α-$Ca(BH_4)_2$. There were two increases in sp^2 boron environments. The first increase was observed up to a temperature of 120°C. As discussed previously the formation of material containing boron in sp^2

environments was initially primarily related to the decomposition pathway of NH_3BH_3. However, figure 6.35 shows that this initial increase was also related to the decrease in BH_4 environments, another indication that unidentified side reactions took place during the reaction. The second increase in boron within an sp^2 environment, above 225°C, matched the percentage decrease in BH_4 environment, which therefore suggested that the decomposition products of $Ca(BH_4)_2$ contained sp^2 boron.

There are no reported studies regarding the decomposition of $Ca(BH_4)_2$ that have used solid state ^{11}B NMR to identify the thermal decomposition products and so a direct comparison of spectra is not possible. Both XRD and Raman spectroscopy have been used to identify CaB_6 as a decomposition product.[20, 28] The solid state ^{11}B NMR chemical shift of CaB_6 has been found to be 1.26 ppm.[43] Therefore this material could not have contributed to the observed increase in sp^2 environment. Powder XRD only showed evidence of CaB_6 in the pattern obtained after reaction at 800°C and therefore a resonance due to CaB_6 would reasonably also only be expected in this spectrum. Previous studies of $Ca(BH_4)_2$ decomposition have also shown that CaB_6 has only been observed as a decomposition product at temperatures above 400°C and so would not have been expected in the lower temperature spectra.[20, 23] Examination of the NMR spectrum obtained after reaction at 800°C showed that a broad signal was present between 0 ppm and 10 ppm, figure 6.37, and so it was not possible to identify CaB_6. This broad feature also meant it was not possible to identify whether any elemental boron was present in this spectrum. Elemental boron shows a broad resonance at 2 ppm, which has been identified by ^{11}B NMR spectroscopy following decomposition of $LiBH_4$ heated to 500°C.[44] Elemental boron has been predicted as a decomposition product of $Ca(BH_4)_2$, although it has not been identified.[18, 20]

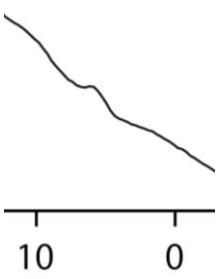

Figure 6.37 – The solid state ^{11}B MAS NMR spectrum of the product of the CaH_2 + $4NH_3BH_3$ reaction after heating to 800°C between 0 ppm and 10 ppm

A number of studies have also discussed the formation of an unidentified boron containing intermediate during $Ca(BH_4)_2$ decomposition. Riktor *et al.*[23] postulated that this intermediate was of composition CaB_2H_2, although, a theoretical study reported that the reaction energy for formation of CaB_2H_2 was too high for this to be the favoured $Ca(BH_4)_2$ decomposition pathway.[45] A second possibility for the intermediate is $CaB_{12}H_{12}$, although its formation during $Ca(BH_4)_2$ decomposition has not been directly identified. ^{11}B NMR spectroscopy has been utilised to identify both $MgB_{12}H_{12}$ and $Li_2B_{12}H_{12}$ as decomposition products from the respective metal borohydrides.[44] The solid state ^{11}B NMR spectrum of $CaB_{12}H_{12}$ shows a single resonance at −14.5 ppm.[46] During our study a resonance of similar chemical shift (−16.0 ppm) was observed between 250°C and 300°C. Figure 6.35 shows that in this temperature range the intensity of both the α and β polymorphs decreased. Therefore, the observation of the resonance at −16.0 ppm provides some evidence that $CaB_{12}H_{12}$ could be an intermediate in the decomposition of $Ca(BH_4)_2$.

The potential boron containing decomposition products of $Ca(BH_4)_2$ discussed so far, CaB_6, B, CaB_2H_2 and $CaB_{12}H_{12}$, offer no explanation as to why there was a growth in the broad sp^2 feature above 225°C. This large sp^2 feature showed that boron was present in either BN_2H or BN_3 environments.[42] As previously discussed, part of this signal was due to the presence of $(NHBH)_n$ in the sample. Above 400°C, this material had the potential to further desorb H_2 to form BN.[36, 47] BN exists in two polymorphs. The cubic form adopts the zinc blende structure and the structure is comprised of local BN_4 tetrahedra, figure 6.38a, whereas the hexagonal polymorph has a structure similar to graphite, involving planar layers of B_3N_3 hexagons, stacked so that there is alternation between B and N in the layers, figure 6.38b. This difference in structure results in different chemical shifts in ^{11}B NMR spectroscopy, with the cubic polymorph producing a resonance at 1.6 ppm, while the hexagonal polymorph produces a feature at 30 ppm with a quadrupolar line shape.[48] Only a weak feature was observed at 1.6 ppm, which suggested that H_2 loss from $(NHBH)_n$ yielded hexagonal BN and hence contributed to the strong quadupolar sp^2 feature above 400°C. However, as $(NHBH)_n$ was already contributing to the resonance below 400°C, this decomposition step would not have resulted in increased intensity.

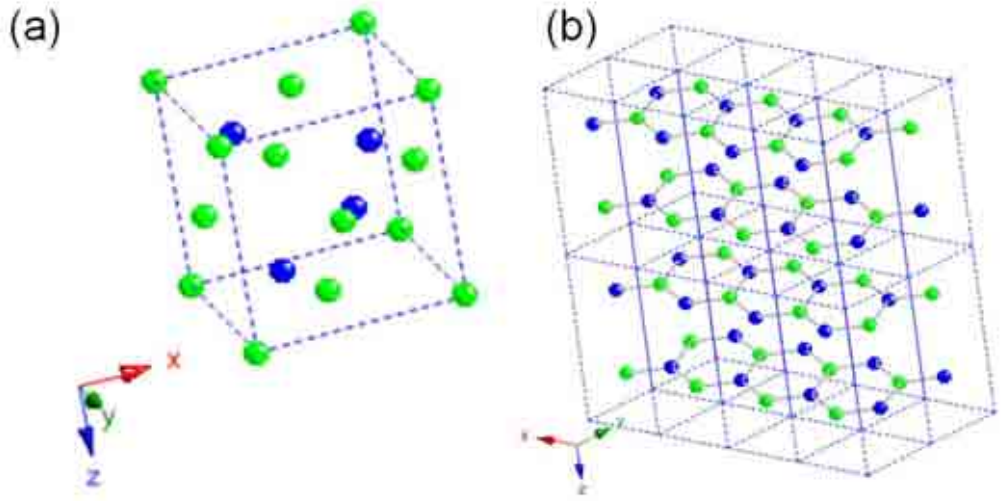

Figure 6.38 – The crystal structures of (a) cubic BN[49] (b) hexagonal BN[50]

The increased strength of the sp^2 resonance may therefore be related to the decomposition of $Ca(BH_4)_2$. Chu *et al.*[13] reported that the decomposition pathway followed by $Ca(BH_4)_2 \cdot 2NH_3$ was dependent on the conditions employed. Under dynamic flow mode, a two step deammoniation pathway proceeded, whereas in a closed system where NH_3 remained within the vicinity of the complex, H_2 was released. The sample collected after dehydrogenation at 250°C was studied by solid state ^{11}B NMR and the spectrum showed two overlapping quadrupolar peaks at similar chemical shift to the broad sp^2 resonance observed in this study. The overall dehydrogenation reaction was thought to have proceeded as shown below:

$$Ca(BH_4)_2 \cdot 2NH_3 \rightarrow \tfrac{1}{4}Ca(BH_4)_2 + \tfrac{1}{4}Ca_3(BN_2)_2 + BN + 6H_2 \qquad \text{Reaction 6.13}$$

The $CaH_2 + 4NH_3BH_3$ reactions in this study were carried out on a flowing argon gas line, with the sample contained within a quartz tube and therefore NH_3 would be expected to desorb. However, as argon flowed over the top of the quartz tube, the desorbed NH_3 gas may not have been removed from the vicinity of the sample quickly enough to prevent a similar decomposition reaction to that shown in reaction 6.13 from proceeding. $Ca_3(BN_2)_2$ possesses boron in an sp environment and the ^{11}B NMR spectrum of this material has been shown to produce a quadrupolar resonance with a similar chemical shift to that observed here.[29] Furthermore, the BN formed during this reaction would have also contributed to the strong sp^2 resonance and the

$Ca(BH_4)_2$ formed would have decomposed according to its known decomposition pathway, resulting in the previously discussed formation of $CaB_{12}H_{12}$ and CaB_6.

A similar phenomenon was observed in the decomposition of $Ca(NH_2BH_3)_2{\cdot}2NH_3$, with a dynamic flowing mode favouring NH_3 release, while a closed system resulted in H_2 desorption.[12] Following H_2 desorption a broad feature with a quadrupolar lineshape compiled of two environments was observed in the solid state ^{11}B NMR spectrum. Therefore, the most satisfactory explanation for the growth in the broad sp^2 feature above 225°C would be the formation of $Ca_3(BN_2)_2$ and BN. As discussed in section 6.3, the powder XRD pattern of the sample collected after reaction at 800°C showed poorly crystalline $Ca_3(BN_2)_2$.The high temperature required for this material to crystallise satisfactorily (1200°C) means that it may have been present in an amorphous form at lower temperatures, and was not detected by powder XRD.[29]

6.8 Overall Discussion and Conclusion

6.8.1 The $CaH_2 + 4NH_3BH_3$ Reaction Pathway

The results of powder XRD, thermal desorption and solid state ^{11}B NMR spectroscopy have led to the following proposed reaction scheme for the $CaH_2 + 4NH_3BH_3$ reaction.

The volume expansion that the sample underwent on heating, coupled with the thermal desorption results, which showed a H_2 release profile similar in nature to NH_3BH_3, suggested that the first step in the reaction pathway could be the same as that in the decomposition mechanism of NH_3BH_3. The network of dihydrogen bonding is disrupted through heating, forming a more mobile phase of NH_3BH_3, figure 6.39, which then undergoes a rearrangement reaction, forming DADB, figure 6.40. This could be a crucial step in the formation of $Ca(BH_4)_2{\cdot}2NH_3$ as DADB possesses the BH_4^- anion required for $Ca(BH_4)_2$ formation.

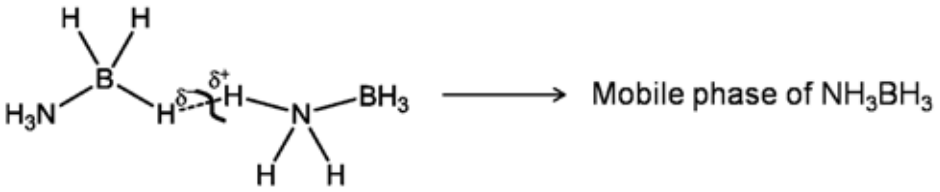

Figure 6.40 – Disruption of dihydrogen bonding network

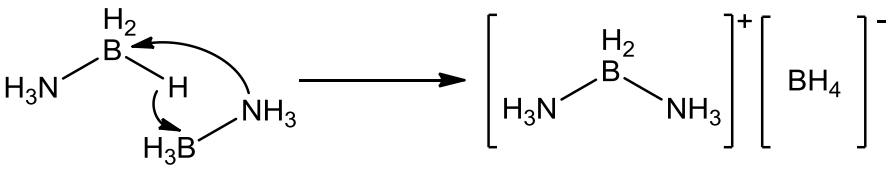

Figure 6.40 – The formation of DADB

It is, however, the cationic segment of DADB that may be involved in the next stage of the reaction mechanism. The hydride ions present in CaH_2 have the potential to attack the cation in one of two ways. An S_N2 type reaction could proceed, whereby the H attacks the B, expelling NH_3 and forming NH_3BH_3, figure 6.41. Alternatively a hydride abstraction reaction could occur, figure 6.42, where the hydride attacks a protic H of one of the NH_3 groups, which would result in the formation of $H_2B{=}NH_2$ and the release of NH_3.

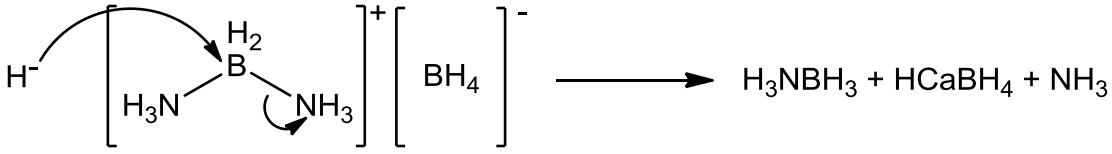

Figure 6.41 – The proposed S_N2 step during the $CaH_2 + 4NH_3BH_3$ reaction

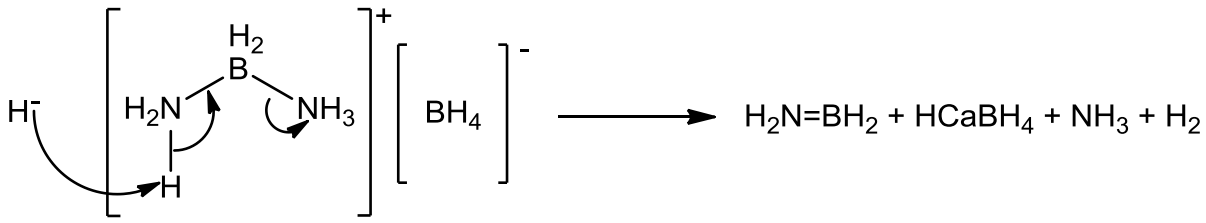

Figure 6.42 – The proposed hydride abstraction step during the $CaH_2 + 4NH_3BH_3$ reaction

Due to the 1:4 reaction stoichiometry, two moles of DADB would have formed and therefore the second H of CaH_2 would be able to undergo a similar reaction to the first and hence a second mole of NH_3 would be released as well as resulting in the formation of $Ca(BH_4)_2$, as shown below.

$$HCaBH_4 + DADB \rightarrow Ca(BH_4)_2 + H_3NBH_3 + NH_3 \qquad \text{Reaction 6.14}$$

$$HCaBH_4 + DADB \rightarrow Ca(BH_4)_2 + H_2N{=}BH_2 + NH_3 + H_2 \qquad \text{Reaction 6.15}$$

The reaction vessel would now contain one mole of $Ca(BH_4)_2$ and two moles of NH_3. NH_3 has been shown to form adduct complexes of Li, Mg and Ca borohydrides under mild conditions and therefore the $Ca(BH_4)_2$ and $2NH_3$ would have formed $Ca(BH_4)_2{\cdot}2NH_3$.[13, 51, 52] This mechanism also offers an explanation for the importance of the 1:4 reaction stoichiometry: Two DADB molecules are required for $Ca(BH_4)_2$ to form and so four NH_3BH_3 molecules were initially required.

In order to determine whether an S_N2 or hydride abstraction reaction occurred, it is necessary to consider the products from the two reactions. The S_N2 would result in NH_3BH_3, but at the temperatures employed in the reactions, in excess of 80°C, it would have been unstable and undergone decomposition, leading to $(NH_2BH_2)_n$. The hydride abstraction reaction would have formed the highly unstable $H_2N{=}BH_2$ monomer, which itself could have undergone two stabilising reactions, forming either $(NH_2BH_2)_n$, figure 6.43, or a cyclic dimer $(H_2NBH_2)_2$, figure 6.44. This cyclic dimer has been shown to be unstable and the ring structure breaks upon heating, also resulting in $(NH_2BH_2)_n$.[38]

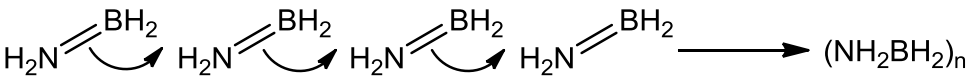

Figure 6.43 – Polymerisation of $H_2N{=}BH_2$ to form $(NH_2BH_2)_n$

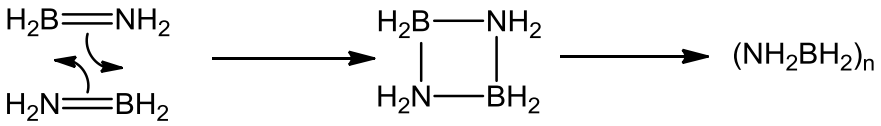

Figure 6.44 – Cyclic dimer, $(NH_2BH_2)_2$ formation from $H_2N{=}BH_2$

There was a subtle decrease in the onset temperature of the second H_2 release step in the $CaH_2 + 4NH_3BH_3$ desorption profile compared to that of NH_3BH_3, as well as the two desorption profiles being significantly different following the initial H_2 desorption, figure 6.20. The S_N2 mechanism essentially releases NH_3BH_3 and so a much better agreement between the two profiles would be expected. Therefore, the large

differences between the two desorption profiles suggests that the abstraction mechanism may have taken place.

Following the formation of $Ca(BH_4)_2{\cdot}2NH_3$ and $(NH_2BH_2)_n$, to a first approximation the decomposition pathways of each material appear to proceed more or less separately, under certain conditions, as previously discussed. $Ca(BH_4)_2{\cdot}2NH_3$ desorbs NH_3 in a stepwise process, forming $Ca(BH_4)_2{\cdot}2NH_3$ and $Ca(BH_4)_2$, sequentially. $Ca(BH_4)_2$ subsequently decomposed leading to CaH_2, and possibly CaB_6 and $CaB_{12}H_{12}$. This decomposition pathway was complicated by the presence of NH_3 in the reaction vessel, resulting also in the formation of $Ca_3(BN_2)_2$. $(NH_2BH_2)_n$ desorbed H_2 forming $(NHBH)_n$, which itself desorbs H_2 at elevated temperatures, eventually leading to BN formation.

6.8.2 Potential as Hydrogen Storage Materials

The goal of this study was to improve the hydrogen desorption properties of the NH_3BH_3 system through the reaction with CaH_2. However, the proposed mechanism of this reaction shows that the formation of DADB was in fact the key event that allowed the reaction with CaH_2 to proceed. Thermal desorption studies showed that there were significant differences between the H_2 release profile of the CaH_2 + $4NH_3BH_3$ reaction and that of NH_3BH_3, with additional H_2 desorption events from the reaction mixture, due to unidentified side reactions involving the interaction of NH_3 released from the ammoniates with other components of the reaction mixture, highlighting the complex nature of the desorption pathway. The product of this reaction, $Ca(BH_4)_2{\cdot}2NH_3$, released NH_3 when it was heated under dynamic flowing conditions. The contamination of the H_2 stream by NH_3 is undesirable when it is to be used in fuel cells as NH_3 will poison the fuel cell and therefore have a negative effect on its performance. As the CaH_2 + $4NH_3BH_3$ reaction pollutes the H_2 desorbed from NH_3BH_3 with large amounts of NH_3, its potential as a method of hydrogen storage seems to be limited. However, $Ca(BH_4)_2{\cdot}2NH_3$ has been shown by Chu *et al.*[13] to offer potential as a hydrogen storage material when thermal decomposition is carried out within a closed system as H_2 is the only gas desorbed.

6.9 References

1. Filinchuk, Y. E.; Yvon, K.; Meisner, G. P.; Pinkerton, F. E.; Balogh, M. P., On the composition and crystal structure of the new quaternary hydride phase $Li_4BN_3H_{10}$. *Inorganic Chemistry* **2006,** 45, 1433–1435.

2. Noritake, T.; Aoki, M.; Towata, S.; Ninomiya, A.; Nakamori, Y.; Orimo, S., Crystal structure analysis of novel complex hydrides formed by the combination of $LiBH_4$ and $LiNH_2$. *Applied Physics A* **2006,** 83, 277–279.

3. Chater, P. A.; Anderson, P. A.; Prendergast, J. W.; Walton, A.; Mann, V. S. J.; Book, D.; David, W. I. F.; Johnson, S. R.; Edwards, P. P., Synthesis and characterisation of amide-borohydrides: New complex light hydrides for potential hydrogen storage. *Journal of Alloys and Compounds* **2007,** 446–447, 350–354.

4. Chater, P. A.; David, W. I. F.; Johnson, S. R.; Edwards, P. P.; Anderson, P. A., Synthesis and crystal structure of $Li_4BH_4(NH_2)_3$. *Chemical Communications* **2006**, 2439–2441.

5. Chater, P. A.; David, W. I. F.; Anderson, P. A., Synthesis and structure of the new complex hydride $Li_2BH_4NH_2$. *Chemical Communications* **2007**, 4770–4772.

6. Yang, J. B.; Wang, X. J.; Cai, Q.; Yelon, W. B.; James, W. J., Crystal and electronic structures of the complex hydride $Li_4BN_3H_{10}$. *Journal of Applied Physics* **2007,** 102, 033507.

7. Wu, H.; Zhou, W.; Udovic, T. J.; Rush, J. J.; Yildirim, T., Structures and crystal chemistry of Li_2BNH_6 and $Li_4BN_3H_{10}$. *Chemistry of Materials* **2008,** 20, 1245–1247.

8. Meisner, G. P.; Scullin, M. L.; Balogh, M. P.; Pinkerton, F. E.; Meyer, M. S., Hydrogen release from mixtures of lithium borohydride and lithium amide: A phase diagram study. *Journal Of Physical Chemistry B* **2006,** 110, 4186–4192.

9. Diyabalanage, H. V.; Shrestha, R. P.; Semelsberger, T. A.; Scott, B. L.; Bowden, M. E.; Davis, B. L.; Burrell, A. K., Calcium Amidotrihydroborate: A Hydrogen Storage Material. *Angewandte Chemie-International Edition* **2007,** 46, 8995–8997.

10. Wu, H.; Zhou, W.; Yildirim, T., Alkali and alkaline-earth metal amidoboranes: Structure, crystal chemistry, and hydrogen storage properties. *Journal of the American Chemical Society* **2008,** 130, 14834–14839.

11. Zhang, Y.; Shimoda, K.; Miyaoka, H.; Ichikawa, T.; Kojima, Y., Thermal decomposition of alkaline-earth metal hydride and ammonia borane composites. *International Journal of Hydrogen Energy* **2010,** 35, 12405–12409.

12. Chua, Y. S.; Wu, G.; Xiong, Z.; He, T.; Chen, P., Calcium Amidoborane Ammoniate – Synthesis, Structure, and Hydrogen Storage Properties. *Chemistry of Materials* **2009,** 21, 4899–4904.

13. Chu, H.; Wu, G.; Xiong, Z.; Guo, J.; He, T.; Chen, P., Structure and hydrogen storage properties of calcium borohydride diammoniate. *Chemistry of Materials* **2010,** 22, 6021–6028.

14. Majzoub, E. H.; Rönnebro, E., Crystal structures of calcium borohydride: Theory and experiment. *Journal Of Physical Chemistry C* **2009,** 113, 3352–3358.

15. Miwa, K.; Aoki, M.; Noritake, T.; Ohba, N.; Nakamori, Y.; Towata, S.; Züttel, A.; Orimo, S., Thermodynamical stability of calcium borohydride $Ca(BH_4)_2$. *Physical Review B* **2006,** 74, 155122.

16. Buchter, F.; Łodziana, Z.; Remhof, A.; Friedrichs, O.; Borgschulte, A.; Mauron, P.; Züttel, A.; Sheptyakov, D.; Barkhordarian, G.; Bormann, R.; Chłopek, K.; Fichtner, M.; Sørby, M. H.; Riktor, M. D.; Hauback, B. C.; Orimo, S., Structure of $Ca(BD_4)_2$ β-phase from combined neutron and synchrotron X-ray powder diffraction data and density functional calculations. *Journal Of Physical Chemistry B* **2008,** 112, 8042–8048.

17. Filinchuk, Y. E.; Rönnebro, E.; Chandra, D., Crystal structures and phase transformations in $Ca(BH_4)_2$. *Acta Materialia* **2009,** 57, 732–738.

18. Kim, J.-H.; Jin, S.-A.; Shim, J.-H.; Cho, Y. W., Thermal decomposition behavior of calcium borohydride $Ca(BH_4)_2$. *Journal of Alloys and Compounds* **2008,** 461, L20–L22.

19. Kim, J.-H.; Jin, S.-A.; Shim, J.-H.; Cho, Y. W., Reversible hydrogen storage in calcium borohydride $Ca(BH_4)_2$. *Scripta Materialia* **2008,** 58, 481–483.

20. Kim, Y.; Reed, D.; Lee, Y.-S.; Y., L. J.; Shim, J.-H.; Book, D.; Cho, Y. W., Identification of the dehydrogenated product of $Ca(BH_4)_2$. *Journal Of Physical Chemistry C* **2009,** 113, 5865–5871.

21. Aoki, M.; Miwa, K.; Noritake, T.; Ohba, N.; Matsumoto, M.; Li, H.-W.; Nakamori, Y.; Towata, S.; Orimo, S., Structural and dehydriding properties of $Ca(BH_4)_2$. *Applied Physics A* **2008,** 92, 601–605.

22. Riktor, M. D.; Sørby, M. H.; Chłopek, K.; Fichtner, M.; Buchter, F.; Züttel, A.; Hauback, B. C., In situ synchrotron diffraction studies of phase transitions and thermal decomposition of $Mg(BH_4)_2$ and $Ca(BH_4)_2$. *Journal of Materials Chemistry* **2007,** 17, 4939–4942.

23. Riktor, M. D.; Sørby, M. H.; Chłopek, K.; Fichtner, M.; Hauback, B. C., The identification of a hitherto unknown intermediate phase CaB_2H_x from decomposition of $Ca(BH_4)_2$. *Journal of Materials Chemistry* **2009,** 19, 2754–2759.

24. Buchter, F.; Łodziana, Z.; Remhof, A.; Friedrichs, O.; Borgschulte, A.; Mauron, P.; Züttel, A.; Sheptyakov, D.; Palatinus, L.; Chłopek, K.; Fichtner, M.; Barkhordarian, G.; Bormann, R.; Hauback, B. C., Structure of the orthorhombic γ-phase and phase transitions of $Ca(BD_4)_2$. *Journal Of Physical Chemistry C* **2009,** 113, 17223–17230.

25. Lee, J. Y.; Ravnsbaek, D.; Lee, Y. S.; Kim, Y.; Cerenius, Y.; Shim, J.-H.; Jensen, T. R.; Nur, N. H.; Cho, Y. W., Decomposition reactions and reversibility of the $LiBH_4$-$Ca(BH_4)_2$ composite. *Journal Of Physical Chemistry C* **2009,** 113, 15080–15086.

26. Wu, H.; Zhou, W.; Pinkerton, F. E.; Meyer, M. S.; Srinivas, G.; Yildirim, T.; Udovic, T. J.; Rush, J. J., A new family of metal borohydride ammonia borane complexes: Synthesis, structures, and hydrogen storage properties. *Journal of Materials Chemistry* **2010,** 20, 6550–6556.

27. Durojaiye, T.; Ibikunle, A.; Goudy, A. J., Hydrogen storage in destabilized borohydride materials. *International Journal of Hydrogen Energy* **2010,** 35, 10329–10333.

28. Rönnebro, E.; Majzoub, E. H., Calcium borohydride for hydrogen storage: Catalysis and reversibility. *Journal of Physical Chemistry B* **2007,** 111, 12045–12047.

29. Worle, M.; Meyer zu Altenschildescheb, H.; Nesper, R., Synthesis, properties and crystal structures of α-$Ca_3(BN_2)_2$ and $Ca_{9+x}(BN_2, CBN)_6$ – two compounds with BN_2^{3-} and CBN^{4-} anions. *Journal of Alloys and Compounds* **1998,** 264, 107–114.

30. Hu, J.; Xiong, Z.; Wu, G.; Chen, P.; Murata, K.; Sakata, K., Hydrogen releasing reaction between $Mg(NH_2)_2$ and CaH_2. *Journal of Power Sources* **2006,** 159, 116–119.

31. Coelho, A. A., Indexing of powder diffraction patterns by iterative use of singular value decomposition. *Journal of Applied Crystallography* **2003,** 36, 86–95.

32. Coelho, A. A. *Topas, General Profile and Structure Analysis Software for Powder Diffraction Data*, Bruker AXS, Karlsruhe, Germany, 3rd edition: 2004.

33. Noritake, T.; Aoki, M.; Matsumoto, M.; Miwa, K.; Towata, S.; Li, H.-W.; Orimo, S., Crystal structure and charge density analysis of $Ca(BH_4)_2$. *Journal of Alloys and Compounds* **2010,** 491, 57–62.

34. Xiong, Z.; Wu, G.; Hu, J.; Chen, P., Ca–Na–N–H system for reversible hydrogen storage. *Journal of Alloys and Compounds* **2007,** 441, 152–156.

35. Pinkerton, F. E., Decomposition kinetics of lithium amide for hydrogen storage materials. *Journal of Alloys and Compounds* **2005,** 400, 76–82.

36. Bowden, M. E.; Autrey, T.; Brown, I.; Ryan, M., The thermal decomposition of ammonia borane: A potential hydrogen storage material. *Current Applied Physics* **2008,** 8, 498–500.

37. Reiter, J. W.; Zan, J. A.; Bowman Jr, R. C.; Hwang, S.-J., Development and evaluation of advanced hydride systems for reversible hydrogen storage. *DoE 2009 Annual Progress Report* **2009**.

38. Stowe, A. C.; Shaw, W. J.; Linehan, J. C.; Schmid, B.; Autrey, T., *In situ* solid state ^{11}B MAS-NMR studies of the thermal decomposition of ammonia borane: mechanistic studies of the hydrogen release pathways from a solid state hydrogen storage material. *Physical Chemistry Chemical Physics* **2007,** 9, 1831–1836.

39. Gervais, C.; Framery, E.; Duriez, C.; Maquet, J.; Vaultier, M.; Babonneau, F., ^{11}B and ^{15}N solid state NMR investigation of a boron nitride preceramic polymer prepared by ammonolysis of borazine. *Journal of the European Ceramic Society* **2005,** 25, 129–135.

40. Gervais, C.; Babonneau, F.; Maquet, J.; Bonhomme, C.; Massiot, D.; Framery, E.; Vaultier, M., ^{15}N Cross-polarization using the Inversion-Recovery Cross-Polarization technique and ^{11}B Magic Angle Spinning NMR studies of reference compounds containing B–N bonds. *Magnetic Resonance in Chemistry* **1998,** 36, 407–414.

41. Gervais, C.; Maquet, J.; Babonneau, F.; Duriez, C.; Framery, E.; Vaultier, M.; Florian, P.; Massiot, D., Chemically derived BN ceramics: Extensive ^{11}B and ^{15}N solid-state NMR study of a preceramic polyborazilene. *Chemistry of Materials* **2001,** 13, 1700–1707.

42. Gervais, C.; Babonneau, F., High resolution solid state NMR investigation of various boron nitride preceramic polymers. *Journal of Organometallic Chemistry* **2002,** 657, 75–82.

43. Sears, R. E. J., ^{11}B chemical shifts and quadrupole coupling constants in the alkaline-earth hexaborides. *Journal of Chemical Physics* **1982,** 76, 5651–5652.

44. Hwang, S.-J.; Bowman Jr, R. C.; Reiter, J. W.; Rijssenbeek, J.; Soloveichik, G. L.; Zhao, J.-C.; Kabbour, H.; Ahn, C. C., NMR confirmation for formation of $[B_{12}H_{12}]^{2-}$ complexes during hydrogen desorption from metal borohydrides. *The Journal of Physical Chemistry C* **2008,** 112, 3164–3169.

45. Frankcombe, T. J., Calcium borohydride for hydrogen storage: A computational study of $Ca(BH_4)_2$ crystal structures and the CaB_2H_x intermediate. *Journal of Physical Chemistry C* **2010,** 114, 9503–9509.

46. Stavila, V.; Her, J.-H.; Zhou, W.; Hwang, S.-J.; Kim, C.; Ottley, L. A. M.; Udovic, T. J., Probing the structure, stability and hydrogen storage properties of calcium dodecahydro-*closo*-dodecaborate. *Journal of Solid State Chemistry* **2010,** 183, 1133–1140.

47. Sit, V.; Geanangel, R. A.; Wendlandt, W. W., The thermal dissociation of NH_3BH_3. *Thermochimica Acta* **1986,** 113, 379–382.

48. Marchetti, P. S.; Kwon, D.; Schmidt, W. R.; Interrante, L. V.; Maciel, G. E., High-field ^{11}B Magic-Angle Spinning NMR characterization of boron nitrides. *Chemistry of Materials* **1991,** 3, 482–486.

49. Eichhorn, K. D.; Kirfel, A.; Grochowski, J.; Serda, P., Accurate structure analysis with synchrotron radiation. An application to borazone, cubic BN. *Acta Crystallographica B* **1992,** 47, 843–848.

50. Pease, R. S., An X-ray study of boron nitride. *Acta Crystallographica* **1952,** 5, 356–361.

51. Guo, Y.; Xia, G.; Zhu, Y.; Gao, L.; Yu, X., Hydrogen release from amminelithium borohydride, $LiBH_4.NH_3$. *Chemical Communications* **2010,** 46, 2599–2601.

52. Soloveichik, G. L.; Her, J.-H.; Stephens, P. W.; Gao, Y.; Rijssenbeek, J.; Andrus, M.; Zhao, J.-C., Ammine magnesium borohydride complex as a new material for hydrogen storage: Structure and properties of $Mg(BH_4)_2{\cdot}2NH_3$. *Inorganic Chemistry* **2008,** 47, 4290–4298.

Chapter 7

Conclusions and Suggestions for Further Work

7.1 Conclusions

The thermal decomposition pathway of ammonia borane has been investigated. It was observed that upon heating ammonia borane foamed, due to the release of gaseous products of decomposition, identified to be hydrogen by TPD–MS investigations. A sharp hydrogen release began at 85°C, while subsequent desorptions were much broader, with releases commencing at 125°C and 290°C. Following the first decomposition step powder XRD analysis showed there were no crystalline materials present. Solid state ^{11}B MAS NMR spectroscopy played a more important role in determining the composition of the amorphous decomposition products. A number of boron environments were present in the samples after heating NH_3BH_3 to 80°C and 200°C. The observed environments showed that DADB played an important role in the decomposition pathway. The appearance of N_2BH_2 environments revealed the initial decomposition products were polyaminoboranes, $(NH_2BH_2)_n$, while further heating resulted in boron predominantly residing in sp^2 environments, in the form of polyiminoboranes, $(NHBH)_n$. The formation of these polymeric products was further supported by Raman spectroscopic studies.

The bulk of this research focused on the thermal reactions of metal hydrides with ammonia borane. The products of the reactions were initially investigated by powder XRD. In the case of NaH, the reaction was found to be able to proceed with a reaction stoichiometry of 1:1 at a temperature of 40°C, forming $NaNH_2BH_3$. A

reaction stoichiometry of 1:2 in favour of NH_3BH_3 led to the formation of a new previously unreported crystalline phase at a reaction temperature of 60°C. The powder XRD pattern collected for this material was indexed to a trigonal unit cell, with a suggested space group of *P*31*c*. The *a* and *c* lattice constants were refined through a Pawley fit to values of 4.3389(4) Å and 17.859(1) Å, respectively. It was subsequently determined that the first step in the reaction pathway was the reaction of 1 mole of NaH with 1 mole of NH_3BH_3, forming $NaNH_2BH_3$, which then reacted with the excess NH_3BH_3 forming the trigonal phase. The trigonal phase was observed to exist until a reaction temperature of 150°C was achieved. Powder XRD analysis revealed that the only crystalline decomposition product was $NaBH_4$, which implied that there were also amorphous decomposition products present. Thermal desorption investigations showed that the formation of $NaNH_2BH_3$ was exclusively accompanied by H_2 release, while the formation of the trigonal phase was accompanied by the release of both H_2 and NH_3. The desorption of NH_3 was concluded to be related to the formation of the trigonal phase, reaction 7.1, which led to the conclusion that the trigonal phase was of composition $Na^+(BH_3NH_2BH_3)^-$. The desorption of H_2 was attributed to side reactions.

$$NaNH_2BH_3 + NH_3BH_3 \rightarrow Na^+(BH_3NH_2BH_3)^- + NH_3 \qquad \text{Reaction 7.1}$$

The reaction of LiH with NH_3BH_3 was observed to proceed differently to that of NaH. A reaction stoichiometry of 1:1 failed to yield $LiNH_2BH_3$ and it was only when a reaction stoichiometry of 1:2 in favour of NH_3BH_3 was employed that a single crystalline product could be obtained. The powder XRD pattern collected for this material was indexed to a tetragonal unit cell with a suggested space group of $P4_2mc$. The *a* and *c* lattice parameters were refined through a Pawley fit, to values of 4.0288(2) Å and 16.958(2) Å, respectively. A powder XRD investigation revealed that this tetragonal phase existed until a reaction temperature of 150°C was reached. At this temperature there was some evidence that $LiBH_4$ had formed, although the decomposition products were predominantly amorphous. Thermal desorption investigations showed that the formation of the tetragonal phase was exclusively accompanied by the release of H_2, while both H_2 and NH_3 were desorbed during this

materials decomposition. These observations helped reach the conclusion that the tetragonal phase was of composition $[Li(NH_3)]^+[BH_3NH_2BH_3]^-$.

The reaction of CaH_2 with NH_3BH_3 was found to require a reaction stoichiometry of 1:4 and a reaction temperature of 80°C in order to yield a product free from starting materials. The crystalline products of the reaction were analysed by powder XRD and a literature search allowed this product to be identified as $Ca(BH_4)_2{\cdot}2NH_3$. Further heating to 120°C yielded a second crystalline material, which was identified as $Ca(BH_4)_2{\cdot}NH_3$, before this material decomposed to form α-$Ca(BH_4)_2$ at 225°C. Powder XRD data was employed to solve the previously unreported structure of $Ca(BH_4)_2{\cdot}NH_3$ using Rietveld refinements. The structure was found to possess an orthorhombic unit cell in the *Pnam* space group with a = 8.1991(3) Å, b = 11.8406(4) Å and c = 5.8369(2) Å. The structure of $Ca(BH_4)_2{\cdot}2NH_3$ was also solved from powder XRD data, although this structure has previously been reported. Thermal desorption investigations showed that only H_2 was released during the formation of $Ca(BH_4)_2{\cdot}2NH_3$ from starting materials, while both H_2 and NH_3 were desorbed in subsequent reaction steps.

In order to obtain a more complete picture of the three reaction pathways discussed above, solid state ^{11}B MAS NMR spectroscopy was employed, primarily to provide information about amorphous components of reaction mixtures. In all three reaction pathways the NMR spectra revealed that amorphous materials were significant decomposition products. The crystalline products of the lithium and sodium reactions possessed boron in only sp^3 environments, however, the NMR spectra revealed sp^2 boron was present in all samples, even at reaction temperatures that were lower than the decomposition temperature of the crystalline products. This low temperature presence of sp^2 boron showed that there were competing reactions taking place. Following decomposition of $Na^+(BH_3NH_2BH_3)^-$ boron was found to exist in approximately equal amounts in sp^2 and BH_4 environments. Solid state ^{23}Na MAS NMR spectroscopy revealed that all of the sodium in the decomposition products was found in the form of $NaBH_4$, leading to the conclusion that the amorphous decomposition products were polyiminoboranes, $(NHBH)_n$. The ^{11}B NMR spectrum of the sample collected following the decomposition of $[Li(NH_3)]^+[BH_3NH_2BH_3]^-$ was

dominated by an sp^2 boron feature, as well as possessing a small BH_4 resonance. The chemical shift of the sp^2 feature was similar to that of the one observed in the spectrum collected from decomposed $Na^+(BH_3NH_2BH_3)^-$, implying that the same amorphous material had formed, namely polyiminoborane.

The solid state ^{11}B MAS NMR spectra of the $CaH_2 + 4NH_3BH_3$ reaction pathway showed BH_4 and sp^2 features at all temperatures. The BH_4 environment showed slight changes in chemical shift as the crystalline material present in the reaction mixture changed, while the appearance of sp^2 boron at low temperature gave an important insight into the reaction pathway. The observation of both BH_4 and sp^2 features following the first step in the reaction pathway led to the conclusion that the decomposition of NH_3BH_3 had an integral role in the reaction pathway, specifically the decomposition step resulting in the formation of DADB. DADB formation provided the BH_4^- anion necessary to effect formation of $Ca(BH_4)_2{\cdot}2NH_3$. This reaction step rationalised the need for a reaction stoichiometry of 1:4, as two DADB units were required for $Ca(BH_4)_2{\cdot}2NH_3$ formation, which initially required four NH_3BH_3 molecules. The $NH_3BH_2NH_3$ unit present in DADB underwent chain growth and released hydrogen, following the same decomposition pathway as NH_3BH_3, forming an amorphous material possessing sp^2 boron. The observed sp^2 environment had the same chemical shift to that of polyiminoborane.

The desorption profile of the $NaH + 2NH_3BH_3$ reaction mixture showed that H_2 release commenced almost instantaneously, with the first peak in the H_2 trace observed at 40°C. A second H_2 release began at 55°C and peaked at 80°C. The $LiH + 2NH_3BH_3$ reaction mixture showed H_2 release did not commence until 50°C, with a peak at 75°C. The observed lower onset temperature of H_2 release from the NaH containing reaction mixture was due to the initial formation of $NaNH_2BH_3$, a reaction step that was not observed in the $LiH + 2NH_3BH_3$ reaction pathway. The second H_2 desorption from the $NaH + 2NH_3BH_3$ reaction mixture was due to $Na^+(BH_3NH_2BH_3)^-$ formation. The first H_2 desorption from the $LiH + 2NH_3BH_3$ reaction mixture was due to the equivalent step in this reaction pathway, the formation of $[Li(NH_3)]^+[BH_3NH_2BH_3]^-$, showing that the two materials formed at similar temperatures. A significant difference between the desorption profiles was the

release of NH_3 from the NaH + $2NH_3BH_3$ reaction mixture between 65°C and 140°C, which occurred during $Na^+(BH_3NH_2BH_3)^-$ formation, whereas the formation of $[Li(NH_3)]^+[BH_3NH_2BH_3]^-$ did not involve NH_3 desorption.

A comparison of the desorption profiles of $Na^+(BH_3NH_2BH_3)^-$ and $[Li(NH_3)]^+[BH_3NH_2BH_3]^-$ showed decomposition of these materials began at similar temperatures, with the onset of H_2 release observed at 135°C and 130°C, respectively. The observed weight loss for $[Li(NH_3)]^+[BH_3NH_2BH_3]^-$ in this initial decomposition step, 9.4 wt%, was greater than that observed for $Na^+(BH_3NH_2BH_3)^-$, 5 wt%. Heating the materials to 350°C resulted in total weight losses due to H_2 release of 12.5 wt% for $[Li(NH_3)]^+[BH_3NH_2BH_3]^-$ and 7.5 wt% for $Na^+(BH_3NH_2BH_3)^-$. The higher weight loss from $[Li(NH_3)]^+[BH_3NH_2BH_3]^-$ suggests that it has more potential as a hydrogen storage material than $Na^+(BH_3NH_2BH_3)^-$. However, a further difference between the two desorption profiles was that $[Li(NH_3)]^+[BH_3NH_2BH_3]^-$ showed a weight loss of 3.6 wt% between 75°C and 150°C due to NH_3 release, whereas decomposition of $Na^+(BH_3NH_2BH_3)^-$ was free from NH_3 desorption. This NH_3 release is a significant drawback in the potential of $[Li(NH_3)]^+[BH_3NH_2BH_3]^-$ as a hydrogen storage material and so unless this release can be suppressed, it is $Na^+(BH_3NH_2BH_3)^-$ that shows the greatest potential as a hydrogen store.

It was observed that the reactions of LiH and NaH with NH_3BH_3 proceeded through different mechanisms, despite yielding similar products. A significant difference between the two reactions was that the LiH and NH_3BH_3 reaction mixture foamed, whereas, the NaH reaction did not, providing an insight into the mechanism of the crystalline phase formation. The hydride ion of MH is a strong base and is potentially capable of removing a protic H from the NH_3 group in NH_3BH_3. In the case of the more basic NaH, deprotonation of NH_3BH_3 was facile and so $NaNH_2BH_3$ could form. Lithium is less electron donating than sodium, meaning the H^- is a weaker base and so it was not capable of acquiring a protic H from NH_3BH_3. This meant that the NaH reaction could proceed when NH_3BH_3 was in its most stable state, before disruption of the dihydrogen bonding network, initially forming $NaNH_2BH_3$, before this material reacted with the second mole of NH_3BH_3 to yield $Na^+(BH_3NH_2BH_3)^-$. The fact that the LiH reaction mixture foamed showed that this metal hydride reacted with the more

mobile phase of NH_3BH_3. Following foaming LiH would have been able to react with one mole of NH_3BH_3 to form $LiNH_2BH_3$, but as the second mole of NH_3BH_3 was also labile, a subsequent reaction of $LiNH_2BH_3$ with NH_3BH_3 would also have been able to proceed. This meant that $LiNH_2BH_3$ was never observed as a reaction product and $[Li(NH_3)]^+[BH_3NH_2BH_3]^-$ formed instead.

Thermal desorption investigations of the reaction pathways showed a significant amount of ammonia was released during the NaH reaction, whereas the formation of $[Li(NH_3)]^+[BH_3NH_2BH_3]^-$ was exclusively accompanied by hydrogen release. The lithium cation is a stronger Lewis acid than the sodium cation and so it is more facile for the released NH_3 to form an adduct with the lithium cation compared to sodium. Consequently, ammonia desorption was observed during the decomposition of $[Li(NH_3)]^+[BH_3NH_2BH_3]^-$, whereas hydrogen desorption was exclusively observed during $Na^+(BH_3NH_2BH_3)^-$ decomposition.

The reaction of CaH_2 with NH_3BH_3 yielded a borohydride containing product, showing that this reaction mechanism involved the formation of DADB, a very different mechanism to that observed in the cases of LiH and NaH. The reason behind this is that LiH and NaH are both metallic hydrides, whereas CaH_2 is an insulator. This means a thermal reaction involving CaH_2 could not proceed until the more reactive DADB had formed in the reaction mixture, which resulted in a reaction product unrelated to $[Li(NH_3)]^+[BH_3NH_2BH_3]^-$ and $Na^+(BH_3NH_2BH_3)^-$.

7.2 Suggestions for Further Work

This research has opened up avenues to further research into metallated derivatives of ammonia borane. In terms of the products already synthesised in this research, namely $Na^+[BH_3NH_2BH_3]^-$, $[Li(NH_3)]^+[BH_3NH_2BH_3]^-$, $Ca(BH_4)_2{\cdot}2NH_3$ and $Ca(BH_4)_2{\cdot}NH_3$, it would be beneficial to continue crystallographic studies on all materials. The acquisition of synchrotron powder diffraction data would be desirable. This higher quality data would allow the diffraction data to be indexed and refined to a higher degree of accuracy. Furthermore, the crystal structures solved for

$Ca(BH_4)_2{\cdot}2NH_3$ and $Ca(BH_4)_2{\cdot}NH_3$ could be more accurately determined with synchrotron powder diffraction data.

The crystalline phases $Na^+[BH_3NH_2BH_3]^-$ and $[Li(NH_3)]^+[BH_3NH_2BH_3]^-$ have been characterised by a variety of techniques in this research, however, the crystal structures of both materials remained unsolved. Further work related to these two materials should therefore focus on the successful solution of both of these crystal structures.

The research could be further extended to investigate the interaction of ammonia borane with other group 1 and group 2 light hydrides as well as incorporating light transition metal hydrides. The possibility of synthesising mixed metal products would also be an interesting avenue to explore as a potential method of optimising hydrogen release.

This research investigated the hydrogen desorption properties of the synthesised materials. However, in order to fully evaluate the potential of these materials for hydrogen storage it will be necessary to investigate their capability to be rehydrogenated following dehydrogenation. Hydrogenation at a variety of temperatures and pressures should be undertaken to investigate this potential. If hydrogenation proves successful, the systems capability to be recycled numerous times should be investigated.

Appendix 1

Table A1.1 – The Raman shifts and assignments of bands observed in the Raman spectra of ammonia borane heated at various temperatures

NH_3BH_3 RT		NH_3BH_3 80°C		NH_3BH_3 200°C	
Assignment	Raman Shift (cm^{-1})	Assignment	Raman Shift (cm^{-1})	Assignment	Raman Shift (cm^{-1})
$N–H^{st}_{asym}$ (NH_3)	3317m	$N–H^{st}_{asym}$ (NH_3)	3319m	$N–H^{st}_{asym}$ (NH)	3339s
$N–H^{st}_{sym}$ (NH_3)	3252vs	$N–H^{st}_{sym}$ (NH_3)	3254m	$N–H^{st}_{sym}$ (NH)	3273vs
Overtone	3177m	Overtone	3178w	$B–H^{st}$	2444s
Unknown	2377s	Unknown	2375m	$B–H^{st}$	2393s
$B–H^{st}_{asym}$ (BH_3)	2330s	$B–H^{st}_{asym}$ (BH_3)	Unobserved	$B–H^{st}$	2329s
$B–H^{st}_{sym}$ (BH_3)	2280vs	BH^{st}_{sym} (BH_3)	2283s	$B–H^{st}$	2278s
$NH_3{}^{ds}_{asym}$	1600w	$NH_3{}^{ds}_{asym}$	1605vw	$N–H^{b}$	1575w
Overtone	1450vw	Overtone	1452vw	$N–H^{b}$	1570w
$NH_3{}^{du}_{sym}$	1375w	$NH_3{}^{du}_{sym}$	1381vw	$B–H^{b}$	1405vw
$BH_3{}^{ds}_{asym}$	1190w	$BH_3{}^{ds}_{asym}$	1193w	$B–H^{b}$	1202w
$BH_3{}^{du}_{sym}$	1160w	$BH_3{}^{du}_{sym}$	1161w	$B–H^{b}$	1043vw
NBH^{r}	1070vw	NBH^{r}	Unobserved	$^{11}B–N^{st}$	880vw
$^{10}B–N^{st}$	800w	$^{10}BN^{st}$	Unobserved	$^{11}B–N^{st}$	787vw
$^{11}B–N^{st}$	783m	$^{11}BN^{st}$	786m		
NBH^{r}	728w	NBH^{r}	Unobserved		
		$N–H^{st}_{asym}$ (NH_2)	3312s		
		$N–H^{st}_{sym}$ (NH_2)	3270vs		
		$B–H^{st}_{asym}$ (BH_2)	2422s		
		$B–H^{st}_{sym}$ (BH_2)	2322s		
		Unknown	2252m		
		$N–H^{b}$ (NH_2)	1566m		
		$B–H^{b}_{asym}$ (BH_2)	1208w		
		$B–H^{b}_{sym}$ (BH_2)	1167w		
		$B–N^{st}$	811w		
		B–H or N–H deformations	1286w		
			1230w		
			1020w		
			876w		

st = stretch
ds = scissors
du = umbrella
r = rock
b = bend

vs = very strong
s = strong
m = medium
w = weak
vw = very weak

Table A1.2 – The chemical shifts and assignments of features observed in the solid state ^{11}B MAS NMR spectra of ammonia borane heated at various temperatures

Environment	Chemical Shift (ppm)		
	Room Temperature	80°C	200°C
BH_4	Not observed	−38.0	−39.8
NBH_3	−26.0	−26.0	−23.7
N_2BH_2	Not observed	−13.0	Not observed
N_3BH	Not observed	−0.5	Not observed
BO_x	Not observed	Not observed	1.0
sp^2 B	Not observed	27.0	Not observed
sp^2 B	Not observed	Not observed	30.0

Appendix 2

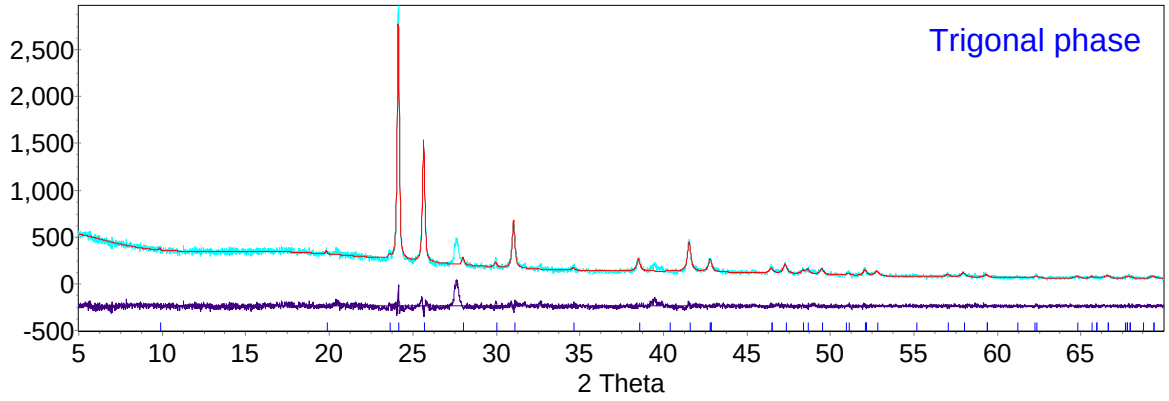

Figure A2.1 – Pawley refinement for the product synthesised through the NaH + $2NH_3BH_3$ reaction at 80°C. The observed pattern is shown in sky blue, the calculated pattern in red and the difference in purple. Bragg peak positions of the trigonal phase are shown in blue. R_{wp} = 9.434%, χ^2 = 1.907

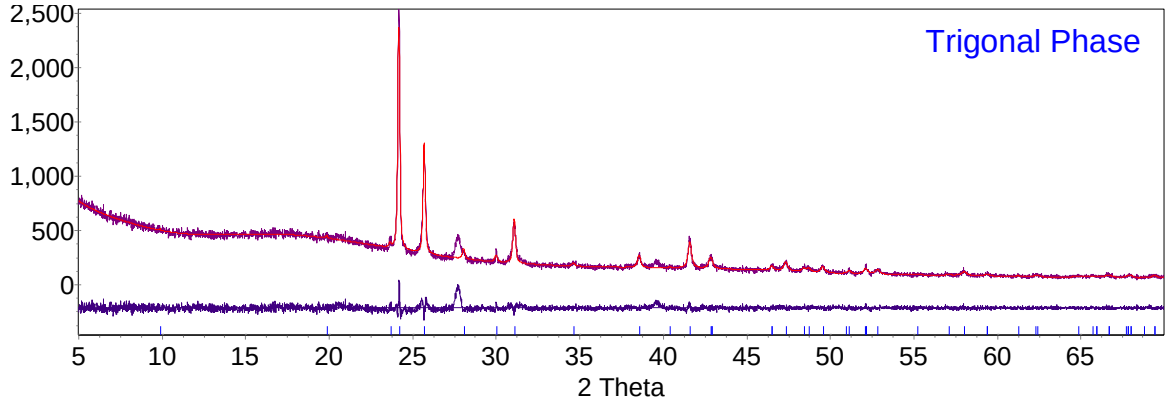

Figure A2.2 – Pawley refinement for the product synthesised through the NaH + $2NH_3BH_3$ reaction at 100°C. The observed pattern is shown in violet, the calculated pattern in red and the difference in purple. Bragg peak positions of the trigonal phase are shown in blue. R_{wp} = 7.798%, χ^2 = 1.573

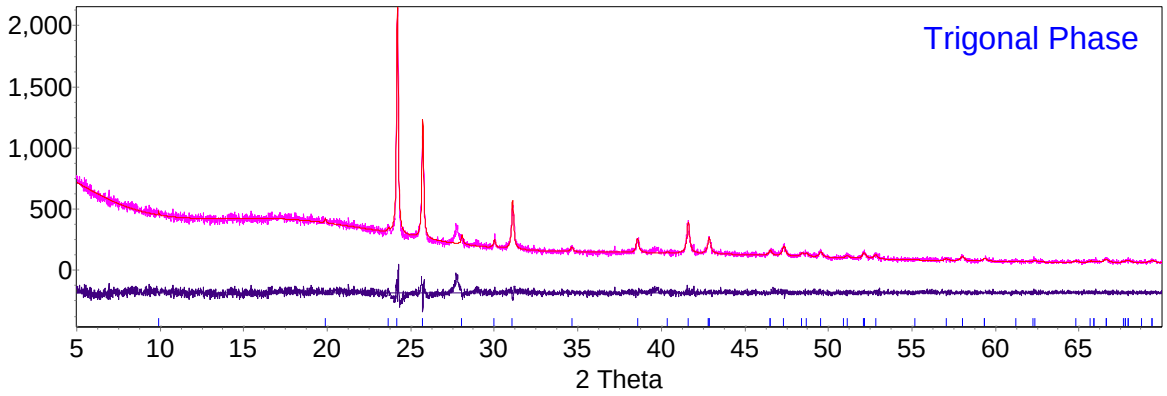

Figure A2.3 – Pawley refinement for the product synthesised through the NaH + $2NH_3BH_3$ reaction at 110°C. The observed pattern is shown in pink, the calculated pattern in red and the difference in purple. Bragg peak positions of the trigonal phase are shown in blue. R_{wp} = 7.779%, χ^2 = 1.413

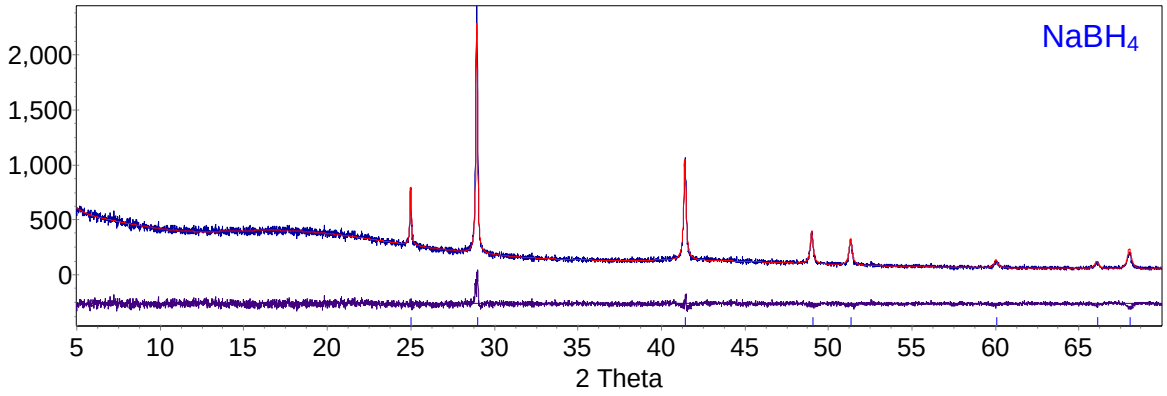

Figure A2.4 – Pawley refinement for the product synthesised through the NaH + $2NH_3BH_3$ reaction at 150°C. The observed pattern is shown in blue, the calculated pattern in red and the difference in purple. Bragg peak positions of $NaBH_4$ are shown in blue. R_{wp} = 7.513%, χ^2 = 1.234

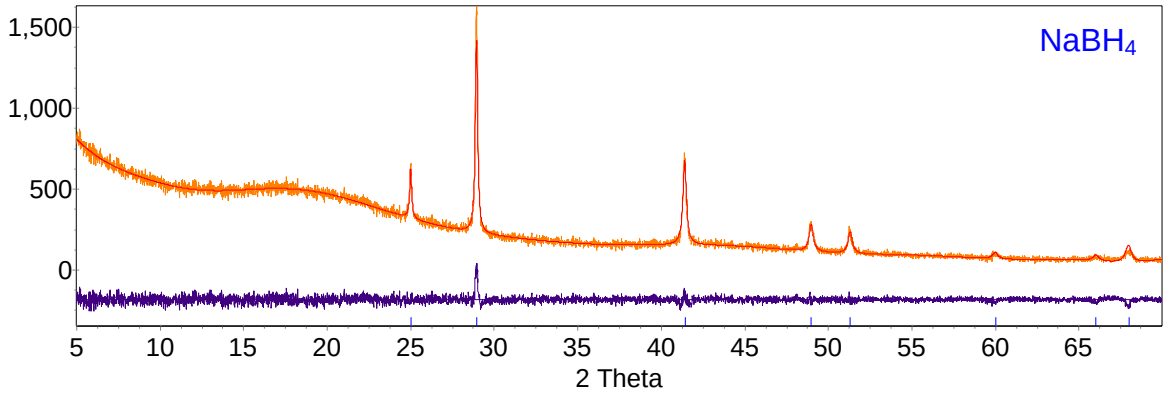

Figure A2.5 – Pawley refinement for the product synthesised through the NaH + $2NH_3BH_3$ reaction at 200°C. The observed pattern is shown in orange, the calculated pattern in red and the difference in purple. Bragg peak positions of $NaBH_4$ are shown in blue. R_{wp} = 6.927%, χ^2 = 1.259

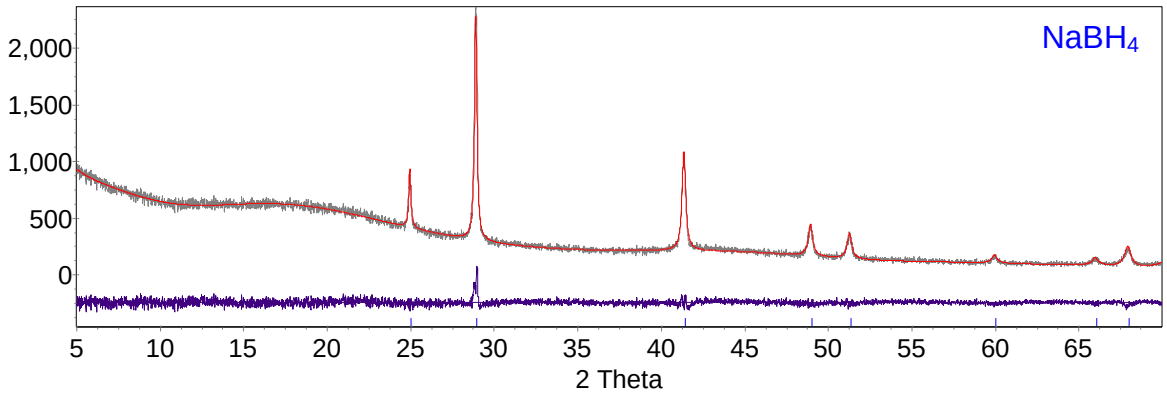

Figure A2.6 – Pawley refinement for the product synthesised through the NaH + $2NH_3BH_3$ reaction at 250°C. The observed pattern is shown in grey, the calculated pattern in red and the difference in purple. Bragg peak positions of $NaBH_4$ are shown in blue. R_{wp} = 6.187%, χ^2 = 1.318

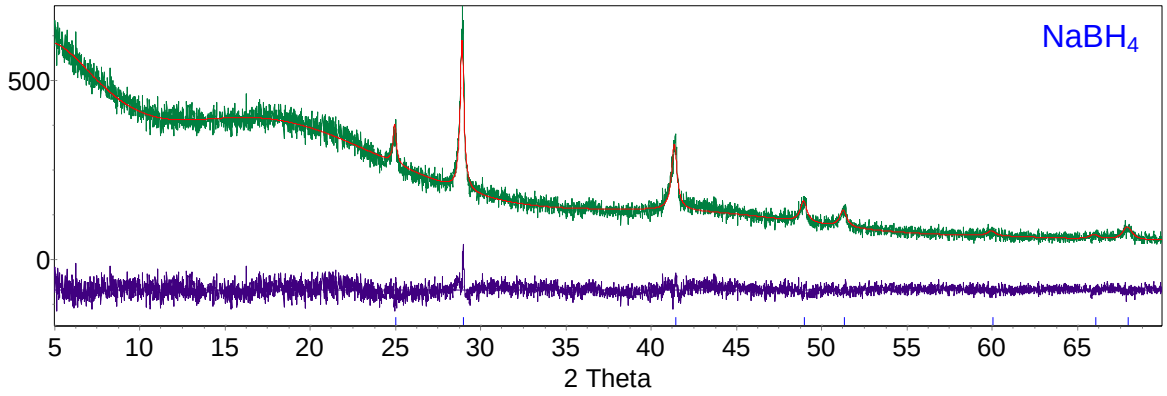

Figure A2.7 – Pawley refinement for the product synthesised through the NaH + $2NH_3BH_3$ reaction at 300°C. The observed pattern is shown in green, the calculated pattern in red and the difference in purple. Bragg peak positions of $NaBH_4$ are shown in blue. R_{wp} = 7.516%, χ^2 = 1.199

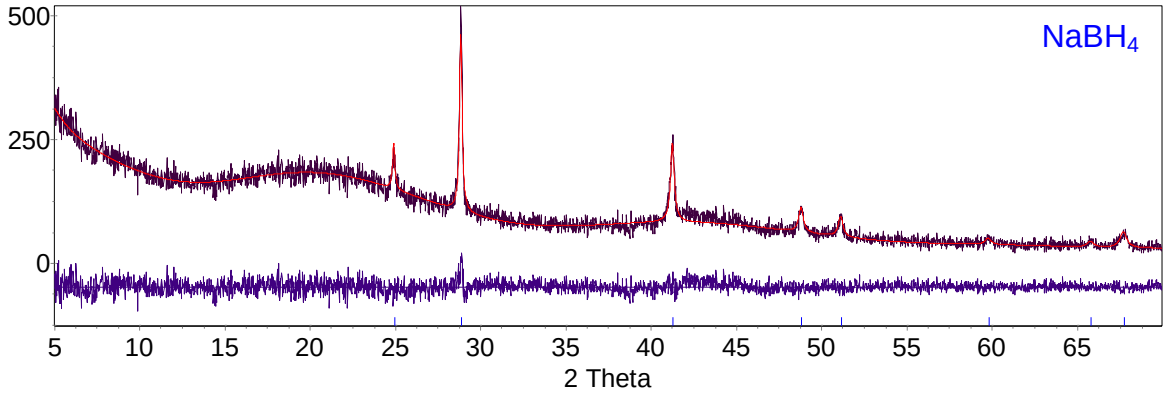

Figure A2.8 – Pawley refinement for the product synthesised through the NaH + $2NH_3BH_3$ reaction at 400°C. The observed pattern is shown in dark purple, the calculated pattern in red and the difference in purple. Bragg peak positions of $NaBH_4$ are shown in blue. R_{wp} = 10.826%, χ^2 = 1.166

Table A2.1 – Refinement of the $NaBH_4$ phase synthesised in the NaH + $2NH_3BH_3$ reaction in the temperature range 120°C – 400°C

Reaction Temperature (°C)	*a* (Å)	Cell Volume (Å^3)
120	6.1888(2)	236.98(8)
150	6.1557(3)	233.26(3)
200	6.1622(5)	233.10(6)
250	6.1613(4)	233.90(5)
300	6.160(2)	233.8(2)
400	6.180(1)	236.0(2)
$NaBH_4$[1]	6.13080(10)	230.43

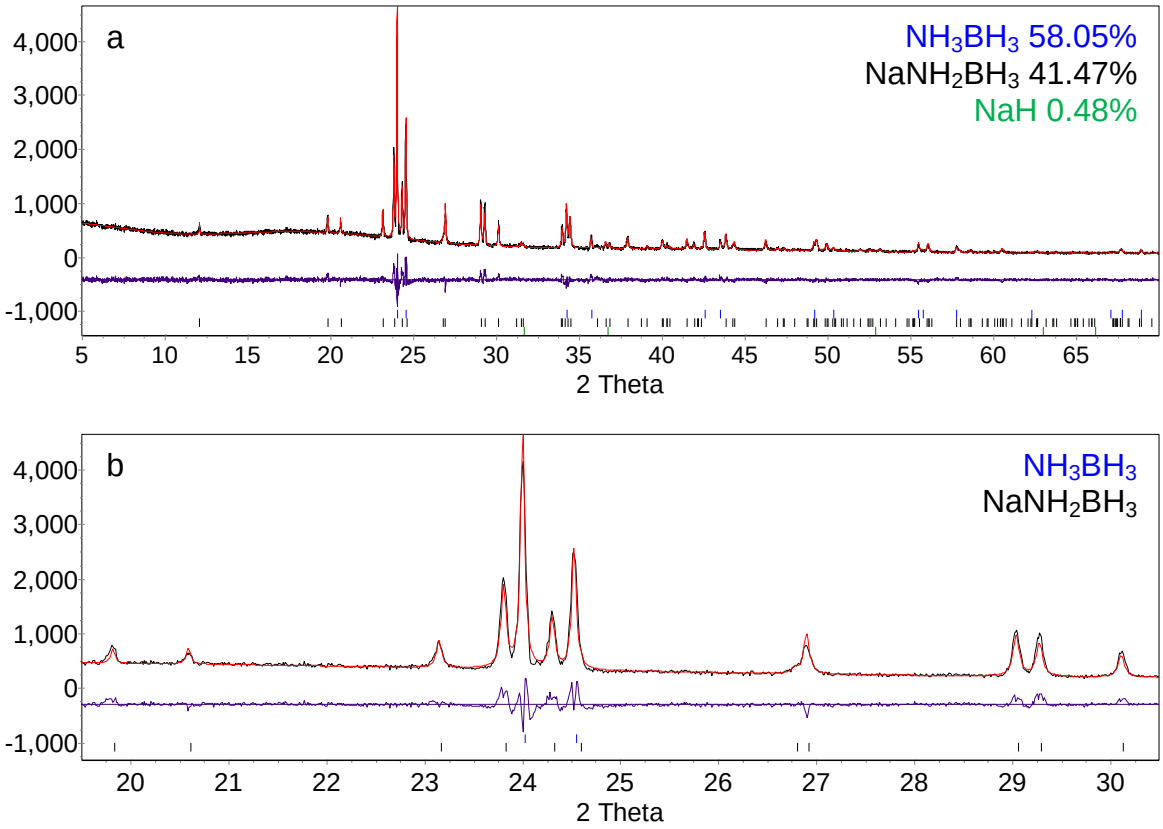

Figure A2.9 – Pawley refinement of the product from the NaH + $2NH_3BH_3$ reaction at room temperature after ten days (a) the full 2θ range (b) 20 – 30° 2θ. The observed pattern is shown in black, the calculated pattern in red and the difference in purple. Bragg peak positions due to NH_3BH_3 (blue), $NaNH_2BH_3$ (black) and NaH (green) are indicated. R_{wp} = 8.514%, χ^2 = 2.008

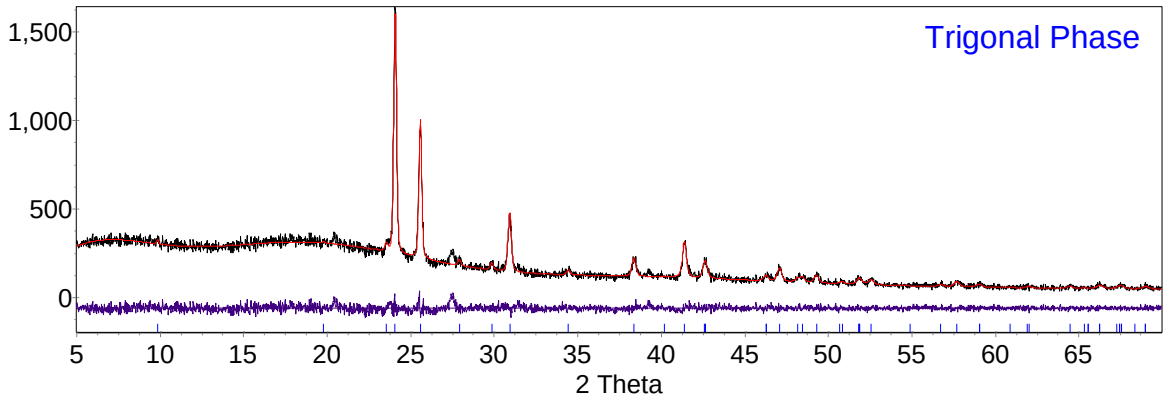

Figure A2.10 – Pawley refinement of the product from the NaH + $2NH_3BH_3$ reaction at room temperature after two months. The observed pattern is shown in black, the calculated pattern in red and the difference in purple. Bragg peak positions of the trigonal phase are shown in blue. R_{wp} = 8.581%, χ^2 = 1.223

Table A2.2 – Refined values of *a*, *b* and *c* lattice constants and selected bond lengths from the NaH + $2NH_3BH_3$ reaction at room temperature

Parameter	$NaNH_2BH_3$ Fig. A1.9.	NH_3BH_3 Fig. A1.9.	Trigonal Phase Fig. A1.10.
***a* (Å)**	7.4633(3)	5.2350(2)	4.3600(2)
***b* (Å)**	14.6262(6)	5.2350(2)	4.3600(2)
***c* (Å)**	5.6530(2)	5.0223(2)	17.950(2)
Na-N bond length (Å)	2.42(1)	Not applicable	Not applicable
B-N bond length (Å)	1.459(9)	1.589	Not applicable

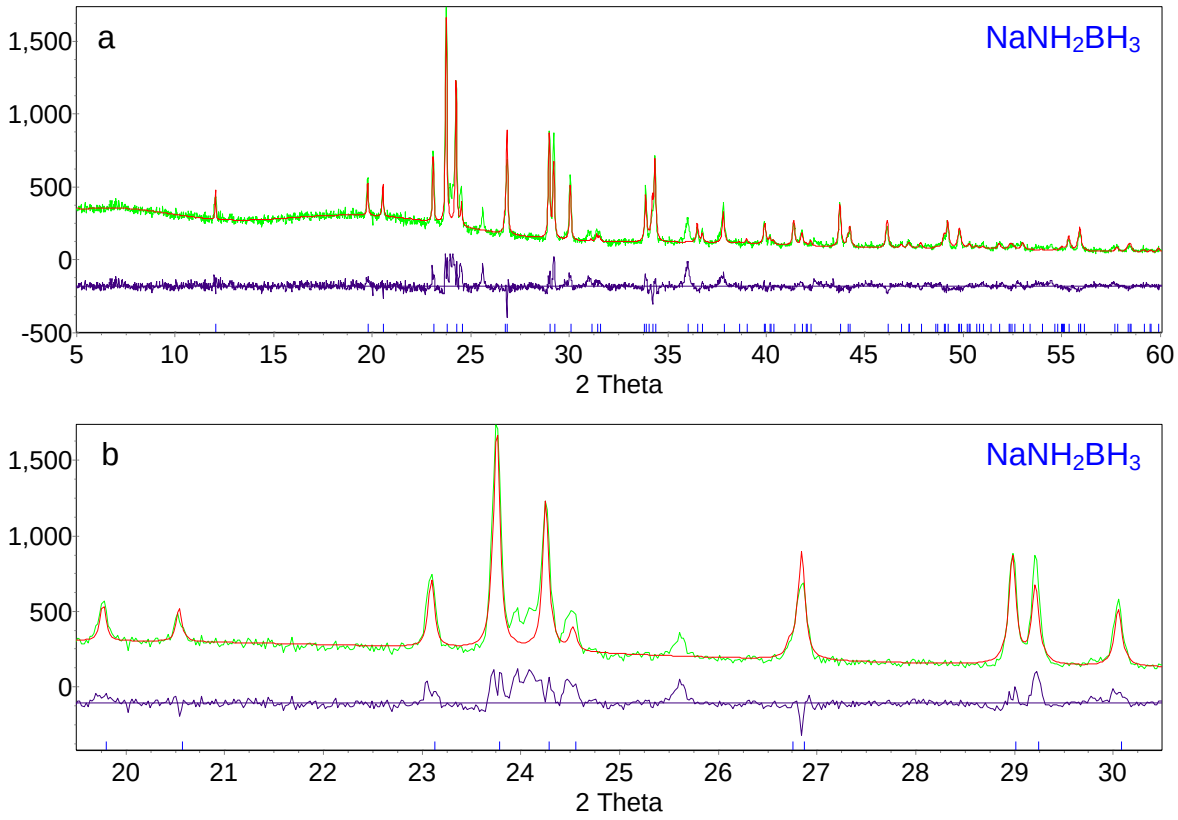

Figure A2.11 – Pawley refinement of the product from the NaH + NH_3BH_3 reaction at 50°C (a) the full 2θ range (b) 20 - 30° 2θ. The observed pattern is shown in green, the calculated pattern in red and the difference in purple. Bragg peak positions of $NaNH_2BH_3$ are shown in blue. R_{wp} = 12.183%, χ^2 = 3.066

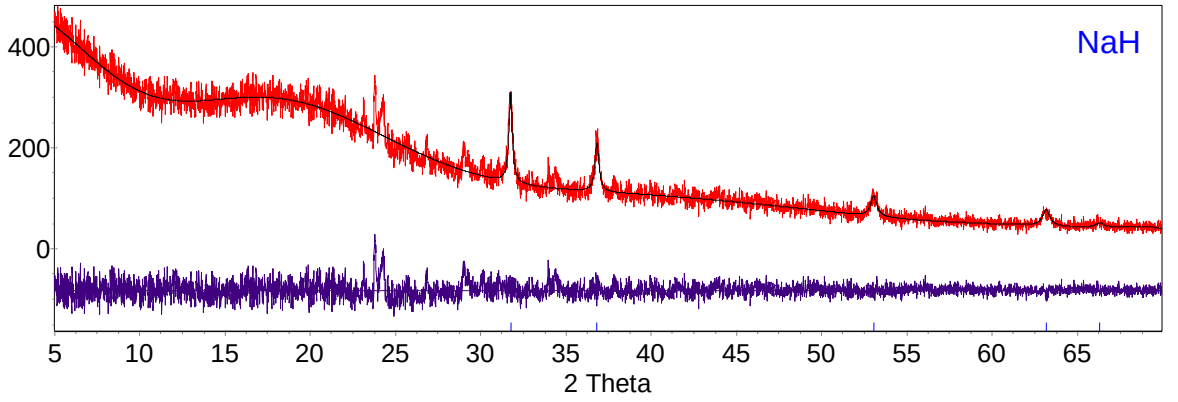

Figure A2.12 – Pawley refinement of the product from the NaH + NH_3BH_3 reaction at 60°C. The observed pattern is shown in red, the calculated pattern in black and the difference in purple. Bragg peak positions of NaH are shown in blue. R_{wp} = 11.131%, χ^2 = 1.153

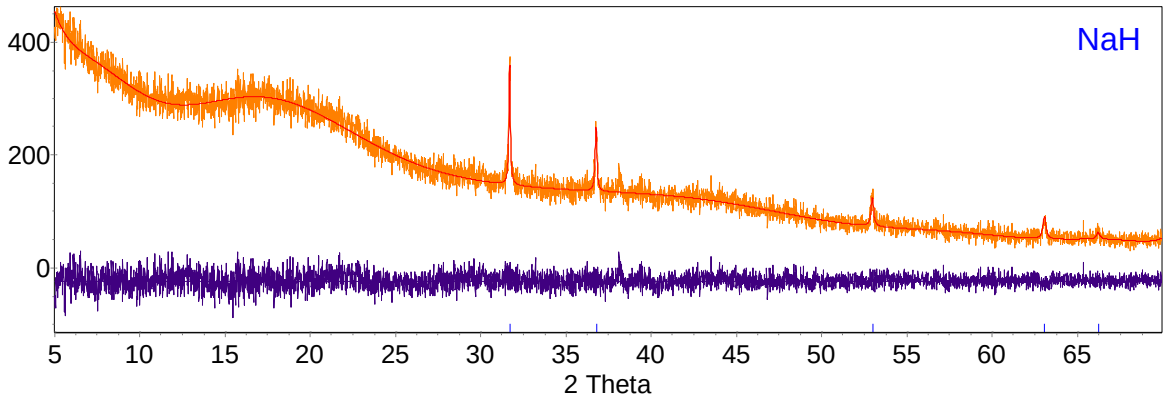

Figure A2.13 – Pawley refinement of the product from the NaH + NH_3BH_3 reaction at 200°C. The observed pattern is shown in orange, the calculated pattern in red and the difference in blue. Bragg peak positions of NaH are shown in blue. R_{wp} = 8.081%, χ^2 = 1.082

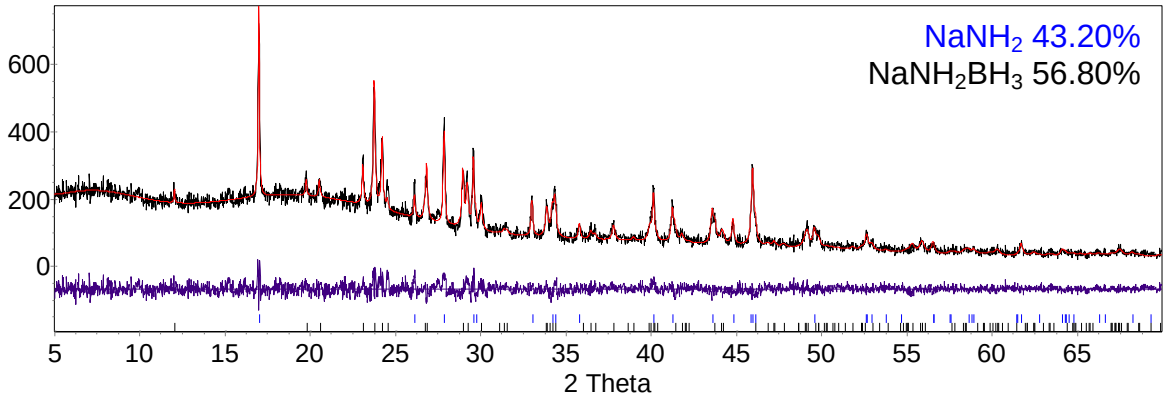

Figure A2.14 – Pawley refinement of the product from the $NaNH_2$ + NH_3BH_3 reaction at room temperature. The observed pattern is shown in black, the calculated pattern in red and the difference in blue. Bragg peak positions due to $NaNH_2$ (blue) and $NaNH_2BH_3$ (black) are indicated. R_{wp} = 10.361%, χ^2 = 1.228

Reference

1. Filinchuk, Y.; Hagemann, H., Structure and properties of $NaBH_4.2H_2O$ and $NaBH_4$. *European Journal of Inorganic Chemistry* **2008,** 20, 3127-3133.

Appendix 3

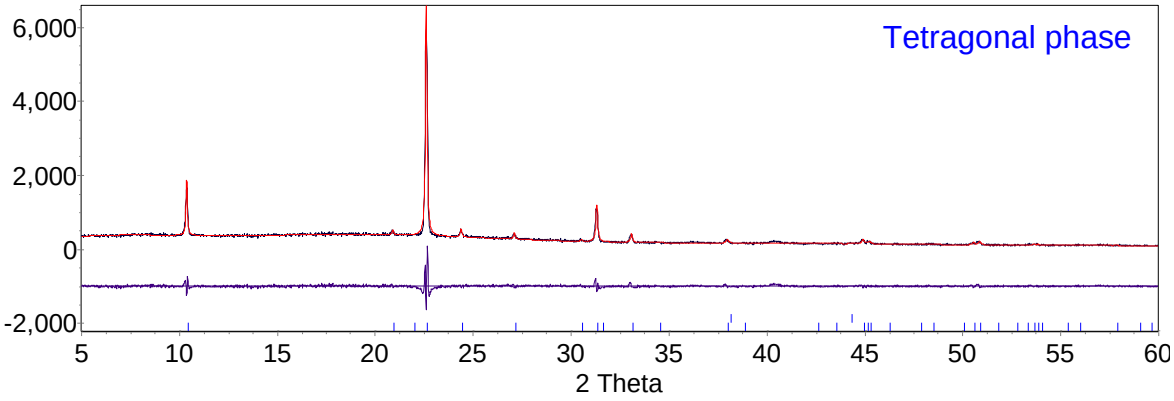

Figure A3.1 – Pawley refinement for the product from the LiH + $2NH_3BH_3$ reaction at room temperature. The observed pattern is shown in black, the calculated pattern in red and the difference in purple. Bragg peak positions of the tetragonal phase are indicated in blue. R_{wp} = 9.340%, χ^2 = 2.051

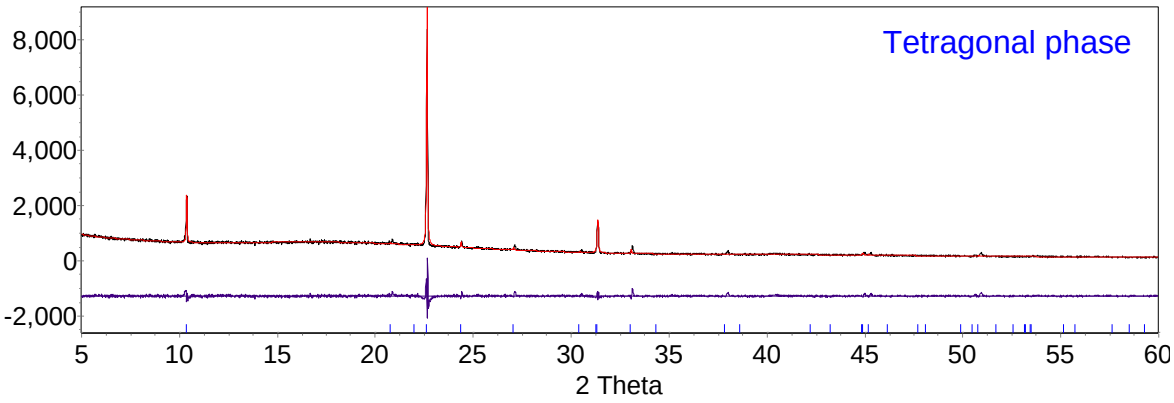

Figure A3.2 – Pawley refinement for the product from the LiH + $2NH_3BH_3$ reaction at 40°C. The observed pattern is shown in black, the calculated pattern in red and the difference in purple. Bragg peak positions of the tetragonal phase are indicated in blue. R_{wp} = 7.732%, χ^2 = 2.126

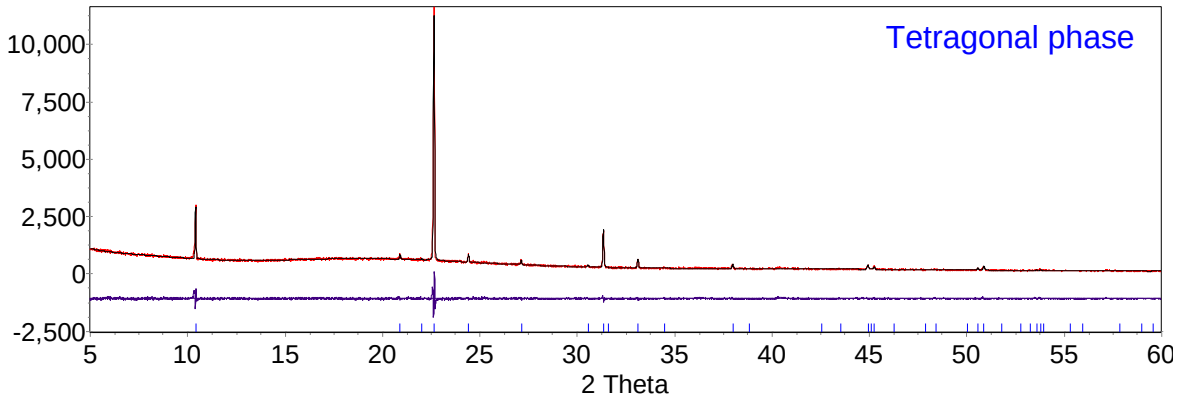

Figure A3.3 – Pawley refinement for the product from the LiH + $2NH_3BH_3$ reaction at 60°C. The observed pattern is shown in red, the calculated pattern in black and the difference in purple. Bragg peak positions of the tetragonal phase are indicated in blue. R_{wp} = 6.257%, χ^2 = 1.664

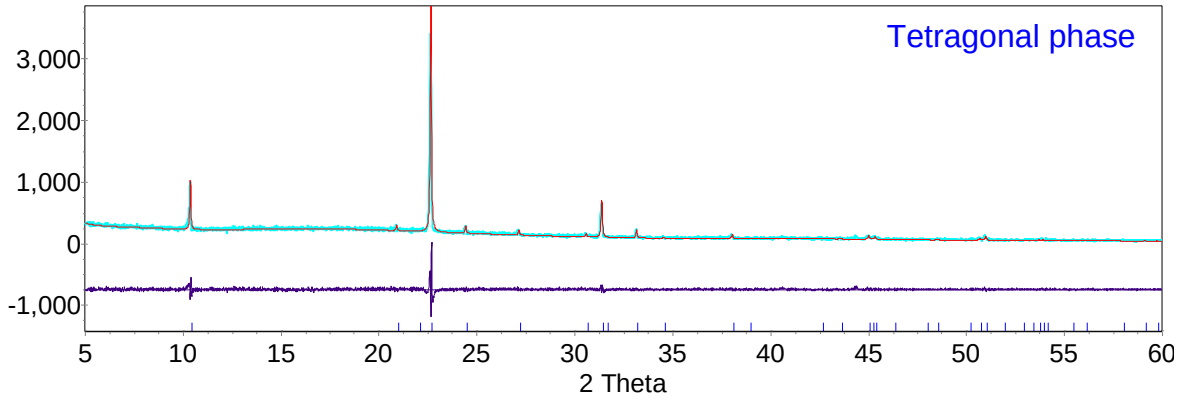

Figure A3.4 – Pawley refinement the product from the LiH + $2NH_3BH_3$ reaction at 80°C. The observed pattern is shown in sky blue, the calculated pattern in red and the difference in purple. Bragg peak positions of the tetragonal phase are indicated in blue. R_{wp} = 11.017%, χ^2 = 1.628

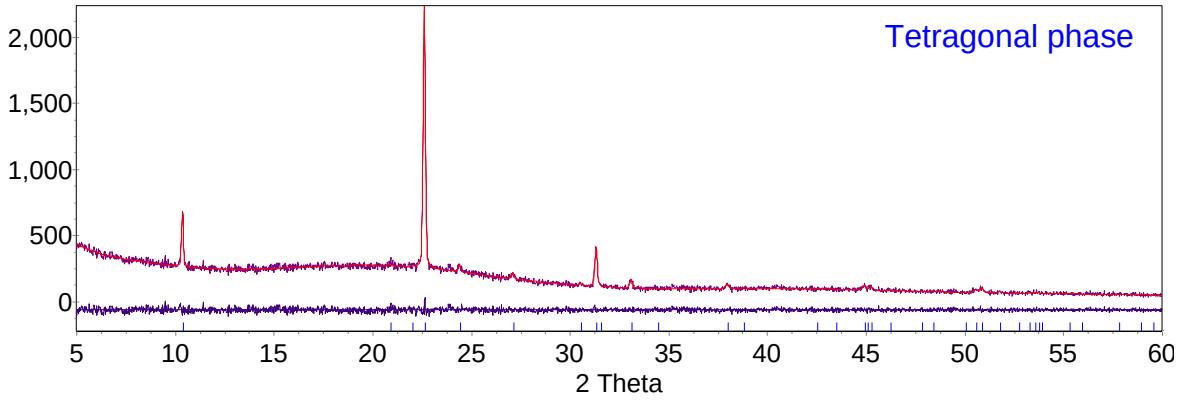

Figure A3.5 – Pawley refinement for the product from the LiH + $2NH_3BH_3$ reaction at 100°C. The observed pattern is shown in violet, the calculated pattern in red and the difference in purple. Bragg peak positions of the tetragonal phase are indicated in blue. R_{wp} = 8.425%, χ^2 = 1.014

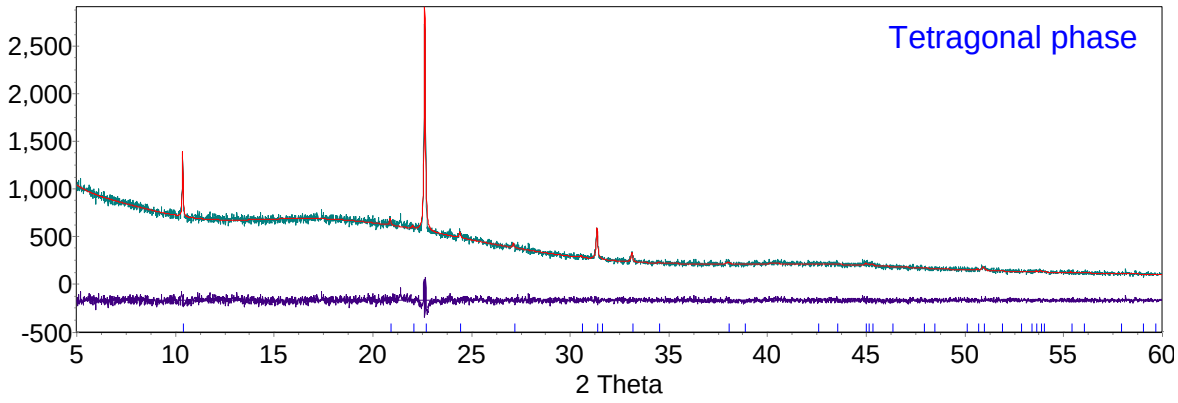

Figure A3.6 – Pawley refinement for the product from the LiH + $2NH_3BH_3$ reaction at 120°C. The observed pattern is shown in teal, the calculated pattern in red and the difference in purple. Bragg peak positions of the tetragonal phase are indicated in blue. R_{wp} = 5.655%, χ^2 = 1.141

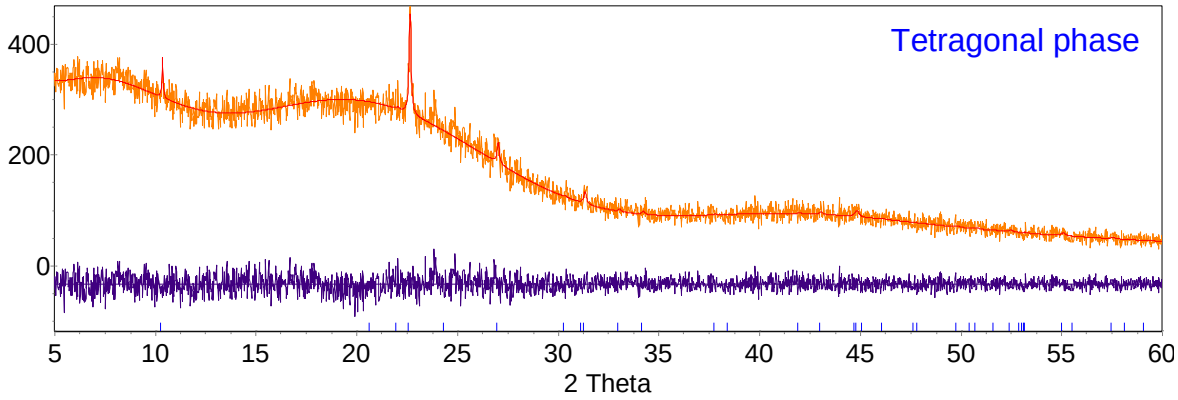

Figure A3.7 – Pawley refinement for the product from the LiH + $2NH_3BH_3$ reaction at 140°C. The observed pattern is shown in orange, the calculated pattern in red and the difference in purple. Bragg peak positions of the tetragonal phase are indicated in blue. R_{wp} = 8.578%, χ^2 = 1.026

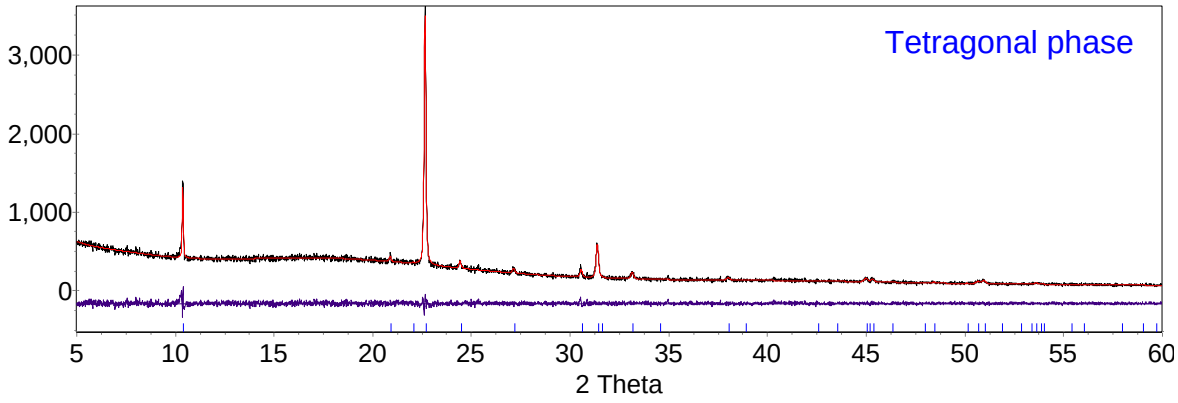

Figure A3.8 – Pawley refinement for the product from the $LiNH_2BH_3$ + NH_3BH_3 reaction at 50°C. The observed pattern is shown in black, the calculated pattern in red and the difference in purple. Bragg peak positions of the tetragonal phase are indicated in blue. R_{wp} = 7.093%, χ^2 = 1.126